Stability of Zero-gap CO_2 Electrolyzers for Electrochemical CO Production

Inaugural dissertation

of the Faculty of Science,

University of Bern

presented by

Menglong Liu (刘梦龙)

from China

Supervisor of the doctoral thesis:

Prof. Dr. Peter Broekmann

Department of Chemistry, Biochemistry and Pharmaceutical Sciences

Stability of Zero-gap CO_2 Electrolyzers for Electrochemical CO Production

Inaugural dissertation

of the Faculty of Science,

University of Bern

presented by

Menglong Liu (刘梦龙)

from China

Supervisor of the doctoral thesis:

Prof. Dr. Peter Broekmann

Department of Chemistry, Biochemistry and Pharmaceutical Sciences

Accepted by the Faculty of Science.

Bern, January 15th, 2024

The Dean

Prof. Dr. Marco Herwegh

Abstract

The unchecked massive emissions of the greenhouse gas CO_2 through the continued use of fossil fuels is the main cause of global warming of the earth's atmosphere with dramatic consequences for our environment. Reducing global CO_2 emissions and controlling CO_2 concentrations in the atmosphere are currently among the greatest global challenges facing our society.

The electrochemical CO_2 reduction reaction (referred to as ec-CO_2RR), capable of converting polluting CO_2 back into valuable chemicals such as carbon monoxide (CO) and formate using excess renewable energy, offers a promising approach to mitigate this problem.

Socio-economic assessments have shown that carbon monoxide is a high-value ec-CO_2RR product and a platform chemical in the chemical industry. This is why this PhD project focused on the optimization of CO_2-to-CO conversion by electrochemical means.

To achieve industrially relevant current densities in the order of several hundred milliamperes per square centimeter, the use of so-called gas diffusion electrodes (GDEs) is essential. One of the biggest problems currently preventing the use of this technology on a large scale is the stability of these GDEs. In this PhD project, the stability of GDEs is therefore systematically investigated using nanoparticulate silver catalysts in combination with a so-called semi-zero-gap test cell configuration (Arenz design). Using novel analytical approaches that can detect and quantify the transport of electrolyte through GDEs during CO_2 electrolysis (referred to as perspiration), various experimental factors (e.g., the use of binder materials, harmful use of capping agents, defectivity of GDEs, chemical nature of alkali metal cations, etc.) that stabilize or destabilize the GDEs could be identified. Active water/electrolyte management has been shown to be essential for prolonged operation of this kind of electrolyzers.

Furthermore, a novel concept for stabilizing the nanoparticulate silver catalysts was developed. This is based on embedding the nanoparticles in a matrix of anion-conductive binder materials, which largely suppresses cathodic corrosion of the catalyst material during extended electrolysis.

The results of this PhD thesis pave the way for a rational design of GDEs for future industrial applications of electrochemical CO_2 conversion.

Table of Contents

Abstract ..... **I**

Chapter 1: Introduction **1**

Chapter 2: Concepts of CO_2 fixation, its storage and valorization **7**

Chapter 3: The electrochemical CO_2 reduction reaction (ec-CO_2RR) **10**

3.1 Thermodynamic considerations 10

3.2 Kinetic considerations and beyond 13

3.3 Metrics for the ec-CO_2RR performance evaluation 17

3.4 Assessment of potential ec-CO_2RR products: Definition of CO as the target product 18

3.5 Experimental configurations and cell designs for the ec-CO_2RR 20

3.5.1 Cell design based on a solid-("bulk")liquid interface (→ two-phase boundary concept) 23

3.5.2 Cell designs based on a solid/liquid/gas interface (→ three-phase boundary concept) 24

Chapter 4: Definition of the scientific problem addressed in this doctoral project and the experimental approach followed **28**

4.1 Stability of the electrocatalysts 28

4.2 Stability of the gas diffusion electrode (GDE) 30

4.3 Experimental approach 32

Chapter 5: Main findings **34**

5.1 Catalyst degradation during CO_2RR at high current densities and possible concepts of catalyst protection (→ publications 1 and 2) 34

5.2 GDE degradation during CO_2RR at high current densities and possible concepts of GDE stabilization (→ publications 2, 3, 4, and 5) 38

Conclusions and outlook **42**

Disclosure of use of AI-assisted technologies **44**

References **45**

Publications **53**

1. The capping agent is the key: Structural alterations of Ag NPs during CO_2 electrolysis probed in a zero-gap gas-flow configuration 54

2. The role of ionomers in the electrolyte management of zero-gap MEA-based CO_2 electrolysers: A Fumion vs. Nafion comparison 81

3. Visualization and quantification of flooding phenomena in gas diffusion electrodes used for electrochemical CO_2 reduction: A combined EDX/ICP–MS approach 101

4. Cracks as Efficient Tools to Mitigate Flooding in Gas Diffusion Electrodes Used for the Electrochemical Reduction of Carbon Dioxide 110

5. Effective perspiration is essential to uphold the stability of zero-gap MEA-based cathodes used in CO_2 electrolysers 127

6. Activation Matters: Hysteresis Effects During Electrochemical Looping of Colloidal Ag Nanowire (Ag-NW) Catalysts 140

7. Limitations of Identical Location SEM as a Method of Degradation Studies on Surfactant Capped Nanoparticle Electrocatalysts 153

8. Size-Dependent Structural Alterations in Ag Nanoparticles during CO_2 Electrolysis in a Gas-Fed Zero-Gap Electrolyzer 163

Appendix 174

1. List of publications 174

2. Conferences 175

3. Acknowledgements 176

4.致我的父母 (Dedication to my parents) 178

5. Declaration of consent 180

Chapter 1: Introduction

The so-called natural greenhouse effect describes the phenomenon that certain parts of our Earth's atmosphere behave like the glass of a greenhouse. It is transparent to electromagnetic radiation in the, at least for human beings, visible wavelength ranges of solar radiation (~ 400 – 780 nm), but less permeable for longer-wave radiation in the infrared (IR) range (ca. 780 nm – 1 mm). The origin of this natural phenomenon is related to certain components of Earth's atmosphere that are capable of absorbing electromagnetic radiation in the infrared range as illustrated in Figure 1.1.

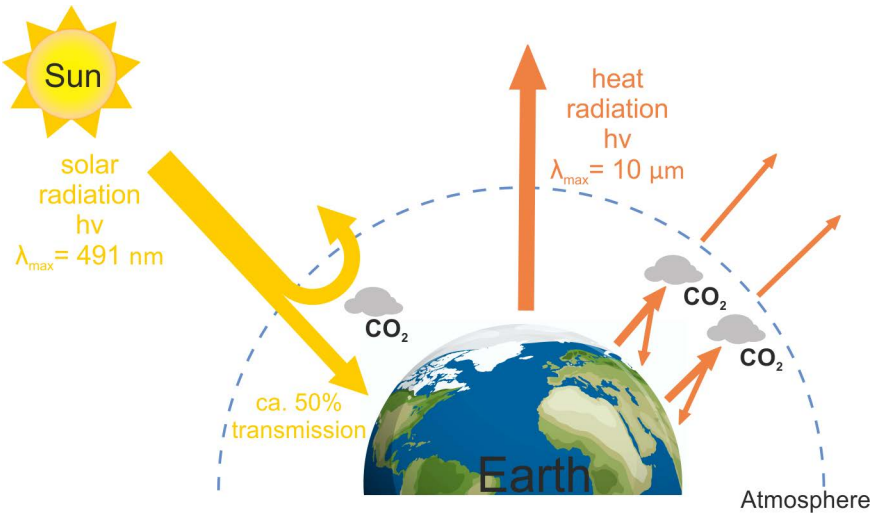

Figure 1.1. Illustration of the **greenhouse effect**. "Heat energy" is trapped in Earth's atmosphere through the (partial) absorption of infrared radiation by the greenhouse gases, e.g., CO_2 and H_2O (vapor).

Most of the gaseous components of Earth's atmosphere (nitrogen: 78.08%, oxygen: 20.95%, and argon: 0.93%,[1, 2] based on dry air) are, however, "IR-inactive". It is the approximately only 0.05% of trace components in our atmosphere that are responsible for the greenhouse effect. These so-called **greenhouse gases** (denoted **GHGs**) include CO_2, CH_4, N_2O, O_3, and water (vapor).[3, 4] Their capability of adsorbing IR radiation can easily be made visible by (IR) spectroscopic means. As a representative example, see the absorption spectrum for CO_2 in Figure 1.2.[5] Often, infrared radiation is referred to as "thermal radiation". Based on the so-called Wien's displacement law, one can *roughly estimate* the maximum intensity of the electromagnetic radiation emitted by a solid body at a given temperature T. If we assume a mean temperature of the Earth surface of about 290 K, Wien's displacement law predicts an intensity maximum of emitted radiation in the infrared range ($\lambda_{max} \approx 10$ µm). This explains why the natural greenhouse effect in our atmosphere is directly linked to the ability of atmospheric components to absorb infrared radiation, which typically occurs through the excitation of vibrational modes in the IR-active GHGs.

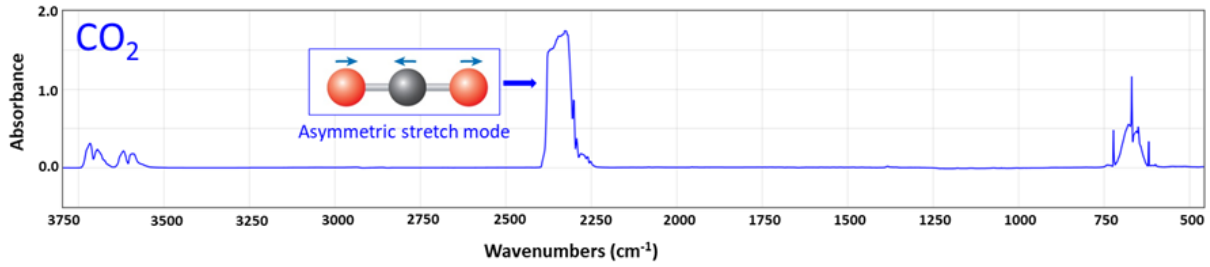

Figure 1.2. Representative absorption spectrum for gaseous CO_2 indicating prominent absorption features (vibrational modes) in the infrared range.

The absorption of electromagnetic radiation by exciting vibrational modes of a molecule means that the kinetic energy of the respective molecule is increased. In addition to translation and rotation, vibrations are another form in which a multiatomic molecule can store kinetic energy. According to kinetic gas theory, any increase in the kinetic energy of gases corresponds to an increase in the gas temperature. To put it simplistic, "thermal energy" is captured to certain extent in the atmosphere by this natural greenhouse effect. In principle, IR radiation can be re-emitted by these gases when returning from the excited vibrational state to the corresponding initial ground state. Because this is an entirely unidirectional process, a significant portion of the IR radiation, emitted by the Earth's surface, cannot escape the atmosphere into free space (Figure 1.1).

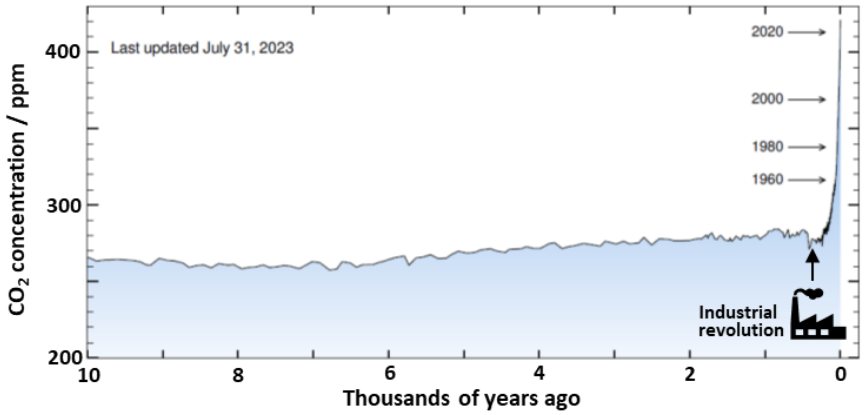

Figure 1.3. Changes of the atmospheric CO_2 concentration on the time scale of thousands of years as derived from the analysis of ice cores (adapted from https://keelingcurve.ucsd.edu/pdf-downloads/).

At this point it should be emphasized that the natural greenhouse effect is a basic prerequisite for the development of all life on Earth, without which, hostile temperatures in the range of -15 to -21 °C would prevail on its surface.[6] Before the era of the **industrial revolution**, which started with the invention of the steam engine in the late 18th century, atmospheric CO_2 levels were rather stable for thousands of years at levels in the range between 270 and 290 ppm (Figure 1.3). It has been

the massive use and combustion of fossil energy carriers (initially coal, oil, and later also natural gas) starting with the industrial revolution which led to the CO_2 level substantially raise within a relatively short period of time, at least on the scale of thousands of years. Figure 1.3 leaves no doubt about the direct correlation between anthropogenic, i.e. non-natural, man-made CO_2 emissions and the increase in atmospheric CO_2 concentration.

In the late 1950s, **Charles Keeling** pioneered the on-line detection and quantification of atmospheric CO_2 based on infrared spectroscopic techniques with the aim of following general trends in the temporal evolution of trace gas concentrations in the atmosphere.[7] This kind of time-resolved monitoring is typically carried out far away from local CO_2 point sources, e.g., on the Mauna Loa in Hawaii. In principle, the so-called Keeling curve, shown in the lower left panel of Figure 1.4, reflects the mean global concentration profile of CO_2 gas in the Earth's atmosphere since 1958. [8] The rising trend in CO_2 concentration is apparently overlaid by a seasonal modulation reflecting the Northern Hemisphere vegetation cycle. While the annual mean increase in CO_2 concentration on Mauna Loa was 0.55 ppm in the late 1950s, the global trend has risen to an alarmingly high mean value of approximately 2.3 ppm per year over the past 15 years. This indicates that the increase in CO_2 concentration in the atmosphere is accelerating even at present. The lower right panel in Figure 1.4 shows the most recent data from Mauna Loa with a current reading of ca. **422 ppm in CO_2 concentration** (on July 31, 2023). [8]

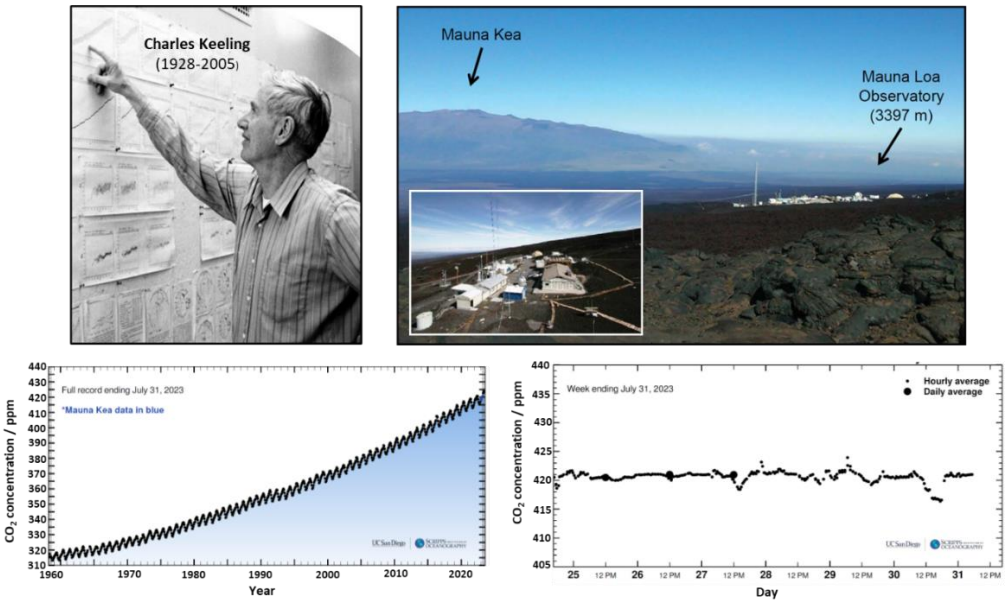

Figure 1.4. Shown is Charles Keeling (top left) from the Scripps Institution of Oceanography (California, US), who pioneered in the late 1950s atmospheric CO_2 monitoring on Mauna Loa (top right), Hawaii, US. The lower left panel shows the so-called Keeling curve based on data measured at the Mauna Loa observatory. The lower right panel shows most recent data from the week ending July 31, 2023, reaching CO_2 concentrations above 420 ppm (adapted from https://keelingcurve.ucsd.edu/pdf-downloads/).

Charles Keeling's work was crucial in providing experimental evidence that increases in atmospheric CO_2 levels are indeed coupled to global warming, an effect which has been corroborated and is now being monitored by numerous independent research institutions worldwide. Figure 1.5 shows representative data from NASA (US) indicating very drastic increases in temperature anomalies relative to mean values from the period between 1951 and 1980. These results agree well with the observed accelerated raise of the atmospheric CO_2 levels in recent years (Figure 1.5). In relation to the pre-industrial age, the average temperature has already increased by around 1.1 °C. This value continues to rise at a rate of approximately 0.2°C per decade.[9, 10]

It should be noted that the connection between CO_2 content in the atmosphere and the temperature at the ground is not in itself a new finding in science but has been discussed in scientific publications already since the 19th century. As early as **1824**, **Jean-Baptiste Fourier** explained how trace gases in the atmosphere warm up the climate.[11] One of the most important contributors to this field is the Swedish chemist and Nobel laureate **Svante Arrhenius**, who published in **1896** a seminal work entitled

On the Influence of Carbonic Acid in the Air upon the Temperature of the Ground

Philosophical Magazine and Journal of Science, Series 5, Volume 41,
April 1896, 237-276

An excerpt from his original work is shown in Figure 1.6. Based on his findings and data, he could estimate already in 1896 that doubling the carbon dioxide content of the atmosphere would lead to a temperature increase in the range of four to six degrees Celsius.[12]

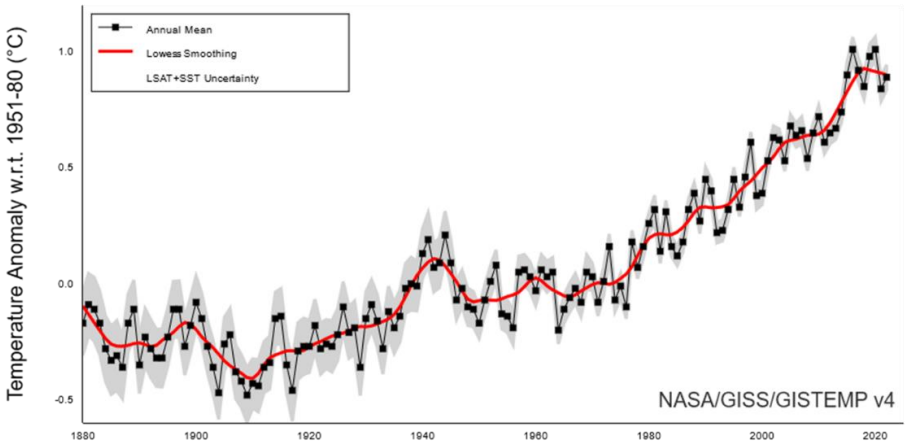

Figure 1.5. Global mean estimates of temperature anomalies based on land and ocean data, with base period 1951-1980 (adapted from https://data.giss.nasa.gov/gistemp/graphs_v4/).

What is interesting to note is that anthropogenic CO_2 emissions and the expected rise in temperature on the ground were by no means considered harmful at that time, but rather positive for agricultural yields and thus also for the prosperity of our society. This viewpoint was detailed also by Arrhenius in a monograph from 1908.[13]

It took several decades before it was recognized, first in science and later also in other areas of society and politics, that man-made related climate change will not only have devastating consequences for the environment, but ultimately also for society's prosperity. Entire terrestrial and marine ecosystems will negatively be impacted by the CO_2-related climate change resulting in rising sea levels, the melting of glaciers and polar caps, the acidification of the oceans, salination of soils, lowering of the ground water table, and the proliferation of desert areas.[14-16] Ultimately, these processes will go hand in hand with the loss of biodiversity in living Nature. These negative environmental developments will directly affect human health, global food and freshwater supplies, and pose a global challenge to various branches of our society including the agricultural sector, transportation sector, energy sector and ultimately also of course the industrial sector.

LONDON, EDINBURGH, AND DUBLIN

PHILOSOPHICAL MAGAZINE

AND

JOURNAL OF SCIENCE.

[FIFTH SERIES.]

APRIL 1896.

XXXI. *On the Influence of Carbonic Acid in the Air upon the Temperature of the Ground.* By Prof. SVANTE ARRHENIUS *.

1. *Introduction: Observations of* Langley *on Atmospherical Absorption.*

A GREAT deal has been written on the influence of the absorption of the atmosphere upon the climate. Tyndall † in particular has pointed out the enormous importance of this question. To him it was chiefly the diurnal and annual variations of the temperature that were lessened by this circumstance. Another side of the question, that has long attracted the attention of physicists, is this: Is the mean temperature of the ground in any way influenced by the presence of heat-absorbing gases in the atmosphere? Fourier‡ maintained that the atmosphere acts like the glass of a hot-house, because it lets through the light rays of the sun but retains the dark rays from the ground. This idea was elaborated by Pouillet §; and Langley was by some of his researches led to the view, that "the temperature of the earth under direct sunshine, even though our atmosphere were present as now, would probably fall to −200° C., if that atmosphere did not possess the quality of selective

* Extract from a paper presented to the Royal Swedish Academy of Sciences, 11th December, 1895. Communicated by the Author.
† 'Heat a Mode of Motion,' 2nd ed. p. 405 (Lond., 1865).
‡ *Mém. de l'Ac. R. d. Sci. de l'Inst. de France*, t. vii. 1827.
§ *Comptes rendus*, t. vii. p. 41 (1838).

Figure 1.6. Excerpt from the original work of Svante Arrhenius from 1898 published in *Philosophical Magazine and Journal of Science* which discusses the influence of atmospheric CO_2 on the temperature on the ground. Adapted with permission from *Lond. Edinb. Dublin philos. mag. j. sci.* 1896, 41 (251), 237-276. Rights managed by Taylor & Francis.

The worldwide rethinking in society and politics about the risks of man-made climate change ultimately led **at the UN Climate Change Conference** (COP21) in **2015** in Paris (France) to the adoption of the so-called **Paris Agreement**.[17] This legally binding treaty has now been ratified by 198 nations and institutions, including the largest CO_2 emitters worldwide like China, USA, the European Union (EU), and India. The overall goal of this concerted action is to keep

"the increase in the global average temperature to well below 2 °C above pre-industrial levels".

This ambitious goal can only be achieved by restructuring the entire society towards a truly **circular economy**. The vision of a carbon-neutral society is a truly intersectorial challenge and can only become a reality through the rigorous implementation of various complementary measures: [18-20]

(i) The drastic reduction in primary CO_2 emissions (avoidance of fossil fuels as primary energy carriers);

(ii) The large-scale fixation and long-term storage of emitted CO_2;

(iii) The sustainable valorization of emitted CO_2.

In general, this doctoral project contributes to the development of novel technologies for the utilization of CO_2 through its sustainable conversion into value-added products.

Chapter 2: Concepts of CO_2 fixation, its storage and valorization

The reduction of anthropogenic CO_2 emissions by minimizing the consumption of fossil fuels with the use of various forms of renewable energy (solar, wind, hydropower) will certainly be the most important contribution to achieving the goals of the **Paris Agreement** in the future. However, given the increase in world population and the demand to improve living standards in low- and middle-income countries, fossil fuels will certainly remain the most important primary energy source for, at least the next few decades. For this reason, various alternative technologies are currently being developed with the aim to first fix CO_2 and to store it permanently afterwards.[18] This combination of CO_2 capture and storage is often referred to as **CCS technology**, which is at present already in use in oil and gas industry.[21, 22] One prime example hereof is the Sleipner field in the North Sea where CO_2 gets separated from natural gas and re-injected and stored far below the seabed.[23] More recently, the concept of CO_2 capture has been successfully extended to various industrial CO_2 (point) emitters such as fossil fuel power plants, the cement industry, and the steel industry, where otherwise the flue gas containing 10-30% CO_2, gets directly released into the atmosphere.[24]

CO_2 capture itself is a (reversible) chemisorption process which occurs through the interaction of CO_2 with primary amine functionalities of organic sorbents, which can be either monomeric or polymeric,[25, 26] CO_2 can be released again by thermal treatment. It should be noted, however, that the operation temperature for the CO_2 desorption is relatively high (120-140 °C) in the regenerator unit.[27] CO_2 separation is therefore considered to be a very energy-intensive process that can only be operated in an economically viable manner in regions where cheap thermal energy is available (e.g., in Iceland). CO_2 capture, based on monoethanolamides, has already been demonstrated on a large industrial scale with a CO_2 capture capacity of one million tons per year.[28]

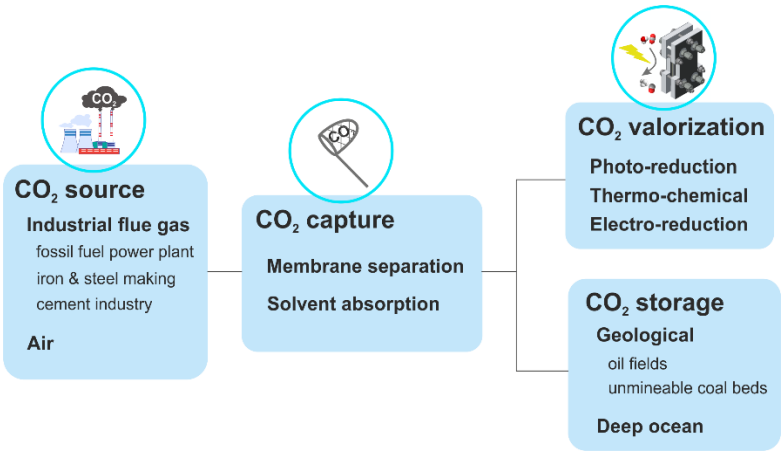

Figure 2.1. Strategies of CO_2 capture, CO_2 storage, and CO_2 valorization.

A (more expensive) alternative to the CO_2 capture from air is the so-called **direct air capture** (DAC) which is currently being pioneered by the Swiss company **Climeworks**.[29] There are already existing pilot projects in Iceland combining the amine scrubbing (capture) technology with a geological storage approach, denoted geo-sequestration. CO_2 is pressed under the ground and mineralized in basalt rocks thereby forming carbonates.[30]

Aside from environmental concerns, a major disadvantage of all CO_2 storage technologies is that CO_2 itself is not further used. In contrast to that, so-called **CO_2 valorization technologies** regard CO_2 as chemical raw material and abundant C_1 feedstock rather than polluting waste.[20, 31] Most of these CO_2 valorization concepts rely in general on catalytic approaches and more specifically on (i) **thermal catalysis**, (ii) **photocatalysis**, or (iii) **direct electrocatalysis**. Figure 2.1 illustrates the main strategies of CO_2 capture, CO_2 storage, and CO_2 valorization.

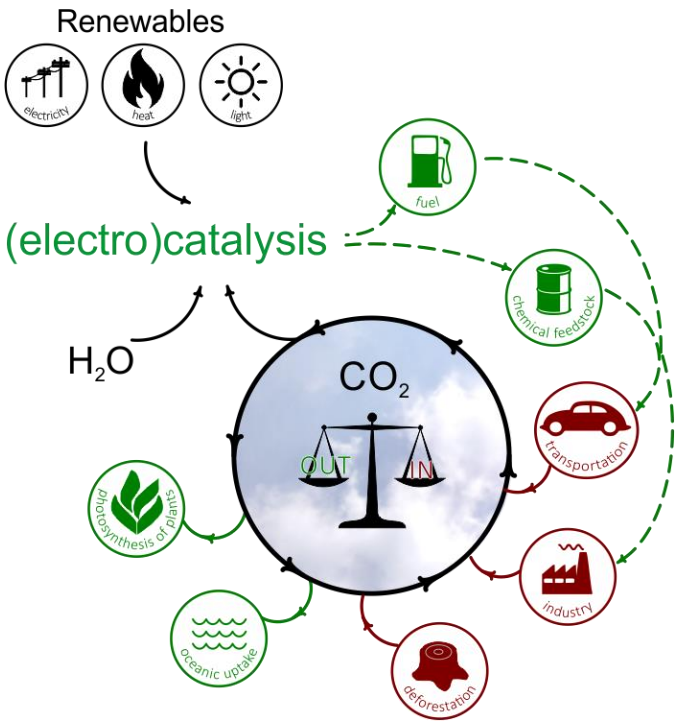

Figure 2.2. Schematic depicting the vision of **closing the anthropogenic carbon cycle** through contributions from the electrocatalytic conversion of CO_2. Adapted from reference 32.

CO_2 valorization through electrochemical means warrants particular attention because of its ability to transform environmentally harmful CO_2 into platform chemicals or directly into synthetic fuels of higher value. The CO_2 reduction reaction might become not only economically feasible but also truly sustainable in the future, particularly when the surplus of renewable energy originating from solar radiation, wind power, and hydroelectric sources is used as energy input to drive the highly

energy demanding CO_2 conversion. In this context, the so-called "**power-to-X**" concept will be particularly important in helping to close the anthropogenic carbon cycle. The commissioning of the first industrial pilot plant by the Siemens-Evonik consortium in September 2020,[33] using CO_2 electroreduction for the production of carbon monoxide (CO), has been a milestone on the path to economically feasible electrochemical CO_2 valorization ('Rheticus project'). Figure 2.2 summarizes the overall vision of the power-to-X concept.

More specifically, this PhD project contributes to the development of electrocatalytic CO_2 conversion processes.

Chapter 3: The electrochemical CO_2 reduction reaction (ec-CO_2RR)

In principle, an electrochemical redox process can be subdivided into two individual half-reactions, a reduction reaction (RR) and the corresponding oxidation reaction (OR). By definition, the reduction reaction occurs on the cathode of the electrochemical cell and the oxidation takes place on the anode side of the electrochemical cell. In a classical three electrode configuration, used throughout this PhD thesis, the working electrode (WE) refers to the electrode where the half-cell reaction of interest takes place which in the present case the electrochemical CO_2 reduction reaction (denoted hereinafter ec-CO_2RR). The counter reaction to the ec-CO_2RR is typically the oxygen evolution reaction (OER) taking place on the so-called counter electrode (CE). In the three-electrode configuration, a non-current-carrying reference electrode (RE) is typically integrated into the WE compartment with the aim to measure changes of the potential difference between WE and RE during the electrolysis reaction of interest. Note that in this thesis a somehow different configuration is used, in which in a so-called zero-gap configuration the RE is placed in the CE (anode) compartment (for technical details see section 3.5.2).

3.1 Thermodynamic considerations

Thermodynamics is a branch of physical chemistry dealing with (electro)chemical systems under equilibrium conditions. Related to electrochemical systems, equilibrium means that no net current is flowing through the external circuit of the electrochemical cell. In thermodynamics, certain state functions and changes thereof are typically used to define chemical equilibrium and to predict the spontaneity and direction of a reaction when leaving the equilibrium. For practical reasons (constant temperature (T) and pressure (p)), these considerations are often based on the Gibb's free energy (G) and changes thereof ($\Delta_r G$). In electrochemistry, changes of the Gibb's free energy for the half-cell reaction of interest under standard conditions ($\Delta_r G^0$, at 1.0 atm and 298.15 K) can be related to the so-called standard potential (E_{eq}^0 in V vs. the **S**tandard **H**ydrogen **E**lectrode (**SHE**)) defining electrochemical equilibrium:

$$\Delta_r G^0 = -nFE_{eq}^0$$

Where n refers to the number of electrons transferred during reaction whereas F represents the Faraday constant. When referring to the standard potential E_{eq}^0 of the half-cell reaction of interest, the "counter" half-cell reaction is, by convention, the hydrogen reaction defining the zero point of the relative potential scale. Of note is that the standard potentials are not measured but typically derived, this means calculated, from the corresponding thermodynamic data ($\rightarrow \Delta_r G^0$).

Leaving equilibrium and initiating a non-spontaneous, i.e. forced, electrochemical process requires the application of potentials different from the equilibrium potential. In case of a spontaneous electrochemical process, this means an exergonic electrochemical reaction, such deviation from the equilibrium potential/potential difference occurs without any external "bias". The difference between the applied potential under non-equilibrium conditions and the equilibrium potential is defined as the so-called **overpotential $\boldsymbol{\eta}$**.

Table 3.1 lists the half-cell standard potentials (E_{eq}^0) of the most relevant CO_2 reduction reactions and the oxidative OER which is the common anodic counter reaction to the ec-CO_2RR. Initiating the ec-CO_2RR under standard conditions requires potentials which are more negative than the ones listed in Table 3.1. This means, cathodic/negative overpotentials must be applied to initiate the ec-CO_2RR.

Table 3.1. Standard electrode potentials for some half-cell reactions related to ec-CO_2RR, HER and OER at 1.0 atm and 298.15 K.[34]

Products	half-cell reactions	n	E_{eq}^0 / V vs. SHE
Carbon monoxide	$CO_2 + 2H_2O + 2e^- \rightarrow CO + 2OH^-$	2	-0.934
	$CO_2 + 2H^+ + 2e^- \rightarrow CO + H_2O$		-0.106
Formic acid/ Formate	$CO_2 + 2H^+ + 2e^- \rightarrow HCOOH$	2	-0.250
	$CO_2 + 2H_2O + 2e^- \rightarrow HCOO^- + OH^-$		-1.078
Methane	$CO_2 + 8H^+ + 8e^- \rightarrow CH_4 + 2H_2O$	8	0.169
Ethylene	$2CO_2 + 8H_2O + 12e^- \rightarrow CH_2CH_2 + 12OH^-$	12	-0.764
	$2CO_2 + 12H^+ + 12e^- \rightarrow CH_2CH_2 + 4H_2O$		0.064
Ethanol	$2CO_2 + 9H_2O + 12e^- \rightarrow CH_3CH_2OH + 12OH^-$	12	-0.744
	$2CO_2 + 12H^+ + 12e^- \rightarrow CH_3CH_2OH + 3H_2O$		0.084
Hydrogen	$2H_2O + 2e^- \rightarrow H_2 + 2OH^-$	2	-0.830
	$2H^+ + 2e^- \rightarrow H_2$		0
Oxygen	$2H_2O \rightarrow O_2 + 4H^+ + 4e^-$	4	1.23

For deriving the so-called cell voltages under standard conditions (ΔE^0), this means the potential difference between the anode/CE and the cathode/WE, the half-cell standard potentials of the ec-CO_2RR and the OER must be combined. This PhD work focuses, however, exclusively on the cathode side of the electrolysis cell where the ec-CO_2RR takes place. An optimization of the OER

was not foreseen. For this reason, only the potentials of the cathode/WE were considered and referenced in a three-electrode configuration versus common reference electrodes (see discussion below).

From the formulation of the half-cell reactions in Table 3.1 it becomes also evident that the ec-CO_2RR is pH dependent as it either consumes protons (acidic conditions) or produces hydroxide ions (neutral or alkaline pH). This also implies that the ec-CO_2RR equilibrium potentials themselves are pH dependent. Under pH neutral or alkaline conditions, water serves as the required proton source.

An important result of the thermodynamic analysis based on the data presented in Table 3.1 is that the targeted **ec-CO_2RR is inevitably superimposed on a parasitic hydrogen evolution reaction (HER)** when the electrolysis is carried out in an **aqueous reaction environment**, since its standard potential is in the same range as the ones of the ec-CO_2RRs.

Typically, electrolysis reactions are not carried out under standard conditions. The activity/concentration dependence of the equilibrium potentials is expressed by the so-called **Nernst equation**, a fundamental equation of electrochemical thermodynamics. It links the equilibrium potential of a given half-cell reaction at nonstandard conditions (E_{eq}) to the corresponding standard potential (E_{eq}^0) and the activities (α) of all involved oxidized (ox) and reduced (red) species according to:

$$E_{eq} = E_{eq}^0 - \frac{RT}{nF} ln \frac{\alpha_{red}}{\alpha_{ox}}$$

where R represents the universal gas constant (R = 8.314 J mol^{-1} K^{-1}), T defines the system temperature (in K), n refers the number of electrons involved in the redox process, F stands for the Faraday constant (96 485.3 C mol^{-1}), and α represents the activity of the reduced and oxidized species, respectively (in mol L^{-1}). Note that, for the sake of simplicity, the respective concentrations (c) are commonly used to formulate the Nernst equation instead of the activities:

$$E_{eq} = E_{eq}^0 - \frac{RT}{nF} ln \frac{c_{red}}{c_{ox}}$$

In the context of this PhD project, the Nernst equation found a practical application in the (re)definition of the potential scales. The SHE is an idealized reference electrode which cannot be realized experimentally. SHE represents a platinum electrode exposed to an ideal electrolyte solution containing 1 M (effective concentration) protons and bubbling hydrogen gas at a pressure of 100 kPa. For practical reasons and to allow for comparison of electrolysis and catalyst

performance data acquired at different pH values, the experimentally applied (or measured) potentials are commonly referenced versus the so-called **R**eversible **H**ydrogen **E**lectrode (**RHE**) which accounts for the pH dependence of the hydrogen reaction (see also Table 3.1) according to:

$$E_{eq}\ (V\ vs\ RHE) = E_{eq}^{0}(V\ vs\ SHE) + \frac{RT}{F}\ln(c_{H^+})$$

For the hydrogen reaction (H^+/H_2), the expression $E_{eq}^{0}(V\ vs\ SHE)$ is per definition set to 0 V. Considering the definition of the pH, this equation simplifies at 25° C to:

$$E_{RHE}\ (V) = -0.059\ V \cdot pH$$

In practice, electrode potentials were measured throughout this PhD project versus a Ag | AgCl | 3 mol L^{-1} KCl double junction reference electrode. It is of note that, although not recommended in textbooks of electrochemistry, we did not notice any failure (e.g., in the form of potential shifts) of the used Ag | AgCl | 3 mol L^{-1} KCl reference electrode when working in pH neutral or slightly alkaline conditions. Its exact reference potential depends on the concentration of chloride anions in solution. This anion concentration dependence is typical for so-called "**electrodes of the second kind**". The anion concentration dependence can also be described based on the Nernst equation.

3.2 Kinetic considerations and beyond

Thermodynamics provides valuable insights on the conditions under which an (electro)chemical reaction can in principle take place. However, specific rates of an electrolysis reaction as function of its key reaction parameters (e.g., the applied overpotential η, the system temperature T, or the concentration of the reactants) cannot be derived based on thermodynamic considerations. In this context, the so-called **(Erdey-Grúz) Butler-Volmer equation** is of central importance for **electrochemical kinetics**. This equation relates the current density j (surface area normalized current) under steady-state conditions to the overpotential η as the key electrochemical parameter determining the overall reaction rate of an electrochemical process ($\rightarrow$ kinetic regime), at least in the absence of any mass transport effects or other limiting factors (e.g., ohmic effects/losses originating from the finite electrolyte resistance, and the resistance of the membrane etc.). For a simple, reversible one electron transfer process the equation consists of an anodic (oxidation: j^+) and a cathodic (reduction: j^-) term according to:

$$j = j^+ + j^- = j_0 \cdot \left[exp\left(\frac{(1-\alpha)nF}{RT}\eta\right) - exp\left(-\frac{\alpha nF}{RT}\eta\right)\right]$$

where j is the net current density (in A cm^{-2}), j_0 represents the exchange current density (in A cm^{-2}), α is the dimensionless asymmetry factor, n the number of transferred electrons, R represents the universal gas constant (R = 8.314 J mol^{-1} K^{-1}), F is the Faraday constant (96485.3 C mol^{-1}), and T the absolute temperature (in K). At moderate (cathodic) overpotentials (| η | > 0.1 V), the anodic term can be neglected, and the equation simplifies to:

$$j \approx j^{-} = -j_0 \cdot exp\left(-\frac{\alpha n F}{RT}\eta\right)$$

The (Erdey-Grúz) Butler-Volmer equation and its simplified form describe an exponential relation between the applied overpotential η and the resulting electric net current (proportional to the reaction rate) flowing through external electric circuit of the electrochemical cell during the electrolysis reaction. Deviations from this exponential correlation can occur at high overpotentials (→ reaction rates) where the process can become affected or even limited by reactant mass transport effects. Other deviations from this relationship originate from ohmic effects which scale with the current (density). The origin of these ohmic losses can be manifold (electrolyte resistance, membrane resistance etc.).

A simple kinetic description of the ec-CO_2RR is typically hampered by the fact that this reaction is actually a sequential multi-step/multi-electron transfer process. In addition, more than one ec-CO_2RR product is often formed at the same time (see discussion below). In addition, the ec-CO_2RR is in most cases superimposed on the parasitic HER (→ occurrence of parallel reactions) if the electrolysis is performed in aqueous media (see Table 3.1). This circumstance makes it necessary to combine electrochemical (kinetic) analyses of experimentally derived current density/potential relationships with further chemical product analyses to disentangle the complex ec-CO_2RR product distribution and related partial current densities ($j = j_{CO} + j_{CH4} + j_{HER} \ldots$).

Electrocatalysts are typically required not only to accelerate the intrinsically sluggish ec-CO_2RR but also to improve the product selectivity with the aim to direct the CO_2 electrolysis reaction towards the desired target product (e.g., CO). According to the German chemist **Wilhelm Ostwald (1895)** a **catalyst** is defined as

"…a substance that increases the rate of a chemical reaction without itself being consumed and without changing the final state of the thermodynamic equilibrium of that reaction."

This also means that a catalyst ideally leaves the catalyzed reaction unchanged. However, in this thesis it is shown for the ec-CO_2RR that this statement is not always true, meaning that the electrocatalysts and their specific reaction environments are often structurally and chemically

altered and degraded during the (electro)catalyzed reaction, which inevitably leads to losses in the process performance over time. With regard to the (Erdey-Grúz) Butler-Volmer equation, the role of the catalyst is to increase the exchange current density of the targeted parallel reaction (e.g., j_0^{CO} for CO production) and to diminish the respective exchange current density of the non-desired reaction products (e.g., j_0^{HER}).

Early work on ec-CO_2RR particularly focused on mono-metallic catalyst systems. In a pioneering work, **Hori et al.**[35] classified the studied metals into **four fundamental catalyst groups** according to the major products formed during ec-CO_2RR (see Table 3.2): **(i)** A first group contains metals like Au, Ag, Zn, and Pd and form preferentially carbon monoxide (CO). **(ii)** Pb, Hg, In, Sn, Cd, and Tl produce formate (HCO_2^-) as main reaction product whereas **(iii)** the parasitic HER dominates the product distribution when metals like Ni, Fe, and Pt are used as catalyst. **(iv)** Cu stands out among the mono-metallic systems as it is the only known ec-CO_2RR catalyst which can form C_{n+} hydrocarbons and alcohols.

Table 3.2. Classification scheme of ec-CO_2RR catalysts according to Hori et al.[35] Adapted with permission from Electrochim. Acta, 1994, 39 (11).[35] Copy right 1994 Elsevier.

Catalyst	Potential vs. NHE / V	Current density / mA cm^{-2}	Faradaic efficiency / %						
			CH_4	C_2H_4	EtOH	PrOH	CO	$HCOO^-$	H_2
Au	–1.14	5.0	0.0	0.0	0.0	0.0	87.1	0.7	10.2
Ag	–1.37	5.0	0.0	0.0	0.0	0.0	81.5	0.8	12.4
Zn	–1.54	5.0	0.0	0.0	0.0	0.0	79.4	6.1	9.9
Pd	–1.20	5.0	2.9	0.0	0.0	0.0	28.3	2.8	26.2
Ga	–1.24	5.0	0.0	0.0	0.0	0.0	23.2	0.0	79.0
Pb	–1.63	5.0	0.0	0.0	0.0	0.0	0.0	97.4	5.0
Hg	–1.51	0.5	0.0	0.0	0.0	0.0	2.1	99.5	0.0
In	–1.55	5.0	0.0	0.0	0.0	0.0	7.1	94.9	3.3
Sn	–1.48	5.0	0.0	0.0	0.0	0.0	13.9	88.4	4.6
Cd	–1.63	5.0	1.3	0.0	0.0	0.0	0.0	78.4	9.4
Tl	–1.60	5.0	0.0	0.0	0.0	0.0	0.0	95.1	6.2
Ni	–1.48	5.0	1.8	0.1	0.0	0.0	0.0	1.4	88.9
Fe	–0.91	5.0	0.0	0.0	0.0	0.0	0.0	0.0	94.8
Pt	–1.07	5.0	0.0	0.0	0.0	0.0	0.0	0.1	95.7
Ti	–1.60	5.0	0.0	0.0	0.0	0.0	tr.	0.0	99.7
Cu	–1.44	5.0	33.3	25.5	5.7	3.0	1.3	9.4	20.5

Electrolyte: 0.1 M $KHCO_3$; Temperature: 18.5 ± 0.5 °C.

Atomic scale ec-CO_2RR mechanisms have intensively been studied in the past for these mono-metallic systems using various *in situ*/*operando* spectroscopic methods (e.g., Raman spectroscopy) and DFT based approaches.[36-39] Figure 3.1 schematically shows the most widely accepted reaction

pathways of CO_2 conversion focusing on the $2e^-$transfer processes of CO and formate production (see also Table 3.1). The catalyzed reaction starts with the chemisorption of CO_2 on the metal surface either through the carbon (→ carbophilic catalysts) or through the oxygen atoms of the CO_2 (→ carbophilic catalysts). Of note is that some catalysts even allow both binding modes and reaction pathways (e.g., Ag and Cu). A first electron transfer transforms the linear CO_2 molecule into a bended radical mono-anion species ($^*CO_2^{\bullet-}$, the asterisk * represents an adsorption state). This initial electron transfer is often considered as rate determining in the multi-step ec-CO_2RR reaction pathway. Depending on the initial $^*CO_2^{\bullet-}$ binding mode either through the oxygens or through the carbon, *OCHO or *COOH intermediates may be formed following a proton transfer step with typically water serving as the proton source (→ pH neutral and alkaline conditions). Both intermediates can in principle yield formate as the final product following a second electron transfer. The formate pathway through the oxygen atoms is, however, clearly the more common one. A further electron transfer along with an OH^- elimination yields chemisorbed $^*CO$ which can either desorb from the catalyst surface (e.g., on Ag and Au) or undergo further electron transfer and C-C coupling reactions (e.g., on Cu) to form multi-carbon oxygenates or hydrocarbons.

The binding strength of the $^*CO$ intermediate has been identified as one of the most important descriptors in the analysis of reaction pathways governing the resulting ec-CO_2RR product distribution.[40, 41] Those catalysts which strongly bind $^*CO$ intermediates on their surface, e.g., Fe, Ni, and Pt, suffer from irreversible CO poisoning and therefore produce mainly hydrogen (see Table 3.2). Weak $^*CO$ *binding* leads to the ease CO desorption from the catalyst surface resulting in CO as the main ec-CO_2RR product (e.g., over Ag and Au). Moderately bound $^*CO$ (e.g., over Cu) will, however, allow for C-C coupling reactions and the ultimate production of C_{2+} chemicals (→ synthetic fuels). It is this balanced CO-catalyst interaction which makes Cu unique among the mono-metallic ec-CO_2RR catalysts in accordance to the so-called **Sabatier principle**.[42]

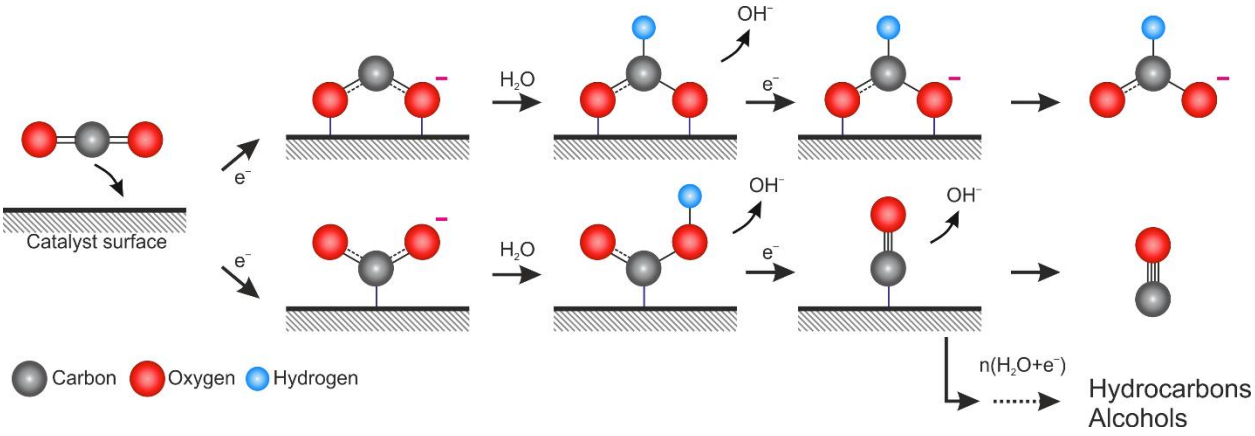

Figure 3.1. Possible ec-CO_2RR pathways according to the literature.[36-39]

3.3 Metrics for the ec-CO_2RR performance evaluation

Generally accepted evaluation metrics and criteria are essential for the optimization of catalysts and catalyzed processes and allow for the comparison of electrolysis data obtained from different laboratories. Given that the ec-CO_2RR can deliver different products simultaneously, the product-specific **Faraday efficiency** (**FE**) is central to catalyst evaluation as it reflects **product distribution** and reaction **selectivity**. FE is typically expressed as a percentage and quantifies how much of the charge passed through the electrochemical cell during electrolysis results into a certain reaction product *i*, as opposed to unwanted by-products:

$$FE_i = \frac{nx_iF}{Q} \cdot 100\%$$

In this equation, *n* represents the number of electrons exchanged to form a certain product *i*, x_i is amount of product *i* (in mol) formed during electrolysis, *F* represents the Faraday constant, and *Q* is the total charge (in C) passed through the cell during the electrolysis. Note that for potentiostatic electrolysis, *Q* is typically derived from an integration of the electrolysis current over time.

A supplementary quantity for the catalyst evaluation is the so-called **partial current density** (j_i or PCD_i in mA cm^{-2}) which defines how much current, normalized to the surface area of the cathode, is consumed during electrolysis to form a certain product *i*. This quantity can simply be derived from the respective FE value and the experimentally measured (or applied) **total current density** (j_{tot} or *TCD* in mA cm^{-2}). This quantity reflects not only the product distribution (such as the Faradaic efficiency) of the electrolysis reaction, but also the surface-normalized **activity** of the catalyst, as it scales directly with the specific reaction rate for a given product *i*.

Besides the product selectivity and the catalyst activity, also the catalyst **stability** is of central importance for the performance evaluation, if considering in particular a future (industrial) application of the catalyzed process. Catalyst instabilities in the form of chemical or structural (morphological) alterations may lead to losses in the catalyst performance in the form of changed product distributions (e.g., favoring the parasitic HER) or in the form of catalyst surface area changes. These performance losses can be monitored by the (electrolysis) time dependence of the FE_i and j_i values. As it will be demonstrated in this PhD work, stability issues do not remain restricted to the catalyst itself. The entire **reaction environment** (e.g., membrane, gas diffusion electrode etc.) of the catalyst material need to be considered when analyzing and rationalizing observed process performance losses. Performance losses related to structural alterations of the catalyst or its environment can be made visible by post-electrolysis imaging of processed electrodes as detailed below.

The ultimate metric evaluating the performance of the complete electrolysis process is the **Energy Efficiency** (**EE**). This metric typically considers both the cathodic target reaction (e.g., a specific ec-CO_2RR) and the anodic counter reaction (e.g., the OER). The EE_i of a specific target product *i* (e.g., CO) can be written in a general form as follows[43]:

$$EE_i = \frac{\Delta E_{eq}^0 \cdot FE_i}{\Delta E_{eq}^0 + |\eta| + iR_s}$$

where ΔE_{eq}^0 is the equilibrium cell voltage (potential difference) for the desired product *i* ($E_{eq(cathode)}^0 - E_{eq(anode)}^0$ *or* $E_{eq(CO2RR)}^0 - E_{eq(OER)}^0$), FE_i refers to the Faradaic efficiency of the target product *i*, the term iR_s represents the ohmic losses of the complete electrolysis cell, and $|\eta|$ stands for the cell overpotential ($|\eta| = |\eta_{cathode}| + |\eta_{anode}|$) during electrolysis.

Within the frame of this PhD work, only the cathodic sub-process (ec-CO_2RR part) was addressed and further optimized. The anodic OER was typically neglected in the optimization process. From this consideration it becomes obvious that an improvement of the electrolysis process and its energy efficiency regarding a specific target product *i* (e.g., CO) can be achieved by maximizing its Faradaic efficiency FE_i ($\rightarrow$ direct proportionality) and/or by minimizing the cathodic overpotential $|\eta_{cathode}|$ ($\rightarrow$ inverse proportionality).

3.4 Assessment of potential ec-CO_2RR products: Definition of CO as the target product

As discussed above, the ec-CO_2RR can in principle yield a variety of different reaction products, which can be either liquid (e.g., formate, alcohols) or gaseous (e.g., CO, methane etc.). Any process optimization should therefore start with the definition of the target product which then further defines the actual starting point of catalyst development and, as it will be demonstrated herein, also the choice of the catalyst's reaction environment which includes the design of the (gas-diffusion) electrode and the entire cell design. The definition of the ec-CO_2RR target product thereby not only addresses the question of **technical feasibility** but also includes a **socio-economical assessment of the possible target products**. Such assessment has been carried out at the beginning of our group's activities in the field of ec-CO_2RR process development by considering the market prize of a given ec-CO_2RR product at that time and the estimated production costs based on published data on Faradaic efficiencies and cell potentials (see previous section).[44] Of further interest to this assessment is the "size" of the market for a particular product (production volume). Table 3.3 summarizes results of this assessment by also comparing the estimated production costs based on an electrocatalytic processing with the respective mature and well-established synthesis routes. From this analysis it becomes clear that methane can clearly be

excluded from the list of target products as the electrochemical CO_2 conversion will by no means be able to compete with the production of natural gas. Among the C_1, CO and formate stand out, as in both cases an electrochemical conversion seems to be competitive compared to the state-of-the art technologies in terms of production costs. What, however, speaks for CO as the ec-CO_2RR target product is its huge market volume with a yearly production in the range of ca. 210000 Mt. CO is a platform chemical in industry and starts at the beginning of various large-scale production processes, e.g. for the production of methanol.

Table 3.3. Estimated production costs for several ec-CO_2RR products at 2015 according to Durst et al.[44] Adapted from reference 44.

Product	Produced by	Market price [\$ kg^{-1}]	Production volume [Mt y^{-1}]	Price of production via electrolysis [\$ kg^{-1}]
H_2	Steam reforming, partial oxidation of methane or gasification of coal	2-4	65	4
CH_4	Methanogenesis or hydrogenation of CO_2	<0.08	2400	2-4
C_2H_4	Pyrolysis or vapor cracking	0.8 - 105	141	1.6-3.2
CO	Boudouard reaction	0.65	210000	0.27-0.54
$HCOO^-$ /HCOOH	Hydrolysis from methyl formate and formamide or by-product of acetic acid production	0.8-1.2	0.8	0.17-0.34
CH_3OH	From natural gas, coal biomass, waste	0.4-0.6	100	0.70-1.4

Based on this assessment, this doctoral project will focus on CO as the ec-CO_2RR target product.

3.5 Experimental configurations and cell designs for the ec-CO_2RR

Based on the considerations above, it becomes clear that any optimization of the ec-CO_2RR process cannot be restricted solely to the catalyst material itself but must be extended to the entire reaction environment of the catalyst. A maximizing of the partial current density regarding a specific product (e.g., CO) implies that the ec-CO_2RR is typically carried out under experimental conditions of high overpotentials and CO_2 conversion rates. Of note is that industry aims for ec-CO_2RR current densities ranging from several hundred milliamperes per square centimeter to even amperes per square centimeter. These target current densities are comparable to what is already realized in commercial water electrolyzer systems. With respect to CO_2 electrolysis, this means that effects of reactant mass transport must not be neglected in the design of the electrolysis cell. This is exemplified in Figure 3.2 illustrating the CO_2-to-CO conversion in a "classical" experimental configuration in which the catalyst surface is in contact with a "bulk" electrolyte solution. The CO_2 reactant is physically dissolved in the electrolyte solution.

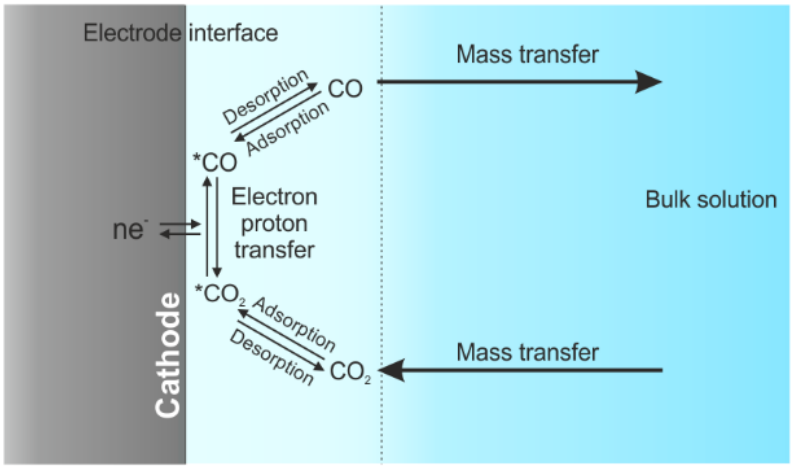

Figure 3.2. Mass transfer and charge transfer effects exemplified for the CO_2-to-CO conversion.

As illustrated in Figure 3.2, the overall reaction can be subdivided into three fundamental steps[45-47] consisting of (i) the diffusional/convectional transport of CO_2 from the interior of the liquid electrolyte solution phase to the solid catalyst surface, (ii) the electrocatalytic conversion itself involving the reactant adsorption, multiple electron/proton transfer steps, and the product (e.g., CO) desorption followed by (iii) the transport of the released product from the catalyst back into the liquid "bulk" electrolyte solution through diffusion/convection. In case the (applied) overpotentials and the resulting reaction rates (current densities) are low, the reaction is solely determined by the intrinsic "kinetics" of the process which can in principle be described by the (Erdey-Grúz) Butler-Volmer equation or its simplified forms (→ kinetic regime). In case the (applied) overpotentials and the resulting reaction rates (current densities) are so high that the local

reactant concentration at the catalyst surface drops down to zero, the (Erdey-Grúz) Butler-Volmer equation fails in describing the overpotentials/current density relationship as the process becomes limited by the reactant mass transport (→ transport regime). A diffusion boundary layer (reactant depletion layer) forms at the interface, which further grows into the electrolyte solution with reaction time/rate and can be several hundred micrometers thick. A further increase of the overpotential does, under these limiting conditions, not lead to a further increase of the partial current density associated to certain ec-CO_2RR products. Note that this does not necessarily mean that the total current density becomes limited in this configuration by the CO_2 mass transport. As argued above, the ec-CO_2RR is typically superimposed by the parasitic HER which, if fed through reductive water splitting, does not become mass transport limited at all at high overpotentials and reaction rates.

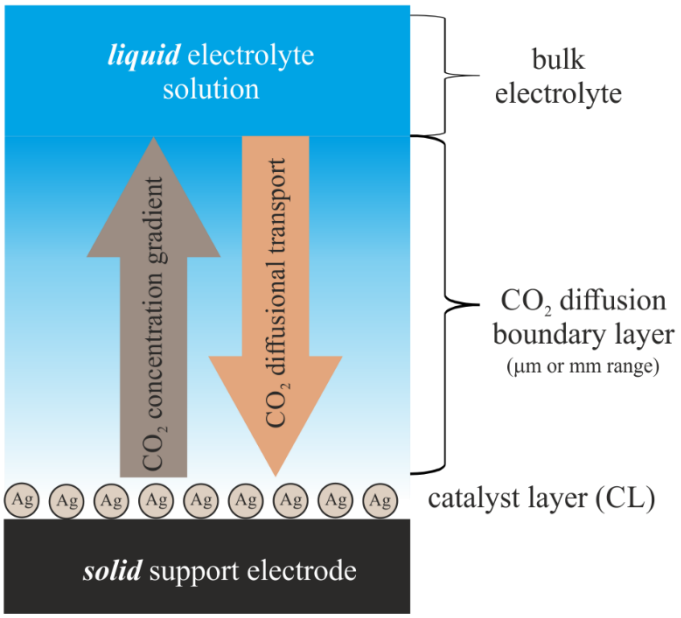

Figure 3.3. Schematic representation of a solid-liquid (catalyst-electrolyte) interface relevant to ec-CO_2RR.

These considerations demonstrate that the electrode and the cell design become crucial for the ec-CO_2RR product distribution particularly when operating the CO_2 electrolysis at high overpotentials and reaction rates. The resulting mass transport effects are particularly severe when using experimental cell/electrode designs based on two-phase (solid-liquid) phase boundaries (see Figure 3.3), which are typically realized in classical H-type cell configurations where the CO_2 reactant is dissolved in the liquid electrolyte phase (see also discussion below). The solubility of CO_2 in aqueous media is, however, limited at room temperature to ca. 30-35 mM L^{-1}.[48] In this configuration, the diffusion path length of the CO_2 reactant is determined by the spatial extent of

the diffusion boundary layer which can, under limiting mass transport conditions and the absence of any convectional mass transport, exceed several hundred micrometers, as mentioned above.

A common strategy to improve the reactant (CO_2) mass transport consists in introducing a third, this means gaseous, phase into the experimental configuration thus (ideally) producing a three-phase solid/liquid/gas boundary (see Figure 3.4-1). In this *idealized scenario*, the catalyst (e.g., Ag nanoparticles) can get in direct contact with the *gaseous* reactant and the liquid/aqueous electrolyte solution. Note, the latter is essential for the ec-CO_2RR by providing the required protons (see Table 3.1). This experimental configuration can in principle be realized by using so-called gas diffusion electrodes (GDEs, see details below). The gaseous CO_2 is typically transported through convective gas flow to the catalytic site where the reaction takes place. Mass transport limitations of the ec-CO_2RR can thus be avoided through the high abundance of the CO_2 reactant, so that other factors may become limiting the reaction rate, e.g., the finite ohmic resistance of the cell (or specific components thereof, e.g., the membrane). However, another scenario appears to be more realistic in representing the phase boundaries under reactive conditions. Depending on the specific experimental configuration, it is more likely that the catalyst becomes at least partially "flooded" by either pure water or by liquid electrolyte (see Figure 3.4-2). The origin of these flooding phenomena will be addressed separately below. In this more *realistic scenario*, a solid/liquid (catalyst/electrolyte) and a liquid/gas (electrolyte/CO_2) interface are combined with each other (→ interconnection of 2 two-phase boundaries).

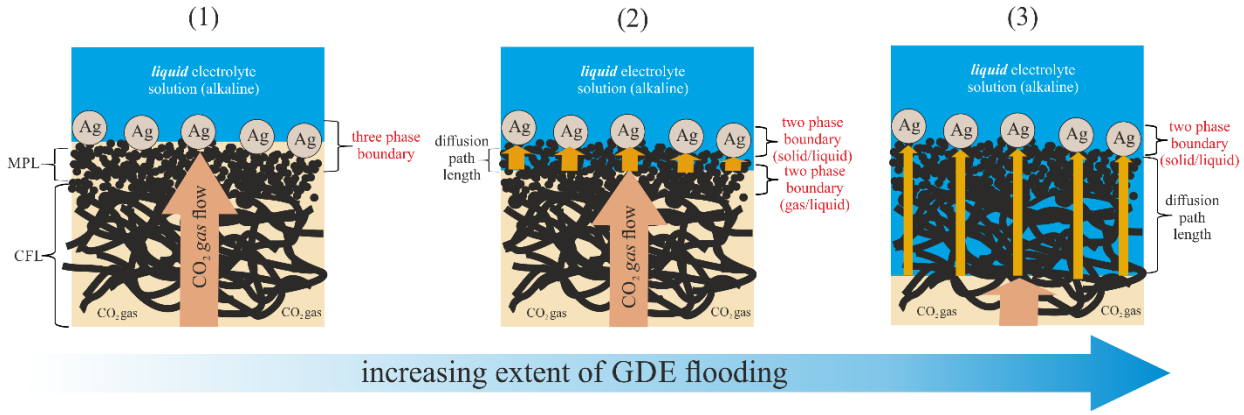

Figure 3.4. Alteration of the interfaces in a GDE due to an increased extent of electrolyte flooding (schematic is not on scale).

If the electrolyte phase, separating the solid catalyst from the gaseous CO_2, remains spatially confined with resulting CO_2 diffusion path lengths in the range of a few micrometers, the CO_2 mass transport can be still considered as fast (see Figure 3.4-3).[49] From these considerations it becomes obvious that there is a gradual transition possible from an ideal three-phase to a two-

phase boundary scenario, the latter representing a completely flooded, this means degraded, GDE (see discussion below). Depending on the extent of electrolyte flooding, the length of the CO_2 diffusion path increases accordingly. Such GDE failure mode is closely related to the (re)appearance of CO_2 mass transport limitations in GDE configurations and not due a failure of the catalyst itself.

3.5.1 Cell design based on a solid-("bulk")liquid interface ($\rightarrow$ two-phase boundary concept)

The most common cell design based on a single solid-liquid interface, i.e. a catalyst/bulk electrolyte interface, is an "H-type" electrolysis cell. This cell is shaped like an H letter. It represents a standard cell confirmation for initial ec-CO_2RR catalyst screening which is characterized by its accessibility and ease of use.[50-52] As shown in Figure 3.5, the H-type cell consists of an anode and cathode compartment which are separated by either a cation (e.g., Nafion®) or an anion exchange (e.g., Sustainion®) membrane. The use of a membrane ($\rightarrow$ divided cell design) is essential for ec-CO_2RR applications to prevent any transport of ec-CO_2RR products from the cathode to the anode where reoxidation processes may occur (e.g., CO $\rightarrow$ CO_2, or formate $\rightarrow$ CO_2) and possibly falsify ec-CO_2RR product quantification. Throughout this PhD project a three-electrode configuration was employed by including a double-junction $Ag/AgCl_{3M}$ electrode (Metrohm) as reference (RE) into the cathode compartment. The anode (CE) typically consisted of a Pt or Ir foil/mesh electrode with a sufficiently high active surface area where the OER as the counter-reaction to the ec-CO_2RR takes place. It should be noted that the use of Pt as anode material in electrolysis reactions is often considered disadvantageous due to possible Pt dissolution into the electrolyte solution with time and its possible re-deposition on the cathode where HER might become favored. ICP-MS analyses of the catholyte and the processed cathode material did, however, never indicate any noticeable cross-contamination with Pt.[53] Ec-CO_2RR product distributions were found similar no matter whether Pt or Ir was used as the anode material.

An aqueous and CO_2-saturated $KHCO_3$ solution was typically applied as the electrolyte in both the anode and cathode compartment. Saturation with CO_2 was achieved through bubbling of CO_2 through the electrolyte. The bubbling of CO_2 through the catholyte continued throughout the electrolysis. The detection and quantification of gaseous ec-CO_2RR products was performed from the catholyte outlet gas stream by means of (online) gas chromatography. This type of setup is easy to operate making it feasible for fast (initial) catalyst screening purposes. For this reason, this experimental configuration was used in particular in the early (pioneering) stage of ec-CO_2RR research.[54-56] As already mentioned, the main experimental drawback of this approach lies in the limited solubility of CO_2 in aqueous media which is in the range of 30-35 mmol L^{-1}.[48] This low solubility limits the achievable partial current density of the targeted CO_2-to-CO conversion to ca.

j_{co_2RR} ≈ 50 mA cm^{-2} thus increasingly favoring the parasitic HER particularly at high overpotentials.[52] Of note is that, in this experimental configuration, the diffusional CO_2 transport might become assisted to some extent by convectional CO_2 transport originating from (i) the continued CO_2 gas bubbling, and (ii) by gas evolution on the cathode caused by the parasitic HER. From these considerations it becomes obvious that industrially relevant partial current densities, e.g., for CO_2-to-CO conversion, higher than 200 mA cm^{-2} cannot be reached with this cell configuration.

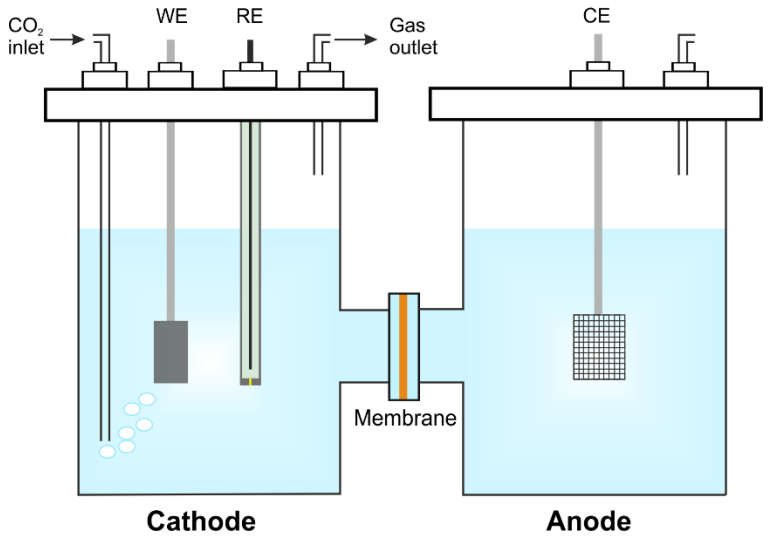

Figure 3.5. Schematic of an H-type electrolysis cell.

3.5.2 Cell designs based on a solid/liquid/gas interface (→ three-phase boundary concept)

To improve the electrolysis cell design regarding its CO_2 transport characteristics, the two-phase boundary concept needs to be replaced by the three-phase boundary approach (Figure 3.4-1) in which CO_2 gets access to the catalyst sites in the form of a gas which can ideally be transported through convection to the place where the reaction takes place (→ gas-fed electrolyzer system). This concept is realized in the form of so-called **gas-diffusion electrodes** (**GDEs**) consisting of a highly porous **gas-diffusion layer** (**GDL**) which serves as the electrical/mechanical support for the covering **catalyst layer** (**CL**) on-top of it.

A representative example of such a GDE with a nanoparticulate Ag catalyst, used in this work for CO_2-to-CO applications, is presented in Figure 3.6. The GDLs commonly used for the ec-CO_2RR are bilayer systems consisting of a porous **carbon fiber layer** (**CFL**) with a thickness in the three-digit micrometer range which provides mechanical stability and excellent electric conductivity to the GDL. On-top of this fibrous CFL there is typically a carbon **microporous layer** (**MPL**) which

serves as support for the catalyst layer and, due to its (super)hydrophobic characteristics (e.g., based on extra PTFE surface coating), prevents rapid and uncontrolled water/electrolyte penetration into the GDL during the electrolysis (→ electrolyte flooding). The MPL, as it will be discussed in more detail below, plays a crucial role in the **active electrolyte/water management** of the electrolyzer which keeps the cathode GDE stable during extended CO_2 electrolysis. The CO_2 reactant is typically transported in gaseous form from the backside of the GDE through the porous CFL and the MPL to the active catalyst sites. The formed gaseous ec-CO_2RR products (e.g., CO) can leave the cathode GDE along with the outward CO_2 gas stream also through the GDL.

The active catalyst is typically dispersed onto the MPL by means of drop-casting or air-brushing techniques. It should be noted that, depending on the deposition technique used, the catalyst layer either remains spatially confined on the MPL or is distributed further in the MPL or sometimes even in the CFL.

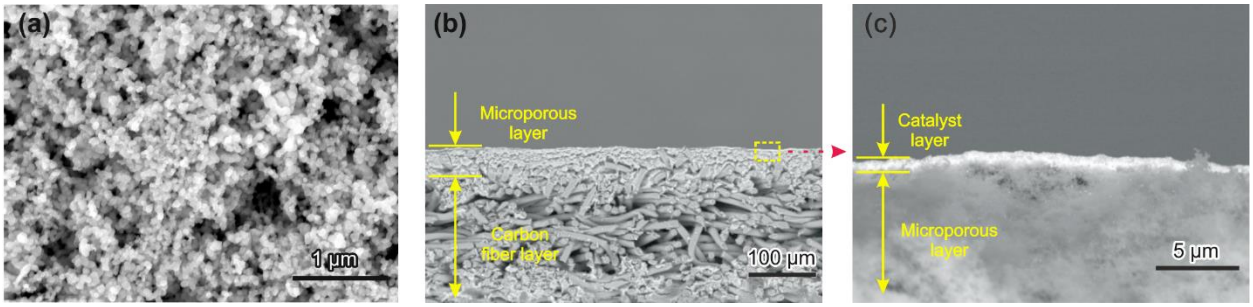

Figure 3.6. (a) Top-down scanning electron microscopy (SEM) image of GDL (catalyst-free). (b) and (c) SEM images showing the cross-sectional structure of a representative GDE modified by a nanoparticulate Ag catalyst for CO_2-to-CO conversion.

In the field of CO_2 electrolysis, two fundamentally different cell concepts are used, depending on how the contact of the cathode GDE with the other essential components of the electrolysis cell (→ electrolyte, membrane and anode compartment) is realized. Which cell design is chosen does also depend on the desired ec-CO_2RR product (→ liquid versus gaseous products). A common cell design is shown in Figure 3.7a, also known as a (micro)fluidic electrolyzer concept, in which the cathode GDE is direct contact with a liquid electrolyte (catholyte). This set-up appears to be particularly advantageous if, in addition to gaseous products (e.g., CO and methane), liquid and/or water-soluble products (e.g. alcohols, formate, etc.) are also produced during CO_2 electrolysis, which can be dissolved by the aqueous electrolyte and transported out of the cell together with the electrolyte (→ laminar flow). Important for the stability of the cathode GDE is not only the structure and the hydrophobic characteristics of the MPL but also experimental conditions (flow rates, gas pressure etc.) which regulate the pressure gap across the GDE. It should be noted here that this cell is designed in such a way that it can also accommodate a reference electrode in the

catholyte. Electrolysis can therefore carried out not only galvanostatically (→ constant current) but also potentiostatically (→ constant potential), like in the classical three-electrode configuration.

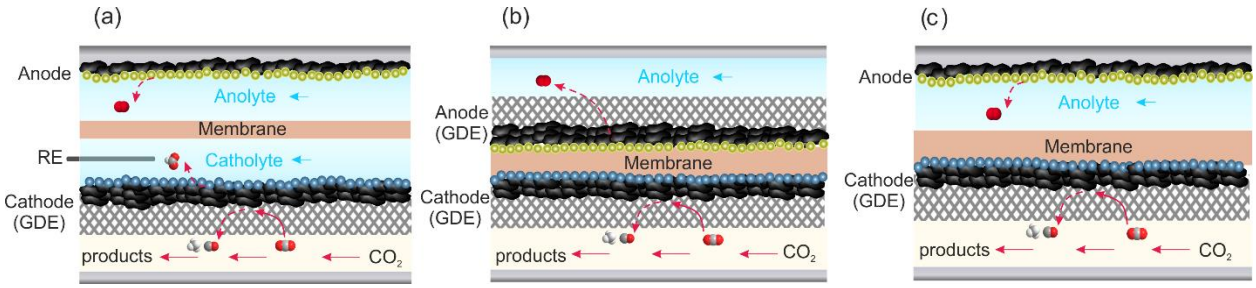

Figure 3.7. Schematic representation of (a) a (micro)fluidic cell configuration, (b) a zero-gap cell configuration, and (c) a semi-zero-gap cell design.

During electrolysis, the hydrophobic characteristics of the MPL effectively prevents electrolyte penetration through CL into the GDL and enables thereby the creation of a gas-liquid-solid (CO_2/electrolyte/catalyst) three-phase interface.[57, 58] The diffusion pathway length for the CO_2 is thereby substantially reduced compared to the classical H-type cell configuration[59, 60] which is a prerequisite for reaching industrially relevant current densities.[57, 61, 62]

Another advantage of using highly porous MPLs is their large inner surface area. When this support is combined with nanoparticulate catalyst materials (e.g., Ag nanoparticles (Ag-NPs)), the result is an electrode with an exceptionally **large electrochemically active surface area** (**ECSA**). These porous supports make it possible to extend the geometric surface area from a few square centimeters to hundreds of square centimeters active area.[63] On the anode side the configuration cathode GDE is in principle mirrored (→ solid/liquid electrolyte interface) with, however, a certain difference related to the support material. For OER applications, a GDL support is not necessarily needed as the reactant for the oxidative water splitting is the aqueous solvent of the anolyte.

One drawback of using this kind of gas-fed electrode systems for routine catalyst screening experiments, e.g. compared to classical H-cells, is certainly related to the time needed to prepare these GDEs and to assemble the flow-cells.[64]

An alternative concept for CO_2 electrolysis cells originates from already mature water electrolysis or fuel cell applications and is based on a so-called **zero-gap configuration**, which is realized in **membrane electrode assemblies** (**MEAs**), as shown in Figure 3.7b. Both, the anode and the cathode catalyst layers are in direct contact with an ion-conducting **polymer electrolyte membrane**. Thus, no liquid electrolyte phase is interfaced with the cathode, at least in the early stage of the electrolysis process. However, in literature it has been reported that water can accumulate in the catalyst layer or, in some cases, throughout the cathode GDE.[65-67] CO_2 and

product transport in the cathode GDE is similarly efficient as in the fluidic cell design resulting also in ec-CO_2RR current densities in the range of several hundred milliamps per square centimeter.[68, 69] This cell design finds application in the field of CO_2 electrolysis when gaseous reaction products (e.g., CO) are primarily formed. It finds applications in more *realistic* electrolyzer systems which are operated under galvanostatic conditions in a two-electrode configuration. If, however, applied for catalyst screening approaches or other more fundamental studies, one certain drawback of this zero-gap design is certainly related to the circumstance that a reference electrode cannot be accommodated in the cathode compartment.

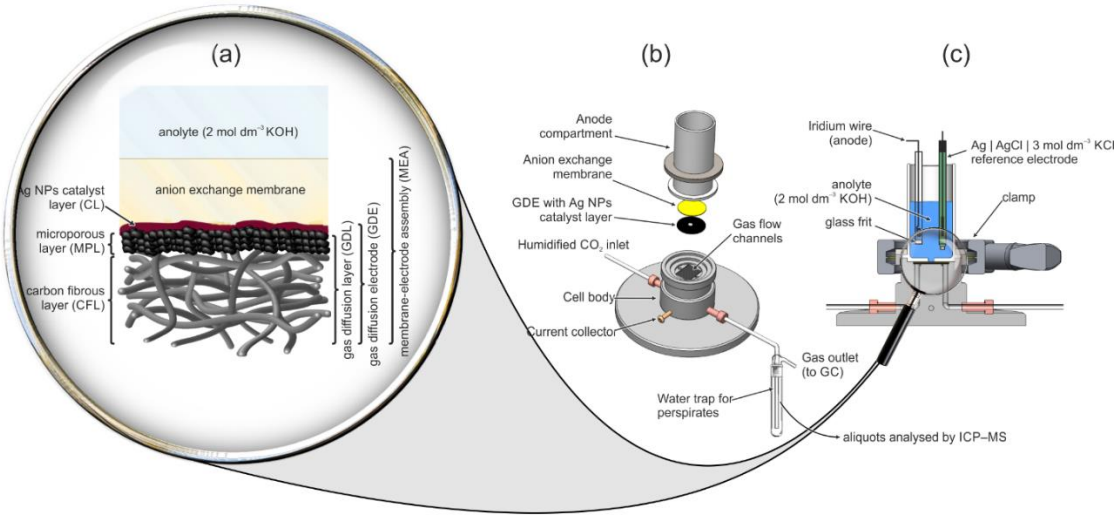

Figure 3.8. The semi-zero-gap configuration for CO_2 electrolysis used in this PhD project. Part (a) shows a close-up view of the MEA, parts (b) and (c) show the exploded and the cross-sectional view of the electrolyzer. Adapted from ref. 70.

In this PhD project a "hybrid" cell design was consistently used which was developed by Arenz et al.[71, 72] originally to study water electrolysis and processes relevant for fuel cell applications and later extended towards ec-CO_2RR applications, as illustrated in Figure 3.8.[73, 74] In this test cell, only the cathode compartment mimics the zero-gap configuration whereas the anode (Pt or Ir foil/mesh) is in contact with a liquid (aqueous) electrolyte solution. This design can therefore be considered as a "**semi-zero-gap" configuration** (see Figure 3.7c). A three-electrode configuration is realized by accommodating the reference electrode into the anode compartment.

A clear advantage of this test cell is the ease of handling at current densities that are comparable to real zero-gap electrolyzers (MEAs).[71] A further advantage of this design consists in the relatively small geometric surface area of the cathode (several square millimeters) which requires only small amounts of newly synthesized catalyst materials.[74, 75]

Chapter 4: Definition of the scientific problem addressed in this doctoral project and the experimental approach followed

The commercialization of ec-CO_2RR requires a high-performance catalyst that is not only selective for a specific product but can also be operated stably in the long term (→ evaluation metrics). In the past, most studies in the field have mainly focused on improving the catalysts regarding the ec-CO_2RR *selectivity* and *activity* by modifying its structure and chemical composition.[76-78] Various catalyst concepts have been successfully applied (e.g., colloidal approaches) or even newly developed (e.g., electrodeposited metal foams) for ec-CO_2RR applications resulting in nanoparticulate or "bulk" materials having different particle shapes (e.g., spherical, cubic, wires etc.) and morphologies (e.g., dendritic, porous etc.).[55, 76, 79, 80] In early work, the problem of *stability* was often neglected, which is, however, of enormous important for the transfer of basic research into a real, commercial process.

4.1 Stability of the electrocatalysts

When discussing the topic of stability, the first thing that comes to mind is of course the catalyst material itself. Efforts to improve catalyst performance also target the electrochemically active surface area, which can be significantly increased, particularly through the use of nanoparticulate materials with a high surface area to volume ratio.[81] However, an intrinsic disadvantage of this colloidal approach is the **thermodynamic instability of such nanoparticulate systems** (compared to the respective "bulk" material), which always strive to minimize their surface energy.[78] As a result of this driving force to minimize surface energy, drastic changes in catalyst morphology can occur, which in turn may have significant consequences for product selectivity (→ impact on catalytic characteristics) and overall current densities (→ surface area effects).

An important scientific question to be addressed here concerns structural modifications of nanoparticulate Ag model catalysts used for the conversion of CO_2 to CO.

These structural changes will be investigated as a function of current density, applied potential and electrolysis time. Before this systematic investigation, it was not clear which factor, e.g. the applied electrolysis potential, the current density or the total transferred charge, was responsible for the structural changes that the Ag nanoparticles underwent as a result of prolonged electrolysis.

A specific aspect of novelty introduced into the field by this PhD thesis concerns the detrimental effect of so-called **capping agents**. These are often used in colloid synthesis to control the particle size distribution and the shape of the nanoparticulate catalyst materials.[82-84] Suspensions of colloidal catalysts, e.g., used to formulate catalyst inks for electrode preparation, typically contain not only capping agents adsorbed on the surface of the nanoparticles, but also an excess of free

capping agents in the solvent. If capping agents remain adsorbed on the particle surface, they may continue to the stabilization of the catalyst during electrolysis. Their presence on the catalyst surface may, however, also affect the ec-CO_2RR product selectivity and the electrochemically accessible surface area of the catalyst.[85, 86] Within this work, **it should be studied in detail under which experimental conditions the capping agents remain adsorbed on the catalyst surface**. It can be hypothesized that this will depend on the applied/resulting current density during electrolysis. Therefore, different results are expected for CO_2 electrolysis performed in H-type cell configurations ($\rightarrow$ low current densities $\leq$ 50 mA cm^{-2}) and in gas-fed systems ($\rightarrow$ high current densities reaching 300 mA cm^{-2}). Representative capping agents used in this PhD project are polymeric additives such as polyethyleneglycol (PEG), polyvinylpyrrolidone (PVP), branched polyethyleneimine (BPEI) and monomers such as citrate. These and other capping agents (e.g., oleylamine (OAm)) were successfully applied in colloidal chemistry to produce nanoparticulate materials of Au[87, 88], Ag[89, 90], Pd[86, 91] Pt[92], and Cu[78, 93] with various shapes and size distributions. As an example, Alinejad et al.[75] investigated the catalytic performance of PVP-stabilized Au-NP catalysts for the ec-CO_2RR using a semi-zero-gap flow-cell cell design. Their experimental results demonstrated that PVP-stabilized Au-NP catalysts favor the HER instead of ec-CO_2RR (see also discussion below on this specific aspect). Safo et al.[92] compared the catalytic performance and structural stability of PVP- and OAm-stabilized platinum nanocubes (Pt-NCs). After partially removing the capping agents by chemical washing, PVP-capped Pt-NCs demonstrated a lower catalytic performance than the corresponding OAm-stabilized catalysts which was attributed to an adsorption which is stronger in case of the PVP. It was concluded in this work that polymeric PVP blocks therefore more efficiently the active catalytic surface sites than the monomeric OAm. A beneficial effect of the stronger adsorbing PVP is, however, related to a more effective stabilizing effects against structural alterations during electrolysis compared to the OAm-capped catalysts which were shown to degrade faster.

So far, most studies addressing stability issues of CO_2 electrolysis were carried out using H-type cell configurations where high performances could be maintained even for longer electrolysis times of days. The current densities remained, however, on the lower milliampere per square centimeter range in these works.[55, 76, 80, 94, 95] In this PhD project, the stability aspects of the **nanoparticulate Ag catalysts** are systematically investigated using a **semi-zero-gap cathode design** that allows the application of **high current densities** of industrial relevance in the range of up to **300 mA cm^{-2}**.

In this study, the stability aspect is not limited to the catalyst itself but is extended to the entire catalytic environment of the zero-gap cathode configuration.

It will be shown here that it is not only the catalyst and its structural changes that determine the time-dependent performance of electrolysis, but also the GDL support and its changes over time. One origin of instability is related to the local pH and changes thereof during electrolysis as the pH dependent ec-CO_2RR either consumes protons or produces hydroxide anions (see Table 3.1). For instance, the near surface pH in an H-type cell configuration at a current density of ca. 10 mA cm^{-2} was approximated to 9. In a CO_2-fed electrolyzer systems and at a current density of ca. 200 mA cm^{-2} the local pH can rise to 13 which will lead, as discussed in detail in the next section, to extra degradation phenomena which are not known from classical H-type cell configrations.[59]

4.2 Stability of the gas diffusion electrode (GDE)

Performance losses of gas-operated cells during extended CO_2 electrolysis can often be attributed to instabilities of the GDEs, which result in the reduced accessibility of the catalyst to the gaseous (or dissolved) CO_2 reactant. Various detrimental effects can contribute to such a GDE instability. An obvious effect is related to the **phenomenon of water/electrolyte flooding**, in which liquid electrolyte not only wets the catalyst layer but also penetrates deeper layers of the MPL, thus blocking the transport channels for the gaseous CO_2. Of note is that these flooding phenomena can occur no matter whether a (micro)fluidic design or a (quasi)zero-gap configuration is used as cathode. Electrolyte flooding promoted by so-called **electrowetting**,[96] which refers to an enhancement of hydrophilic properties when the electrode is electrically charged, thereby overcoming the intrinsic hydrophobic properties of the MPL. In the case of a (semi-)zero-gap configuration, anolyte can cross the membrane and accumulate in the CL and MPL unless transported out of the cathode by active electrolyte management.[97, 98] Under the conditions of a fully flooded cathode, the CO_2 transport situation approaches that present in the H-type cell configuration ($\rightarrow$ solid/liquid interface).[96] Reyer et al.[99] demonstrated for a CO_2-to-CO process over Ag powder catalysts that cathode flooding occurs in a zero-gap electrolyzer when an excess water is transported from the anode to the cathode side, which resulted into ~37% lower Faradaic efficiency for CO and a 450 mV higher cell voltage. It was also demonstrated that water flooding can in principle be mitigated to some extent in such a zero-gap configuration by (i) optimizing the membrane transport properties (e.g., its thickness) preventing massive water transport and (ii) by increasing the hydrophobicity of the CL/MPL. By optimizing the thickness of the membrane, the fluxed water from the anode to the cathode was decreased, and the ec-CO_2RR performance was found to be significantly improved. Lim et al.[100] compared the performance of Ag-NPs dispersed on different carbon supports (e.g., carbon black, carbon nanofibers, and carbon nanocages etc.). The most hydrophobic systems (carbon nanocages) indeed showed the highest Faraday efficiency for CO, which was explained by effective prevention of water/electrolyte flooding. These results already demonstrate that GDE/GDL engineering is the key to optimizing the ec-CO_2RR.

A common strategy to design the local reaction environment of the catalyst is the use of ionomer binders added to the catalyst inks for the CL preparation.[101-107] As an example, Liu et al.[107] demonstrated that hydrophobic Nafion and PTFE nanoparticles can create stable triple-phase boundaries inside SnO_2 nanosheets resulting in partial current densities for formate in the range of 380 mA cm^{-2} and corresponding Faradaic efficiencies in the range of 88%. Dinh et al.[101] optimized a copper based ec-CO_2RR catalyst for ethylene production by "sandwiching" the Cu between a hydrophobic PTFE layer and a supporting layer of carbon-NPs thus preventing flooding to a large extent. This made it possible to maintain an ethylene Faraday efficiency of 75% and current densities between 75 and 100 mA cm^{-2} for 150 operating hours. Similar results were also discussed by Pham et al.[102] reporting a Cu catalysts coated with a thin layer of fluorinated ethylene propylene binder. The changed local reaction environment improved the ec-CO_2RR product distribution even towards C_{2+} products.

In addition to flooding with liquid water/electrolyte, there is a second detrimental process that must be considered when discussing GDE stability. As mentioned above, the application of high current densities in the gas-fed electrolyzers can lead to a considerable alkalization of both the CL and the MPL. As a result, CO_2 can be converted into bicarbonate and carbonate salts according to:

$$CO_2 + 2OH^- \rightarrow CO_3^{2-} + H_2O$$

$$CO_3^{2-} + 2K^+ \rightarrow K_2CO_3 \downarrow \text{ (precipitation)}$$

$$or\ CO_2 + CO_3^{2-} + H_2O + 2K^+ \rightarrow 2KHCO_3 \downarrow \text{ (precipitation)}$$

The precipitation of salts has indeed proven to be one of the biggest obstacles to the long-term stability of ec-CO_2RR liquid flow-through cells and zero-gap electrolyzers.[70, 74, 108-111] A prerequisite for these harmful precipitation processes is the presence of alkali cations on the cathode side (e.g., K^+) which typically stem from the anolyte. An important aspect here is the ability of the commonly used anion exchange membranes (e.g., Sustainion®) to also allow the transfer of metal cations during electrolysis which is further facilitated by the extremely high electrolyte concentrations (in the molar range) often used on the anode side.[69, 109] As a consequence **a solid plaque of alkali carbonates** is formed on the CL or in extreme cases also inside the MPL thus hindering the CO_2 transport through the GDL to the CL and resulting in reduced ec-CO_2RR performances.[69, 112] What accelerates the degradation of the cathode is the hydrophilic/hygroscopic nature of the precipitated carbonates, which further drains water/electrolyte from the anode to the cathode side.[113]

Recent works suggest replacing the alkaline electrolytes by pure water to prevent salt precipitation. It has been, however, also demonstrated that the alkali cations play a crucial role in the catalytic process itself (e.g., though site blocking[114] or the modulation of the interfacial pH[115, 116]) and for

establishing ionic conductivity. As an example, Endrődi et al.[69] demonstrated an increased Faradaic efficiency for CO and a three-times higher current density when using a 0.1 M KOH anolyte in a zero-gap electrolyzer compared to pure water. Since it is unlikely to avoid completely the use of alkali cations, it is preferable to keep the (bi)carbonate concentrations below their solubility limit. To avoid saturation of (bi)carbonate salt concentrations, Xu et al.[111] proposed a cyclic two-step electrolysis of ec-CO_2RR between so-called operational and regeneration voltages. The (bi)carbonate ions generated were transported to the anode electrolyte via electromigration and diffusion, reducing their concentrations on the cathode side. This strategy successfully extended the operation time from ~10 h to 157 h while maintaining a C_2 partial current density of 138 mA cm^{-2} at 80% C_2 selectivity.

In this work, the detrimental carbonate salt precipitation phenomena in the semi-zero-gap cathode configuration are investigated with the aim of following this process as a function of the electrolysis time and depending on the nature of the GDL, the alkali cations, the capping agents, and the binders present at the CL. A concept of active water/electrolyte management shall be developed.

4.3 Experimental approach

The experimental approach to target these goals was based on the use of a semi-zero-gap testing device according to the **Arenz design** which is shown in Figure 3.8. This electrochemical test device is coupled to *online* gas chromatography (GC) which can be complemented by post-electrolysis ion-exchange chromatography (IC) for the detection of non-volatile ec-CO_2RR products.

Processed cathode GDEs were subsequently subjected to a comprehensive post-electrolysis analysis which includes the *top-down* and *cross-sectional* electron microscopic characterization of the Ag-NP catalyst layer. For this purpose, the GDEs were punched and segmented into segments. To gain deeper insights into the structural alterations the used Ag-NPs experienced during electrolysis, the so-called **identical location SEM imaging technique** was applied.[117] As a reference, the unprocessed GDEs were also regularly imaged before electrolysis. For the visualization of changes in the size distribution of the Ag-NPs, meaningful data sets of SEM images were created and subjected to **statistical analysis** (→ size distribution functions).

To visualize and quantify the flooding/salt precipitation phenomena, structural and elemental SEM with energy dispersive X-ray analysis (EDX) were combined with a **newly developed ICP-MS technique** after dissolution of the CL and the precipitated salts from the GDE. 2D-EDX imaging thereby provides the spatial distribution of the Ag catalyst and the potassium (→ chemical "fingerprint" of the presence of (bi)carbonates) whereas corresponding quantitative ICP-MS data

is used for the normalization of the otherwise non-quantitative EDX results. Figure 4.1 demonstrates the general workflow of these standardized microscopic and spectroscopic/spectrometry analyses.

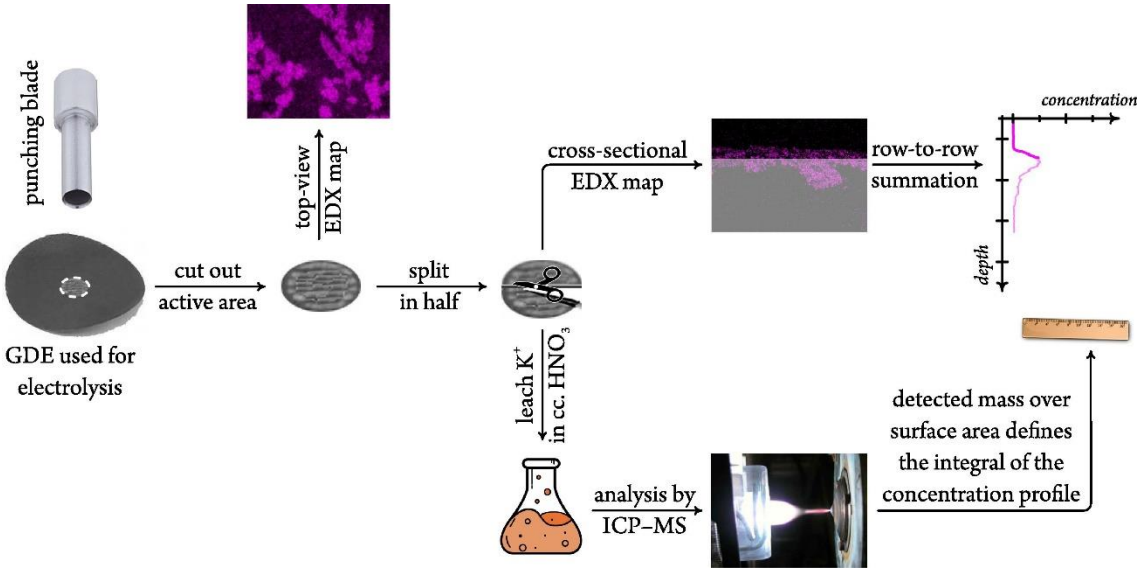

Figure 4.1. Schematic showing the workflow of analyses applied for the visualization of flooding/precipitation phenomena. Adapted from ref. 118.

To relate the (online) electrochemical performance data with electrolyte transport processes through the cathode GDE, the CO_2 outlet was for dedicated experiments attached to a water trap in which transported precipitates could be accumulated and further analyzed also by means of ICP-MS. Again, potassium served as chemical fingerprint for the presence/transport of alkali metal (bi)carbonates.

This PhD project specifically addresses stability aspects of model cathode GDEs in a semi-zero-gap configuration and attempts to link performance degradation in ec-CO_2RR to either structural changes in the nanoparticulate Ag catalyst or to other adverse effects of electrolyte/water flooding and salt precipitation phenomena which may lead to reduced catalyst accessibility to the CO_2 reactant. For this special cell design, concepts for stabilizing the Ag-NPs and active water/electrolyte management will be presented.

Chapter 5: Main findings

5.1 Catalyst degradation during CO_2RR at high current densities and possible concepts of catalyst protection (→ publications 1 and 2)

The first main finding concerns the structural alterations which Ag-NP model catalysts experience during ec-CO_2RR at high applied cathodic potentials (e.g., at –2.354 V vs. Ag/AgCl → high current densities). In fact, it is shown here that **nanoparticulate catalysts are extremely unstable at high current densities**, regardless of which polymeric or monomeric capping agents (e.g., PEG, PVP, or citrate) were used for GDE preparation. An exception to the trend is observed with strongly adsorbing BPEI surfactants, which attenuate the structural degradation of Ag-NPs, but at the expense of losses in the Faraday efficiency for CO formation and of the total/partial current densities (→ **publication 1**).

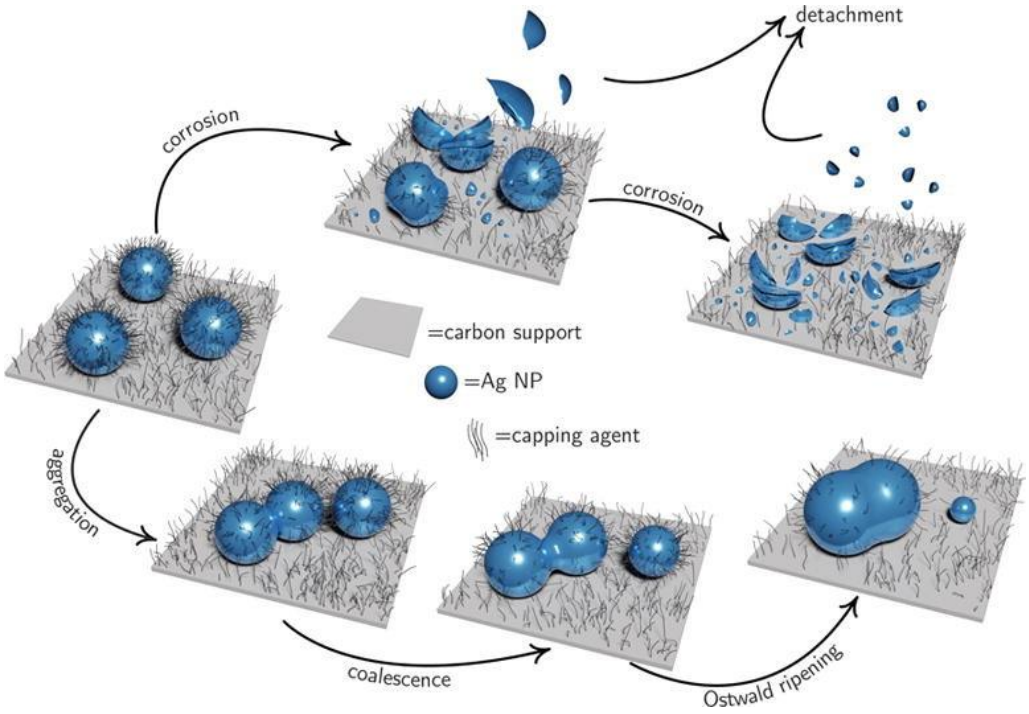

Figure 5.1. Schematic demonstrating various forms of structural degradation nanoparticulate catalysts experience during ec-CO_2RR at high current densities. Adapted from ref. 70.

All forms of structural changes could be observed in top-down SEM analysis, including ***cathodic corrosion***, ***aggregation***, ***particle coalescence*** and ***Ostwald ripening,*** as demonstrated in Figure 5.1. **The type of capping merely determines which of the various degradation pathways is the dominant one**.

It is not, as is sometimes assumed in the literature, the applied potential that governs the extent of structural degradation of the NPs, but rather the **total charge transferred at the given current density**. These extremely strong morphological changes are made possible by the extremely high mobility of nanoparticles or corroded, i.e., decomposed, catalyst material at these high current densities. It is assumed that these structural degradation pathways in the use of nanoparticulate catalysts are of a general nature and are not limited to the specific CO_2-to-CO conversion process. A representative example of such a drastic change in particle size distribution is shown in Figure 5.2. Starting from Ag-NPs with a mean diameter of about 40 nm dispersed on a Freudenberg H23C8 GDL support, coalescence of the Ag catalyst material into micrometer-sized objects is observed after passing a charge of only -300 C cm^{-2} through the cell. The particle size distribution broadens considerably in the course of CO_2 electrolysis.

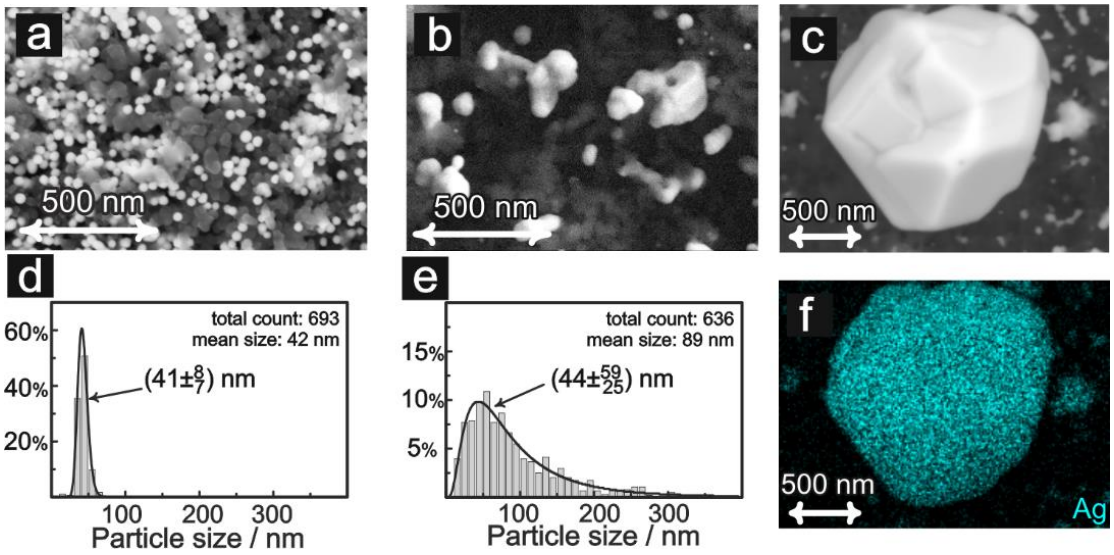

Figure 5.2. (a), (b) Representative top-down SEM images of the GDEs loaded with citrate-capped 40nmAg-NPs. (a) represents the starting situation before electrolysis and (b) shows the Ag catalyst after potentiostatic electrolysis at –2.354 V vs. Ag/AgCl and 300 C cm^{-2} transferred charge. (d), (e) Corresponding particle size distributions derived from more than 500 particles in each case (analyses of multiple SEM images of larges size!). (c) and (f) SEM and EDX imaging of a coalesced Ag particle with a diameter of about 1 µm. Adapted from ref. 70.

Another important finding of this study was that the Faradaic efficiency for CO_2-to-CO conversion is not necessarily affected by these structural changes as long as the electrochemically active surface area (ECSA) of the Ag catalyst remains high enough to feed the current density for ec-CO_2RR. The CO_2-to-CO conversion can be considered as a reaction that is largely insensitive to structural changes of the catalyst. However, far more serious changes in product distribution are to be expected in more structure-dependent reactions, e.g., the conversion of CO_2 into hydrocarbons or alcohols on nanoparticulate Cu catalysts. Performance losses, which were also

observed in CO_2-to-CO conversion, could clearly be attributed to other adverse effects such as electrolyte flooding or salt precipitation (see discussion below).

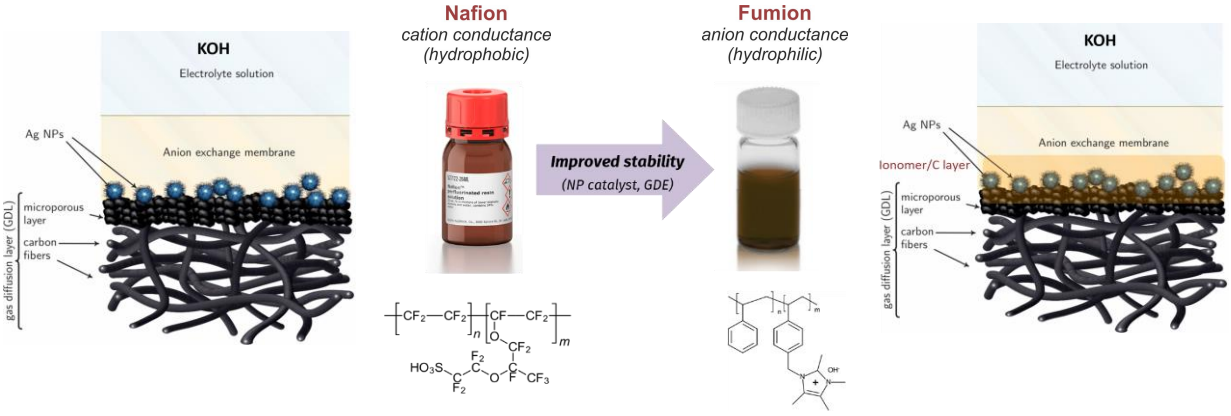

Figure 5.3. Exchange the commonly used **(hydrophobic) Nafion®** binder by an anion conducting **(hydrophilic) Fumion®** binder is the key element of the stabilization concept followed herein.

Based on the analysis of the possible degradation pathways and the unfavorable factors that accelerate this structural change of the Ag-NPs (high current density → high mobility of the catalyst material), **we were able to develop a possible strategy to mitigate the structural degradation of the nanoparticulate catalysts**. This novel approach is based on the immobilization of the Ag-NPs in an ion-conductive, gel-like ionomer matrix as schematically depicted in Figure 5.3.

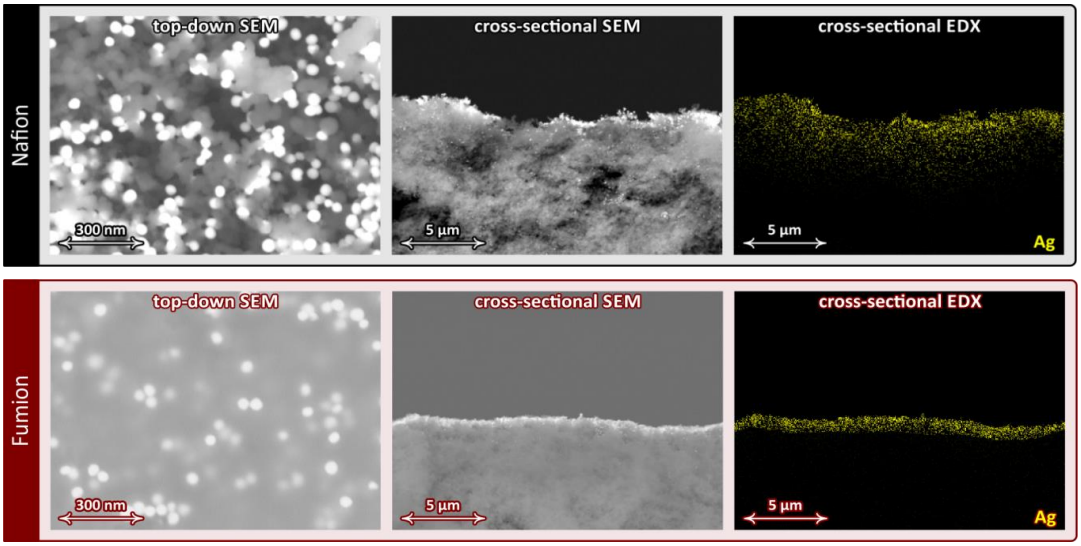

Figure 5.4. Top-down and cross-sectional SEM/EDX characterization of the 50 nm Ag-NPs containing CL prepared either by using Nafion® or Fumion® as the binder material. Adapted from ref. 119.

The main difference lies in the increased hydrophilicity of the Fumion® binder used, which prevents its dispersion together with the Ag-NPs on and in the superhydrophobic MPL of the GDL during electrode preparation (→ **publication 2**). The latter is typically observed when Nafion® is used as a binder for the preparation of the CL. Instead, a jelly-like film forms on the MPL in which the Ag-NPs are embedded and immobilized. However, this anion conducting ionomer matrix remains permeable for the CO_2 reactant and for the transport of the alkaline electrolyte (like the used anion exchange membrane). These differences in the structure of the CL mediated by the used binder material is exemplified in Figure 5.4. Combined top-down and cross-sectional SEM/EDX imaging clearly proves the higher degree of Ag catalyst dispersion into the GDL in the Nafion® case whereas the Ag-NPs remain spatially confined on-top of the MPL in case of the Fumion® binder. The conclusion of Ag-NPs embedded into a Fumion® matrix is further corroborated by the top-down SEM imaging in Figure 5.4. Ag-NPs appear sharp and well resolved in the Nafion® case whereas the catalyst particles and the carbon support appear "blurry" in the Fumion® case due to the presence of the ionomer film. The beneficial effect of the protecting jelly Fumion® film on the structural stability of the Ag-NPs is significant as exemplarily demonstrated in Figure 5.5.

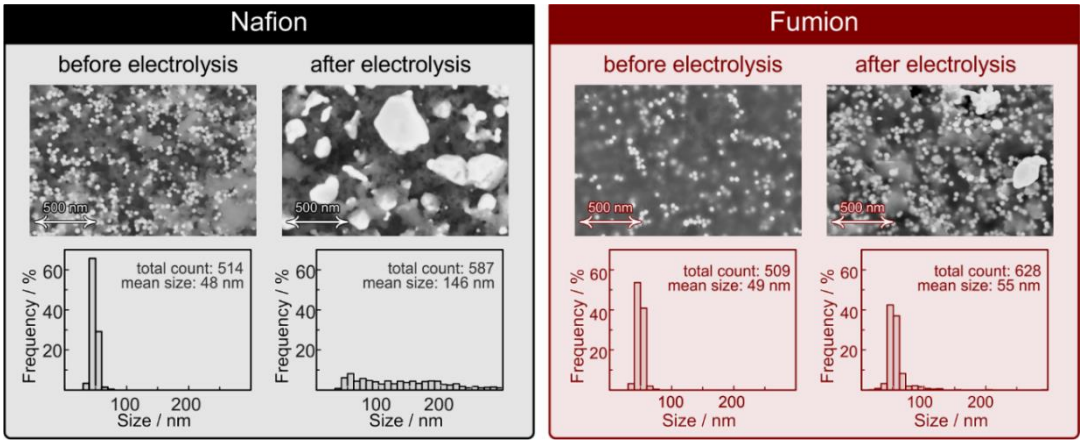

Figure 5.5. Proof of concept: Stabilization of LA (lipoic acid)-capped Ag-NPs by their embedment and immobilization in an anion conducting and hydrophilic Fumion® matrix. The structural degradation of Ag-NPs in the Nafion®/LA system is like what has been observed for citrate-capped Ag-NPs. Adapted from ref. 119.

5.2 GDE degradation during CO_2RR at high current densities and possible concepts of GDE stabilization (→ publications 2, 3, 4, and 5)

As discussed above, catalyst degradation is only one possible cause of performance losses often observed in CO_2 electrolysis and may even not be the most important factor, at least for the CO_2-to-CO conversion. Electrolyte flooding and (bi)carbonate salt formation typically lead to massive structural changes in the GDE, which may block the CL itself and clog the transport channels for the CO_2 reactant in the MPL. A blockage of the Ag-NP CL and related performance losses are exemplary demonstrated in Figure 5.6. Contact angle measurements are typically used to show how the initial hydrophobic characteristics of the GDE (mainly introduced by the MPL and the binder) are changed after electrolysis due to precipitation of hygroscopic salts in and on the CL.

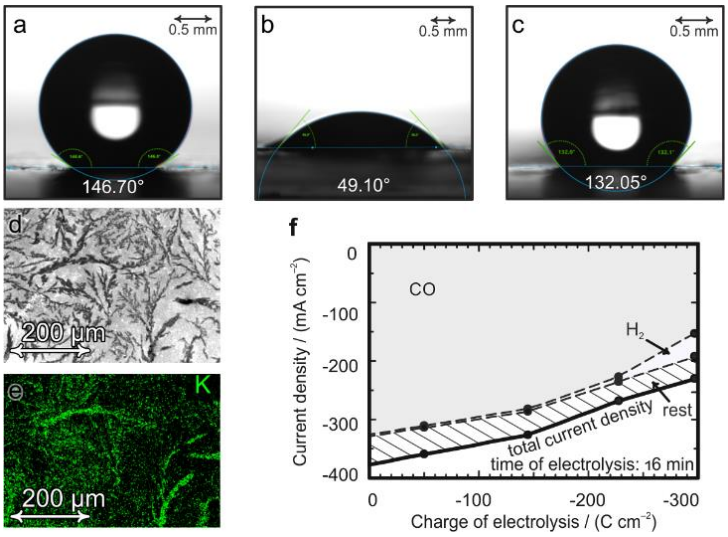

Figure 5.6. Contact angle measurements of (a) an as-prepared GDE, (b) GDE after electrolysis, and (c) GDE after cleaning by washing with Milli-Q water. (d) Top-down SEM of the GDE after electrolysis and (e) the corresponding EDX mapping. (f) Total and partial current densities indicating the resulting products distribution electrolysis plotted as a function of the passed charge density at a constant electrolysis potential of –2.354 vs. Ag/AgCl. The "rest" could be attributed to formate formation. Adapted from ref. 70.

An important finding in this context is that the hydrophobic properties of the GDE and electrolysis performance can in principle be recovered by removing the salt precipitates from the GDE surface, e.g., by washing with Milli-Q water.

With zero-gap and semi-zero-gap cell designs, it is not possible to completely prevent water/electrolyte transport across the membrane. Without proper water/electrolyte management, liquid electrolyte accumulates in the CL and can even flood the MPL. The reaction of gaseous CO_2 with the alkaline electrolyte could further lead to precipitation of alkali (bi)carbonate salts, thus further aggravating the situation in the GDE during CO_2 electrolysis. As long as the transport channels in the GDE are open, electrolyte and water can in principle be transported out of the cathode GDE together with the CO_2 gas stream. The transport of *liquid* electrolyte through the GDL and its accumulation/condensation on the backside of the GDL in the form of droplets is also known as (liquid) **electrolyte perspiration**.[66, 120]

Key to the successful correlation of GDE stabilizing/destabilizing factors and electrolyte transport phenomena through the cathode GDE was the development of ICP-MS-based analytical techniques that enabled the detection and quantification of perspired electrolyte in an external water trap outside the electrolysis cell (→ **publication 3**). Based on this general analytical approach, it has been shown that **introducing larger voids and larger, micron-sized cracks** into the MPL **is** extremely **beneficial to the electrolyte perspiration process** and thus contributes substantially to the stabilization of the GDE (→ **publication 4**) as this opens more and larger transport channels for the liquid electrolyte. It should be also noted that water and electrolyte can in principle be transported also in the form of aerosols (mini droplets) directly with the outward CO_2 gas stream. This transport pathway would not necessarily lead to the condensation of water/electrolyte droplets on the backside of the GDL.

An excess of polymeric capping agents (e.g., PEG, PVP and BPEI) dispersed in the MPL during CL preparation has been also proved to be detrimental to the stability of the GDE, as they can also clog the transport channels inside the MPL and inhibit electrolyte perspiration. Possible concepts of GDE stabilization therefore involve NP synthesis approaches minimizing or even avoiding completely the use of capping agents. Post-synthesis removal of capping agents via centrifugation immediately before CL preparation is also a viable approach to stabilize the GDE while maintaining the NP catalyst concept **(→ publication 5**).

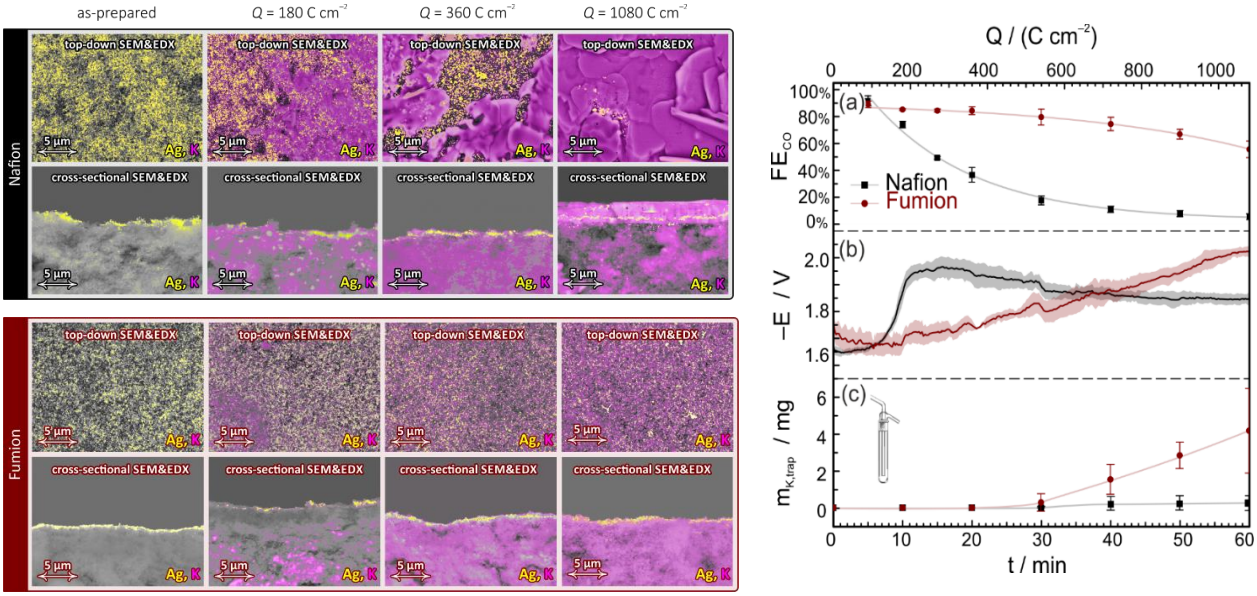

Figure 5.7. Top-down and cross-sectional SEM/EDX analysis of GDEs before and after electrolysis (left panel). Correlation of ec performance data, cell voltages and electrolyte perspiration (right panel). Adapted from ref. 119.

The embedding of the nanoparticulate catalyst in an ionomer matrix, as described in section 5.1, not only stabilizes the NPs by immobilization, but also facilitates the transport of the hydroxide ions away from the catalyst that form during electrolysis (→ pH dependence of the HER and ec-CO_2RR), provided an ion conducting ionomer like Fumion® is used. This facilitated hydroxide transport is discussed as the reason why the solubility product of the alkali metal (bi)carbonates within the CL layer is not exceeded so quickly during ec-CO_2RR at high current densities (→ **publication 2**). A prime example of this concept of GDE stabilization is presented in Figure 5.7. If Nafion® is used as the binder, a thick potassium carbonate plaque forms quickly after initiating the ec-CO_2RR thus physically blocking the Ag catalyst layer as evidenced by top-down and cross-sectional SEM/EDX imaging (Figure 5.7, left panel).

With the Fumion® binder, the Ag catalyst layer remains, however, accessible for the CO_2. Accordingly, the CO_2-to-CO efficiency drops down quickly in the Nafion® but not in the Fumion® case. In the latter case, the sustained ec-CO_2RR performance clearly correlates with the GDE's ability to effectively perspire the electrolyte (Figure 5.7, right panel). The suppression of the ec-CO_2RR leads to an increase in the cell voltage due to a feedback reaction of the system during operation under galvanostatic conditions and thus to the activation of the carbon carrier for the parasitic HER, which begins to dominate the product distribution in the failure scenario.

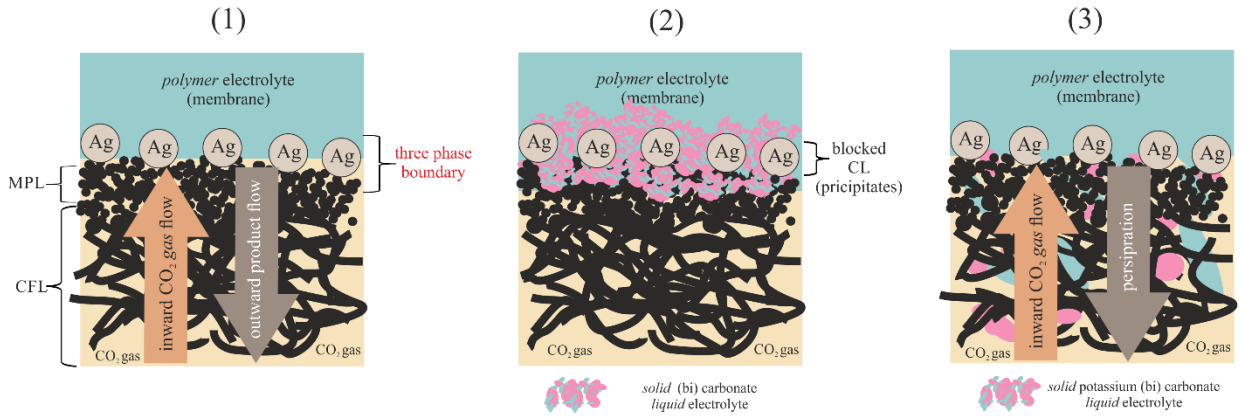

Figure 5.8. Schematic representation of (1) an ideal semi-zero-gap configuration, (2) a GDE degraded by confined (bi)carbonate precipitation, and (3) a stabilized GDE with a functioning electrolyte management (effective perspiration).

Figure 5.8 summarized the results graphically. Scenario 1 represents an idealized semi-zero-gap configuration (e.g., initial stage of electrolysis), scenario 2 shows a GDE degraded by spatially confined alkali (bi)carbonate precipitation blocking the CL and the MPL, and scenario 3 shown a functioning GDE with active water/electrolyte management (effective perspiration).

It should be noted that that the amount of potassium accumulated in the external water trap is enormous (scenario 3 in Figure 5.8). Milligrams of potassium were detected after passing ca. 1000 C cm^{-2} through the cell.

These studies clearly showed that the precipitation of *solid* salts during ec-CO_2RR may be even more severe for the GDE stability than the "flooding" with *liquid* electrolyte. This finding became supported by further control experiments varying the nature of the alkali cation in the anolyte**. It could be shown in this work that the rate at which the GDE degrades scales with the solubility of the alkali metal (bi)carbonate salt** (abbreviated as "s") which depends on the nature of the alkali metal cations (→ **publication 2**) and decreases in the sequence of

$$s(Cs^+) > s(K^+) > s(Na^+) > s(Li^+)$$

Table 5.1 provides the respective information on the solubility of alkali metal salts which may precipitate during ec-CO2RR at high current densities.

Table 5.1. Solubility of the alkali (bi)carbonate salts.[121]

Cations	Solubility (M) at 20 °C		
	OH^-	HCO_3^-	CO_3^{2-}
Li^+	5.34	-	0.18
Na^+	25.0	1.23	2.90
K^+	21.6	3.62	8.03
Cs^+	20.0	10.78	8.01

Conclusions and outlook

In this PhD project, a semi-zero-gap electrolysis test cell (Arenz design) was successfully applied to study the structural (in)stability of nanoparticulate Ag model catalysts at ec-CO_2RR current densities of industrial relevance. Post-electrolysis analyses by means of SEM/EDX imaging demonstrated a rapid degradation of the Ag-NPs catalysts, no matter which capping agent was used. Based on in-depth analyses, we developed a promising concept of NP stabilization which is based on their embedment and immobilization in an anion conducting (Fumion®) ionomer matrix. As the most severe sources of GDE degradation, we identified, however liquid electrolyte flooding and carbonate salt precipitation phenomena. This PhD work demonstrated that active water/electrolyte management is essential for the GDE stabilization if working with (semi)-zero-gap cell configurations.

A certain disadvantage of the analytical post-electrolysis applied herein is that this approach cannot in all cases distinguish between alkali metal salts that have formed within the GDL after the electrolysis in the sense of a drying effect or already during the electrolysis. To address this certain weakness of the analytical approach, our post-electrolysis analyzes will be complemented in the future by advanced *operando* tomographic techniques based on X-ray diffraction and X-ray scattering. These enable the spatially resolved distinction between liquid electrolyte and solid precipitates within the GDE during ec-CO_2RR. Our own cross-sectional SEM/EDX technique is further developed into a 3D tomography technique by processing numerous analyzes of sectioned GDEs. Advanced laser techniques will be applied to slice the processed GDEs.

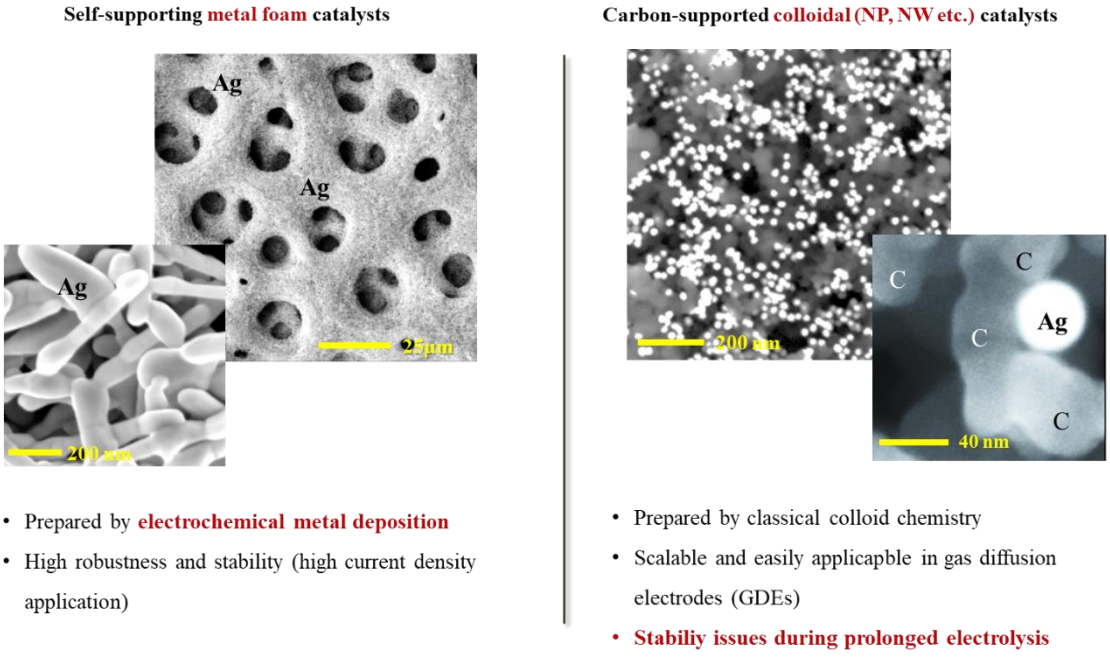

Certain factors that can also contribute to the stabilization of cathode GDEs have not yet been taken into account in this doctoral project and concern physical cell parameters, e.g. the so-called pressure gap, the cell temperature and the gas flow velocity. The role of these factors will be investigated in detail in the future using advanced and automated parallel electrolyzer setups that are currently being set up as an initiative of the collaborative research center NCCR *Catalysis*.

Capping agents, used for the synthesis of nanoparticulate catalyst, have been identified as one potential source for GDE instabilities. In the future we will also explore other approaches of catalyst synthesis and GDE fabrication which are based on catalyst (metal) electrodeposition at high current densities thus avoiding any use of capping agents. Well-studied nanoparticulate catalysts will be compared to respective high surface area metal foam catalysts (see Figure above).

Disclosure of use of AI-assisted technologies

Disclosure of use of AI-assisted technologies

☒ During the preparation of this work, I have **NOT** used any AI-assisted technologies.

☐ During the preparation of this work, I used the following tools:

1. [NAME TOOL / SERVICE] - reason for use
2. [NAME TOOL / SERVICE] - reason for use
3. [NAME TOOL / SERVICE] - reason for use

After using these tools/services, I reviewed and edited the content as needed and take full responsibility for the content of the publication. I am aware that in case of dis-compliance, the generated text is considered plagiarism with its legal consequences.

20.11.2023 Bern

Mengfang Liu

References

1. Cox, A. N., *Allen's astrophysical quantities*. Springer: 2015.
2. Atmosphere, U. S., *US standard atmosphere*. National Oceanic and Atmospheric Administration: 1976.
3. Lacis, A. A.; Schmidt, G. A.; Rind, D.; Ruedy, R. A., Atmospheric CO_2: Principal Control Knob Governing Earth's Temperature. *Science* **2010,** *330* (6002), 356-359.
4. Ledley, T. S.; Sundquist, E. T.; Schwartz, S. E.; Hall, D. K.; Fellows, J. D.; Killeen, T. L., Climate change and greenhouse gases. *Eos* **1999,** *80* (39), 453-458.
5. Linstorm, P., NIST chemistry webbook, NIST standard reference database number 69. *J. Phys. Chem. Ref. Data, Monograph* **1998,** *9*, 1-1951.
6. Mitchell, J. F., The "greenhouse" effect and climate change. *Rev. Geophys.* **1989,** *27* (1), 115-139.
7. Keeling, C. D., The concentration and isotopic abundances of atmospheric carbon dioxide in rural areas. *Geochim. Cosmochim. Acta* **1958,** *13* (4), 322-334.
8. C. D. Keeling, S. C. P., R. B. Bacastow, M. Wahlen, T. P. Whorf, M. Heimann, and H. A. Meijer Exchanges of atmospheric CO_2 and $^{13}CO_2$ with the terrestrial biosphere and oceans from 1978 to 2000.
9. Armstrong McKay, D. I.; Staal, A.; Abrams, J. F.; Winkelmann, R.; Sakschewski, B.; Loriani, S.; Fetzer, I.; Cornell, S. E.; Rockstrom, J.; Lenton, T. M., Exceeding 1.5 °C global warming could trigger multiple climate tipping points. *Science* **2022,** *377* (6611), eabn7950.
10. Davis, S. J.; Caldeira, K.; Matthews, H. D., Future CO_2 Emissions and Climate Change from Existing Energy Infrastructure. *Science* **2010,** *329* (5997), 1330-1333.
11. Fourier, J. B. J., *Théorie du mouvement de la chaleur dans les corps solides*. 1824.
12. Arrhenius, S., XXXI. On the influence of carbonic acid in the air upon the temperature of the ground. *Lond. Edinb. Dublin philos. mag. j. sci.* **1896,** *41* (251), 237-276.
13. Arrhenius, S., *Worlds in the making: the evolution of the universe*. Harper: 1908.
14. Wheeler, T.; von Braun, J., Climate Change Impacts on Global Food Security. *Science* **2013,** *341* (6145), 508-513.
15. Müller, J. D.; Schneider, B.; Rehder, G., Long-term alkalinity trends in the Baltic Sea and their implications for CO_2-induced acidification. *Limnol. Oceanogr.* **2016,** *61* (6), 1984-2002.
16. Ekwurzel, B.; Boneham, J.; Dalton, M. W.; Heede, R.; Mera, R. J.; Allen, M. R.; Frumhoff, P. C., The rise in global atmospheric CO_2, surface temperature, and sea level from emissions traced to major carbon producers. *Clim. Change* **2017,** *144* (4), 579-590.
17. The Paris Agreement. https://unfccc.int/process-and-meetings/the-paris-agreement (accessed August 30).
18. Bui, M.; Adjiman, C. S.; Bardow, A.; Anthony, E. J.; Boston, A.; Brown, S.; Fennell, P. S.; Fuss, S.; Galindo, A.; Hackett, L. A.; Hallett, J. P.; Herzog, H. J.; Jackson, G.; Kemper, J.; Krevor, S.; Maitland, G. C.; Matuszewski, M.; Metcalfe, I. S.; Petit, C.; Puxty, G.; Reimer, J.; Reiner, D. M.; Rubin, E. S.; Scott, S. A.; Shah, N.; Smit, B.; Trusler, J. P. M.; Webley, P.; Wilcox, J.; Mac Dowell, N., Carbon capture and storage (CCS): the way forward. *Energy Environ. Sci.* **2018,** *11* (5), 1062-1176.

19. Vega, F.; Baena-Moreno, F. M.; Gallego Fernández, L. M.; Portillo, E.; Navarrete, B.; Zhang, Z., Current status of CO_2 chemical absorption research applied to CCS: Towards full deployment at industrial scale. *Appl. Energy* **2020,** *260*.

20. Chery, D.; Lair, V.; Cassir, M., Overview on CO_2 Valorization: Challenge of Molten Carbonates. *Front. Energy Res.* **2015,** *3*.

21. Viebahn, P.; Vallentin, D.; Höller, S., Prospects of carbon capture and storage (CCS) in China's power sector – An integrated assessment. *Appl. Energy* **2015,** *157*, 229-244.

22. Merkel, T. C.; Wei, X.; He, Z.; White, L. S.; Wijmans, J.; Baker, R. W., Selective exhaust gas recycle with membranes for CO_2 capture from natural gas combined cycle power plants. *Ind. Eng. Chem. Res.* **2013,** *52* (3), 1150-1159.

23. Zweigel, P.; Arts, R.; Lothe, A. E.; Lindeberg, E. B., Reservoir geology of the Utsira Formation at the first industrial-scale underground CO_2 storage site (Sleipner area, North Sea). *Geol. Soc. Spec. Publ.* **2004,** *233* (1), 165-180.

24. Bains, P.; Psarras, P.; Wilcox, J., CO_2 capture from the industry sector. *Prog. Energy Combust. Sci.* **2017,** *63*, 146-172.

25. Madejski, P.; Chmiel, K.; Subramanian, N.; Kuś, T., Methods and techniques for CO_2 capture: Review of potential solutions and applications in modern energy technologies. *Energies* **2022,** *15* (3), 887.

26. Liang, Z.; Rongwong, W.; Liu, H.; Fu, K.; Gao, H.; Cao, F.; Zhang, R.; Sema, T.; Henni, A.; Sumon, K.; Nath, D.; Gelowitz, D.; Srisang, W.; Saiwan, C.; Benamor, A.; Al-Marri, M.; Shi, H.; Supap, T.; Chan, C.; Zhou, Q.; Abu-Zahra, M.; Wilson, M.; Olson, W.; Idem, R.; Tontiwachwuthikul, P., Recent progress and new developments in post-combustion carbon-capture technology with amine based solvents. *Int. J. Greenhouse Gas Control* **2015,** *40*, 26-54.

27. Zhao, B.; Liu, F.; Cui, Z.; Liu, C.; Yue, H.; Tang, S.; Liu, Y.; Lu, H.; Liang, B., Enhancing the energetic efficiency of MDEA/PZ-based CO_2 capture technology for a 650 MW power plant: Process improvement. *Appl. Energy* **2017,** *185*, 362-375.

28. Li, Y.; Rui, W.; Qingmin, Z.; Zhaojie, X., Technological advancement and industrialization path of Sinopec in carbon capture, utilization and storage, China. *Energy Geosci.* **2022**, 100107.

29. Beuttler, C.; Charles, L.; Wurzbacher, J., The Role of Direct Air Capture in Mitigation of Anthropogenic Greenhouse Gas Emissions. *Front. Clim.* **2019,** *1*.

30. Gutknecht, V.; Snæbjörnsdóttir, S. Ó.; Sigfússon, B.; Aradóttir, E. S.; Charles, L., Creating a carbon dioxide removal solution by combining rapid mineralization of CO_2 with direct air capture. *Energy Procedia* **2018,** *146*, 129-134.

31. Aresta, M.; Dibenedetto, A.; Angelini, A., Catalysis for the valorization of exhaust carbon: from CO_2 to chemicals, materials, and fuels. technological use of CO_2. *Chem. Rev.* **2014,** *114* (3), 1709-42.

32. Rudnev, A. V.; Fu, Y. C.; Gjuroski, I.; Stricker, F.; Furrer, J.; Kovacs, N.; Vesztergom, S.; Broekmann, P., Transport Matters: Boosting CO_2 Electroreduction in Mixtures of [BMIm][BF_4]/Water by Enhanced Diffusion. *ChemPhysChem* **2017,** *18* (22), 3153-3162.

33. Haas, T.; Krause, R.; Weber, R.; Demler, M.; Schmid, G., Technical photosynthesis involving CO_2 electrolysis and fermentation. *Nat. Catal.* **2018,** *1* (1), 32-39.

34. Qiao, J.; Liu, Y.; Hong, F.; Zhang, J., A review of catalysts for the electroreduction of carbon dioxide to produce low-carbon fuels. *Chem. Soc. Rev.* **2014,** *43* (2), 631-75.

35. Hori, Y.; Wakebe, H.; Tsukamoto, T.; Koga, O., Electrocatalytic process of CO selectivity in electrochemical reduction of CO_2 at metal electrodes in aqueous media. *Electrochim. Acta* **1994,** *39* (11-12), 1833-1839.

36. Zang, Y.; Wei, P.; Li, H.; Gao, D.; Wang, G., Catalyst Design for Electrolytic CO_2 Reduction Toward Low-Carbon Fuels and Chemicals. *Electrochem. Energy Rev.* **2022,** *5* (S1).

37. Rahaman, M.; Dutta, A.; Zanetti, A.; Broekmann, P., Electrochemical Reduction of CO_2 into Multicarbon Alcohols on Activated Cu Mesh Catalysts: An Identical Location (IL) Study. *ACS Catal.* **2017,** *7* (11), 7946-7956.

38. Nam, D. H.; De Luna, P.; Rosas-Hernandez, A.; Thevenon, A.; Li, F.; Agapie, T.; Peters, J. C.; Shekhah, O.; Eddaoudi, M.; Sargent, E. H., Molecular enhancement of heterogeneous CO_2 reduction. *Nat. Mater.* **2020,** *19* (3), 266-276.

39. Xiao, H.; Cheng, T.; Goddard, W. A., 3rd, Atomistic Mechanisms Underlying Selectivities in C_1 and C_2 Products from Electrochemical Reduction of CO on Cu(111). *J. Am. Chem. Soc.* **2017,** *139* (1), 130-136.

40. Hatsukade, T.; Kuhl, K. P.; Cave, E. R.; Abram, D. N.; Jaramillo, T. F., Insights into the electrocatalytic reduction of CO_2 on metallic silver surfaces. *PCCP* **2014,** *16* (27), 13814-9.

41. Peterson, A. A.; Nørskov, J. K., Activity Descriptors for CO_2 Electroreduction to Methane on Transition-Metal Catalysts. *J. Phys. Chem. Lett.* **2012,** *3* (2), 251-258.

42. Cheng, J.; Hu, P., Utilization of the three-dimensional volcano surface to understand the chemistry of multiphase systems in heterogeneous catalysis. *Journal of the American Chemical Society* **2008,** *130* (33), 10868-10869.

43. Sajna, M. S.; Zavahir, S.; Popelka, A.; Kasak, P.; Al-Sharshani, A.; Onwusogh, U.; Wang, M.; Park, H.; Han, D. S., Electrochemical system design for CO_2 conversion: A comprehensive review. *J. Environ. Chem. Eng.* **2023,** *11* (5).

44. Durst, J.; Rudnev, A.; Dutta, A.; Fu, Y.; Herranz, J.; Kaliginedi, V.; Kuzume, A.; Permyakova, A. A.; Paratcha, Y.; Broekmann, P.; Schmidt, T. J., Electrochemical CO_2 Reduction - A Critical View on Fundamentals, Materials and Applications. *Chimia (Aarau)* **2015,** *69* (12), 769-776.

45. Noel, T.; Cao, Y.; Laudadio, G., The Fundamentals Behind the Use of Flow Reactors in Electrochemistry. *Acc. Chem. Res.* **2019,** *52* (10), 2858-2869.

46. Qu, D.; Wang, G.; Kafle, J.; Harris, J.; Crain, L.; Jin, Z.; Zheng, D., Electrochemical Impedance and its Applications in Energy-Storage Systems. *Small Methods* **2018,** *2* (8).

47. Gu, M.; Kim, B. S., Electrochemistry of Multilayer Electrodes: From the Basics to Energy Applications. *Acc. Chem. Res.* **2021,** *54* (1), 57-69.

48. Chen, Y.; Lewis, N. S.; Xiang, C., Operational constraints and strategies for systems to effect the sustainable, solar-driven reduction of atmospheric CO_2. *Energy Environ. Sci.* **2015,** *8* (12), 3663-3674.

49. Johnson, E. F.; Boutin, E.; Liu, S.; Haussener, S., Pathways to enhance electrochemical CO_2 reduction identified through direct pore-level modeling. *EES Catal.* **2023,** *1* (5), 704-719.

50. Zhang, N.; Zhang, X.; Tao, L.; Jiang, P.; Ye, C.; Lin, R.; Huang, Z.; Li, A.; Pang, D.; Yan, H.; Wang, Y.; Xu, P.; An, S.; Zhang, Q.; Liu, L.; Du, S.; Han, X.; Wang, D.; Li, Y., Silver Single-Atom Catalyst for Efficient Electrochemical CO_2 Reduction Synthesized from Thermal Transformation and Surface Reconstruction. *Angew. Chem. Int. Ed.* **2021,** *60* (11), 6170-6176.

51. Liu, S.; Sun, C.; Xiao, J.; Luo, J.-L., Unraveling Structure Sensitivity in CO_2 Electroreduction to Near-Unity CO on Silver Nanocubes. *ACS Catal.* **2020,** *10* (5), 3158-3163.

52. Liang, S.; Altaf, N.; Huang, L.; Gao, Y.; Wang, Q., Electrolytic cell design for electrochemical CO_2 reduction. *J. CO2 Util.* **2020,** *35*, 90-105.

53. Hu, H.; Liu, M.; Kong, Y.; Mysuru, N.; Sun, C.; Galvez-Vazquez, M. d. J.; Müller, U.; Erni, R.; Grozovski, V.; Hou, Y., Activation Matters: Hysteresis Effects during Electrochemical Looping of Colloidal Ag Nanowire Catalysts. *ACS Catal.* **2020,** *10* (15), 8503-8514.

54. Rahaman, M.; Dutta, A.; Broekmann, P., Size-Dependent Activity of Palladium Nanoparticles: Efficient Conversion of CO_2 into Formate at Low Overpotentials. *ChemSusChem* **2017,** *10* (8), 1733-1741.

55. Liu, S.; Wang, X.-Z.; Tao, H.; Li, T.; Liu, Q.; Xu, Z.; Fu, X.-Z.; Luo, J.-L., Ultrathin 5-fold twinned sub-25 nm silver nanowires enable highly selective electroreduction of CO_2 to CO. *Nano Energy* **2018,** *45*, 456-462.

56. Wei, L.; Li, H.; Chen, J.; Yuan, Z.; Huang, Q.; Liao, X.; Henkelman, G.; Chen, Y., Thiocyanate-Modified Silver Nanofoam for Efficient CO_2 Reduction to CO. *ACS Catal.* **2019,** *10* (2), 1444-1453.

57. García de Arquer, F. P.; Dinh, C.-T.; Ozden, A.; Wicks, J.; McCallum, C.; Kirmani, A. R.; Nam, D.-H.; Gabardo, C.; Seifitokaldani, A.; Wang, X., CO_2 electrolysis to multicarbon products at activities greater than 1 A cm^{-2}. *Science* **2020,** *367* (6478), 661-666.

58. Nesbitt, N. T.; Burdyny, T.; Simonson, H.; Salvatore, D.; Bohra, D.; Kas, R.; Smith, W. A., Liquid–Solid Boundaries Dominate Activity of CO_2 Reduction on Gas-Diffusion Electrodes. *ACS Catal.* **2020,** *10* (23), 14093-14106.

59. Burdyny, T.; Smith, W. A., CO_2 reduction on gas-diffusion electrodes and why catalytic performance must be assessed at commercially-relevant conditions. *Energy Environ. Sci.* **2019,** *12* (5), 1442-1453.

60. Ma, M.; Clark, E. L.; Therkildsen, K. T.; Dalsgaard, S.; Chorkendorff, I.; Seger, B., Insights into the carbon balance for CO_2 electroreduction on Cu using gas diffusion electrode reactor designs. *Energy Environ. Sci.* **2020,** *13* (3), 977-985.

61. Salvatore, D. A.; Weekes, D. M.; He, J.; Dettelbach, K. E.; Li, Y. C.; Mallouk, T. E.; Berlinguette, C. P., Electrolysis of Gaseous CO_2 to CO in a Flow Cell with a Bipolar Membrane. *ACS Energy Lett.* **2017,** *3* (1), 149-154.

62. Lees, E. W.; Mowbray, B. A. W.; Salvatore, D. A.; Simpson, G. L.; Dvorak, D. J.; Ren, S.; Chau, J.; Milton, K. L.; Berlinguette, C. P., Linking gas diffusion electrode composition to CO_2 reduction in a flow cell. *J. Mater. Chem. A* **2020,** *8* (37), 19493-19501.

63. Zheng, T.; Jiang, K.; Ta, N.; Hu, Y.; Zeng, J.; Liu, J.; Wang, H., Large-Scale and Highly Selective CO_2 Electrocatalytic Reduction on Nickel Single-Atom Catalyst. *Joule* **2019,** *3* (1), 265-278.

64. Liu, K.; Smith, W. A.; Burdyny, T., Introductory Guide to Assembling and Operating Gas Diffusion Electrodes for Electrochemical CO_2 Reduction. *ACS Energy Lett.* **2019,** *4* (3), 639-643.

65. Kong, Y.; Liu, M.; Hu, H.; Hou, Y.; Vesztergom, S.; Galvez-Vazquez, M. J.; Zelocualtecatl Montiel, I.; Kolivoska, V.; Broekmann, P., Cracks as Efficient Tools to Mitigate Flooding in Gas Diffusion Electrodes Used for the Electrochemical Reduction of Carbon Dioxide. *Small Methods* **2022,** *6* (9), e2200369.

66. Hu, H.; Kong, Y.; Liu, M.; Kolivoska, V.; Rudnev, A. V.; Hou, Y.; Erni, R.; Vesztergom, S.; Broekmann, P., Effective perspiration is essential to uphold the stability of zero-gap MEA-based cathodes used in CO_2 electrolysers. *J. Mater. Chem. A* **2023,** *11* (10), 5083-5094.

67. Luo, X.; Wright, A.; Weissbach, T.; Holdcroft, S., Water permeation through anion exchange membranes. *J. Power Sources* **2018,** *375*, 442-451.

68. Endrődi, B.; Kecsenovity, E.; Samu, A.; Halmágyi, T.; Rojas-Carbonell, S.; Wang, L.; Yan, Y.; Janáky, C., High carbonate ion conductance of a robust PiperION membrane allows industrial current density and conversion in a zero-gap carbon dioxide electrolyzer cell. *Energy Environ. Sci.* **2020,** *13* (11), 4098-4105.

69. Endrodi, B.; Samu, A.; Kecsenovity, E.; Halmagyi, T.; Sebok, D.; Janaky, C., Operando cathode activation with alkali metal cations for high current density operation of water-fed zero-gap carbon dioxide electrolyzers. *Nat. Energy* **2021,** *6* (4), 439-448.

70. Liu, M.; Kong, Y.; Hu, H.; Kovács, N.; Sun, C.; Zelocualtecatl Montiel, I.; Gálvez Vázquez, M. d. J.; Hou, Y.; Mirolo, M.; Martens, I.; Drnec, J.; Vesztergom, S.; Broekmann, P., The capping agent is the key: Structural alterations of Ag NPs during CO_2 electrolysis probed in a zero-gap gas-flow configuration. *Journal of Catalysis* **2021,** *404*, 371-382.

71. Wiberg, G. K.; Fleige, M.; Arenz, M., Gas diffusion electrode setup for catalyst testing in concentrated phosphoric acid at elevated temperatures. *Rev. Sci. Instrum.* **2015,** *86* (2), 024102.

72. Inaba, M.; Jensen, A. W.; Sievers, G. W.; Escudero-Escribano, M.; Zana, A.; Arenz, M., Benchmarking high surface area electrocatalysts in a gas diffusion electrode: measurement of oxygen reduction activities under realistic conditions. *Energy Environ. Sci.* **2018,** *11* (4), 988-994.

73. Galvez-Vazquez, M. J.; Alinejad, S.; Hu, H.; Hou, Y.; Moreno-Garcia, P.; Zana, A.; Wiberg, G. K. H.; Broekmann, P.; Arenz, M., Testing a Silver Nanowire Catalyst for the Selective CO_2 Reduction in a Gas Diffusion Electrode Half-cell Setup Enabling High Mass Transport Conditions. *Chimia (Aarau)* **2019,** *73* (11), 922-927.

74. de Jesus Gálvez-Vázquez, M.; Moreno-García, P.; Xu, H.; Hou, Y.; Hu, H.; Montiel, I. Z.; Rudnev, A. V.; Alinejad, S.; Grozovski, V.; Wiley, B. J.; Arenz, M.; Broekmann, P., Environment Matters: CO_2RR Electrocatalyst Performance Testing in a Gas-Fed Zero-Gap Electrolyzer. *ACS Catal.* **2020,** *10* (21), 13096-13108.

75. Alinejad, S.; Quinson, J.; Wiberg, G. K. H.; Schlegel, N.; Zhang, D.; Li, Y.; Reichenberger, S.; Barcikowski, S.; Arenz, M., Electrochemical Reduction of CO_2 on Au Electrocatalysts in a Zero‐Gap, Half‐Cell Gas Diffusion Electrode Setup: a Systematic Performance Evaluation and Comparison to an H‐cell Setup. *ChemElectroChem* **2022,** *9* (12).

76. Xi, W.; Ma, R.; Wang, H.; Gao, Z.; Zhang, W.; Zhao, Y., Ultrathin Ag Nanowires Electrode for Electrochemical Syngas Production from Carbon Dioxide. *ACS Sustainable Chem. Eng.* **2018,** *6* (6), 7687-7694.

77. Dong, W. J.; Yoo, C. J.; Lim, J. W.; Park, J. Y.; Kim, K.; Kim, S.; Lee, D.; Lee, J.-L., Tailoring electronic structure of bifunctional Cu/Ag layered electrocatalysts for selective CO_2 reduction to CO and CH_4. *Nano Energy* **2020,** *78*.

78. Popovic, S.; Smiljanic, M.; Jovanovic, P.; Vavra, J.; Buonsanti, R.; Hodnik, N., Stability and Degradation Mechanisms of Copper-Based Catalysts for Electrochemical CO_2 Reduction. *Angew. Chem. Int. Ed.* **2020**.

79. Liu, S.-Q.; Wu, S.-W.; Gao, M.-R.; Li, M.-S.; Fu, X.-Z.; Luo, J.-L., Hollow Porous Ag Spherical Catalysts for Highly Efficient and Selective Electrocatalytic Reduction of CO_2 to CO. *ACS Sustainable Chem. Eng.* **2019,** *7* (17), 14443-14450.

80. Liu, S.; Tao, H.; Zeng, L.; Liu, Q.; Xu, Z.; Liu, Q.; Luo, J. L., Shape-Dependent Electrocatalytic Reduction of CO_2 to CO on Triangular Silver Nanoplates. *J. Am. Chem. Soc.* **2017,** *139* (6), 2160-2163.

81. Lu, Q.; Rosen, J.; Zhou, Y.; Hutchings, G. S.; Kimmel, Y. C.; Chen, J. G.; Jiao, F., A selective and efficient electrocatalyst for carbon dioxide reduction. *Nat. Commun.* **2014,** *5*, 3242.

82. Gao, Y.; Jiang, P.; Song, L.; Liu, L.; Yan, X.; Zhou, Z.; Liu, D.; Wang, J.; Yuan, H.; Zhang, Z.; Zhao, X.; Dou, X.; Zhou, W.; Wang, G.; Xie, S., Growth mechanism of silver nanowires synthesized by polyvinylpyrrolidone-assisted polyol reduction. *J. Phys. D: Appl. Phys.* **2005,** *38* (7), 1061-1067.

83. Chen, Z.; Chang, J. W.; Balasanthiran, C.; Milner, S. T.; Rioux, R. M., Anisotropic Growth of Silver Nanoparticles Is Kinetically Controlled by Polyvinylpyrrolidone Binding. *J. Am. Chem. Soc.* **2019,** *141* (10), 4328-4337.

84. Guo, H.; Chen, Y.; Cortie, M. B.; Liu, X.; Xie, Q.; Wang, X.; Peng, D.-L., Shape-Selective Formation of Monodisperse Copper Nanospheres and Nanocubes via Disproportionation Reaction Route and Their Optical Properties. *J. Phys. Chem. C* **2014,** *118* (18), 9801-9808.

85. Luo, M.; Hong, Y.; Yao, W.; Huang, C.; Xu, Q.; Wu, Q., Facile removal of polyvinylpyrrolidone (PVP) adsorbates from Pt alloy nanoparticles. *J. Mater. Chem. A* **2015,** *3* (6), 2770-2775.

86. Naresh, N.; Wasim, F. G. S.; Ladewig, B. P.; Neergat, M., Removal of surfactant and capping agent from Pd nanocubes (Pd-NCs) using tert-butylamine: its effect on electrochemical characteristics. *J. Mater. Chem. A* **2013,** *1* (30).

87. Xiao, C.; Chen, S.; Zhang, L.; Zhou, S.; Wu, W., One-pot synthesis of responsive catalytic Au@ PVP hybrid nanogels. *Chem. Commun.* **2012,** *48* (96), 11751-11753.

88. Tsunoyama, H.; Tsukuda, T., Magic numbers of gold clusters stabilized by PVP. *J. Am. Chem. Soc.* **2009,** *131* (51), 18216-18217.

89. Pastoriza-Santos, I.; Liz-Marzán, L. M., Formation of PVP-protected metal nanoparticles in DMF. *Langmuir* **2002,** *18* (7), 2888-2894.

90. Mdluli, P. S.; Sosibo, N. M.; Mashazi, P. N.; Nyokong, T.; Tshikhudo, R. T.; Skepu, A.; van der Lingen, E., Selective adsorption of PVP on the surface of silver nanoparticles: A molecular dynamics study. *J. Mol. Struct.* **2011,** *1004* (1-3), 131-137.

91. Collins, G.; Schmidt, M.; McGlacken, G. P.; O'Dwyer, C.; Holmes, J. D., Stability, Oxidation, and Shape Evolution of PVP-Capped Pd Nanocrystals. *J. Phys. Chem. C* **2014,** *118* (12), 6522-6530.

92. Safo, I. A.; Dosche, C.; Ozaslan, M., Effects of Capping Agents on the Oxygen Reduction Reaction Activity and Shape Stability of Pt Nanocubes. *ChemPhysChem* **2019,** *20* (22), 3010-3023.

93. Guo, H.; Lin, N.; Chen, Y.; Wang, Z.; Xie, Q.; Zheng, T.; Gao, N.; Li, S.; Kang, J.; Cai, D.; Peng, D. L., Copper nanowires as fully transparent conductive electrodes. *Sci. Rep.* **2013,** *3*, 2323.

94. Kim, C.; Jeon, H. S.; Eom, T.; Jee, M. S.; Kim, H.; Friend, C. M.; Min, B. K.; Hwang, Y. J., Achieving Selective and Efficient Electrocatalytic Activity for CO_2 Reduction Using Immobilized Silver Nanoparticles. *J. Am. Chem. Soc.* **2015,** *137* (43), 13844-50.

95. Sun, C.; Hou, Y.; Lüdi, N.; Hu, H.; de Jesús Gálvez-Vázquez, M.; Liechti, M.; Kong, Y.; Liu, M.; Erni, R.; Rudnev, A. V.; Broekmann, P., Improving the lifetime of hybrid CoPc@MWCNT catalysts for selective electrochemical CO_2-to-CO conversion. *J. Catal.* **2022,** *407*, 198-205.

96. Li, M.; Idros, M. N.; Wu, Y.; Burdyny, T.; Garg, S.; Zhao, X. S.; Wang, G.; Rufford, T. E., The role of electrode wettability in electrochemical reduction of carbon dioxide. *J. Mater. Chem. A* **2021,** *9* (35), 19369-19409.

97. Mardle, P.; Cassegrain, S.; Habibzadeh, F.; Shi, Z.; Holdcroft, S., Carbonate Ion Crossover in Zero-Gap, KOH Anolyte CO_2 Electrolysis. *J. Phys. Chem. C* **2021,** *125* (46), 25446-25454.

98. El-Nagar, G. A.; Haun, F.; Gupta, S.; Stojkovikj, S.; Mayer, M. T., Unintended cation crossover influences CO_2 reduction selectivity in Cu-based zero-gap electrolysers. *Nat. Commun.* **2023,** *14* (1), 2062.

99. Reyes, A.; Jansonius, R. P.; Mowbray, B. A. W.; Cao, Y.; Wheeler, D. G.; Chau, J.; Dvorak, D. J.; Berlinguette, C. P., Managing Hydration at the Cathode Enables Efficient CO_2 Electrolysis at Commercially Relevant Current Densities. *ACS Energy Lett.* **2020,** *5* (5), 1612-1618.

100. Lim, C.; Lee, W. H.; Won, J. H.; Ko, Y. J.; Kim, S.; Min, B. K.; Lee, K. Y.; Jung, W. S.; Oh, H. S., Enhancement of Catalytic Activity and Selectivity for the Gaseous Electroreduction of CO_2 to CO: Guidelines for the Selection of Carbon Supports. *Adv. Sustainable Syst.* **2021,** *5* (12).

101. Dinh, C.-T.; Burdyny, T.; Kibria, M. G.; Seifitokaldani, A.; Gabardo, C. M.; García de Arquer, F. P.; Kiani, A.; Edwards, J. P.; De Luna, P.; Bushuyev, O. S.; Zou, C.; Quintero-Bermudez, R.; Pang, Y.; Sinton, D.; Sargent, E. H., CO_2 electroreduction to ethylene via hydroxide-mediated copper catalysis at an abrupt interface. *Science* **2018,** *360* (6390), 783-787.

102. Pham, T. H. M.; Zhang, J.; Li, M.; Shen, T. H.; Ko, Y.; Tileli, V.; Luo, W.; Züttel, A., Enhanced Electrocatalytic CO_2 Reduction to C_{2+} Products by Adjusting the Local Reaction Environment with Polymer Binders. *Adv. Energy Mater.* **2022,** *12* (9).

103. Chang, M.; Ren, W.; Ni, W.; Lee, S.; Hu, X., Ionomers Modify the Selectivity of Cu-Catalyzed Electrochemical CO_2 Reduction. *ChemSusChem* **2023,** *16* (5), e202201687.

104. Xing, Z.; Hu, L.; Ripatti, D. S.; Hu, X.; Feng, X., Enhancing carbon dioxide gas-diffusion electrolysis by creating a hydrophobic catalyst microenvironment. *Nat. Commun.* **2021,** *12* (1), 136.

105. Xing, Z.; Hu, X.; Feng, X., Tuning the Microenvironment in Gas-Diffusion Electrodes Enables High-Rate CO_2 Electrolysis to Formate. *ACS Energy Lett.* **2021,** *6* (5), 1694-1702.

106. Rabiee, H.; Ge, L.; Zhao, J.; Zhang, X.; Li, M.; Hu, S.; Smart, S.; Rufford, T. E.; Zhu, Z.; Wang, H.; Yuan, Z., Regulating the reaction zone of electrochemical CO_2 reduction on gas-diffusion electrodes by distinctive hydrophilic-hydrophobic catalyst layers. *Appl. Catal., B* **2022,** *310*.

107. Liu, H.; Su, Y.; Liu, Z.; Chuai, H.; Zhang, S.; Ma, X., Tailoring microenvironment for enhanced electrochemical CO_2 reduction on ultrathin tin oxide derived nanosheets. *Nano Energy* **2023,** *105*.

108. Rabinowitz, J. A.; Kanan, M. W., The future of low-temperature carbon dioxide electrolysis depends on solving one basic problem. *Nat. Commun.* **2020,** *11* (1), 5231.

109. Sassenburg, M.; Kelly, M.; Subramanian, S.; Smith, W. A.; Burdyny, T., Zero-Gap Electrochemical CO_2 Reduction Cells: Challenges and Operational Strategies for Prevention of Salt Precipitation. *ACS Energy Lett.* **2023,** *8* (1), 321-331.

110. Ramdin, M.; Moultos, O. A.; van den Broeke, L. J. P.; Gonugunta, P.; Taheri, P.; Vlugt, T. J. H., Carbonation in Low-Temperature CO_2 Electrolyzers: Causes, Consequences, and Solutions. *Ind. Eng. Chem. Res.* **2023,** *62* (18), 6843-6864.

111. Xu, Y.; Edwards, J. P.; Liu, S.; Miao, R. K.; Huang, J. E.; Gabardo, C. M.; O'Brien, C. P.; Li, J.; Sargent, E. H.; Sinton, D., Self-Cleaning CO_2 Reduction Systems: Unsteady Electrochemical Forcing Enables Stability. *ACS Energy Lett.* **2021,** *6* (2), 809-815.

112. Wang, R.; Haspel, H.; Pustovarenko, A.; Dikhtiarenko, A.; Russkikh, A.; Shterk, G.; Osadchii, D.; Ould-Chikh, S.; Ma, M.; Smith, W. A.; Takanabe, K.; Kapteijn, F.; Gascon, J., Maximizing Ag Utilization in High-Rate CO_2 Electrochemical Reduction with a Coordination Polymer-Mediated Gas Diffusion Electrode. *ACS Energy Lett.* **2019,** *4* (8), 2024-2031.

113. Cofell, E. R.; Nwabara, U. O.; Bhargava, S. S.; Henckel, D. E.; Kenis, P. J. A., Investigation of Electrolyte-Dependent Carbonate Formation on Gas Diffusion Electrodes for CO_2 Electrolysis. *ACS Appl. Mater. Interfaces* **2021,** *13* (13), 15132-15142.

114. Bhargava, S. S.; Cofell, E. R.; Chumble, P.; Azmoodeh, D.; Someshwar, S.; Kenis, P. J. A., Exploring multivalent cations-based electrolytes for CO_2 electroreduction. *Electrochim. Acta* **2021,** *394*.

115. Singh, M. R.; Kwon, Y.; Lum, Y.; Ager, J. W., 3rd; Bell, A. T., Hydrolysis of Electrolyte Cations Enhances the Electrochemical Reduction of CO_2 over Ag and Cu. *J. Am. Chem. Soc.* **2016,** *138* (39), 13006-13012.

116. Zhang, F.; Co, A. C., Direct Evidence of Local pH Change and the Role of Alkali Cation during CO_2 Electroreduction in Aqueous Media. *Angew. Chem. Int. Ed.* **2020,** *59* (4), 1674-1681.

117. Hou, Y.; Kovács, N.; Xu, H.; Sun, C.; Erni, R.; Gálvez-Vázquez, M. d. J.; Rieder, A.; Hu, H.; Kong, Y.; Liu, M.; Wiley, B. J.; Vesztergom, S.; Broekmann, P., Limitations of identical location SEM as a method of degradation studies on surfactant capped nanoparticle electrocatalysts. *J. Catal.* **2021,** *394*, 58-66.

118. Kong, Y.; Hu, H.; Liu, M.; Hou, Y.; Kolivoška, V.; Vesztergom, S.; Broekmann, P., Visualisation and quantification of flooding phenomena in gas diffusion electrodes used for electrochemical CO_2 reduction: A combined EDX/ICP–MS approach. *J. Catal.* **2022,** *408*, 1-8.

119. Liu, M.; Hu, H.; Kong, Y.; Montiel, I. Z.; Kolivoška, V.; Rudnev, A. V.; Hou, Y.; Erni, R.; Vesztergom, S.; Broekmann, P., The role of ionomers in the electrolyte management of zero-gap MEA-based CO_2 electrolysers: A Fumion vs. Nafion comparison. *Appl. Catal., B* **2023,** *335*.

120. Jeanty, P.; Scherer, C.; Magori, E.; Wiesner-Fleischer, K.; Hinrichsen, O.; Fleischer, M., Upscaling and continuous operation of electrochemical CO_2 to CO conversion in aqueous solutions on silver gas diffusion electrodes. *J. CO2 Util.* **2018,** *24*, 454-462.

121. Haynes, W. M., *CRC handbook of chemistry and physics*. CRC press: 2014.

Publications

The following section presents the main research outcomes (published papers) in which I participated during my PhD. The first five publications form the essence of this PhD project and the subsequent ones represent additional works in which I was involved.

1. The capping agent is the key: Structural alterations of Ag NPs during CO_2 electrolysis probed in a zero-gap gas-flow configuration

Authors: Menglong Liu, Ying Kong, Huifang Hu, Noémi Kovács, Changzhe Sun, Iván Zelocualtecatl Montiel, María de Jesús-Gálvez Vázquez, Yuhui Hou, Marta Mirolo, Isaac Martens, Jakub Drnec, Soma Vesztergom, and Peter Broekmann.

***Journal of Catalysis*, 404 (2021), 371–382. DOI: 10.1016/j.jcat.2021.10.016**

Highlight: The effect of capping agents (i.e., BPEI, PVP, PEG, and citrate) on the morphological change and catalytic performance of Ag-NPs during ec-CO_2RR was studied in a semi-zero-gap electrolyzer. While PVP-, PEG-, and citrate-capped Ag-NPs show similar activity and selectivity towards CO formation, the Ag-NPs follow different structural alteration pathways; predominant cathodic corrosion is observed for PVP-capped Ag-NPs; Ag-NPs undergo mainly coalescence in the case of PEG, and severe change occur for citrate-capped Ag-NPs through Ostwald ripening. No obvious morphology change was observed for BPEI-capped Ag-NPs due to strong binding between the amino groups and Ag-NPs. However, strong PEI-Ag bonding blocked active sites for ec-CO_2RR, thus resulting in a relatively poor catalytic performance. These differences were attributed to the chemical nature of capping agents. It is also pointed out that, besides the capping agents that were absorbed on the Ag-NPs, the excess capping agents in the ink solution (and co-deposited on the GDL) also play a significant role for the resulting morphology changes of the catalysts.

Contribution: I carried out most of the electrochemical experiments, the particle size distribution analysis, the contact angle measurements, and participated discussion of the results. I contributed to the preparation of the figures and revised the text of the manuscript.

Journal of Catalysis 404 (2021) 371–382

Contents lists available at ScienceDirect

Journal of Catalysis

journal homepage: www.elsevier.com/locate/jcat

The capping agent is the key: Structural alterations of Ag NPs during CO_2 electrolysis probed in a zero-gap gas-flow configuration

Menglong Liu [a,b], Ying Kong [a,b], Huifang Hu [a], Noémi Kovács [a], Changzhe Sun [a,b], Iván Zelocualtecatl Montiel [a], María de Jesús Gálvez Vázquez [a], Yuhui Hou [a,*], Marta Mirolo [c], Isaac Martens [c], Jakub Drnec [c], Soma Vesztergom [a,d,*], Peter Broekmann [a,b,*]

[a] University of Bern, Department of Chemistry, Biochemistry and Pharmaceutical Sciences Freiestrasse 3, 3012 Bern, Switzerland
[b] National Centre of Competence in Research (NCCR) Catalysis, University of Bern Freiestrasse 3, 3012 Bern, Switzerland
[c] European Synchrotron Radiation Facility, Experimental Division, Avenue des Martyrs 71, 38000 Grenoble, France
[d] Eötvös Loránd University, Department of Physical Chemistry Pázmány Péter sétány 1/A, 1117 Budapest, Hungary

ARTICLE INFO

Article history:
Received 16 August 2021
Revised 1 October 2021
Accepted 13 October 2021
Available online 21 October 2021

Keywords:
Power to value
Carbon dioxide electroreduction
Catalyst degradation
Particle sizing
Scanning electron microscopy
Wide-angle X-ray scattering

ABSTRACT

We apply silver nanoparticles (Ag NPs) as catalysts of CO_2 reduction in a zero-gap gas-flow electrolyser. Ag NPs stabilized by different ligands —branched polyethylenimine (BPEI), polyvinylpyrrolidone (PVP), polyethylene glycol (PEG), and citrate— are used in the experiments. The as-prepared NPs have almost identical initial size distributions, yet their catalytic performance, in terms of achievable current and CO selectivity, is different. During electrolysis all Ag NPs exhibit unambiguous morphology changes; the degradation pathway they follow, however, markedly depends on the chemical nature of the capping agent stabilizing them. Scanning electron micrographs obtained before and after constant-charge electrolyses carried out at different potentials reveal that amongst the studied ligands, BPEI seems to be the most effective stabilizer of Ag NPs; in turn, however, BPEI also limits CO formation the most. In case of PVP, mostly corrosion (particle shrinkage) is observed at practically relevant electrolysing potentials, while the application of PEG leads more to particle coalescence. Ostwald ripening seems to appear only at high applied (H_2 forming) potentials in case of the three afore-mentioned ligands while in case of citrate it becomes significant already at mild (CO forming) voltages. By studying the effects of capping agent removal and exchange we demonstrate that apart from ligands directly attached to the Ag NPs, also the excess of capping agents (adsorbed on the electrode surface) plays a decisive role in determining the extent and mode of catalyst degradation. The results of SEM-based particle sizing are also confirmed by synchrotron based wide-angle X-ray scattering measurements that provide further insight into the evolution of crystallite size and lattice strain in the applied Ag NPs during electrolysis.

1. Introduction

The electrochemical reduction of CO_2 into value-added products is a quickly developing field of electrocatalysis, mostly because it opens new perspectives in front of climate change mitigation [1]. Due to the considerable thermodynamic stability of carbon dioxide, the electrochemical CO_2 reduction reaction (CO_2RR) requires high negative potentials, and the application of catalyst materials that favour CO_2RR over the competing hydrogen evolution reaction (HER). The design of new catalyst materials that not only meet this requirement, but can also selectively direct CO_2RR towards the formation of a desired product at suitable rate and at low energy cost has thus become the forefront of electrochemical research in the past 20 years [2].

Although examples to the contrary already exist [3], metals or metal oxides (either in bulk [4], foam [5], or nanoparticulate [6] form) are still considered as catalysts of first choice for CO_2RR. While on bulk metal electrodes with large planar surfaces it is primarily the chemical nature of the metal [4] that determines the

* Corresponding authors at: University of Bern, Department of Chemistry, Biochemistry and Pharmaceutical Sciences, Freiestrasse 3, 3012 Bern, Switzerland (Y. Hou and P. Broekmann); Eötvös Loránd University, Department of Physical Chemistry, Pázmány Péter sétány 1/A, 1117 Budapest, Hungary (S. Vesztergom).

E-mail addresses: menglong.liu@unibe.ch (M. Liu), ying.kong@unibe.ch (Y. Kong), huifang.hu@unibe.ch (H. Hu), noemi.kovacs@unibe.ch (N. Kovács), changzhe.sun@unibe.ch (C. Sun), ivan.zelocualtecatl@unibe.ch (I. Zelocualtecatl Montiel), maria.galvez@dcb.ch (M.J. Gálvez Vázquez), yuhui.hou@unibe.ch (Y. Hou), marta.mirolo@esrf.fr (M. Mirolo), isaac.martens@esrf.fr (I. Martens), jakub.drnec@esrf.fr (J. Drnec), vesztergom@chem.elte.hu (S. Vesztergom), peter.broekmann@dcb.unibe.ch (P. Broekmann).

https://doi.org/10.1016/j.jcat.2021.10.016
0021-9517/

majority product (CO, formate, hydrocarbons, alcohols), in case of catalysts with nanosized features (nanoparticles or hierarchic foams) also the nanoscale structure has a pivotal role in determining selectivity [6,7]. In case of Cu nanoparticles (NPs), for example, a direct correlation between particle size and product distribution has already been established [8], and also for other metallic NPs (like Sn [9] or Ag [10]) intense research has been carried out to correlate the activity and selectivity of nanoparticulate catalysts to their morphology and physical structure. To use metals (or their oxides) in a nanoparticulate form for the catalysis of the CO_2RR is a very straightforward approach especially because of the many facile synthesis routes available that allow the design of NPs with fine-tuned catalytic properties.

Using metals in a nanoparticulate form for the catalysis of CO_2-RR has the obvious advantage that comes with the low raw material cost — small sized NPs can be applied in a relatively low loading to achieve an already considerable current of CO_2 reduction [5]. A significant drawback of nanoparticulate catalysts stems, however, also from the small size of NPs, which makes them thermodynamically unstable. Maintaining the stability of NPs under the operating conditions of electrolysis, that is, at high applied potentials, strong flow of current and intense gas formation, thus becomes a key question of research. In other fields of electrocatalysis (*e.g.,* in fuel cell research [11]) the degradation of catalyst NPs is well studied. In relation to CO_2RR on the other hand, only a few researchers seem to place emphasis on elucidating possible degradation mechanisms [9,10,12–16].

Ag is considered an appealing catalyst material for CO_2 reduction because it produces a single yet very sought-after product over a broad potential window and under different operating conditions: CO. CO is a remarkably versatile precursor of the production of synthetic fuels [17], and industrial applications already exist, for example, for the coupling of CO_2-to-CO/water-to-H_2 electrolysers to a fermentation module where CO and H_2 are converted to butanol and hexanol with high carbon selectivity [18]. In addition, the two-electron transfer required by the CO_2-to-CO conversion provides a large profit margin compared to other multiple-electron transfer products requiring larger energy inputs [17].

While in existing industrial electrolysers Ag is usually applied in a bulk form for the production of CO [18], it was recently shown in lab scale experiments that when Ag is used in a nanoparticulate form, stable CO formation can be achieved over a much broader potential window, and thus better conversion metrics can be achieved compared to the case when electrolysis is carried out on planar Ag cathodes [10].

In a recent study we made the first step in the direction of upscaling towards practical application by using Ag NPs as catalysts of CO_2RR in a zero-gap gas-flow electrolyser unit [15]. Zero-gap gas-flow electrolysers allow the realisation of large current densities ($\gg$300 mA cm^{-2}, normalized to geometric cathode surface area) and create an ideal playground for catalyst stability testing under harsh operating conditions.

The use of capping agents is essential in Ag nanoparticle synthesis as they control the shape and size of the grown nanoparticles, and prevent their aggregation over time [19]. Capping agents usually achieve long-term stabilization of the particle size [20] either by steric hindrance (such ligands usually have bulky protecting groups) or by an electrostatic repulsion between ligands bearing the same charge (such capping agents are usually ionic species). While essentially both types of ligands can work well in stabilizing NPs in dispersion, they both have significant drawbacks when it comes to fixing the NPs on an electrode surface and using them as electrocatalysts. In such cases NPs stabilized by charged ligands are often found to quickly agglomerate either due to screening effects arising from high ionic strengths or as a result of the electric field of the working electrode. NPs stabilized by steric hindrance are usually more stable, however in this case the strong adsorption of ligands often blocks the access of reactants to the NPs, leading to an overall decrease of the catalytic activity.

The structural changes metallic NP-based catalyst layers undergo in the course of the catalysed process can take many forms, including the *detachment* of particles from the support (which ultimately results in catalyst loss), the *corrosion* of the NPs (leading to an overall decrease of the average nanoparticle size), the *aggregation* of NPs on the catalyst support (leading to the formation of larger particles) and the phenomenon known as Ostwald ripening (as a result of which some particles grow larger on the expense of smaller ones disappearing). These structural changes (an illustration is shown in Fig. 1) all result in distortions of the particle size distribution of the NPs, and as such, they are commonly referred to as means of *degradation* — practically regardless to whether they have any measurable effect, either negative or positive, on the observed catalytic performance.

In practical electrolysers degradation rarely takes a single route, and in most cases it is a combination of several of the above-described degradation phenomena that determines the fate of catalyst NPs. The means and extent of degradation heavily depends on the operating conditions of the electrolyser (voltage and current, the intensity of gas formation, etc.), as well as on the chemical nature of the stabilizing (capping) agents applied either during the synthesis of the NPs or later for the formulation of the catalyst ink.

As capping agents not only adsorb on the surface of the NPs but also on the (usually carbon) cathode support, they may also play a decisive role in determining the surface adherence and the mobility of the NPs. While strongly bonding capping agents may preserve the initial particle size distribution of the NPs more efficiently than others, such ligands may also decrease catalytic performance by blocking the access of reactants to active catalyst sites. In such cases, the onset of "degradation" can even have an unexpected positive effect on the performance of electrolysis, as it can enable the participation of new, previously unaccessible sites in the catalysed process [21]. Apart from such exceptions, however, the degradation of NPs usually manifests in a long-term loss of the catalytic performance. This is primarily due to a loss of the active catalyst surface area that accompanies all degradation modes (including corrosion that often leads to the detachment of the smaller particles). A secondary degradation effect that may also account for performance losses is related not to the changing size distribution of the particles, but rather to a consequence of this: an internal structural change of the NPs, during which the (from a catalytic point of view, highly active) open crystalline sites re-organize to less ordered and more compact amorphous structures.

In this study we use Ag NPs capped by different ligands — branched polyethylenimine (BPEI), polyvinylpyrrolidone (PVP), polyethylene glycol (PEG), and citrate— with an initially narrow size distribution centred at $\sim$ 40 nm for the preparation of catalyst inks that we disperse on a gas diffusion layer. The thus prepared Ag NP GDE (Fig. 2) is in direct contact with the anion exchange membrane of the zero-gap gas-flow electrolyser (see also Figure S1 of the Supporting Information) that contains an electrolyte solution only on the anode side. The reactant gas (CO_2) is directly fed by a constant flow to the GDE, and the configuration does not only assure reduced ohmic losses but it also attenuates complications that arise from poor membrane hydration and electrode flooding at high current densities [15].

We show that in case of all four applied capping agents, the efficiency of CO_2RR considerably drops over time in a manner that is similar for all capping agents. While this performance loss, occurring due to the formation of carbonate plaques at high current densities over the electrode surface, is not a direct result of the structural changes that catalyst NPs suffer during electrolysis, the zero-gap gas flow cell still provides means to study the morpholog-

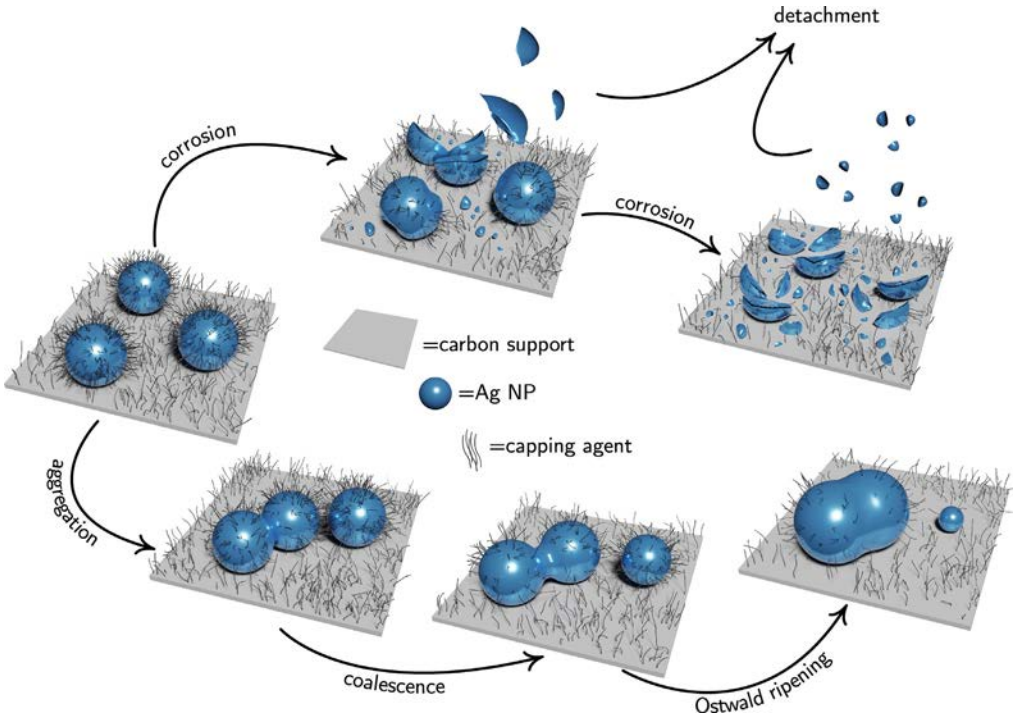

Fig. 1. Degradation pathways of Ag NPs used for CO_2RR.

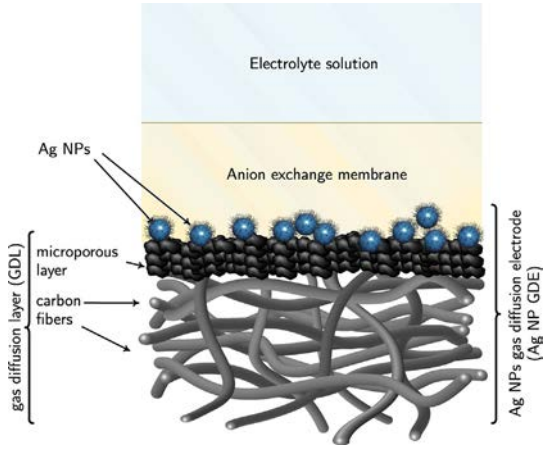

Fig. 2. The gas diffusion electrodes (Ag NP GDEs) used in this study are formed by drop-casting an Ag NPs containing catalyst ink on a gas diffusion layer (GDL). The latter is a bilayer structure consisting of a macroporous backing material (carbon fiber paper support) and a carbon-based microporous layer. The Ag NP GDE is separated by an anion exchange membrane from the electrolyte solution that contains the anode and a reference electrode.

ical changes of Ag NPs during intense CO_2RR/HER stressing. Following a removal of the formed carbonate plaques by careful dip-washing, structural changes can be investigated by a set of state-of-the-art nanoparticle characterization techniques including scanning electron microscopy (SEM) and wide-angle X-ray scattering (WAXS) measurements. These methods can clearly demonstrate that depending on the nature of their stabilizing ligands, Ag NPs undergo different degradation pathways on the course of electrolysis. By a set of ligand removal and exchange experiments we also demonstrate that apart from ligand molecules directly attached to the NPs, ligands adsorbed on the supporting carbon matrix also play a role in determining the dominant degradation mode.

2. Experimental Section

Preparation of the Ag NPs-containing catalyst ink. To prepare the carbon-supported Ag NP catalyst ink, 0.25 cm^3 of the as-received parent catalyst suspension (NanoComposix, Ag mass concentration of 1 mg cm^{-3}) was diluted to 0.55 cm^3 by the addition of Milli-Q water. A second suspension (volume: 0.44 cm^3) was made by dispersing carbon black (Vulcan XC 72r, Cabot) in isopropanol (VLSI Selectipur, BASF SE, Ludwigshafen, Germany) in a 0.1 mg cm^{-3} concentration. Both suspensions were sonicated separately for 10 and 30 min, respectively, following which the suspensions were intermixed and, after the addition of 10 $\mu\ell$ Nafion solution (5% Nafion, 15–20% water, Sigma–Aldrich), the new suspension was sonicated for further 10 min. The same ink preparation protocol was applied to all four nanoparticulate catalysts used herein. BPEI, PVP, PEG and citrate-capped Ag NPs with an average particle size of $\sim$ 40 nm were purchased from a supplier (NanoComposix) and were used directly for the ink preparation. In order to carry out experiments by removing some of the excess PVP capping agent, the parent Ag NP suspension was first subjected to centrifugation (at 35 000 rpm, 40 min, Beckmann Coulter ultracentrifuge, SW60 rotor). This treatment allowed for a separation of the surfactant-capped Ag NPs and the free surfactants that remained, at least to a large extent, in the liquid (aqueous) phase. The separated Ag NPs were then suspended in Milli-Q water to keep the Ag concentration the same as that of the parent suspension, and the ink preparation protocol described above was followed. The separated Ag NPs and the aqueous matrix phase were both subjected to a total organic carbon concentration (TOC) analysis with the aim to estimate the amount of surfactants that is either attached to the Ag NPs or is present in solution (see Table S5 in Supporting Information).

Preparation of the Ag NP GDEs. GDEs were formed by drop-casting 40 $\mu\ell$ of either one of the above-described catalyst inks onto the masked hydrophobic surface of a GDL (H23C8, FuelCellStore, see Figure S2 of the Supporting Information for SEM charac-

terization). The GDE was in contact with the membrane through a circular opening with a diameter of 3 mm, and the corresponding geometric area (7.07 mm^2) is used for the surface normalization of current to current density. The catalyst ink was percolated through the porous body of the GDE by a vacuum filtration system placed on the backside of the electrode, followed by drying at ambient conditions. The resulting mass loading was in the range of (43±5) $\mu g\ cm^{-2}$, as confirmed by inductively coupled plasma mass spectrometry (ICP–MS, see Table S1 in Supporting Information for detailed loading data).

Assembly of the gas flow-cell. The assembly and main components of the zero-gap gas-flow cell employed in this work have been described elsewhere [15]. The cell (see also Figure S1 in Supporting Information) consists of a stainless steel body with the gas flow channels used to feed the CO_2 from the backside of the prepared Ag NPs GDE mounted on the outermost location of the central portion. Other components incorporated into the cell include a current collector and a gas inlet and outlet to control the supply of the CO_2 reactant (99.999%, Carbagas, Switzerland) and analysis of gaseous products, respectively. All the CO_2 reduction experiments were set up by placing a freshly prepared Ag NPs GDE on top of the gas flow channels, with its catalyst modified surface facing upward. Subsequently, a new hydroxide-functionalised Sustainion alkaline membrane (X3750 RT, Dioxide materials) and a poly-(tetrafluoroethylene) anolyte compartment were placed on top of the GDE. A clamp was then used to guarentee cell tightness and mechanical stability. 10 cm^3 of 2.0 mol dm^{-3} KOH was used as electrolyte for the anolyte compartment. An Ag|AgCl|3 mol dm^{-3} KCl electrode (double junction design, Metrohm) was used as a reference, and an Ir wire (99.9%, MaTeck Material-Technologie & Kristalle GmbH, Germany) separated by a glass frit was used as a counter electrode. Note that the PTFE anolyte compartment has a central orifice (of 3 mm diameter, corresponding to a geometric surface area of 7.07mm^2) in its bottom part that provides direct contact between the electrolyte and the underlying anion-exchange membrane, while the Ag NPs GDE is prevented from direct contact with the supporting anolyte. During electrolysis, a humidified CO_2 stream (16 $cm^3\ min^{-1}$) was continuously fed through the gas flow channels of the stainless steel cell body, adjacent to the GDE.

Electrochemical measurements and product distribution studies. An ECi-200 potentiostat (Nordic Electrochemistry) was used to perform all electrolysis experiments. The electro-generated gaseous products (CO and H_2) were determined by means of on-line gas chromatography (SRI Instruments) in fixed (10 or 4 min) time intervals. The electrolyte solution was also analysed after full electrolyses, to check for any soluble products formed, by means of ion exchange chromatography (Metrohm Ltd., Switzerland). As formate (in different amounts, see Table S3 in Supporting Information) was found as the sole dissolved product in the electrolyte solution, it was assumed that whenever the GC-based detection of volatile products could not account for a 100% of Faradaic efficiency, the rest of the passed current was turned into formate production.

Electron microscopy measurements. For the morphological characterization of the Ag NPs on GDEs, a Zeiss Gemini 450 scanning electron microscope equipped with an InLens secondary electron detector and a back-scattering detector was used. An accelerating voltage of 5 kV and a current of 120 pA were applied at a working distance of 3.8–4.2 mm. Using the Smile View software for particle sizing, ca. 500–900 particles were analysed per experimental setting for the creation of the particles size distribution shown in Figs. 7, 9 and 10. The particle size was defined as the longest measurable dimension in case of anisotropic NPs, see Figure S13 in the Supporting Information. To acquire EDX point spectra and 2D surface mappings of selected samples, the AZtec 4.2 software (Oxford Instruments) was used. An acceleration voltage of 10 kV and a current of 500 pA were applied at a working distance of 8.5 mm for EDX measurements. For high-angle annular dark-field scanning transmission electron microscopy (HAADF–STEM) combined with energy-dispersive X-ray spectroscopy (EDX), a Talos F200X (Thermo Fisher Scientific) instrument equipped with a SuperEDX detector was used with an acceleration voltage of 200 kV.

Contact angle measurements. Contact angle measurements were carried out using a Krüss Advance Drop Shape Analyzer DSA25 (Krüss GmbH, Hamburg, Germany). Electrodes were mounted on a flat stage and water drops (milli-Q water, 1.4 μL) were deposited at room temperature.

Synchrotron Wide-Angle X-ray Scattering (WAXS) measurements. Crystallite size and microstrain were measured via WAXS measurements at the ID31 beamline of the European Synchrotron Radiation facility (ESRF) in Grenoble, France. The high energy X-ray beam (75 keV) was focused on the Ag NP GDEs, and the scattered signal was collected using a Dectris Pilatus CdTe 2 M detector positioned 520 mm behind the sample. The energy, detector distance and tilts were calibrated using a standard CeO_2 powder and the 2D diffraction patterns were reduced to the presented 1D curves using the pyFAI software package [22]. Rietveld refinement of the WAXS patterns was performed to extract the phase structure, crystallite size, lattice parameter and microstrain using the cubic *Fm–3 m* structure of Ag metal and the GSASII software [23], see Figure S14 in Supporting Information for a representative fit. The instrumental parameters were determined by the refinement of a CeO_2 standard sample. Air scattering was removed from each pattern. The measurement consists in a height scan acquiring WAXS pattern at different positions in the sample. The pattern of the GDE is considered as background and removed for each sample. The fitting is performed using crystallites of uniaxial orientation along the (111) direction.

White light interferometry (WLI) analysis. The mesoscopic surface morphology of the Ag NP GDEs was analyzed by means of white light interferometry (Contour GT, Bruker, see Figure S5). Vision64 software (Bruker) was used for operating the instrument and for data analysis.

Inductively coupled plasma mass spectrometry (ICP-MS). GDE samples were immersed for 24 h in 1 cm^3 HNO_3 (69.3%, BASF SE, Ludwigshafen, Germany) to dissolve all Ag NPs. The resulting solutions were diluted with 3% HNO_3 solution by a factor of 500 and were then fed into a NExION 2000 ICP-MS instrument (Perkin Elmer) to obtain the Ag mass loading of the electrodes (see Tables S1 and S4 in Supporting Information).

Total organic content (TOC) determination. To quantify surfactants in each solution, 100 $\mu\ell$ of free surfactant solutions obtained by centrifugation of Ag NP suspensions (0.25 mg cm^{-3}) and surfactant-capped Ag NP suspensions (0.25 mg cm^{-3}) which do not contain free surfactants were fed into a DIMATOC 2100 instrument (Dimatec, Essen, Germany). The organic compounds were oxidized at 850 °C with Pt as catalyst to CO_2/NO. Non-dispersive infrared (NDIR) gas sensor with a reflective diffuser and a chemiluminescence detector were used to detect CO_2 and NO, respectively.

3. Results and Discussion

Characterization of the as-prepared Ag NP GDEs. Essentially regardless to the nature of the stabilizing ligand (BPEI, PVP, PEG or citrate), all our studied Ag NP GDEs exhibited very similar physical characteristics (Fig. 3). Representative SEM images of (PVP-capped) Ag NP GDEs are shown in Fig. 3a and c, revealing isotropic and uniformly dispersed NPs with an almost uniform particle size

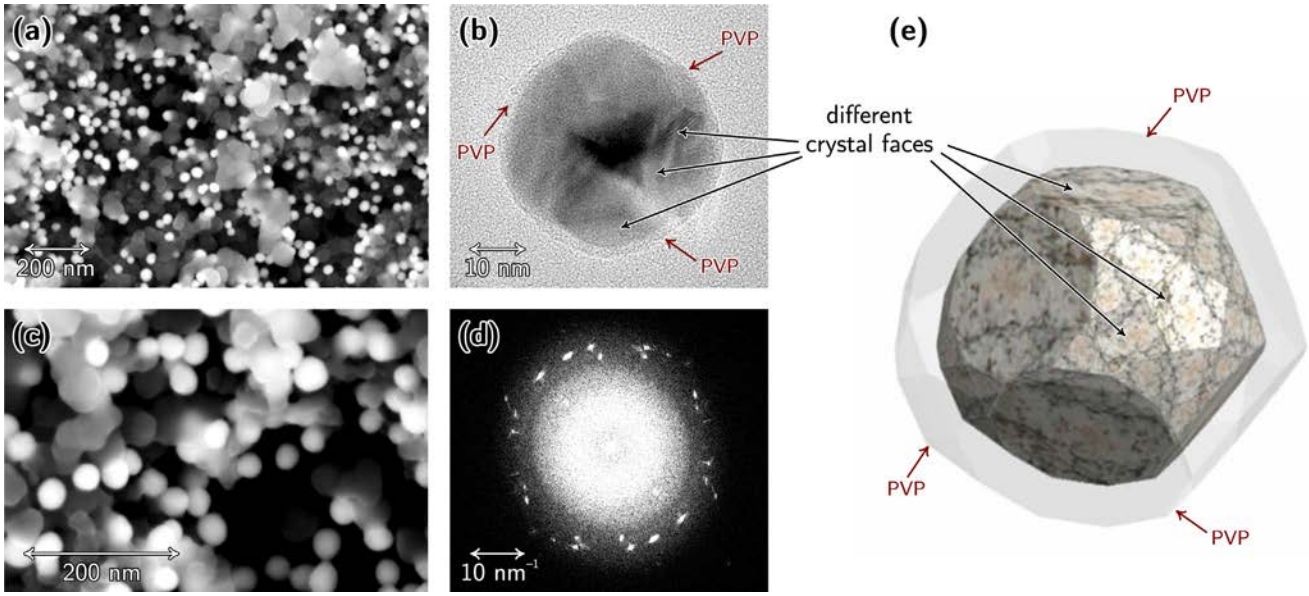

Fig. 3. Representative top-down SEM images (a, c) of PVP-capped Ag NPs dispersed on the carbon microporous layer of the GDE. The HR–TEM image (b) of an individual PVP-capped Ag NP, and its Fourier-transformed representation (d) demonstrate the polycrystalline nature of the nanoparticle, exhibiting different crystalline domains. Schematic drawing of the PVP-capped Ag NP is shown in (e). For a complete (top-down) SEM and TEM view of GDEs prepared by the use of Ag NPs capped with different ligands, see Figure S3 and S4 in the Supporting Information.

of about 37 nm. The HR–TEM image and the corresponding FFT representation of an individual PVP-capped Ag NP, shown in Fig. 3b and d, reveal the polycrystalline nature of the NPs. The drawing in Fig. 3e, inspired by the result of electron micrography, attempts to show a single Ag NP in three dimensions. Similar initial states were found in the case of Ag NPs capped by other ligands (BPEI, PEG and citrate). Independently of the nature of the capping agent used by the provider (NanoComposix) for the synthesis of the studied Ag NPs, we found that all NPs used in this work are of an (almost) spherical shape, as shown in Fig. 3e, and that the NPs exhibit no preferential faceting. The uniformly dispersed particles were isotropic but polycrystalline, and their average size was between 30 and 40 nm in all cases. Corresponding SEM and TEM images of all four types of surfactant-capped Ag NPs are shown in Figures S3 and S4, respectively, of the Supporting Information, where white-light interferometry images (top view of the catalyst layer, Figure S5), as well as cross-sectional (side view) SEM and EDX images (Figure S6) can also be found. The latter show that the majority of Ag NPs does not penetrate the GDE, and remains dispersed on top of the microporous layer.

CO_2RR/HER stressing. In order to study the electrochemical performance of Ag NP GDEs, potentiostatic electrolyses in the configuration shown in Fig. 2 were carried out at three different applied potentials. Keeping comparability in mind, all electrolyses were performed until the same amount of charge (300 C cm^{-2}, normalized to the geometric surface area of the circular opening of the zero-gap cell) passed through the electrolyser. The product distribution (that is, the partial current densities of CO and H_2 formation, see the dashed lines) were reconstructed on the basis of on-line GC measurements at given fixed time intervals, shown by the dots in Fig. 4.

As the amount of CO and H_2 detected by on-line GC measurements did not account for a 100% Faradaic efficiency, contents of the electrolyte were analysed post-electrolysis by ionic liquid chromatography (IC), which revealed a significant amount of formate production at each setting (see Table S3 in Supporting Information). As no water-soluble products apart from formate were detected after electrolysis by IC, it is safe to assign the missing fraction of the current density (hatched areas in Fig. 4 labelled "rest") to the production of formate [15,24].

Fig. 4 reveals a rather similar behaviour of three out of four studied catalysts. Namely, the PVP-, PEG- and citrate-capped Ag NPs all seem to exhibit a remarkable selectivity towards the production of CO, although especially at larger electrolysing potentials this selectivity, as well as the overall current, significantly decrease with time. That the catalytic performance of these NPs seems not to depend significantly on the nature of the applied capping agents suggests that already at initial stages of the electrolysis at least a partial removal of the capping shell from the surface of the NPs may have occurred, leaving catalytically active sites available to participate in CO_2RR [13,16,21].

As for BPEI-capped Ag NPs, both the overall current and the selectivity of CO production are considerably smaller (essentially at all three applied potentials), and this observation can be explained by the exceptionally strong bonding interactions between the amino groups of BPEI and the Ag NPs. Due to this strong bonding it seems plausible to assume that the BPEI-capped particles remain at least partially inaccessible for the reactants of electrolysis. As a result, the observed performance loss is in turn also smaller compared to the case of NPs capped by other agents (PVP, PEG or citrate).

In case of all four types of NPs, a clear decrease is observed in both the Faradaic efficiencies of CO formation and the current density as a function of time (*i.e.*, charge) at each potential. The performance decay is especially rapid at the electrolysing potential of –2.354 V, where the Faradaic efficiency of CO formation very quickly drops due to intense hydrogen evolution. Although less severe, performance losses can also be observed in the cases of lower electrolysing potentials in Fig. 4. The question whether the observed performance loss has anything to do with the actual morphology changes of the NPs during the electrolysis immediately follows: we found, however, that although by SEM and WAXS investigations significant morphology changes can indeed be monitored, these structural alterations are not the main cause of the performance losses observed in Fig. 4.

The obvious decrease of the overall current density and the relative selectivity of the catalyst NPs to produce CO is rather connected to another phenomenon, namely the formation of a mostly potassium carbonate-based precipitate over the GDE. This

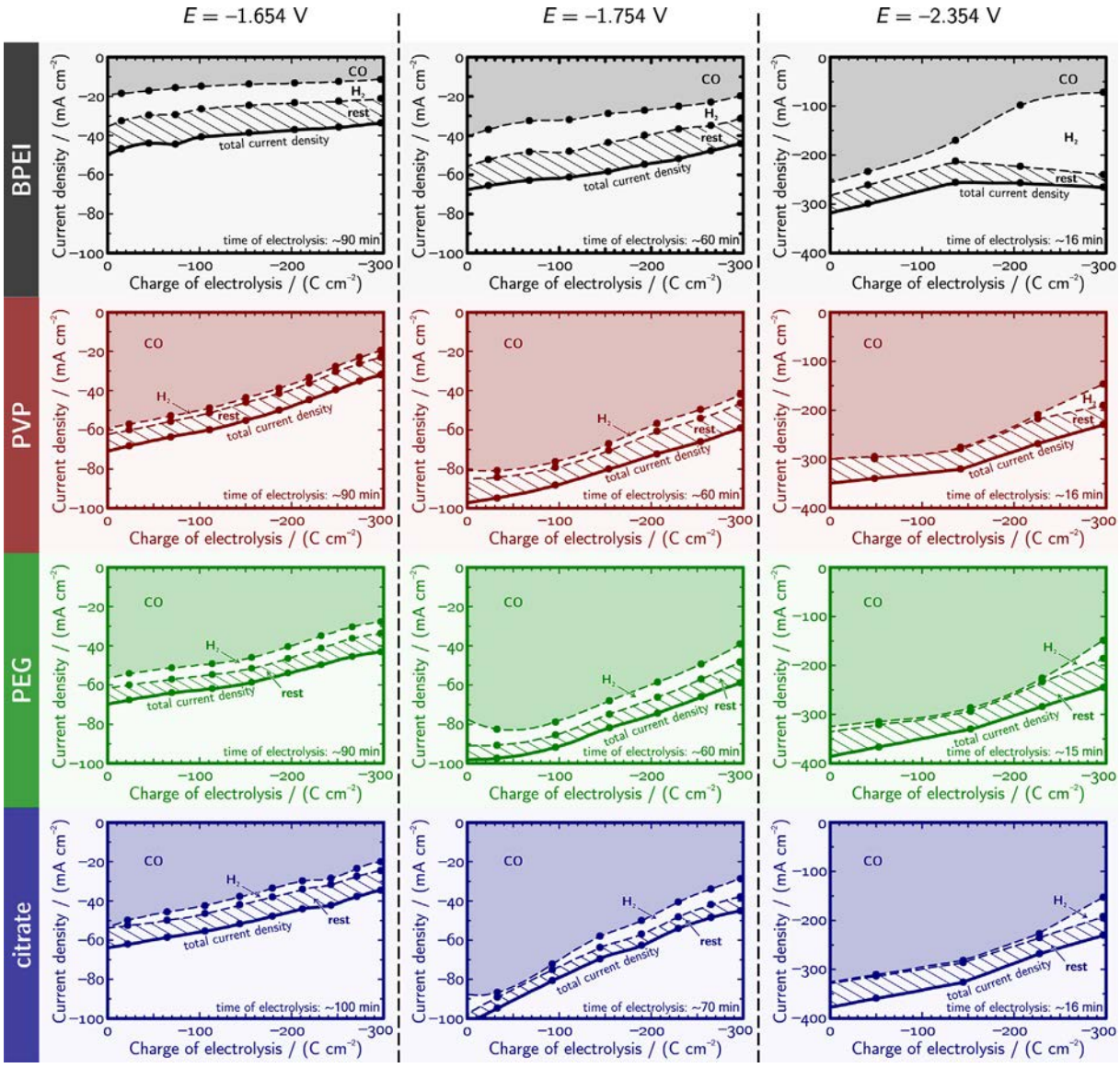

Fig. 4. Total current densities (full thick curves) plotted as a function of the passed charge density at different constant electrolysis potentials (measured vs. Ag/AgCl) for differently capped Ag NP GDEs. Electrolyses were stopped in all cases after the same amount of charge (−300 C cm^{-2}) was passed through the electrode. Shaded areas and dashed curves show the product distribution as reconstructed by GC measurements at different times (indicated by dots). Note that CO and H_2 were the only GC-detectable products that however did not account for a 100% of Faradaic efficiency. The "rest" of the current (hatched area in the graphs) can most probably be assigned to formate production (see the text and Tables S2 and S3 in Supporting Information for more details).

serious effect —that however does not hinder the observation of actual morphology changes on the nanoscale— is exemplified in Fig. 5.

As shown in Fig. 5, the pristine GDL we start out from (see Fig. 5a for a photograph) exhibits a clear surface, and the top- and side-view SEM images (Fig. 5b and c) reveal the expected structure of the surface microporous layer and the underlying carbon fibers. The surface of the top microporous layer is hydrophobic, as demonstrated by contact angle measurements on a sessile water drop, Fig. 5d. The EDX mapping analysis (Fig. 5q) reveals only carbon and fluorine signals in the elemental composition (the latter arises due to the PTFE treatment of the GDL applied by the manufacturer).

Fig. 5e shows a photograph of the (PVP-capped) catalyst ink drop-cast on the GDL. The circular area that will serve as the active cathode surface of the electrolyser (this will be in direct contact with the membrane) is shown here by a dashed circle. The catalyst NPs are clearly visible by SEM (Fig. 5f) and EDX-based elemental mapping (Fig. 5g) confirms that the NPs are clearly composed of Ag. Drop-casting the catalyst ink on the surface does not significantly decrease the hydrophobicity of the GDE (Fig. 5h), while in the EDX spectrum (Fig. 5h) the signal of Ag clearly appears.

When this GDE is subjected to CO_2RR/HER stressing, the formation of a potassium carbonate/bicarbonate based precipitate immediately becomes visible also to the bare eye, as shown in the photograph of Fig. 5i. An SEM image of the formed carbonate plaque is shown in Fig. 5j, and the elemental composition map of Fig. 5k reveals K as a major component of this plaque. Due to the formation of the carbonate precipitate the surface of the GDE becomes hydrophilic (Fig. 5l) and the signals of both K and O appear in the EDX spectra of Fig. 5q.

That the formed carbonate plaque is beyond doubt responsible for the performance losses observed before in Fig. 4 can be proven by a set of "recovery" experiments. These show (see Figure S12 in

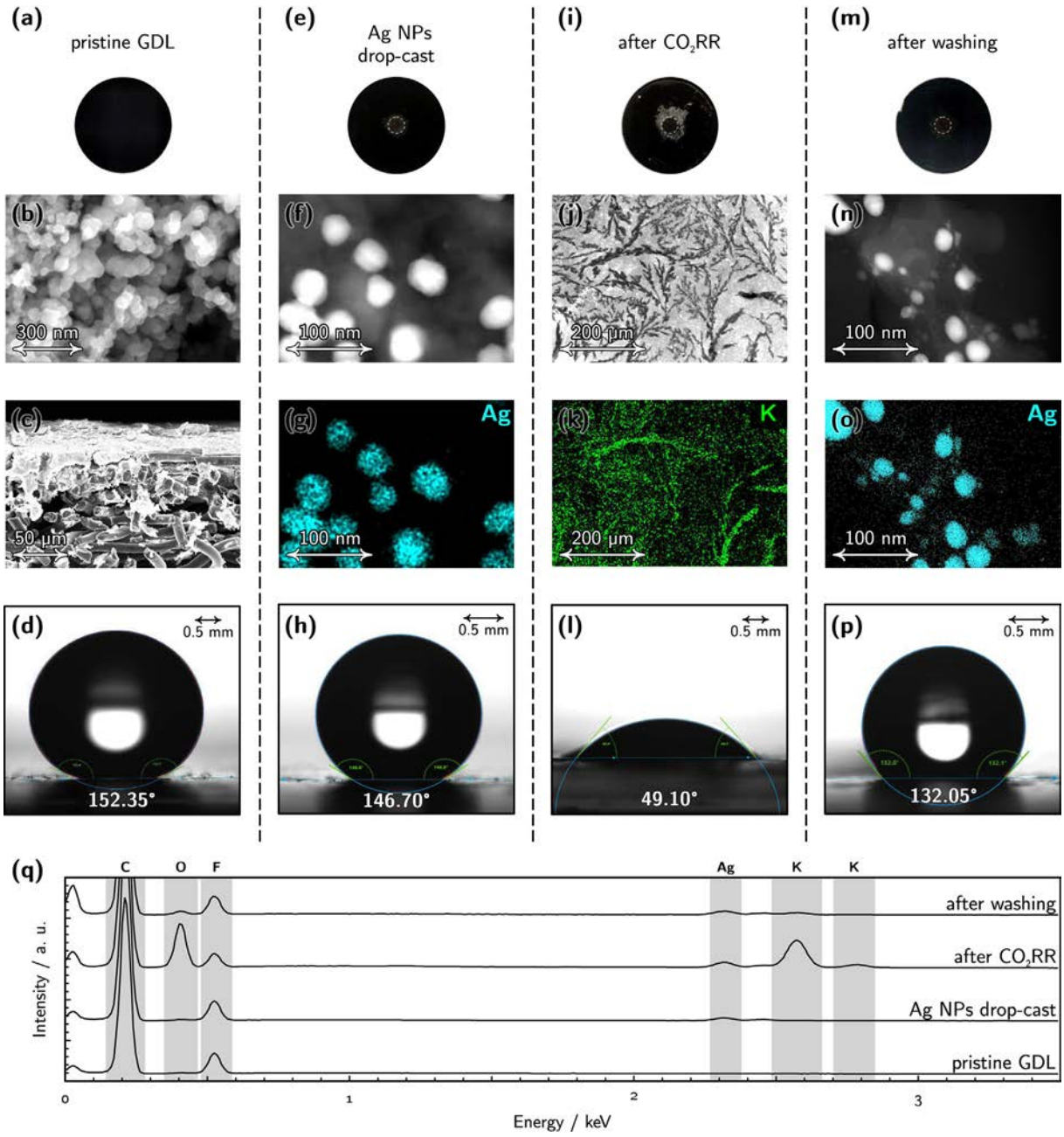

Fig. 5. The characteristic features of a pristine GDL significantly change after surfactant-capped Ag NPs are drop-cast on it, the thus prepared GDE is used for electrolysis, and finally, after the carbonate precipitate formed during CO_2RR/HER stressing is washed away. See the text for an exact description of each panel, and Figures S7–S11 of the Supporting Information for more details.

Supporting Information) that following a removal of the carbonate layer by dip-washing, already used GDEs can almost completely regain their efficiency in a subsequent electrolysis.

As the formed carbonate plaque makes us unable to study the degradation of NPs during CO2RR/HER stressing, the carbonate precipitate was removed from the surface following electrolysis by careful dip-washing (see Figure S8 in Supporting Information for details). A photograph of the GDE following the dissolution of the carbonate plaque is shown in Fig. 5m, and the subsequently taken SEM images (Fig. 5n and o) clearly indicate that this cleaning method does leave the actual catalyst NPs intact (compare panels n and o with f and g in Fig. 5). The accuracy of the dip-washing method is also proven by EDX (Fig. 5q) showing that the K and O signals almost fully disappear and the Ag signal is regained after washing. That the dip-washing technique we used to remove the carbonate plaque from over the catalyst surface did not result in any significant catalyst (Ag) loss was confirmed by ICP–MS analysis (see Table S4 in Supporting Information).

Morphology changes of Ag NPs on GDEs studied by SEM. The reliability of the applied dip-washing method allowed us to apply SEM analysis in order to study the structural changes that the differently capped Ag NPs undergo during extensive CO_2RR/HER stressing. Representative SEM images of pre- and post-electrolysis (dip-washed) samples are shown in Fig. 6 for the studied four types of surfactant-capped Ag NP catalysts. The histograms shown in Fig. 7 were prepared by manually processing several micrographs similar to those shown in Fig. 6: the size of each NP, regardless

to form, was determined by measuring its longest dimension as illustrated by Figure S13 in the Supporting Information.

Expectation ranges of the particle sizes (mode±deviation) were determined by making the histograms shown in Fig. 7 subject to probability distribution fitting. Histograms exhibiting a single mode were fitted by log-normal distributions yielding an unsymmetrical (skewed) expectation range, while in case of bimodal distributions the linear combination of two (symmetric) Gaussians were used to describe our datasets. Expectation ranges for the average particle size are specified for all panels of Fig. 7, making it apparent that the morphology of the Ag NPs evolved differently in case of the four different capping agents.

In case of BPEI, the observed particle size distributions are bimodal both before and after electrolyses. Interestingly, the second characteristic particle size (corresponding to a smaller peak) is twice of the first one, which implies, taking into consideration that we used the longest measurable dimension for particle sizing, two-particle aggregates were present at the GDE surface, already before electrolysis. As also shown in Fig. 7, however, no significant change of the characteristic particle sizes are observed when BPEI-capped Ag NPs are exposed to electrolysis stressing at different potentials, and this is in agreement with the results of Fig. 4 that also show a relatively stable catalytic performance of BPEI-capped Ag NPs.

The situation is markedly different in the case of PVP-capped nanoparticles that, as shown in Fig. 7, tend to corrode during electrolysis. Corrosion in case of PVP-capped Ag NPs leads to a significant decrease of the characteristic particle size, as well as to a general broadening and a larger skewness of the distribution.

In the case of PEG, stressing by CO_2RR/HER seems to have rather the opposite effect. While the first characteristic particle size remains essentially unchanged, as a result of electrolysis a second peak becomes visible in the histograms, and the maximum of this peak is approximately twice of that of the first one. This is a clear hint [25] to that in case of PEG, particle coalescence is the most favoured mode of catalyst degradation (see also the micrographs of Fig. 6).

The general increase of particle sizes is also apparent in the case of citrate-capped Ag NPs, as shown in the last row of Fig. 7, although in this case no evolution of further, distinct modes are seen: the histograms, instead, get significantly broadened and skewed as a result of electrolysis. In this particular case we assume that due to the relative instability of the citrate shell at the applied (negative) potentials, the NPs quickly become almost totally unprotected [26]. As a result, their aggregation/coalescence becomes unhindered, and apart from the coalescence of neighbouring particles, also Ostwald ripening (either its two or three-dimensional form) occurs in this case [27,28].

To conclude, the SEM analyses seem to suggest that PVP-capped particles undergo more the corrosion pathway of degradation (Fig. 1), while PEG- and citrate-capped NPs tend more to aggregate, coalesce, and (especially in case of citrate) some form of Ostwald

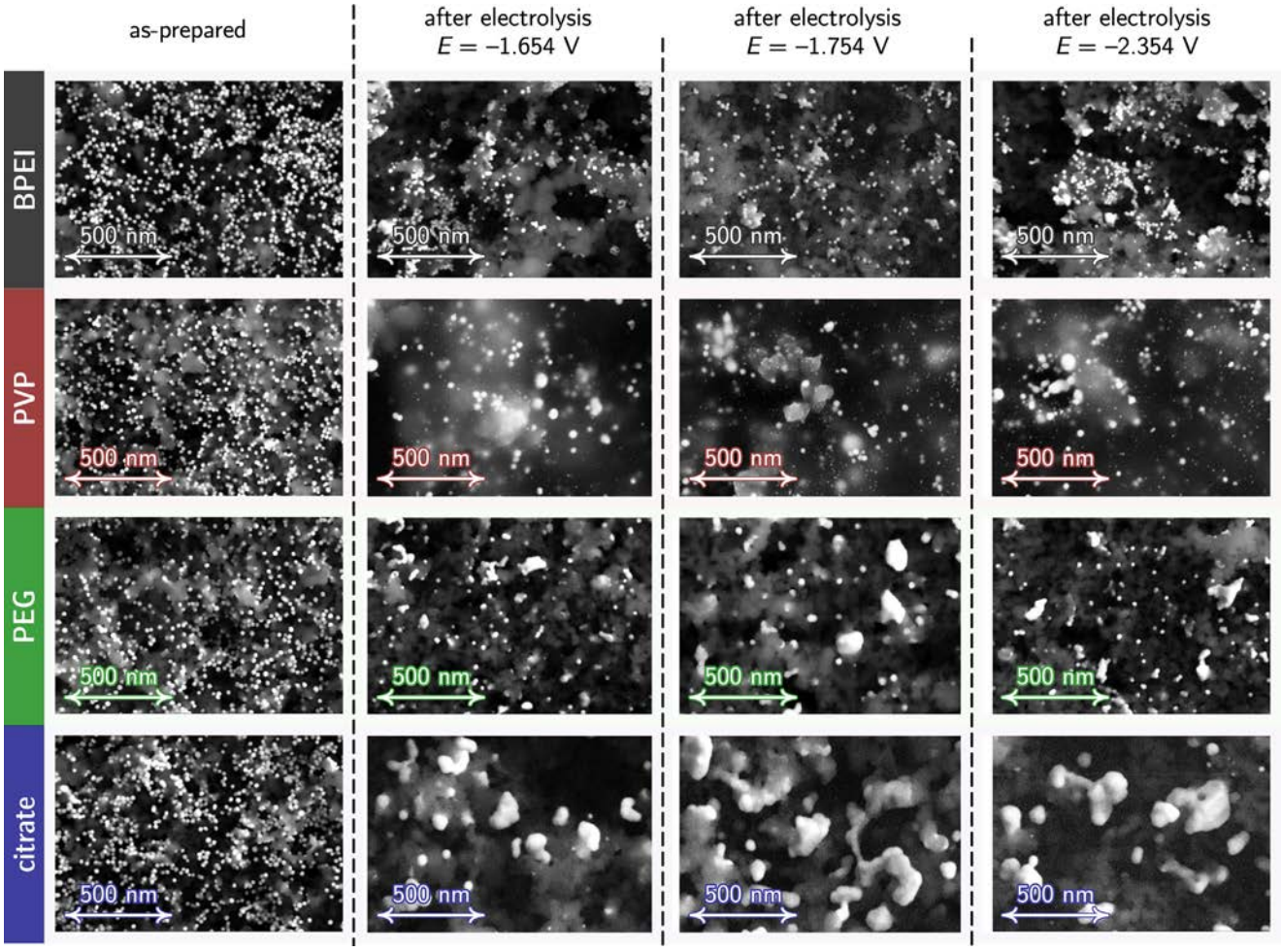

Fig. 6. Representative SEM micrographs of GDEs prepared using Ag NPs stabilized by different capping agents, recorded before ("as-prepared") and after constant charge electrolyses at different potentials (cf. to Fig. 4). These, as well as some other similar SEM images were used to construct the histograms shown in Fig. 7.

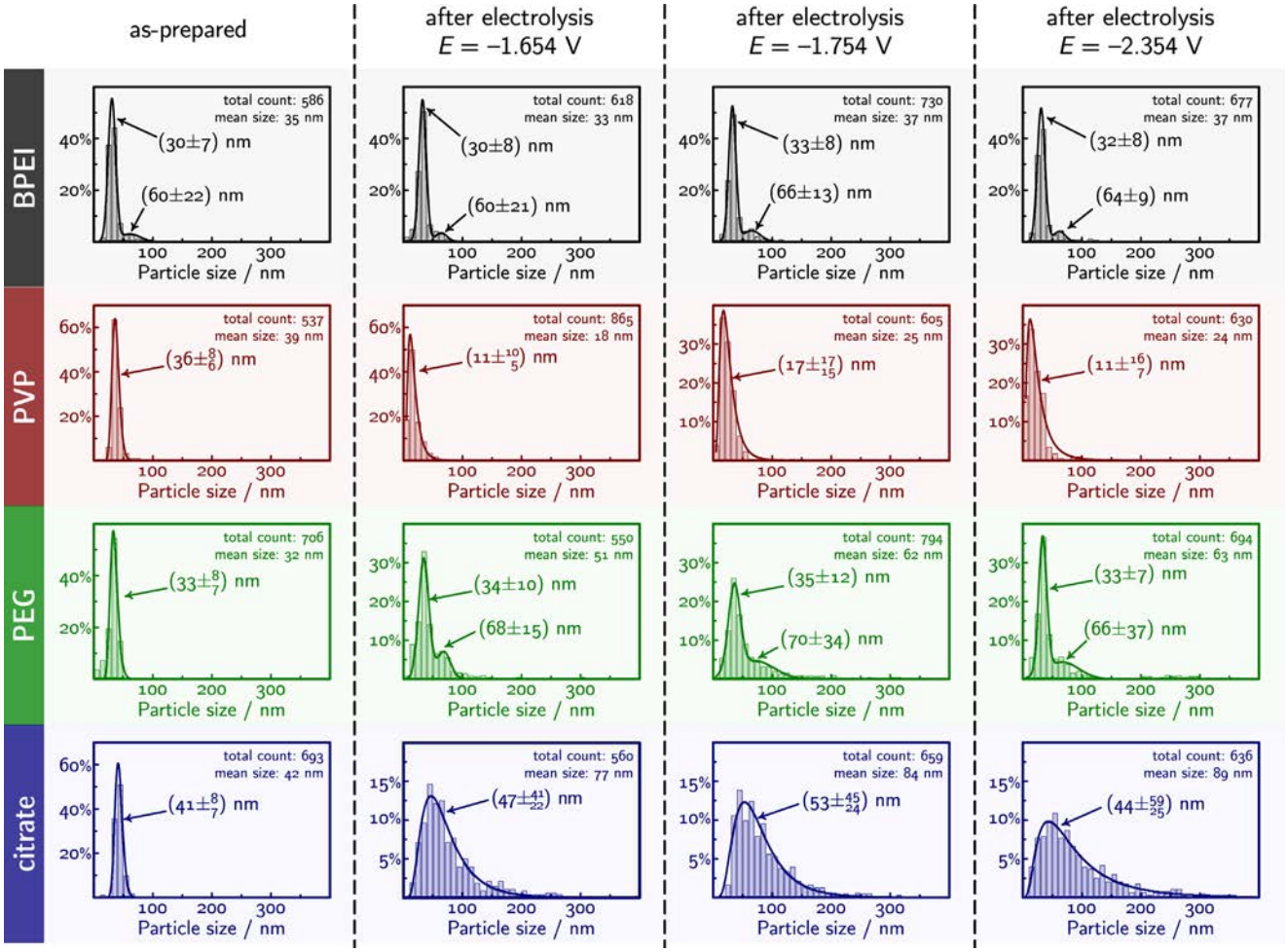

Fig. 7. Histograms showing the particle size distribution of Ag NPs, capped by different ligands, before and after electrolysis at a given potential. Expectation ranges of the particle size are shown for the fitted peak(s).

ripening also seems to take place. Amongst the studied capping agents, BPEI seems to be the most protecting one, as in this case no particular changes of the size distribution was observed when comparing post- to pre-electrolysis SEM images.

Morphology changes of Ag NPs on GDEs studied by WAXS analysis. The above picture can further be nuanced if we also use WAXS measurements to characterize the morphology changes of Ag NP catalysts during electrolysis (Fig. 8). The width of the WAXS peaks have two main contributions —apart from instrumental broadening—, and these are the size of coherently scattering domain (crystallite size) and microstrain (deviation from perfect order). These different characteristic parameters were determined by Rietveld fits of the diffraction pattern. Because the size determined by Rietveld fit maps crystallite sizes rather than full geometrical sizes, direct comparison between the WAXS and SEM-based analysis can reveal new insights about the degradation phenomena. First we note that using only the isotropic size model did not fit the data well. The fits improved significantly only after a size anisotropy had been included, implying that the nanoparticles have preferred growth orientation along the (111) direction (Fig. 8 and Figure S16 in Supporting Information). Along this direction, the crystallite size is about two times longer when compared to the short directions.

In the case of BPEI, the crystallite size is smaller than the particle size determined by the SEM analysis. This hints that the particles are composed from several crystallites, in agreement with the TEM observations. In this case the size does not change significantly, supporting the conclusions from the SEM analysis that the particles are stable during electrolysis. The microstrain shows a very low value for as-prepared NPs, but increases significantly for the samples measured after electrolysis. Given that the microstrain is a direct measure of internal disorder of the crystallites, the electrolysis seems to distort the local order which is typically linked to the increase of grain boundaries length. However, as in our case we do not observe any decrease in crystallite dimensions, the increase of microstrain should either be linked to surface phenomena caused by changes in the BPEI surface structure [29], or, alternatively, could be explained by some carbonate precipitates (that were not entirely removed by dip-washing) remaining adherent to the catalyst NPs (cf. to Fig. 5 exhibiting a small K signal even after washing).

The PVP case shows different behaviour. After electrolysis, the crystallite size increases in both directions, independently of the applied current, and the microstrain values increase moderately. This crystallite size increase is apparently opposite to the SEM-derived trend in particle size and the crystallites appear significantly larger than the physical size measured by SEM. This is caused by a broadening of the particle size distribution during electrocatalysis that is due to the formation of some amount of larger NPs while the average size shows a general decrease in the SEM measurements. It is of worth to note that while SEM results a number-weighted distribution, the diffraction amplitude is weighted by the volume of the NPs, therefore the crystallite size

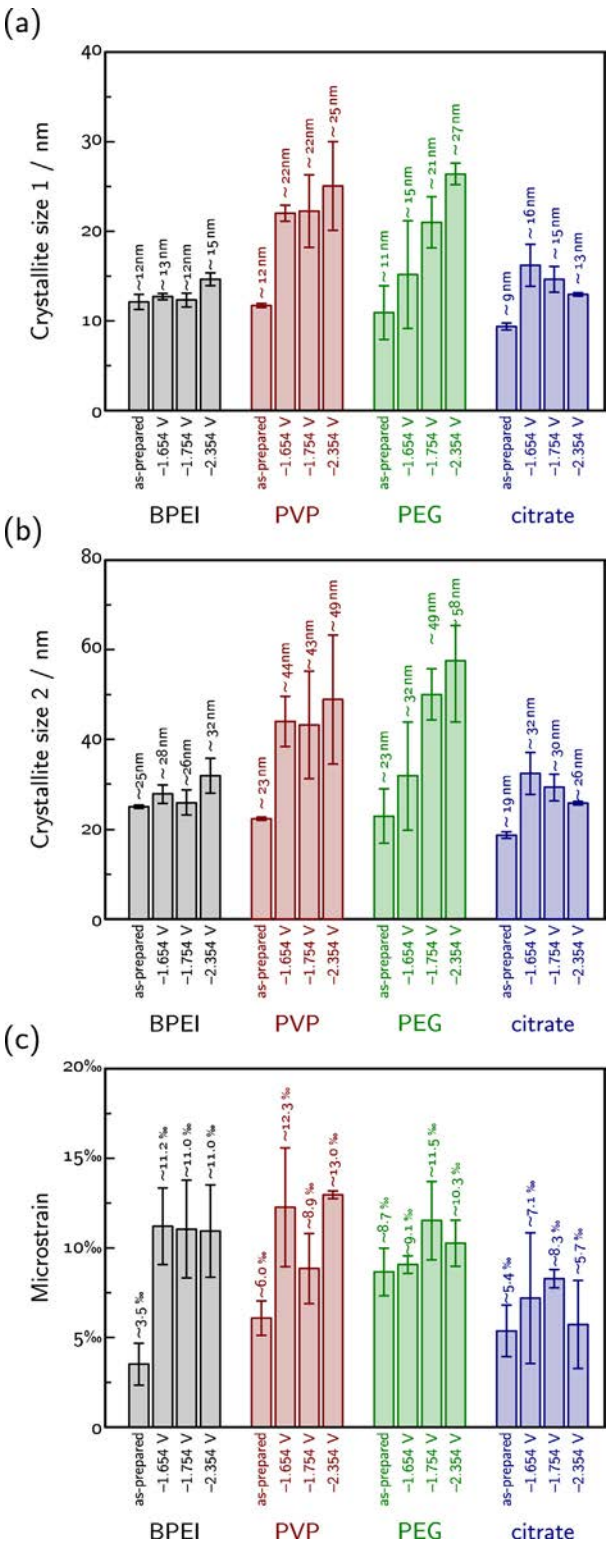

Fig. 8. Crystallite sizes (a, b) and microstrain (c) measured by WAXS of Ag NPs, capped by different ligands, before and after electrolysis at a given potential.

is much more sensitive to the appearance of larger NPs in the whole ensemble. This can result in crystallite sizes seemingly larger than the size of the NPs as determined by SEM using the distribution maximum. Based on the above observations we can conclude that apart from corrosion, that is a dominant pathway of the degradation of PVP-capped Ag NPs, Ostwald ripening also takes place in this case — and this causes both the increase of crystallite sizes (Fig. 8) and the broadening towards bigger sizes of the SEM-based size distribution (Fig. 7).

WAXS measurements on PEG-capped Ag NPs show a similar trend of increasing crystallite size, consistently with the appearance of bimodality in the SEM-based size distribution. PEG-capped NPs are not only aggregated, but the individual crystallites are also fused together through coalescence during electrolysis. The picture is somewhat different for citrate capped NPs that although as evidenced by SEM clearly undergo coalescence to a large extent during electrolysis, at the same time show only a moderate increase of the crystallite size. This is a hint to that the fusion of the NPs does not necessarily involve the merging of crystallites and that the enormously large Ag particles formed from citrate-capped Ag NPs during electrolysis (see, e.g, Fig. 6) can be composed of several distinct crystalline domains. The relatively low changes of microstrain observed in the case of PEG- and citrate-capped NPs are likely linked to the fact that the capping agent is only loosely bound to the surface of these NPs.

Ligand removal and exchange experiments. That in our investigations we saw the most severe degradation taking place in the case of citrate-capped Ag NPs can plausibly be explained by the fact that citrate stabilizes the NPs not by a steric effect as the other three studied ligands do, but by an electrostatic force. It can thus safely be assumed that under the operating conditions of electrolyses — that is, at high cathodic potentials— most of the negatively charged citrate ions will leave not only the surface of the NPs but they would also desorb from the surface of the carbon support. This can enhance the surface mobility of the particles, leading to their more rapid aggregation and then coalescence.

In order to check whether ligand molecules that may have remained adsorbed on the support in the three other (non-citrate) case have any role in determining the degradation pathway of the NPs, we designed a set of ligand exchange/removal experiments. These were based on separating the NPs from their parent dispersion by centrifugation, which left the majority of the capping agents —that would necessarily end up on the support surface during the GDE preparation— in the supernatant (see Table S5 and Figure S14 in Supporting Information). Filtering and re-dispersing the nanoparticles in Milli-Q water after centrifugation (see Section 2 for details) thus allowed us the (at least partial) removal of the carbon substrate-attached ligands or, if re-dispersion took place in the solution of another capping agent, the (again, at least partial) exchange of ligands.

The effect of ligand removal on electrolysis-induced degradation is shown in Fig. 9 for PVP-capped Ag NPs (this time, electrolysis took place at $E = -1.754$ V, see Figure S15a in Supporting Information for more details). We can see a notable difference if we compare this figure to the appropriate panels of Figs. 6 and 7: namely, that while the initial size distribution of the NPs is seemingly unaffected by the removal of excess PVP, the degradation pathway markedly changes. While in the previous case, when excess PVP was adsorbed on the carbon support layer, we primarily observed corrosion (and the change of the average particle size from around 39 to 25 nm), in Fig. 9 we see an increase of the average size (from 42 to 67 nm) and a significant broadening of the distribution. It seems to be a plausible assumption that the apparent coalescence we observe here was in the previous case hindered by support-adsorbed PVP, rendering the degrading NPs immobile. Alternatively, the removal of a significant portion of PVP from the surface of the NPs might have also lead to an increase of the average particle size by allowing quicker Ostwald ripening.

The role of support-adsorbed ligands can further be emphasized if we carry out a ligand exchange (as opposed to removal) experiment with citrate-capped Ag NPs that we in this case after centrifugation re-disperse in a PVP solution. As shown in Fig. 10, this

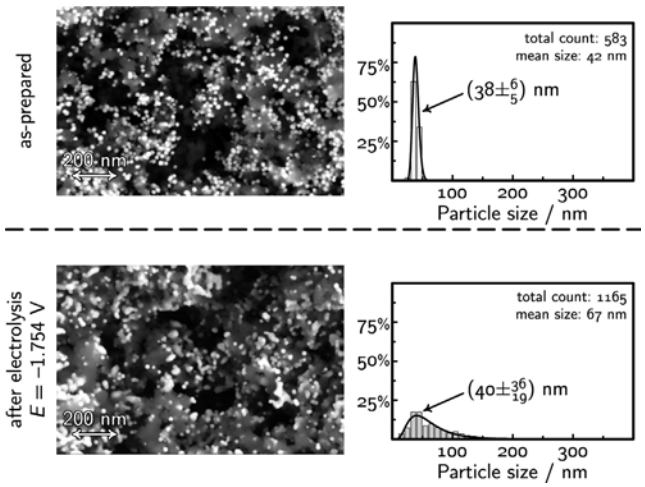

Fig. 9. The partial removal of the excess PVP from the catalyst ink results in less PVP adsorbed on the carbon support, facilitating more the aggregation (rather than the corrosion) of Ag NPs. (Cf. to Figs. 6 and 7).

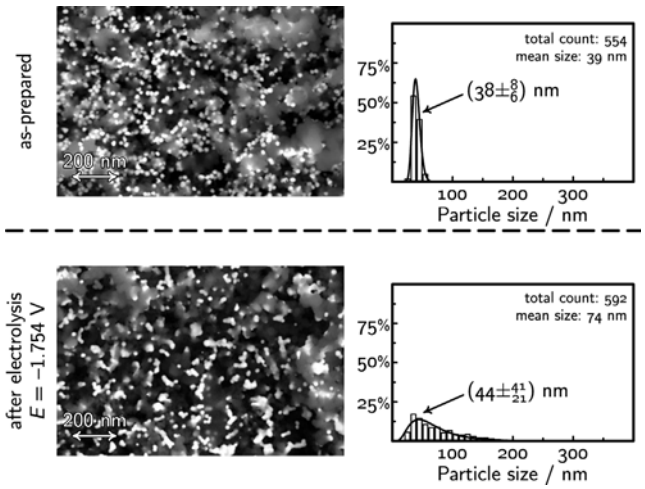

Fig. 10. The partial citrate → PVP ligand exchange in the catalyst ink results in more PVP adsorbed on the carbon support, somewhat hindering the coalescence degradation pathway otherwise observable for citrate-capped NPs. (Cf. to Figs. 6 and 7.).

can milden the coalescence of particles (otherwise characteristic for citrate-capped NPs, see Fig. 6 and 7), and this effect can also be explained by the adsorption of the extra PVP amount on the support surface, hindering the motion of the degrading NPs. (For more details of the electrolysis experiments, see Figure S15b of the Supporting Information.).

4. Conclusion

In this paper we used Ag NPs capped by different stabilizing ligands to prepare gas diffusion electrodes that we applied for CO_2 electroreduction in a zero-gap gas-flow electrolyser. This configuration allowed a high current stressing of the NPs. After careful cleaning of the GDE from the carbonate precipitates formed during electolysis, we compared SEM images of the catalyst NPs obtained before and after the high current testing, and made these subject to a statistical analysis.

We showed that amongst the studied capping agents, BPEI is the most protective one; in turn, however, it also limits CO formation the most. In case of PVP, mostly corrosion (particle shrinkage) was observed at practically relevant electrolysing potentials, while the application of PEG and that of citrate lead more to particle coalescence. In parallel with the SEM-based investigations, WAXS analysis was also used to follow the evolution of crystallite size and lattice strain during CO_2RR/HER stressing, and the results were compared to those of SEM mapping.

By studying the effects of capping agent removal and exchange we demonstrated that apart from ligands directly attached to the Ag NPs, also the excess of capping agents (adsorbed on the carbon support surface) plays a decisive role in determining the extent and mode of catalyst degradation.

Declaration of Competing Interest

The authors declare that they have no known competing financial interests or personal relationships that could have appeared to influence the work reported in this paper.

Acknowledgement

P. B. acknowledges financial support by NCCR Catalysis. S. V. acknowledges support from the National Research, Development and Innovation Office of Hungary (NKFIH grant FK135375). M. L., Y. K., H. H., and C. S. acknowledge the financial support by the Chinese Scholarship Council (CSC).

Appendix A. Supplementary material

Supplementary data associated with this article can be found, in the online version, at https://doi.org/10.1016/j.jcat.2021.10.016.

References

[1] D.R. Feldman, W.D. Collins, P.J. Gero, M.S. Torn, E.J. Mlawer, T.R. Shippert, Observational determination of surface radiative forcing by CO_2 from 2000 to 2010, Nature 519 (2015) (2000) 339–343, https://doi.org/10.1038/nature14240.

[2] D.T. Whipple, P.J.A. Kenis, Prospects of CO_2 utilization via direct heterogeneous electrochemical reduction, J. Phys. Chem. Lett. 1 (2010) 3451–3458, https://doi.org/10.1021/jz1012627.

[3] H. Coskun, A. Aljabour, P.D. Luna, D. Farka, T. Greunz, D. Stifter, M. Kus, X. Zheng, M. Liu, A.W. Hassel, W. Schöfberger, E.H. Sargent, N.S. Sariciftci, P. Stadler, Biofunctionalized conductive polymers enable efficient CO_2 electroreduction, Sci. Adv. 3 (8) (2017) e1700686, https://doi.org/10.1126/sciadv.1700686.

[4] Y. Hori, Electrochemical CO_2 reduction on metal electrodes, in: C.G. Vayenas, R.E. White, M.E. Gamboa-Aldeco (Eds.), Modern Aspects of Electrochemistry, Vol. 42, Springer, 2008, pp. 89–189.

[5] S. Vesztergom, A. Dutta, M. Rahaman, K. Kiran, I.Z. Montiel, P. Broekmann, Hydrogen bubble templated metal foams as efficient catalysts of CO_2 electroreduction, ChemCatChem 13 (2020) 1039–1058, https://doi.org/10.1002/cctc.202001145.

[6] F. Yu, P. Wei, Y. Yang, Y. Chen, L. Guo, Z. Peng, Material design at nano and atomic scale for electrocatalytic CO_2 reduction, Nano, Mater. Sci. 1 (2019) 60–69, https://doi.org/10.1016/j.nanoms.2019.03.006.

[7] D. Sun, X. Xu, Y. Qin, S.P. Jiang, Z. Shao, Rational design of Ag-based catalysts for the electrochemical CO_2 reduction to CO: A review, ChemSusChem 13 (2019) 39–58, https://doi.org/10.1002/cssc.201902061.

[8] R. Reske, H. Mistry, F. Behafarid, B.R. Cuenya, P. Strasser, Particle size effects in the catalytic electroreduction of CO_2 on Cu nanoparticles, J. Am. Chem. Soc. 136 (19) (2014) 6978–6986, https://doi.org/10.1021/ja500328k.

[9] A. Dutta, A. Kuzume, V. Kaliginedi, M. Rahaman, I. Sinev, M. Ahmadi, B. Roldán Cuenya, S. Vesztergom, P. Broekmann, Probing the chemical state of tin oxide NP catalysts during CO_2 electroreduction: A complementary operando approach, Nano Energy 53 (2018) 828–840, https://doi.org/10.1016/j.nanoen.2018.09.033.

[10] Y. Hou, N. Kovács, H. Xu, C. Sun, R. Erni, M. Gálvez-Vázquez, A. Rieder, H. Hu, Y. Kong, M. Liu, B.J. Wiley, S. Vesztergom, P. Broekmann, Limitations of identical location SEM as a method of degradation studies on surfactant capped nanoparticle electrocatalysts, J. Catal. 394 (2020) 58–66, https://doi.org/10.1016/j.jcat.2020.12.006.

[11] P.C. Okonkwo, O.O. Ige, E.M. Barhoumi, P.C. Uzoma, W. Emori, A. Benamor, A. M. Abdullah, Platinum degradation mechanisms in proton exchange membrane fuel cell (PEMFC) system: A review, Int. J. Hydrog. Energy 46 (29) (2021) 15850–15865, https://doi.org/10.1016/j.ijhydene.2021.02.078.

[12] J. Huang, N. Hörmann, E. Oveisi, A. Loiudice, G.L. De Gregorio, O. Andreussi, N. Marzari, R. Buonsanti, Potential-induced nanoclustering of metallic catalysts during electrochemical CO_2 reduction, Nat. Commun. 9 (1) (2018) 3117, https://doi.org/10.1038/s41467-018-05544-3.
[13] J.R. Pankhurst, P. Iyengar, A. Loiudice, M. Mensi, R. Buonsanti, Metal–ligand bond strength determines the fate of organic ligands on the catalyst surface during the electrochemical CO_2 reduction reaction, Chem. Sci. 11 (2020) 9296–9302, https://doi.org/10.1039/d0sc03061a.
[14] S. Popović, M. Smiljanić, P. Jovanovič, J. Vavra, R. Buonsanti, N. Hodnik, Stability and degradation mechanisms of copper-based catalysts for electrochemical CO_2 reduction, Angew. Chem. 132 (35) (2020) 14844–14854, https://doi.org/10.1002/ange.202000617.
[15] M.de.J. Gálvez-Vázquez, P. Moreno-García, H. Xu, Y. Hou, H. Hu, I. Zelocualtecatl Montiel, A.V. Rudnev, S. Alinejad, V. Grozovski, B.J. Wiley, M. Arenz, P. Broekmann, Environment matters: CO_2RR electrocatalyst performance testing in a gas-fed zero-gap electrolyzer, ACS Catal. 10 (21) (2020) 13096–13108, https://doi.org/10.1021/acscatal.0c03609.
[16] H. Hu, M. Liu, Y. Kong, N. Mysuru, C. Sun, M. d. J. Gálvez-Vázquez, U. Müller, R. Erni, V. Grozovski, Y. Hou, P. Broekmann, Activation matters: Hysteresis effects during electrochemical looping of colloidal Ag nanowire catalysts, ACS Catal. 10 (2020) 8503–8514. doi:https://doi.org/10.1021/acscatal.0c02026.
[17] C.-T. Dinh, F.P.G. de Arquer, D. Sinton, E.H. Sargent, High rate, selective, and stable electroreduction of CO_2 to CO in basic and neutral media, ACS Energy Lett. 3 (2018) 2835–2840, https://doi.org/10.1021/acsenergylett.8b01734.
[18] T. Haas, R. Krause, R. Weber, M. Demler, G. Schmid, Technical photosynthesis involving CO_2 electrolysis and fermentation, Nat. Catal. 1 (2018) 32–39, https://doi.org/10.1038/s41929-017-0005-1.
[19] C.V. Restrepo, C.C. Villa, Synthesis of silver nanoparticles, influence of capping agents, and dependence on size and shape: A review, Environ. Nanotechnol. Monit. Manag. 15 (2021) 100428, https://doi.org/10.1016/j.enmm.2021.100428.
[20] R. Szűcs, D. Balogh-Weiser, E. Sánta-Bell, E. Tóth-Szeles, T. Varga, Z. Kónya, L. Poppe, I. Lagzi, Green synthesis and in situ immobilization of gold nanoparticles and their application for the reduction of p-nitrophenol in continuous-flow mode, RSC Adv. 9 (2019) 9193–9197, https://doi.org/10.1039/c8ra10373a.
[21] M. d. J. Gálvez-Vázquez, H. Xu, P. Moreno-García, Y. Hou, H. Hu, B.J. Wiley, S. Vesztergom, P. Broekmann, Unwrap them first: Operando potential-induced activation is required when using PVP-capped Ag nanocubes as catalysts of CO_2 electroreduction, Chimia 75 (2021) 163–168. doi:https://doi.org/10.2533/chimia.2021.163.
[22] J. Kieffer, J.P. Wright, PyFAI: A Python library for high performance azimuthal integration on GPU, Powder Diffr. 28 (2013) S339–S350, https://doi.org/10.1017/s0885715613000924.
[23] B.H. Toby, R.B.V. Dreele, GSAS-II: The genesis of a modern open-source all purpose crystallography software package, J. Appl. Crystallogr. 46 (2013) 544–549, https://doi.org/10.1107/s0021889813003531.
[24] J.S. Yoo, R. Christensen, T. Vegge, J.K. Nørskov, F. Studt, Theoretical insight into the trends that guide the electrochemical reduction of carbon dioxide to formic acid, ChemSusChem 9 (2015) 358–363, https://doi.org/10.1002/cssc.201501197.
[25] C. Spöri, J.T.H. Kwan, A. Bonakdarpour, D.P. Wilkinson, P. Strasser, The stability challenges of oxygen evolving catalysts: Towards a common fundamental understanding and mitigation of catalyst degradation, Angew. Chem. Int. Ed. 56 (2017) 5994–6021, https://doi.org/10.1002/anie.201608601.
[26] I. Schrader, J. Warneke, S. Neumann, S. Grotheer, A.A. Swane, J.J.K. Kirkensgaard, M. Arenz, S. Kunz, Surface chemistry of "unprotected" nanoparticles: A spectroscopic investigation on colloidal particles, J. Phys. Chem. C 119 (31) (2015) 17655–17661, https://doi.org/10.1021/acs.jpcc.5b03863.
[27] J.A.S. Bett, K. Kinoshita, P. Stoneheart, Crystallite growth of platinum dispersed on graphitized carbon black II. Effect of liquid environment, J. Catal. 41 (1976) 124–133, https://doi.org/10.1016/0021-9517(76)90207-4.
[28] P.J. Ferreira, G.J. la O', Y. Shao-Horn, D. Morgan, R. Makharia, S. Kocha, H.A. Gasteiger, Instability of Pt/C electrocatalysts in proton exchange membrane fuel cells, J. Electrochem. Soc. 152 (2005) A2256. doi:https://doi.org/10.1149/1.2050347.
[29] R. Chattot, P. Bordet, I. Martens, J. Drnec, L. Dubau, F. Maillard, Building practical descriptors for defect engineering of electrocatalytic materials, ACS Catal. 10 (2020) 9046–9056, https://doi.org/10.1021/acscatal.0c02144.

Supporting Information
to the paper entitled

The Capping Agent is the Key: Structural Alterations of Ag NPs during CO_2 Electrolysis Probed in a Zero-Gap Gas-Flow Configuration

M. Liu, Y. Kong, H. Hu, N. Kovács, Ch. Sun, I. Zelocualtecatl Montiel, M. de J. Gálvez-Vázquez, Y. Hou, M. Mirolo, I. Martens, J. Drnec, S. Vesztergom, P. Broekmann

Contents

Figure S1. Schematics of the zero-gap gas-flow electrolyser....2
Figure S2. SEM investigation of the pristine GDL....2
Figure S3. SEM investigation of as-prepared Ag NP GDEs (different capping agents)....3
Table S1. Mass loading data....3
Figure S4. TEM image of individual Ag NPs capped by different ligands....4
Figure S5. White light interferometry of GDEs....5
Figure S6. Side-view of the catalyst layer (SEM and EDX)....6
Table S2. Electrochemical measurement data on Ag NP GDEs....7
Table S3. The amount of formate produced during electrolyses....8
Table S4. Changes of Ag mass loading during electrolyses....8
Figure S7. Photos of the GDE at different stages of experiment....8
Figure S8. Photo of carbonate plaque removal....9
Figure S9. Characterization of the formed carbonate plaque....9
Figure S10. Contact angle measurements, microporous layer (top) side....10
Figure S11. Contact angle measurements, fibrous layer (bottom) side....11
Figure S12. Recovery after dip-washing....11
Figure S13. Illustration of the particle sizing by SEM....12
Table S5. TOC and TON measurements of NP-bound and free ligands....12
Figure S14. Separation of NPs from dispersion by centrifugation....13
Figure S15. Electrochemistry and GC data for surfactant removal and exchange experiments....14
Table S6. Numerical data for Figure S15....14
Figure S16. Example of Rietveld refinement of WAXS data....14

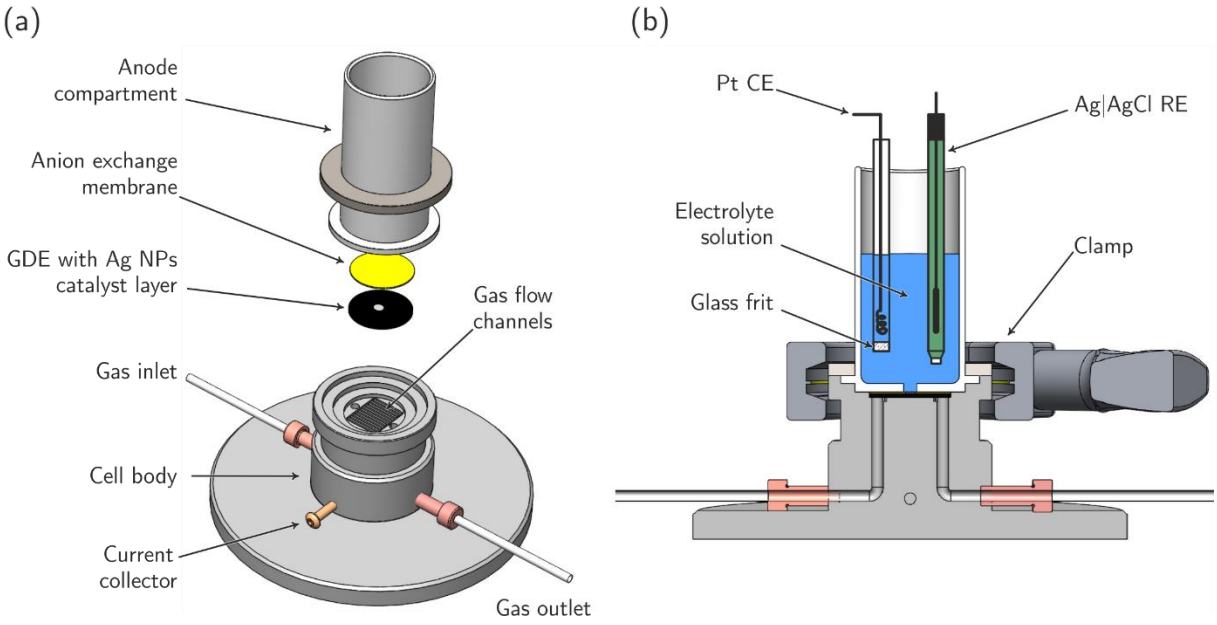

Figure S1. Schematics of the zero-gap gas-flow electrolyser. (a) Exploded drawing of the electrolyser used in this work for studying the morphological evolution of different surfactant-capped Ag nanoparticles (Ag NPs) applied as catalyst material for electrochemical CO_2 conversion. (b) Cross-sectional drawing of the assembled flow cell during operation. Adapted from *ACS Catal.* **2020**, *10*, 13096–13108.

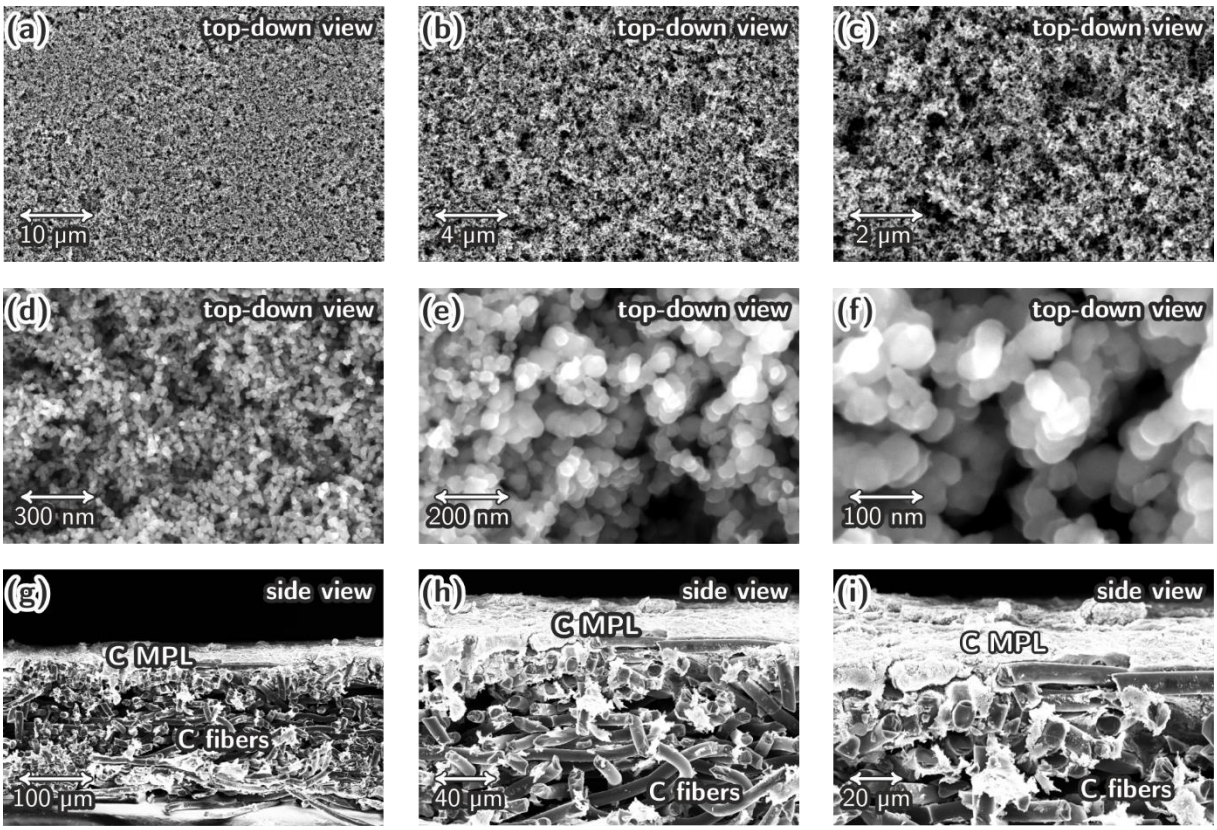

Figure S2. SEM investigation of the pristine GDL. (a-f) Top-down SEM inspection of H23C8 carbon paper gas diffusion layer (GDL) at different magnifications. The images show the morphology of the bare carbon microporous layer (MPL) of the GDL onto which the catalyst ink is drop-cast during the electrode preparation procedure. (g-i) Cross-sectional SEM inspection of the H23C8 carbon paper showing the C-fiber core covered by the C-MPL at different magnifications.

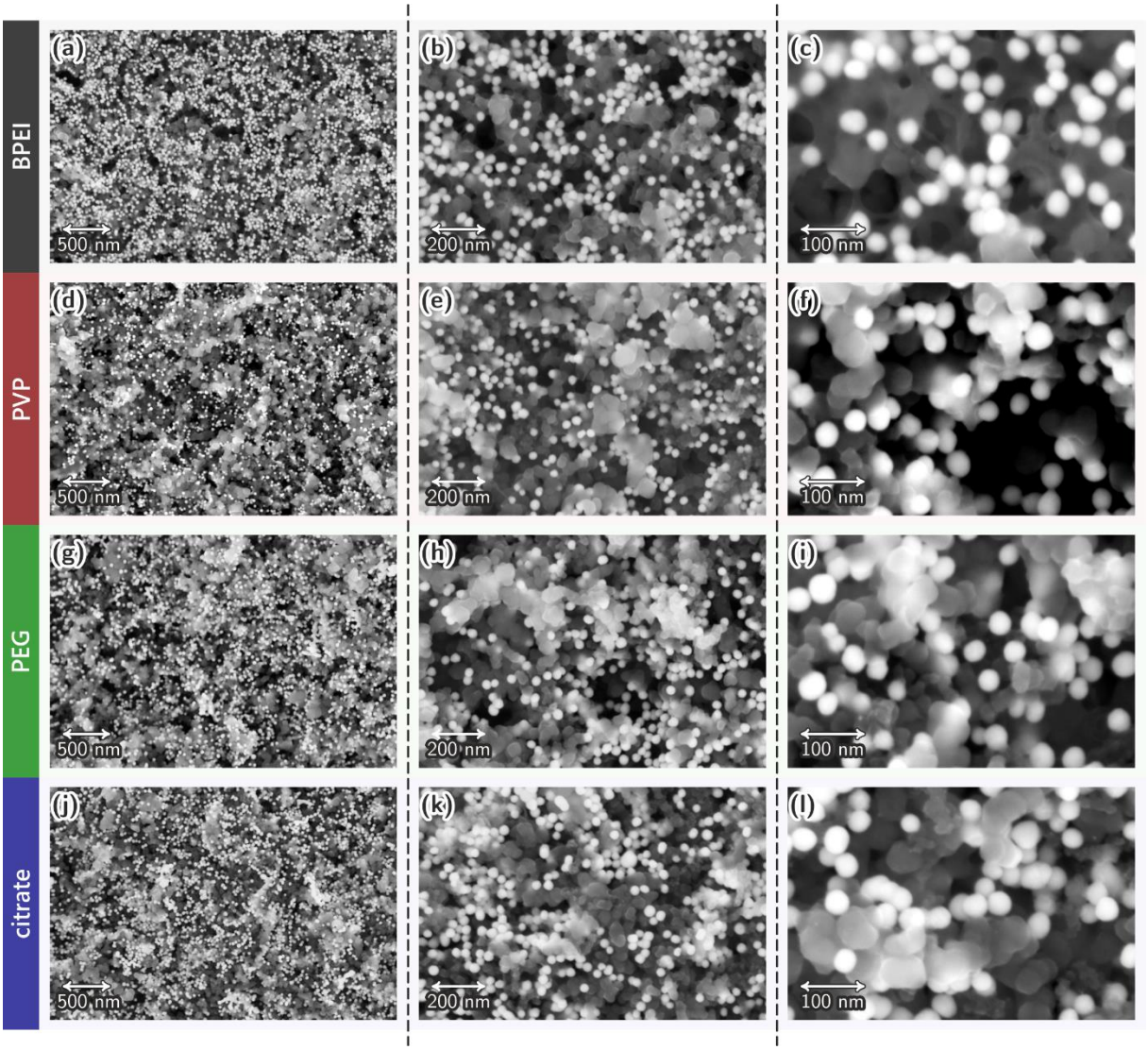

Figure S3. SEM investigation of as-prepared Ag NP GDEs (different capping agents). Representative top-down SEM images showing the studied four types of surfactant-capped Ag NPs (mixed with 15 wt% carbon black) dispersed on H23C8 carbon paper GDL at three different magnifications. (a-c) BPEI-capped Ag NPs; (d-f) PVP-capped Ag NPs; (g-i) PEG-capped Ag NPs; (j-l) citrate-capped Ag NPs. The nominal Ag NP mass loading of the electrodes (normalized to the geometric surface area) was 80 μg cm^{-2} in all cases; the actual loading (which proved to be lower than the nominal loading due to the vacuum-assisted sample preparation technique) determined by ICP-MS is indicated below in Table S1.

Table S1. Mass loading data of the different surfactant-capped Ag NP GDEs determined by inductively coupled plasma mass spectrometry normalized to the geometric surface area. Intervals reflect confidence levels of 95%.

Capping agent	Loading / (μg cm^{-2})
BPEI	41 ± 4
PVP	45 ± 5
PEG	41 ± 5
citrate	43 ± 8

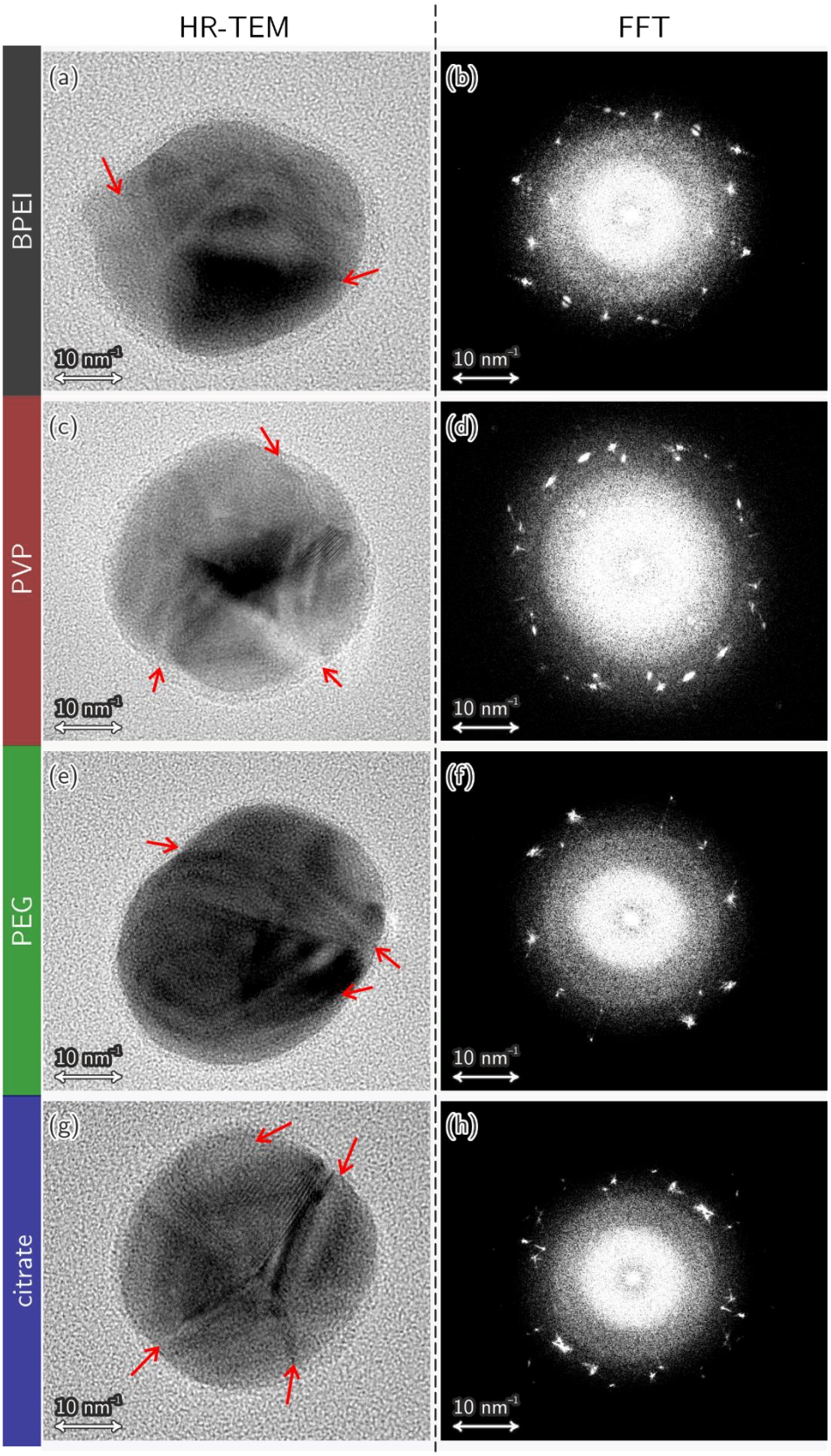

Figure S4. Representative high-resolution transmission electron microscopy (HR-TEM) images of individual, surfactant-capped Ag NPs and their corresponding fast Fourier transform (FFT) patterns in the case of the studied four types of capping agents. (a-b) BPEI-capped Ag NP; (c-d) PVP-capped Ag NP; (e-f) PEG-capped Ag NP; (g-h) citrate-capped Ag NP.

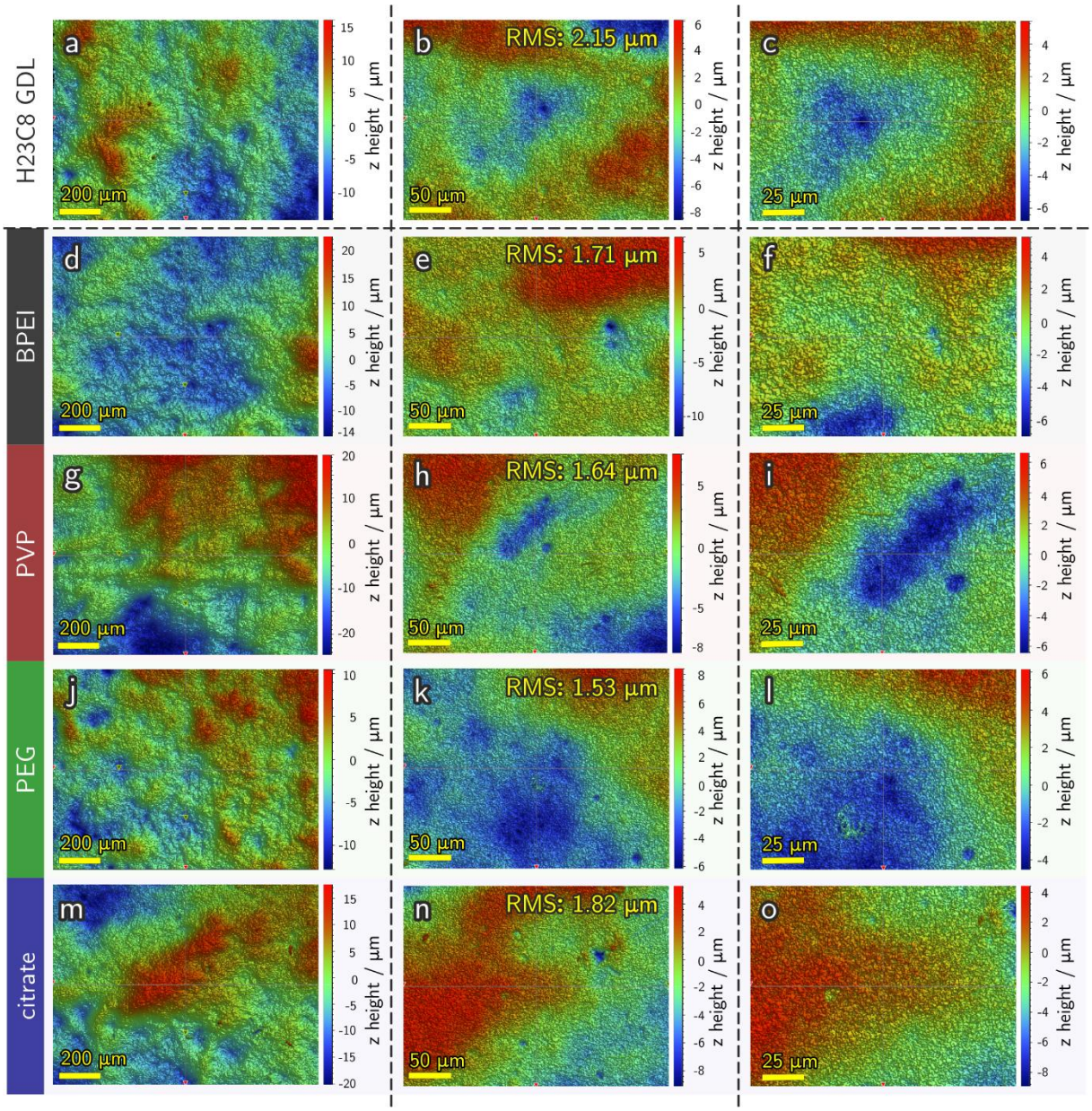

Figure S5. Representative top-down surface images of the blank GDL and the as-prepared Ag NP GDEs obtained by white light interferometry at three different magnifications. The surface roughness is given as the root mean square (RMS) for each presented sample. (a-c) As-received H23C8 carbon paper – mapping of the unmodified C-MPL; (d-f) BPEI-capped Ag NP GDE; (g-i) PVP-capped Ag NP GDE; (j-l) PEG-capped Ag NP GDE; (m-o) citrate-capped Ag NP GDE.

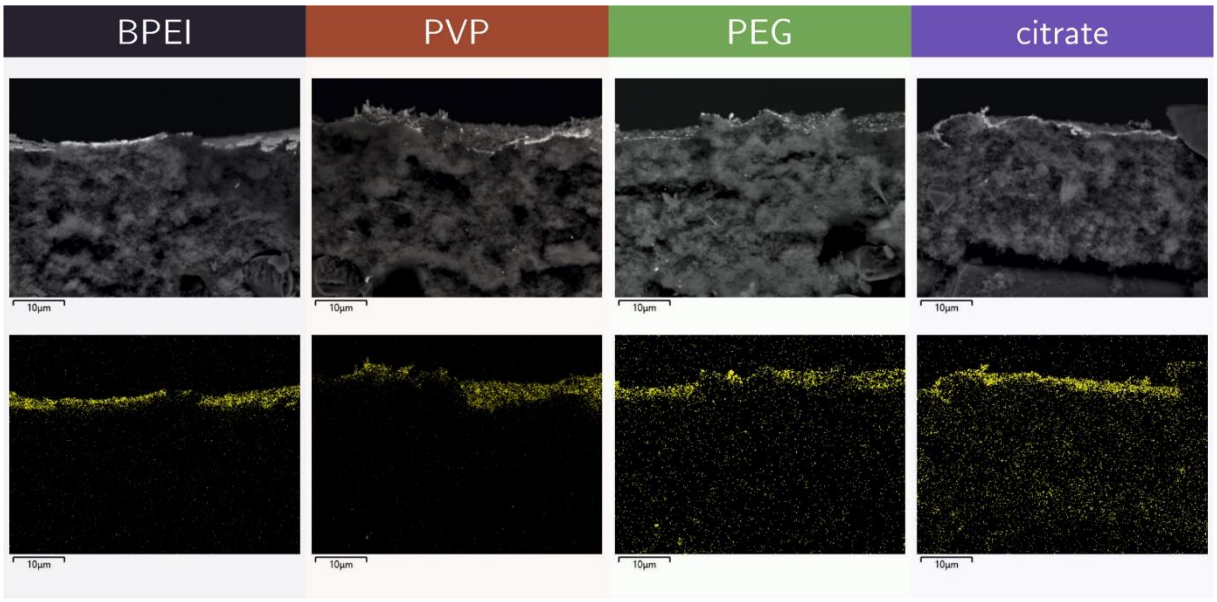

Figure S6. Cross-sectional side-view of the microporous layer of the GDE after drop-casting the catalyst ink, as shown by SEM (top row). EDX (bottom row) reveals that most of the silver nanoparticles remain on top of the GDE.

Table S2. Time-resolved current density data and distribution of gaseous products formed during electrochemical CO_2 reduction using surfactant-capped Ag NP catalysts in a gas-fed zero-gap flow cell at different applied potentials in the case of the studied four types of capping agents: BPEI, PVP, PEG, and citrate. The presented data (also used for the creation of Figure 4 of the main text) are average values of data points determined in 3 parallel experiments. Each electrolysis was carried out until a total of $Q = -300$ C cm^{-2} charge was transferred. The product distribution was determined by means of on-line gas chromatography. Intervals reflect confidence levels of 95%.

BPEI

$E = -1.654$ V				$E = -1.754$ V				$E = -2.354$ V			
t / min	$-j_{CO}$ / (mA cm^{-2})	$-j_{H_2}$ / (mA cm^{-2})	$-j_{tot}$ / (mA cm^{-2})	t / min	$-j_{CO}$ / (mA cm^{-2})	$-j_{H_2}$ / (mA cm^{-2})	$-j_{tot}$ / (mA cm^{-2})	t / min	$-j_{CO}$ / (mA cm^{-2})	$-j_{H_2}$ / (mA cm^{-2})	$-j_{tot}$ / (mA cm^{-2})
10	18.54±0.88	14.12±0.03	46.75±0.73	10	36.92±0.36	15.4±0.36	65.7±1.1	4	234.1±6.0	27.39±0.69	299.9±2.1
20	17.11±0.15	12.47±0.26	43.85±0.81	20	32.6±1.3	15.66±0.73	62.85±0.15	9	170.2±3.5	42.35±0.99	256.0±3.2
30	15.66±0.31	13.60±0.27	44.34±0.26	30	31.9±1.2	16.36±0.09	61.3±1.3	13	98.2±4.0	125.4±4.1	257.4±3.2
40	14.86±0.42	11.48±0.04	40.64±0.75	40	28.95±0.61	14.76±0.55	58.46±0.45	18	71.89±0.41	168.1±4.4	265.9±6.5
60	13.79±0.20	10.78±0.44	38.76±0.51	50	27.21±0.29	12.85±0.15	54.7±1.1				
80	13.23±0.43	10.17±0.43	37.06±0.6	60	25.12±0.63	11.59±0.06	51.86±0.70				
100	12.48±0.37	10.03±0.10	35.79±0.47	70	23.14±0.09	11.75±0.18	47.85±0.05				
120	11.25±0.40	10.04±0.06	33.52±0.81	80	19.82±0.55	11.66±0.17	44.1±1.0				

PVP

$E = -1.654$ V				$E = -1.754$ V				$E = -2.354$ V			
t / min	$-j_{CO}$ / (mA cm^{-2})	$-j_{H_2}$ / (mA cm^{-2})	$-j_{tot}$ / (mA cm^{-2})	t / min	$-j_{CO}$ / (mA cm^{-2})	$-j_{H_2}$ / (mA cm^{-2})	$-j_{tot}$ / (mA cm^{-2})	t / min	$-j_{CO}$ / (mA cm^{-2})	$-j_{H_2}$ / (mA cm^{-2})	$-j_{tot}$ / (mA cm^{-2})
10	57.1±2.6	3.08±0.07	68.2±1.4	10	80.9±2.7	3.46±0.13	94.9±1.8	4	295.4±9.5	4.25±0.01	339.5±7.7
20	52.99±0.84	2.72±0.07	63.7±1.6	20	76.4±1.2	2.95±0.14	88.45±0.24	8	276±13	2.75±0.07	320.6±2.4
30	48.95±0.63	2.33±0.11	60.0±1.2	30	67.25±0.44	3.51±0.01	80.21±0.40	12	209.2±8.1	8.32±0.17	268.3±2.2
40	43.75±0.52	2.37±0.07	55.2±1.4	40	56.9±1.9	4.09±0.10	72.37±0.71	16	147.11±0.9	43.36±0.27	230.1±4.8
50	38.8±1.6	2.63±0.02	50.12±0.92	50	49.79±0.73	4.45±0.16	66.2±1.1				
60	33.45±0.43	2.85±0.06	44.70±0.64	60	42.1±1.9	4.44±0.20	59.17±0.41				
70	27.8±1.3	2.79±0.11	39.75±0.15								
80	23.14±0.11	3.01±0.11	35.17±0.02								
90	19.46±0.93	3.63±0.12	32.06±0.13								

PEG

$E = -1.654$ V				$E = -1.754$ V				$E = -2.354$ V			
t / min	$-j_{CO}$ / (mA cm^{-2})	$-j_{H_2}$ / (mA cm^{-2})	$-j_{tot}$ / (mA cm^{-2})	t / min	$-j_{CO}$ / (mA cm^{-2})	$-j_{H_2}$ / (mA cm^{-2})	$-j_{tot}$ / (mA cm^{-2})	t / min	$-j_{CO}$ / (mA cm^{-2})	$-j_{H_2}$ / (mA cm^{-2})	$-j_{tot}$ / (mA cm^{-2})
10	54.23±0.39	5.85±0.02	67.7±1.6	10	82.7±2.1	8.23±0.25	97.6±2.1	4	314.9±8.1	6.42±0.91	366.8±5.2
20	51.28±0.49	5.83±0.16	64.12±0.96	20	79.0±1.4	6.73±0.05	92.0±1.5	8	2871±8.4	7.43±0.19	330.5±1.7
30	49.15±0.41	5.49±0.24	61.9±0.50	30	68.17±2.5	6.84±0.32	82.0±1.5	11.5	226.4±6.4	7.63±0.58	284.3±1.5
40	45.96±2.07	5.59±0.06	58.7±0.32	40	58.6±2.7	7.65±0.09	74.49±0.73	15	148.8±4.8	37.88±0.99	245.2±5.4
50	40.57±0.56	5.94±0.24	54.1±1.1	50	49.5±1.4	7.7±0.02	66.2±0.02				
60	35.02±0.12	6.2±0.04	49.74±0.45	60	39.3±1.5	9.12±0.44	58.93±0.15				
70	30.3±1.0	6.03±0.29	45.54±0.19								
80	27.9±0.58	5.73±0.24	43.1±1.1								

Citrate

$E = -1.654$ V				$E = -1.754$ V				$E = -2.354$ V			
t / min	$-j_{CO}$ / (mA cm^{-2})	$-j_{H_2}$ / (mA cm^{-2})	$-j_{tot}$ / (mA cm^{-2})	t / min	$-j_{CO}$ / (mA cm^{-2})	$-j_{H_2}$ / (mA cm^{-2})	$-j_{tot}$ / (mA cm^{-2})	t / min	$-j_{CO}$ / (mA cm^{-2})	$-j_{H_2}$ / (mA cm^{-2})	$-j_{tot}$ / (mA cm^{-2})
10	50.0±1.6	2.75±0.02	62.23±0.09	10	87.0±1.4	2.54±0.01	95.1±1.5	4	310.9±1.2	3.56±0.07	360.2±5.5
20	45.8±1.2	4.18±0.18	58.75±0.80	20	72.5±1.6	2.91±0.14	81.00±0.26	8	282.1±4.8	4.44±0.13	326.73±8.1
30	42.49±0.32	4.18±0.10	55.6±1.0	30	58.3±1.9	5.82±0.07	69.7±1.5	12	227.2±2.5	8.6±0.39	268.7±1.7
40	37.9±1.5	4.23±0.05	51.86±0.95	40	50.23±0.76	6.94±0.32	62.94±0.53	16	153.0±5.9	40.1±1.9	231.0±1.5
50	33.70±0.37	4.33±0.15	47.81±0.66	50	40.7±1.1	7.68±0.01	54.2±1.2				
60	29.98±0.62	4.22±0.05	44.2±1.1	60	34.0±1.6	8.11±0.37	48.7±0.45				
70	28.48±0.72	3.27±0.13	42.29±0.16	70	28.8±1.4	9.39±0.41	45.26±0.27				
80	23.46±0.26	4.04±0.18	37.81±0.86								
90	20.18±0.68	4.42±0.03	34.56±0.33								

Table S3. Faradaic efficiency of formate production ($FE_{formate}$) during electrochemical CO_2 reduction using surfactant-capped Ag NP catalysts in a gas-fed zero-gap flow cell at different applied potentials ($Q = -300$ C cm^{-2}) in the case of the studied four types of capping agents: BPEI, PVP, PEG, and citrate. The formate content of the electrolyte was determined post-electrolysis by means of ion exchange chromatography.

Applied potential / V (vs. Ag/AgCl)	BPEI	PVP	PEG	Citrate
	$FE_{formate}$			
−1.654	0.5%	2.7%	1.0%	0.3%
−1.754	1.1%	2.7%	2.0%	1.4%
−2.354	19.9%	15.8%	8.2%	12.5%

Table S4. Mass loading of PVP-capped Ag NP GDEs determined by ICP-MS prior to and after electrochemical CO_2 reduction carried out in a gas-fed zero-gap flow cell at −2.354 V vs. Ag/AgCl ($Q = -300$ C cm^{-2}). Intervals reflect confidence levels of 95%.

	Mass loading / (μg cm^{-2})
As-prepared	45 ± 5
After electrolysis and washing	36 ± 5

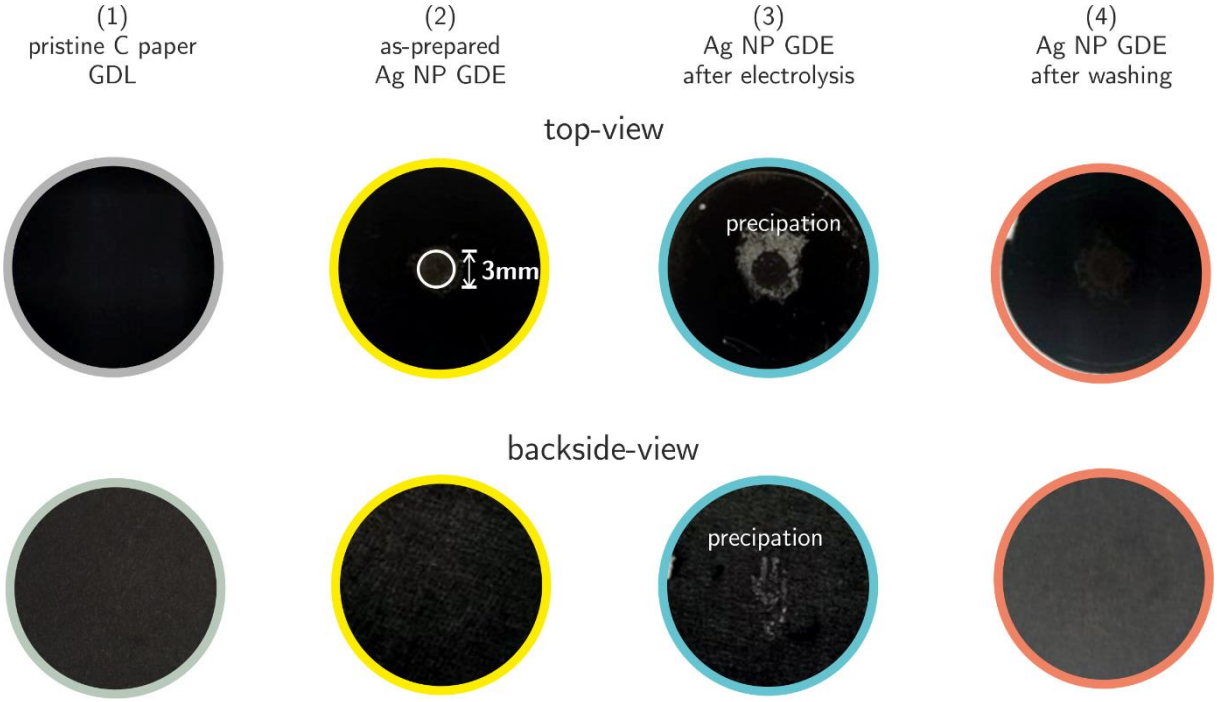

Figure S7. Representative optical micrographs of both the top and back sides of the applied H23C8 carbon paper at different experimental stages. (1) Pristine carbon paper cut to size. (2) Ag NP modified gas diffusion layer (as-prepared Ag NP GDE); the white circle in the central part of the carbon paper shows the 3 mm diameter electrochemically active area, which is in direct contact with the anion exchange membrane in the flow cell setup. (3) Ag NP GDE after being subjected to electrochemical CO_2 reduction in a gas-fed zero-gap flow cell at −2.354 V vs. Ag/AgCl ($Q = -300$ C cm^{-2}). (4) Post-electrolysis Ag NP GDE after applying a careful washing step to remove the $KHCO_3/K_2CO_3$ precipitates (see details of the precipitate removal in the caption of Figure S8 below). The presented images were taken of a sample prepared using PVP-capped Ag NPs.

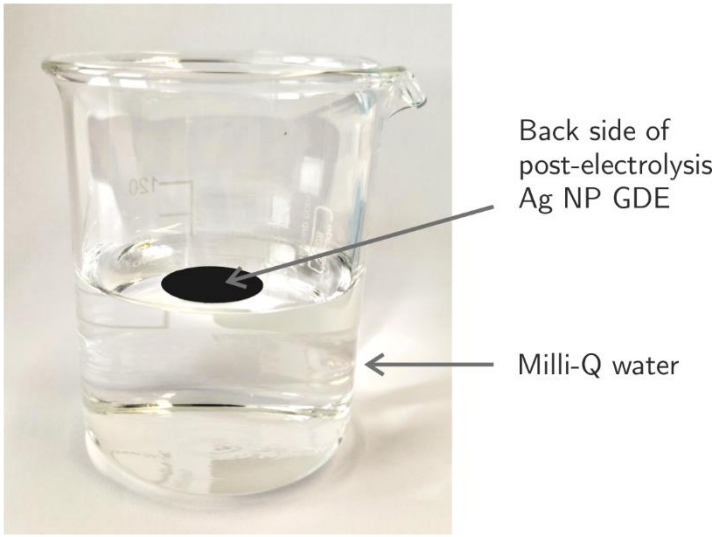

Figure S8. Illustration of $KHCO_3/K_2CO_3$ precipitate removal: the post-electrolysis Ag NP GDE was carefully placed onto the surface of ~80 cm^3 Milli-Q water in a beaker with the catalyst-modified side facing downward. The water was exchanged five times in the case of each sample, after every 15 minutes.

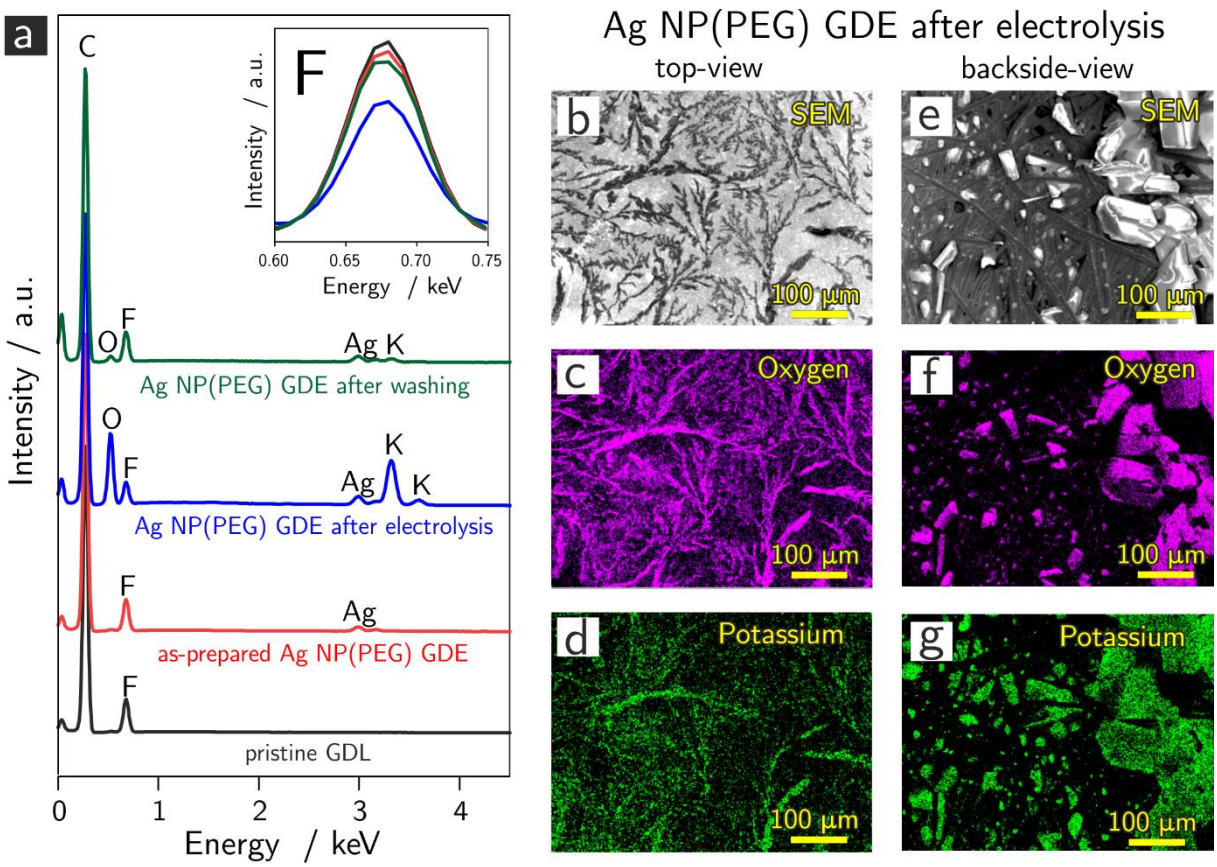

Figure S9. (a) Representative energy dispersive X-ray (EDX) spectra recorded on the top side of Ag NP GDEs at different experimental stages. The inset shows emissions assigned to fluorine (F); (b-d) SEM and corresponding 2D-EDX mapping of the top side of an Ag NP GDE after being subjected to electrochemical CO_2 reduction in a gas-fed zero-gap flow cell at –2.354 V vs. Ag/AgCl (Q=–300 C cm^{-2}). (e-g) SEM and corresponding 2D-EDX mapping of the back side of the same post-electrolysis Ag NP GDE. The presented spectra and images were taken of a sample prepared using PEG-capped Ag NPs (Ag NP(PEG) GDE).

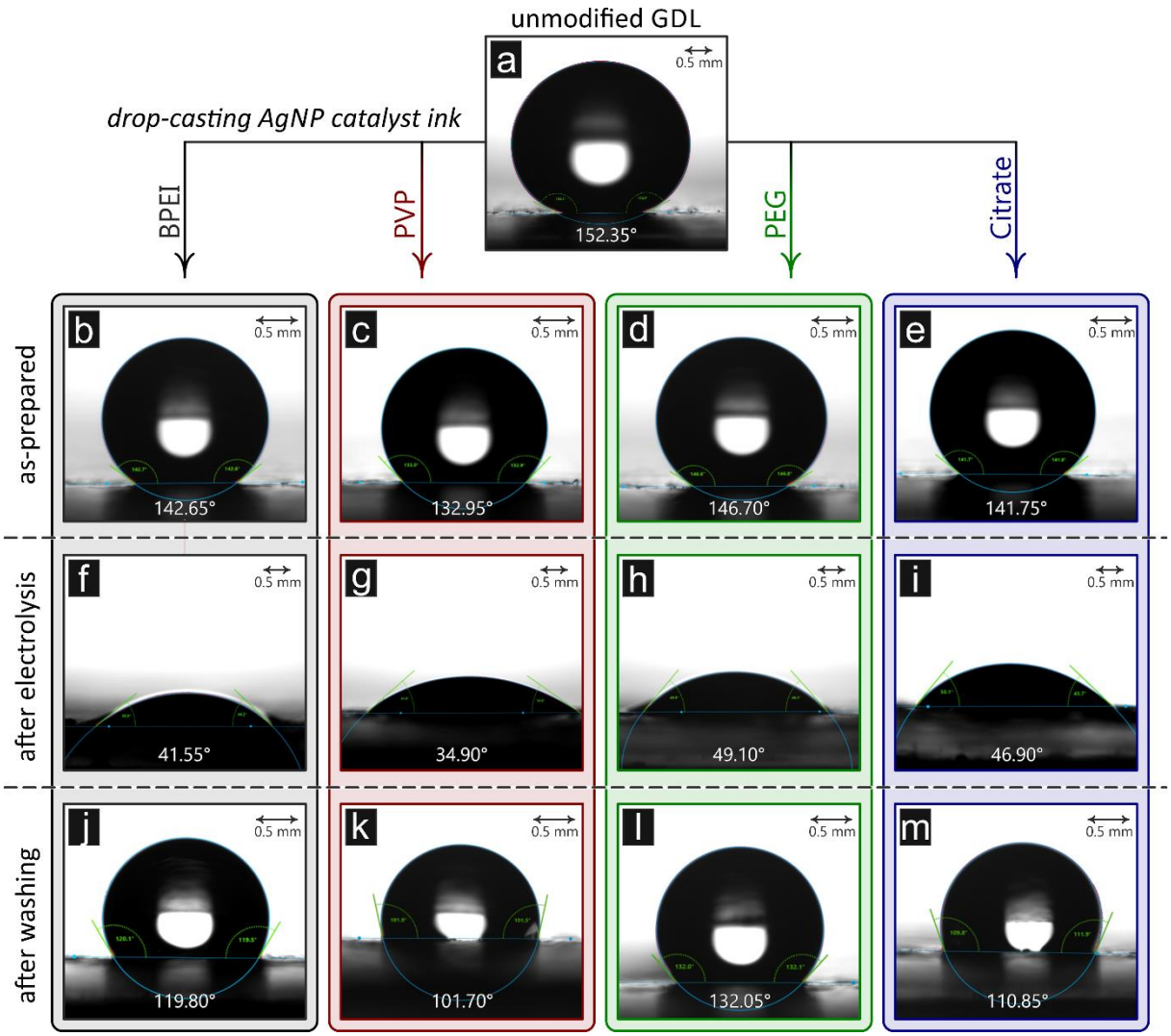

Figure S10. Sessile water drop measurements carried out on the different surfactant-capped Ag NP GDEs show that the initially hydrophobic GDL surface remains water repellent after a catalyst ink is drop-cast on it, practically regardless of the chemical nature of the applied capping agent. Following electrolyses, due to $KHCO_3/K_2CO_3$ formation, the surface becomes hydrophilic. The initial hydrophobicity may however be restored if a careful washing step (see Figure S8) is applied to the post-electrolysis GDE. (a) Blank measurement on pristine C paper. (b-e) As-prepared Ag NP GDEs. (f-i) Ag NP GDEs after being subjected to electrochemical CO_2 reduction in a gas-fed zero-gap flow cell at –2.354 V vs. Ag/AgCl (Q = –300 C cm^{-2}); corresponding electrochemical data are shown in Figure 4 of the main text). (j-m) Post-electrolysis Ag NP GDEs after applying a careful washing step (see Figure S8) in order to remove the $KHCO_3/K_2CO_3$ precipitates. Results of similar measurements carried out on the back side of the same GDEs are presented in Figure S11.

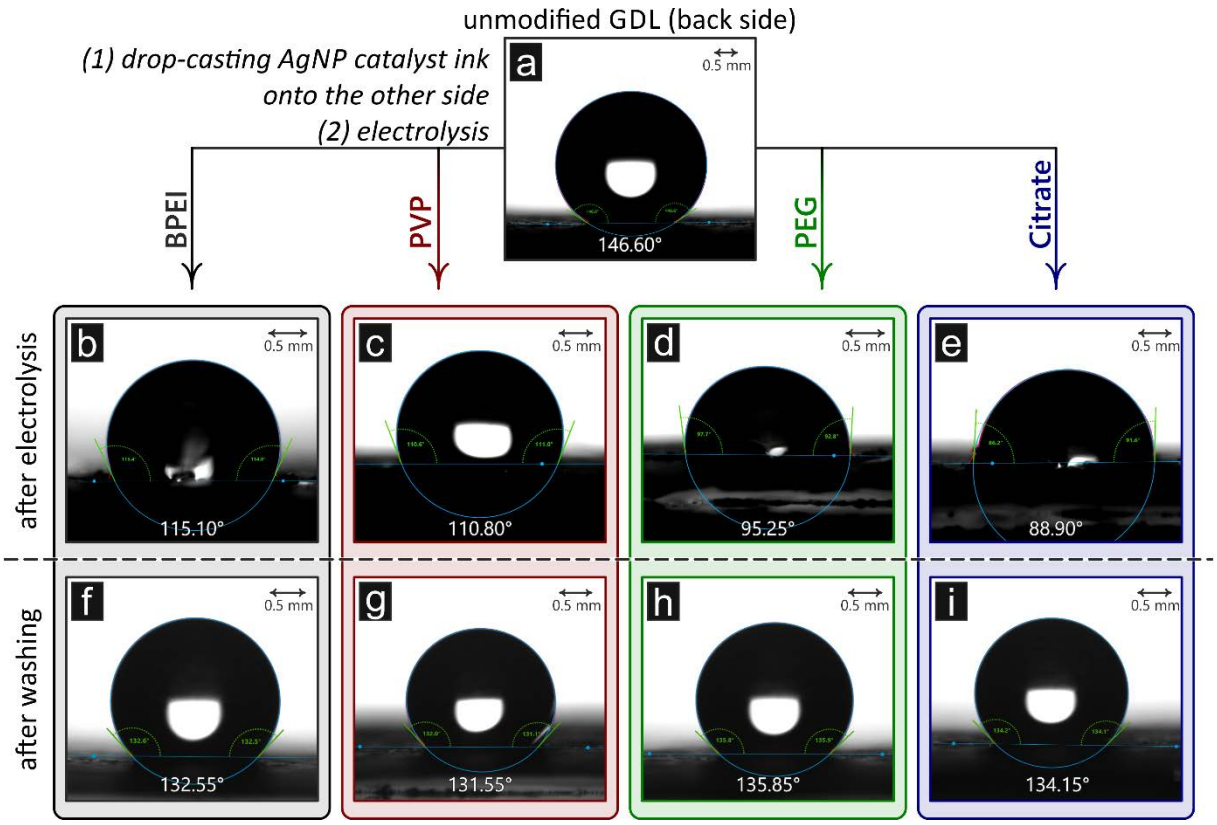

Figure S11. Sessile water drop measurements carried out on the back side (which is exposed to the gas-flow channels in the experimental set-up shown in Figure S1) of the different surfactant-capped Ag NP GDEs. (a) Blank measurement on pristine C paper. (b-e) Ag NP GDEs after being subjected to electrochemical CO_2 reduction in a gas-fed zero-gap flow cell at –2.354 V vs. Ag/AgCl ($Q = -300\ C\ cm^{-2}$); corresponding electrochemical data are shown in Figure 4 of the main text). (f-i) Post-electrolysis Ag NP GDEs after applying a careful washing step (see Figure S8) to remove the $KHCO_3/K_2CO_3$ precipitates.

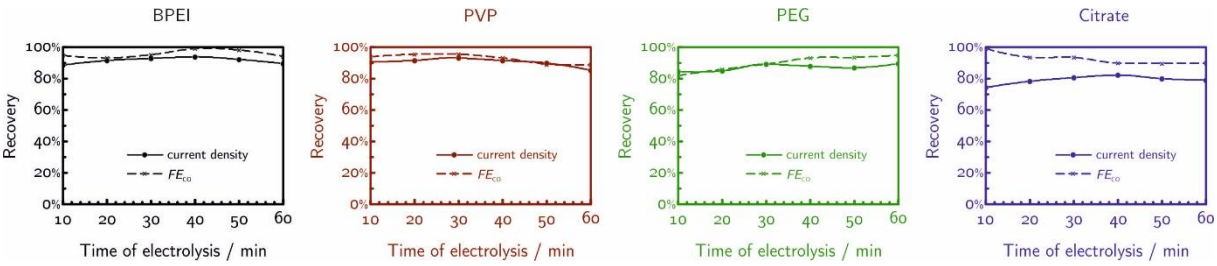

Figure S12. Recovery experiments. Electrolyses lasting 1 hour are carried out at –1.765 V, and are repeated following the removal of the formed precipitate layer by dip-washing. During this second electrolysis both the total current density and the Faradaic efficiency remain close to the values initially measured, indicating that by dip-washing the catalytic performance of the GDE can, within range of experimental error, fully be recovered.

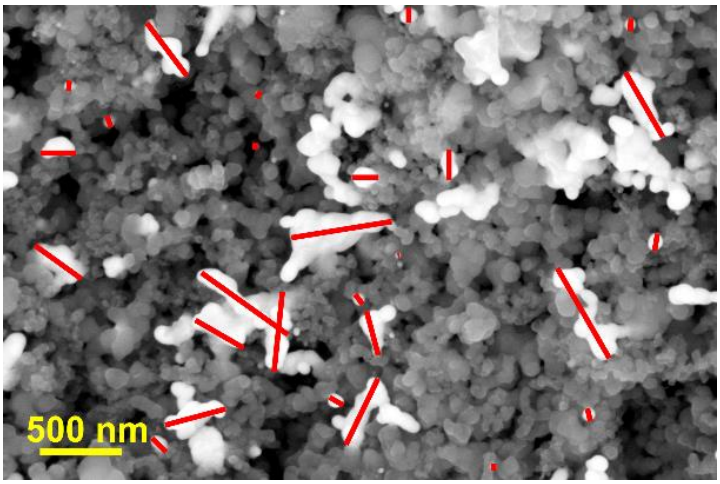

Figure S13. The method of particle size determination: particle size was defined as the longest measurable dimension in case of anisotropic NPs.

Table S5. Estimation of the amount of capping agents attached to the different surfactant-capped Ag NPs and the extent of capping agents present in the liquid phase of the as-received Ag NP suspensions by means of total organic carbon (TOC) and nitrogen (TON) content determination. 1 cm^3 of each as-received Ag NP suspension (provided by NanoComposix) was diluted to 4 cm^3 with Milli-Q water resulting suspensions of 0.25 mg cm^{-3} Ag content. The diluted suspensions were then subjected to centrifugation (at 35000 rpm, 40 min, Beckmann Coulter ultracentrifuge, SW60 rotor). This treatment allowed for a separation of the surfactant-capped Ag NPs (as pellet) and the free surfactants that remained at least to a large extent in the supernatant (see Figure S14). The separated (surfactant-capped) Ag NPs were redispersed in Milli-Q water to keep the Ag concentration of 0.25 mg cm^{-3}. Each obtained supernatant and newly prepared Ag NP suspension was subjected to TOC and TON analysis: 0.1 cm^3 of the samples were fed into a DIMATOC 2100 instrument (Dimatec, Essen, Germany). The organic compounds were oxidized at 850 °C with Pt as catalyst to CO_2/NO. Non-dispersive infrared (NDIR) gas sensor with a reflective diffuser and a chemiluminescence detector were used to detect CO_2 and NO, respectively.

Samples	Supernatant		Redispersed Ag NP suspension	
	TOC / (mg dm^{-3})	TON / (mg dm^{-3})	TOC / (mg dm^{-3})	TON / (mg dm^{-3})
Milli-Q water	0.15	0.02		
BPEI-capped Ag NP suspension	20.15	3.88	2.92	0.53
PVP-capped Ag NP suspension	70.93	9.44	5.73	0.89
PEG-capped Ag NP suspension	15.96	0.16	2.11	0.05
Citrate-capped Ag NP suspension	64.92	0.31	2.11	0.01

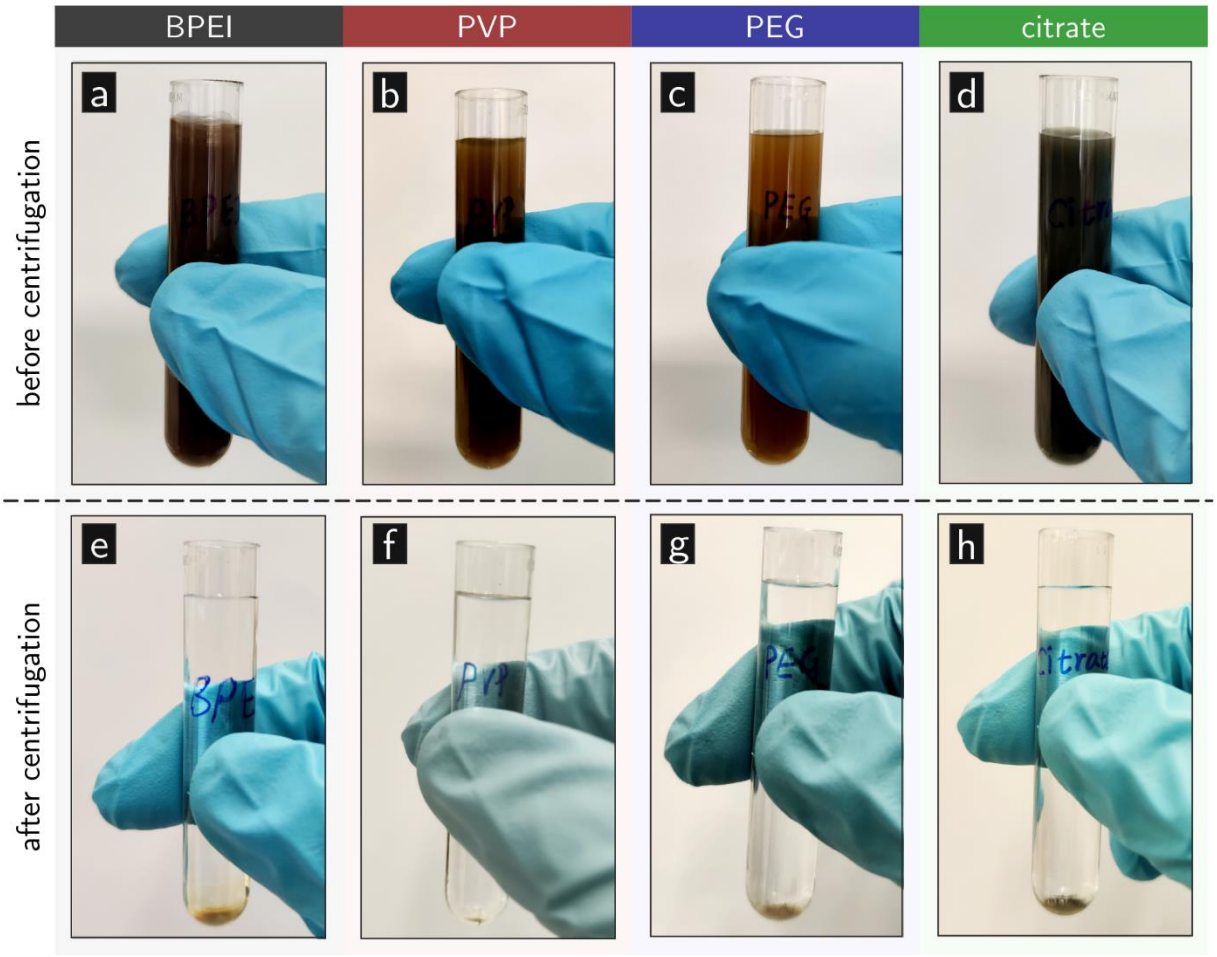

Figure S14. (a-d) Photos of as-received Ag NP suspensions (diluted to four times volume) in test tubes before applying centrifugation to separate excess capping agents dissolved in the liquid phase of the suspension and the surfactant-capped Ag NPs (at least to a large extent) in the case of the studied four types of surfactants. (e-h) Photos of the test tubes taken after centrifugation (at 35000 rpm for 40 min, Beckmann Coulter ultracentrifuge, SW60 rotor).

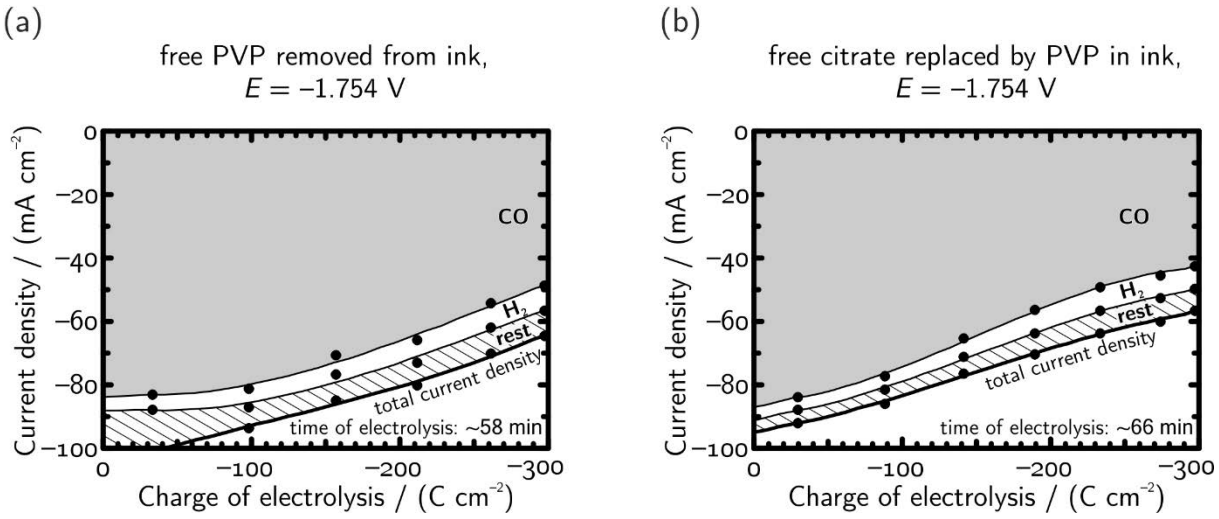

Figure S15. EC & GC data of PVP removal and citrate-to-PVP experiments (cf. to Figures 9 and 10 of the main text) in a representation similar to what was applied in Figure 4 of the main text. Note the apparent similarity to Figure 4, applied potential: $E = -1.754$ V.

Table S6. Numerical results based on which Figure S15 was created. Confidence intervals (95%) are estimated based on at least three parallel measurements.

PVP removed from ink, $E = -1.754$ V				free citrate replaced by PVP in ink, $E = -1.754$ V			
t / min	$-j_{CO}$ / (mA cm^{-2})	$-j_{H_2}$ / (mA cm^{-2})	$-j_{tot}$ / (mA cm^{-2})	t / min	$-j_{CO}$ / (mA cm^{-2})	$-j_{H_2}$ / (mA cm^{-2})	$-j_{tot}$ / (mA cm^{-2})
10	82,98±0,81	4,73±0,04	101,1±2,1	10	83,8±3,2	4,08±0,09	91,94±0,08
20	81,2±1,5	5,85±0,29	93,6±1,9	20	77,4±2,1	4,13±0,06	85,9±1,9
30	70,7±2,7	6,10±0,16	84,9±1,9	30	65,46±0,18	5,67±0,13	76,38±0,89
40	66,00±0,95	6,92±0,08	80,2±1,2	40	56,4±2,4	7,25±0,07	70,3±1,1
50	54,26±0,55	7,68±0,04	70,16±0,58	50	49,3±2,4	7,36±0,20	63,65±0,73
58	48,66±0,34	7,84±0,27	64,5±1,28	60	45,58±0,14	7,08±0,23	60,11±1,1
				66	42,5±1,1	7,2±0,03	56,58±1,1

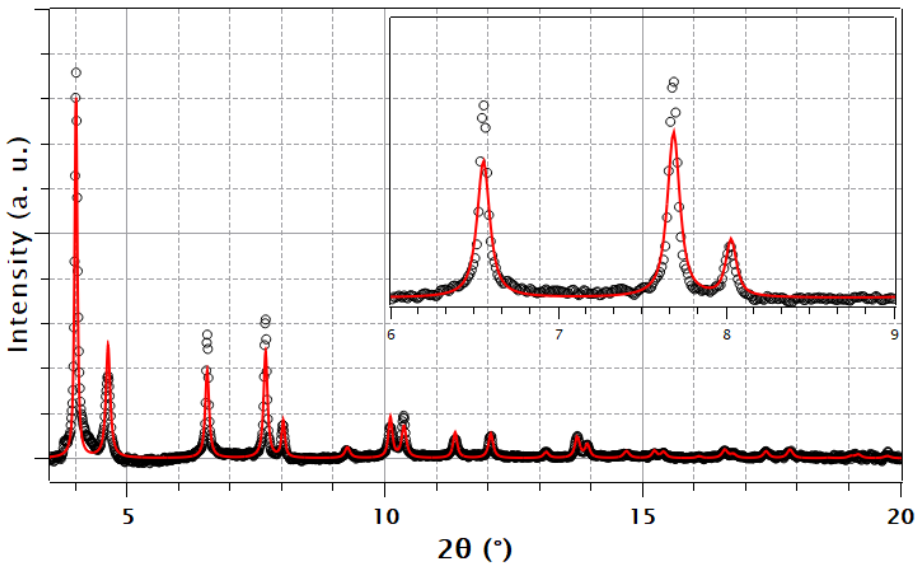

Figure S16. Example of Rietveld refinement performed on an as-prepared citrate-capped Ag NP GDE sample. The circles represent the raw data (after background removal), while the red line shows the fitting.

2. The role of ionomers in the electrolyte management of zero-gap MEA-based CO_2 electrolysers: A Fumion vs. Nafion comparison

Authors: Menglong Liu, Huifang Hu, Ying Kong, Iván Zelocualtecatl Montiel, Viliam Kolivoška, Alexander V. Rudnev, Yuhui Hou, Rolf Erni, Soma Vesztergom, and Peter Broekmann.

***Applied Catalysis B: Environmental*, 335 (2023). 122885. DOI: 10.1016/j.apcatb.2023.122885**

Highlight: The role of binders in determining the stability of GDEs for ec-CO_2RR in a semi-zero-gap electrolyzer was studied with two widely used commercial binder materials, Nafion® and Fumion®. Although Fumion®-modified GDEs exhibit hydrophilic characteristics (this is usually considered to be detrimental compared hydrophobic surfaces, e.g., Nafion®-modified GDEs), the Fumion®-modified GDEs maintained high selectivity towards CO for a much more extended electrolysis time compared to Nafion® case. SEM/EDX imaging demonstrated that potassium (bi)carbonate plaques of ca. 3 μm thickness were formed during electrolysis covering and the entire CL when Nafion® was used as the binder. The use of anion-conducting Fumion®-modified GDEs prevented (bi)carbonate salt precipitation in the CL in the transport channels of the MPL and facilitated thereby active water/electrolyte management (perspiration). The embedment of the Ag-NPs in the matrix of the anion-conducting Fumion® film prevented rapid degradation of the nanoparticulate Ag catalysts.

Contribution: I discovered the beneficial effect of the Fumion® binder. I conducted most of the electrochemical experiments and all the SEM/EDX analyses. Also, I prepared the figures and wrote the first draft of the manuscript. I contributed to the revision of the manuscript.

Applied Catalysis B: Environmental 335 (2023) 122885

Contents lists available at ScienceDirect

Applied Catalysis B: Environmental

journal homepage: www.elsevier.com/locate/apcatb

The role of ionomers in the electrolyte management of zero-gap MEA-based CO_2 electrolysers: A Fumion *vs.* Nafion comparison

Menglong Liu [a], Huifang Hu [a], Ying Kong [a], Iván Zelocualtecatl Montiel [a], Viliam Kolivoška [b], Alexander V. Rudnev [a,c], Yuhui Hou [a], Rolf Erni [d], Soma Vesztergom [a,e,*], Peter Broekmann [a,**]

[a] NCCR Catalysis, University of Bern, Department of Chemistry, Biochemistry and Pharmaceutical Sciences, Freiestrasse 3, 3012 Bern, Switzerland
[b] J. Heyrovský Institute of Physical Chemistry of the Czech Academy of Sciences, Dolejškova 3, 182 23 Prague, Czechia
[c] A. N. Frumkin Institute of Physical Chemistry and Electrochemistry, Russian Academy of Sciences, Leninsky Prospekt 31, 119071 Moscow, Russia
[d] Electron Microscopy Center, Swiss Federal Laboratories for Materials Science and Technology (EMPA), Überlandstrasse 129, 8600 Dübendorf, Switzerland
[e] Eötvös Loránd University, MTA–ELTE Momentum Interfacial Electrochemistry Research Group, Pázmány Péter sétány 1/A, 1117 Budapest, Hungary

ARTICLE INFO

Keywords:
Power to value
Carbon dioxide electroreduction
Stability
Precipitation
GDE flooding

ABSTRACT

We study the role of binders (ionomers) in determining the life-span of gas diffusion electrodes (GDEs) used for high throughput CO_2-to-CO electrolysis. We compare two typical ionomer materials (Nafion and Fumion, both are widely used for the preparation of Ag nanoparticles-based catalyst inks) to show that when used in zero-gap membrane/electrode assemblies, Fumion-containing inks are superior to Nafion-based ones and can uphold a very high CO-selectivity in the electrochemical CO_2 reduction reaction for longer time. This is due to the ability of Fumion containing inks to suppress precipitation inside the GDE structure. As Fumion-fixed GDEs are significantly less hydrophobic than Nafion-fixed ones, our results contradict the widely accepted opinion that it is their non-wettability what mostly protects CO_2-reducing GDEs from flooding. In turn, we argue that it is more important to maintain efficient electrolyte drainage pathways in the GDE structure, and explain the superiority of Fumion-fixed GDEs on this basis.

1. Introduction

The increasing level of atmospheric carbon dioxide (CO_2) and its climatic and environmental consequences, such as global warming and ocean acidification, present a serious threat to the sustainable development of human society [1]. Propelled by the excess of intermittent energy sources, the electrochemical CO_2 reduction reaction (*ec*–CO_2RR) is a promising approach to convert CO_2 into valuable fuels and commodity chemicals [1–3], and thereby to restore the global carbon cycle.

Depending on the catalyst applied for the reaction, *ec*–CO_2RR can yield a variety of products that even include hydrocarbons [4] and alcohols [5,6] of various (typically 1–3 carbon atoms) chain lengths [7,8]. However, from an economic point of view, those that lead to the formation of carbon monoxide (CO) and formate ($HCOO^-$) are considered the most viable amongst the various possible reaction routes. This is mostly because the two-electron transfer that leads to CO and formate production offers a large profit margin over other multi-electron transfer products that require heavier energy inputs [9]. Strong cases of commercial viability can be made especially for the production of CO, as CO is considered a remarkably versatile precursor of the production of synthetic fuels [9], and industrial applications already exist for the coupling of CO_2 and water co-electrolysers to fermentation modules where CO and H_2 are converted to butanol and hexanol with high carbon selectivity [10]. Amongst the various metal catalysts (Au, Ag, Zn, Pd, Ga) that direct *ec*–CO_2RR towards the formation of CO [11], Ag-based ones seem to be the most promising [12–14].

By using Ag especially in the form of nanoparticles (NPs) for the catalysis of *ec*–CO_2RR, Faradaic efficiencies (*FEs*) reaching almost 100% in the CO_2-to-CO conversion can be achieved [12], and at least in standard lab-scale experiments utilising conventional "H-type" cells, the reaction can remain stable for a very long time. The up-scaling of the reaction in the direction of reaching industrially relevant reaction rates is still hindered, however, by several tough challenges, and addressing these requires not only the study of new catalyst materials, but also that

* Corresponding author at: Eötvös Loránd University, MTA–ELTE Momentum Interfacial Electrochemistry Research Group, Pázmány Péter sétány 1/A, 1117 Budapest, Hungary.
** Corresponding author.
E-mail addresses: vesztergom@chem.elte.hu (S. Vesztergom), peter.broekmann@dcb.unibe.ch (P. Broekmann).

https://doi.org/10.1016/j.apcatb.2023.122885
Received 17 October 2022; Received in revised form 25 April 2023; Accepted 13 May 2023
Available online 16 May 2023

of entire electrolyser designs [16,17].

In a conventional H-type cell, where CO_2 dissolved in an aqueous phase undergoes reduction at the electrode surface, the reaction quickly becomes mass transport limited at high enough cathodic potentials, and the reaction rate will thus not be determined by the catalytic activity of the cathode but rather by the slow diffusion and low concentration of water-dissolved CO_2 molecules, allowing current densities typically not exceeding a few mA cm^{-2} in quiescent solutions. To overcome this limitation, and to achieve current densities that are orders of magnitude higher, the application of gas diffusion electrodes (GDEs) seems to be intuitive [18–28].

In GDEs, the catalyst is supported by a gas diffusion layer (GDL) that is composed of a carbon fibrous layer (CFL) and a microporous layer (MPL), as shown in Fig. 1a, and this bi-layer structure allows CO_2 to reach the catalyst layer essentially in gas phase, relieving the mass transport limitations that apply to H-type cells. Besides enabling fast reactant delivery, the GDL also facilitates the release of gaseous reaction products, serves as a mechanical support and electrical contact for the catalyst, and plays important role in controlling the amount of electrolyte in the catalyst layer [29].

In practical electrolysers producing mostly gaseous products, GDEs are often applied as parts of so-called zero-gap membrane-electrode assemblies (MEAs, Fig. 1), where the GDE is directly interfaced to an anion exchange membrane [30,31]. The membrane [32] assures that no volatile cathode-generated products cross over to the anode, which would reduce the efficiency of electrolysis. Another important role of the anion exchange membrane in zero-gap MEAs is that it controls the access of water to the catalyst layer while making sure that anionic reaction byproducts and products of CO_2 neutralisation —e.g., hydroxide and (bi-)carbonate ions— can be transported away from it.

Water plays a very ambiguous role in MEA-based CO_2-to-CO electrolysers [23,33]. Since water appears as a reactant in the target reaction

$$CO_2 + H_2O + 2e^- \rightarrow CO + 2OH^-, \quad \text{(R1)}$$

the presence of some amount of water in or nearby the catalyst layer is essential. If, however, an excess amount of water penetrates not only the catalyst layer but the underlying MPL as well, it may flood micropores, thereby blocking the access of CO_2 to the catalyst and giving rise to parasitic hydrogen evolution:

$$2H_2O + 2e^- \rightarrow H_2 + 2OH^-. \quad \text{(R2)}$$

As of today, it is probably the above-mentioned proneness of GDE micropores to flooding that presents the main obstacle in front of the scale-up prospects of CO_2 electroreduction [21,34–39]. When flooding in a GDE-based electrolyser occurs to such extent that the reactant CO_2 can no longer reach the catalyst layer, severe stability issues —a shifting from Reaction (R1) to (R2)— occur, and as a result, the *FE* of CO formation drops down during long-time electrolyses.

In zero-gap MEAs, the penetration of water (or in fact, that of the KOH solution) through the membrane cannot be precisely controlled, and usually the amount of electrolyte passing through the membrane is more than what could be consumed by Reaction (R1). In order to avoid that this excess amount of electrolyte gets trapped within (and ultimately floods) the micropores of the GDL, measures have to be taken to allow its drainage through the microporous and then the carbon fibrous layer, so that it can eventually exit the electrolyser with the outward gas flow. As it was pointed out recently [15,40–42], maintaining the efficacy of drainage channels by which the above-described perspiration [43,44] occurs seems to be a key strategic line in avoiding the flooding of MPL micropores, and thus extending the lifetime of zero-gap MEA-based CO_2 electrolysers.

The task of optimising electrolyte management in zero-gap MEAs is further complicated by the fact that most of these constructions apply heavily alkaline electrolyte solutions (to keep the anode process fast enough) and by that the anion exchange membranes used for the separation of the cathode GDE from the anode compartment are to some extent permeable also to cations.

When cations of the anolyte (in our case, K^+ ions) appear on the cathode GDE, they react with the CO_2 supply and form K_2CO_3/$KHCO_3$ salts. If these salts are formed only in a small amount, they present less of a threat as they can perspire through the GDL and exit the electrolyser dissolved in aerosol. If, on the other hand, K_2CO_3/$KHCO_3$ salts are formed at large concentrations, they precipitate inside the GDE structure or over the catalyst layer, which can have a detrimental effect on the electrolysis process [43,45]. Following electrolysis, K_2CO_3/$KHCO_3$ precipitates can often be visualised, e.g., by energy dispersive X-ray (EDX)-based analysis, inside or on top of the GDE structure [41].

The EDX elemental mapping-based analysis of precipitate formation patterns in GDEs, combined with the inductively coupled plasma mass

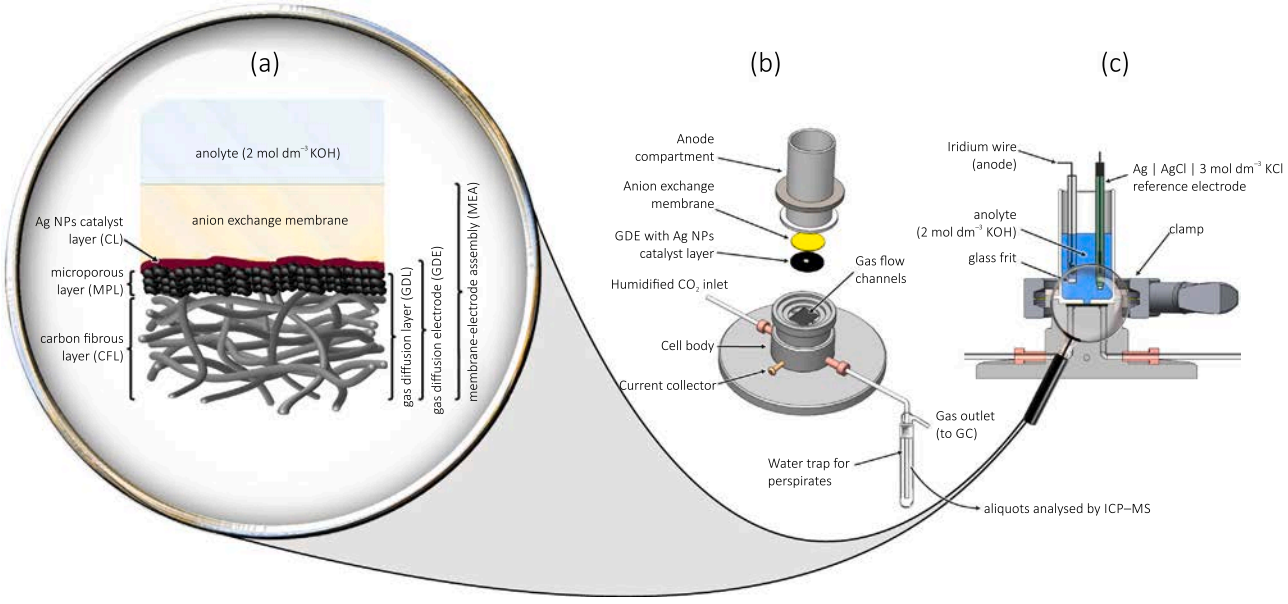

Fig. 1. A zero-gap membrane-electrode assembly (MEA) employing a gas diffusion electrode in contact with an anion exchange membrane, used in a gas-flow cell for the electrolysis of CO_2. Part (a) shows a close-up view of the MEA, parts (b) and (c) show the exploded and the cross-sectional view of the electrolyser. Adapted from [15].

spectrometry (ICP–MS) -based monitoring of K^+ outflow can lead to a better understanding of the often-observed stability losses of zero-gap MEA-based CO_2 electrolysers [41], and the combination of these methods have already led to the successful identification of design strategies that could help prolong electrolyser lifespans. These strategies included the preferential application of GDLs with a cracked MPL structure (over GDLs of compact MPLs, [42]) or the practice of avoiding the use of polymeric capping agents when formulating Ag NP-based catalyst inks [15].

In the present paper we focus on another important constituent of zero-gap MEAs that has crucial effect on the water (electrolyte) management of electrolysers. This constituent is the binder: an ionomer that is added to the catalyst ink in order to improve its consistency, its electrical (ionic) conductivity, and its adherence to the MPL surface. In this paper we compare two well-known binders, Nafion and Fumion, in order to study their effect on the lifespan of electrolyses.

The major difference between the two applied binders is that Nafion, a sulphonated tetrafluoroethylene-based polymer, is an essentially H^+-conducting material, while Fumion, a polyaromatic polymer with quaternary ammonium functional groups, conducts electricity by counterion (in the studied media, OH^- or CO_3^{2-}/HCO_3^-) hopping. While, probably mostly out of tradition, Nafion is still used by a vast majority of researchers of *ec*–CO_2RR as the ionomer of cathode catalyst layers (see [46] for a Review), the advantages of using anion exchange ionomers (especially in order to hinder cation penetration and precipitation at the cathode) were also identified [47].

Working under the hypothesis that upholding effective perspiration is essential in order to avoid the entrapment of electrolyte (flooding) in the GDE structure, as well as that the appearance of K^+ ions inside the GDE can directly be interpreted as a tracer of flooding, we utilise our recently developed approach [31] that combines post-experimental EDX-based analysis of GDEs with the ICP–MS-based monitoring of perspired electrolytes in order to shed light on the reasons why the application of Fumion as a binder leads to more prolonged electrolysis stability compared to when a Nafion ionomer is used for the fixation of the catalyst ink.

We note here that a recent comparative study by Nwabara et al. on different ionomers [48], the scope of which also initially included Fumion, concluded —based on contact angle measurements screening— that Fumion would not be an efficient binder because of its hydrophobicity being significantly lower than that of Nafion. While this observation is generally valid (and in contact angle measurements we also observed the same difference), this paper points out that the ability of ionomers to assure effective electrolyte perspiration, thus enabling longer electrolysis stability, is a more important factor than hydrophobicity alone. This observation, we believe, is an important addition to existing screening strategies that seem to emphasise mostly the role of non-wettability in GDE design for stable *ec*–CO_2RR [48–51].

With regard to the zero-gap cathode MEA configuration used in our experiments (see Fig. 1) we note here that this set-up was created specifically for the accelerated durability testing of CO_2 electrolysing GDEs [22]. As opposed to devices of higher effective surface areas employing a true zero-gap configuration that also includes an anode GDE, the effective area of our small-scale electrolyser is only a few square-millimetres, and it features a semi-zero gap design, meaning that the membrane is brought into direct contact with the anolyte solution containing an Ir wire anode and is not interfaced to an anode GDE. As a result of these two conceptual differences, stability defects in our small-scale electrolyser can be observed after much shorter times of electrolysis, compared to semi-industrial scale reactors where durability issues similar to those reported in our paper would occur only after weeks of stable operation [52].

2. Experimental

2.1. Chemicals used

All chemicals were used as purchased, without further purification. Potassium hydroxide (reagent grade, 90%, flakes) and Nafion (Nafion 117, $w \approx 5\%$, dissolved in a mixture of lower aliphatic alcohols and water) were purchased from Sigma-Aldrich. Dispersions of lipoic acid capped —for some experiments, polyvinylpyrrolidone (PVP) capped or branched polyethylene-imine (BPEI) capped— Ag NPs (1 mg cm^{-3} Ag in 2 mmol dm^{-3} aqueous K_2CO_3 solution) were purchased from Nano-Composix. The Freudenberg H23C8 GDL and Fumion solution (Fumion FAA-3-SOLUT-10) were purchased from Fuel Cell Store. Carbon black (Vulcan XC 72 R) was purchased from Cabot. Isopropanol (VLSI Selectipur) was obtained from BASF. The anion exchange membrane (X3750 RT) was purchased from Dioxide materials. Ir wire (99.9%) was obtained from MaTeck Material Technologie & Kristalle GmbH. An Ag | AgCl | 3 mol dm^{-3} KCl reference electrode (double junction design) was purchased from Metrohm. Carbon dioxide (99.999%) was purchased from Carbagas. Ultra-pure water (Milli-Q by Merck Millipore, 18.2 MΩ cm specific resistance) was used in all experiments.

2.2. Catalyst ink preparation

0.25 cm^3 of the dispersion containing lipoic acid (alternatively, for some experiments, PVP or BPEI) capped Ag NPs and 0.74 cm^3 of carbon black in isopropanol (carbon concentration: 0.059 mg cm^{-3}) were separately sonicated for 10 min. Then, the two solutions were mixed, and 0.01 cm^3 of either Nafion or Fumion binder solutions (as purchased) was added, following which the resulting ink was sonicated for another 10 min. We note here that if no binder is used, the ink becomes unstable and already within 10 min, agglomeration of particles can be observed (see the photos of Fig. S1 in Supporting Information). The amount of binders to add (0.01 cm^3 in 1 cm^3 ink, corresponding to 1% binder volume fraction) was determined based on pre-screening experiments, results of which are shown in Fig. S2 of Supporting Information. In case when the Fumion binder was used, the ink of 1% binder volume fraction exhibited the longest durability during electrolyses. In case of Nafion, the binder concentration had little effect on the stability of electrolysis, thus we decided to compare inks with the same, 1% binder volume fraction. As seen in Fig. S1, these catalyst inks were homogeneous, with an Ag NP concentration of 0.25 mg cm^{-3} and an Ag/carbon black mass ratio of 85:15.

2.3. Preparation of the GDEs

0.04 cm^3 of the prepared catalyst ink was drop-cast on the centre of the microporous surface of a circular Freudenberg H23C8 (FuelCell-Store) GDL of 2 cm diameter by using vacuum filtration. By applying a silicone plate mask, the drop-cast area was limited to a circle of 4 mm diameter. The thus prepared GDE was dried in a vacuum drying chamber overnight.

2.4. Assembly of the electrolyser

The electrolyser shown in Fig. 1 was used to carry out electrochemical CO_2 reduction. The bottom part of the electrolyser is made of stainless steel and is equipped with gas flow channels, on which the prepared GDEs were placed with the catalyst layer facing upwards and the bottom carbon fibre layer facing the gas flow channels. The GDE was covered by a hydroxide functionalised Sustainion anion exchange membrane from above, before fixing the Teflon-made anode compartment on top. The anode compartment has a central orifice on its bottom, allowing access of the anolyte to the membrane. The orifice is of 3 mm diameter, determining the geometric surface area (0.0707 cm^2) of the GDE. The anode compartment is filled with 10 cm^3 of 2 mol dm^{-3} KOH

solution, and contains an Ag | AgCl | 3 mol dm^{-3} KCl reference electrode and an Ir wire anode. The anode is placed inside a small chamber and is separated from the rest of the analyte by glass frit, as shown in Fig. 1.

2.5. Electrochemical measurements and product analysis

All galvanostatic electrolysis experiments were carried out using an ECi-200 potentiostat (Nordic Electrochemistry), by applying a current of − 21.2 mA (corresponding to a geometric surface area-normalised current density of −300 mA $cm^{-2)}$ for a duration of 1 h, resulting in a passage of −76.34 C of charge (−1080 C cm^{-2} normalised to geometric surface area). Cathode potentials reported in the paper are all referred to the applied Ag | AgCl | 3 mol dm^{-3} KCl reference electrode. Potential values were IR-corrected based on an impedimetric determination of the series cell resistance. Gaseous reaction products (CO and H_2) were analysed by connecting the gas outlet of the electrolyser to a gas chromatograph (GC, SRI Instruments Multigas Analyzer). The continuous flow of the carrier CO_2 gas through the cathode flow channels carried reaction products from the gas outlet of the electrolyser into the sampling loop of the gas chromatograph. The partial current I_i, corresponding to the formation of a gaseous product *i*, can be calculated [53] as

$$I_i = x_i\, n_i\, F\, v_{\mathrm{m}}, \tag{1}$$

where x_i denotes the mole fraction of the products, determined by GC using an independent calibration standard gas (Carbagas); n_i is the number of electrons involved in the reduction reaction to form a particular product ($n = 2$ for both CO and H_2 formation); F = 96,485.3 C mol^{-1} is Faraday's constant; and v_{m} is the molar CO_2 gas flow rate determined by a universal flowmeter (7000 GC flowmeter, Ellutia) at the gas outlet of the electrolyser. The Faradaic efficiency (*FE*) of a given reaction product was determined by dividing the respective partial current, calculated from Eq. (1), by the total current. A thermal conductivity detector (TCD, for the detection of H_2) and a flame ionisation detector (FID, for the detection of CO) were equipped to the gas chromatograph. In all our experiments, the formed CO and H_2 amounts accounted for an altogether 90–99% *FE*. Following 1-hour electrolyses, some amounts of formate ($HCOO^-$) were detected in the anolyte compartment, which could account for the less than 100% total *FE*, although an exact quantification of this product is not possible (due to the fact that it is partially consumed by oxidation at the anode).

2.6. Scanning electron microscope (SEM), energy-dispersive X-ray spectroscopy (EDX) and transmission electron spectroscopy (TEM)

A Zeiss Gemini 450 scanning electron microscope with InLens secondary electron detector and backscattering detector was used to study the surface and the interior of GDEs prior to, and after electrolysis. An accelerating voltage of 5 kV and a beam current of 120 pA were applied at working distances between 5.0 and 5.5 mm. The SmileView software was used to measure the particle size of Ag NPs, 500–700 particles were analyzed at each experimental setting to create particles size distribution charts. To study the morphological evolution of Ag NPs upon electrolysis, all GDEs were immersed into Milli-Q water at least 15 min for three times, to remove K_2CO_3/$KHCO_3$ precipitates from their surface. (This step was obviously omitted before the SEM/EDX-based characterisation of the formed precipitate patterns.) An Energy Dispersive X-Ray Analyzer (EDX) was used to provide elemental identification and compositional information of Ag and K for after-electrolysis GDE samples. To obtain surface or cross-sectional mapping of GDEs, the Aztec 5.0 software (Oxford Instruments) was used, with an acceleration voltage of 10 kV, current of 1 nA and working distance of 8.5 mm. Cross-sectional SEM and EDX analysis was carried out using the GDE cut by a knife in the middle, by applying pressure to the knife from the back side. For the transmission electron microscopy (TEM) imaging, an FEI Titan Themis instrument was used with an accelerating voltage of 300 kV.

2.7. Inductively coupled plasma mass spectrometry (ICP–MS)

ICP–MS (NExION 2000, Perkin Elmer) was applied to determine the mass of potassium that perspired through the membrane and the GDE, and exited the electrolyser through the gas outlet. A trap containing 10 cm^3 of ultrapure water was used to collect perspired potassium salts (Fig. 1b). 0.02 cm^3 aliquots of the trap content, collected every 10 min, were 500-fold diluted by an appropriate amount of 2% HNO_3 solution (BASF SE, Ludwigshafen, Germany) and the resulting solution samples were injected into the ICP–MS to obtain the content of potassium in perspiration. To determine the Ag mass loading of the GDE samples, the GDEs were immersed in 1 cm^3 of concentrated HNO_3 (69.3%, BASF SE, Ludwigshafen, Germany) for 24 h to dissolve all Ag NPs. 0.02 cm^3 of the resulting solutions was diluted with 3% HNO_3 solution by a factor of 500, and was then fed into the ICP–MS. Loading values reported in the paper are 95% confidence intervals, calculated from 6 independent measurements.

2.8. Contact angle measurements

Contact angle measurements were carried out using a Krüss Advance Drop Shape Analyzer DSA25 (Krüss GmbH, Hamburg, Germany). GDEs were mounted on a flat stage and water drops (milli-Q water, 0.0014 cm^3) were deposited at room temperature.

Raw data, as well as unprocessed measurement files serving as a basis of this publication can be downloaded from Zenodo [54].

3. Results and discussion

The aim of this paper is to study the effect of two chosen ionomers (Nafion and Fumion) on the stability of *ec*–CO_2RR carried out in the electrolyser shown in Fig. 1. This reactor is a small-scale version of catholyte-free (also known as zero-gap) gas fed MEA-based electrolysers [45] in which cathode GDEs are directly interfaced to an anion exchange membrane. Although its small active GDE area (0.0707 cm^2, see the Experimental section for details) limits the operating current of the device (so that it definitely falls short of industrial requirements), the electrolyser can be operated at high (> 100 mA cm^{-2}) current densities. Since it was designed [30,31], the device has become a useful tool for the simulation of close-to application electrolysis conditions, and —complemented by the quantitative monitoring of perspired electrolyte amounts and by the post-mortem SEM/EDX-based analysis of GDEs— the small-scale electrolyser has already successfully been used to identify the major causes of efficiency losses [15,40–42] in GDE-based CO_2-to-CO converters.

Due to its limited size, our small-scale electrolyser device is more sensitive to edge effect-related stability losses, thus when operated at suitably high current densities, a break-down of the electrolysis efficiency can be observed relatively early (usually, within an hour). This allows the identification of major malfunction causes without the need of long-lasting electrolyses, and the device can thus serve for the accelerated durability testing of GDEs, the need of which has been pointed out recently [22].

3.1. Characterisation of as-prepared GDEs

Nafion- and Fumion-fixed GDEs were prepared as described in the Experimental Section by keeping the following two points in mind: First, we intentionally applied a Freudenberg H23C8 GDL, the MPL of which is free of any cracks or voids, the size of which would exceed the submicron region. This choice was necessary in order to make sure that we study a "worst-case scenario", in which larger cracks can provide no drainage channels in addition to those provided by micropores [42]. Second, we chose an Ag NP dispersion for the formulation of the catalyst

ink in which the NPs were capped by lipoic acid, a non-polymeric agent that stabilises the NPs mostly by Coulomb interactions, and that does not get adhered to the MPL, clogging its micropores [15].

Although the applied silver loading was almost the same in case of the Nafion-fixed ((37.7 ± 6.0) μg cm^{-2}) and the Fumion-fixed ((40.0 ± 6.5) μg cm^{-2}) GDE, sessile water drop tensiometry (respective contact angles: 150.9° ± 0.1° and 99.8° ± 0.5°) revealed that the surface of the Fumion-bound catalyst layer is significantly less hydrophobic, in agreement with previous reports of Nwabara et al. [48].

While TEM investigations (see Fig. S3 of Supporting Information) reveal that Ag NPs originating from Nafion- and Fumion-containing samples have a rather similar nanoscale structure, the SEM/EDX-based imaging of as-prepared GDEs exhibit significant differences. The top-down SEM micrographs (Fig. 2) of the Fumion-bound catalyst layer were relatively blurry, and they showed an apparently smaller number of Ag NPs compared to the much sharper micrographs taken from the Nafion-bound catalyst layer where not only the Ag NPs, but also flakes of the Vulcan carbon support could well be identified. We ascribe the observed blurriness of the SEM images taken from the Fumion-bound catalyst to the formation of an electron-optically dense, jelly-like Fumion layer that covers most of the Ag NPs, keeping them partially inaccessible to the electron beam. This argument is further supported by the cross-sectional SEM micrographs and elemental (Ag) EDX maps of the GDEs. These show that while the Ag NPs of Nafion-bound catalyst inks can relatively deeply penetrate the MPL (to an approximate depth of ~10 μm), such penetration does not occur in Fumion-fixed GDEs. In the latter case it seems that Fumion, probably due to its hydrophilic nature, cannot enter the (hydrophobic) MPL, and as a result, the catalyst forms a well-discernible (about 500 nm thick) layer on top of the GDE.

3.2. Electrolysis stress tests: stability–perspiration relations

Nafion-fixed and Fumion-fixed GDEs also exhibit several differences when made subject to 1 h *ec*–CO_2RR stressing experiments at a high current density (–300 mA cm^{-2}, Fig. 3). Fig. 3a shows that at the start of electrolysis, both GDEs perform well and yield CO with a Faradaic efficiency of $FE_{CO} \geq 90\%$. The performance of the GDEs will then decrease, however, and a shift from CO_2-to-CO reduction (Reaction (R1)) to hydrogen evolution (Reaction (R2)) is clearly indicated both by

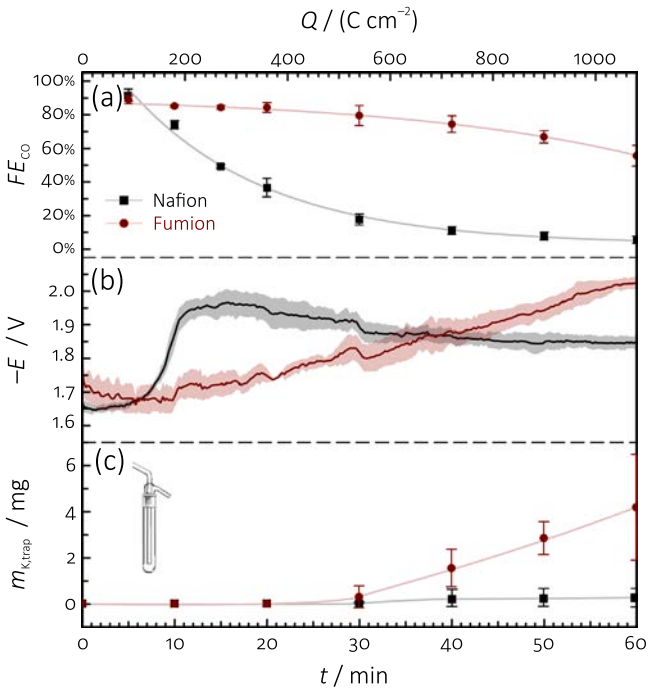

Fig. 3. Results of *ec*–CO_2RR stressing of Nafion-fixed (black) and Fumion-fixed (red) GDEs. Panel (a) shows the variation of the Faradaic efficiency of CO, FE_{CO}, over time. Panel (b) shows the temporal variation of the measured electrode potential *E*, while in panel (c) we plotted the amount of K^+ that perspired through the electrolyser and was detected in the water trap equipped to its gas outlet channels (cf. to Fig. 1). Error bars and shaded areas indicate 95% confidence intervals calculated from at least three independent measurements, raw data that served the construction of the figure are accessible online [54].

the instantaneous increase of the cathodic potential shown in Fig. 3b, and by the (due to the nature of GC-based sampling, much slower) decrease of the measured FE_{CO} values. The trend of this shift is, however, distinctly different for the two GDEs, and while for the Nafion-bound catalyst layer a deterioration of electrolyser stability is imminent

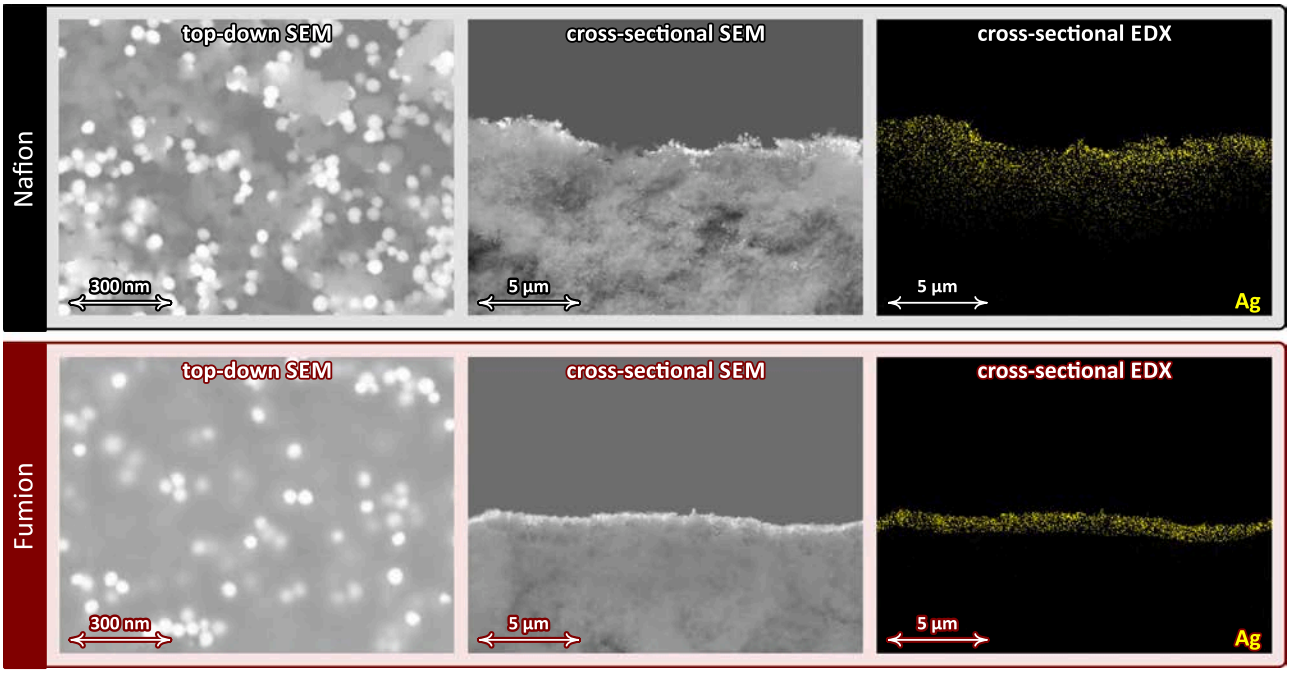

Fig. 2. SEM/EDX-based characterisation of Nafion-fixed (top row) and Fumion-fixed (bottom row) GDEs.

—already after the first 15 min of electrolysis, FE_{CO} drops to below 50%—, the Fumion-bound catalyst layer holds on for longer times, and even after 1 h long electrolysis, CO is still the majority product.

The reason of this difference in the electrolysis stability is not that electrolyte could not enter the Fumion-fixed GDE: as it can be seen in Fig. 3c, the amount of K^+ exiting through the outflow of the electrolyser is quite significant and the K^+ content of the trap keeps increasing steadily for the Fumion-containing GDE. The Nafion-fixed electrode, on the other hand, seems to allow no significant perspiration of K^+ ions through the electrolyser.

3.3. *Fumion vs. Nafion: reasons behind different electrolysis lifespans unravelled by post mortem SEM–EDX investigations of GDEs*

That the appearance of membrane-transported electrolytes have a key role in determining the stability of electrolyses is directly proven by the top-down and crosssectional SEM investigation of the two GDEs at different stages of electrolysis. The SEM micrographs in Fig. 4 were colourised based on the EDX-based elemental mapping of K and Ag to show the exact spots where precipitates and catalyst particles are located.

The as-prepared Nafion and Fumion-fixed electrodes look different in terms of apparent loading (top-down view) and the distribution of the catalyst particles (crosssectional view), due to reasons already described previously, in relation to Fig. 2. When the electrolysis starts, K^+-containing precipitates begin to appear (and their concentration evidently increases with the time of electrolysis) in both GDEs, however the spatial distribution and the accumulated amount of precipitates will be completely different for the two studied systems.

In Nafion-fixed GDEs, K^+ preferentially appears on-top of the catalyst layer, and plaques of precipitates tend to cover rather quickly the Ag NP catalyst particles. At the final stage of electrolysis, and this is well observable both in the top-down and cross-sectional SEM images, only some very little part of the catalyst layer remains active due to the formation of an about 3 μm thick $K_2CO_3/KHCO_3$ plaque formed over it. This is clearly the reason for which the Nafion-fixed GDE at this point already loses almost all its ability to reduce CO_2 to CO. The amount of K^+ that could enter —primarily at the beginning of electrolysis— the deeper layers of the MPL is significantly less than what is retained in the plaque. Note that after it is formed, the plaque should not only inhibit the electrolysis process, but should also hinder the further entry of K^+ ions into the MPL, which explains why the Nafion-fixed GDE allows almost no K^+ perspiration (Fig. 3c).

Fumion-fixed GDEs behave utterly differently compared to Nafion-fixed ones: not in the sense that in this case, clear signs of precipitate formations would not be visible (the amount of K^+, both on-top and within the GDL, clearly increases with the time of electrolysis, Fig. 4) but rather because the distribution of the precipitates is clearly more

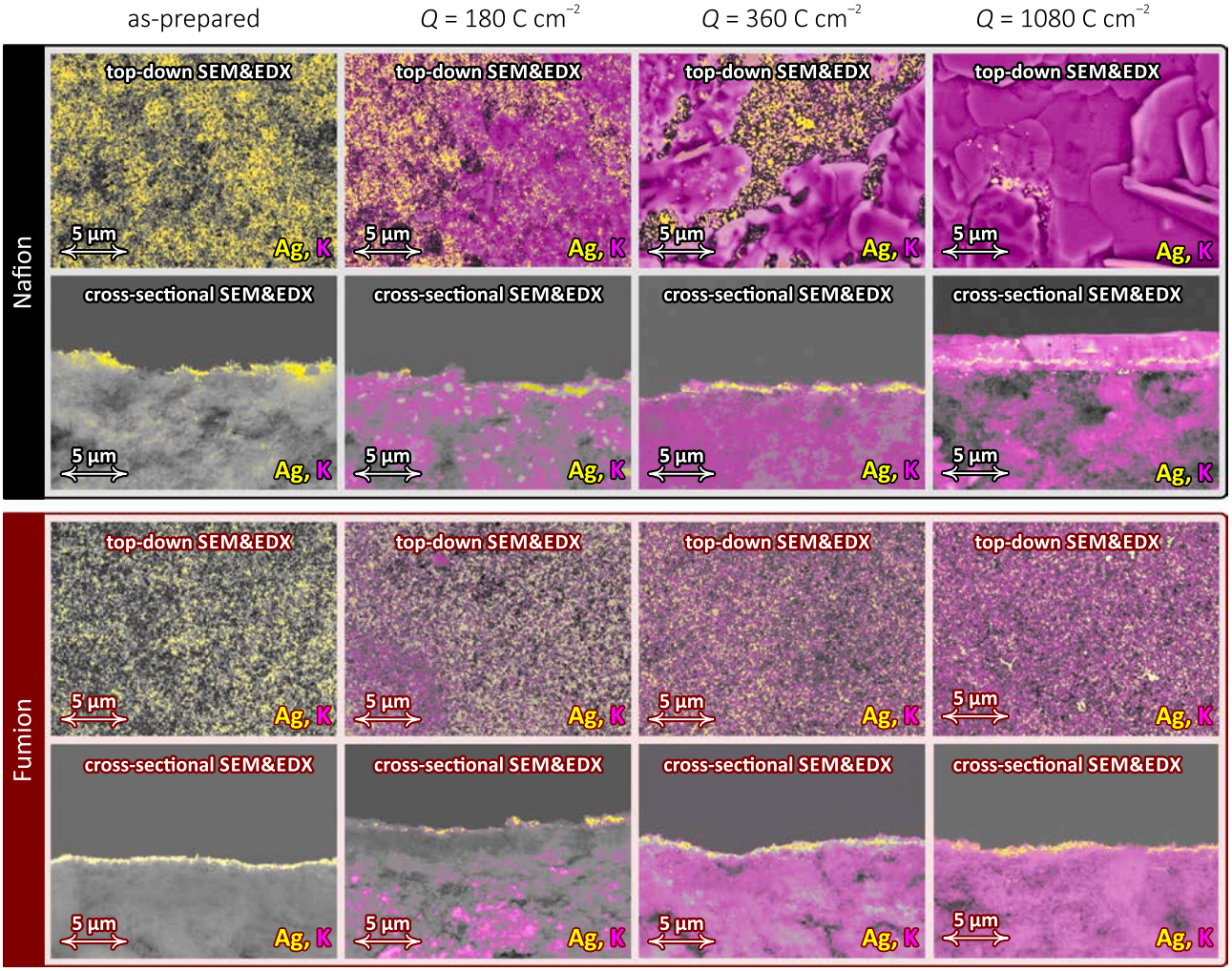

Fig. 4. Top-down and cross-sectional images recorded of Nafion and Fumion-fixed GDEs at different stages of electrolysis (after the passage of the indicated amount of charge). The images were colourised based on elemental EDX mapping: yellow colour stands for Ag, magenta for K-rich spots. The original SEM images and corresponding EDX maps are accessible online [54].

homogeneous in Fumion-fixed GDEs. Here, no distinct plaque formation is observed, and the formed precipitates seem to penetrate more uniformly the deeper regions of the MPLs. For the majority of the formed K^+ salts it is still possible to perspire through the GDE structure, and eventually to exit the electrolyser—these salts can be detected in the water trap equipped to the gas outflow (Fig. 3c).

That the Fumion-fixed GDE retains its activity for a longer time than its Nafion-fixed alternative can clearly be explained by that the formed precipitates cover much less of the catalyst layer on-top of the Fumion-fixed GDE. Formed precipitates, on the other hand, do seem to penetrate the GDL structure to considerable extent, where they probably flood some portion of the micropores —this causes the about 50% drop of the Faradaic efficiency over the 1-hour electrolysis—, but this effect seems to be less detrimental than that of the plaque formation on-top of the catalyst layer, seen in the case of Nafion-fixed electrodes. It seems to be a plausible assumption that this improved performance of Fumion-fixed GDEs is due to the relatively compact, jelly film-like nature of Fumion that, as opposed to Nafion, does not penetrate and clogs the micropores of the MPL, however that is still somewhat permeable to K^+ ions.

As the ultimate source of K^+ ions in the studied electrolyser configuration is the anolyte, we carried out additional experiments utilising a 0.2 (instead of 2.0) mol dm^{-3} KOH solution as anolyte (see Figs. S4 and S5 in Supporting Information). It seemed, however, that also this decreased anolyte concentration is high enough to cause very similar stability issues and plaque formation during electrolysis on Nafion-bound GDEs.

In order to further support the hypothesis that Fumion-bound GDEs are superior to Nafion-bound electrodes due to that they enable more effective electrolyte perspiration, we had to rule out two alternative explanations; namely, that *i.)* the deficient stability of Nafion-bound GDEs could also be caused by the deeper penetration (and, as a result, partial deactivation) of the Ag NPs into the MPL, as was shown in Fig. 2; and *ii.)* that specific chemical interactions between the lipoic acid capping agent and the used ionomers may also be responsible for the observed durability differences of Fumion and Nafion-bound GDEs.

As to the first point, we found that in case we apply spray coating (instead of vacuum filtration) to cover the GDL with the catalyst ink, the aforementioned penetration of Ag NPs will occur to a considerably less extent (see Fig. S7 of Supporting Information), while the same difference between the stability of Nafion and Fumion fixed GDEs will remain to be observed (Fig. S8 of Supporting Information).

As to the second point, we also prepared GDEs using another two capping agents —PVP and BPEI— with structures very different from that of lipoic acid, and we still observed (see Fig. S9 in Supporting Information) that Fumion-fixed GDEs retain their stability for longer times than Nafion-fixed ones, in a way that is rather similar for lipoic acid stabilised NPs.

The above experiments further support the conclusion of findings shown in Figs. 3 and 4: that is, efficient perspiration needs to be maintained in the zero-gap MEA to avoid plaque formation over the catalyst layer and resulting stability losses. From this point of view, Fumion-bound GDEs seem to perform better than their Nafion-fixed alternatives—however, upholding the efficiency of electrolysis is not the only advantage that Fumion offers.

3.4. The role of ionomers in protecting catalyst NPs from degradation

Another beneficial effect of the Fumion layer is that it protects most Ag NPs from degradation. If after 1 h electrolysis, we clean away (by water rinsing, see the Experimental Section) the formed precipitates from the top of the GDEs, we can use SEM-based analysis to detect the morphological changes of catalyst particles. Fig. 5 shows that in case of both electrodes, the initial size distribution of the NPs was almost monodisperse, centred around approximately 50 nm. During electrolysis, in case of the Nafion-bound electrode, severe degradation occurred, as a result of which many particles merged into large conglomerates, and the size distribution became flattened. A tendency towards the formation of large aggregates can also be noticed in the case of the Fumion-fixed GDE; however, in this case the protective Fumion layer seems to keep the big majority of the particles immobile, and as a result, the initial size distribution still remains dominant also after the electrolysis testing. We note here that following long-lasting electrolyses, the sharpness of the top-down SEM micrographs taken from Fumion-bound GDEs has apparently improved, and thus the number of exhibited NPs also seemed to increase (compare the SEM images of the "Fumion" panel in Fig. 5). This probably has to do with the degradation of the protective Fumion layer during electrolysis. That the large agglomerates formed to more extent on the Nafion-bound and to less on the Fumion-bound GDEs during electrolyses consist of Ag, is clearly proven by the EDX maps of Fig. S6 in Supporting Information.

3.5. Testing Fumion-bound GDEs with anolytes of different compositions

The experiments described above all indicate that it is the relatively

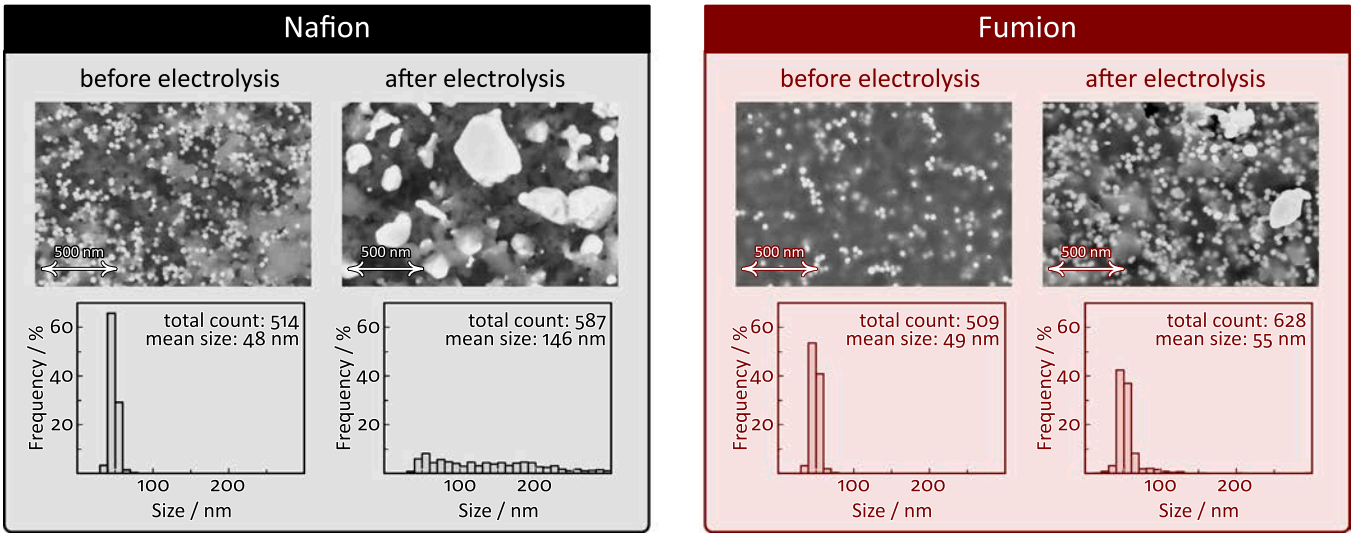

Fig. 5. Top-down and cross-sectional images recorded of Nafion and Fumion-fixed GDEs at different stages of electrolysis (after the passage of the indicated amount of charge). The images were colourised based on elemental EDX mapping: yellow colour stands for Ag, magenta for K-rich spots. The original SEM images and corresponding EDX maps are accessible online [54].

good permeability of the Fumion layer to K^+ ions that enables a more long-lasting cell stability (compared to what can be achieved by using Nafion-bound GDEs), and that the ability of Fumion in upholding electrolyte perspiration is essential for the stable operation of CO_2 electrolysing zero-gap MEAs.

In order to further test the validity of this statement and to define its boundaries, we performed a set of further experiments in which Fumion-fixed GDEs (MEAs) were used in combination with anolytes of different compositions. Apart from KOH, LiOH, NaOH and CsOH solutions of 2 mol dm^{-3} concentration were used as anolyte in these experiments. As shown in Fig. 6, we found during electrolysis at a constant current density of 150 mA cm^{-2} that in case of a CsOH anolyte, the stability of electrolysis could slightly be improved (compared to when a KOH anolyte was applied). In case of NaOH, the durability of the electrolysis has already significantly decreased, and HER became prevailing over *ec*–CO_2RR already after 2 h of electrolysis. Furthermore, if NaOH was used as an electrolyte, results (see Fig. 6) also indicated the production formate ions at large scale (something that was not seen either in case of KOH or of CsOH). In the case when LiOH was used as an anolyte, the electrolysis broke down almost immediately —so that no product distribution could be determined— and the measured potential reached a saturation value, indicating that the control circuit cannot provide sufficient current for the electrolysis.

Also in these experiments we found that stability losses during electrolysis usually occur as a result of plaque (precipitate) formation over the GDE surfaces (Fig. 7), and that the time at which the electrolysis breaks down is mostly determined by two factors: the transport properties (the mobility) of the cations and the solubility of their carbonate salts. The SEM/EDX characterisation of GDEs at different stages of the electrolysis show that in case of K^+ and Cs^+, precipitates appear rather late over the catalyst layer, while the formation of Na^+ and, in particular, Li^+ carbonates on top of GDEs commences much earlier. This has to do with the greater (hydrodynamic) radius and the resulting reduced mobility of hydrated Na^+ and Li^+ ions, as well as with the limited solubility of their carbonate salts (see Table 1 for data). A correlation between the diffusion coefficients of the cations and the solubility of their carbonate salts, as well as the stability time of electrolyses when different alkali hydroxides are used as anolytes are shown in Fig. 8. (The time of electrolysis stability we define here as the electrolysis time required for FE_{H_2} to grow higher than 50%.).

The above experiments demonstrate that while the application of Fumion as an ionomer of catalyst inks usually leads to more prolonged electrolyser stabilities compared to when, e.g., a Nafion binder is used, precipitation inside Fumion-bound GDEs can still be observed, and this is what at the end determines the stability of the process. Apart from choosing the right ionomer material for the fabrication of GDEs, also the composition of the anolyte has thus to be taken into account in order to establish proper electrolyte management within CO reducing GDE-based MEAs, in alignment with novel findings of Garg et al. [56] and of Burdyny et al. [57].

4. Conclusion

In this paper we prepared Ag NPs containing catalyst inks by the application of two different binders: Nafion and Fumion. By using these inks, we created GDEs that we subjected, in a zero-gap MEA configuration, to *ec*–CO_2RR experiments. Although based on their wettabilities (Nafion-fixed GDEs are more hydrophobic than Fumion-fixed ones) we expected the opposite [48,49], we found that on Fumion-containing GDEs the selectivity of CO_2-to-CO conversion can be upheld for longer times.

By a post-electrolysis EDX-based elemental (K) analysis of precipitation patterns inside and on-top of the GDEs, combined with a mass spectrometric monitoring of the perspired electrolyte amount, we concluded that the poor performance of Nafion-fixed GDEs is due to the formation of K_2CO_3/$KHCO_3$ precipitate plaques over the catalyst layer that breaks down its activity in *ec*–CO_2RR. On Fumion-fixed GDEs this plaque formation was avoided, and while a protective ionomer layer

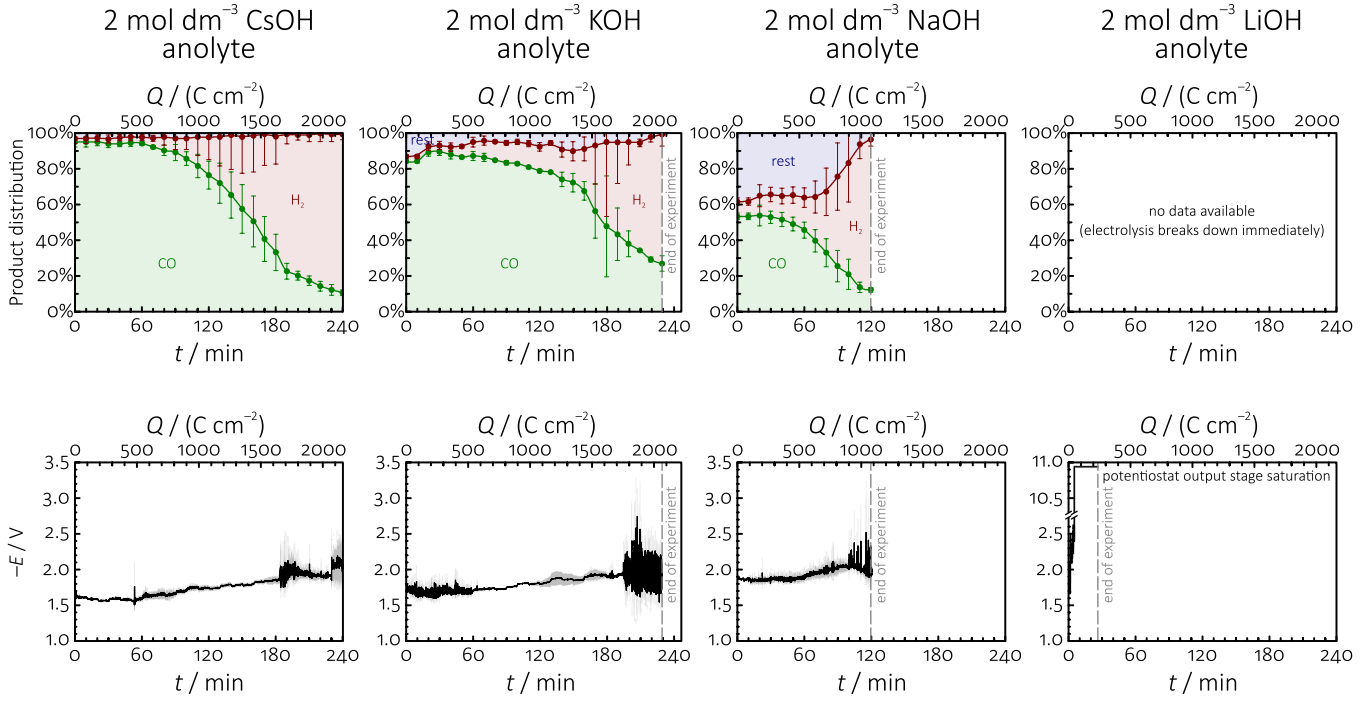

Fig. 6. Fumion-fixed GDEs are tested in *ec*–CO_2RR experiments in the cell shown in Fig. 1, using different anolyte compositions. The top row shows the time (charge) dependence of the product distribution, the bottom row the time (charge) dependence of the measured cathode potential. Applied current density: 150 mA cm^{-2}. Regions marked as "rest" in the product distribution plots probably correspond to the production of formate. (Slight amounts of formate were detected in the anode compartment of the electrolyser following the experiments: the amount of formate can however not be exactly quantified in the used set-up, due to its possible oxidation at the anode.)

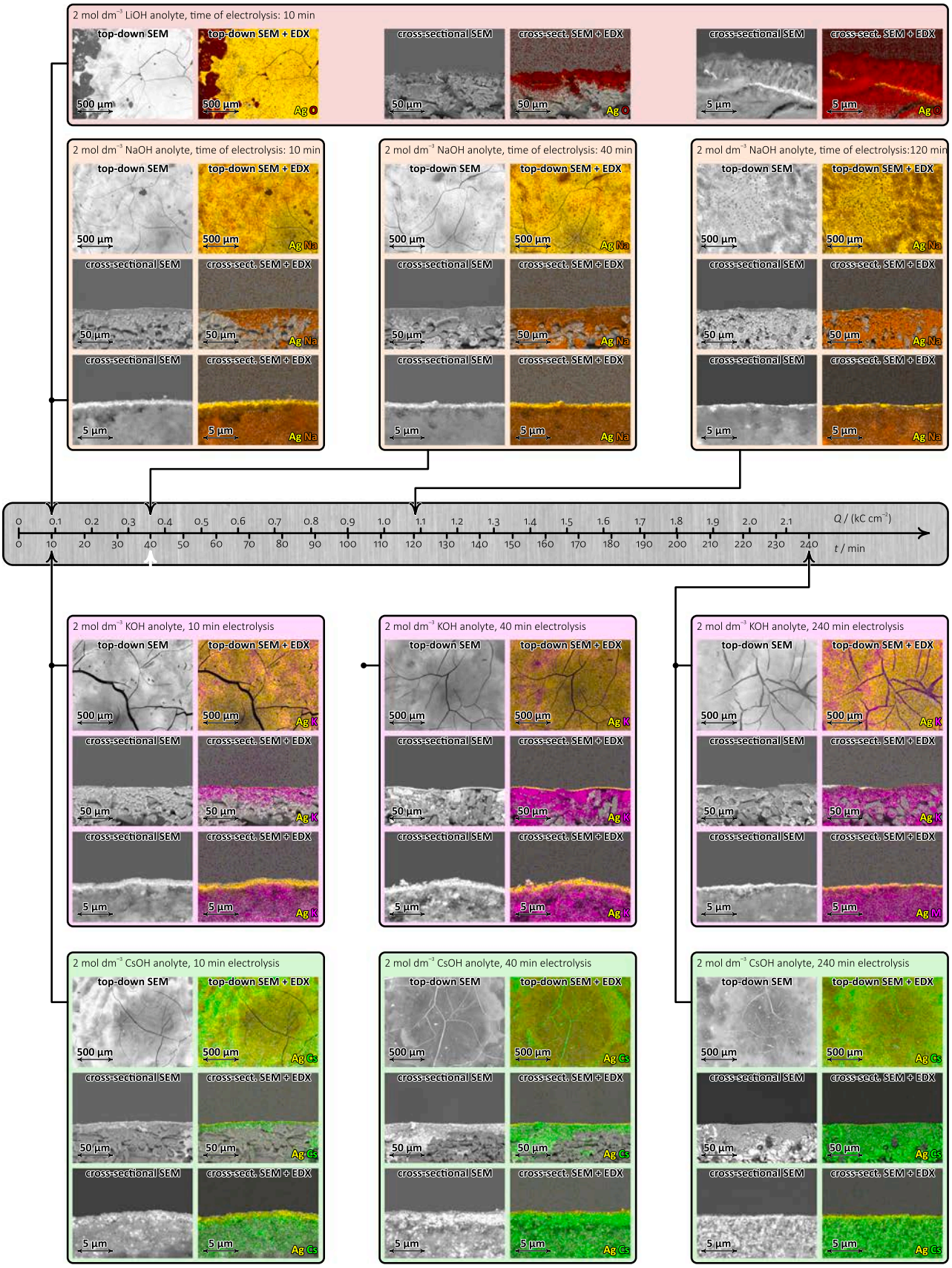

Fig. 7. Top-down and cross-sectional SEM and EDX investigation of Fumion-fixed GDEs following *ec*–CO_2RR stressing after electrolysis lasting different times (corresponding to different passed charge densities). LiOH, NaOH, KOH and CsOH were used as anolytes of the electrolyser. Elemental EDX mapping shows the formation of growing amounts of precipitates inside and on-top of the GDE structure as a function of increasing charge. For visualising Li^+ carbonate precipitates, elemental O mapping was applied. Applied current density: 150 mA cm^{-2}. Cf. to Fig. 6 for electrochemical measurement data.

Table 1
Physico-chemical parameters (Λ_0: molar conductivity at infinite dilution, D_0: diffusion coefficient at infinite dilution, r_{Stokes}: hydrodynamic radius) of the different hydrated alkali cations studied in this paper, as well as the solubility of their carbonate salt ($b_{max,\ M_2CO_3}$) expressed in molality and the approximate stability time (t_{stab}) of electrolyses when the given alkali hydroxide is used as anolyte of the electrolyser. Data are taken from Ref. [55]; transport parameters correspond to 25 °C, solubilities to 15 °C temperature.

	Li^+	Na^+	K^+	Cs^+
Λ_0 / (S cm^2 mol^{-1})	38.66	50.08	73.48	77.20
D_0 / (10^{-5} cm^2 s^{-1})	1.029	1.333	1.957	2.056
r_{Stokes} / Å	2.386	1.842	1.255	1.195
$b_{max,\ M_2CO_3}$ / (mol kg^{-1})	0.1894	1.581	7.839	8.011
t_{stab} / s	~5	~80	~178	~189

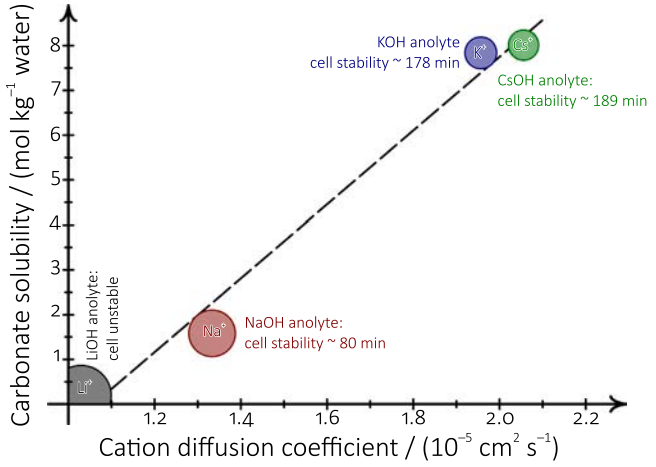

Fig. 8. Plot showing a direct correlation between the diffusion coefficients (scaled mobilities) of the studied cations and the solubilities of their carbonate salts, as well as the stability of electrolyser cells operated with the corresponding 2 mol dm^{-3} hydroxide solutions. See Table 1 for numerical data.

kept most of the Ag NP catalyst particles active, a majority amount of the K^+-containing electrolyte that penetrated through the membrane could perspire through the GDE and exit the electrolyser through the gas outflow line.

Our results indicate that from the point of view of upholding the stability of CO_2 electrolyses in zero-gap MEA-based cathode configurations, the importance of good electrolyte management (effective perspiration) is even higher than that of the wettability properties of GDEs [48–51].

By carrying out experiments with Fumion-fixed GDEs in combination with anolytes of different compositions (KOH, CsOH, NaOH and LiOH), we demonstrated that stable electrolysis (efficient perspiration) can more be upheld in the order $Cs^+ > K^+ > Na^+ >> Li^+$; that is, in case when smaller (more mobile) cations are used, the carbonates of which exhibit greater solubility in water.

CRediT authorship contribution statement

Menglong Liu: Investigation, Experiments, Data curation, Writing – first draft. **Ying Kong:** Investigation, Experiments. **Huifang Hu:** Investigation, Experiments. **Iván Zelocualtecatl Montiel:** Investigation, Experiments. **Viliam Kolivoška:** Conceptualization, Methodology. **Alexander V. Rudnev:** Conceptualization, Methodology. **Yuhui Hou:** Conceptualization, Methodology. **Rolf Erni:** TEM measurements. **Soma Vesztergom:** Conceptualization, Methodology, Visualization, Data analysis, Writing, Funding acquisition. **Peter Broekmann:** Conceptualization, Methodology, Writing – review & editing, Supervision, Funding acquisition.

Declaration of Competing Interest

The authors declare the following financial interests/personal relationships which may be considered as potential competing interests: Peter Broekmann reports financial support was provided by National Center of Competence in Research Catalysis. Soma Vesztergom reports financial support was provided by National Research Development and Innovation Office. Viliam Kolivoska reports financial support was provided by Czech Science Foundation.

Data availability

The Zenodo service will be used for the publication of ALL relevant research data. Using the doi shown in Ref. 54 of the paper, all research data will be made accessible upon publication of the paper.

Acknowledgements

This publication was created as part of NCCR Catalysis (grant number 180544), a National Centre of Competence in Research funded by the Swiss National Science Foundation. V. K. acknowledges financial support from the Czech Science Foundation (project number 18-09848S). A. R. acknowledges support from the Ministry of Science and Higher Education of the Russian Federation. H. H., Y. K. and M. L. acknowledge the financial support by the China Scholarship Council (CSC). S. V. acknowledges support from the National Research, Development and Innovation Office of Hungary (NKFIH grants FK135375 and K129210) and from the Lendület Programme of the Hungarian Academy of Sciences (grant LP2022-18/2022).

Appendix A. Supplementary material

Supplementary data associated with this article can be found in the online version at doi:10.1016/j.apcatb.2023.122885.

References

[1] X. Tan, C. Yu, Y. Ren, S. Cui, W. Li, J. Qiu, Recent advances in innovative strategies for the CO_2 electroreduction reaction, Energy Environ. Sci. 14 (2021) 765–780, https://doi.org/10.1039/d0ee02981e.
[2] G. Centi, S. Perathoner, Z.S. Rak, Reduction of greenhouse gas emissions by catalytic processes, Appl. Catal. B 41 (2003) 143–155, https://doi.org/10.1016/s0926-3373(02)00207-2.
[3] Z.W. Seh, J. Kibsgaard, C.F. Dickens, I. Chorkendorff, J.K. Nørskov, T.F. Jaramillo, Combining theory and experiment in electrocatalysis: insights into materials design, Science 355 (2017) eaad4998, https://doi.org/10.1126/science.aad4998.
[4] S. Ma, M. Sadakiyo, M. Heima, R. Luo, R.T. Haasch, J.I. Gold, M. Yamauchi, P.J. A. Kenis, Electroreduction of carbon dioxide to hydrocarbons using bimetallic Cu–Pd catalysts with different mixing patterns, J. Am. Chem. Soc. 139 (2017) 47–50, https://doi.org/10.1021/jacs.6b10740.
[5] T. Jaster, A. Gawel, D. Siegmund, J. Holzmann, H. Lohmann, E. Klemm, U.-P. Apfel, Electrochemical CO_2 reduction toward multicarbon alcohols — the microscopic world of catalysts & process conditions, iScience 25 (2022), 104010, https://doi.org/10.1016/j.isci.2022.104010.
[6] J. Albo, A. Sáez, J. Solla-Gullón, V. Montiel, A. Irabien, Production of methanol from CO_2 electroreduction at Cu_2O and Cu_2O/ZnObased electrodes in aqueous solution, Appl. Catal. B 176–177 (2015) 709–717, https://doi.org/10.1016/j.apcatb.2015.04.055.
[7] Y. Zheng, A. Vasileff, X. Zhou, Y. Jiao, M. Jaroniec, S.-Z. Qiao, Understanding the roadmap for electrochemical reduction of CO_2 to multi-carbon oxygenates and hydrocarbons on copper-based catalysts, J. Am. Chem. Soc. 141 (2019) 7646–7659, https://doi.org/10.1021/jacs.9b02124.
[8] X. Su, Y. Sun, L. Jin, L. Zhang, Y. Yang, P. Kerns, B. Liu, S. Li, J. He, Hierarchically porous Cu/Zn bimetallic catalysts for highly selective CO_2 electroreduction to liquid C_2 products, Appl. Catal. B 269 (2020), 118800, https://doi.org/10.1016/j.apcatb.2020.118800.
[9] C.-T. Dinh, F.P.G. de Arquer, D. Sinton, E.H. Sargent, High rate, selective, and stable electroreduction of CO_2 to CO in basic and neutral media, ACS Energy Lett. 3 (2018) 2835–2840, https://doi.org/10.1021/acsenergylett.8b01734.

[10] T. Haas, R. Krause, R. Weber, M. Demler, G. Schmid, Technical photosynthesis involving CO_2 electrolysis and fermentation, Nat. Catal. 1 (2018) 32–39, https://doi.org/10.1038/s41929-017-0005-1.

[11] Y. Hori, Electrochemical CO_2 reduction on metal electrodes, in: C.G. Vayenas, R. E. White, M.E. Gamboa-Aldeco (Eds.), Modern Aspects of Electrochemistry Vol. 42, Springer, New York, 2008, pp. 89–189, https://doi.org/10.1007/978-0-387-49489-0.

[12] S.A. Mahyoub, F.A. Qaraah, C. Chen, F. Zhang, S. Yan, Z. Cheng, An overview on the recent developments of Ag-based electrodes in the electrochemical reduction of CO_2 to CO, Sustain. Energy Fuels 4 (2020) 50–67, https://doi.org/10.1039/c9se00594c.

[13] D. Sun, X. Xu, Y. Qin, S.P. Jiang, Z. Shao, Rational design of Ag based catalysts for the electrochemical CO_2 reduction to CO: A review, ChemSusChem 13 (2019) 39–58, https://doi.org/10.1002/cssc.201902061.

[14] Y. Li, C. Chen, R. Cao, Z. Pan, H. He, K. Zhou, Dual-atom Ag_2/graphene catalyst for efficient electroreduction of CO_2 to CO, Appl. Catal. B 268 (2020), 118747, https://doi.org/10.1016/j.apcatb.2020.118747.

[15] H. Hu, M. Liu, Y. Kong, V. Kolivoška, A. Rudnev, Y. Hou, R. Erni, S. Vesztergom, P. Broekmann, Effective perspiration is essential to uphold the stability of zero-gap MEA-based CO_2 electrolysers, J. Mater. Chem. A 11 (2023) 5083–5094, https://doi.org/10.1039/D2TA06965B.

[16] Z. Yang, D. Li, L. Xing, H. Xiang, J. Xuan, S. Cheng, E.H. Yu, A. Yang, Modeling and upscaling analysis of gas diffusion electrode-based electrochemical carbon dioxide reduction systems, ACS Sustain. Chem. Eng. 9 (2020) 351–361, https://doi.org/10.1021/acssuschemeng.0c07387.

[17] A. Gawel, T. Jaster, D. Siegmund, J. Holzmann, H. Lohmann, E. Klemm, U.-P. Apfel, Electrochemical CO_2 reduction – the macroscopic world of electrode design, reactor concepts & economic aspects, iScience 25 (2022), 104011, https://doi.org/10.1016/j.isci.2022.104011.

[18] D.M. Weekes, D.A. Salvatore, A. Reyes, A. Huang, C.P. Berlinguette, Electrolytic CO_2 reduction in a flow cell, Acc. Chem. Res. 51 (2018) 910–918, https://doi.org/10.1021/acs.accounts.8b00010.

[19] D. Higgins, C. Hahn, C. Xiang, T.F. Jaramillo, A.Z. Weber, Gas-diffusion electrodes for carbon dioxide reduction: a new paradigm, ACS Energy Lett. 4 (2019) 317–324, https://doi.org/10.1021/acsenergylett.8b02035.

[20] T. Burdyny, W.A. Smith, CO_2 reduction on gas-diffusion electrodes and why catalytic performance must be assessed at commercially relevant conditions, Energy Environ. Sci. 12 (2019) 1442–1453, https://doi.org/10.1039/c8ee03134g.

[21] N.T. Nesbitt, T. Burdyny, H. Simonson, D. Salvatore, D. Bohra, R. Kas, W.A. Smith, Liquid–solid boundaries dominate activity of CO_2 reduction on gas-diffusion electrodes, ACS Catal. 10 (2020) 14093–14106, https://doi.org/10.1021/acscatal.0c03319.

[22] U.O. Nwabara, M.P. de Heer, E.R. Cofell, S. Verma, E. Negro, P.J.A. Kenis, Towards accelerated durability testing protocols for CO_2 electrolysis, J. Mater. Chem. A 8 (2020) 22557–22571, https://doi.org/10.1039/d0ta08695a.

[23] E.W. Lees, B.A.W. Mowbray, F.G.L. Parlane, C.P. Berlinguette, Gas diffusion electrodes and membranes for CO_2 reduction electrolysers, Nat. Rev. Mater. 7 (2021) 55–64, https://doi.org/10.1038/s41578-021-00356-2.

[24] Y. Luo, K. Zhang, Y. Li, Y. Wang, Valorizing carbon dioxide via electrochemical reduction on gas-diffusion electrodes, InfoMat 3 (2021) 1313–1332, https://doi.org/10.1002/inf2.12253.

[25] W. Liu, S. Wei, P. Bai, C. Yang, L. Xu, Robust coal matrix intensifies electron/substrate interaction of nickel-nitrogen (Ni-N) active sites for efficient CO_2 electroreduction at industrial current density, Appl. Catal. B 299 (2021), 120661, https://doi.org/10.1016/j.apcatb.2021.120661.

[26] H. Rabiee, L. Ge, X. Zhang, S. Hu, M. Li, S. Smart, Z. Zhu, H. Wang, Z. Yuan, Stand-alone asymmetric hollow fiber gas-diffusion electrodes with distinguished bronze phases for high-efficiency CO_2 electrochemical reduction, Appl. Catal. B 298 (2021), 120538, https://doi.org/10.1016/j.apcatb.2021.120538.

[27] H. Rabiee, L. Ge, J. Zhao, X. Zhang, M. Li, S. Hu, S. Smart, T.E. Rufford, Z. Zhu, H. Wang, Z. Yuan, Regulating the reaction zone of electrochemical CO_2 reduction on gas-diffusion electrodes by istinctive hydrophilic-hydrophobic catalyst layers, Appl. Catal. B 310 (2022), 121362, https://doi.org/10.1016/j.apcatb.2022.121362.

[28] D. Giusi, M. Miceli, C. Genovese, G. Centi, S. Perathoner, C. Ampelli, In situ electrochemical characterization of Cu_xO-based gasdiffusion electrodes (GDEs) for CO_2 electrocatalytic reduction in presence and absence of liquid electrolyte and relationship with c2+ products formation, Appl. Catal. B 318 (2022), 121845, https://doi.org/10.1016/j.apcatb.2022.121845.

[29] K. Yang, R. Kas, W.A. Smith, T. Burdyny, Role of the carbon-based gas diffusion layer on flooding in a gas diffusion electrode cell for electrochemical CO_2 reduction, ACS Energy Lett. 6 (2020) 33–40, https://doi.org/10.1021/acsenergylett.0c02184.

[30] S. Alinejad, J. Quinson, G.K.H. Wiberg, N. Schlegel, D. Zhang, Y. Li, S. Reichenberger, S. Barcikowski, M. Arenz, Electrochemical reduction of CO_2 on Au electrocatalysts in a zero-gap, half-cell gas diffusion electrode setup: a systematic performance evaluation and comparison to an H-cell setup, ChemElectroChem 9 (12) (2022), e202200341, https://doi.org/10.1002/celc.202200341.

[31] M. de, J. Gálvez-Vázquez, P. Moreno-García, H. Xu, Y. Hou, H. Hu, I.Z. Montiel, A. V. Rudnev, S. Alinejad, V. Grozovski, B.J. Wiley, M. Arenz, P. Broekmann, Environment matters: CO_2 electrocatalyst performance testing in a gas-fed zero-gap electrolyzer, ACS Catal. 10 (2020) 13096–13108, https://doi.org/10.1021/acscatal.0c03609.

[32] D.A. Salvatore, C.M. Gabardo, A. Reyes, C.P. O'Brien, S. Holdcroft, P. Pintauro, B. Bahar, M. Hickner, C. Bae, D. Sinton, E.H. Sargent, C.P. Berlinguette, Designing anion exchange membranes for CO_2 electrolysers, Nat. Energy 6 (2021) 339–348, https://doi.org/10.1038/s41560-020-00761-x.

[33] A. Reyes, R.P. Jansonius, B.A.W. Mowbray, Y. Cao, D.G. Wheeler, J. Chau, D. J. Dvorak, C.P. Berlinguette, Managing hydration at the cathode enables efficient CO_2 electrolysis at commercially relevant current densities, ACS Energy Lett. 5 (2020) 1612–1618, https://doi.org/10.1021/acsenergylett.0c00637.

[34] M.E. Leonard, L.E. Clarke, A. Forner-Cuenca, S.M. Brown, F.R. Brushett, Investigating electrode flooding in a flowing electrolyte, gas-fed carbon dioxide electrolyzer, ChemSusChem 13 (2020) 400–411, https://doi.org/10.1002/cssc.201902547.

[35] B. Kim, F. Hillman, M. Ariyoshi, S. Fujikawa, P.J.A. Kenis, Effects of composition of the micro porous layer and the substrate on performance in the electrochemical reduction of CO_2 to CO, J. Power Sources 312 (2016) 192–198, https://doi.org/10.1016/j.jpowsour.2016.02.043.

[36] G.O. Larrazábal, P. Strøm-Hansen, J.P. Heli, K. Zeiter, K.T. Therkildsen, I. Chorkendorff, B. Seger, Analysis of mass flows and membrane cross-over in CO_2 reduction at high current densities in an MEA-type electrolyzer, ACS Appl. Mater. Interfaces 11 (44) (2019) 41281–41288, https://doi.org/10.1021/acsami.9b13081.

[37] B. Endrődi, E. Kecsenovity, A. Samu, F. Darvas, R.V. Jones, V. Török, A. Danyi, C. Janáky, Multilayer electrolyzer stack converts carbon dioxide to gas products at high pressure with high efficiency, ACS Energy Lett. 4 (2019) 1770–1777, https://doi.org/10.1021/acsenergylett.9b01142.

[38] W.H. Lee, Y.-J. Ko, Y. Choi, S.Y. Lee, C.H. Choi, Y.J. Hwang, B.K. Min, P. Strasser, H.-S. Oh, Highly selective and scalable CO_2 to CO electrolysis using coral-nanostructured Ag catalysts in zero-gap configuration, Nano Energy 76 (2020), 105030, https://doi.org/10.1016/j.nanoen.2020.105030.

[39] A.A. Samu, A. Kormányos, E. Kecsenovity, N. Szilágyi, B. Endrődi, C. Janáky, Intermittent operation of CO_2 electrolyzers at industrially relevant current densities, ACS Energy Lett. 7 (2022) 1859–1861, https://doi.org/10.1021/acsenergylett.2c00923.

[40] M. Liu, Y. Kong, H. Hu, N. Kovács, C. Sun, I. Zelocualtecatl Montiel, M. de, J. Gálvez Vázquez, Y. Hou, M. Mirolo, I. Martens, J. Drnec, S. Vesztergom, P. Broekmann, The capping agent is the key: Structural alterations of ag NPs during CO_2 electrolysis probed in a zero-gap gas-flow configuration, J. Catal. 404 (2021) 371–382, https://doi.org/10.1016/j.jcat.2021.10.016.

[41] Y. Kong, H. Hu, M. Liu, Y. Hou, V. Kolivoška, S. Vesztergom, P. Broekmann, Visualisation and quantification of flooding phenomena in gas diffusion electrodes used for electrochemical CO_2 reduction: a combined EDX/ICP–MS approach, J. Catal. 408 (2022) 1–8, https://doi.org/10.1016/j.jcat.2022.02.014.

[42] Y. Kong, M. Liu, H. Hu, Y. Hou, S. Vesztergom, M. de, J. Gálvez Vázquez, I. Zelocualtecatl Montiel, V. Kolivoška, P. Broekmann, Cracks as efficient tools to mitigate flooding in gas diffusion electrodes used for the electrochemical reduction of carbon dioxide, Small Methods (2022), 2200369, https://doi.org/10.1002/smtd.202200369.

[43] P. Jeanty, C. Scherer, E. Magori, K. Wiesner-Fleischer, O. Hinrichsen, M. Fleischer, Upscaling and continuous operation of electrochemical CO_2 to CO conversion in aqueous solutions on silver gas diffusion electrodes, J. CO_2 Util. 24 (2018) 454–462, https://doi.org/10.1016/j.jcou.2018.01.011.

[44] B. De Mot, J. Hereijgers, M. Duarte, T. Breugelmans, Influence of flow and pressure distribution inside a gas diffusion electrode on the performance of a flow-by CO_2 electrolyzer, Chem. Eng. J. 378 (2019), 122224, https://doi.org/10.1016/j.cej.2019.122224.

[45] B. De Mot, M. Ramdin, J. Hereijgers, T.J.H. Vlugt, T. Breugelmans, Direct water injection in catholyte-free zero-gap carbon dioxide electrolyzers, ChemElectroChem 7 (2020) 3839–3843, https://doi.org/10.1002/celc.202000961.

[46] U.O. Nwabara, E.R. Cofell, S. Verma, E. Negro, P.J.A. Kenis, Durable cathodes and electrolyzers for the efficient aqueous electrochemical reduction of CO_2, ChemSusChem 13 (2020) 855–875, https://doi.org/10.1002/cssc.201902933.

[47] A. Pătru, T. Binninger, B. Pribyl, T.J. Schmidt, Design principles of bipolar electrochemical co-electrolysis cells for efficient reduction of carbon dioxide from gas phase at low temperature, J. Electrochem. Soc. 166 (2019) F34–F43, https://doi.org/10.1149/2.1221816jes.

[48] U.O. Nwabara, A.D. Hernandez, D.A. Henckel, X. Chen, E.R. Cofell, M.P. de Heer, S. Verma, A.A. Gewirth, P.J.A. Kenis, Binderfocused approaches to improve the stability of cathodes for CO_2 electroreduction, ACS Appl. Energy Mater. 4 (2021) 5175–5186, https://doi.org/10.1021/acsaem.1c00715.

[49] M. Li, M.N. Idros, Y. Wu, T. Burdyny, S. Garg, X.S. Zhao, G. Wang, T.E. Rufford, The role of electrode wettability in electrochemical reduction of carbon dioxide, J. Mater. Chem. A 9 (2021) 19369–19409, https://doi.org/10.1039/d1ta03636j.

[50] Z. Xing, L. Hu, D.S. Ripatti, X. Hu, X. Feng, Enhancing carbon dioxide gas-diffusion electrolysis by creating a hydrophobic catalyst microenvironment, Nat. Commun. 12 (2021) 136, https://doi.org/10.1038/s41467-020-20397-5.

[51] K.U. Hansen, F. Jiao, Hydrophobicity of CO_2 gas diffusion electrodes, Joule 5 (2021) 754–757, https://doi.org/10.1016/j.joule.2021.02.005.

[52] Z. Liu, H. Yang, R. Kutz, R.I. Masel, CO_2 electrolysis to CO and O_2 at high selectivity, stability and efficiency using Sustainion membranes, J. Electrochem. Soc. 165 (2018) J3371, https://doi.org/10.1149/2.0501815jes.

[53] A.V. Rudnev, Online chromatographic detection, in: K. Wandelt (Ed.), Encyclopedia of Interfacial Chemistry, Elsevier, Amsterdam, 2018, pp. 321–325, https://doi.org/10.1016/b978-0-12-409547-2.13564-4.

[54] M. Liu, H. Hu, Y. Kong, I. Zelocualtecatl Montiel, V. Kolivoška, A.V. Rudnev, Y. Hou, S. Vesztergom, P. Broekmann, Raw data for the article "The role of ionomers in the electrolyte management of zero-gap MEA-based CO2 electrolysers: A Fumion vs. Nafion comparison", Zenodo. ⟨https://doi.org/10.5281/zenodo.7117080⟩.

[55] W.M. Haynes. CRC Handbook of Chemistry and Physics, 97th ed., CRC Press, Boca Raton FL, 2017. Section 5.
[56] S. Garg, Q. Xu, A.B. Mossa, M. Mirolo, W. Denga, I. Chorkendorff, J. Drnec, B. Seger, How alkali cations affect salt precipitation and CO2 electrolysis performance in membrane electrode assembly electrolyzers Energy, Environ. Sci. 16 (2023) 1631–1643, https://doi.org/10.1039/D2EE03725D.
[57] M. Sassenburg, M. Kelly, S. Subramanian, W.A. Smith, T. Burdyny, Zero-gap electrochemical CO_2 reduction cells: challenges and operational strategies for prevention of salt precipitation, ACS Energy Lett. 8 (2023) 321–331, https://doi.org/10.1021/acsenergylett.2c01885.

Supporting Information
to the paper entitled

The role of ionomers in the electrolyte management of zero-gap MEA-based CO_2 electrolysers: A Fumion *vs.* Nafion comparison

M. Liu, H. Hu, Y. Kong, I. Zelocualtecatl Montiel, V. Kolivoška, A. V. Rudnev, Y. Hou, R. Erni, S. Vesztergom, P. Broekmann

Contents

Fig. S1. Photographs of catalyst inks containing Nafion, Fumion, or no added binder 2
Fig. S2. Experiments for optimizing the binder volume fraction 2
Fig. S3. TEM characterization of Ag NPs 3
Fig. S4. Results of electrolysis stress tests, using 0.2 mol dm^{-3} KOH anolyte 4
Fig. S5. SEM and EDX maps recorded post-electrolysis, using 0.2 mol dm^{-3} KOH anolyte 5
Fig. S6. SEM and EDX maps of Ag agglomerates formed during electrolysis on Nafion-fixed GDEs 5
Fig. S7. Vacuum filtration vs. spray coating comparison (SEM and EDX characterization) 6
Fig. S8. Vacuum filtration vs. spray coating comparison (*ec*–CO_2RR performance testing) 6
Fig. S9. Comparison of performance of Ag NPs stabilized by different capping agents 7

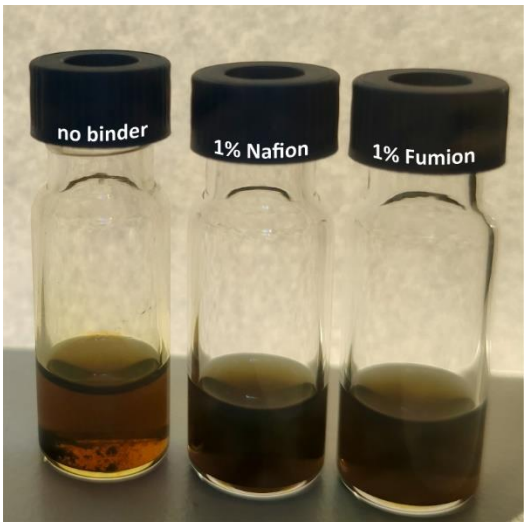

Fig. S1. Photographs of catalyst inks prepared by the addition of no binder (to the left), by the addition of Nafion (middle) and by that of Fumion (to the right). Binders were added in 1% volume fractions. In case no binder is added, the ink is unstable and agglomeration of particles can be observed within minutes.

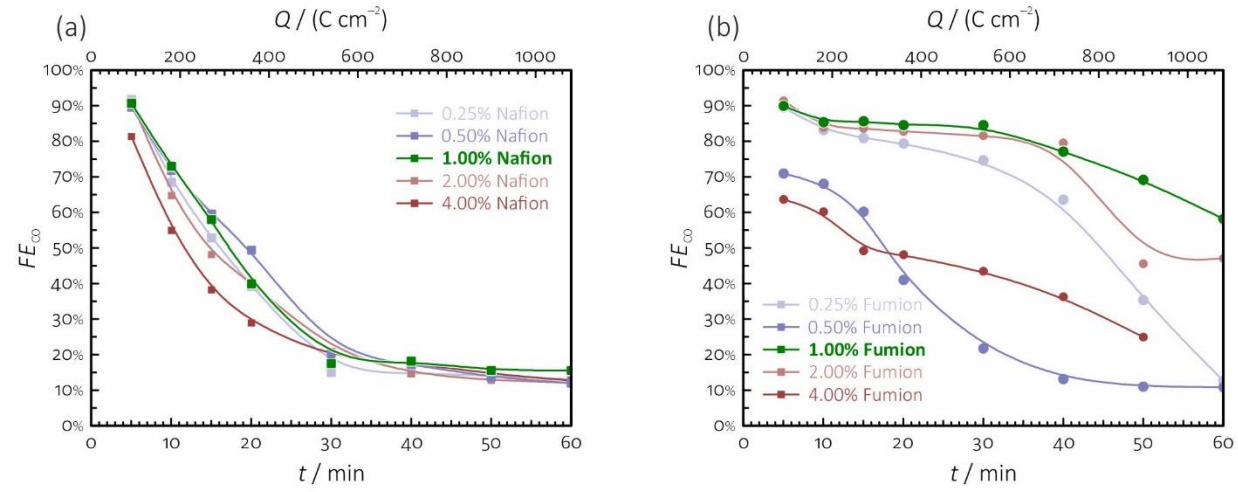

Fig. S2. Results of *ec*–CO_2RR stressing (the variation of the Faradaic efficiency of CO, FE_{CO}, over time) of catalyst inks of different binder concentrations. The volume fraction of Nafion (a) and Fumion (b) is varied between 0.25% and 4%. For Fumion-containing inks, the ideal binder volume fraction is 1%: for Nafion-containing inks, the binder concentration seems not to determine the (generally low) stability of electrolysis. In the paper, inks with a binder volume fraction of 1% are compared (both for Fumion and for Nafion containing inks) based on this screening experiment.

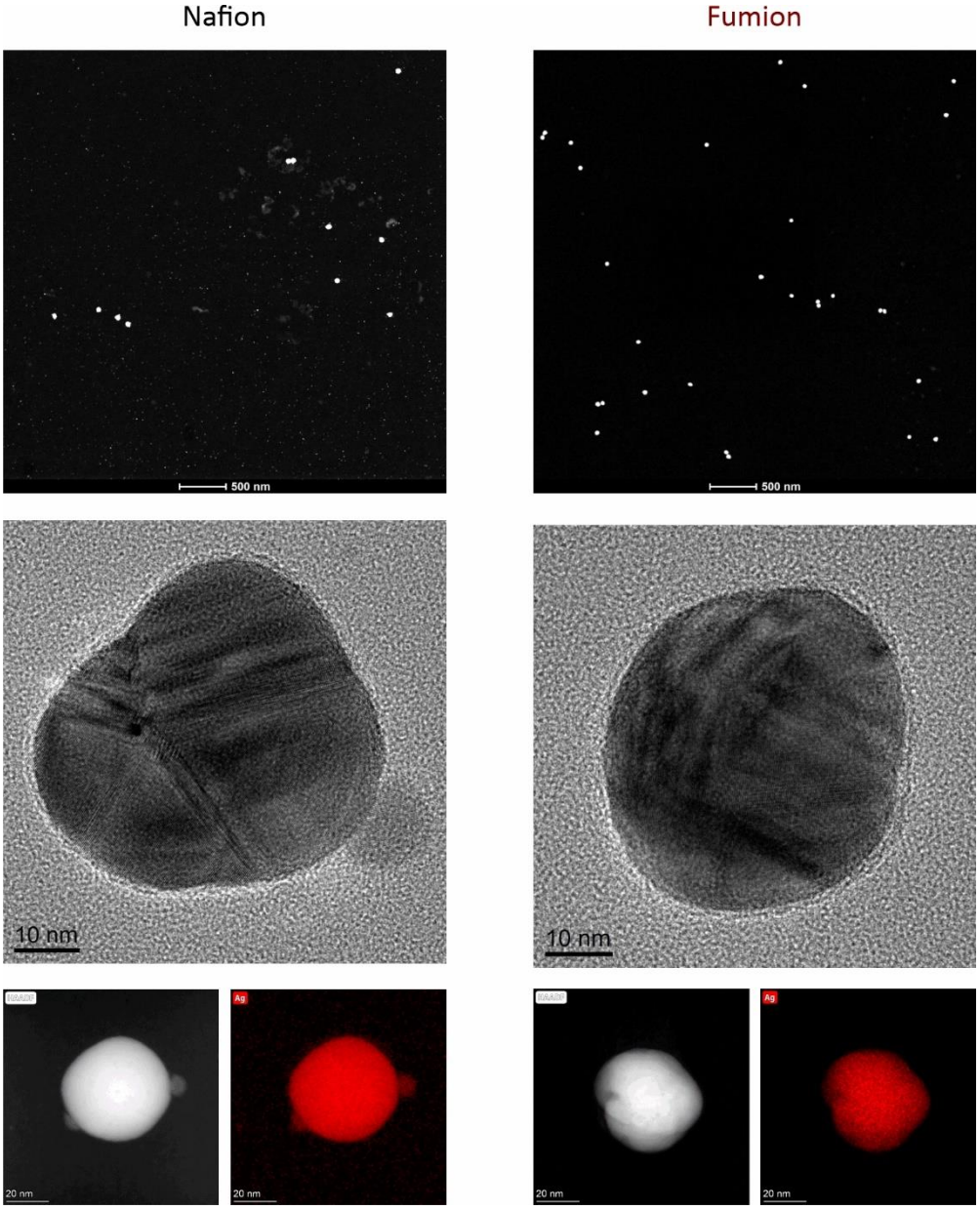

Fig. S3. Transmission Electron Micrography (TEM)-based comparison of lipoic acid capped Ag NPs originating from Nafion and Fumion-containing inks show no major structural differences. Top row: HAADF STEM overview showing homogeneous particle sizes. Middle row: high-resolution TEM micrographs of individual particle. Bottom row: HAADF images and EDX (Ag) elemental maps of individual particles.

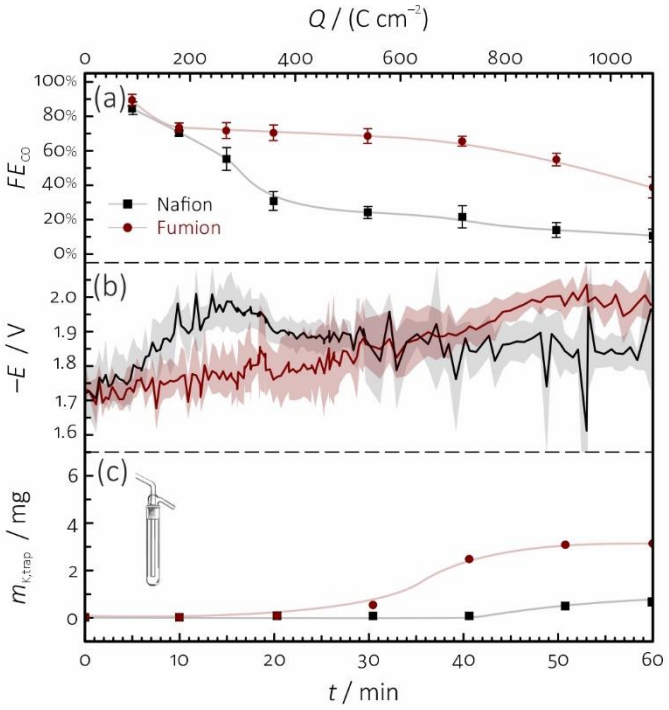

Fig. S4. Results of *ec*–CO_2RR stressing of Nafion-fixed (black) and Fumion-fixed (red) GDEs. Panel (a) shows the variation of the Faradaic efficiency of CO, FE_{CO}, over time. Panel (b) shows the temporal variation of the measured electrode potential *E*, while in panel (c) we plotted the amount of K^+ that perspired through the electrolyser and was detected in the water trap equipped to its gas outlet channels (cf. to Figure 1 of the main text). Error bars and shaded areas indicate 95% confidence intervals calculated from at least three independent measurements, raw data that served the construction of the figure are accessible online, See Ref. [52] of the paper. As opposed to Figure 3 of the main manuscript (where an anolyte concentration of 2 mol dm^{-3} was applied), the anolyte in these experiments was a 0.2 mol dm^{-3} KOH solution.

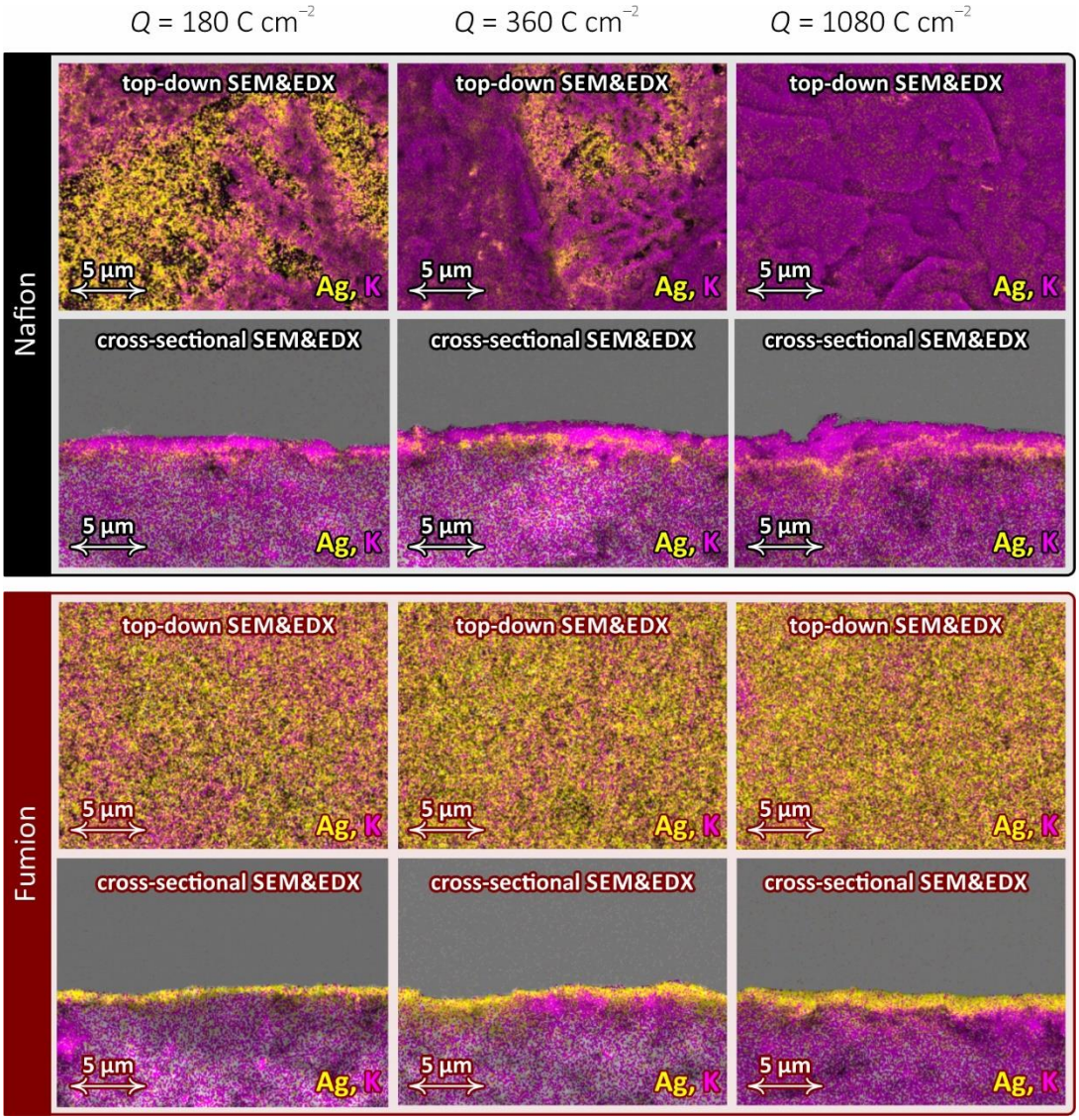

Fig. S5. Top-down and cross-sectional images recorded of Nafion and Fumion-fixed GDEs at different stages of electrolysis (after the passage of the indicated amount of charge). The images were colourised based on elemental EDX mapping: yellow colour stands for Ag, magenta for K-rich spots. The original SEM images and corresponding EDX maps are accessible online (see Ref. [52] of the main manuscript). As opposed to Figure 4 of the main manuscript (where an anolyte concentration of 2 mol dm^{-3} was applied), the anolyte in these experiments was a 0.2 mol dm^{-3} KOH solution.

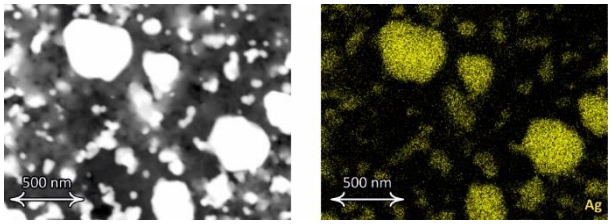

Fig. S6. SEM micrograph and EDX elemental map showing that the large agglomerates formed during electrolyses on Nafion-fixed GDEs consist of Ag.

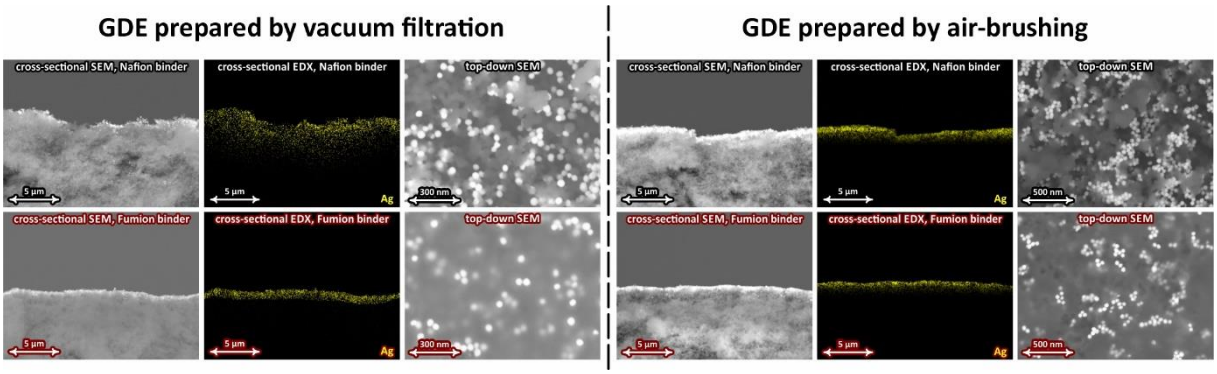

Fig. S7. If instead of vacuum filtration (to the left) spray coating is used for the preparation of GDEs (to the right), the penetration of the Ag NPs into the MPL remains limited also in case of Nafion-bound catalyst inks.

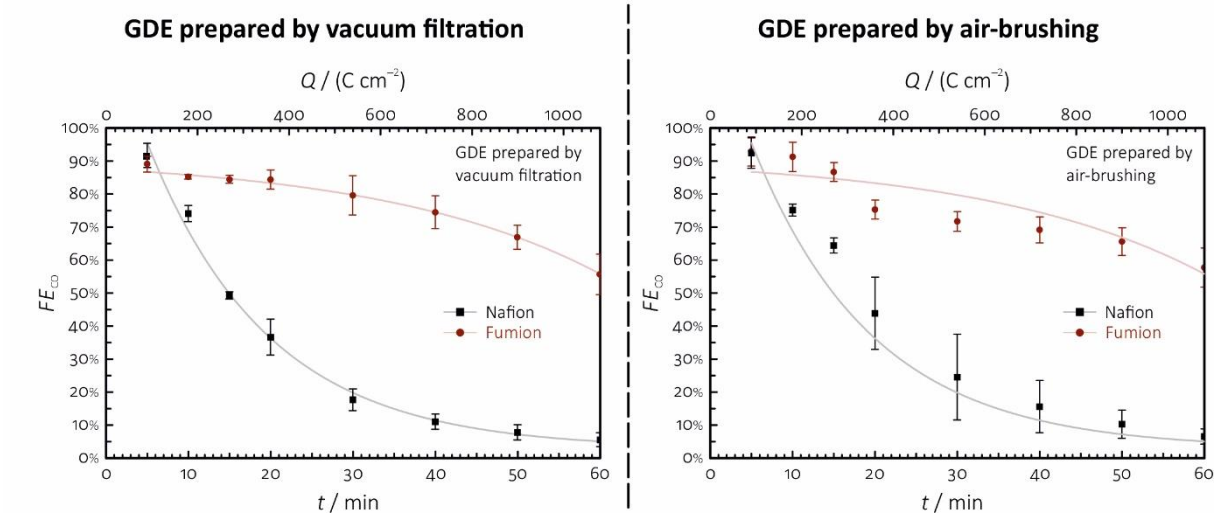

Fig. S8. Despite the different penetration depths of Ag NPs (see Figure S7 above), the durability of Nafion-bound GDEs still falls short that of Fumion-bound ones, even if the GDEs are prepared by air-brushing the ink rather than by vacuum filtration. (While measured data points differ on the two graphs, the trend lines shown are the same).

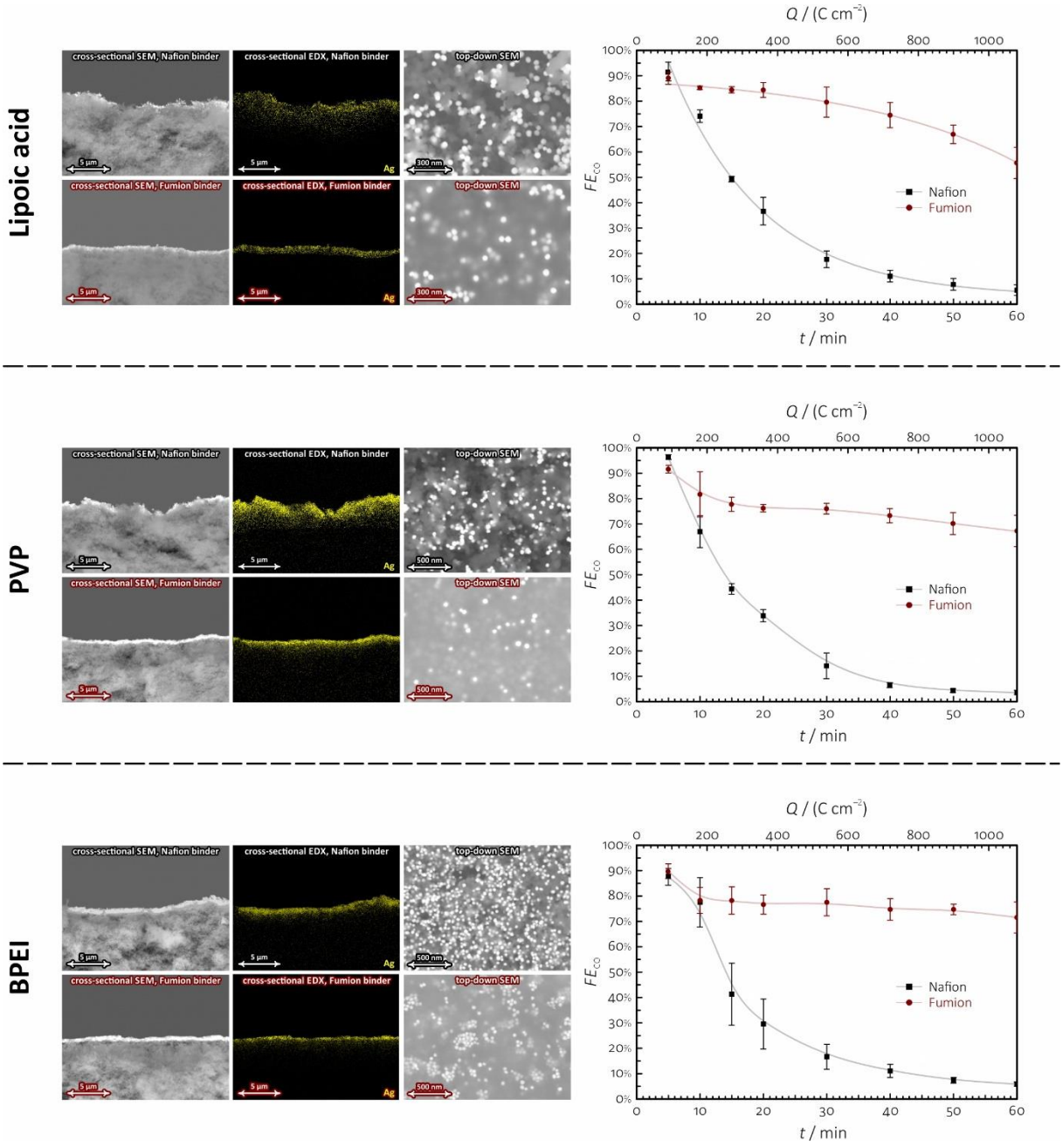

Fig. S9. GDEs were prepared from Ag NP suspensions stabilized by different capping agents with both Nafion and Fumion as a binder. The characterization (by top-down as well as cross-sectional) SEM and EDX measurements of the GDEs is shown in panels to the right. The stability of electrolyses shows little if any dependence on the nature of the applied capping agent.

3. Visualization and quantification of flooding phenomena in gas diffusion electrodes used for electrochemical CO_2 reduction: A combined EDX/ICP–MS approach

Authors: Ying Kong, Huifang Hu, Menglong Liu, Yuhui Hou, Viliam Kolivoška, Soma Vesztergom and Peter Broekmann.

***Journal of Catalysis*, 408, (2022) 1–8. DOI: 10.1016/j.jcat.2022.02.014**

Highlight: Electrolyte flooding and (bi)carbonate salt precipitation were herein shown to be the main sources for performance losses in ec-CO_2RR when carried out in a semi-zero-gap cell configuration. In this contribution we developed a new analytical approach for the visualization and quantification of detrimental flooding/precipitation phenomena which are based on the combination of non-quantitative (cross-sectional) SEM/EDX imaging ($\rightarrow$ spatial distribution of elements) and quantitative ICP-MS analyses. This new approach allowed for identifying factors which (de)stabilize the GDE during extended ec-CO_2RR.

Contribution: I carried out some parts of the GDE performance evaluation experiments and has been involved in the discussion of results. I contributed to the revision of the manuscript text.

Journal of Catalysis 408 (2022) 1–8

Contents lists available at ScienceDirect

Journal of Catalysis

journal homepage: www.elsevier.com/locate/jcat

Visualisation and quantification of flooding phenomena in gas diffusion electrodes used for electrochemical CO_2 reduction: A combined EDX/ICP–MS approach

Ying Kong [a,b], Huifang Hu [a], Menglong Liu [a,b], Yuhui Hou [a,b], Viliam Kolivoška [c], Soma Vesztergom [a,d,*], Peter Broekmann [a,b,*]

[a] University of Bern, Department of Chemistry, Biochemistry and Pharmaceutical Sciences, Freiestrasse 3, 3012 Bern, Switzerland
[b] National Centre of Competence in Research (NCCR) Catalysis, University of Bern, Freiestrasse 3, 3012 Bern, Switzerland
[c] J. Heyrovský Institute of Physical Chemistry of the Czech Academy of Sciences, Dolejškova 2155/3, 18223 Prague, Czech Republic
[d] Eötvös Loránd University, Department of Physical Chemistry, Pázmány Péter sétány 1/A, 1117 Budapest, Hungary

ARTICLE INFO

Article history:
Received 7 January 2022
Revised 10 February 2022
Accepted 15 February 2022
Available online 22 February 2022

Keywords:
Carbon dioxide electroreduction
Gas diffusion electrodes
Flooding
Precipitate formation

ABSTRACT

The most promising strategy to scale up the electrochemical CO_2 reduction reaction (*ec*-CO_2RR) is based on the use of gas diffusion electrodes (GDEs) that allow current densities close to the range of 1 A/cm^2 to be reached. At such high current densities, however, the flooding of the GDE cathode is often observed in CO_2 electrolysers. Flooding hinders the access of CO_2 to the catalyst, and by thus leaving space for (unwanted) hydrogen evolution, it usually leads to a decrease of the observable Faradaic efficiency of CO_2 reduction products. To avoid flooding as much as possible has thus become one of the most important aims of to-date *ec*-CO_2RR engineering, and robust analytical methods that can quantitatively assess flooding are now in demand. As flooding is very closely related to the formation of carbonate salts within the GDE structure, in this paper we use alkali (in particular, potassium) carbonates as a tracer of flooding. We present a novel analytical approach —based on the combination of cross-sectional energy-dispersive X-ray (EDX) mapping and inductively coupled plasma mass spectrometry (ICP–MS) analysis— that can not only visualise, but can also quantitatively describe the electrolysis time dependent flooding in GDEs, leading to a better understanding of electrolyser malfunctions.

1. Introduction

Great progress has recently been made towards the development of new technologies that enable a large-scale reduction of the atmospheric concentration of CO_2, one of the most important contributors of global warming [1]. Among these technologies, electrochemical ones deserve special attention as electrolysers — ideally powered by renewable energy sources— can effectively be used to convert CO_2 into a variety of commodity chemicals and synthetic fuels, such as CO, formic acid, different alcohols and hydrocarbons [2].

In the past few years, the efficiency of newly developed catalysts for the electrochemical CO_2 reduction reaction (*ec*-CO_2RR) has become so high that under ambient conditions it is not any longer the catalytic activity but rather the limited rate of liquid-phase CO_2 transport that hinders the process [3]. Several attempts have thus been made to boost *ec*-CO_2RR by increasing the rate of CO_2 transport, and the most promising of these scale-up strategies involve the use of gas diffusion electrodes (GDEs) [4–7].

The use of GDEs enables current densities that are at least one order of magnitude larger than those measurable in standard H-type cells [3,7]. The benefit of achieving high currents comes, however, at the cost of stability issues, and it is primarily the rapid flooding of GDEs that raises most concerns [7–11].

CO_2 electrolysers where the catalyst dispersed over a gas diffusion layer (GDL) contacts the electrolyte solution through a wet membrane —that is, in so-called zero-gap cathode half-cell configurarions [7]— flooding usually occurs at high current densities where either the CO_2 reduction reaction itself or its parasitic side-process, hydrogen evolution reaction (HER) cause a significant

* Corresponding authors at: University of Bern, Department of Chemistry, Biochemistry and Pharmaceutical Sciences, Freiestrasse 3, 3012 Bern, Switzerland (P. Broekmann); Eötvös Loránd University, Department of Physical Chemisty, Pázmány Péter sétány 1/A, 1117 Budapest, Hungary (S. Vesztergom).

E-mail addresses: ying.kong@unibe.ch (Y. Kong), huifang.hu@unibe.ch (H. Hu), menglong.liu@unibe.ch (M. Liu), viliam.kolivoska@jh-inst.cas.cz (V. Kolivoška), vesztergom@chem.elte.hu (S. Vesztergom), peter.broekmann@dcb.unibe.ch (P. Broekmann).

https://doi.org/10.1016/j.jcat.2022.02.014
0021-9517/

near-electrode *p*H increase. The CO_2 supply of the GDE reacts with the electro-generated OH^- ions, which leads to the localised formation of carbonate salts that in turn increases the wettability [8–10] of the GDE and intensifies flooding.

As flooding limits the access of CO_2 to the catalyst, it usually leads to a decrease of the observable Faradaic efficiency of CO_2 reduction products, and leaves space for unwanted hydrogen evolution. To suppress flooding as much as possible, and to understand its mechanism and key factors has thus become one of the most important aims of to-date *ec*-CO_2RR research, and analytical tools that can quantitatively assess the means and extent of flooding are now in demand.

The mechanism of flooding depends on several processes occurring in GDE-based CO_2 electrolysers, and system properties influencing flooding include the wettability of GDEs [12–17] and its dependence on the applied electrode potential (also called electrowetting [18]), the flow-rate [19] and humidity [20,21] of the CO_2 supply, the presence of reaction products [10], and the thickness of the employed membrane [17]. Flooding is very often accompanied by the massive formation of carbonate precipitates on-top, and within deeper layers of the GDE [7–11,18,22–24], and the amount and distribution of carbonates —in case of CO_2 electrolysers operated with a KOH anolyte, these are typically potassium carbonates and bicarbonates— seem to be an important tracer of flooding within the three-dimensional GDE structure.

The aim of this paper is to show that the post-electrolysis analysis of GDE samples by energy-dispersive X-ray (EDX) elemental mapping can easily be used to visualise the electrolysis time dependent penetration of K^+-containing precipitates into the GDE. In order to make the obtained distribution profiles comparable for electrodes that received different electrolysis treatments, it is necessary to convert the relative distribution profiles to absolute concentration *vs.* depth plots that already bear quantitative information. This latter aim can be achieved by an inductively coupled plasma mass spectrometry (ICP–MS)-based determination of the total potassium content of the GDE [25]. The described EDX/ICP–MS combination is a powerful and very robust technique that allows a better understanding of *ec*-CO_2RR electrolyser malfunctions by enabling the accurate visualisation and quantification of flooding phenomena in GDE samples.

2. The method

The scheme of a typical gas-fed CO_2 electrolyser employing a zero-gap cathode half-cell configuration is shown in Fig. 1, with the blown-up section depicting the GDE cathode in direct contact with the anion exchange membrane. The GDE cathode is created by evenly covering the surface of a gas diffusion layer (GDL) with a catalyst ink that can be achieved by using several techniques [3] including drop-casting, airbrushing, vacuum filtering, etc. The uniformity of the catalyst layer thickness depends however not only on the applied technique but also on the imperfections of the gas diffusion layer: especially cracks found on the GDL surface (see, *e.g.*, Fig. 5.b in Section 4) may lead to non-uniform coverage [26–28] and to the burial of some catalyst particles in deeper trenches.

The GDL itself is a bilayer structure that consists of an upper (microporous) and an underlying (fibrous) layer. The microporous layer acts as an electrically conductive mechanical support to the catalyst, holding it in direct contact with the membrane. In many electrolysers, the applied catalyst ink contains silver nanoparticles that direct *ec*-CO_2RR towards the formation of CO as a dominant reaction product [8,11,17,21,24,29]. Note here that CO belongs to the most economically viable *ec*-CO_2RR products [30] and has large global annual production [3]. The cathode reaction of CO_2-to-CO conversion can be written as

$$CO_2 + H_2O + 2e^- \rightarrow CO + 2OH^-, \quad (1)$$

and the operation of the electrolyser should be optimised so that parasitic hydrogen evolution reaction (HER),

$$2H_2O + 2e^- \rightarrow H_2 + 2OH^-, \quad (2)$$

would take place only incidentally.

In the design shown in Fig. 1, a constant (humidified) CO_2 flow penetrates the fibrous part of the GDL, and the CO_2 molecules are transported through the pores of the thin microporous layer to reach the catalyst where they are reduced to CO.

The (essentially wet) membrane has two important roles in the electrolyser: one is that it enables water (a reactant of *ec*-CO_2RR) to access the catalyst, and another is that it allows the passage of the formed OH^- ions (a by-product of CO_2 reduction) from the cathode surface to the anode compartment of the cell. The anode compartment is filled with a solution of KOH, and OH^- ions are oxidised on the Ir anode to form O_2 gas:

$$4OH^- \rightarrow 2H_2O + O_2 + 4e^-. \quad (3)$$

The wettability of the GDL plays a crucial role in determining the cathode performance of gas-fed CO_2 electrolysers. The presence of some amount of water, based on Eq. (1), is essential; however, if too much water enters the GDL structure, it may block the access of CO_2 to the catalyst, shifting the balance of the cathode reaction from the preferred *ec*-CO_2RR towards the parasitic HER [31].

For this reason, GDLs are usually made hydrophobic by the manufacturer (*e.g.*, by a treatment with polytetrafluoroethylene, PTFE) and the conditions of the electrolysis are optimized to uphold hydrophobicity as long as possible. From this point of view, the imperfections of the anion exchange membrane deserve special attention, especially if the membrane allows not only the transfer of OH^- ions, but also the transference of cations. As the real-life behaviour of anion exchange membranes is far from ideal [32], the transference of cations very often occurs, and for example in case of the electrolyser shown by Fig. 1, K^+ ions of the anolyte can thus appear on the cathode side of the cell.

The alkalination of the cathode surface —note that OH^- ions are produced both by Reaction (1) and (2)— clearly acts as a driving force for the transport of K^+ ions from the anode compartment to the cathode, where the alkaline conditions and the presence of CO_2 facilitate the formation of K_2CO_3 or $KHCO_3$ salts. If concentrations are high enough [9], both K_2CO_3 and $KHCO_3$ can form precipitates on-top and within the deeper layers of the GDE. This reduces the hydrophobicity of the GDE and triggers flooding, which ultimately breaks down the overall cell performance.

There seems to be a consensus in literature with regard to that the formation of carbonate precipitates on the cathode side of *ec*-CO_2RR electrolysers is an important indicator of flooding [9–11,20,21,33,34]. In spite of this, scanning electron microscopy (SEM)-based imaging techniques like EDX elemental mapping have only scarcely been used to study the penetration of carbonate precipitates into GDE structures [7,11,34]. The reason behind this is obvious: while EDX elemental (K) mapping, applied in a cross-sectional view to study the penetration of K_2CO_3/$KHCO_3$ precipitates into the GDE structure can give a good qualitative picture about the relative distribution of the formed K^+ salts, the comparison of such elemental maps is by no means straightforward. Such comparisons would require EDX elemental mapping to provide truly quantitative information, which is usually not the case.

Indeed, the quantification of elemental maps is a very demanding task that would not only necessitate the acquisition, storage, and subsequent analysis of entire spectra, pixel-by-pixel [35], but it would also require the in-depth understanding of electron

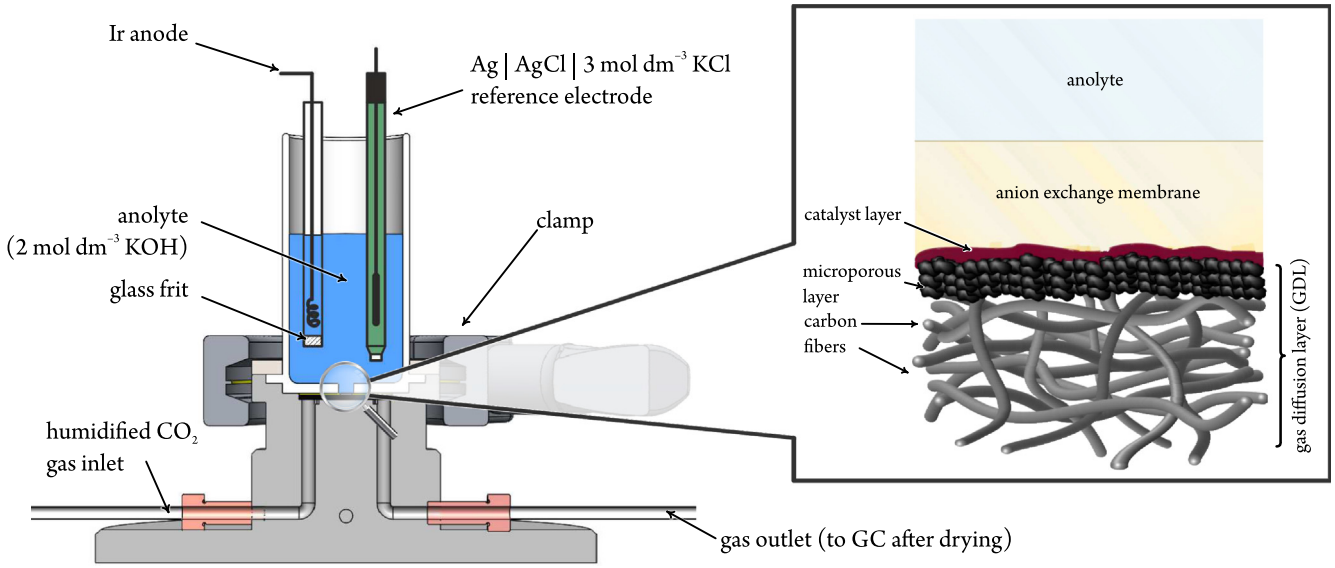

Fig. 1. Scheme of a gas-flow CO_2 electrolyser employing a zero-gap cathode half-cell configuration. The gas diffusion electrode/membrane assembly is shown by the inset at the initial stage of electrolysis.

beam/material interactions, which is particularly challenging when working with heterogeneous and highly porous materials (*e.g.*, GDEs).

X-ray signal intensities are known to depend largely on (amongst other parameters) the applied acceleration voltage [35], and this is exemplarily demonstrated by the cross-sectional EDX elemental (K) maps of Fig. 2. These maps, taken at different applied accelerating voltages, show the same GDE sample that exhibits marks of *ec*-CO_2RR-induced K_2CO_3/$KHCO_3$ precipitation within its structure.

Maps of the top row of Fig. 2 are those shown by the operating software of the SEM instrument. The automatic colouration of these maps is optimised for human perception, and as a result, the maps could lead us to the erroneous conclusion that the potassium concentrations visualised by them are markedly different. As, however, the four maps are made of the very same sample, this is certainly not the case: the maps are differently coloured only because the corresponding K peaks in the EDX spectra become more intense at higher accelerating voltages.

Fortunately, from most SEM operating software, EDX maps can be exported not only in the form of images but also in the form of two-dimensional numerical arrays that represent the (in our case, K) signal intensities over the sampled area. If we create such numerical representations from the four maps shown in the top row of Fig. 2, we get four arrays on which we can perform mathematical operations. We can, for example, normalise the arrays to their (overall) maximum, and we can then convert the arrays back into images. If we use the same colour-code that was applied before, we obtain the images shown by the middle row of Fig. 2. These coloured maps already give a trustworthy representation of intensity ratios; however, at low accelerating voltages, the normalised intensities happen to be so low that we see almost entirely dark fields.

In order to reduce the dependency of intensities on the applied accelerating voltage, we have to normalise each array individually, using their respective maxima as an individual norm. By this approach, we get to the images shown in the bottom row of Fig. 2. These elemental maps, while they all appear a bit dark for the human eye, all look essentially the same. Subtle differences between the images do exist, however, primarily because not only the overall intensity of the spectrum peaks but also the penetration depth of the electron beam depends on the accelerating voltage [35]. This dependence, while it affects the measured absolute intensities, exerts only a minor effect on the observed relative intensity distributions.

The above two normalisation concepts are illustrated also by the graphs of Fig. 2 that contain sums of intensities for each image row, plotted *vs.* the respective row index. The graphs clearly show that while the recorded K signal intensity does vary greatly with the applied accelerating voltage, and while the exact relationship between local K concentration and intensity may not be known, EDX mapping is still robust enough to deliver a relative distribution of potassium-containing precipitates along the line normal to the GDE surface.

Such relative distributions, obtained from GDEs that had undergone different *ec*-CO_2RR stressing treatment can of course not directly be compared, unless we determine by some other analytical method the total potassium content of the GDE. A variety of elemental analysis methods can be used to achieve this goal; in our practice we favour ICP–MS-based determination.

The essence of the method described here is schematically shown in Fig. 3. On the top surface of GDEs that have previously been used for *ec*-CO_2RR, the appearance of precipitates is usually visible already to the bare eye. The centrally located, salt-covered part (of known geometric area) is removed by a punching blade, and the resulting 'coin' is cut into two by a sharp knife. One part of the coin is briefly sonicated and then left for over-night in a known volume (usually 1 cm^3) of cc. HNO_3, so that its K_2CO_3/$KHCO_3$ content is quantitatively leached. The concentration of the resulting solution is then determined by ICP–MS in known (usually 500 or 1000 times) dilutions: by this method, the total potassium mass that is contained by the given volume of the GDE is calculated and normalised to the base area of the analysed sample. This yields a total surface area-normalised concentration that is usually in the range of a few mg cm^{-2}.

The other half of the coin (Fig. 3) is used for cross-sectional EDX K elemental mapping, without any additional treatment other than drying the sample. In order to improve statistics, usually multiple locations of the same cut are mapped, and sometimes, even additional cuts are made and sampled. The resulting EDX maps are then exported in numerical form, and depth profiles of the relative K distribution are created by row-wise summation. Row indices

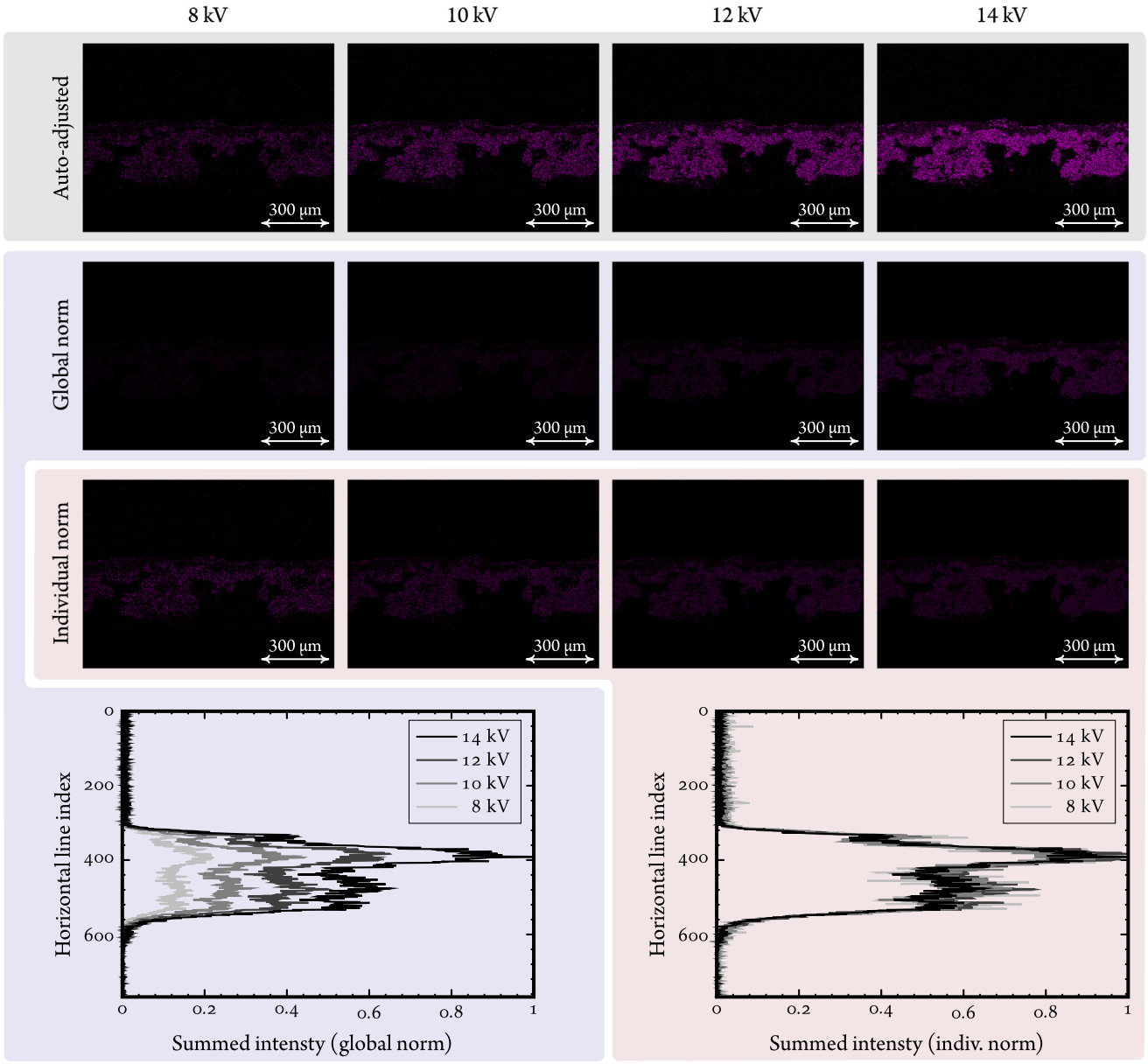

Fig. 2. Electrolysis-induced potassium penetration into a GDE sample visualised by EDX elemental maps (cross-sectional view), recorded using different accelerating voltages as shown. Images of the same column show maps of the exact same intensity dataset, coloured differently. The brightness and the contrast of images in the top row was automatically adjusted for optimal perception by the human eye — this is how most SEM operating software would show these maps. Colour intensities in the middle row were normalised to the largest intensity value detected. In case of the third row, the maps were normalised individually, each to its own maximum intensity. The graphs show the differences of the two normalisation concepts in row-by-row intensity summation. The EDX measurements were made on sample GDE#2, following passage of −1839 C cm^{-2} charge (cf. to Sections 3 and 4, as well as to Fig. 5).

are turned into spatial coordinates knowing the resolution of the map.

The individual relative distributions are aligned on the distance scale by means of (differential) edge detection, and an averaged curve is calculated. The relative distributions are subsequently re-scaled into absolute concentration profiles (usually expressed in units of µg cm^{-3}); the applied scaling factor is chosen so that the full space integral of the averaged absolute concentration profile equals the surface area-normalised concentration determined by ICP–MS.

The described cross-sectional EDX/ICP–MS combination approach yields concentration depth profiles that are comparable for GDE samples that are either of different original structure or that underwent different *ec*-CO_2RR stressing treatment (see later Fig. 5), and can lead to a better understanding of flooding-related phenomena. Note here that in order to obtain statistically reliable data, both the ICP–MS and the EDX mapping measurements are to be repeated several times, using GDE samples that received the very same treatment. As it will be shown later in Fig. 5, this approach helps to identify possible outliers. Also note that ICP–MS measurements may not have to be performed on all (rather just on a few) studied samples, which may reduce the time demand of the analysis.

As the described EDX/ICP–MS combination approach is a post-experimental characterisation technique, it cannot be used for a real-time observation of flooding-related phenomena like it is possible, for example, in *operando* tomographic X-ray absorption spectroscopy [36]. The EDX/ICP–MS combination is, however, a more

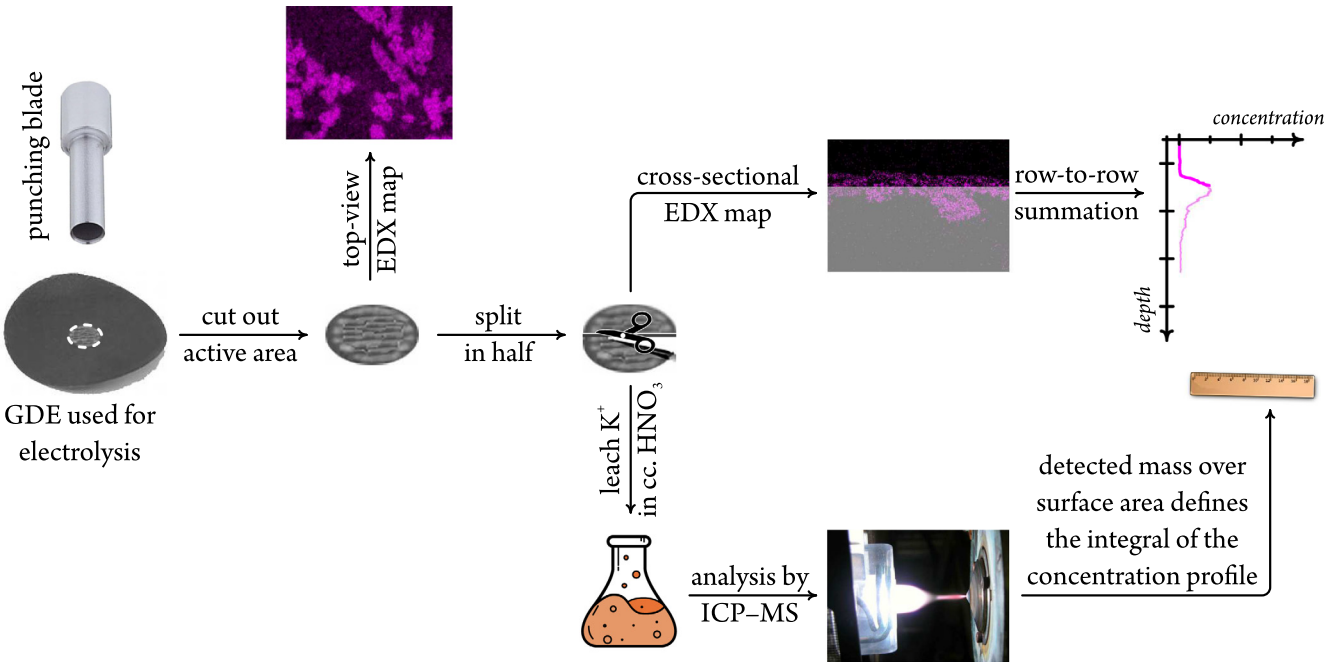

Fig. 3. The strategy to quantitatively assess flooding phenomena in GDEs uses $K_2CO_3/KHCO_3$ precipitates as a tracer of flooding. Following electrolysis, the carbonate precipitates formed over the GDE are visible to the bare eye (and can also be seen by top-down EDX mapping). By cross-sectional EDX, the relative distribution of K can be mapped along the surface normal. Absolute concentration (mass over volume) profiles can be created by applying a scaling factor that sets the integral of the profile equal to the (surface area normalised) K mass determined by ICP–MS analysis.

robust and a considerably cheaper method than X-ray absorption or scattering measurements that require specially designed cells and a significant amount of synchrotron beam-time, and the amount of information gathered from EDX/ICP–MS studies may effectively complement the results of *operando* investigations.

The versatility of the method will be illustrated in Section 4, where we used two different gas diffusion electrodes for CO_2 electrolysis in a gas-fed CO_2 electrolyser employing a zero-gap cathode half-cell configuration, finding that the different structure of the two GDLs result in different $K_2CO_3/KHCO_3$ deposition patterns and, ultimately, different electrolyser stabilities.

3. Experimental

Two commercial gas diffusion layers (Table 1), a Freudenberg H23C8 (GDL#1) and a Sigracet 36BB (GDL#2) paper, were used in this study. The microporous layers of both GDLs contain ~ 5% PTFE as a water repelling agent.

To prepare a catalyst ink, 4.5 mg of silver nanowires (Ag NWs, prepared as described in [37]) and 0.8 mg of carbon black (VULCAN^{TM} VXC72R, Cabot) were separately dispersed in 20 cm^3 of isopropanol (BASF SE, assay ⩾ 99.0%) by half hour of sonication. Both suspensions were intermixed and sonicated for an additional half hour, then dried by a rotary evaporator (Büchi R210, 40 °C, 65 mbar). The resulting mixture was then re-dispersed in 18 cm^3 of isopropanol containing 180 $\mu\ell$ of Nafion 117 solution (Sigma–Aldrich, ~ 5 wt% in a mixture of lower aliphatic alcohols and water) and subjected to 20 min of sonication. Subsequently, the resulting ink was carefully dispersed by using an airbrush pistole (Infinity CR plus) propelled by nitrogen gas (99.999%, Carbagas, Switzerland) onto the GDL substrate.

Table 1
Parameters of the gas diffusion layers used in this study.

	GDL#1, Freudenberg H23C8	GDL#2, Sigracet 36BB
Microporous layer thickness*	41 µm	97 µm
Fibrous layer thickness*	194 µm	160 µm
Electrical resistivity†	8 mΩ cm^2	9 mΩ cm^2
Area density†	135 g cm^{-2}	105 g cm^{-2}
Air permeability†	90 Gurley s	3 Gurley s

* Average values, determined by cross-sectional SEM.
† Values provided by the manufacturer.

A CO_2 electrolyser with a zero-gap cathode half-cell configuration (see Fig. 1, details of the electrolyser were described previously in [7,38–41]) was used for the electrochemical reduction of CO_2. The Ag NW-coated GDEs were placed on the stainless steel body, with the Ag NW layer directed upwards. The such formed cathode was then covered by an anion exchange membrane (AEM, X37-50 RT, Dioxide materials), on top of which a PTFE chamber was placed to support the anolyte, a 2.0moldm^{--3} aqueous KOH solution (KOH, analytical grade, was purchased from Sigma Aldrich). A central orifice with a diameter of 3 mm at the bottom of the anode compartment provided contact between the anolyte and the membrane-cathode assembly, and the area of this opening (0.0707 cm^2) was considered the geometric surface area of the cathode, used for the normalization of current to current density. An iridium (Ir) wire (99.9%, MaTeck Material-Technologie & Kristalle GmbH, Germany) separated by a glass frit from the anolyte compartment, and a Ag|AgCl|3moldm^{--3} KCl electrode (double junction design, Metrohm) immersed directly into the anolyte were used as counter and reference electrodes. A humidified CO_2 stream (99.999%, Carbagas, Switzerland) was fed to the fibrous layer of the cathode from the backside of the cell at a constant volumetric flow rate of 18 cm^3 min^{-1}. Electrolyses were carried out using an ECi-200 potentiostat (Nordic Electrochemistry) at a constant current of −20 mA, resulting in a current density of −283 mA cm^{-2}, during which the formed gaseous reaction products were quantified by online gas chromatography (GC, SRI Instruments), as described elsewhere [7].

For the SEM and EDX studies presented in the paper, a Zeiss Gemini 450 SEM was applied, equipped with an InLens secondary electron (SE), a backscatter electron detector (BSD) and a SuperEDX detector.

Contact angle measurements were carried out using a Krüss Advance Drop Shape Analyzer DSA25 (Krüss GmbH, Hamburg, Germany). Electrodes were mounted on a flat stage and water drops (milli-Q water, 1.4 $\mu\ell$) were deposited at room temperature.

Raw data, as well as unprocessed measurement files serving as a basis of this publication can be downloaded from Zenodo [42].

4. Demonstrative experiments

Two gas diffusion electrodes —one supported by a Freudenberg H23C8 paper (GDL#1), and another by a Sigracet 36BB paper (GDL#2)— were created and used in our experiments. The two GDLs, as can be seen in Table 1, are of different structure, and the majority of differences arise from that while the microporous layer of GDL#1 is thinner but more compact (Fig. 4.a), the relatively thick microporous layer of GDL#2 is laced by small cracks that are visible also to the bare eye (Fig. 4.b).

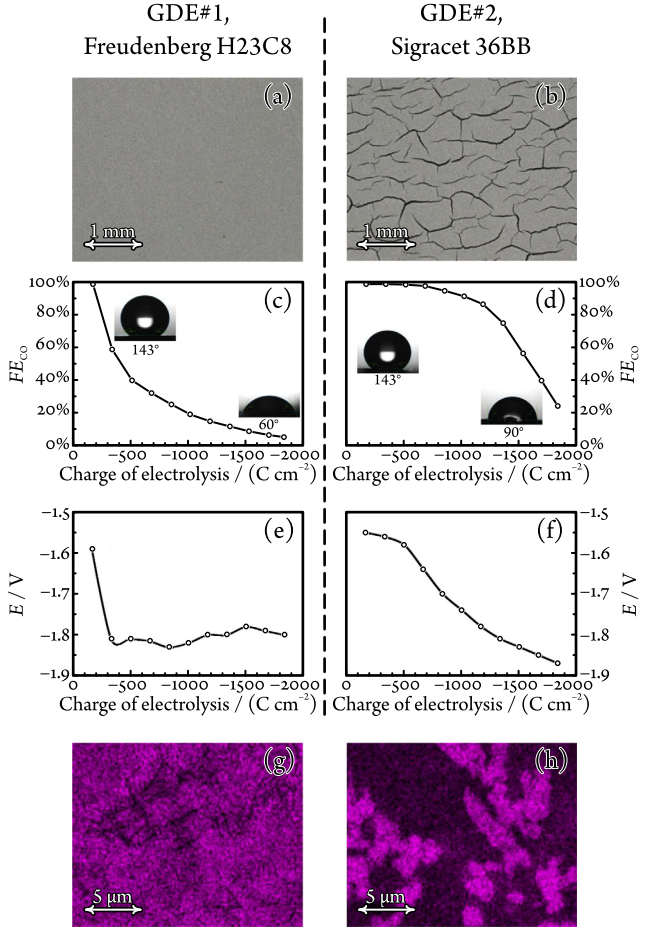

Fig. 4. The top-down optical microscopy image of the two studied gas diffusion electrodes exhibit a compact microporous layer in case of GDE#1 (a), while the top surface of GDE#2 (b) is laced by small cracks. Both GDEs exhibit severe stability losses (a decrease of the Faradaic efficiency of CO production as a function of the passed charge) when made subject to electrolysis at a constant current density of –283 mA cm^{-2}. While GDE#1 quickly loses stability (c), GDE#2 remains stable for longer time (d). The hydrophobicity of both GDLs decrease heavily during prolonged *ec*-CO_2RR stressing (consumed charge: –1839 C cm^{-2}), as revealed by the pre- and post-electrolysis contact angle measurements shown in the insets of (c) and (d). The shift from *ec*-CO_2RR to HER is also indicated by changes of the measured electrode potentials shown in panels (e) and (f). That the mentioned hydrophobicity loss is caused by the appearance of K_2CO_3 or $KHCO_3$ precipitates on-top of both GDEs during electrolysis is clearly shown by the top-down EDX elemental maps of (g) and (h), recorded after the total charge of –1839 C cm^{-2} is passed through the GDEs.

When made subject to constant-current electrolyses experiments (applied current density: –283 mA cm^{-2}), both GDEs initially produce CO at close to 100% Faradaic efficiency. As the electrolysis continues to longer times, the observed Faradaic efficiency however drops down (Fig. 4.c and 4.d), and the observed stability loss commences earlier in case of GDE#1 (with the compact structure) than in case of GDE#2 (having a cracked microporous layer).

The observed efficiency loss is due to the flooding of the GDEs, which can be inferred not only from pre- and post-electrolysis sessile drop goniometry that clearly demonstrates a significant decrease of the surface hydrophobicity during electrolysis (insets of Fig. 4.c and 4.d), but also from top-down EDX elemental mapping that exhibits the formation of massive amounts of K_2CO_3/$KHCO_3$ precipitates on top of both GDE samples (Fig. 4.e and 4.f).

These top-down EDX elemental maps provide a straightforward explanation of the observed stability differences: while at the end of electrolysis, GDE#1 is more or less uniformly covered by K_2CO_3/$KHCO_3$ precipitates (and it is safe to assume that this uniform precipitate layer practically blocks all active Ag catalyst sites), we observe a rather non-uniform coverage (and an only partially blocked catalytic activity) in case of GDE#2. As to why the two GDEs are covered differently by the formed carbonate precipitates, top-down EDX mapping provides no answer, however. In order to address this question we have to rely on the combined cross-sectional EDX/ICP–MS method described previously in Section 2.

When GDE samples are made subject to electrolyses consuming different amounts of charge, and the samples are processed as was shown before in Fig. 3, the obtained absolute concentration *vs.* depth profiles are those shown by Fig. 5. Based on these profiles, a very important observation can be made: namely, that the total amount of formed precipitates, as well as the extent to which they penetrate the GDE structure is markedly different on GDE#1 and #2.

On GDE#1 —with the compact surface— K_2CO_3 and $KHCO_3$ precipitates are mainly formed (and remain) inside the catalyst layer and inside the pores of the microporous layer, and appear only in little amount in the underlying (fibrous) structure. As the microporous layer has a very limited capacity to store the formed carbonates —note that with increasing charge, the concentration profiles seem to saturate—, catalytic sites become blocked, and this results in the quick break-down of the measured Faradaic efficiency (cf. to Fig. 4.c). This saturation effect can well be observed in case of GDE#1, where at charges of −510.0 C cm^{-2} and −1839 C cm^{-2} the K concentration distribution (Fig. 5) within the microporous layer varies only a little, while the Faradaic efficiency of CO production is already significantly lowered at −510.0 C cm^{-2}. In case of GDE#2, the (cracked) microporous layer has a higher capacity to store potassium precipitates, and saturation of the microporous layer (resulting in a significant decrease of the Faradaic efficiency) seems to occur only at −1839 C cm^{-2}.

The higher durability of GDE#2 is probably a result of the presence of cracks in its microporous layer. These cracks allow a direct access of electrolyte solution to the fibrous layer, hence carbonates will also be able to precipitate in deeper parts of the GDE structure. Neither the electrolyte that penetrates the fibrous layer, nor the carbonate crystals which are formed there will block the active catalytic sites on-top of the microporous layer. As a result, the break-down of the Faradaic efficiency of CO production will commence on GDE#2 much later than on GDE#1, since in the (due to the

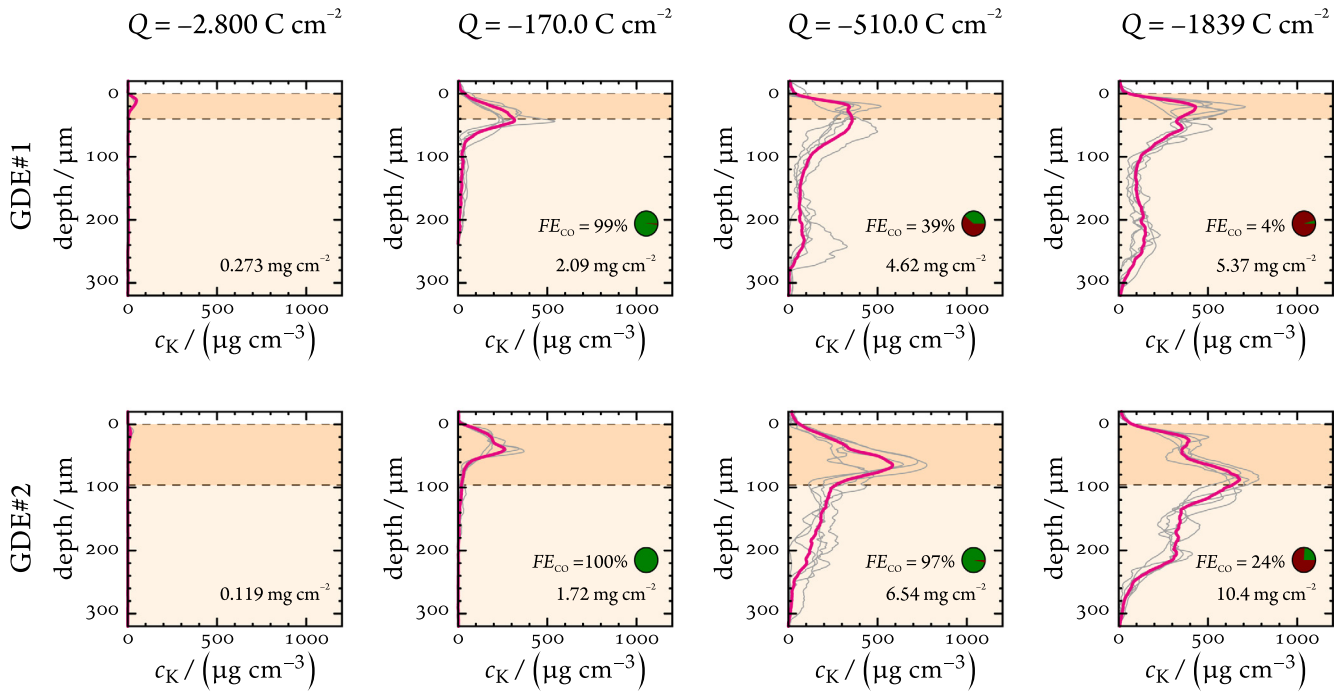

Fig. 5. Depth profiles of the absolute K^+ concentrations in different GDE samples, following electrolyses consuming different charges. The profiles were created by the cross-sectional EDX mapping/ICP–MS combination described in Section 2. (Grey curves show individual, magenta curves the averaged profiles.) The integral of each profile —that is, the total potassium content of the GDE normalised to surface area, determined by ICP–MS—, as well as the Faradaic efficiency of CO production, measured at the moment before the electrolysis was stopped, is given in each panel. The background shading of the panels pictures the GDL as a bi-layer structure (darker shading corresponds to the mic.roporous layer).

cracks, more penetrable) structure of GDE#2 a significantly bigger amount of K^+-containing precipitates has to be formed to effectively block the access of CO_2 to the catalyst layer. In case of GDE#1, blockage to the same effect occurs earlier, as in the absence of eluviation accelerating cracks, the formed precipitates quickly reach a critical concentration in the microporous layer.

Our results thus demonstrate that the crackedness of the GDL surface (maybe, somewhat counter-intuitively) plays a seemingly beneficial role in the water management of the GDE.

5. Conclusion

When *ec*-CO_2RR is carried out in a gas-fed CO_2 electrolyser with a zero-gap cathode half-cell configuration, K_2CO_3/$KHCO_3$ precipitation inside the GDE structure is a sovereign symptom (and probably an important driving force) of flooding. By determining, following electrolysis, the concentration distribution of carbonate salt leftovers within a GDE, we can assess the extent of flooding that occurred during the operation of the electrolyser, and we can better explain any observed stability losses and electrolyser malfunctions.

In this paper, a robust analytical method, based on the combination of cross-sectional EDX elemental mapping and ICP–MS-based analysis, was suggested in order to achieve the above goal. The novelty of this combination is that by ICP–MS measurements we turn EDX elemental —an essentially qualitative technique— into a quantitative characterisation tool that makes the obtained concentration profiles comparable across different GDE samples.

The basic concept and the technical details of the method were accurately described in the paper, and we also presented a short case study that demonstrated the applicability of the method.

We prepared two gas diffusion electrodes (one with a compact, another with a cracked microporous layer support) and made these subject to *ec*-CO_2RR stressing. We found that while the GDE with the compact surface looses stability (in terms of CO producing efficiency) rather quickly, the one with the cracked surface preserves its stability for a longer time. The newly developed, cross-sectional EDX elemental mapping/ICP–MS-based depth profiling tool provided an insight to the background of these efficiency losses. We found that the fibrous layer of GDEs (provided that it is accessible to water through the cracks of the microporous layer) may act as a reservoir for flooding, and as such, it can prevent (or at least postpone) the flooding-related deactivation of the catalyst layer.

The EDX/ICP–MS-based K precipitation mapping approach described in this paper will in future be used for the creation of statistically meaningful datasets based on which a systematic comparison of various gas diffusion layers and catalyst design concepts can be carried out.

Declaration of Competing Interest

The authors declare that they have no known competing financial interests or personal relationships that could have appeared to influence the work reported in this paper.

Acknowledgement

This publication was created as part of NCCR Catalysis (Grant No. 180544), a National Centre of Competence in Research funded by the Swiss National Science Foundation. V. Kolivoška acknowledges financial support from the Czech Science Foundation (project number 18-09848S). S. Vesztergom acknowledges support from the National Research, Development and Innovation Office of Hungary (NKFIH grant FK135375). Y. Kong, M. Liu and H. Hu acknowledge the financial support by the Chinese Scholarship Council (CSC).

References

[1] C. Hepburn, E. Adlen, J. Beddington, E.A. Carter, S. Fuss, N.M. Dowell, J.C. Minx, P. Smith, Ch.K. Williams, The technological and economic prospects for CO_2 utilization and removal, Nature 575 (7781) (2019) 87–97, https://doi.org/10.1038/s41586-019-1681-6.

[2] C.A.R. Pappijn, M. Ruitenbeek, M.-F. Reyniers, K.M. Van Geem, Challenges and opportunities of carbon capture and utilization: Electrochemical conversion of CO_2 to ethylene, Front. Energy Res. 8 (2020) 557466, https://doi.org/10.3389/fenrg.2020.557466.

[3] B. Endrődi, G. Bencsik, F. Darvas, R. Jones, K. Rajeshwar, Cs. Janáky, Continuous-flow electroreduction of carbon dioxide, Prog. Energy Combust. Sci. 62 (2017) 133–154, https://doi.org/10.1016/j.pecs.2017.05.005.

[4] J.-B. Vennekoetter, R. Sengpiel, M. Wessling, Beyond the catalyst: How electrode and reactor design determine the product spectrum during electrochemical CO_2 reduction, Chem. Engin. J. 364 (2019) 89–101, https://doi.org/10.1016/j.cej.2019.01.045.

[5] Y. Gu, J. Wei, X. Wu, X. Liu, A study on improving the current density performances of CO_2 electrolysers, Sci. Rep. 11 (2021) 11136, https://doi.org/10.1038/s41598-021-90581-0.

[6] B. Jung, S. Park, C. Lim, W.H. Lee, Y. Lim, J. Na, Ch.-J. Lee, H.-S. Oh, U. Lee, Design methodology for mass transfer-enhanced large-scale electrochemical reactor for CO_2 reduction, Chem. Eng. J. 424 (2021) 130265, https://doi.org/10.1016/j.cej.2021.130265.

[7] M.deJ. Gálvez-Vázquez, P. Moreno-García, H. Xu, Y. Hou, H. Hu, I.Z. Montiel, A. V. Rudnev, Sh. Alinejad, V. Grozovski, B.J. Wiley, M. Arenz, P. Broekmann, Environment matters: CO_2RR electrocatalyst performance testing in a gas-fed zero-gap electrolyzer, ACS Catal. 10 (2020) 13096–13108, https://doi.org/10.1021/acscatal.0c03609.

[8] K. Yang, R. Kas, W.A. Smith, Th. Burdyny, Role of the carbon-based gas diffusion layer on flooding in a gas diffusion electrode cell for electrochemical CO_2 reduction, ACS Energy Lett. 6 (2020) 33–40, https://doi.org/10.1021/acsenergylett.0c02184.

[9] M.E. Leonard, L.E. Clarke, A. Forner-Cuenca, S.M. Brown, F.R. Brushett, Investigating electrode flooding in a flowing electrolyte, gas-fed carbon dioxide electrolyzer, ChemSusChem 13 (2) (2019) 400–411, https://doi.org/10.1002/cssc.201902547.

[10] M.E. Leonard, M.J. Orella, N. Aiello, Y. Román-Leshkov, A. Forner-Cuenca, F.R. Brushett, Flooded by success: On the role of electrode wettability in CO_2 electrolyzers that generate liquid products, J. Electrochem. Soc. 167 (2020) 124521, https://doi.org/10.1149/1945-7111/abaa1a.

[11] B. Endrődi, A. Samu, E. Kecsenovity, T. Halmágyi, D. Sebők, Cs. Janáky, Operando cathode activation with alkali metal cations for high current density operation of water-fed zero-gap carbon dioxide electrolysers, Nature Energy 6 (2021) 439–448, https://doi.org/10.1038/s41560-021-00813-w.

[12] Z. Xing, X. Hu, X. Feng, Tuning the microenvironment in gas-diffusion electrodes enables high-rate CO_2 electrolysis to formate, ACS Energy Lett. 6 (2021) 1694–1702, https://doi.org/10.1021/acsenergylett.1c00612.

[13] Z. Xing, L. Hu, D.S. Ripatti, X. Hu, X. Feng, Enhancing carbon dioxide gas-diffusion electrolysis by creating a hydrophobic catalyst microenvironment, Nature Comm. 12 (2021) 1–11, https://doi.org/10.1038/s41467-020-20397-5.

[14] B. Kim, F. Hillman, M. Ariyoshi, S. Fujikawa, P.J.A. Kenis, Effects of composition of the micro porous layer and the substrate on performance in the electrochemical reduction of CO_2 to CO, J. Power Sources 312 (2016) 192–198, https://doi.org/10.1016/j.jpowsour.2016.02.043.

[15] W.H. Lee, Y.-J. Ko, Y. Choi, S.Y. Lee, C.H. Choi, Y.J. Hwang, B.K. Min, P. Strasser, H.-S. Oh, Highly selective and scalable CO_2 to CO - electrolysis using coral-nanostructured Ag catalysts in zero-gap configuration, Nano Energy 76 (2020) 105030, https://doi.org/10.1016/j.nanoen.2020.105030.

[16] U.O. Nwabara, A.D. Hernandez, D.A. Henckel, X. Chen, E.R. Cofell, M.P. de Heer, S. Verma, A.A. Gewirth, P.J.A. Kenis, Binder-focused approaches to improve the stability of cathodes for CO_2 electroreduction, ACS Appl. Energy Mater. 4 (2021) 5175–5186, https://doi.org/10.1021/acsaem.1c00715.

[17] A. Reyes, R.P. Jansonius, B.A.W. Mowbray, Y. Cao, D.G. Wheeler, J. Chau, D.J. Dvorak, C.P. Berlinguette, Managing hydration at the cathode enables efficient CO_2 electrolysis at commercially relevant current densities, ACS Energy Lett. 5 (2020) 1612–1618, https://doi.org/10.1021/acsenergylett.0c00637.

[18] F. Bienen, J. Hildebrand, D. Kopljar, N. Wagner, E. Klemm, K.A. Friedrich, Importance of time-dependent wetting behavior of gas-diffusion electrodes for reactivity determination, Chem. Ing. Tech. 93 (2021) 1015–1019, https://doi.org/10.1002/cite.202000192.

[19] B. De Mot, J. Hereijgers, M. Duarte, T. Breugelmans, Influence of flow and pressure distribution inside a gas diffusion electrode on the performance of a flow-by CO_2 electrolyzer, Chem. Eng. J. 378 (2019) 122224, https://doi.org/10.1016/j.cej.2019.122224.

[20] B. Endrődi, E. Kecsenovity, A. Samu, F. Darvas, R.V. Jones, V. Török, A. Danyi, Cs. Janáky, Multilayer electrolyzer stack converts carbon dioxide to gas products at high pressure with high efficiency, ACS Energy Lett. 4 (2019) 1770–1777, https://doi.org/10.1021/acsenergylett.9b01142.

[21] D.G. Wheeler, B.A.W. Mowbray, A. Reyes, F. Habibzadeh, J. He, C.P. Berlinguette, Quantification of water transport in a CO_2 electrolyzer, Energy Environ. Sci. 13 (12) (2020) 5126–5134, https://doi.org/10.1039/d0ee02219e.

[22] D. McLaughlin, M. Bierling, R. Moroni, Ch. Vogl, G. Schmid, S. Thiele, Tomographic reconstruction and analysis of a silver CO_2 reduction cathode, Adv. Energy Mater. 10 (19) (2020) 2000488, https://doi.org/10.1002/aenm.202000488.

[23] F. Bienen, D. Kopljar, A. Löwe, S. Geiger, N. Wagner, E. Klemm, K.A. Friedrich, Revealing mechanistic processes in gas-diffusion electrodes during CO_2 reduction via impedance spectroscopy, ACS Sustainable Chem. Eng. 8 (2020) 13759–13768, https://doi.org/10.1021/acssuschemeng.0c04451.

[24] E.R. Cofell, U.O. Nwabara, S.S. Bhargava, D.E. Henckel, P.J.A. Kenis, Investigation of electrolyte-dependent carbonate formation on gas diffusion electrodes for CO_2 electrolysis, ACS Appl. Mater. Interfaces 13 (2021) 15132–15142, https://doi.org/10.1021/acsami.0c21997.

[25] B. De Mot, M. Ramdin, J. Hereijgers, Th.J.H. Vlugt, T. Breugelmans, Direct water injection in catholyte-free zero-gap carbon dioxide electrolyzers, ChemElectroChem 7 (2020) 3839–3843, https://doi.org/10.1002/celc.202000961.

[26] D. Raciti, T. Braun, B.M. Tackett, H. Xu, M. Cruz, B.J. Wiley, Th.P. Moffat, High-aspect-ratio Ag nanowire mat electrodes for electrochemical CO production from CO_2, ACS Catal. 11 (2021) 11945–11959, https://doi.org/10.1021/acscatal.1c02783.

[27] A.J. Welch, A.Q. Fenwick, A. Böhme, H.-Y. Chen, I. Sullivan, X. Li, J.S. DuChene, C. Xiang, H.A. Atwater, Operando local pH measurement within gas diffusion electrodes performing electrochemical carbon dioxide reduction, J. Phys. Chem. C 125 (2021) 20896–20904, https://doi.org/10.1021/acs.jpcc.1c06265.

[28] H.-R. Jhong, F.R. Brushett, P.J.A. Kenis, The effects of catalyst layer deposition methodology on electrode performance, Adv. Energy Mater. 3 (2013) 589–599, https://doi.org/10.1002/aenm.201200759.

[29] H. Haspel, J. Gascon, Is hydroxide just hydroxide? Unidentical CO_2 hydration conditions during hydrogen evolution and carbon dioxide reduction in zero-gap gas diffusion electrode reactors, ACS Appl. Energy Mater. 4 (2021) 8506–8516, https://doi.org/10.1021/acsaem.1c01693.

[30] S. Verma, B. Kim, H.-R. Jhong, S. Ma, P.J.A. Kenis, A gross-margin model for defining technoeconomic benchmarks in the electroreduction of CO_2, ChemSusChem 9 (2016) 1972–1979, https://doi.org/10.1002/cssc.201600394.

[31] N.T. Nesbitt, Th. Burdyny, H. Simonson, D. Salvatore, D. Bohra, R. Kas, W.A. Smith, Liquid–solid boundaries dominate activity of CO_2 reduction on gas-diffusion electrodes, ACS Catal. 10 (2020) 14093–14106, https://doi.org/10.1021/acscatal.0c03319.

[32] T. Luo, S. Abdu, M. Wessling, Selectivity of ion exchange membranes: A review, J. Membr. Sci. 555 (2018) 429–454, https://doi.org/10.1016/j.memsci.2018.03.051.

[33] R. Wang, H. Haspel, A. Pustovarenko, A. Dikhtiarenko, A. Russkikh, G. Shterk, D. Osadchii, S. Ould-Chikh, M. Ma, W.A. Smith, K. Takanabe, F. Kapteijn, J. Gascon, Maximizing Ag utilization in high-rate CO_2 electrochemical reduction with a coordination polymer-mediated gas diffusion electrode, ACS Energy Lett. 4 (2019) 2024–2031, https://doi.org/10.1021/acsenergylett.9b01509.

[34] M. Liu, Y. Kong, H. Hu, N. Kovács, Ch. Sun, I.Z. Montiel, M.deJ. Gálvez Vázquez, Y. Hou, M. Mirolo, I. Martens, J. Drnec, S. Vesztergom, P. Broekmann, The capping agent is the key: Structural alterations of Ag NPs during CO_2 electrolysis probed in a zero-gap gas-flow configuration, J. Catal. 404 (2021) 371–382, https://doi.org/10.1016/j.jcat.2021.10.016.

[35] J.J. Friel, Ch.E. Lyman, Tutorial review: X-ray mapping in electron-beam instruments, Microsc. Microanal. 12 (2006) 2–25, https://doi.org/10.1017/s1431927606060211.

[36] N.J. Firet, Th. Burdyny, N.T. Nesbitt, S. Chandrashekar, A. Longo, W.A. Smith, Copper and silver gas diffusion electrodes performing CO_2 reduction studied through operando X-ray absorption spectroscopy, Catal. Sci. Technol. 10 (2020) 5870–5885, https://doi.org/10.1039/d0cy01267j.

[37] H. Hu, M. Liu, Y. Kong, N. Mysuru, Ch. Sun, M.deJ. Gálvez-Vázquez, U. Müller, R. Erni, V. Grozovski, Y. Hou, P. Broekmann, Activation matters: Hysteresis effects during electrochemical looping of colloidal ag nanowire catalysts, ACS Catal. 10 (2020) 8503–8514, https://doi.org/10.1021/acscatal.0c02026.

[38] M.deJ. Gálvez Vázquez, Sh. Alinejad, H. Hu, Y. Hou, P. Moreno-García, A. Zana, G.K.H. Wiberg, P. Broekmann, M. Arenz, Testing a silver nanowire catalyst for the selective CO_2 reduction in a gas diffusion electrode half-cell setup enabling high mass transport conditions, Chimia 73 (2019) 922–927, https://doi.org/10.2533/chimia.2019.922.

[39] Sh. Alinejad, J. Quinson, G.K.H. Wiberg, N. Schlegel, D. Zhang, Y. Li, S. Reichenberger, St. Barcikowski, M. Arenz, Electrochemical reduction of CO_2 on Au electrocatalysts in a zero-gap, half-cell gas diffusion electrode setup: a systematic performance evaluation and comparison to a H-cell setup, in: ChemRxiv, Cambridge Open Engage, 2021. https://doi.org/10.33774/chemrxiv-2021-1t50s-v3.

[40] G.K.H. Wiberg, M. Fleige, M. Arenz, Gas diffusion electrode setup for catalyst testing in concentrated phosphoric acid at elevated temperatures, Rev. Sci. Instrum. 86 (2015) 024102, https://doi.org/10.1063/1.4908169.

[41] M. Inaba, A.W. Jensen, G.W. Sievers, M. Escudero-Escribano, A. Zana, M. Arenz, Benchmarking high surface area electrocatalysts in a gas diffusion electrode: Measurement of oxygen reduction activities under realistic conditions, Energy Environ. Sci. 11 (2018) 988–994, https://doi.org/10.1039/c8ee00019k.

[42] Y. Kong, H. Hu, M. Liu, Y. Hou, V. Kolivoška, S. Vesztergom, P. Broekmann, Raw data for the article Visualisation and quantification of flooding phenomena in gas diffusion electrodes used for electrochemical CO_2 reduction: A combined EDX/ICP–MS approach (2022). https://doi.org/10.5281/ZENODO.6037503.

4. Cracks as Efficient Tools to Mitigate Flooding in Gas Diffusion Electrodes Used for the Electrochemical Reduction of Carbon Dioxide

Authors: Ying Kong, Menglong Liu, Huifang Hu, Yuhui Hou, María de Jesús Gálvez-Vázquez, Iván Zelocualtecatl Montiel, Soma Vesztergom, Viliam Kolivoška and Peter Broekmann.

Small Methods **2022, 6, 2200369. DOI: 10.1002/smtd.202200369**

Highlight: For the first time, cracks inside the GDLs were studied and correlated to the stability of a semi-zero-gap ec-CO_2RR electrolyzer. The electrolyte flooding and salt precipitation phenomena were shown to be detrimental to the system stability when GDL-based electrodes were applied for ec-CO_2RR. Ag-NWs-containing catalyst inks were airbrushed onto four types of commercial GDLs (different crack ratios) as GDEs for galvanostatic ec-CO_2RRs to study their stability. The stability of the semi-zero-gap cell was found to increase as the GDL crack ratio increases. While non-cracked GDL can only sustain efficient selectivity towards CO within 10 min, the GDL with the highest crack ratio remains high FE for CO longer than 2 h of electrolysis. Combined SEM/EDX and ICP-MS approaches revealed that the cracks helped to perspire electrolyte through the GDE, thus maintaining the catalytic performance on a high level.

Contribution: I conducted some parts of the electrochemical measurements, the perspiration experiments, and actively participated in discussion of the results. I participated in the revision of the manuscript text.

small methods
www.small-methods.com

Cracks as Efficient Tools to Mitigate Flooding in Gas Diffusion Electrodes Used for the Electrochemical Reduction of Carbon Dioxide

Ying Kong, Menglong Liu, Huifang Hu, Yuhui Hou, Soma Vesztergom, María de Jesus Gálvez-Vázquez, Iván Zelocualtecatl Montiel, Viliam Kolivoška, and Peter Broekmann**

The advantage of employing gas diffusion electrodes (GDEs) in carbon dioxide reduction electrolyzers is that they allow CO_2 to reach the catalyst in gaseous state, enabling current densities that are orders of magnitude larger than what is achievable in standard H-type cells. The gain in the reaction rate comes, however, at the cost of stability issues related to flooding that occurs when excess electrolyte permeates the micropores of the GDE, effectively blocking the access of CO_2 to the catalyst. For electrolyzers operated with alkaline electrolytes, flooding leaves clear traces within the GDE in the form of precipitated potassium (hydrogen)carbonates. By analyzing the amount and distribution of precipitates, and by quantifying potassium salts transported through the GDE during operation (electrolyte perspiration), important information can be gained with regard to the extent and means of flooding. In this work, a novel combination of energy dispersive X-ray and inductively coupled plasma mass spectrometry based methods is employed to study flooding-related phenomena in GDEs differing in the abundance of cracks in the microporous layer. It is concluded that cracks play an important role in the electrolyte management of CO_2 electrolyzers, and that electrolyte perspiration through cracks is paramount in avoiding flooding-related performance drops.

1. Introduction

Rising levels of atmospheric CO_2 as a dominant greenhouse gas have motivated endeavors to curb carbon emissions and utilize excess CO_2 to produce valuable resources.[1] The electrochemical reduction of CO_2 (denoted hereafter $ERCO_2$) allows not only its conversion to fuels and feedstock chemicals of high added value, but also the simultaneous storage of electrical energy originating from intermittent renewable sources.[2]

$ERCO_2$ operating at commercially relevant reaction rates (current densities) requires efficient and stable catalysts and facile mass transport of reactants and products with minimized energy losses.[3] Gas diffusion electrodes (GDEs) circumvent the problem of limited solubility and slow diffusion of CO_2 in aqueous media by delivering this reactant to the catalyst layer via gas phase.[3–6]

In GDEs, the catalyst layer is located on a supportive gas diffusion layer (GDL) that is composed of a carbon fiber layer (CFL) and a microporous layer (MPL),[4] as shown in **Figure 1**. Besides the reactant delivery, the GDL enables the release of gaseous reaction products, serves as a mechanical support and electrical contact for the catalyst, and plays important role in controlling the amount of electrolyte in the catalyst layer.[4,7,8] GDEs operating in alkaline aqueous electrolytes show highly active and selective $ERCO_2$ toward target products (like CO) due to the combination of reduced ohmic drops,[3,9] favorable electrode kinetics,[3,10–14] and suppression of the electrochemical reduction of water (ERH_2O) as a parasitic reaction.[15]

Y. Kong, M. Liu, H. Hu, Y. Hou, S. Vesztergom, M. de J. Gálvez-Vázquez, I. Zelocualtecatl Montiel, P. Broekmann
Department of Chemistry, Biochemistry and Pharmaceutical Sciences
University of Bern
3012 Bern, Switzerland
E-mail: peter.broekmann@unibe.ch

The ORCID identification number(s) for the author(s) of this article can be found under https://doi.org/10.1002/smtd.202200369.

DOI: 10.1002/smtd.202200369

Y. Kong, M. Liu, Y. Hou, P. Broekmann
National Centre of Competence in Research (NCCR) Catalysis
University of Bern
3012 Bern, Switzerland

S. Vesztergom
Department of Physical Chemistry
Eötvös Loránd University
1117 Budapest, Hungary

V. Kolivoška
J. Heyrovský Institute of Physical Chemistry of the Czech Academy of Sciences
18223 Prague, Czech Republic
E-mail: viliam.kolivoska@jh-inst.cas.cz

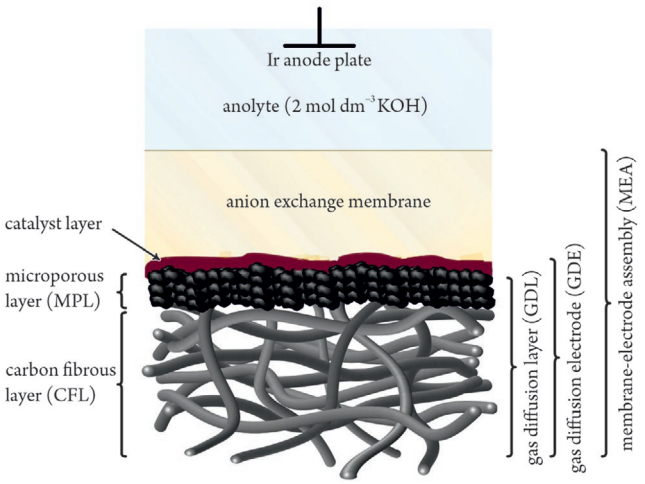

Figure 1. Schematic depiction of the zero-gap gas diffusion electrode (ZG GDE).

GDEs interfaced to ion exchange membranes, as shown in Figure 1, constitute membrane-electrode assemblies (MEAs),[16] allowing for decreased ohmic losses,[17] improved catalyst stability, and avoidance of problems due to the formation of gaseous products directly at electrode/electrolyte interfaces.[18]

Reactor arrangements based on MEAs were originally developed in the field of proton exchange membrane fuel cells (PEMFCs).[19] In PEMFCs, both the cathode and the anode are of a GDE structure, and are separated by a thin membrane. $ERCO_2$ electrolyzers often involve a configuration (see Figure 1 for a scheme; Figure S1, Supporting Information for detailed assembly) in which only the cathode is of a MEA structure.[20–22] This configuration is denoted further as a zero-gap GDE (ZG GDE) because the GDE cathode is in a direct contact with the membrane that separates it from the electrolyte solution (the anolyte) that contains the anode.

Despite differences in their mode of operation (electrical-to-chemical vs chemical-to-electrical energy conversion) and in their underlying chemistry, ZG GDE $ERCO_2$ electrolyzers and PEMFCs share several important aspects considering their water (electrolyte) management. In PEMFCs, H^+ ions resulting from the anodic oxidation of hydrogen are transported through the membrane to the cathode, where they are combined with electrons and oxygen to form water as the reaction product. In ZG GDE $ERCO_2$ electrolyzers, the membrane has essentially two roles: it controls the amount of water (that acts as a reactant of $ERCO_2$, and the absence of which can cause kinetic limitations[6]) and ensures that gaseous products formed by $ERCO_2$ in the catalyst layer cannot enter the anode compartment.

Insufficient hydration of the membrane can cause, both in PEMFCs and ZG GDE $ERCO_2$ electrolyzers, an increased cell resistance and pronounced energy losses, while excess hydration can lead to the flooding of the GDL and hence compromised transport of gaseous reactants toward the catalyst.[4]

The flooding of GDLs should be understood as a complex phenomenon that depends on diverse physico-chemical processes. System properties influencing flooding include the wettability of GDEs[8,23–29] and its dependence on the applied electrode potential (electrowetting),[30–40] the pH of the electrolyte,[30] the humidity of the reactant gases,[41,42] the presence of reaction intermediates[30] and products,[43] the temperature[30] and pressure[31,32,37,38] gradients across the cell, as well as the thickness of the employed membranes.[29]

In PEMFC research, the inspection of flooding phenomena has reached a significant degree of maturity.[19,44–47] The distribution of water in the interior of fuel cell structures has been visualized under operando conditions, for example, by optical microscopy (OM), magnetic resonance imaging, neutron imaging, environmental scanning electron microscopy (SEM), X-ray computed tomography, and fluorescence microscopy.[48–50]

Strategies to mitigate flooding in PEMFCs involve the use of MPLs with large voids[51,52] comprising both naturally formed structures (pores[53,54] and cracks[55–58]) and artificially designed architectures (holes[59] and grooves[60]). These bigger voids in the MPLs exhibit a smaller capillary pressure and hydrodynamic resistance compared to that of micropores. Thus, water formed in the cathode catalyst layer can preferentially be drained through the larger voids, reaching the CFL and finally escaping the fuel cell via flow channels and gas outlet. When large voids with appropriate abundance and distribution are present, micropores remain dry and keep their ability to function as efficient transport channels for gaseous reactants.

In the $ERCO_2$ field, flooding has been reported for GDEs either directly interfaced to liquid electrolytes[8,10,11,25,26,28,32–34,36–40,61–70] or blanketed by ion exchange membranes.[22,27,29,41,42,65,71–74] Flooding in $ERCO_2$ electrolyzers was often found to be accompanied by the appearance of precipitated salts inside or on the surface of GDEs.[9,11,22,28,33,34,36,38,39,41,42,61,64–66,68,69,74–76] These salts are either themselves constituents of the electrolyte solution or are formed when such a constituent reacts with CO_2. Both flooding and salt precipitation can hinder or even completely block the transport of CO_2 to the catalyst. As a result, a transition from $ERCO_2$ to ERH_2O is observed, leading to a significant drop of the overall Faradaic efficiency of $ERCO_2$.

In $ERCO_2$ electrolyzers employing alkaline electrolytes, the flooding of GDEs, and the appearance of precipitates within the GDE structure are mutually perpetuating processes. As some of the alkaline electrolyte appears in the GDE, it combines with the CO_2 supply gas to form potassium carbonate (or bicarbonate) precipitates. These salt formations decrease the hydrophobicity of the GDE, resulting in the permeation of even more electrolyte to the MPL and the formation of additional amounts of the precipitate.[68]

As a consequence, the appearance of carbonate precipitates within a GDE structure during electrolysis can be regarded as a tracer of flooding. In this vein, several authors have described flooding phenomena by visualizing potassium (as the electrolyte cation) on the surface[22,28,66] or within the interior[34,35,68,69,72,76] of GDEs, by the application of SEM complemented by energy dispersive X-ray (EDX) elemental mapping or by X-ray micro-computed tomography.[66,76] While these SEM-EDX works successfully showed that the appearance of potassium containing precipitates in GDE structures can be interpreted as a sign of flooding, they did not attempt to quantify the distribution of precipitates within the GDE, and to establish a correlation between the latter and the observed performance losses of the electrolyzer. The reason behind this is most likely that EDX is mostly considered a qualitative technique, yielding elemental maps that are not directly (that is, not quantitatively) comparable. This gap can however be bridged by the application of a novel method, based on the combination of cross-sectional EDX measurements

with an inductively coupled plasma mass spectrometry (ICP-MS) based determination of the total potassium content accumulated within a GDE structure upon the electrolysis.[77]

Note here that from the viewpoint of catalytic performance and stability, not only the total electrolyte content in a GDE but also its spatial distribution may become decisive. While the occurrence of potassium inside the micropores of the MPL can be interpreted as a sign of flooding with high certainty, its appearance in the CFL is not necessarily to be linked to flooding of micropores. In several works, the transport of the liquid electrolyte through the entire GDE (further referred to as electrolyte perspiration) was reported.[37–39,41,66,68,70] It is likely—especially based on what was said above about PEMFCs[51–60]—that the electrolyte perspiration through larger structures in the MPL involving cracks can prevent or at least delay the flooding of the micropores.

In the $ERCO_2$ field, recent works have demonstrated that cracks in the MPL facilitate the reaction due to augmented mass transport of gaseous CO_2 to the catalyst[78] and removal of excess electrolyte from the catalyst layer.[37] To the best of our knowledge, however, there is no systematic work studying the impact of MPL cracks on the catalytic activity and water management in $ERCO_2$ electrolyzers, as was carried out for PEMFCs.[55,57] While flooding of GDEs by liquid water formed as the reaction product represents the only barrier for the gas transport in PEMFCs, $ERCO_2$ is further complicated by the intrusion of the electrolyte ions into GDEs, potentially leading to salt precipitation. Exploring the electrolyte transport through MPLs with systematically varied architectures thus becomes the aim of this paper, with the ultimate goal of avoiding electrode flooding and salt precipitation in commercial $ERCO_2$ reactors.

Here we perform a series of galvanostatic experiments in a ZG GDE electrolyzer operated with alkaline anolyte. We employ different GDEs, the MPLs of which exhibit a varied abundance of cracks. To allow for a straightforward monitoring of reaction rates, we employ silver as the $ERCO_2$ catalyst, capable of producing CO with near-unity Faradaic efficiency.[8,10,12–14,16,21,22,27–29,36,38,39,41,42,66,68,70,71,75,76] The evolution of the catalytic performance is inspected by online gas chromatographic monitoring of CO and H_2, the latter being the product of ERH_2O and hence a fingerprint of electrolyte management deficiencies. Additionally, cell resistance and voltage and surface wettability of GDEs are monitored in the course of the electrolysis. We further utilize potassium as the cation of the employed electrolyte to visualize and quantify flooding and perspiration in the interior of GDEs, based on a recently developed, robust analytical approach that combines cross-sectional EDX elemental mapping and ICP-MS methods.[77] In addition, we monitor the perspiration rate by determining the amount of potassium in the perspirate, employing ICP-MS.

To the best of our knowledge, we perform and present here the first systematic study of flooding phenomena in GDEs at varied stages of the electrolysis, for GDEs with systematically varied microarchitecture. Our results shed light on an important, yet still unaddressed question of $ERCO_2$ engineering, namely, that submillimeter cracks in the MPL of GDEs applied for CO_2 electrolysis play a key role in the electrolyte management, and that by providing direct means for electrolyte drainage, cracks can efficiently prevent (or at least delay) the flooding of the catalyst layer.

2. Results and Discussion

The presented work aims at exploring the impact of the MPL structure with the emphasis on naturally occurring cracks on the catalytic activity and electrolyte management in $ERCO_2$ realized in an alkaline ZG GDE-based electrolyzer (full and cross-sectional drawings are shown in Figure S1, Supporting Information).[22,79]

We have selected four commercial GDLs as catalyst supports for our experiments, all of them having a bilayer structure composed of a CFL and an MPL. Three GDLs (36BB, 39BB, and 39BC) contain cracks in their MPLs. The fourth GDL (H23C8) has a crack-free MPL and is utilized as a reference system. For all four GDLs, the CFL is composed of coarse fibers. The surfaces of all GDLs were air-brushed with a catalyst ink containing silver nanowires (see the Experimental Section for details). The use of a catalyst ink based on nanowires was motivated by the assumption that assemblies of these quasi-1D objects form thin layers uniformly covering MPL surfaces and crack walls, without permeating into the interior of micropores.[70] For all four GDEs, the mass loading of silver was constant and equal to ≈40 μg cm^{-2}, as verified by ICP-MS analysis (see the Experimental Section for details). Representative top-down OM images of as-prepared GDEs are shown in **Figure 2**.

The optical micrographs of Figure 2 are very similar to those shown in Figure S2, Supporting Information, taken from bare GDL surfaces unmodified by catalyst ink deposition. This suggests that the air brush deposition leads to uniform catalyst layers without localized accumulation of deposits on the GDL surface or in cracks.

To inspect the structure of the formed catalyst layers in more detail, surfaces of as-prepared GDEs were further imaged by top-down SEM (also shown in Figure 2). For all four GDEs, Ag nanowires are well discerned, appearing as a collection of cylindrical objects with a diameter of ≈100 nm and a length of several micrometers, oriented parallel to the electrode surface. The small spherical features seen in the top-down SEM images of Figure 2 are attributed to the carbon black particles of the catalyst ink. High-resolution cross-sectional focused ion beam SEM images of top parts of MPLs (Figure S3, Supporting Information) demonstrate that the formed catalyst layers are 100 to 300 nm thick and involve one to three layers of Ag nanowires.

To investigate the permeation of the catalyst ink into the interior features of MPLs (micropores and cracks), cross sections of as-prepared GDEs were further inspected by SEM imaging combined with the EDX mapping of silver (Figure 2). For the non-cracked MPL (H23C8), the silver signal is confined to the top part of the MPL, confirming that Ag nanowires do not permeate micropores.

For cracked MPLs (36BB, 39BB, and 39BC) we first focused (in Figure 2) on regions containing cracks appearing as shaded features in the centers of cross-sectional SEM images. The corresponding EDX maps show a strong silver signal in the cracks, confirming that the catalyst ink permeates into the interior of the GDE through the cracks. For all three cracked MPLs, we performed the same analysis for regions with no cracks, with results shown in Figure S3, Supporting Information. In all cases, the silver signal is confined to the top of MPLs, similarly as for the non-cracked MPL (H23C8, Figure 2).

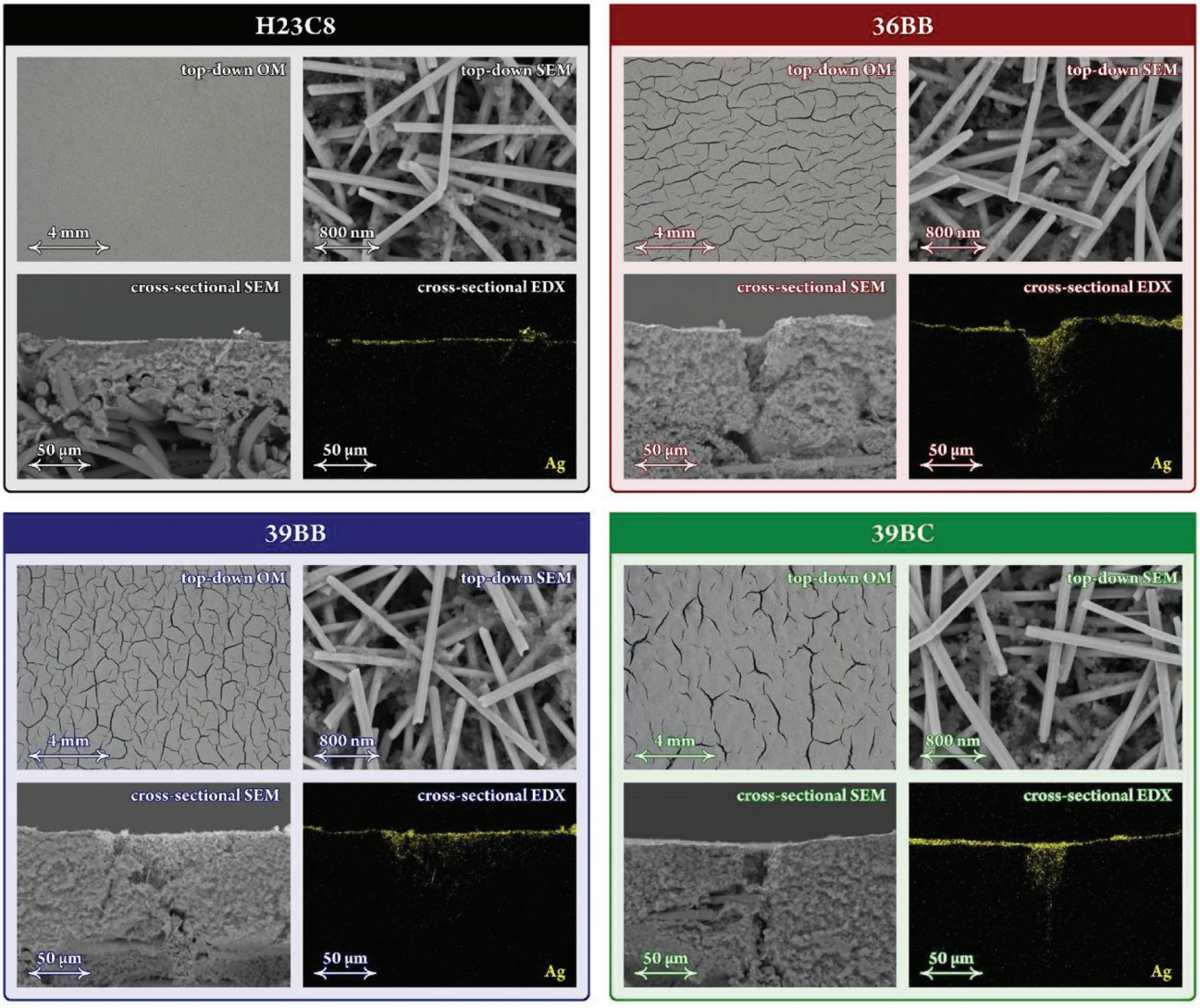

Figure 2. Representative top-down OM and SEM images, and cross-sectional SEM images and silver EDX maps of as-prepared GDEs.

One can conclude that the employed air brush deposition protocol leads to surfaces of MPLs completely covered by a thin catalyst layer that permeates into cracks, but leaves micropores unmodified. Such arrangement of the catalyst layer spatially decouples the target electrochemical process ($ERCO_2$) from the mass transport and charge transport phenomena occurring in the MPL, which is essential for the rigorous interpretation of relationships between the MPL structure, catalytic performance, and electrolyte management characteristics addressed in this work.

With regard to the distribution of cracks (see the optical micrographs of Figure 2 for catalyst ink-covered and Figure S2, Supporting Information for bare GDLs), it can be said that the H23C8 MPL has an almost featureless surface. Surfaces of the other three MPLs contain cracks that appear as distinct, elongated, and dark features. Cracks have no preferential orientation and enclose otherwise flat regions. White-light interferometry images of the pristine GDLs, as well as those of GDLs covered by a catalyst ink (taken before or following electrolysis, Figure S4, Supporting Information) exhibit the same crack distribution that seems undisturbed both by the catalyst ink coating and by subsequent electrolysis.

The pixel-by-pixel analysis of the top-down optical micrographs shown in Figure 2 allowed us to determine the relative occurrence of cracks on the MPL surface, denoted further as the surface crack ratio (CR). Obtained values are listed in **Table 1** and range from 0% to 21%. The characteristic width of cracks (≈100 µm for 36BB and 39BB, 100 to 200 µm for 39BC) is comparable to the thickness of the MPLs (also listed in Table 1), suggesting that most cracks span over the entire MPL depth.

Table 1 also lists void ratio values of entire GDLs, CFLs, and MPLs. These values were determined by densitometry, as described in the Experimental Section. The void ratio values of MPLs (further referred to as VR values) represent the cumulative porosity of MPLs; that is, the porosity that accounts for both cracks and micropores. The structure of micropores is partially resolved in SEM images presented in Figure S2, Supporting Information. As seen in Table 1, VR values scale with CR values, indicating that cracks are significant contributors to the overall porosity of MPLs. However, the differences

Table 1. Physical characteristics of GDLs used in this work. See the Statistical Analysis in the Experimental Section for more information on statistics.

	Entire GDL		CFL		MPL			
	Thickness [µm]	Void ratio [%]	Thickness [µm]	Void ratio [%]	Thickness [µm]	Void ratio (VR) [%]	Crack ratio (CR) [%]	Pores in solid (PS) [%]
H23C8	235 ± 3	60 ± 4	194 ± 5	67 ± 4	41 ± 2	30 ± 8	0 ± 0	30 ± 8
36BB	256 ± 9	70 ± 3	160 ± 20	73 ± 1	97 ± 11	68 ± 4	9 ± 2	64 ± 4
39BB	295 ± 15	81 ± 5	197 ± 22	82 ± 2	98 ± 7	78 ± 8	16 ± 4	74 ± 10
39BC	267 ± 7	72 ± 1	138 ± 21	66 ± 2	129 ± 14	78 ± 4	21 ± 4	72 ± 5

between VR values of cracked MPLs and the one obtained for the non-cracked MPL are more pronounced than the respective CR values, suggesting that cracked MPLs also exhibit a higher microporosity than crack-free MPLs. To quantify this observation, we introduce here a parameter termed the porosity of solid regions (PS) of MPLs, defined as

$$\mathrm{PS} = \frac{\mathrm{VR} - \mathrm{CR}}{1 - \mathrm{CR}} \tag{1}$$

Obtained PS values of all applied MPLs are also presented in Table 1. We presume that cracks formed in MPLs result from drying as a part of the manufacturing process of GDLs.[28] The comparison of PS and CR values suggests that the formation of cracks during the drying process is more likely for more porous MPLs. Results of combined OM and SEM imaging (Figure S2, Supporting Information) further show that the characteristic dimensions of cracks and micropores differ by at least two orders of magnitude. This difference has, as will be demonstrated, a huge impact on the capillary phenomena occurring in MPLs, being one of the key factors influencing the electrolyte management and hence catalytic performance of ZG GDEs.

For $ERCO_2$ testing, each GDE prepared and characterized as described above was blanketed by an anion exchange membrane and integrated in the electrolyzer, forming a ZG GDE (see Figure S1, Supporting Information for the arrangement of the electrolyzer and the Experimental Section for details). The electrolysis was performed and monitored under galvanostatic conditions with the GDE being continuously fed by a stream of humidified CO_2. **Figure 3** shows the evolution of the Faradaic efficiency (FE) values of CO obtained for all four ZG GDEs, expressed as a function of time as well as normalized charge passed in the electrolysis.

The charge normalization is based on the geometric area of the ZG GDE/anolyte interface, and the presented FE(CO) values were obtained by gas chromatography (GC) monitoring of the formed CO quantity during electrolysis (see the Experimental Section). For all ZG GDEs, CO is initially formed with near-unity FE, confirming that the catalyst shows high activity toward $ERCO_2$.

In the course of the electrolysis, significant differences in the evolution of FE(CO) values are noticed. For the crack-free MPL (H23C8), a fast decline in the CO production rate and a concomitant increase of the H_2 production rate are observed. The observed loss of CO production specificity may either be caused by a gradual degradation of the active catalyst sites, or by the retarded mass transport of CO_2 toward the catalyst layer.

For GDEs involving cracked MPLs, a markedly different evolution of FE(CO) values is observed. The GDE with the intermediate abundance of cracks (36BB, red) starts losing its catalytic activity roughly upon one-third of the electrolysis time. GDEs with higher crack abundance (39BB and 39BC, blue and green) continue to generate CO with near-unity FE values till the very end of the electrolysis. To reveal the origin of differences in the catalytic behavior, we performed identical location SEM studies of the catalyst layers deposited on H23C8 and 39BC GDLs (systems showing the smallest and the largest drop in the catalytic activity) before and after the electrolysis. For both systems, the obtained micrographs (Figure S5, Supporting Information) demonstrate that the electrolysis causes no visible changes in the nanomorphology of the catalyst. To exclude the influence of the electron beam used in SEM on the catalytic behavior and subsequent imaging,[80] we have further inspected random

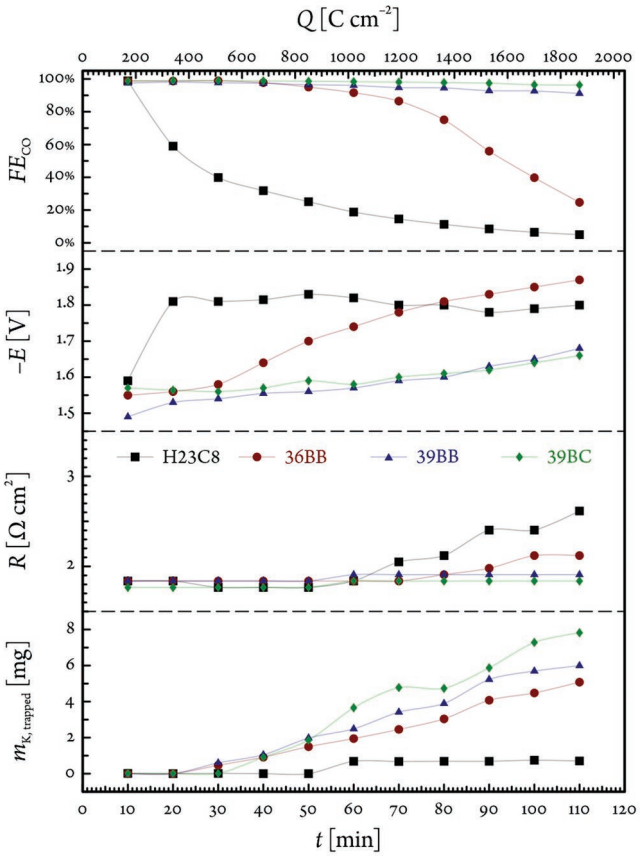

Figure 3. Faradaic efficiency of CO, ohmic drop-corrected cell voltage, normalized cell resistance, and the amount of potassium found by ICP-MS in the outlet trap plotted as a function of time and normalized charge passed in the electrolysis. Experiments were performed in the galvanostatic regime at –283 mA cm^{-2}, employing aqueous 2 M KOH as anolyte. A humidified CO_2 stream was fed to the GDE during the experiment at constant flow rate of 18 mL min^{-1}.

locations of the catalyst layer, not imaged prior to the electrolysis, again showing no signs of degradation (random location SEM micrographs are also shown in Figure S5, Supporting Information). Keeping in mind that catalyst loading and conditions applied in the electrolysis were identical for all four ZG GDEs, this suggests that a decline of the CO production rate observed for H23C8 and 36BB is not caused by the degradation of catalytic sites.

Employing a 36BB GDE selected for the demonstration, we further performed a follow-up electrolysis with a previously once-used electrode, preceded by a rinsing/drying step (see the Experimental Section for details). The catalytic activity of the electrode at the beginning of the follow-up electrolysis was largely restored (Figure S6, Supporting Information). This result not only confirms that the flooded electrolyte may be at least partially removed from the interior of the GDE, but additionally demonstrates that electrodes may be reused. The degradation of the catalyst was further excluded by identical and random location SEM studies performed before the initial and after the follow-up electrolysis (micrographs are also shown in Figure S6, Supporting Information).

The observed differences in the evolution of FE(CO) values among the investigated ZG GDEs are thus clearly attributed to the dissimilar rate of the CO_2 mass transport due to the different structure of MPLs.

It is important to remind that apart from the abundance of cracks (Figure 2; Figure S2, Supporting Information), the investigated MPLs also differ in void structure and, more specifically, in the porosity in solid regions, as documented by the CR, VR, and PS values (see Table 1). To investigate the effect of cracks and micropores on the observed differences in the catalytic behavior, we plotted FE(CO) values found at the end of the electrolysis as a function of the above three structural parameters in Figure S7, Supporting Information. FE(CO) data plotted on the CR basis shows more evident correlation compared to VR and PS parameters, suggesting that the crack abundance is the most important descriptor of differences in the catalytic behavior. Importantly, results of electrolysis experiments combined with the gas chromatographic product analysis suggest that cracks formed in the MPL prevent (39BB and 39BC) or at least delay (36BB) flooding as an adverse phenomenon frequently reported for $ERCO_2$ employing GDEs.

Apart from FE(CO) values, we also monitored the cell resistance as described in the Experimental Section, and plotted it as a function of time (as well as a function of the passed charge) in Figure 3. For MPLs with high crack abundance (39BB and 39BC), almost constant cell resistance values were found after a short initial period, suggesting that the concentration and mobility distribution of ions in these ZG GDEs reach a steady state. For the ZG GDE with lower crack abundance (36BB), a slight increase in resistance values is detected in later stages of the electrolysis, lagging the decrease of FE(CO) values. The resistance increase is either due to decreased electrolyte conductivity upon the reaction between CO_2 and OH^-[3,9] or a decrease of the active electrode area upon flooding or salt precipitation. Resistance values recorded for the non-cracked ZG GDE (H23C8) show an initial, transient decrease (presumably due to the accumulation of electrolyte ions in the catalyst layer and MPL, vide infra), followed by a pronounced increase toward the end of the electrolysis. The observed time shifts suggest that the cell resistance monitoring can only detect severe flooding events where the concentration and mobility of ions and/or active area of electrodes are affected significantly. The low flooding predicting power of cell resistance measurements is ascribed to significant resistance contributions originating from the anion exchange membrane and the anolyte, which are not affected by flooding of the GDE. The cell resistance thus cannot be used as an early warning signal to detect the onset of flooding.

Figure 3 further shows electrode potential values, mathematically corrected for the ohmic drop based on the measured cell resistance. Values obtained for ZG GDEs with high abundance of cracks (39BB and 39BC) show only subtle (and uniform) shifts, while more pronounced changes are noticed for the crack-free ZG GDE (H23C8) and the ZG GDE with moderate abundance of cracks (36BB). Such changes are probably due to the transition from the $ERCO_2$ to the ERH_2O regime. Importantly, the onset of changes observed in the electrode potential has no lag to the changes noticed in FE(CO) profiles. This suggests that electrode potential monitoring is applicable as an online tool for the detection of flooding of GDEs at commercially relevant current densities.

In experiments performed with all four ZG GDEs, small amounts of liquids and solids were observed at the back of CFLs, that is, in the gas flow channels and in the outlet equipped with a trap (see Experimental Section for details). After making sure that no electrolyte can escape the electrolyzer via leaking due to loosely assembled parts, we arrived at the conclusion that the observed liquids and solids originate from the transport of the electrolyte through ZG GDEs.

In the literature, the appearance of liquid electrolyte at the back of CFLs (termed as electrolyte perspiration) was attributed to the combination of pressure difference between the electrolyte and the gas phase and the electrowetting phenomena in the interior of GDEs.[37,38] For the ZG GDE electrolyzer employed in our study, the former contribution is given by the difference of the hydrostatic pressure acting on the top of the anion exchange membrane and the pressure in the gas flow channel beneath the CFL (see Figure S1, Supporting Information for the electrolyzer design). The magnitude of the hydrostatic pressure was estimated as 2.5 mbar, being much lower than the value needed to trigger electrolyte perspiration through the 39BC based GDE embedded in a flow-by electrolyzer (15 mbar) reported in the work of DeMot et al.[37]

In our study, the stream of gas (humidified CO_2) was fed to the flow channel at atmospheric pressure. Thus, we conclude that a differential pressure of 2.5 mbar (constant for all four ZG GDEs) was applied to the top of the anion exchange membrane. The pressure exerted on the top of GDE may additionally be influenced by the electroosmotic drag[29] resulting from the electric field (formed due to voltage applied across the cell), acting on the electric double layer in the interior of the membrane. The total pressure applied to the top of GDE is opposed by the capillary pressure originating from its hydrophobic interior structures. It is important to note that the ability of GDEs to resist external pressure may be compromised by electrowetting (an increase of wettability upon applying electric voltage between the electrode and the electrolyte).[30–40]

The magnitude of the capillary pressure is inversely proportional to the characteristic dimensions of interior structures. For hydrophobic surfaces, the electrolyte first enters structures with larger dimensions (cracks in this work), while leaving smaller structures (micropores) dry. For hydrophilic surfaces, the order of the electrolyte intrusion is just the opposite.[81] While wettability is not easily measurable in the interior of GDEs, it may be explored on their surfaces by contact angle measurements. In this work, we have monitored values of the contact angle on the surface of GDEs in the course of their preparation and upon subsequent electrolysis[22,26,27,66,70] performed with systematically varied charge consumption (Figures S8,S9, Supporting Information; see also the Statistical Analysis in the Experimental Section).

All four as-purchased (pristine) GDLs have strongly hydrophobic surfaces, with contact angle values obtained for cracked MPLs (164° ± 1°) being slightly lower than that of the crack-free MPL (170°). This is either due to crack walls having higher wettability than solid MPL regions or due to effects of highly curved surfaces. The deposition of the catalyst ink on MPLs leads to the uniform value of 143° ± 1°. This is in line with results of above-presented microscopic observations which demonstrate that the catalyst ink permeates to cracks (Figure 2).

Following electrolysis, the measured contact angle values diverge significantly among the employed electrodes. Values obtained for GDEs with high CR values (39BB and 39BC) are time-independent and equal to 106° ± 2°, indicating that their surfaces retain hydrophobic character. The value obtained for the GDE with the intermediate CR value (36BB) approaches 90°, being at the borderline between hydrophobicity and hydrophilicity. For the crack-free GDE (H23C8), contact angle values fall deep in the hydrophilic region. Washing GDEs with deionized water after completing the electrolysis led to uniform contact angle values of 135° ± 2°, being slightly lower than that obtained for as-prepared GDEs (143° ± 1°). This partial recovery implies that wettability changes observed upon the electrolysis are largely due to electrolyte accumulated in the GDE and not due to the catalyst degradation. This is in accord with results of identical and random location SEM studies of the catalyst layers presented in Figures S5,S6, Supporting Information.

Besides contact angle measurements, we further monitored the rate of electrolyte perspiration in the course of electrolysis by quantifying the amount of potassium in the outlet trap (Figure 3), employing ICP-MS analysis (see Experimental Section for details). For charge below 510 C cm^{-2}, no potassium was found. For non-cracked ZG GDE, the potassium amount remains low till the end of the electrolysis. For cracked ZG GDEs, amounts are significantly higher, scaling with passed charge and abundance of cracks.

As was already outlined above, the presence of cracks in MPLs helps to retain the catalytic activity of GDEs for a longer time (see the end-electrolysis FE(CO) values correlation with the CR parameter in Figure S7, Supporting Information). This is in agreement with the observation that the surface of GDE cathodes constructed of 39BB and 39BC GDLs show less hydrophobicity loss during electrolysis (Figures S8,S9, Supporting Information), because—as will be demonstrated below—of the cracks of these MPL surfaces act as dominant electrolyte transport pathways. For 36BB, the combination of lower CR value and hydrophobicity loss leads to slower electrolyte perspiration (Figure 3). Low amounts of potassium found for the non-cracked H23C8 suggest that the capacity of micropores to transport the electrolyte is very limited.

Besides the capillary action originating from interfacial forces, one also needs to consider that the flow of liquids through porous media is affected by viscous forces acting in the liquid. For laminar flow of water through pores of cylindrical geometry, Poiseuille law predicts that the flow rate is proportional to the second power of the cross-sectional pore area. This implies that cracks allow the passage of water at faster rate compared to micropores, additionally supporting the dominant role of cracks in the electrolyte transport. In addition to the presented reasoning, the difference in perspiration rates may further be rationalized by unequal rates of water consumption in the $ERCO_2$ and ERH_2O reactions. The two reactions proceed according to

$$CO_2 + H_2O + 2e^- \rightarrow CO + 2OH^- \quad (2)$$

and

$$2H_2O + 2e^- \rightarrow H_2 + 2OH^- \quad (3)$$

indicating that for ERH_2O, the consumption of water per unit passed charge is twice as high as for $ERCO_2$. For the non-cracked ZG GDE, where ERH_2O becomes the dominant process soon after the beginning of the electrolysis (Figure 3), higher consumption of water may contribute to the pronounced accumulation of electrolyte ions in the GDE interior, increasing the viscosity and impeding perspiration.

In the following, we further estimate the impact of the electrolyte perspiration on the carbon mass balance in $ERCO_2$, considering the data obtained for ZG GDEs based on 39BB and 39BC as best performing catalytic systems (Figure 3).

As mentioned above, the perspiration results in the accumulation of solids and liquids in gas flow channels and subsequently in the gas outlet equipped with the trap. During the electrolysis, it is not possible to monitor the amount of perspirate in gas flow channels and gas outlet and further analysis is thus restricted to the perspirate found in the trap (see Experimental Section for details). For both ZG GDEs (39BB and 39BC), the amount of potassium found in the trap scales linearly with the consumed charge. For the highest charge (1839 C cm^{-2}), it equals to 6.0 and 7.8 mg, respectively. The electrolyte transported through the GDE is in a permanent contact with gaseous CO_2 that is continuously delivered to flow channels. For stoichiometric excess of CO_2, we expect that its neutralization proceeds only to the first step, that is, producing HCO_3^- (and not CO_3^{2-}). Assuming this stoichiometry, the found mass of potassium corresponds to 1.53 and 1.99×10^{-4} mol of CO_2. We further discuss these amounts in the relation to the amount of CO_2 electrochemically converted to CO (6.74×10^{-4} mol) obtained considering FE(CO) of 100% for the sake of simplicity. The obtained CO_2 loss due to neutralization amounts to 23% and 30% indicating that the electrolyte perspiration cannot be ignored when drawing the total carbon mass balance of $ERCO_2$. Noteworthy, perspiration-related CO_2 losses in the ZG GDE electrolyzer as determined in this work

are significantly lower than those reported for CO_2 neutralization in the interior of GDEs embedded in membrane-based flow-by electrolyzers (≈70%).[82,83]

To provide microscopic insight to the electrolyte intrusion in GDEs, we utilized post-experimental SEM imaging to visualize the surfaces and cross sections of electrodes subjected to the electrolysis (see Experimental Section for details). In all inspections, SEM imaging was complemented by EDX mapping of potassium (shown as purple) utilized in this work as the electrolyte cation, to specifically reveal locations to which the electrolyte has permeated. A collection of top-down and cross-sectional SEM images and EDX-K elemental maps are shown in Figure S10, Supporting Information for four different GDE samples and four different electrolysis treatments.

Here, **Figure 4** shows representative top-down EDX maps obtained for surfaces of GDEs subjected to electrolyzes terminated at the charge consumption of 2.8, 170, 510, and 1839 C cm^{-2}. In these surface maps, the deposited salt appears as fuzzy features, sometimes forming islands that, with on-going electrolysis, tend to cover the catalyst layer. Cross-sectional

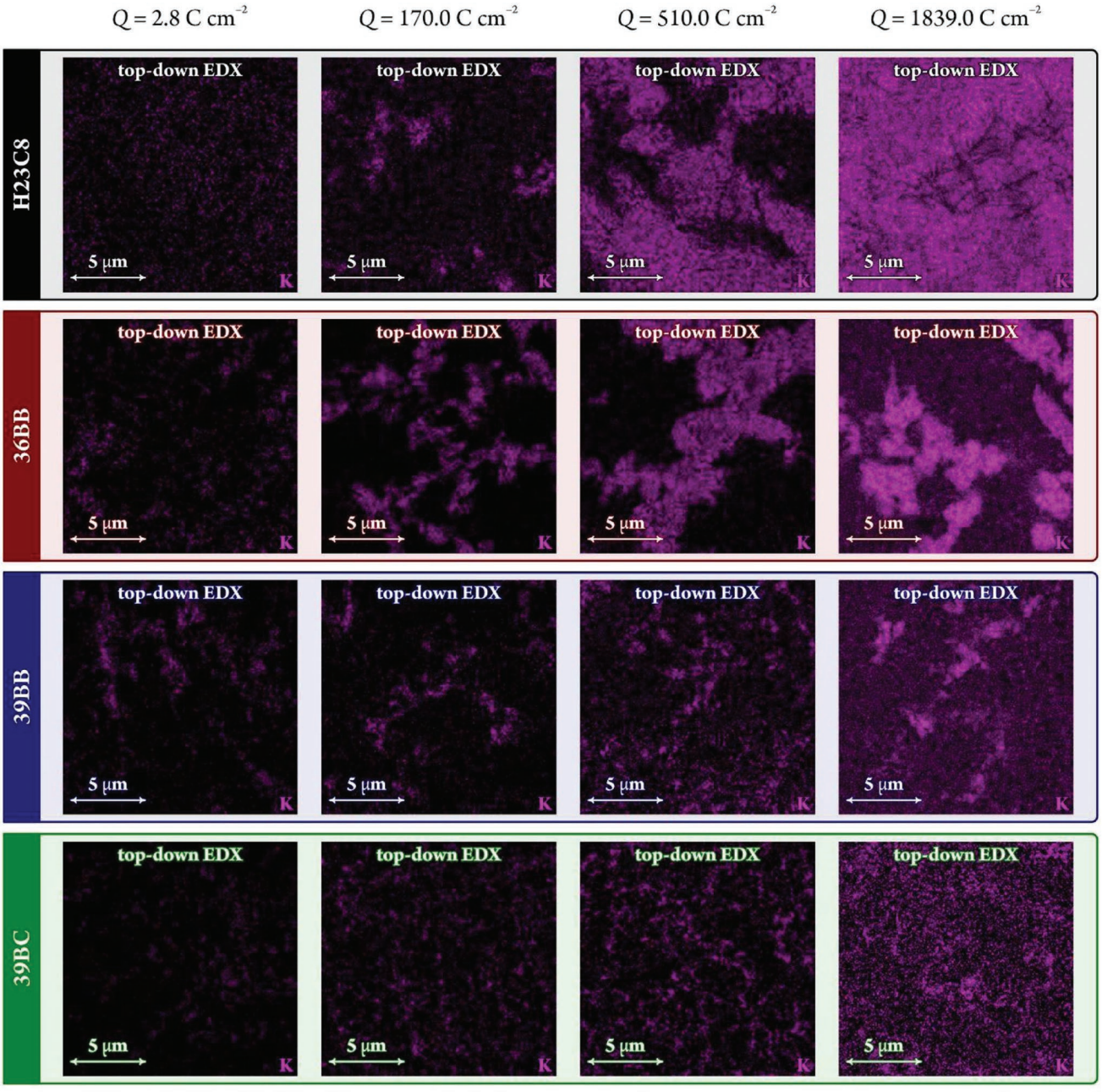

Figure 4. Representative top-down potassium EDX maps obtained for GDEs subjected to electrolyzes performed with varied charge consumption (for a comparison to corresponding top-down SEM images, as well as to cross-sectional SEM images and EDX maps, see Figure S10, Supporting Information).

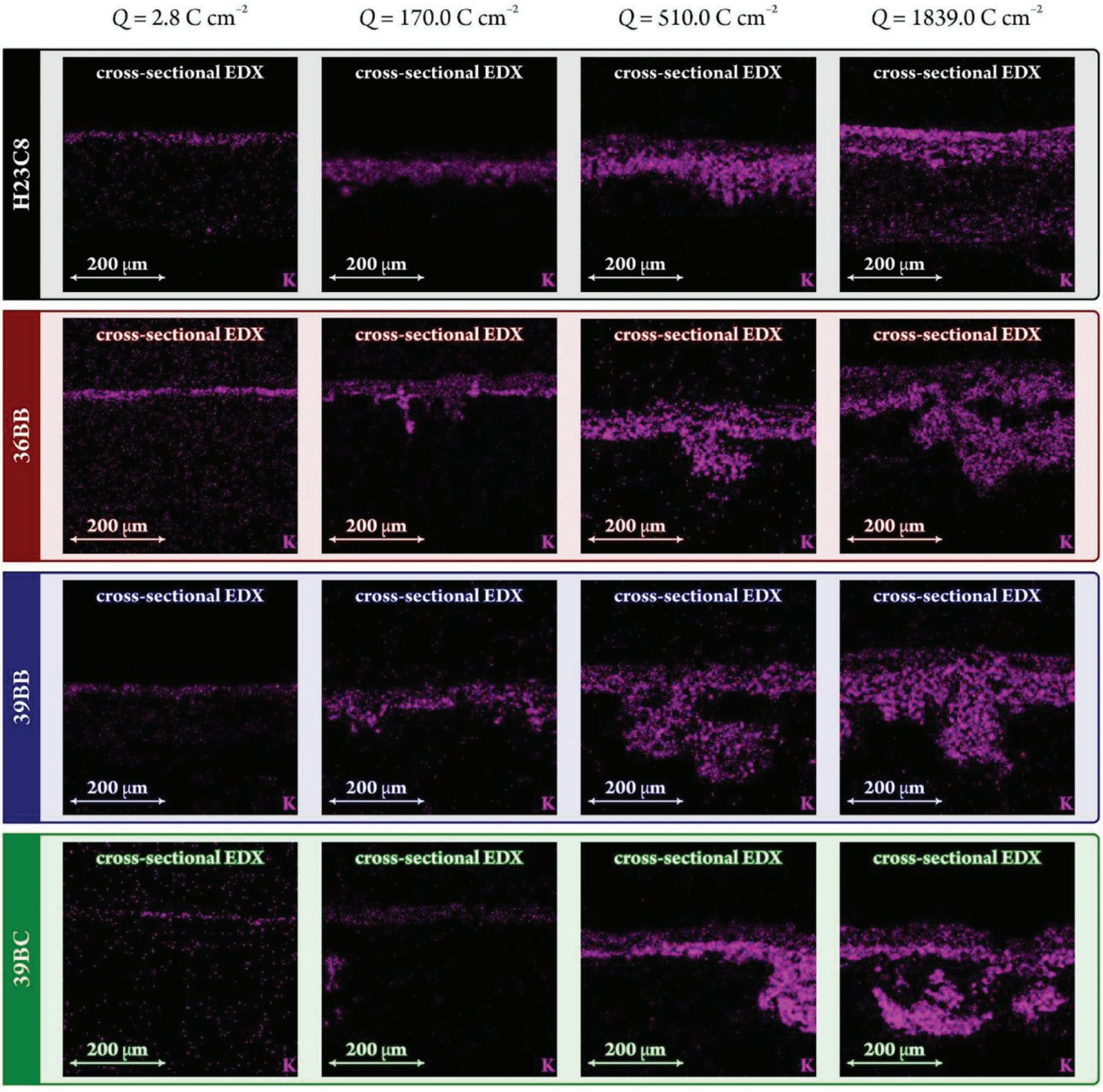

Figure 5. Representative cross-sectional potassium EDX maps obtained for GDEs subjected to electrolyzes performed with varied charge consumption (for a comparison to corresponding cross-sectional SEM images, as well as to top-down SEM images and EDX maps, see Figure S10, Supporting Information).

K EDX maps, shown in **Figure 5**, confirm that salt deposits (these are assumed to be potassium carbonates or hydrocarbonates), while initially formed only on the surface of the MPL, can later penetrate deeper layers of the GDL structure to different extent. Deposits appear already at the early stage of the electrolysis (2.8 C cm^{-2}) on all four GDE types, however they are confined to the surface of GDEs and show sparse coverage. For later stages of the electrolysis (170, 510, and 1839 C cm^{-2}) the amount and the pattern of deposits markedly differ among electrodes.

For the non-cracked GDE (H23C8), the electrolysis ends up with the deposit completely covering the electrode surface (Figure 4), being largely confined to the MPL (Figure 5). Only a minor amount of the deposit is found at the bottom of the CFL. This observation is in accordance with the low electrolyte perspiration rate found for this system (Figure 3). For the GDE with the intermediate CR value (36BB), the electrolysis leads to patched deposits covering significant portion of the electrode surface (Figure 4) and more pronounced electrolyte intrusion to the interior of the GDL (Figure 5). Higher amounts of the deposit found at the bottom of the CFL are consistent with higher perspiration rate. For GDEs with high CR values (39BB and 39BC), very little amounts of deposits were found at the

electrode surface (Figure 4), with significant intrusion toward the bottom of the CFL (Figure 5), which is in line with the highest electrolyte perspiration rate.

To reveal relationships between the structure of MPLs and patterns of formed deposits, we further performed SEM imaging at higher magnification, together with combined EDX mapping of silver and potassium, with representative results shown in Figure S11, Supporting Information. All inspections were performed on GDEs subjected to electrolyzes terminated after 510 C cm^{-2}. The non-cracked GDE (H23C8) shows that the silver signal is confined to the top of the MPL and the potassium signal is evenly distributed mainly in the MPL, with little intrusion toward the CFL, all being in accord with the above-presented results (Figures 2,4,5). The SEM image obtained for 36BB shows a crack in the middle, with a corresponding region of increased silver signal. The potassium signal is localized mostly beneath this crack. A very similar scenario is observed for 39BB, with the crack, silver signal and potassium signal being in the left part of the inspected region. For 39BC, the SEM image depicts a horizontal rupture in the MPL in the central part of the micrograph with corresponding increase of the silver signal and the potassium signal located mostly below the rupture.

To conclude, high-resolution cross-sectional imaging of GDEs combined with EDX mapping of silver and potassium as signatures of cracks and electrolyte intrusion clearly demonstrate that these features correlate. This unique approach thus provides microscopic evidence that cracks drain excess electrolyte from the MPL, which is macroscopically observed in the form of electrolyte perspiration.

Samples of electrodes subjected to electrolyzes terminated at varied stages were further analyzed by ICP-MS with the goal of determining the total amount of potassium in their interior (see Experimental Section for details). Results are shown as potassium mass normalized to the electrode area (numbers stated in mg cm^{-2} shown in the panels of **Figure 6**). It is worth noting that the ICP-MS technique, while it can provide the absolute amount of potassium in the entire volume of the GDE,[74] lacks information about its spatial distribution. On the contrary, cross-sectional EDX mapping of potassium gives access to the spatial distribution,[34,35,68,69,72,76] but provides no information in terms of the absolute concentration. The two techniques may be combined to provide spatially resolved absolute potassium profiling as demonstrated by our recent contribution.

Following the approach described before,[77] we quantified the potassium distribution in GDEs subjected to electrolysis with the charge consumption varied as described above. Obtained local absolute potassium concentration values were averaged along horizontal lines of EDX maps and plotted as a function of the vertical position (i.e., depth in the GDE), with results depicted as shaded profiles in Figure 6. To provide statistically relevant information, such obtained profiles were further averaged over five individually prepared GDE cross sections, with results shown as thick curves. The concentration scale is established based on the ICP-MS based measurement of the total (surface area normalized) K content of the studied GDE section, providing the integral of the thick curves in Figure 6.

The MPL regions are visualized by shaded bands in Figure 6. The thickness of CFLs as imaged upon the electrolysis was generally found to differ a little from that determined for as-purchased GDLs (see Table 1). We attribute these differences to the swelling of the CFL structure due to electrolyte intrusion.

At early stages of electrolysis (charge consumption of 2.8 C cm^{-2}), little amounts of potassium were observed inside the investigated GDEs (Figure 6), being confined to the top of MPLs. At 170 C cm^{-2}, potassium permeated deeper to the GDE structure, with more pronounced accumulation noticed for systems losing their catalytic activity (H23C8 and 36BB, Figure 3) in top regions of the MPL. Differences among GDEs are most marked at later stages of the electrolysis (510 and 1839 C cm^{-2}). For H23C8, potassium stays localized mostly in the MPL and the top part of the CFL, with very little intrusion found in its bottom part, which is in line with the low perspiration rate observed for this GDE (Figure 3). For 36BB, the intrusion advances deeper to the CFL, being consistent with higher perspiration rate. Among all four GDEs, 36BB shows the highest total potassium content in the GDE presumably due to the combination of highly porous MPL (Table 1), high wettability of the catalyst layer (Figures S8,S9, Supporting Information) and low abundance of cracks as draining features (Table 1, Figure 2; Figure S2, Supporting Information). For 39BB and 39BC, overall lower concentration values in both MPL and CFL are observed, being in accord with the highest perspiration rates and the highest abundance of cracks.

For all four ZG GDEs, the total amount of potassium (numbers in mg cm^{-2} in Figure 6) grows up to 510 C cm^{-2} and converges to a plateau for 1839 C cm^{-2}, suggesting that a steady-state electrolyte intrusion is approached. No distinct correlations were found between the total amount of potassium in GDEs after completing the electrolysis at 1839 C cm^{-2} and the void parameters of MPLs (Figure S7, Supporting Information) suggesting that both cracks and micropores play a role in the accumulation of potassium in MPLs. The highest amount of potassium observed for 36BB presumably reflects a relatively high porosity of its MPL (Table 1) and high wettability of the catalyst layer (Figures S8,S9, Supporting Information), both favoring electrolyte intrusion, combined with low abundance of cracks (Figure 2; Figure S2, Supporting Information) impeding electrolyte perspiration.

For the three cracked GDEs (36BB, 39BB, and 39BC), the amount of potassium found in their interior (Figure 6) is insignificant compared to that determined in the outlet trap (Figure 3). This finding corroborates that cracks function as efficient pathways for the electrolyte transport and indicates that the total amount of CO_2 deposited as carbonates in the interior of GDEs can be neglected in the total carbon balance of $ERCO_2$.

We further inspected the back sides of GDEs subjected to the electrolysis by SEM/EDX analysis, finding only little amounts of potassium (Figure S12, Supporting Information). Contact angle measurements performed after the electrolysis with 1839 C cm^{-2} also confirmed that back sides of GDEs largely retained their hydrophobic character (Figure S13, Supporting Information).

To explore the extent of the electrolyte flooding in the absence of CO_2, we further carried out an electrolytic experiment employing argon-fed 36BB based ZG GDE selected for the demonstration. The catalytic activity of such treated

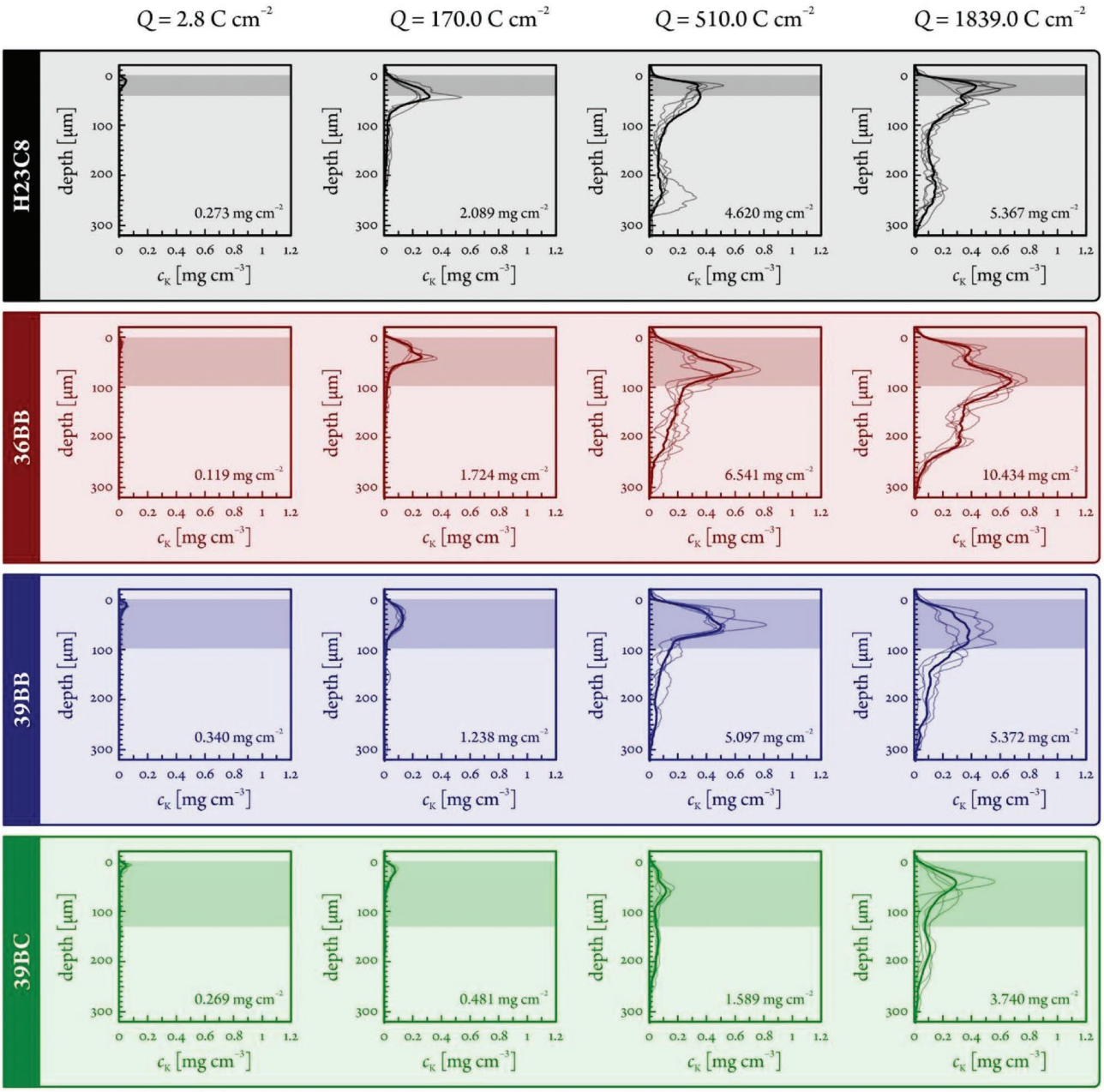

Figure 6. Potassium concentration as a function of depth in cross sections of GDEs subjected to electrolysis performed with varied charge consumption, obtained by combined EDX/ICP-MS approach. Shaded bands indicate MPL regions. The total amount of potassium found in the GDE by ICP-MS, normalized to its surface area, is indicated by numbers. See the Statistical Analysis in the Experimental Section for more information on data processing.

electrode was subsequently inspected in a follow-up electrolysis performed with CO_2. Resulting FE(CO) values (Figure S14, Supporting Information, left panel) were significantly lower compared to those obtained for the as-prepared GDE (Figure 3). This indicates that flooding in the GDE takes place also in the absence of CO_2 and in situ generated (hydrogen)carbonate salts. Nonetheless, when a cleaning/drying step (see the Experimental Section for details) was inserted between the argon-fed and the follow-up CO_2-fed electrolysis, the evolution of the catalytic activity (Figure S14, Supporting Information, right panel) well resembled that obtained for the as-prepared GDE. This demonstrates that flooded electrolyte may be removed from the interior of GDE when flooding has taken place in the absence of CO_2.

Results of the multi-methodological experimental approach presented above have revealed significant differences in the evolution of catalytic activity and the character of the electrolyte intrusion among inspected ZG GDEs due to varied structure of their MPLs. In the following, we aim to find relationships between the MPL structure, electrolyte intrusion pattern, and

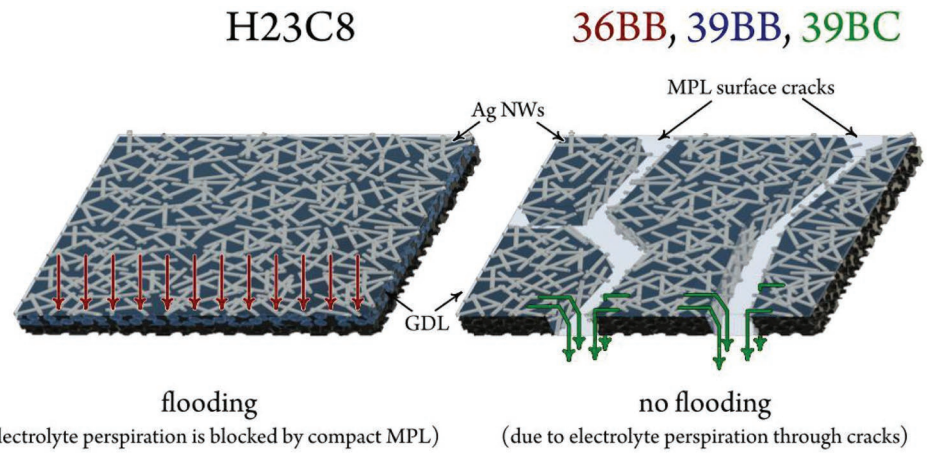

Figure 7. Schematic depiction of the catalyst layer supported with non-cracked (left) and cracked (right) MPL, visualizing electrode flooding and electrolyte perspiration phenomena.

catalytic activity, and provide mechanistic insights in these phenomena, employing a schematic depiction of the catalyst layers supported by non-cracked and cracked MPLs shown in **Figure 7**.

The MPL of H23C8 contains no cracks (Figure 2; Figure S2, Supporting Information) and shows low internal porosity (Table 1). The electrolysis performed with such ZG GDE leads to an immediate and pronounced decline in FE(CO), significant increase in cell resistance and voltage (Figure 3), loss of hydrophobilicy (Figures S8,S9, Supporting Information) and electrode surface completely covered with potassium (Figure 4) that additionally accumulates in the MPL and top part of CFL (Figures 4,5). All these characteristics are indicative of severe flooding of the MPL (Figure 7, left), with the proposed mechanism presented as follows. The combination of the hydrostatic pressure and electroosmotic drag drives the electrolyte through the anion exchange membrane to the catalyst layer, where water is partially consumed in cathodic processes (first $ERCO_2$, later mainly ERH_2O). In the absence of cracks in the MPL, the excess electrolyte floods its micropores.[81] The presence of the liquid electrolyte in micropores significantly reduces the diffusion coefficient of CO_2.[5] The diffusion rate slows down in the course of the electrolysis as the electrolyte intrudes deeper in the GDL (Figures 4,5). The ERH_2O takes place in the GDL,[70] causing more water to be consumed per unit charge. This accelerates the accumulation of OH^- ions (both originally present in the electrolyte and generated as the by-product of ERH_2O) in the GDL. Increased amounts of OH^- ions are balanced by potassium ions that reach the GDL by ionic migration via the anion exchange membrane that can generally have non-perfect permselectivity.[84] Increased ionic concentration may negatively impact the solubility of gases[85] and reaction kinetics.[3,86] The absence of cracks combined with low internal porosity of the MPL and increased electrolyte viscosity due to accumulated ions leads to low perspiration rate (Figure 3). Furthermore, OH^- ions react with CO_2 dissolved in the electrolyte to form (hydrogen)carbonate anions, reducing the electrolyte conductivity and increasing the risk of the salt precipitation in micropores. The accumulation of ions further leads to loss of hydrophobicity facilitating flooding of micropores.[68]

Based on the results of consecutive electrolytic experiments performed with argon and CO_2 (Figure S14, Supporting Information), we support the view that flooding is not initiated by the carbonate precipitation, being in contradiction to the interpretation presented by Leonard et al.[68] In fact, the intrusion of the electrolyte to micropores may be triggered by electrowetting at extreme cathodic potentials (Figure 3).[30–40] It is important to note that the ex situ SEM/EDX analysis of GDE cross sections, as performed in this work (Figures 4,5), can visualize areas to which the electrolyte has permeated during the electrolysis but cannot distinguish whether solid precipitates are formed during or after the electrolysis.[69]

The MPL of 36BB contains cracks in low abundance (Figure 2; Figure S2, Supporting Information) and has high internal porosity (Table 1). Compared to the crack-free system, this ZG GDE sustains $ERCO_2$ for longer time, shows lower increase in the cell resistance and voltage (Figure 3), less pronounced loss of hydrophobicity (Figures S8,S9, Supporting Information) and lower accumulation of potassium on the electrode surface (Figures 4,5). Compared to micropores, cracks have much greater characteristic dimensions (Figure 2; Figure S2, Supporting Information) and thus constitute preferred pathways for the electrolyte intrusion (Figure 7, right), which was microscopically confirmed by the SEM/EDX analysis (Figure S11, Supporting Information) and macroscopically observed as increased perspiration rate (Figure 3). The perspiration through cracks alleviates the flooding of micropores, enabling them to function as channels for the gas transport.[53,54,56–58] However, the loss of catalytic activity (Figure 3) accompanied by a significant buildup of potassium on the surface (Figure 4) and in the interior (Figure 5) of the GDE observed in later stages of the electrolysis indicate that the crack abundance in 36BB is not sufficient to maintain micropores dry. Values of contact angles found in later stages of the electrolysis are close to 90° (Figures S8,S9, Supporting Information), suggesting that capillary forces have minimal effect on the electrolyte transport through the MPL. In such case, the electrolyte transport rate via cracks and micropores is governed by their hydrodynamic resistance.

MPLs of 39BB and 39BC have high abundance of cracks (Figure 2; Figure S2, Supporting Information) and high

internal porosity (Table 1). They differ in the architecture of cracks, with 39BB having higher amount of narrow cracks and 39BC having broader cracks with sparser abundance. Both ZG GDEs show near-unity FE(CO) values, no increase in the cell resistance, only subtle cell voltage shifts, high electrolyte perspiration rates (Figure 3), almost no loss of hydrophobicity (Figures S8,S9, Supporting Information) and little accumulation of potassium on the electrode surface (Figure 4) and in its interior (Figures 4,5), with all these characteristics being retained for the entire time span of the electrolysis. This indicates that MPLs of these two electrodes possess sufficient abundance of cracks enabling efficient electrolyte perspiration that prevents the flooding of micropores (Figure 7, right). A desired electrolyte management in the ZG GDE, with the liquid phase being largely confined to the catalyst layer, is thus established.[4] Slightly higher FE(CO) values obtained for the 39BC based system further corroborate that cracks, and not micropores, are the main drainage pathway for the electrolyte perspiration, providing valuable hints for the design of MPLs in future $ERCO_2$ electrolyzers. Near unity FE(CO) values combined with results of cross-sectional EDX mapping of silver indicate that Ag nanowires deposited on crack walls are catalytically active toward $ERCO_2$. In fact, the catalyst located in the interior of cracks may be more active than that deposited on the MPL surface due to facilitated CO_2 transport, as recently demonstrated by Welch et al.[78] Nevertheless, it is important to note that the electrolyte perspiration through cracks causes parasitic CO_2 losses due to neutralization occurring in gas flow channels, which needs to be accounted for when assessing the overall economic viability of newly designed electrolyzers.

3. Conclusions and Outlook

Cracks as structures naturally occurring in MPLs of GDEs have been reported as beneficial for the water removal in polymer electrolyte membrane fuel cells.

In this work, we have inspected the ability of cracks to improve the electrolyte management and the overall catalytic performance of zero gap GDEs for the electrochemical reduction of carbon dioxide. The employed electrodes contained silver nanowires in a thin catalytic layer and differed in the abundance of cracks in the MPL supporting the catalyst. Utilizing galvanostatic electrolyzes, we demonstrated that electrodes with appropriate abundance of cracks show high and sustained catalytic activity, while a fast transition to parasitic reduction of water was noticed for non-cracked electrodes.

Small amounts of liquids and solids were observed in flow channels and the outlet of the carbon dioxide delivery system indicating that the electrolyte is transported through zero gap GDEs (electrolyte perspiration). For the first time, the amount of the electrolyte in the perspirate was determined, employing ICP-MS, finding that this amount scales with the abundance of cracks.

Cross sections of GDEs subjected to electrolyzes were subsequently inspected by our recently developed analytical approach combining SEM imaging, EDX elemental analysis, and ICP-MS, to obtain absolute concentration profiles of potassium used as the electrolyte intrusion marker. The performed analysis provided the microscopic evidence that cracks serve as preferential pathways for the electrolyte transport through the MPL. Cracks thus drain excess electrolyte from the catalytic layer, which prevents flooding of micropores and enables them to function as efficient transport channels for gaseous carbon dioxide. In the absence of cracks, the electrolyte was found to flood micropores, reflecting itself as greatly reduced catalytic activity.

Our contribution presents the first study focusing on the effect of cracks on the electrolyte management and catalytic activity in the field of electrochemical CO_2 reduction. Besides monitoring the electrolyte intrusion in GDEs as a function of charge consumed in the electrolysis, we found correlations among the catalytic performance, electrochemical characteristics of cells, electrolyte perspiration rates, and surface wettability of electrodes, resolving the influence of cracks and micropores in the electrolyte transport.

While cracks were clearly proven to be beneficial for the electrolyte management, it should not be forgotten that the electrolyte perspiration occurring via these structures leads to non-negligible parasitic losses of carbon dioxide due to its neutralization. Therefore, efforts to optimize the utilization of carbon dioxide in electrolyzers must include searching for conditions under which both electrode flooding and perspiration-related reactant losses are minimized. Following the approaches reported for polymer electrolyte membrane fuel cells, we further aim at manufacturing and inspecting zero gap GDEs based on MPLs modified with artificially created draining elements such as holes or trenches formed by mechanical or laser perforation. The electrolyte perspiration through these structures may be controlled by their dimensions and predicted employing numerical models taking into account the capillary action, hydrodynamic resistance, and electroosmotic drag.

4. Experimental Section

Preparation of Gas Diffusion Electrodes: All experiments performed in this work employed commercial GDLs composed of supporting compressed CFL (carbon without additives) and MPL (carbon black treated with 5% PTFE). MPLs differ in their height, porosity, and abundance of cracks (for details see Results and Discussion). The GDL with crack-free MPL (H23C8) was obtained from Freudenberg, while GDLs involving cracked MPLs (36BB, 39BB, and 39BC) were purchased from Sigracet.

Silver nanowires used in this work as catalysts for $ERCO_2$ were synthesized following the procedure described in the previous work.[87] To prepare the catalyst ink, 4.5 mg of the as-synthesized Ag nanowires and 0.8 mg of carbon black (VULCAN VXC72R, Cabot) were separately dispersed in 20 mL of isopropanol (BASF SE, assay ≥ 99.0%) and sonicated for 30 min. Such prepared dispersions were intermixed, sonicated for 30 min, and dried by a rotary evaporator (Büchi R 210, 40 °C, 65 mbar). The resulting mixture was re-dispersed in 18 mL of isopropanol additionally containing 180 µL of Nafion 117 solution (≈5 wt% in a mixture of lower aliphatic alcohols and water, obtained from Sigma Aldrich) and sonicated for 20 min. The thus prepared catalyst ink was deposited on the MPL surfaces by airbrushing (hand-held Airbrushpistole Infinity CR plus, propelled by nitrogen gas, 99.999%, Carbagas, Switzerland), forming the catalyst layer. Such modified assemblies were dried and used as GDEs in electrolytic experiments performed as follows.

Assembly of the Electrolyzer: All electrochemical experiments performed in this work were realized in the electrolyzer shown in Figure S1,

Supporting Information.[22,79] The electrolyzer was based on ZG GDE arrangement with GDEs prepared as described above, interfaced to the anodic compartment. The assembly of the electrolyzer was carried out as follows. The GDE with the catalyst layer facing upward was placed on a stainless steel support functioning as a current collector and a gas delivery system (it was equipped with flow channels connected to inlet and outlet tubing). The anion exchange membrane (X37-50 RT, Dioxide materials) was subjected to a pre-treatment suggested by the supplier, and gently placed on the top of the GDE. The formed ZG GDE was covered by a Teflon chamber, which was subsequently mounted to the stainless steel support by a clamp. The Teflon chamber was filled with aqueous KOH solution (10 mL, 2 M, pH = 14.3, solid KOH purchased from Sigma Aldrich, prepared employing Milli-Q water) serving as the anolyte. The Teflon chamber contained a central circular orifice (radius of 0.15 cm) in its bottom part defining the geometrical area of the ZG GDE/anolyte interface. Iridium wire (99.9%, MaTeck Material-Technologie & Kristalle GmbH, Germany) separated by glass frit and Ag/AgCl/3 M KCl electrode (double junction design, Metrohm) were immersed in the anolyte and were utilized as the counter electrode and the reference electrode. A flask containing 15 mL of Milli-Q water was placed downstream to the gas outlet and served as a trap to collect the perspirate resulting from the electrolyte transport through the ZG GDE.

Electrochemical Measurements: The catalytic activity of the ZG GDE (set as the working electrode) was inspected by galvanostatic experiments in the electrolyzer assembled as described above, employing an ECi-200 potentiostat (ECi-200, Nordic Electrochemistry). For all four GDEs, the electrolysis was performed at current of −20 mA (corresponding to geometric current density of −283 mA cm^{-2}) for systematically varied time, specifically 10, 600, 1800, and 6500 s. In the Results and Discussion section, the duration of electrolysis is presented as passed charge normalized to the geometrical area of the ZG GDE/anolyte interface (0.0707 cm^2). Unless otherwise specified, a freshly prepared GDE was used in the electrolysis. A humidified gaseous CO_2 stream (99.999%, Carbagas, Switzerland) was continuously supplied to the flow channels of the stainless steel support via the inlet at the rate of 18 mL min^{-1} employing a thermal mass flow controller (red-y smart, Vögtlin Instruments). The gaseous mixture leaving the outlet was fed through a drying tube and its composition was analyzed for CO and H_2 by online GC (SRI Instruments) in 10 min intervals.[21] The formed CO and H_2 quantities, measured during electrolysis, added up to about 100% ± 10% of the quantities that could be expected from the charge of electrolysis. Noting that while the formation of some other products (e.g., that of formate) was possible in very little amount in the studied electrolyzer, it was assumed that the H_2:CO formation ratios detectable by GC were, within range of experimental error, correct. Faradaic efficiency values (e.g., those presented in Figure 3) were thus re-scaled so that the measured H_2:CO ratios were respected, together accounting for a 100% Faradaic efficiency.

The cell voltage and resistance were monitored in 0.1 s intervals. The cell resistance was obtained by superimposing AC perturbation (5 000 Hz, 50 µA) to the current applied to the cell (20 mA) and monitoring the AC component of the cell voltage.

For the GDE based on 36BB GDL, a follow-up electrolysis experiment was performed with the goal of exploring the possibility of restoring the catalytic activity of once used electrode. First, the GDE was subjected to the electrolysis performed as described above. Afterward, the electrolyzer was disassembled and the GDE was immersed in ≈30 mL of quiescent Milli-Q water for 5 min, the procedure being repeated 7 times. Subsequently, the GDE was dried in a vacuum oven for 2 h at ambient temperature. Such treated GDE was reinstalled into the electrolyzer and its catalytic performance was inspected in a follow-up electrolysis carried out under the same conditions.

Also for the GDE based on 36BB GDL, an additional control electrolytic experiment was performed to inspect the occurrence of flooding in the absence of CO_2. First, the GDE was subjected to the electrolysis with humidified CO_2 being replaced by humidified argon (99.9999%, Carbagas, Switzerland). Subsequently, the electrolyzer was disassembled and the GDE was either subjected to the cleaning/drying procedure performed as described above or this step was omitted. Such treated GDE was reinstalled into the electrolyzer and its catalytic performance was inspected in a follow-up electrolysis carried out with humidified CO_2.

Characterization of Electrodes: Surfaces of pristine MPLs and as-prepared GDEs were inspected by optical microscopic imaging employing a VHX600 Keyence digital microscopes. The obtained images were utilized to determine the surface CR based on counting pixels corresponding to cracks and solid regions on the MPL surface. The void ratio of CFLs, MPLs, and entire GDLs was obtained by using a pycnometer, employing isopropanol as a liquid that was assumed to completely fill up the internal structures of layers. Surfaces of as-purchased (pristine) MPLs, as-prepared GDEs, and GDEs subjected to the electrolysis were additionally inspected by white light interferometry (Contour GT, Bruker) equipped with Vision64 software (Vision64, Bruker).

A Zeiss Gemini 450 SEM equipped with an EDX spectroscopy instrument (Aztec, Oxford instruments) was used to investigate the structure and content of silver and potassium on surfaces and in the interior of GDEs. Surfaces of GDEs were inspected before and after electrolytic measurements performed as described above. For selected samples, identical location SEM studies were performed. Subsequently, electrodes subjected to the electrolysis were frozen in liquid nitrogen and cut by a sharp blade and such obtained cross sections were examined by SEM/EDX. To obtain statistically significant information, at least five cross sections were prepared and analyzed for each GDE. The cross-sectional imaging was additionally performed for as-purchased GDLs, to determine the thickness of the CFL and the MPL.

The mass loading of silver in the catalyst layer of as-prepared GDEs was determined by means of ICP-MS (NexION 2000 ICP-MS instrument, PerkinElmer). For this purpose, GDEs of circular shape with the radius of 0.1 cm were prepared and examined. GDE samples were introduced to concentrated nitric acid (69.3%, VLSI selectipur, BASF), sonicated for 30 min and left overnight. Additionally, ICP-MS analysis following the same sample treatment was employed to determine the amount of potassium in the interior of GDEs upon the electrolysis. Furthermore, the ICP-MS was employed to determine the amount of potassium in the perspirate resulting from the electrolyte transport through GDEs, found in the trap following the gas outlet.

The wettability of as-purchased GDLs, as prepared GDEs and GDEs subjected to electrolysis performed as described above was assessed by contact angle measurement (Krüss Advance Drop Shape Analyzer DSA25, Krüss GmbH, Hamburg, Germany). Electrodes subjected to the electrolysis were dried for 2 h before actual measurements. All inspected samples were mounted on a flat stage, sessile water drops (Milli-Q water, 1.4 µL) were deposited on their top at room temperature and contact angles were recorded immediately after creating droplets.

Statistical Analysis: For data presented in the form expected value ± error in the paper, the expected value was determined as the arithemetic mean, and the error as the standard deviation of the dataset. Contact angle intervals reported in the text were calculated using values shown in Figure S7, Supporting Information, by averaging over different GDEs that underwent the same electrolysis treatment. The optical micrographs of the as-prepared GDEs (Figure 2) were used for the calculation of surface CRs of the GDEs. The micrographs were utilized to determine the surface CR based on counting pixels corresponding to cracks and solid regions on the MPL surface: the analysis was done by an in-house developed algorithm written in LabVIEW. The void ratios of the carbon fibrous and MPLs of GDLs, as well as the total void ratios of CFLs, MPLs, and entire GDLs, shown in Table 1, were determined by three parallel pycnometer-based densitometry measurements. The vertical depth profiles of K^+ concentrations, shown in Figure 6, were created using cross-sectional EDX maps obtained from the respective GDEs following electrolyzes. The total (average) K^+ concentrations, corresponding to the integrals of the averaged distribution curves, were determined by a single ICP-MS measurement. In case of each panel of Figure 6, several (five to eight) individual EDX maps were analyzed. These maps were obtained in a numerical format from the Aztec controlling software. Depth profiles were

obtained by a row-to-row summation of the K signal intensity, followed by vertical alignment of the individual distributions. This alignment was based on the assignation of a 0 depth value to the first entry where the detected K intensity reached 3 times the initial noise level. For the alignment, subsequent averaging, and normalization of the distributions, a home-built software (written in LabVIEW) was used; more details of the calculations can be found elsewhere.[77] Raw data serving as a basis for the presented calculations are accessible at Zenodo.[88]

Supporting Information

Supporting Information is available from the Wiley Online Library or from the author.

Acknowledgements

This publication was created as part of NCCR Catalysis (Grant number 180544), a National Centre of Competence in Research funded by the Swiss National Science Foundation. V.K. acknowledges financial support from the Czech Science Foundation (Project number 18-09848S). Y.K., M.L., and H.H. acknowledge the financial support by the Chinese Scholarship Council (CSC). S.V. acknowledges support from the National Research, Development and Innovation Office of Hungary (NKFIH grant FK135375).

Open access funding provided by Universität Bern.

Conflict of Interest

The authors declare no conflict of interest.

Data Availability Statement

The raw data to this paper are made fully accessible to the public via Zenodo (https://doi.org/10.5281/zenodo.6421142) along with the publication of this manuscript.

Keywords

carbon dioxide electroreduction, cracks, flooding, gas diffusion electrodes, microporous layers, perspiration, precipitation

Received: April 7, 2022
Revised: June 28, 2022
Published online: July 10, 2022

[1] I. Ganesh, *Renewable Sustainable Energy Rev.* **2016**, *59*, 1269.
[2] S. Nitopi, E. Bertheussen, S. B. Scott, X. Y. Liu, A. K. Engstfeld, S. Horch, B. Seger, I. E. L. Stephens, K. Chan, C. Hahn, J. K. Norskov, T. F. Jaramillo, I. Chorkendorff, *Chem. Rev.* **2019**, *119*, 7610.
[3] T. Burdyny, W. A. Smith, *Energy Environ. Sci.* **2019**, *12*, 1442.
[4] N. T. Nesbitt, T. Burdyny, H. Simonson, D. Salvatore, D. Bohra, R. Kas, W. A. Smith, *ACS Catal.* **2020**, *10*, 14093.
[5] D. M. Weekes, D. A. Salvatore, A. Reyes, A. X. Huang, C. P. Berlinguette, *Acc. Chem. Res.* **2018**, *51*, 910.
[6] E. W. Lees, B. A. W. Mowbray, F. G. L. Parlane, C. P. Berlinguette, *Nat. Rev. Mater.* **2022**, *7*, 55.
[7] A. Z. Weber, J. Newman, *J. Electrochem. Soc.* **2005**, *152*, A677.
[8] B. Kim, F. Hillman, M. Ariyoshi, S. Fujikawa, P. J. A. Kenis, *J. Power Sources* **2016**, *312*, 192.
[9] E. J. Dufek, T. E. Lister, M. E. McIlwain, *Electrochem. Solid-State Lett.* **2012**, *15*, B48.
[10] S. S. Bhargava, F. Proietto, D. Azmoodeh, E. R. Cofell, D. A. Henckel, S. Verma, C. J. Brooks, A. A. Gewirth, P. J. A. Kenis, *ChemElectroChem* **2020**, *7*, 2001.
[11] S. Verma, Y. Hamasaki, C. Kim, W. X. Huang, S. Lu, H. R. M. Jhong, A. A. Gewirth, T. Fujigaya, N. Nakashima, P. J. A. Kenis, *ACS Energy Lett.* **2018**, *3*, 193.
[12] S. Verma, X. Lu, S. C. Ma, R. I. Masel, P. J. A. Kenis, *Phys. Chem. Chem. Phys.* **2016**, *18*, 7075.
[13] B. Kim, S. Ma, H. R. M. Jhong, P. J. A. Kenis, *Electrochim. Acta* **2015**, *166*, 271.
[14] C. M. Gabardo, A. Seifitokaldani, J. P. Edwards, C. T. Dinh, T. Burdyny, M. G. Kibria, C. P. O'Brien, E. H. Sargent, D. Sinton, *Energy Environ. Sci.* **2018**, *11*, 2531.
[15] V. R. Stamenkovic, D. Strmcnik, P. P. Lopes, N. M. Markovic, *Nat. Mater.* **2017**, *16*, 57.
[16] J. Lee, J. Lim, C. W. Roh, H. S. Whang, H. Lee, *J. CO_2 Util.* **2019**, *31*, 244.
[17] L. C. Weng, A. T. Bell, A. Z. Weber, *Energy Environ. Sci.* **2019**, *12*, 1950.
[18] A. Angulo, P. van der Linde, H. Gardeniers, M. Modestino, D. F. Rivas, *Joule* **2020**, *4*, 555.
[19] L. Cindrella, A. M. Kannan, J. F. Lin, K. Saminathan, Y. Ho, C. W. Lin, J. Wertz, *J. Power Sources* **2009**, *194*, 146.
[20] M. L. Liu, Y. Kong, H. F. Hu, N. Kovacs, C. Z. Sun, I. Z. Montiel, M. D. G. Vazquez, Y. Hou, M. Mirolo, I. Martens, J. Drnec, S. Vesztergom, P. Broekmann, *J. Catal.* **2021**, *404*, 371.
[21] M. D. Galvez-Vazquez, S. Alinejad, H. F. Hu, Y. H. Hou, P. Moreno-Garcia, A. Zana, G. K. H. Wiberg, P. Broekmann, M. Arenz, *Chimia* **2019**, *73*, 922.
[22] M. D. Galvez-Vazquez, P. Moreno-Garcia, H. Xu, Y. H. Hou, H. F. Hu, I. Z. Montiel, A. V. Rudnev, S. Alinejad, V. Grozovski, B. J. Wiley, M. Arenz, P. Broekmann, *ACS Catal.* **2020**, *10*, 13096.
[23] M. Maja, C. Orecchia, M. Strano, P. Tosco, M. Vanni, *Electrochim. Acta* **2000**, *46*, 423.
[24] N. Wagner, M. Schulze, E. Gulzow, *J. Power Sources* **2004**, *127*, 264.
[25] Z. Xing, X. Hu, X. F. Feng, *ACS Energy Lett.* **2021**, *6*, 1694.
[26] Z. Xing, L. Hu, D. S. Ripatti, X. Hu, X. F. Feng, *Nat. Commun.* **2021**, *12*, 136.
[27] W. H. Lee, Y. J. Ko, Y. Choi, S. Y. Lee, C. H. Choi, Y. J. Hwang, B. K. Min, P. Strasser, H. S. Oh, *Nano Energy* **2020**, *76*, 105030.
[28] U. O. Nwabara, A. D. Hernandez, D. A. Henckel, X. Y. Chen, E. R. Cofell, M. P. De-Heer, S. Verma, A. A. Gewirth, P. J. A. Kenis, *ACS Appl. Energy Mater.* **2021**, *4*, 5175.
[29] A. Reyes, R. P. Jansonius, B. A. W. Mowbray, Y. Cao, D. G. Wheeler, J. Chau, D. J. Dvorak, C. P. Berlinguette, *ACS Energy Lett.* **2020**, *5*, 1612.
[30] T. Burchardt, *J. Power Sources* **2004**, *135*, 192.
[31] K. Liu, W. A. Smith, T. Burdyny, *ACS Energy Lett.* **2019**, *4*, 639.
[32] A. Lowe, C. Rieg, T. Hierlemann, N. Salas, D. Kopljar, N. Wagner, E. Klemm, *ChemElectroChem* **2019**, *6*, 4497.
[33] K. J. Puring, D. Siegmund, J. Timm, F. Mollenbruck, S. Schemme, R. Marschall, U. P. Apfel, *Adv. Sustainable Syst.* **2021**, *5*, 2000088.
[34] F. Bienen, A. Lowe, J. Hildebrand, S. Hertle, D. Schonvogel, D. Kopljar, N. Wagner, E. Klemm, K. A. Friedrich, *J. Energy Chem.* **2021**, *62*, 367.
[35] F. Bienen, J. Hildebrand, D. Kopljar, N. Wagner, E. Klemm, K. A. Friedrich, *Chem. Ing. Tech.* **2021**, *93*, 1015.
[36] K. L. Yang, R. Kas, W. A. Smith, T. Burdyny, *ACS Energy Lett.* **2021**, *6*, 33.
[37] B. De Mot, J. Hereijgers, M. Duarte, T. Breugelmans, *Chem. Eng. J.* **2019**, *378*, 122224.
[38] P. Jeanty, C. Scherer, E. Magori, K. Wiesner-Fleischer, O. Hinrichsen, M. Fleischer, *J. CO_2 Util.* **2018**, *24*, 454.
[39] M. Duarte, B. De Mot, J. Hereijgers, T. Breugelmans, *ChemElectroChem* **2019**, *6*, 5596.
[40] S. Sen, S. M. Brown, M. Leonard, F. R. Brushett, *J. Appl. Electrochem.* **2019**, *49*, 917.

[41] D. G. Wheeler, B. A. W. Mowbray, A. Reyes, F. Habibzadeh, J. F. He, C. P. Berlinguette, *Energy Environ. Sci.* **2020**, *13*, 5126.
[42] B. Endrodi, E. Kecsenovity, A. Samu, F. Darvas, R. V. Jones, V. Torok, A. Danyi, C. Janaky, *ACS Energy Lett.* **2019**, *4*, 1770.
[43] M. E. Leonard, M. J. Orella, N. Aiello, Y. Roman-Leshkov, A. Forner-Cuenca, F. R. Brushett, *J. Electrochem. Soc.* **2020**, *167*, 124521.
[44] H. Li, Y. H. Tang, Z. W. Wang, Z. Shi, S. H. Wu, D. T. Song, J. L. Zhang, K. Fatih, J. J. Zhang, H. J. Wang, Z. S. Liu, R. Abouatallah, A. Mazza, *J. Power Sources* **2008**, *178*, 103.
[45] K. Jiao, X. G. Li, *Prog. Energy Combust. Sci.* **2011**, *37*, 221.
[46] N. Yousfi-Steiner, P. Mocoteguy, D. Candusso, D. Hissel, A. Hernandez, A. Aslanides, *J. Power Sources* **2008**, *183*, 260.
[47] P. C. Pei, H. C. Chen, *Appl. Energy* **2014**, *125*, 60.
[48] M. B. Ji, Z. D. Wei, *Energies* **2009**, *2*, 1057.
[49] A. Bazylak, *Int. J. Hydrogen Energy* **2009**, *34*, 3845.
[50] S. Tsushima, S. Hirai, *Prog. Energy Combust. Sci.* **2011**, *37*, 204.
[51] R. Omrani, B. Shabani, *Int. J. Hydrogen Energy* **2017**, *42*, 28515.
[52] S. Tsushima, S. Hirai, *J. Therm. Sci. Technol.* **2015**, *10*, JTST0002.
[53] T. Sasabe, P. Deevanhxay, S. Tsushima, S. Hirai, *Electrochem. Commun.* **2011**, *13*, 638.
[54] E. A. Wargo, V. P. Schulz, A. Cecen, S. R. Kalidindi, E. C. Kumbur, *Electrochim. Acta* **2013**, *87*, 201.
[55] M. P. Manahan, S. Kim, E. C. Kumbur, M. M. Mench, *ECS Trans.* **2009**, *25*, 1745.
[56] H. Markotter, I. Manke, P. Kruger, T. Arlt, J. Haussmann, M. Klages, H. Riesemeier, C. Hartnig, J. Scholta, J. Banhart, *Electrochem. Commun.* **2011**, *13*, 1001.
[57] N. Karst, V. Faucheux, A. Martinent, P. Bouillon, J. P. Simonato, *J. Power Sources* **2010**, *195*, 5228.
[58] J. S. Ma, X. X. Zhang, Z. Y. Jiang, H. Ostadi, K. Jiang, R. Chen, *Fuel* **2014**, *136*, 307.
[59] D. Gerteisen, C. Sadeler, *J. Power Sources* **2010**, *195*, 5252.
[60] K. Nishida, T. Murakami, S. Tsushima, S. Hirai, *J. Power Sources* **2010**, *195*, 3365.
[61] R. L. Cook, R. C. Macduff, A. F. Sammells, *J. Electrochem. Soc.* **1990**, *137*, 607.
[62] G. L. De Gregorio, T. Burdyny, A. Loiudice, P. Iyengar, W. A. Smith, R. Buonsanti, *ACS Catal.* **2020**, *10*, 4854.
[63] M. Jouny, W. Luc, F. Jiao, *Nat. Catal.* **2018**, *1*, 748.
[64] J. J. Lv, M. Jouny, W. Luc, W. L. Zhu, J. J. Zhu, F. Jiao, *Adv. Mater.* **2018**, *30*, 1803111.
[65] C. M. Gabardo, C. P. O'Brien, J. P. Edwards, C. McCallum, Y. Xu, C. T. Dinh, J. Li, E. H. Sargent, D. Sinton, *Joule* **2019**, *3*, 2777.
[66] E. R. Cofell, U. O. Nwabara, S. S. Bhargava, D. E. Henckel, P. J. A. Kenis, *ACS Appl. Mater. Interfaces* **2021**, *13*, 15132.
[67] C. T. Dinh, T. Burdyny, M. G. Kibria, A. Seifitokaldani, C. M. Gabardo, F. P. G. de Arquer, A. Kiani, J. P. Edwards, P. De Luna, O. S. Bushuyev, C. Q. Zou, R. Quintero-Bermudez, Y. J. Pang, D. Sinton, E. H. Sargent, *Science* **2018**, *360*, 783.
[68] M. E. Leonard, L. E. Clarke, A. Forner-Cuenca, S. M. Brown, F. R. Brushett, *ChemSusChem* **2020**, *13*, 400.
[69] D. McLaughlin, M. Bierling, R. Moroni, C. Vogl, G. Schmid, S. Thiele, *Adv. Energy Mater.* **2020**, *10*, 2000488.
[70] D. Raciti, T. Braun, B. M. Tackett, H. Xu, M. Cruz, B. J. Wiley, T. P. Moffat, *ACS Catal.* **2021**, *11*, 11945.
[71] G. O. Larrazabal, P. Strom-Hansen, J. P. Heli, K. Zeiter, K. T. Therldldsen, I. Chorkendorff, B. Seger, *ACS Appl. Mater. Interfaces* **2019**, *11*, 41281.
[72] J. Li, G. X. Chen, Y. Y. Zhu, Z. Liang, A. Pei, C. L. Wu, H. X. Wang, H. R. Lee, K. Liu, S. Chu, Y. Cui, *Nat. Catal.* **2018**, *1*, 592.
[73] A. Patru, T. Binninger, B. Pribyl, T. J. Schmidt, *J. Electrochem. Soc.* **2019**, *166*, F34.
[74] B. De Mot, M. Ramdin, J. Hereijgers, T. J. H. Vlugt, T. Breugelmans, *ChemElectroChem* **2020**, *7*, 3839.
[75] B. Endrodi, E. Kecsenovity, A. Samu, T. Halmagyi, S. Rojas-Carbonell, L. Wang, Y. Yan, C. Janaky, *Energy Environ. Sci.* **2020**, *13*, 4098.
[76] B. Endrodi, A. Samu, E. Kecsenovity, T. Halmagyi, D. Sebok, C. Janaky, *Nat. Energy* **2021**, *6*, 439.
[77] Y. Kong, H. F. Hu, M. L. Liu, Y. Hou, V. Kolivoska, S. Vesztergom, P. Broekmann, *J. Catal.* **2022**, *408*, 1.
[78] A. J. Welch, A. Q. Fenwick, A. Bohme, H. Y. Chen, I. Sullivan, X. Q. Li, J. S. DuChene, C. X. Xiang, H. A. Atwater, *J. Phys. Chem. C* **2021**, *125*, 20896.
[79] G. K. H. Wiberg, M. Fleige, M. Arenz, *Rev. Sci. Instrum.* **2015**, *86*, 024102.
[80] Y. H. Hou, N. Kovacs, H. Xu, C. Z. Sun, R. Erni, M. D. Galvez-Vazquez, A. Rieder, H. F. Hu, Y. Kong, M. L. Liu, B. J. Wiley, S. Vesztergom, P. Broekmann, *J. Catal.* **2021**, *394*, 58.
[81] L. C. Weng, A. T. Bell, A. Z. Weber, *Phys. Chem. Chem. Phys.* **2018**, *20*, 16973.
[82] M. Ma, S. Kim, I. Chorkendorff, B. Seger, *Chem. Sci.* **2020**, *11*, 8854.
[83] M. Ma, E. L. Clark, K. T. Therkildsen, S. Dalsgaard, I. Chorkendorff, B. Seger, *Energy Environ. Sci.* **2020**, *13*, 977.
[84] G. M. Geise, M. A. Hickner, B. E. Logan, *ACS Appl. Mater. Interfaces* **2013**, *5*, 10294.
[85] M. Roehe, A. Botz, D. Franzen, F. Kubannek, B. Ellendorff, D. Oehl, W. Schuhmann, T. Turek, U. Krewer, *ChemElectroChem* **2019**, *6*, 5671.
[86] N. T. Nesbitt, W. A. Smith, *J. Phys. Chem. C* **2021**, *125*, 13085.
[87] H. F. Hu, M. L. Liu, Y. Kong, N. Mysuru, C. Z. Sun, M. D. Galvez-Vazquez, U. Muller, R. Erni, V. Grozovski, Y. H. Hou, P. Broekmann, *ACS Catal.* **2020**, *10*, 8503.
[88] Y. Kong, M. Liu, H. Hu, Y. Hou, S. Vesztergom, M. de J. Gálvez-Vázquez, I. Zelocualtecatl Montiel, V. Kolivoška, P. Broekmann, Raw data for the article "Cracks as efficient tools to mitigate flooding in gas diffusion electrodes used for the electrochemical reduction of carbon dioxide" **2022**, https://doi.org/10.5281/zenodo.6421142.

5. Effective perspiration is essential to uphold the stability of zero-gap MEA-based cathodes used in CO_2 electrolysers

Authors: Huifang Hu, Ying Kong, Menglong Liu, Viliam Kolivoška, Alexander V. Rudnev, Yuhui Hou, Rolf Erni, Soma Vesztergom, and Peter Broekmann.

***J. Mater. Chem. A*, 2023, 11, 5083–5094, e202200615. DOI: 10.1002/smtd.202200369**

Highlight: The effect of the content of capping agents on the stability of a semi-zero-gap electrolyzer was investigated. Capping agents are commonly applied to stabilize Ag-NPs. However, if these surfactant-capped Ag-NPs are co-deposited on the GDLs, the excess polymeric capping agents (i.e., PVP and BPEI) would clog the transport channels of the MPL thus resulting in and accelerated performance loss due to massive flooding/salt precipitation in the CL. The content of excess capping agents in the ink formulation could be substantially reduced by ultracentrifugation of the Ag-NP suspension prior to the ink formulation. This resulted in a higher ability of the GDE to perspire electrolyte during ec-CO_2RR and into sustained GDE stability.

Contribution: I performed some parts of the electrochemical measurements and have been involved in the discussion of the results. I actively contributed to the revision of the manuscript text.

Journal of Materials Chemistry A

ROYAL SOCIETY OF CHEMISTRY

PAPER

View Article Online
View Journal | View Issue

Check for updates

Cite this: J. Mater. Chem. A, 2023, 11, 5083

Effective perspiration is essential to uphold the stability of zero-gap MEA-based cathodes used in CO_2 electrolysers†

Huifang Hu, [a] Ying Kong,[a] Menglong Liu,[a] Viliam Kolivoška, [b] Alexander V. Rudnev, [ac] Yuhui Hou,[a] Rolf Erni, [d] Soma Vesztergom *[ae] and Peter Broekmann *[a]

The application of gas diffusion electrodes (GDEs) for the electrochemical reduction of CO_2 to value-added products creates the possibility of achieving current densities of a few hundred mA cm^{-2}. To achieve stable operation at such high reaction rates remains, however, a challenging task, due to the flooding of the GDE. In order to mitigate flooding in a zero-gap membrane-electrode assembly (MEA) configuration, paths for effective electrolyte perspiration inside the GDE structure have to be kept open during the electrolysis process. Here we demonstrate that apart from the operational parameters of the electrolysis and the structural properties of the supporting gas diffusion layers, also the chemical composition of the applied catalyst inks can play a decisive role in the electrolyte management of GDEs used for CO_2 electroreduction. In particular, the presence of excess amounts of polymeric capping agents (used to stabilize the catalyst nanoparticles) can lead to a blockage of micropores, which hinders perspiration and initiates the flooding of the microporous layer. Here we use a novel ICP-MS analysis-based approach to quantitatively monitor the amount of perspired electrolyte that exits a GDE-based CO_2 electrolyser, and we show a direct correlation between the break-down of effective perspiration and the appearance of flooding—the latter ultimately leading to a loss of electrolyser stability. We recommend the use of an ultracentrifugation-based approach by which catalyst inks containing no excess amount of polymeric capping agents can be formulated. Using these inks, the stability of electrolyses can be ensured for much longer times.

Received 2nd September 2022
Accepted 5th December 2022

DOI: 10.1039/d2ta06965b

rsc.li/materials-a

1 Introduction

Global warming, caused by the burning of fossil fuels and the resulting rapid increase of atmospheric CO_2 levels, is regarded as one of the most serious problems faced by human society. From this respect, electrochemical CO_2 reduction deserves special attention. Propelled by excess renewable energy sources, this process may not only provide viable means to reduce CO_2 emissions, but it can also create the possibility of converting excess energy into the form of storable fuels.[1]

The successful design of industrial level CO_2 electrolysers that can be operated for extended periods of time, converting CO_2 to a set of desired products at high rate and at low energy costs, requires a well-coordinated interplay of all electrolyser constituents.[2–5] From the chemistry, yet not from the overall efficiency point of view, the most essential part of a CO_2 electrolyser unit is the cathode catalyst: this is the scene where the actual transition of CO_2—its reduction to value-added products—takes place. In the past three decades, huge research efforts have thus been invested in the development of electrocatalysts that can achieve considerable reaction yields, preferably at low overvoltages.[6,7]

Today, researchers agree that apart from their chemical composition it is also the nanoscale structure of electrocatalysts that mostly affect their performance in CO_2 electroreduction.[8–10] Metallic catalysts of nanoparticulate (NP) form, for example, usually exhibit a much higher mass-normalised activity than planar metallic surfaces.[11] This is mostly due to the large surface area of NPs that offers more active sites with low coordination numbers, enabling improved performances.[12] Metallic

[a]NCCR Catalysis, University of Bern, Department of Chemistry, Biochemistry and Pharmaceutical Sciences, Freiestrasse 3, 3012 Bern, Switzerland. E-mail: peter.broekmann@unibe.ch; vesztergom@chem.elte.hu

[b]J. Heyrovský Institute of Physical Chemistry of the Czech Academy of Sciences, Dolejškova 3, 182 23 Prague, Czechia

[c]A. N. Frumkin Institute of Physical Chemistry and Electrochemistry, Russian Academy of Sciences, Leninsky Prospekt 31, 119071 Moscow, Russia

[d]Swiss Federal Laboratories for Materials Science and Technology (EMPA), Electron Microscopy Center, Überlandstrasse 129, 8600 Dübendorf, Switzerland

[e]Eötvös Loránd University, MTA-ELTE Momentum Interfacial Electrochemistry Research Group, Pázmány Péter Sétány 1/A, 1117 Budapest, Hungary

† Electronic supplementary information (ESI) available. See DOI: https://doi.org/10.1039/d2ta06965b

NPs thus seem to become the most favoured catalysts used in today's CO_2 electrolysers, and the reason for this is not only their low raw material cost, but also that they can easily be applied in gas diffusion electrodes (GDEs).

The main advantage of using GDEs as cathodes for CO_2 electroreduction is that they circumvent the problem of limited solubility and slow transport in aqueous media, by allowing CO_2 to access the catalyst layer mostly in a gas phase.[13] In GDEs, the catalyst is supported by a gas diffusion layer (GDL) that is composed of a carbon fibrous layer (CFL) and a microporous layer (MPL), as shown in Fig. 1a. Besides enabling fast reactant delivery, the GDL also facilitates the release of gaseous reaction products, serves as a mechanical support and electrical contact for the catalyst, and plays important role in controlling the amount of electrolyte in the catalyst layer.[14]

In so-called zero-gap membrane-electrode assemblies (MEAs, see Fig. 1a for a model-scale version), the GDE is directly interfaced to an anion exchange membrane, the primary role of which is to control the amount of water (an important reactant of cathodic CO_2 reduction) reaching the catalyst layer, while anionic species (carbonate or hydroxide ions) can be transported away from it,[15] in the direction of the anode. The membrane should further assure that no volatile cathode-generated products can cross over to the anode, thereby reducing the efficiency of electrolysis.[16] When zero-gap MEA cathodes are employed in electrolyser set-ups similar to that shown in Fig. 1, current densities ranging a few hundred mA cm^{-2} can be achieved.[17]

Provided that at a given catalyst CO_2 reduction yields only gas-phase carbon-containing products, the configuration shown in Fig. 1 indeed provides an excellent platform for the performance and stability testing of catalyst materials. We have recently shown, for example, that when Ag nanocubes are used to catalyse CO_2 electroreduction (on Ag, the reaction almost exclusively yields CO), catalyst corrosion at stringent cathodic conditions occurs, and leads to truncated cube morphologies and the appearance of smaller Ag NPs.[17] When using, on the other hand, Ag nanospheres protected by different ligands as a catalyst, degradation was shown to follow different pathways including corrosion, aggregation and even Ostwald ripening[18]—all depending on the chemical nature of the stabilizing ligand. In ref. 17 and 18 we have also found, however, that the degradation of Ag NPs, while it does occur at harshly cathodic operating conditions, is not in itself responsible for the observed, often severe, stability issues of the CO_2 electrolysis process performed in zero-gap MEA cathode configurations.

In zero-gap MEA cathode-based electrolysers, stability losses rather occur due to the flooding of the MPL during prolonged electrolyses. Flooding is the excess hydration of the GDE that can severely limit or even block the access of CO_2 to the catalyst layer, leading to the decrease of the observable faradaic efficiency (FE) of CO_2 reduction products and the appearance of parasitic hydrogen evolution.[14,19,20] The rapid flooding of GDEs, and the related stability issues are currently recognised as the biggest obstacle in front of the scale-up prospects[21] of CO_2 electroreduction. As a result, the focus of studies in the field of CO_2 electrolysis has recently shifted from the identification of new catalyst materials to other, more engineering-related tasks that include the optimisation of electrolyser geometries, the design of GDEs and membranes, and the fine-tuning of the applied process parameters.[2]

Amongst these tasks, the adaptation of design strategies that can help prevent, or at least slow down flooding-related stability losses are of prime importance. It was recently shown, for example, that the presence of sub-millimeter wide cracks in the MPL can effectively mitigate the flooding of GDEs during CO_2 electrolysis utilizing Ag nanowire catalysts.[20] Rapid flooding, in this case, was avoided by a pathway that the surface cracks of the MPL enabled for electrolyte perspiration[22,23] in addition to those provided by micropores.[20]

At this point it is important to emphasize the conceptual difference between electrolyte perspiration and flooding.

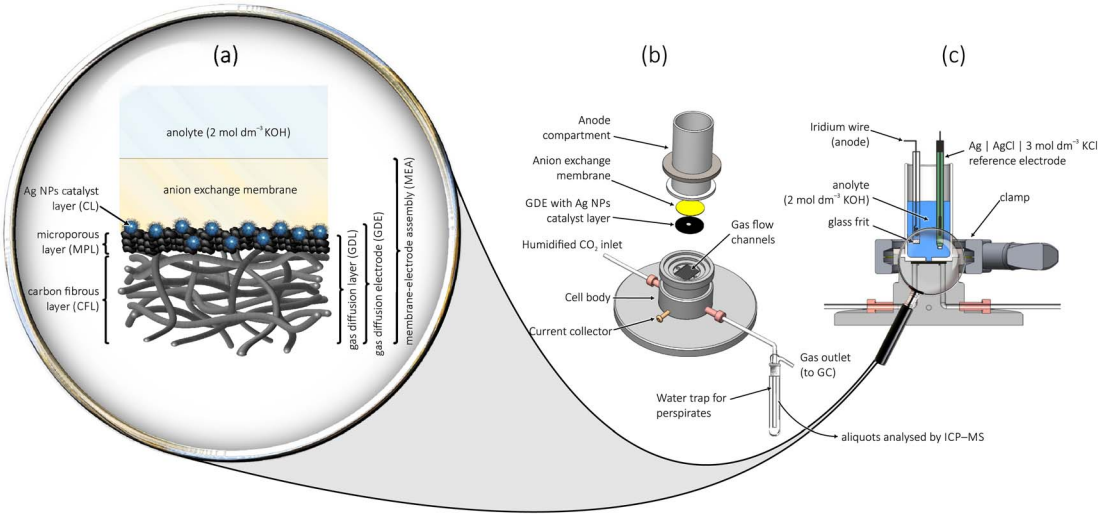

Fig. 1 A zero-gap membrane-electrode assembly (MEA) cathode employing a gas diffusion electrode, used in a flow-cell for the electrolysis of CO_2. Part (a) shows a close-up view of the MEA, parts (b) and (c) show the exploded and the cross-sectional view of the model-scale electrolyser.

Perspiration (a term we owe to Jeanty *et al.*[22]) refers to the crossover of electrolyte through the GDE structure, which ultimately results in the appearance of electrolyte droplets on the back side of the GDE, and even in the gas outflow of the cathode gas compartment. The somewhat interrelated effect of flooding occurs when the electrolyte that entered the GDE structure has no means to escape it, so it remains adhered to the MPL. This trapped electrolyte, due to its large KOH concentration, reacts with CO_2 and forms a large amount of carbonate (or bicarbonate) plaques that will limit and eventually block the access of CO_2 to the catalyst particles.

As was recently pointed out,[20,22,23] the flooding of the catalyst layer and the entrapment of electrolyte inside the GDE structure can be avoided by taking measures to uphold optimal perspiration rates, *e.g.*, by the selection of appropriate cathode-side CO_2 flow rates[22,23] or the application of GDLs with cracked surfaces.[20] Apart from optimizing the structure of MPLs or the operational parameters of electrolyses there is, however, more room for development, especially if we consider that essentially all parts of the MEA can influence flooding and perspiration phenomena. In this vein, the aim of the present paper will be to identify a critical point of zero-gap MEA cathode fabrication for CO_2 reduction: that is, the excess use of polymeric capping agents (CAs) in the catalyst ink formulations of Ag NP-based catalysts, and its flooding promoting—perspiration blocking—effect.

CAs are commonly used in the synthesis of metallic NPs to achieve uniform and stable size distribution of the particles. By adsorbing to the surface of the NPs, CAs prevent their aggregation either by providing sterical or electro-repulsive protection.[24] For the synthesis of Ag NPs, poly-(vinylpyrrolidone) (PVP) and branched polyethylenimine (BPEI) are very often used polymeric CAs that provide sterical protection to the NPs,[17,25–28] while on the other hand citrate ions are often used as a non-polymeric (coulombic repulsion based) stabilizer.[29]

Practically regardless of the nature of the stabilizing CA, in aqueous Ag NP dispersions—either self-synthesised or purchased off-the-shelf—CAs are usually present at a rather high concentration, with not all of the ligand molecules adsorbed on the surfaces of NPs, but a majority of them being dissolved in the liquid phase.

In this study we show that the excess polymeric CA content, if not removed from the catalyst ink, blocks perspiration channels and acts as a promoter of flooding, thereby causing serious stability issues observed in zero-gap MEA cathode-based electrolysers used for CO_2 electroreduction.[30] In the paper we utilize a novel ICP-MS analysis-based approach to quantitatively monitor the amount of perspired electrolyte that exits the zero-gap MEA cathode and ends up in the water trap equipped to the gas outflow channel of the electrolyser (see Fig. 1b). We show a direct correlation between the breakdown of effective perspiration and the appearance of flooding in the MPL—the latter ultimately leading to a loss of electrolyser stability. We also present a simple ultracentrifugation technique, by which the polymeric CA content of formulated catalyst inks can be reduced, and we show that this strategy in itself helps to provide longer time stability to CO_2 electrolysers operated at high current densities. In the paper we work with PVP- and BPEI-capped Ag NPs as representatives of polymeric CA-stabilised catalysts, and we also extend our tests to Ag NPs stabilised by citrate ligands (see Fig. 2 for the applied ligand structures). We come to the conclusion that the small, monomeric ligand (citrate) has less adverse effects on the electrolysis durability.

The use of the model scale electrolyser shown in Fig. 1 for the electrochemical stress-test of GDE cathodes in a zero-gap cathode MEA configuration is particularly advantageous, since due to its small effective cross-section (that limits the geometric surface area of the cathode to 0.0707 cm^2, see the Experimental section for details) the cell enables high current densities to be reached at the cost of relatively small applied currents (see Fig. S1 in ESI†). Furthermore, due to more pronounced edge effects introduced by the small cathode area,[31] cell failures already manifest during relatively short (few hours long) electrolyses, making our test system a promising tool for the accelerated durability testing[32] of CO_2-to-CO converting GDEs.

2 Experimental

Ag NP suspensions: CA removal

PVP-capped spherical Ag NP suspensions (of ~10 nm and ~100 nm diameter), BPEI-capped spherical Ag NP suspensions (of ~50 nm diameter) and citrate-capped Ag NP suspensions (also of ~50 nm diameter) were purchased from Nano-Composix (all water-based, with a concentration of 1 mg cm^{-3}). The suspensions were either used as-purchased for the preparation of catalyst inks, or—in order to remove at least some of their CA content—were made subject to centrifugation. In this latter case, the suspensions were first diluted 8-fold, and then centrifuged in an Optima XPN-80 Ultracentrifuge (Beckman Coulter) for 40 min at 35 000 rpm.

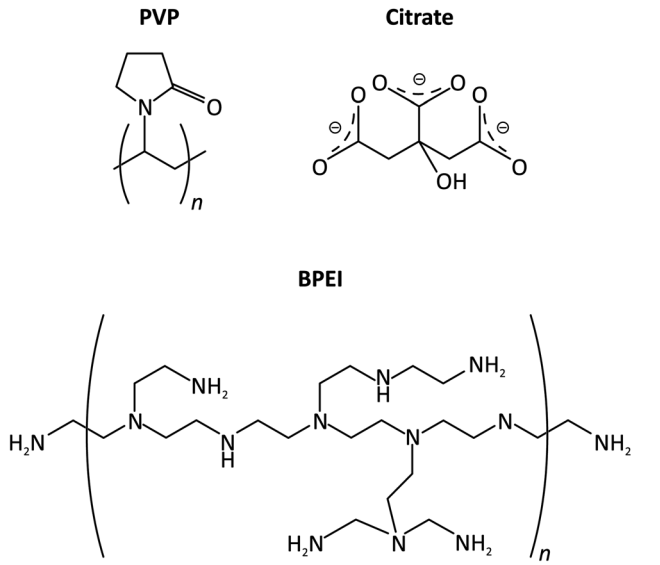

Fig. 2 The structure of CAs studied in this paper, used for the stabilisation of Ag NP suspensions.

(Suspensions with a nanoparticle diameter of ~10 nm were centrifuged for an additional 40 min at 50 000 rpm.) Following decantation of the supernatant, NPs in the pellet were re-dispersed in ultrapure water (Milli-Q by Merck Millipore, 18.2 MΩ cm specific resistance) to restore the original concentration of 1 mg cm^{-3}. The 8-fold dilution/centrifugation/re-dispersion steps were then repeated once for an as thorough as possible removal of the CA content (steps are illustrated by Fig. 3). To quantify the effectiveness of CA removal, total organic carbon content (TOC) and total nitrogen content (TNC) measurements were made for the supernatant of the first centrifugation step and for the finally obtained (for better comparability, 8-fold diluted) CA-deficient suspension (see Table 1 for results). For TOC and TNC determination, 0.1 cm^3 sample volumes were fed into a DIMATOC 2100 instrument (Dimatec Analysentechnik GmbH, Essen, Germany). The organic compounds were oxidized at 850 °C with Pt catalyst to CO_2 and NO, the amounts of which were quantified by a non-dispersive infrared gas sensor with a reflective diffuser and a chemiluminescence detector, respectively.

Catalyst ink preparation

Ag NP suspensions with 1 mg cm^{-3} Ag content (either as-purchased or centrifuged) were used for the catalyst ink preparation. A 1 cm^3 volume of the Ag NP suspension was mixed with 627 µl of isopropanol (VLSI Selectipur, BASF, Germany). A second suspension was then made by dispersing carbon black (Vulcan XC 72R, Cabot) in isopropanol in a 0.5 mg cm^{-3} concentration by 1 hour sonication. The Ag NP suspension and 353 µl of the carbon black suspension were then intermixed, 20 µl of Nafion solution (5% in a mixture of lower aliphatic alcohols and water, Sigma-Aldrich) was added, and the resulting ink was homogenised by 5 min sonication.

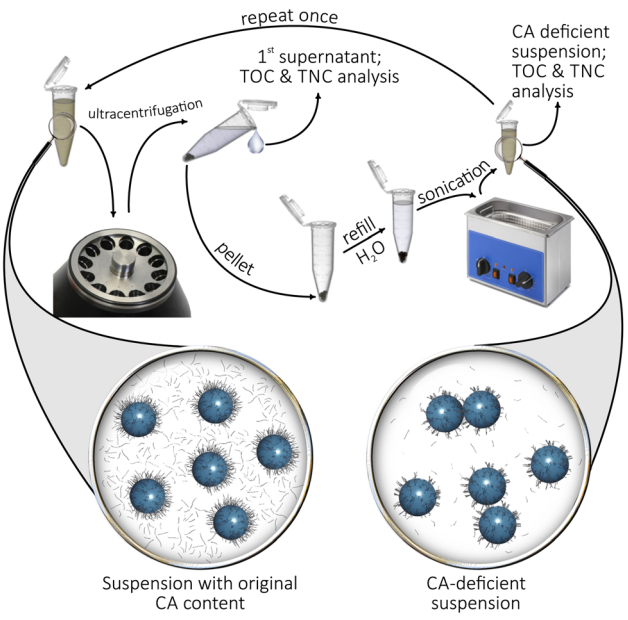

Fig. 3 Scheme of the ultracentrifugation-based method used for the removal of the excess CA content of Ag NP suspensions.

Table 1 Total organic carbon content (TOC) and total nitrogen content (TNC) determined in the Ag NP suspensions. Before: values measured in the supernatant of the first centrifugation step. After: values measured in the finally obtained 1 mg cm^{-3} suspension, following 8-fold dilution. *Cf.* to Fig. 3

Capping agent	Nominal size of Ag NPs	TOC/ppm		TNC/ppm	
		Before	After	Before	After
PVP	~10 nm	43.15	6.12	7.88	0.69
PVP	~100 nm	28.51	4.45	4.24	0.33
BPEI	~50 nm	7.53	3.81	3.09	—
Citrate	~50 nm	15.21	2.88	—	—

Preparation of the GDEs

75 µl of the prepared catalyst ink was drop-cast on the microporous surface of a circular Sigracet 36BB (FuelCellStore) GDL with 4 mm of diameter to form a GDE. Electrodes were dried at ambient conditions. Drop-casting 75 µl of the catalyst ink resulted in a nominal mass loading of ~300 µg cm^{-2} for silver. GDEs with lower loading were prepared by drop-casting proportionally less amount of the catalyst ink.

Assembly of the electrolyser

The electrolyser shown in Fig. 1 was used to carry out electrochemical CO_2 reduction. The bottom part of the electrolyser is made of stainless steel and is equipped with gas flow channels. The small circular GDEs containing the Ag NP catalyst were placed in a centrally located 4 mm diameter hole of a Freudenberg H23C8 (FuelCellStore) carbon paper with an external diameter of 2 cm, with the catalyst layer facing upwards and the bottom CFL facing the gas flow channels. The GDE was covered by a hydroxide-functionalised Sustainion anion exchange membrane (X3750 RT, Dioxide Materials, diameter of 2 cm) from above, before fixing the Teflon-made anode compartment on top. The anode compartment has a central orifice on its bottom, allowing access of the anolyte to the membrane. The orifice is of 3 mm diameter and it determines the geometric surface area (0.0707 cm^2) of the GDE. The anode compartment is filled with 10 cm^3 of 2 mol per dm^3 KOH solution (reagent grade, 90%, Sigma-Aldrich), and contains an Ag|AgCl|3 mol per dm^3 KCl reference electrode (double junction, Metrohm) and an Ir wire anode (99.9%, Goodfellow GmbH). The anode is placed inside a small chamber and is separated from the rest of the anolyte by glass frit, as shown in Fig. 1.

Electrochemical measurements and product analysis

All electrochemical measurements were carried out using an ECi-200 potentiostat (Nordic Electrochemistry) at constant current. The applied currents of −20, −10 and −5 mA correspond to geometric surface area normalised current densities of −283.0, −141.5 and −70.7 mA cm^{-2}. Cathode potentials reported in the paper are all referred to the applied Ag|AgCl|3 mol per dm^3 KCl reference electrode, and are corrected for IR drop (the cell resistance was followed by high frequency impedance measurements). On the Ag NP catalysts used in our studies, CO was the only detectable gaseous

product of CO_2 reduction with H_2 formed as the product of parasitic hydrogen evolution. Gaseous reaction products were analysed by connecting the gas outlet of the electrolyser to a gas chromatograph (SRI Instruments Multigas Analyzer). The continuous flow of the carrier CO_2 gas through the electrolysis cell carried reaction products from the gas outlet of the electrolyser into the sampling loops of the gas chromatograph. The partial current I_i, corresponding to the formation of a gaseous product i, can be calculated[33] as

$$I_i = x_i n_i F v_m, \quad (1)$$

where x_i denotes the mole fraction of the products, determined by GC using an independent calibration standard gas (Carbagas); n_i is the number of electrons involved in the reduction reaction to form a particular product ($n = 2$ for both CO and H_2 formation); $F = 96\,485.3$ C mol^{-1} is Faraday's constant; and v_m is the molar CO_2 gas flow rate measured by a universal flowmeter (7000 GC flowmeter, Ellutia) at the gas outlet of the electrolyser. The faradaic efficiency (FE) of a given reaction product was determined by dividing the respective partial current, calculated from eqn (1), by the total current. A thermal conductivity detector (TCD, for the detection of H_2) and a flame ionization detector (FID, for the detection of CO) were equipped to the gas chromatograph. In our experiments, the formed CO and H_2 amounts accounted for an about 90% FE. Following long time electrolyses, some amounts of formate ($HCOO^-$) were detected in the anolyte compartment, which could account for the less than 100% total FE, although an exact quantification of this product is not possible (due to the fact that formate is partially consumed by oxidation at the anode).

Scanning electron microscopy (SEM), energy-dispersive X-ray spectroscopy (EDX), and transmission electron microscopy (TEM)

A Zeiss Gemini 450 scanning electron microscope equipped with an InLens secondary electron detector and a backscattering detector was used for the morphological analysis of GDEs, prior to and following electrolyses. An accelerating voltage of 5 kV and currents of 70 to 100 pA were applied at a working distance of 4.0 to 5.1 mm. The Smile View software was used to measure the size of particles. Particle size distribution histograms were created by determining the size of at least 500 individual particles based on micrographs taken from at least three randomly selected areas.[18] EDX spectra were acquired and elemental composition maps were composed by using the AZtec 5.0 software (Oxford Instruments). The applied acceleration voltage and current were 10 kV and 1 nA, respectively, and a working distance of 8.5 mm was set for all EDX measurements. For the transmission electron microscopy (TEM) imaging, an FEI Titan Themis instrument was used with an accelerating voltage of 300 kV.

Inductively coupled plasma mass spectrometry (ICP-MS)

ICP-MS (NExION 2000, PerkinElmer) was applied to determine the mass of potassium that perspired through the membrane and the GDE, and exited the electrolyser through the gas outlet. A trap containing 15 cm^3 of ultrapure water was used to collect perspired potassium salts. Aliquots of the collected perspired material were diluted by an appropriate amount of 2% HNO_3 solution (BASF SE, Ludwigshafen, Germany) and the resulting solution samples were injected into the ICP-MS to obtain the content of potassium in perspiration.

Raw data, as well as unprocessed measurement files serving as a basis of this publication can be downloaded from Zenodo.[34]

3 Results and discussion

In this paper we use Ag NPs stabilised by different capping agents (PVP, BPEI and citrate, Fig. 2) for the creation of cathode GDEs that we integrate in the zero-gap MEA configuration (Fig. 1) to carry out durability tests at high current density. In order to study the effect of CAs exerted on the electrolysis stress-tests, in some cases we removed the majority of the CA content from the Ag NP suspensions before preparing the catalyst ink by using the ultracentrifugation-based method described in the Experimental section.

The possibility that (especially, polymeric) CAs can have an adverse effect on the stability of electrolyses first occurred to us when we used as-purchased, PVP-stabilised Ag NPs of ~10 nm nominal diameter in order to formulate catalyst inks with a carbon black support, and we attempted to define the optimal loading of the catalyst by one hour-long galvanostatic electrolyses.

These tests gave the rather counter-intuitive result (Fig. 4) that by increasing the nominal mass loading of Ag, the obtained GDEs became less stable, tending to lose their (initially high) CO production efficiency more quickly, and beginning to form H_2 after shorter and shorter times. Concomitantly with the loss of CO faradaic efficiency, the cathode potential also shifted to more negative values as instead of CO_2 reduction, hydrogen evolution became the dominant electrode reaction.

We found that the above equivocal result (higher loading—less stability) can be explained by another experiment, in which we reduced, by ultracentrifugation, the PVP content of the applied Ag NP dispersion before it was used for the preparation of the catalyst ink. By 2 times centrifugation, the majority of the PVP-content of the ~10 nm Ag NP suspension was removed (see Table 1 in the Experimental section for details), and this helped to maintain the stability of electrolysis even when the catalyst was applied at high loading. Indeed, comparing the plots of the bottom row of Fig. 4 immediately makes it apparent that it was the excess amount of PVP present in the catalyst ink—and not the increase of the silver loading in itself—that exerted a detrimental effect on the stability of electrolysis.

In order to unravel the exact reasons of this effect, we made two GDEs (one prepared from an Ag NP suspension of the original PVP content, other with less PVP) subject to further investigation.

The top-down SEM images (Fig. 5) obtained from the two catalyst layers (one prepared with the original, another with reduced PVP content) reveal only slight differences. Silver NPs well-dispersed in a matrix of carbon flakes over the MPL are well

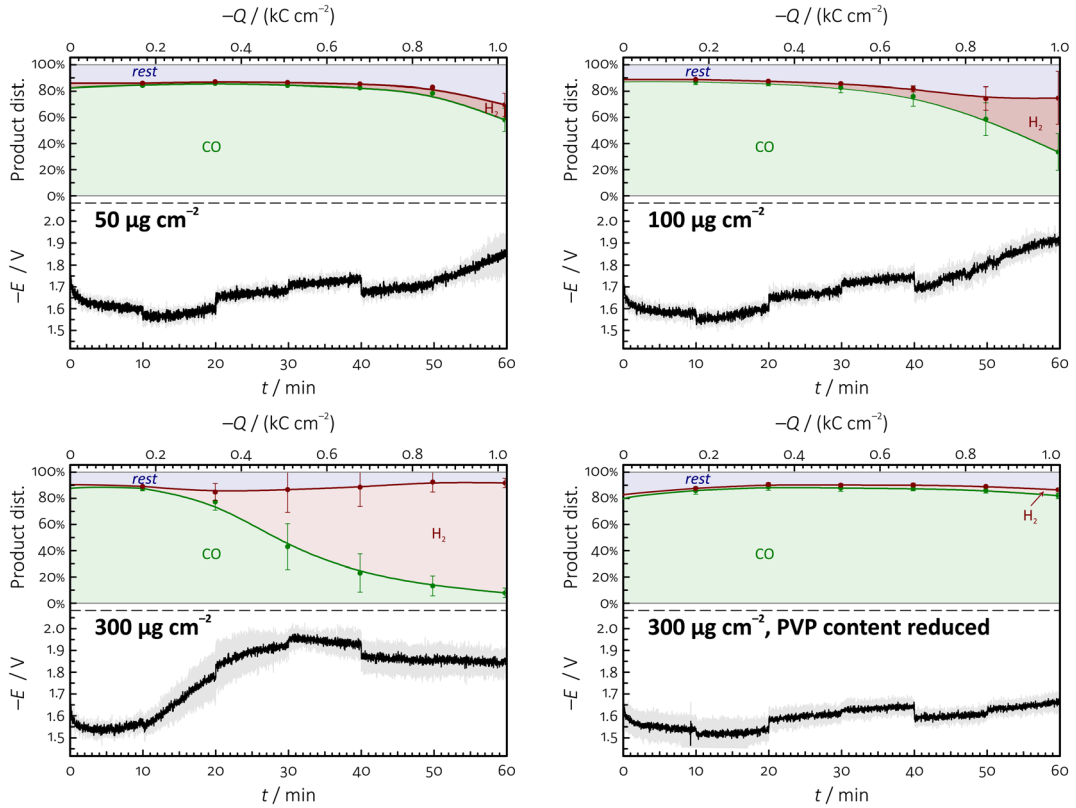

Fig. 4 Temporal variation of the product distribution of CO_2 reduction (top panels) and the measured cathode potential (bottom panels) during one hour long galvanostatic electrolyses (geometric surface area-normalised current density: −283 mA cm^{-2}) conducted on GDEs prepared with different Ag NP loadings shown in the figure. Error bars represent 95% confidence intervals. Nominal size of the Ag NPs used as catalyst: ~10 nm. The area labelled "rest" in the product distribution plots can mostly be attributed to the production of small amounts of formate during electrolyses, see the Experimental section for details.

distinguishable in both cases. If the catalyst ink is prepared using the as-purchased NP suspension (nominal diameter: ~10 nm) of high PVP content, the size distribution of the NPs is fairly symmetric and is centred at about 11.5 nm. If on the other hand the majority of the PVP content is removed by centrifugation, and the catalyst ink is prepared using a suspension gained by re-dispersing the particles in pure water, slight aggregation of the particles can be observed, resulting in a broadened and tailed size distribution histogram with a slightly increased maximum located at 16.2 nm. This indicates that removing the majority of PVP from the suspension of the Ag NPs results in a detectable but minor agglomeration of the particles on the GDE surface.

In order to determine to which extent the catalyst particles penetrate the microporous layer, we carried out cross-sectional SEM/EDX investigations, the results of which are shown in the bottom row of Fig. 5. EDX signals collected from different depth of the MPL all show strong peaks related to Ag, indicating that the NPs well penetrate the micropores of the MPL, practically regardless to whether they originate from as-purchased or centrifuged (PVP-deficient) suspensions.

Fig. 5 thus reveals no significant differences between GDEs prepared from Ag NP suspensions of the originally high PVP content and those prepared from PVP-deficient suspensions. Yet, when the two GDEs are made subject to prolonged electrolysis lasting 2.5 hours, differences between their stability immediately become apparent, as shown in Fig. 6.

It is clearly visible in the product distribution plots of Fig. 6 that both normal and PVP-deficient GDEs exhibit a high (>90%) faradaic efficiency for CO production at the start of the electrolysis. However, in GDEs of high excess PVP content the initially high selectivity towards CO formation is quickly lost, and in less than 30 minutes the FE of CO formation drops down to below 50%. On the other hand, FE_{CO} values measured on PVP-deficient GDEs remain rather high, with significant decrease appearing only after 1 hour, and the efficiency dropping below 50% only after about 90 minutes of electrolysis. That the shortage of CO production is due to the appearance of hydrogen evolution is also indicated by the *E vs. t* plots of Fig. 6, showing cathode potentials shifting to more negative values concomitantly with the observed FE_{CO} loss.

That the observed stability losses—both on GDEs with originally high and of reduced PVP content—occur due to flooding can be demonstrated by the post-electrolysis top-down and cross-sectional SEM and EDX mapping of the GDEs. The SEM micrographs and K elemental maps shown in Fig. 6, recorded after 60 and 150 minutes of electrolyses, clearly indicate the presence of a significant amount of K^+ (in the form of K_2CO_3/

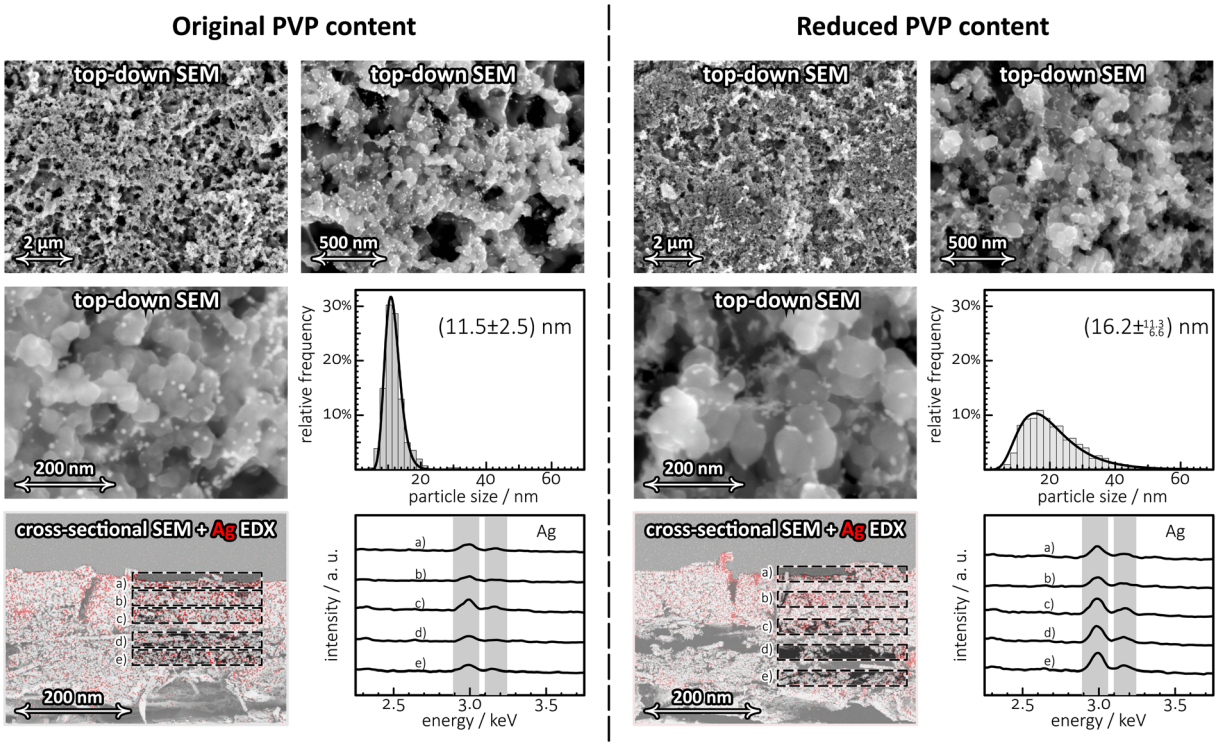

Fig. 5 Top-down SEM images of different magnification, showing catalyst layers containing the original (to the left) and reduced amount of PVP (to the right). Reducing, by ultracentrifugation, the amount of the stabilizing agent PVP leads to a broadening of the size distribution of the NPs as shown by the histograms. The cross-sectional view of the MPLs prove that the partial removal of the PVP content from the Ag NP suspensions exerts no considerable effect on the vertical distribution of the NPs. The EDX-based Ag elemental map (with red pixels corresponding to high Ag concentration) is superimposed on the cross-sectional SEM micrographs. EDX signals averaged over some selected areas, labelled from (a)–(e) clearly exhibit peaks assigned to Ag with no particular vertical intensity variation. Nominal size of the Ag NPs used as catalyst: ~10 nm, applied mass loading: 300 µg per cm^2 Ag. For more details on the structure of PVP-capped Ag NPs (TEM images), see Fig. S2 of the ESI.†

$KHCO_3$ precipitates) both on-top and inside the GDE structure. The appearance of K^+ in the cathode GDE serves as a direct proof of anolyte cross-over through the membrane, and as such, the formation pattern of K^+ precipitates inside the GDE acts as a tracer of electrolyte intrusion to the GDE.[19,20]

While the as-prepared GDEs are essentially potassium-free, the post-electrolysis determination of the K-content of GDEs by digestion in concentrated HNO_3 and follow-up ICP-MS measurements indicate that already at the first 60 minutes of electrolysis, K^+ ions accumulate within the GDE structure in an amount of approximately 4 mg cm^{-2}, normalised to the geometric surface area of the GDE (see Fig. 6 for exact values).

While the total amount of precipitated K^+ (determined by ICP-MS) seems not to vary much (at least, after 60 minutes) with the time of electrolysis, nor it seems to depend significantly on whether the original CA-content of the Ag NPs was reduced, a marked difference with regard to the spatial distribution of the precipitates can clearly be observed in Fig. 6, especially if we compare the top-down EDX elemental maps recorded on the two electrodes (PVP-deficient and original) after 60 min electrolysis.

These elemental maps show that for the GDE containing PVP in the original (high) concentration, precipitates first appear on top of flat parts of the catalyst layer, while in case of the GDE with reduced PVP content, precipitates tend to appear preferentially inside the cracks of the MPL, leaving the catalyst layer—at least, for some time—mostly uncovered. (In a later stage, following 2.5 hours of electrolysis, precipitates already seem to cover the entire MPL.) This observation can be explained by assuming that the excess PVP content of the catalyst ink facilitates the flooding of the GDE, and leads to a blockage of CO_2 access to the catalyst NPs. On GDEs of a reduced PVP content, this effect occurs only in a later stage of electrolysis, with precipitates first appearing not on-top of the active catalyst layer but rather inside cracks of the MPL, also penetrating deeper parts of the GDE structure.

Note here that the cross-over of K^+ ions through the membrane is a naturally occurring (and in fact unavoidable) phenomenon, and does not (or should not) in itself lead to a blockage of the catalyst. *E.g.*, in case of the PVP-deficient catalyst, the electrolyte penetrating the GDE structure does not get trapped in the MPL but—through cracks and micro-pores—drains to deeper layers of the GDE and finally exits the cell in the form of small liquid drops through the gas flow channels of the cathode. This latter phenomenon was termed perspiration by Jeanty *et al.*,[22] and we quantitatively monitor it here for the first time, by applying a liquid trap to collect K_2CO_3/$KHCO_3$ perspirates at the gas out-flow of the electrolyser (see Fig. 1b).

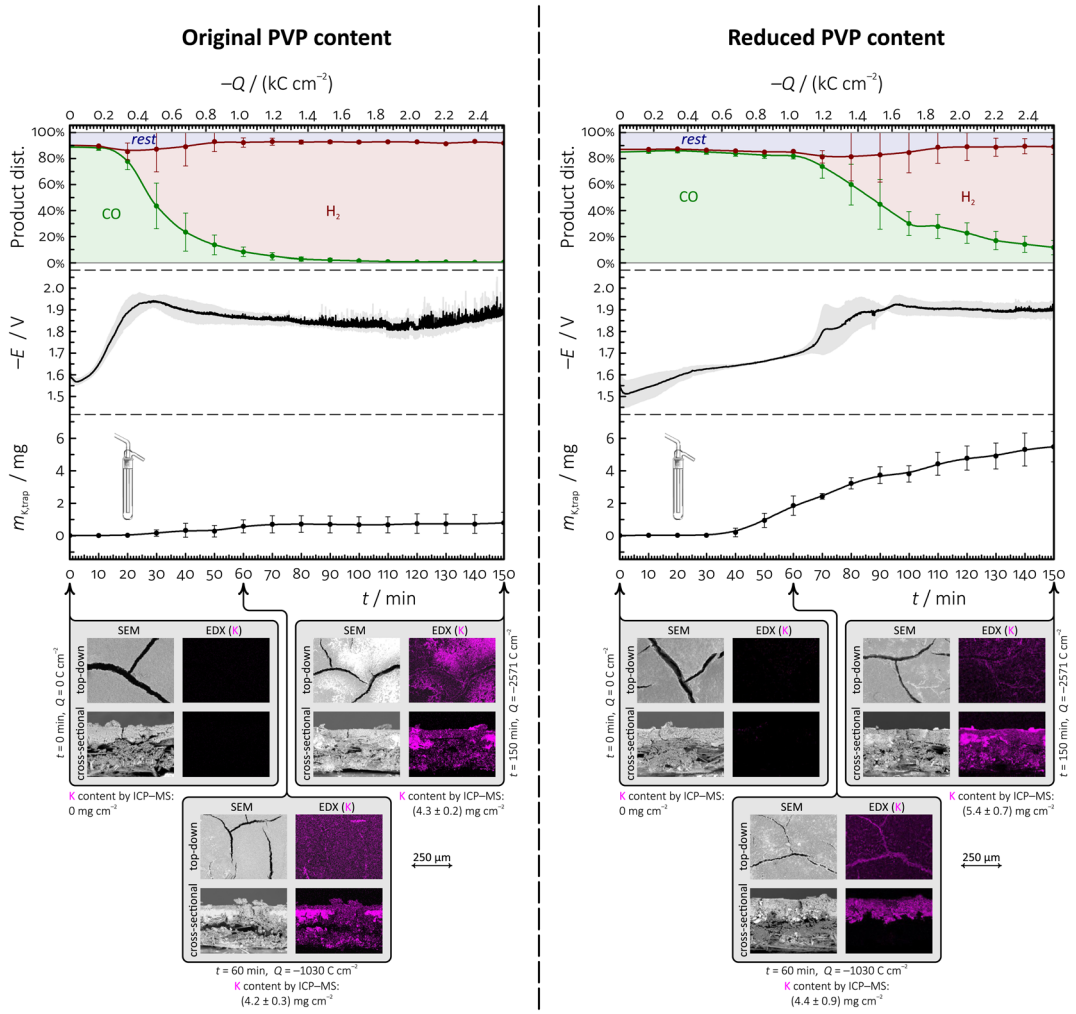

Fig. 6 Comparison of the results of electrolysis stress-tests on two different GDEs prepared with PVP-capped Ag NPs of 10 nm nominal diameter. The PVP content of the Ag NP suspensions was either unchanged (left side) or was reduced by ultracentrifugation (right side) during the course of catalyst ink preparation; in both cases, the catalyst was applied at a mass loading of 300 µg per cm^2 Ag. The plots show the variation of the product distribution of CO_2 reduction, the measured electrode potential E (referenced *vs.* an Ag|AgCl|3 mol per dm^3 KCl electrode), and the mass of K^+ ions collected in the liquid trap equipped to the gas outflow of the electrolyser, as a function of both time and passed charge, for galvanostatic electrolyses carried out at −283 mA cm^{-2}. Structural changes of the applied GDEs were monitored by recording top-down and cross-sectional SEM/EDX images of the GDEs obtained before, as well as 60 and 150 min after the electrolysis.

If we plot the amount of K^+ present in this outlet trap as a function of time (see the $m_{K,trap}$ *vs.* t plots of Fig. 6), we see that perspiration does occur (and the amount of K^+ in the trap constantly rises) up to the point at which the actual flooding of the catalyst layer takes place, the access of CO_2 to the catalyst layer becomes blocked, and the overall performance drops down.

Our results clearly indicate that the (at least partial) removal of PVP from the catalyst layer delays the flooding of the GDE and aids the electrolyte management of the cathode MEA by facilitating perspiration. The correlation of the $m_{K,trap}$ *vs.* t curves and the product distribution plots of Fig. 6 demonstrate that the faradaic efficiency of CO production can only be efficiently upheld until the electrolyte (and, with it, K^+) can effectively perspire through the system. The distribution of precipitates on-top and within the GDE structure, visualised by the EDX maps of Fig. 6, point out that excess amounts of the capping agent PVP can easily clog the micropores of the GDL, and emphasize the role of the PVP content of Ag NP catalyst inks in creating erratic electrolysis performances.

From what was written above, the question immediately follows: is it only PVP, or other polymeric CAs as well, the presence of which in catalyst inks can have such detrimental effect on the operation of CO_2-to-CO electrolysing GDEs? While we cannot give a generally valid answer to this question, we did perform additional tests on BPEI-capped Ag NPs and, similarly to the case of PVP-stabilised ones, we found that the ultracentrifugation-based removal of the excess BPEI content of the Ag NP suspensions increases the durability of GDEs in the course of high current density electrolyses (Fig. 7).

By comparing Fig. 6 and 7 one can immediately see that BPEI, present in catalyst inks at high amount, decreases the FE

of CO formation already at the start of the electrolysis, which is in agreement with previous observations.[18] As the electrolysis proceeds, CO selectivity is dropping quickly and within 25 minutes H_2 already becomes the dominant product. As HER takes over the place of CO_2 reduction, massive precipitate formations can be observed, especially on-top of the catalyst layer, with precipitates showing typical burst patterns around the edges of cracks.

When the catalyst ink is prepared from BPEI-deficient (Table 1) suspensions (Fig. 7, to the right), the formation of the burst-like precipitate patterns can only be observed at later stages of the electrolysis. In this case the (also initially higher) FE of CO production breaks down to below 50% only after ~75 minutes of electrolysis. With a certain delay (that is due to the time needed for the formed precipitates to get transported out of the electrolyser) the measured $m_{K,trap}$ *vs.* t curves of Fig. 7 show the same tendency: following the drop-down of FE_{CO} the amount of K^+ in the down-flow trap will also grow less rapidly. This points to that the cell seems to remain active for CO_2 reduction as long as the pores of the MPL remain unclogged.

From Fig. 6 and 7 it is obvious that removing some of the (originally high) polymeric CA content of Ag NP suspensions before turning these into catalyst inks does seem to be an advisable strategy, as this will increase the durability of the prepared GDEs. We note here, however, that the effect seems observable only in the case when polymeric CAs are used for the Ag NP preparation. The operation of GDEs prepared from Ag NPs stabilised by (monomeric) citrate ligands, for example, seems less to depend on whether the citrate content of the NP suspension was reduced or not (Table 1). As shown in Fig. 8,

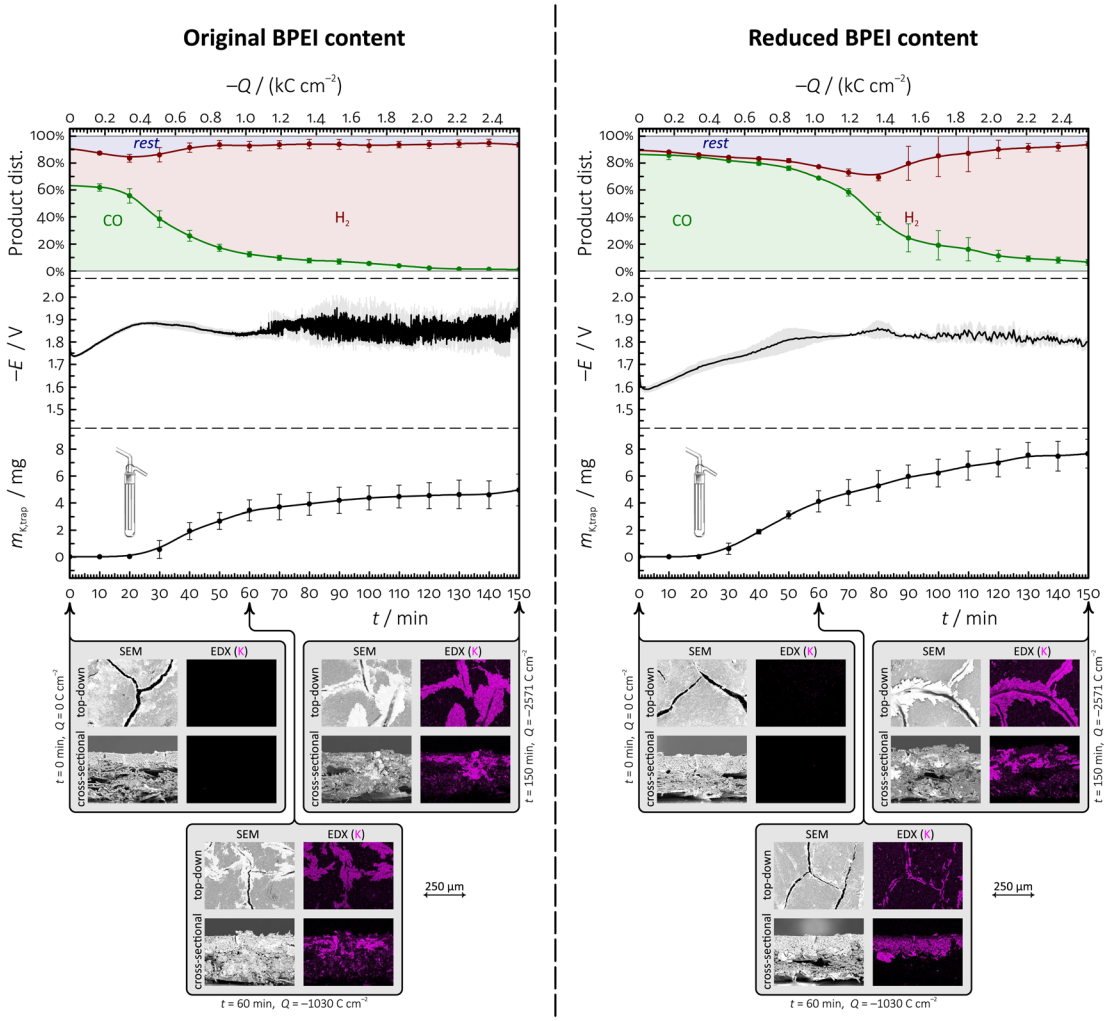

Fig. 7 Comparison of the results of electrolysis stress-tests on two different GDEs prepared with BPEI-capped Ag NPs of 50 nm nominal diameter. The BPEI content of the Ag NP suspensions was either unchanged (left side) or was reduced by ultracentrifugation (right side) during the course of catalyst ink preparation; in both cases, the catalyst was applied at a mass loading of 300 µg per cm^2 Ag. The plots show the variation of the product distribution of CO_2 reduction, the measured electrode potential E (referenced *vs.* an Ag|AgCl|3 mol per dm^3 KCl electrode), and the mass of K^+ ions collected in the liquid trap equipped to the gas outflow of the electrolyser, as a function of both time and passed charge, for galvanostatic electrolyses carried out at −283 mA cm^{-2}. Structural changes of the applied GDEs were monitored by recording top-down and cross-sectional SEM/EDX images of the GDEs obtained before, as well as 60 and 150 min after the electrolysis. For more details on the structure of BPEI-capped Ag NPs (TEM images), see Fig. S3 of the ESI.†

citrate removal seems to exert no considerable effect either on the measurable product distribution, electrode potential and trapped K^+ plots, or on the formed precipitate patterns.

In order to further demonstrate, for the case of polymeric CA-stabilised Ag NPs, the detrimental effect of the excess CA content of catalyst inks on the stability of CO_2 electrolysers, we also created GDEs using PVP-capped Ag NPs of ~100 nm (as opposed to the previously used ~10 nm) diameter. The suspensions of larger size Ag NPs inherently contains less PVP,[28] although the PVP content could again be further reduced by ultracentrifugation (see Table 1). When used for the fabrication of GDEs, the 100 nm diameter NPs seemed to penetrate the MPL lot less efficiently than the ~10 nm particles did, and remained more concentrated in the catalyst layer on-top of the MPL, with some NPs penetrating through cracks of the MPL into the CFL, as shown by the cross-sectional EDX maps of Fig. S4 of the ESI†. Decreasing the amount of PVP in the catalyst ink helped, also in case of the ~100 nm diameter PVP-capped Ag NPs to increase the stability time of electrolysis (see Fig. S5 of the ESI†), proving that the durability impairments reported in this paper are indeed caused by the excess amounts of polymeric CAs clogging the pores (perspiration pathways) of the MPL (scheme shown in Fig. 9) and are not due to particle size effects.

The importance of maintaining the ability of GDEs to uphold effective perspiration pathways is further emphasized by the results of sessile water drop contact angle measurements made on the as-prepared GDEs, shown in Fig. 10. These measurements all show that the ultracentrifugation-based partial removal of the excess amount of capping agents from the NP suspensions in the course of catalyst ink preparation does increase, however only a bit, the hydrophobicity of the catalyst layer. This increase of hydrophobicity can, however, not explain

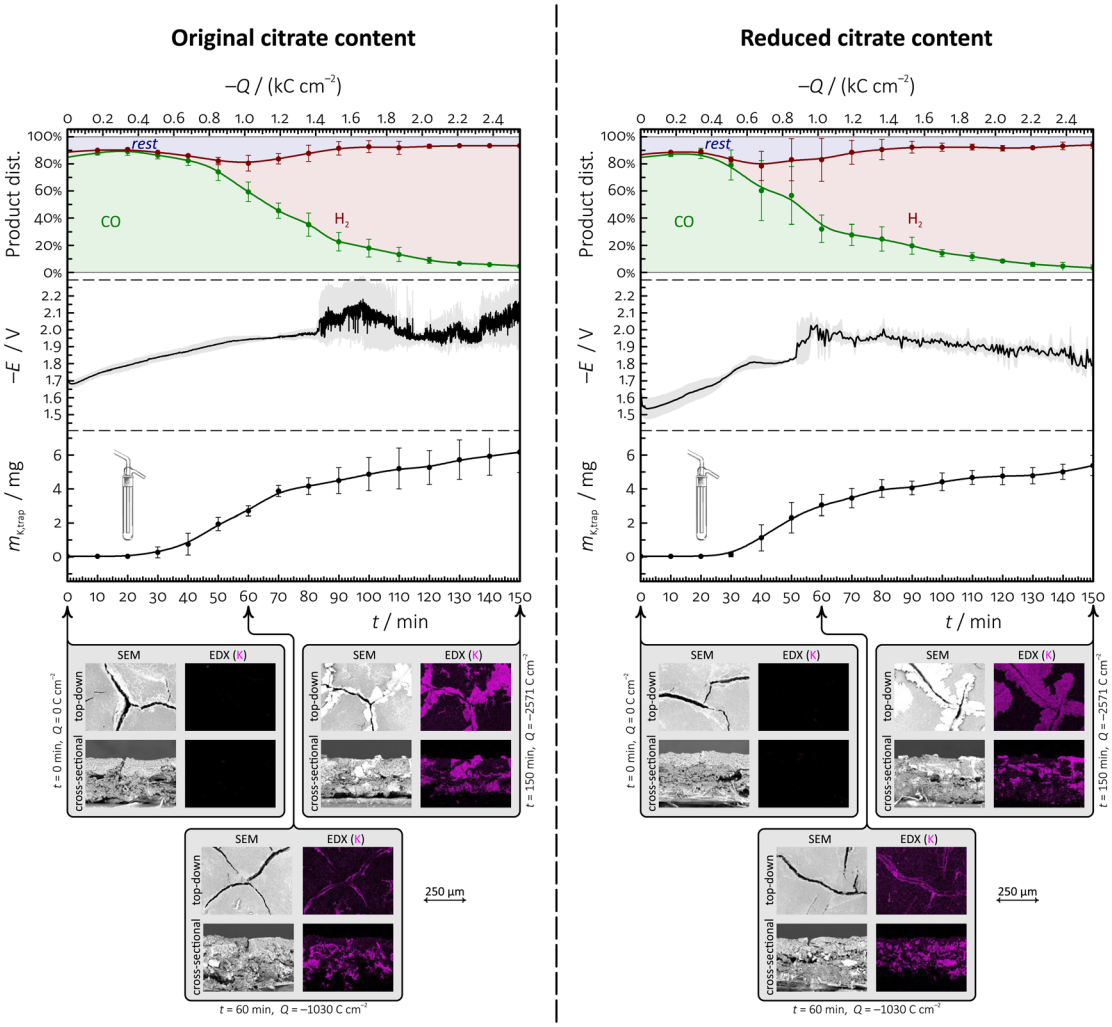

Fig. 8 Comparison of the results of electrolysis stress-tests on two different GDEs prepared with citrate-capped Ag NPs of 50 nm nominal diameter. The citrate content of the Ag NP suspensions was either unchanged (left side) or was reduced by ultracentrifugation (right side) during the course of catalyst ink preparation; in both cases, the catalyst was applied at a mass loading of 300 µg per cm^2 Ag. The plots show the variation of the product distribution of CO_2 reduction, the measured electrode potential E (referenced *vs.* an Ag|AgCl|3 mol per dm^3 KCl electrode), and the mass of K^+ ions collected in the liquid trap equipped to the gas outflow of the electrolyser, as a function of both time and passed charge, for galvanostatic electrolyses carried out at −283 mA cm^{-2}. Structural changes of the applied GDEs were monitored by recording top-down and cross-sectional SEM/EDX images of the GDEs obtained before, as well as 60 and 150 min after the electrolysis.

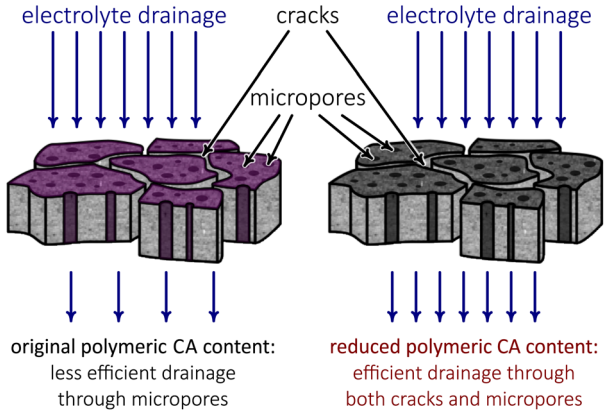

Fig. 9 Schematic illustration of the clogging effect of polymeric CAs, disallowing effective perspiration through the micropores of GDEs. (Figure not to scale, micropores are depicted magnified for better visibility.)

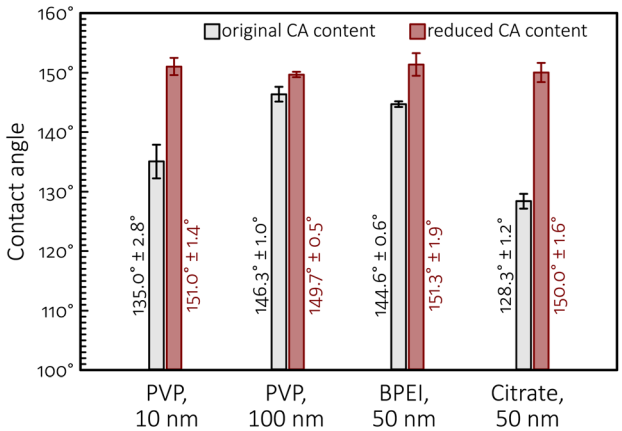

Fig. 10 Contact angles (of sessile water drops) measured on different GDEs (as-prepared, prior to electrolyses) used in this study.

the durability improvements caused by the removal of polymeric capping agents from the catalyst ink, pointing to that—in contrast to prevailing views[5,35,36]—the perspiration properties of GDEs are probably even more important than their non-wettability in efficient, long time CO_2 electrolysis.

4 Conclusion

Zero-gap MEA cathodes employing catalysts distributed over the surface of a gas diffusion layer allow CO_2 reduction to be carried out at extreme high rate and good selectivity. *E.g.*, by using Ag NPs with well-chosen structure and size distribution, current densities in the range of few hundreds of mA cm^{-2} and an almost 100% faradaic efficiency of CO production can be achieved. This efficiency increase comes, however, at the cost of severe stability issues that are mostly all related to the flooding of the GDE by the employed electrolyte. Flooding is currently recognised as the biggest obstacle in front of the scale-up prospects of CO_2 electroreduction, thus the identification and possible elimination of phenomena that can lead to flooding in CO_2 electrolysers is a primary goal of today's electrocatalysis studies.

In the above vein, we identified in this paper one important contributor to flooding; that is, the excessive presence of polymeric capping agents in the catalyst layer of gas diffusion electrodes. CAs have an important role in stabilising Ag NPs in suspension, however when these suspensions are turned into catalyst inks and deposited on the surface of a gas diffusion layer, polymeric CAs can clog the perspiration channels of the MPL and can thus act as an initiator to flooding. The detrimental effect of polymeric CAs (PVP and BPEI were studied in this paper) present in catalyst inks can in fact be so strong that it overshadows other tendencies. *E.g.*, it was shown in the paper that by increasing the mass loading of PVP-capped Ag NP catalysts, a counter-intuitive stability loss can often be observed. This stability loss, as we showed, is however not a result of the increased loading in itself, but of the increase of the PVP concentration in the catalyst layer.

In the paper we used a combination of electrochemical performance tests, during which we monitored the faradaic efficiency of CO production, the cathode potential, and also, using a novel ICP-MS detection-based approach, the outflow of electrolyte perspirates. We combined these measurements with *ex situ* SEM and EDX-based investigations of the GDEs, carried out at various stages of the electrolysis. Our investigations proved that the presence of excess amount of polymeric capping agents (PVP and BPEI) in the catalyst ink can cause a rapid flooding of the GDE cathode and can thus exert disastrous effects on the stability of zero-gap MEA cathode-based electrolysers. No such effects were observed when a monomeric CA (citrate) was used as a stabilizing ligand of Ag NPs. In order to attenuate the concentration of polymeric capping agents in the used catalyst inks, an ultracentrifugation-based method has been described in the paper, the application of which in the catalyst ink formulation immediately resulted in an improved electrolyser stability.

Author contributions

Huifang Hu: investigation, experiments, data curation, writing – first draft. Ying Kong and Menglong Liu: investigation, experiments. Viliam Kolivoška, Alexander V. Rudnev and Yuhui Hou: conceptualization, methodology. Rolf Erni: TEM measurements. Soma Vesztergom: conceptualization, methodology, visualization, data analysis, writing, funding acquisition. Peter Broekmann: conceptualization, methodology, writing – review & editing, supervision, funding acquisition.

Conflicts of interest

There are no conflicts to declare.

Acknowledgements

This publication was created as part of NCCR Catalysis (grant number 180544), a National Centre of Competence in Research funded by the Swiss National Science Foundation. V. K.

acknowledges financial support from the Czech Science Foundation (project number 18-09848S and 23-07292S). A. R. acknowledges support from the Ministry of Science and Higher Education of the Russian Federation. H. H., Y. K. and M. L. acknowledge the financial support by the Chinese Scholarship Council (CSC). S. V. acknowledges support from the Lendület (Momentum) program of the Hungarian Academy of Sciences (grant LP2022-18/2022) and from the National Research, Development and Innovation Office of Hungary (NKFIH grants FK135375 and K129210).

Notes and references

1 D. R. Feldman, W. D. Collins, P. J. Gero, M. S. Torn, E. J. Mlawer and T. R. Shippert, *Nature*, 2015, **519**, 339–343.
2 A. Gawel, T. Jaster, D. Siegmund, J. Holzmann, H. Lohmann, E. Klemm and U.-P. Apfel, *iScience*, 2022, **25**, 104011.
3 J.-B. Vennekoetter, R. Sengpiel and M. Wessling, *Chem. Eng. J.*, 2019, **364**, 89–101.
4 C. M. Gabardo, A. Seifitokaldani, J. P. Edwards, C.-T. Dinh, T. Burdyny, M. G. Kibria, C. P. O'Brien, E. H. Sargent and D. Sinton, *Energy Environ. Sci.*, 2018, **11**, 2531–2539.
5 U. O. Nwabara, A. D. Hernandez, D. A. Henckel, X. Chen, E. R. Cofell, M. P. de Heer, S. Verma, A. A. Gewirth and P. J. A. Kenis, *ACS Appl. Energy Mater.*, 2021, **4**, 5175–5186.
6 J. Li, S. U. Abbas, H. Wang, Z. Zhang and W. Hu, *Nano-Micro Lett.*, 2021, **13**, 216.
7 H.-R. M. Jhong, S. Ma and P. J. A. Kenis, *Curr. Opin. Chem. Eng.*, 2013, **2**, 191–199.
8 F. Yu, P. Wei, Y. Yang, Y. Chen, L. Guo and Z. Peng, *Nano Mater. Sci.*, 2019, **1**, 60–69.
9 D. Sun, X. Xu, Y. Qin, S. P. Jiang and Z. Shao, *ChemSusChem*, 2019, **13**, 39–58.
10 D. Xue, H. Xia, W. Yan, J. Zhang and S. Mu, *Nano-Micro Lett.*, 2020, **13**, 5.
11 J. Y. Choi, W. Choi, J. W. Park, C. K. Lim and H. Song, *Chem.–Asian J.*, 2019, **15**, 253–265.
12 Y. Pei, H. Zhong and F. Jin, *Energy Sci. Eng.*, 2021, **9**, 1012–1032.
13 D. M. Weekes, D. A. Salvatore, A. Reyes, A. Huang and C. P. Berlinguette, *Acc. Chem. Res.*, 2018, **51**, 910–918.
14 N. T. Nesbitt, T. Burdyny, H. Simonson, D. Salvatore, D. Bohra, R. Kas and W. A. Smith, *ACS Catal.*, 2020, **10**, 14093–14106.
15 A. Marcos-Madrazo, C. Casado-Coterillo, J. Iniesta and A. Irabien, *Membranes*, 2022, **12**, 783.
16 G. Díaz-Sainz, M. Alvarez-Guerra, J. Solla-Gullón, L. García-Cruz, V. Montiel and A. Irabien, *J. CO2 Util.*, 2019, **34**, 12–19.
17 M. de J. Gálvez-Vázquez, P. Moreno-García, H. Xu, Y. Hou, H. Hu, I. Z. Montiel, A. V. Rudnev, S. Alinejad, V. Grozovski, B. J. Wiley, M. Arenz and P. Broekmann, *ACS Catal.*, 2020, **10**, 13096–13108.
18 M. Liu, Y. Kong, H. Hu, N. Kovács, C. Sun, I. Z. Montiel, M. de J. G. Vázquez, Y. Hou, M. Mirolo, I. Martens, J. Drnec, S. Vesztergom and P. Broekmann, *J. Catal.*, 2021, **404**, 371–382.
19 Y. Kong, H. Hu, M. Liu, Y. Hou, V. Kolivoška, S. Vesztergom and P. Broekmann, *J. Catal.*, 2022, **408**, 1–8.
20 Y. Kong, M. Liu, H. Hu, Y. Hou, S. Vesztergom, M. de J. G. Vázquez, I. Z. Montiel, V. Kolivoška and P. Broekmann, *Small Methods*, 2022, **6**, 2200369.
21 K. Yang, R. Kas, W. A. Smith and T. Burdyny, *ACS Energy Lett.*, 2020, **6**, 33–40.
22 P. Jeanty, C. Scherer, E. Magori, K. Wiesner-Fleischer, O. Hinrichsen and M. Fleischer, *J. CO2 Util.*, 2018, **24**, 454–462.
23 B. De Mot, J. Hereijgers, M. Duarte and T. Breugelmans, *Chem. Eng. J.*, 2019, **378**, 122224.
24 C. V. Restrepo and C. C. Villa, *Environ. Nanotechnol., Monit. Manage.*, 2021, **15**, 100428.
25 S. H. Im, Y. T. Lee, B. Wiley and Y. Xia, *Angew. Chem.*, 2005, **117**, 2192–2195.
26 J. Zhang, Q. Wang, X. Zhang, J. Wang, M. Guo, B. J. Wiley, C. Li and C. Hu, *Inorg. Chem. Front.*, 2016, **3**, 547–555.
27 M. de J. Gálvez-Vázquez, S. Alinejad, H. Hu, Y. Hou, P. Moreno-García, A. Zana, G. K. H. Wiberg, P. Broekmann and M. Arenz, *Chimia*, 2019, **73**, 922.
28 K. M. Koczkur, S. Mourdikoudis, L. Polavarapu and S. E. Skrabalak, *Dalton Trans.*, 2015, **44**, 17883–17905.
29 Q. Zhang, N. Li, J. Goebl, Z. Lu and Y. Yin, *J. Am. Chem. Soc.*, 2011, **133**, 18931–18939.
30 S. Alinejad, J. Quinson, G. K. H. Wiberg, N. Schlegel, D. Zhang, Y. Li, S. Reichenberger, S. Barcikowski and M. Arenz, *ChemElectroChem*, 2022, **9**, e20220034.
31 K. Ehelebe, D. Seeberger, M. T. Y. Paul, S. Thiele, K. J. J. Mayrhofer and S. Cherevko, *J. Electrochem. Soc.*, 2019, **166**, F1259–F1268.
32 U. O. Nwabara, M. P. de Heer, E. R. Cofell, S. Verma, E. Negro and P. J. A. Kenis, *J. Mater. Chem. A*, 2020, **8**, 22557–22571.
33 A. V. Rudnev, *Encyclopedia of Interfacial Chemistry*, Elsevier, Amsterdam, 2018, pp. 321–325.
34 H. Hu, Y. Kong, M. Liu, V. Kolivoška, A. V. Rudnev, Y. Hou, R. Erni, S. Vesztergom and P. Broekmann, Raw data for the article "Effective perspiration is essential to uphold the stability of zero-gap MEA-based cathodes used in CO_2 electrolysers, *Zenodo*, 2022, **https://doi.org/10.5281/zenodo.7002917**.
35 M. Li, M. N. Idros, Y. Wu, T. Burdyny, S. Garg, X. S. Zhao, G. Wang and T. E. Rufford, *J. Mater. Chem. A*, 2021, **9**, 19369–19409.
36 M. E. Leonard, M. J. Orella, N. Aiello, Y. Román-Leshkov, A. Forner-Cuenca and F. R. Brushett, *J. Electrochem. Soc.*, 2020, **167**, 124521.

6. Activation Matters: Hysteresis Effects During Electrochemical Looping of Colloidal Ag Nanowire (Ag-NW) Catalysts

Authors: Huifang Hu, Menglong Liu, Ying Kong, Nisarga Mysuru, Changzhe Sun, María de Jesús Gálvez-Vázquez, Ulrich Müller, Rolf Erni, Vitali Grozovski, Yuhui Hou, and Peter Broekmann.

***ACS Catal.* 10 (15), 8503–8514 (2020). DOI: 10.1021/acscatal.0c02026**

Highlight: Ag nanowire (Ag-NW) catalysts, synthesized by means of colloidal methods, have been demonstrated to be highly active catalyst to produce CO from CO_2. However, PVP capping agents, typically used during Ag-NW synthesis for shape control, have been shown to have detrimental effects on the product selectivity and the catalyst activity. A removal of the capping agents is essential to achieve high Faradaic efficiencies and partial current densities for CO production, at least when working with a classical H-cell configuration. In this contribution a novel electrochemical looping approach was developed and introduced which allows for the complete removal of the PVP capping agents without affecting the structural integrity of the NW catalysts. Consequently, a near unity Faradaic efficiency for CO could be achieved. The successful PVP removal was experimentally proven by post-electrolysis XPS inspection.

Contribution: I carried out some parts of the electrochemical experiments and have been involved in the discussion of the results. I have been actively involved into the revision of the manuscript text.

ACS Catalysis

pubs.acs.org/acscatalysis Research Article

Activation Matters: Hysteresis Effects during Electrochemical Looping of Colloidal Ag Nanowire Catalysts

Huifang Hu, Menglong Liu, Ying Kong, Nisarga Mysuru, Changzhe Sun, María de Jesús Gálvez-Vázquez, Ulrich Müller, Rolf Erni, Vitali Grozovski, Yuhui Hou,* and Peter Broekmann*

Cite This: ACS Catal. 2020, 10, 8503–8514 Read Online

ACCESS | Metrics & More | Article Recommendations | Supporting Information

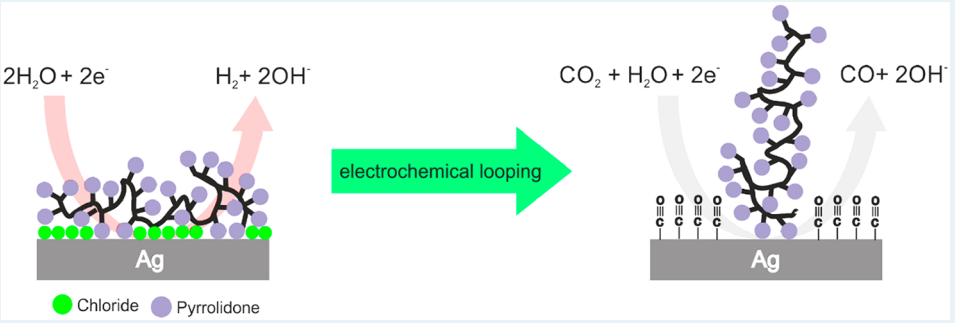

ABSTRACT: Colloidal electrocatalysts are commonly synthesized using organic capping agents (surfactants), which control the size distribution and shape of the resulting nano-objects and prevent them from agglomerating during and after synthesis. However, the presence of a surfactant shell on the catalyst is detrimental, as the resulting performance of the electrocatalyst depends crucially on the ability of reactants to access active surface sites. Techniques for postsynthesis deprotection are therefore mandatory for removing the capping agents from the otherwise blocked reactions sites without compromising the structural integrity of the nanocatalysts. Herein, we present silver nanowires (Ag-NWs)—produced via PVP-assisted polyol synthesis (PVP, polyvinylpyrrolidone)—as effective catalysts for the electrochemical CO_2 reduction reaction (*ec*-CO_2RR), which reach Faradaic efficiencies close to 100% for CO formation after deprotection by a so-called "electrochemical looping" (ec-l) pretreatment. Electrochemical looping refers to a sequence of potentiostatic CO_2 electrolysis experiments that exhibit well-defined starting (E_{start}), vertex (E_{vertex}), and end (E_{end}) potentials. The resulting product distribution undergoes a profound hysteresis in the forward and corresponding backward run of the electrochemical looping experiment, thus pointing to an effective deprotection of the catalyst as made evident by postelectrolysis XPS inspection. These results can be considered as a prime example demonstrating the importance of the catalyst's "history" for the resulting *ec*-CO_2RR performance. These transient (non-steady-state) effects are crucial in particular for the initial stage of the CO_2 electrolysis reaction and for catalyst screening approaches carried out on the time scale of hours.

KEYWORDS: *CO_2 reduction reaction, silver nanowires, surfactant removal, catalyst deprotection, electrochemical looping*

INTRODUCTION

The conversion of environmentally harmful carbon dioxide (CO_2) into value-added products is one of the major intersectoral challenges that we currently face.[1] In this context, electrochemical approaches of CO_2 valorization deserve particular attention as they can utilize the "green" electric power—generated by renewables such as solar or wind energy—as energy input for the highly endergonic process of CO_2 electrolysis, thereby rendering the overall process more sustainable.[2−4] One of the main target products of the electrochemical CO_2 reduction reaction (hereafter referred to as *ec*-CO_2RR) is carbon monoxide (CO), which is currently produced on an industrial scale via the "Boudouard" reaction and reaches a yearly production volume of approximately 210 000 Mt.[5] CO is considered to be a valuable intermediate (current market price: ≈0.65 \$ kg^{-1})[5] and has the potential to be used as a reactant on a large scale (e.g., in the Fischer−Tropsch synthesis of aliphatic hydrocarbons [synthetic fuels] or alcohols).[6] Cost estimates suggest that the electrochemical coelectrolysis of water/CO_2 might indeed become competitive with more well-established routes of CO production.[5] The electrochemical production of CO via the coelectrolysis of water/CO_2 can be considered to be a versatile "synthesis module", which also can be coupled to other process units for

Received: May 6, 2020
Revised: June 26, 2020
Published: July 6, 2020

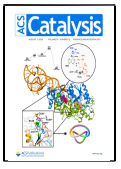

https://dx.doi.org/10.1021/acscatal.0c02026
ACS Catal. 2020, 10, 8503−8514

the production of valuable end products. A promising alternative to interlinking this process to the heterogeneous gas-phase Fischer−Tropsch reaction has recently been proposed by the Siemens/Evonik consortium[1,7] and couples the *ec*-CO_2RR (CO production; Siemens) to a biotechnological fermentation process (Evonik), thereby yielding fine chemicals such as butanol and hexanol as key intermediates for the production of specialty plastics.[7] The first test plant is expected to become operative in 2021[1] and thus demonstrates the enormous efforts that are currently underway to bring the *ec*-CO_2RR process from the lab to the market.[1]

Catalysts are essential for *ec*-CO_2RR, as they direct the electrolytic reaction toward the desired target product (e.g., CO). The pioneering work by Hori et al.[8−10] identified silver (Ag) as one of best (electro)catalysts, in addition to Au and Zn, which yielded CO with Faradaic efficiencies (FEs) that reached 81.5% (E = −1.14 V vs NHE).[8] In these early studies, catalyst screening was mainly based on the use of polycrystalline electrode materials as active catalysts (e.g., metal foils). However, substantial progress has been made during the last two decades in the development of tailored nanomaterials with an improved surface-to-volume ratio and well-defined shapes, the latter being important for the rational design of active surface sites.[11,12] In future, these nanomaterials have the potential to be used in gas diffusion electrodes (GDEs) as a key component of advanced gas-flow electrolyzer systems.[7,13−16] From a technical point of view, it is mandatory to use a gas-flow approach to reach the current densities that are targeted by industry (100 to 1000 mA cm^{-2}) to cover the capital and operating costs of these systems.[13,17,18] Typically, these nanomaterials are produced via colloidal synthesis, which also allows the process to be easily scaled up and which is considered to be a key perquisite for any industrial application. A wide range of particle morphologies can be obtained using this colloidal approach, ranging from spheres,[19] cubic shapes,[20] and triangular platelets (confined 2-D systems)[21] to 1-D nano-objects such as rods[19] and wires.[22−26] To rationally design these nano-objects, a multiparameter space needs to be considered, which includes but is not limited to (i) the reaction temperature, (ii) the convective transport of reactants (e.g., stirring speed), (iii) the ratio of reactants (e.g., metal ion precursor, reducing agent, etc.), (iv) reaction times, and (v) the injection speed of chemicals.[27−29] However, the most important aspect to consider is the action of the so-called surfactants and capping agents.[19,25,30] Their presence in the reaction medium crucially affects the nucleation and growth kinetics of the nano-objects and could even cause crystal growth to be anisotropic, which is required for the synthesis of metallic nanowires (NWs).[31] The physical origin of this anisotropic growth behavior is the preferential surfactant adsorption on certain surface facets (e.g., [100] textured), which reduces their growth rate relative to surfaces with different surface orientations (e.g., [111]).[30,32−35] In this sense, the role of the surfactants is a result of the steric blocking of surface sites that are active for the (e-less) metal deposition by selectively limiting the access of precursor metal ions in the liquid reaction medium to the emerging surface of the nanocrystals (NCs).[36] Note that not only the monomeric[11,37] or polymeric (e.g., polyvinylpyrrolidone, PVP[38]) organic surfactants need to be considered, but also anionic species (e.g., halides) that are added to the reaction media along with the metal precursors. These counteranions usually play a crucial role in the initial nucleation process of the nano-objects (concept of self-seeded growth[25,35]) and further tend to chemisorb on the emerging facets in an advanced stage of NC growth.[31]

While this facet-specific blocking by adsorbed surfactants is a mechanistic prerequisite for any anisotropic growth mode, it is highly detrimental to the desired (electro)catalytic performance of the nanocatalysts. As capping agents sterically block the access of reactants to the active catalyst sites during the electrocatalyzed reaction of interest,[37−40] various "soft" postsynthesis methods have been proposed to deprotect the "capped" nano-objects without compromising their structural integrity (e.g., loss of the shape, changes in size distribution, NP agglomeration, etc.). These deprotection techniques range from purely physical (e.g., thermal annealing[41,42] or exposure to light of particular wavelength and intensity[43,44]) to chemical treatments under nonreactive (e.g., "chemical" washing[38]) or reactive conditions (e.g., plasma treatment, the use of oxidizing or reducing agents, etc.).[37,38,44−51] Note that, under extremely drastic experimental conditions (e.g., thermal treatment at elevated temperatures), this type of catalyst pretreatment could lead to the loss of surface texture or to the agglomeration of nanoparticles.[52]

Also, electrochemical treatments (anodic or cathodic polarization) have successfully been applied to deprotect colloidal catalysts.[53−56] For example, Oezaslan et al.[54] reported on the efficient removal of a PVP capping shell from Pt nanocubes by applying an oxidative stressing protocol (electrochemical cycling up to +0.8 V vs reversible hydrogen electrode [RHE] in 0.1 M $HClO_4$), whereas the electrochemical deprotection failed under alkaline conditions. Also, the chemical nature of the capping agent (PVP versus oleylamine) has been shown to play a crucial role in the structural integrity of the nanocatalysts after electrochemical deprotection.[54]

So far, most studies on catalyst activation have considered only one single electrocatalytic reaction, (e.g., the oxygen reduction reaction [ORR],[53,54] the oxygen evolution reaction [OER], or the hydrogen evolution reaction [HER][37] etc.). For these single reactions, there are straightforward electrochemical descriptors and measuring approaches available to monitor the effectiveness of the applied deprotection technique (e.g., via the electrochemically active surface area [ECSA]), which is probed either by Faradaic or non-Faradaic processes. Their increase is directly proportional to the increase in the ECSA and is related to an overall improvement in the reaction rate.[37,40,49,53,54]

However, the situation is more complex when considering the *ec*-CO_2RR owing to the fact that the CO_2 electroreduction is necessarily superimposed on the parasitic HER when carried out in an aqueous reaction environment, which leads to a less-than-unity Faradaic efficiency of the *ec*-CO_2RR. Thus, the presence of the capping agents and the applied deprotection treatment affect not only the overall reaction rate (current density normalized to the geometric surface area) but also the resulting product distribution.

Herein, we present a comprehensive study on an approach to electrochemical catalyst activation (surfactant removal) that utilizes the *ec*-CO_2RR itself to achieve the desired catalyst deprotection. As the catalyst of choice, we applied silver nanowires (Ag-NWs) that were synthesized by a self-seeding polyol process using high-molecular-weight PVP as the capping agent.[24,27,32,57,58] The coelectrolysis of water/CO_2 that is performed over Ag catalysts yields only H_2 and CO as the reaction products.[8−10,59] In the present study, we sought to demonstrate that the formed CO acts as an excellent surfactant removal agent that is capable of deprotecting the Ag-NWs,

https://dx.doi.org/10.1021/acscatal.0c02026
ACS Catal. 2020, 10, 8503−8514

thereby further self-accelerating the *ec*-CO_2RR at the expense of the parasitic HER and leading to CO efficiencies of nearly 100%. This PVP removal by "cathodic" electrode polarization complements the "oxidative" approach that was proposed by Oezaslan et al.[54]

EXPERIMENTAL SECTION

Catalyst Synthesis. Ag nanowires (Ag-NWs) were synthesized in a three-necked flask according to a modified protocol introduced by Jiu et al. and others.[24,27,32,57,58] For this purpose, 0.2 g of PVP (M_w = 1 300 000 g mol^{-1}, Sigma-Aldrich; see Figure 1) was dissolved at room temperature under

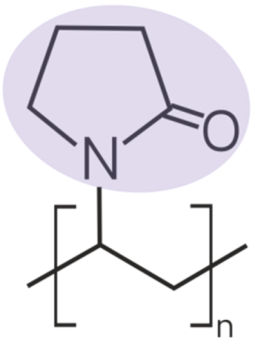

Figure 1. Polyvinylpyrrolidone (PVP) used as the capping agent for the Ag-NW synthesis. The pyrrolidone functionality attached to the linear aliphatic backbone is highlighted purple.

magnetic agitation in 25 mL of ethylene glycol (EG, Sigma-Aldrich, 99.8%). Subsequently, 0.25 g of silver nitrate ($AgNO_3$, Sigma-Aldrich, ACS reagent, ≥99.8%) was added to the PVP containing EG, followed by the addition of a solution of 1.95 mg of $FeCl_3$ (Sigma-Aldrich, 97%) predissolved in 2 mL of EG, which serves as a solvent and reducing agent.[24,32,57,58] This mixture was then stirred for an additional 2 min before the three-necked flask containing the transparent EG solution was transferred to a preheated oil bath. This solution was kept at 130 °C for a total of 5 h. During the first hour, the solution was continuously stirred, while no magnetic agitation was applied during the last 4 h of the thermal treatment. The resulting Ag-NW precipitate was separated from the EG solvent by centrifugation at 4000 rpm for 10 min, followed by three repetitive washing/centrifugation treatments using a mixture of Milli-Q water and acetone (V_{water}:V_{aceton} = 2:1), ultimately yielding 24 mg of the Ag-NW catalyst (denoted "as-synthesized"). The Ag-NW powder was finally redispersed in 8 mL of isopropanol (BASF SE, assay ≥99.0%).

Electrode Preparation. After 30 min of sonication, 50 μL of the Ag-NW suspension was drop-cast onto a glassy carbon support electrode (A = 0.8 cm^{-2}, Alfa Aesar, 2 mm thickness).

For the sake of comparison, Ag-NW catalysts were also dispersed onto a technical carbon support. For this purpose, 12 mg of the as-prepared Ag-NWs was suspended in 15 mL of isopropanol, followed by 1 h of sonication. Technical carbon powder (12 mg, Vulcan XC 72R, Cabot) was dispersed in 15 mL of isopropanol, and this was also followed by 1 h of sonication. Both suspensions were subsequently mixed and homogenized by sonicating for 30 min. The resulting suspension was dried under vacuum conditions and yielded a carbon-supported (C-supported) Ag-NW catalyst powder. This powder was redispersed in 4 mL of isopropanol containing 400 μL of Nafion solution (Aldrich, 5 wt % dissolved in a mixture of lower aliphatic alcohols and water) and subjected to 30 min of sonication. Subsequently, 50 μL of the resulting ink was drop-cast onto the glassy carbon support electrode (see the aforementioned protocol).

Electrode Characterization. The morphologies of the Ag-NW films (nonsupported, C-supported) that were deposited on the glassy carbon support electrodes were characterized by means of scanning electron microscopy (Zeiss Gemini SEM450). Complementary white-light interferometry (ContourGT profilometer, Bruker) was applied to determine the thickness and roughness of the Ag-NW films. For the transmission electron microscopy (TEM) imaging and selective area electron diffraction, an FEI Titan Themis instrument was used with an accelerating voltage of 300 kV.

An X-ray photoelectron (XPS) inspection was performed on a Physical Electronics (PHI) Quantum 2000 scanning ESCA microprobe system using monochromated Al Kα radiation ($h\nu$ = 1486.7 eV). A hemispherical capacitor electron-energy analyzer, equipped with a channel plate and a position-sensitive detector, was operated under an electron takeoff angle of 45°. For the acquisition of the high-resolution Ag3*d*, Cl2*p* and N1*s* photoemission data, the analyzer was operated with a constant pass energy mode at 23.5 eV and an energy step width of 0.20 eV. The X-ray beam diameter was around 150 μm. The binding energy was calibrated using the Cu2$p_{3/2}$, Ag3$d_{5/2}$, and Au4$f_{7/2}$ emissions at 932.62, 368.21, and 83.96 eV, respectively, to within ±0.1 eV [see ISO 15472; 2010-05]. Built-in electron and argon ion neutralizers were applied in order to compensate for eventual surface charging effects. The base pressure of the XPS system was below 5 × 10^{-7} Pa. The XPS spectra were analyzed using the MultiPak 8.2B software package and were subjected to a Shirley background subtraction. The atomic concentrations were determined based on the corrected relative sensitivity factors that were provided by the manufacturer and normalized to 100 atom %. The uncertainty was estimated to be ca. 10%.

Electrochemical Experiments. For all electrochemical experiments, a potentiostat/galvanostat (Metrohm Autolab 302N) was used to control the potential, current density, and transferred charge. The electrolysis experiments were carried out using a custom-built, airtight glass-cell (H-type) as previously described (see Figure S1).[60−62] For the *iR* compensation, cell resistance was determined by means of impedance spectroscopy (FRA module, Autolab Nova). Hence, all potentials provided herein are *iR*-compensated to ∼85% of the measured cell resistance.

The three-electrode arrangement used here consisted of a leakless Ag/$AgCl_{3M}$ electrode (Pine), a bright Pt-foil (15 mm × 5 mm), and the Ag-NW catalyst film (nonsupported, C-supported) serving as the reference, counter, and working electrodes, respectively.

For the sake of comparability, all potentials measured versus Ag/$AgCl_{3M}$ are referenced herein with respect to the reversible hydrogen electrode (RHE). The applied potentials (vs Ag/$AgCl_{3M}$) were converted to the RHE scale using the following equation:

$$E_{RHE}\ (V) = E_{Ag/AgCl(3M)}\ (V) + 0.210\ V + (0.059\ V \times pH)$$

Note that the anolyte and the catholyte were separated by a Nafion 117 membrane (Figure S1). This cell design also prevents the transfer of trace amounts of Pt ions from the anolyte to the catholyte when using Pt as the material for the counter electrode (see reference measurements presented in Figures S2−S5) as made evident by ICP-MS measurements

https://dx.doi.org/10.1021/acscatal.0c02026
ACS Catal. 2020, 10, 8503−8514

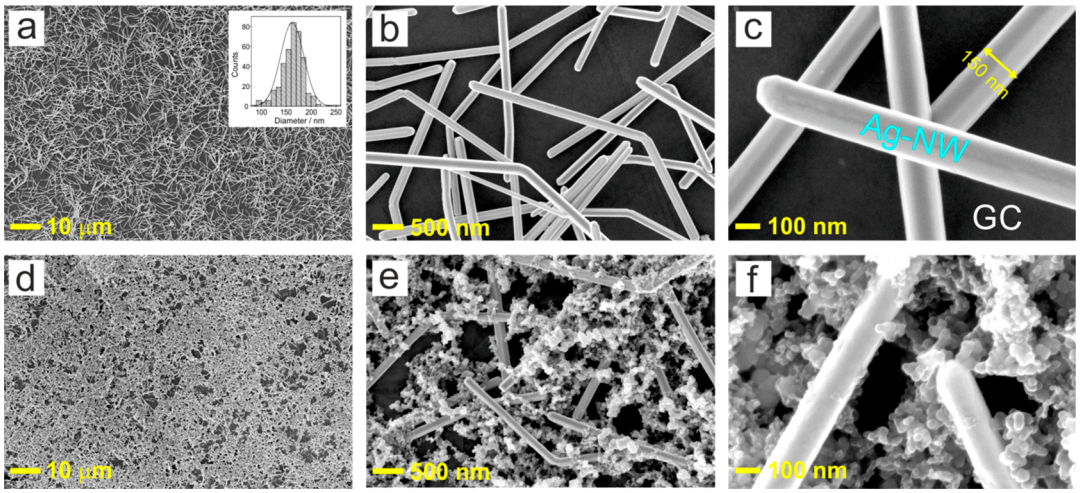

Figure 2. (a–c) Top-down SEM images of the Ag-NW film drop-cast on the glassy carbon (GC) support electrode; the inset in panel a shows a histogram representing the thickness distribution of the Ag-NWs. (d–f) Corresponding SEM images of the C-supported (Vulcan XC 72R) Ag-NWs drop-cast on the GC support electrode (for details, see the Experimental Section).

(NexION 2000 ICP-MS instrument, PerkinElmer). Also note that no change of the *ec*-CO_2RR product distribution is observed when exchanging the Pt counter electrode by Ir (see Figure S5).

Electrolysis experiments were carried out in 0.5 M $KHCO_3$ (ACS grade, Sigma-Aldrich) electrolyte solutions that were saturated with either Ar (blank) or CO_2 gas (99.999%, Carbagas). The pH of the CO_2- and Ar-saturated 0.5 M $KHCO_3$ was 7.5 and 8.9, respectively.

Technical details of the CO_2RR product analysis based on online gas-chromatography have been previously described.[60−62] A so-called single-catalyst approach was applied in order to demonstrate the pronounced hysteresis effects on the potential-dependent CO_2RR product distribution.[63] The same electrode was used for a defined sequence of potentiostatic electrolysis experiments, which differed in both the electrolysis time and the width of the potential window applied to the catalyst. In a further step a multicatalyst approach was applied,[63] in which a newly prepared (preconditioned) catalyst was used for each applied electrolysis potential to demonstrate the performance of the deprotected Ag-NW catalysts.

RESULTS AND DISCUSSION

Structural Characterization. Figure 2 displays top-down SEM images of the two types of Ag-NW catalysts used in this study. A three-dimensional network of randomly distributed and loosely packed Ag-NWs is formed after drop-casting the Ag-NW suspension on the glassy carbon support electrode (Figure 2a–c). Complementary white light interferometry reveals a homogeneous layer of Ag-NWs on the glassy carbon electrode with a root-mean-square (RMS) roughness and film thickness of 76 and 885 nm, respectively (Figure S6a–c). On the nm length scale the network of Ag-NWs shows a more inhomogeneous appearance. Note that the surface of the glassy carbon support remains visible in the top-down SEM inspection (Figure 2c). Therefore, the entirety of the Ag-NW film is, when exposed to the aqueous environment, likely to be wetted by the electrolyte down to the glassy carbon electrode. A statistical analysis of the SEM images reveals that the mean thickness of the Ag-NWs is approximately 162 nm (inset of Figure 2a), whereas they range in length from ca. 1 to several microns. According to the literature,[22,64,65] the Ag-NWs exhibit a 5-fold twinned face-centered cubic (fcc) structure with a preferential orientation along the (110) crystallographic direction. The sidewalls of the Ag-NWs consist of five (100) textured facets, whereas the pentagonal apex of the Ag-NW is (111) terminated. These hexagonal facets represent the actual growth front in the Ag-NW synthesis in which the monovalent Ag^+ precursor ions are reduced and added to the developing nanowire. The origin of this highly anisotropic metal growth is the chemisorption of additives/surfactants (e.g., chloride and PVP), which is supposed to be weaker on the (111) facets, thereby rendering them more active for the e-less metal deposition than the (100) facets.[58] The latter experience a steric blocking by the more strongly chemisorbed surfactants.[22,66]

One drawback of the Ag-NW model catalyst drop-cast on the glassy carbon support is the potential loss of catalyst material during extended electrolysis, in particular when the electrolysis reaction involves massive gas evolution, e.g., by the parasitic HER that is inevitably superimposed on the CO_2RR in an aqueous environment.[43] This loss of catalyst material is a result of the weak adhesion of the NW layer to the glassy carbon support electrode and the loose packing of the Ag-NWs inside the catalyst film. One possible approach to circumventing this structural degradation is based on the mechanical stabilization of the NW film. This stabilization can be achieved by the use of a technical carbon support (e.g., Vulcan) in combination with a Nafion binder, thereby substantially improving both the adhesion of the catalyst film to the glassy carbon support and the cohesion inside the film.[67] Figure 2d–f depicts the corresponding top-down SEM images of the C-supported Ag-NW catalysts that were drop-cast on the glassy carbon electrode, demonstrating that individual Ag-NWs were embedded in the highly porous carbon support. However, one possible drawback of this approach could be an increase in the contribution of the porous carbon material to the resulting product distribution in the form of an increase in the parasitic HER (see the discussion of Figure 6 below). An alternative approach to catalyst stabilization, which is based on a so-called photonic curing, has recently been introduced by Hou et al.[43] This treatment induces a local melting and subsequent solidifying of the NWs at their points of contact. Photonically

https://dx.doi.org/10.1021/acscatal.0c02026
ACS Catal. 2020, 10, 8503−8514

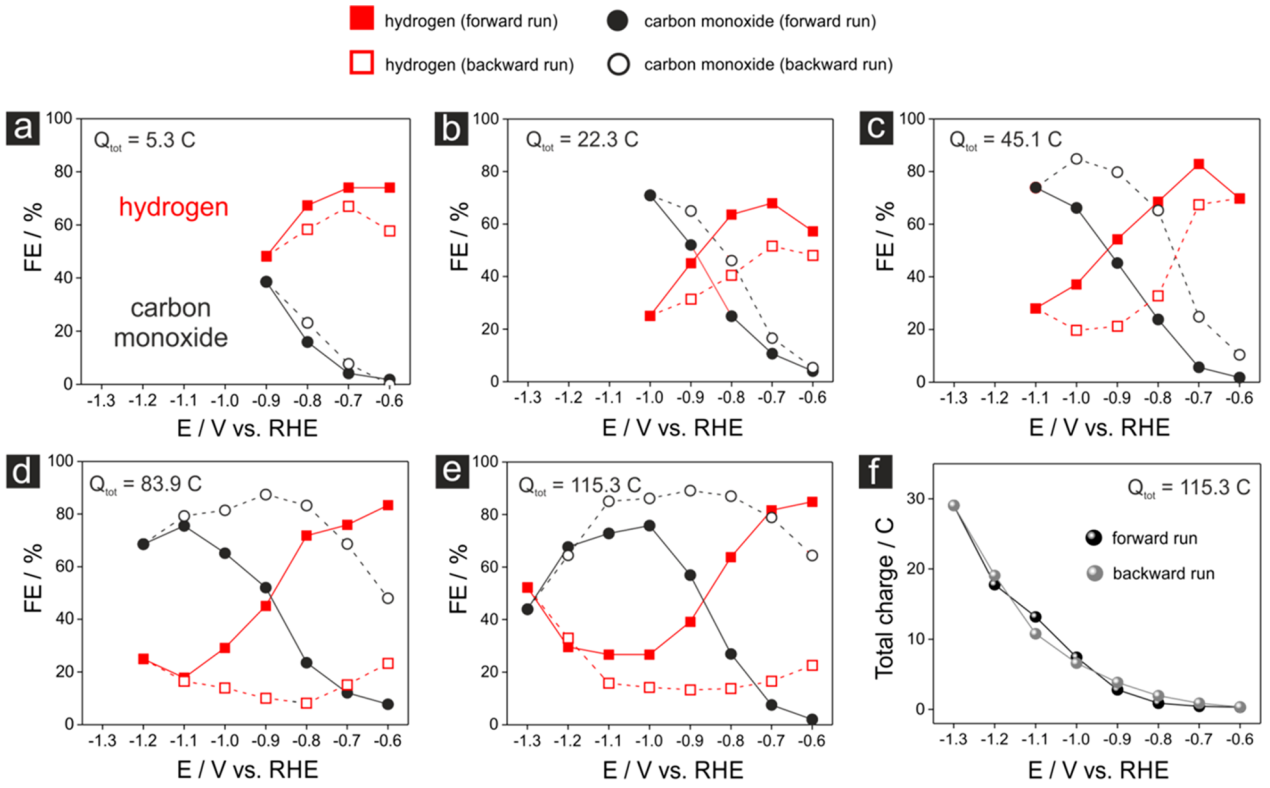

Figure 3. (a–e) Hysteresis effects appearing in the forward and backward runs of the electrochemical looping experiments (40 min duration at each potential) carried out over Ag-NW catalysts (see Figure 2a–c) in CO_2-saturated 0.5 M $KHCO_3$ (single catalyst approach); the total cathodic charges transferred during the "electrochemical looping" are indicated. (f) Graph showing the total integrated charge corresponding to the electrolysis experiments shown in panel e.

cured freestanding films of metallic nanowires were demonstrated to resist even massive gas-evolution reactions without any indication of structural degradation.[43]

Electrochemical Activation of Ag-NW Catalysts by Electrochemical Looping. The working hypothesis, which was to be verified in the following experiments, is that the surfactants (i.e., chloride and PVP) on the Ag surface of the deposited nanowires severely affect the product distribution of *ec*-CO_2RR and undergo substantial alterations over the course of the performed coelectrolysis reaction. An efficient catalyst activation that is induced by the electrolysis reaction itself can be deduced from the pronounced hysteresis characteristics observed in the potential-dependent product distribution, which is displayed in Figure 3 as Faradaic efficiency versus applied potential (FE versus *E*) plots (Table S1). These dedicated electrolysis experiments are referred to as "electrochemical looping" (ec-l), in which the applied electrolysis potentials of the individual 40 min long electrolyses were changed in a stepwise manner from a fixed starting point of E_{start} = −0.6 V vs RHE to a variable "lower" vertex potential (E_{vertex}) that ranged from −0.9 V vs RHE to −1.3 V vs RHE (Figure 3a–e). The electrolysis loop is closed through the corresponding backward run of electrolysis experiments and ends at the initial starting potential (E_{start} = E_{end}). The main products of the electrolysis in the CO_2-saturated 0.5 M $KHCO_3$ aqueous solution are CO (black circles, Figure 3) and H_2 (red squares, Figure 3). The filled and nonfilled circles/squares refer to FE values, which correspond to the forward and the corresponding backward runs of the electrochemical looping campaigns. As long as the lower vertex potential remains larger than or equal to −0.9 V vs RHE (Figure 3a), only a marginal deviation is observed in the product distributions of the forward and the corresponding backward electrolysis runs (see also Figure S7). However, a minor trend toward increased CO efficiencies (decreased H_2 efficiencies) can be observed in the backward run. This positive trend of catalyst activation is continued by further shifting the lower vertex potential to more negative applied electrolysis potentials (Figure 3b–e). When extending the potential window of electrolysis to a vertex potential of E_{vertex} = −1.3 V vs RHE, CO efficiencies of >80% were achieved in the corresponding backward electrolysis run (Table S1e). In general, the shape of the product distribution in the FE versus *E* plot in Figure 3e displays an anticorrelated change in the FE values for CO and H_2, which exceed the maximum in CO efficiency (minimum in H_2 efficiency) at potentials between −1.0 and −1.1 V vs RHE (forward run). Interestingly, a more extended plateau of approximately 300 mV develops in the corresponding backward run in the potential range from −1.1 V to −0.8 V vs RHE, ultimately reaching CO efficiencies of >80%.

The FE_{CO} and FE_{H_2} values were the most substantially impacted by electrochemical looping at medium and low overpotentials (>−1.1 V vs RHE), whereas only minor differences were observed in the forward and backward runs for applied electrolysis potentials of < −1.2 V vs RHE (Figure 3e). In Figure 3e, the differences in potentials between the backward and the respective forward runs were ΔFE_{CO} = +10.3% at −1.0 V vs RHE, ΔFE_{CO} = +32.2% at −0.9 V vs RHE, ΔFE_{CO} = +60.0% at −0.8 V vs RHE, ΔFE_{CO} = +71.4% at −0.7 V vs RHE, and ΔFE_{CO} = +62.3% at −0.6 V vs RHE (see also Figure S7).

The absence of any substantial improvement in the FE_{CO} values at the lowest applied electrolysis potentials (<−1.2 V vs

https://dx.doi.org/10.1021/acscatal.0c02026
ACS Catal. 2020, 10, 8503−8514

RHE) can be rationalized by the onset of CO_2 mass transfer limitations, where the CO_2 concentration in the diffusion boundary layer is expected to drop down to zero as a result of increased CO_2RR rates (partial current densities). Therefore, the continuous activation of the catalyst material under CO_2 mass transport conditions does not lead to a further shift in the product distribution toward CO. The characteristics of pronounced hysteresis that can be seen at medium and low overpotentials (Figure 3a−e, Figure S7) are clearly indicative of the "activation" of the Ag-NW catalyst toward CO formation, which is mediated by the applied electrochemical looping. This is demonstrated in the first experiment, as the coelectrolysis of water/CO_2 resulted in the desired deprotection (chemical cleaning) of the catalyst surface. It can be hypothesized that changes in the composition of the surface are responsible for the observed changes in the potential-dependent product distribution (see discussion on the XPS analysis below). A first control experiment proving that the improved FE values (Figure 3) indeed originate from an effective removal of the surfactants from the catalyst surface during the ec-l treatment is shown in Figure S8. It compares the CO efficiencies of a Ag-NW catalyst before and after the ec-l treatment with the ones of a Ag-foil (GoodFellow, 99.95%, 0.25 mm thickness) which serves as a model system for a surfactant-free Ag catalyst. As expected, the CO efficiencies do not change by the ec-l treatment in the case of the Ag-foil catalyst. Further, we exclude severe structural or morphological changes of the Ag-NW catalyst in the course of the ec-l treatment as origin of the observed catalyst activation (see combined SEM and TEM analysis in Figure S9). It should be noted that, based on our experimental results, it cannot be concluded on which active sites of the Ag-NWs the HER and the *ec*-CO_2RR take place. Both experimental and theoretical studies on Ag single crystals strongly suggest, however, that defects, in particular steps and kink sites, are substantially more active toward CO formation than the planar (100) and (111) facets.[10,68]

One important aspect of this activation effect, discussed herein, is displayed in Figure 3f. In principle, the total (integrated) charge that is transferred at each electrolysis potential—derived from the respective j versus t (40 min) plots—exponentially increases with the applied overpotential (Table S2a). However, when comparing the forward and backward runs, it becomes obvious that the total transferred charge for a given electrolysis potential does not substantially change during electrochemical looping. This implies that only the product distribution (ratio of FE_{CO} and FE_{H_2} values) is altered by this treatment, whereas the total current density normalized to the geometric surface area (total transferred charge) remains unaffected. This is an important distinction between the current study and previous studies on catalyst activation processes in which only a single electrocatalytic reaction needs to be considered (e.g., ORR,[40,49,55] OER,[49] or HER[37]) and where increased reaction rates directly correlate with an increase of the electrochemically active surface area (ECSA).[53,54]

In order to elaborate on which experimental factors contribute to the observed change in the product distribution (e.g., nature of the formed CO_2RR reaction product, applied vertex potential [E_{vertex}], current density [j], electrolysis time, total transferred charge [Q], etc.), an extra electrochemical looping experiment was carried out in an Ar-saturated (CO_2-free) 0.5 M $KHCO_3$ electrolyte (pH = 8.9) while applying the full range of electrolysis potentials (E_{vertex} = −1.3 V vs RHE). This approach excludes CO as a reaction product and exclusively produces H_2 during electrolysis. Note that bicarbonate can be neglected as a reactant when Ag is used as the catalyst.[63] Figure 4a compares the total transferred

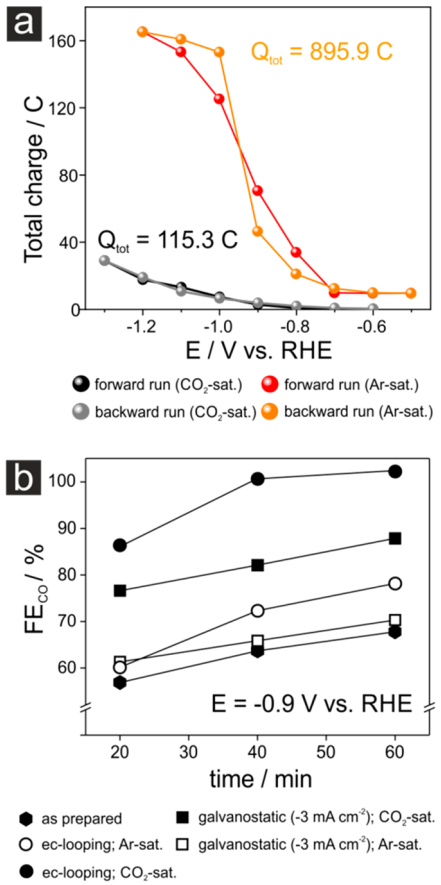

Figure 4. (a) Integrated cathodic charges of potentiostatic electrolysis reactions carried out in Ar- and CO_2-saturated 0.5 M $KHCO_3$ electrolytes (electrochemical looping). (b) Time-resolved FE_{CO} values derived from electrolysis reactions carried out at −0.9 V vs RHE after applying various activation protocols (for details, see the text).

charges of the chemical looping experiments carried out in the Ar- and the CO_2-saturated electrolyte (Table S2a). The most obvious difference is in the total amount of transferred charges, which is substantially higher for the CO_2-free case in which the HER is the only electrolytic reaction. These results suggest that the HER is not effectively hindered by the presence of the surfactants (chloride and PVP). Note that the expected exponential increase in the total transferred charge passes into a plateau regime at applied potentials that are more negative than −1.1 V vs RHE (Figure 4a). This particular feature originates from the partial blocking of the electrode surface by hydrogen bubbles, which appear at elevated current densities (surface area change under massive gas evolution; see Figure S10).

It becomes obvious from Figure 4a that the total transferred charges are substantially lower when CO is formed as one of the reaction products. This is likely owing to a high surface concentration of formed and temporarily adsorbed *CO (the asterisk represents an adsorption state), which therefore effectively sterically blocks those surface sites on the Ag-NW

https://dx.doi.org/10.1021/acscatal.0c02026
ACS Catal. 2020, 10, 8503−8514

that are active toward the competing HER. It is clear that the chemisorbed *CO acts as an efficient "suppressor" with regard to the HER.[63] The binding strength of *CO to the Ag catalyst is generally considered to be relatively low (i.e., in comparison to Cu),[69−71] thereby rationalizing the easy release of the formed *CO from the catalyst surface into the electrolyte phase (Figure 5). However, the *CO binding to the Ag-NW surface seems

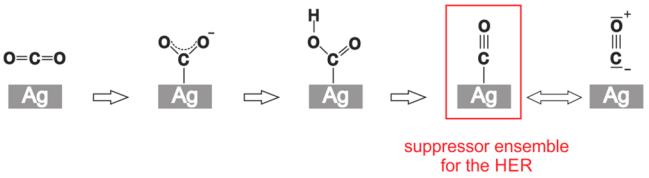

Figure 5. Reaction pathway of CO_2 conversion into CO on Ag catalysts; the strong suppressing action of the chemisorbed CO with regard to the HER is highlighted.

sufficiently high to remove surfactants from the surface during the water/CO_2 coelectrolysis reaction, which can be considered to be the origin of the profound hysteresis effects observed in the FE vs E plots (Figure 3). It can be hypothesized that the observed Ag-NW deprotection is based on the "chemisorptive displacement" of the surfactants by the *CO. The temporary presence of chemisorbed *CO on the Ag-catalyst surface has been previously demonstrated by operando vibrational (IR or Raman) spectroscopy.[72−74] The massive gas evolution (by H_2 and CO)—which is in agreement with the water/CO_2 coelectrolysis at high current densities (Figure S10)—can be considered to be an additional beneficial effect and facilitates the convectional transport of the released PVP from the catalyst surface into the bulk of the electrolyte phase. This process therefore prevents the readsorption of the PVP on the catalyst surface. Possible surfactant readsorption phenomena have been identified by Oezaslan et al.[54] as one possible drawback of the oxidative approach to PVP removal.

The chemical nature of the electrolysis product (H_2 or CO) that is formed during the electrochemical looping clearly plays a vital role in the deprotection of the desired catalyst. This effect can be denoted as surfactant removal by "chemical" cleaning. This has been demonstrated by additional experiments for CO_2 electrolysis, which were performed at a constant electrolysis potential of E = −0.9 V vs RHE using Ag-NW catalysts that had been subjected to a full chemical looping pretreatment (E_{vertex} = −1.3 V vs RHE) in either the CO_2-saturated or the CO_2-free (Ar-saturated) electrolyte. Figure 4b illustrates the time-dependent evolution of the FE_{CO} values of the electrolyses that were carried out in the CO_2-saturated electrolyte following the ec-l treatments.

For the purpose of comparison, the resulting FE_{CO} values of the as-prepared samples are also provided. It is clear that maximal CO efficiency (close to 100%) is most rapidly attained when preconditioning in the CO_2-saturated electrolyte, whereas the one subjected to the chemical looping in the Ar-saturated electrolyte demonstrates only marginally improved CO efficiencies. This finding is striking, as substantially higher charges were transferred, and higher current densities were applied during chemical looping in the Ar-saturated electrolyte (Q_{tot} = 895.9 C, j_{max} = −85.6 mA cm^{-2} at E = −1.3 V vs RHE, see Table S2a) in comparison to the CO_2-saturated electrolyte (Q_{tot} = 115.3 C, j_{max} = −15.1 mA cm^{-2} at E = −1.3 V vs RHE). The total charge is obviously not the key parameter for the activation of the catalyst. Furthermore, the massive gas evolution alone does not seem to be sufficient for the deprotection of the Ag-NW catalyst (see also Figure S11).

As the total transferred charges were different in both electrochemical looping treatments (Ar- and CO_2-saturated electrolytes, Figure 4a) it is hard to compare them directly. We therefore applied two addition pretreatment techniques on the Ag-NW catalysts—based on galvanostatic electrolyses at j = −3 mA cm^{-2}—in both CO_2-saturated and CO_2-free electrolytes. In these cases, the total transferred charge was normalized to Q_{tot} = 115.3 C, which allowed for a direct comparison to the electrochemical looping experiment performed in the CO_2-containing electrolyte (Figure 4a). The corresponding FE_{CO} data for the subsequent CO_2 electrolysis reactions at −0.9 V vs RHE are included in the plot in Figure 4b. Again, pretreatment in the CO_2-free electrolyte yields poor FE_{CO} values in the actual CO_2 electrolysis experiment. Interestingly, the electrochemical looping in the CO_2-saturated electrolyte is superior to the galvanostatic pretreatment at j = −3 mA cm^{-2} that was carried out in the same electrolyte. Obviously, the applied electrolysis potential and the electrolysis time are important factors for the efficiency of surfactant removal (see also Figures S12 and S13, and discussion of the XPS data below). It can be assumed that, due to the increased CO partial current densities, the CO surface coverage is higher at lower vertex potentials thus also rationalizing the observed potential dependence of the hysteresis characteristics (Figure 3).

An extra electrolysis experiment was carried out using C-supported Ag-NWs as the catalyst in order to demonstrate that the electrochemical looping works when the NWs are embedded into a technical carbon matrix. The result of this ec-l experiment exhibits the desired trend of improved FE_{CO} values in the corresponding backward run of the electrochemical looping (Figure 6), in which values of FE_{CO} = 90.7%

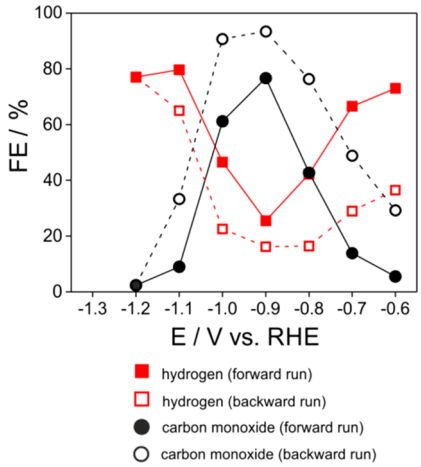

Figure 6. Activation of C-supported Ag-NW catalysts (see Figure 2d–f).

and FE_{CO} = 93.4% at E = −1.0 V and −0.9 V vs RHE were achieved. However, the HER is still dominating the product distribution at lower applied overpotentials in contrast to the nonsupported Ag-NWs (see Figure 3e). This observation can be rationalized by an effect that is mediated by the high surface area of the C-support, which is active toward the HER but not toward the CO_2RR. The increased FE_{H_2} values at the lowest overpotentials (Figure 6) are therefore the result of a surface

https://dx.doi.org/10.1021/acscatal.0c02026
ACS Catal. 2020, 10, 8503−8514

area effect of the component in the catalyst film, which is selective toward the HER (Vulcan and glassy carbon support electrode, see Figure S6d–f).

As the extended electrochemical looping (E_{vertex} = −1.3 V) was identified as the most effective pretreatment for the deprotection of the catalyst, a full set of additional electrolysis experiments were performed using a single catalyst approach[63] in which newly prepared and preconditioned catalyst (see Figures 2a–c and 3e) were used for 1 h long electrolysis experiments and applied potential. This approach guaranteed identical starting conditions for CO_2 electrolysis and minimized time-dependent changes on the selectivity of the CO_2RR products. Figure 7a represents the "true" potential-dependent

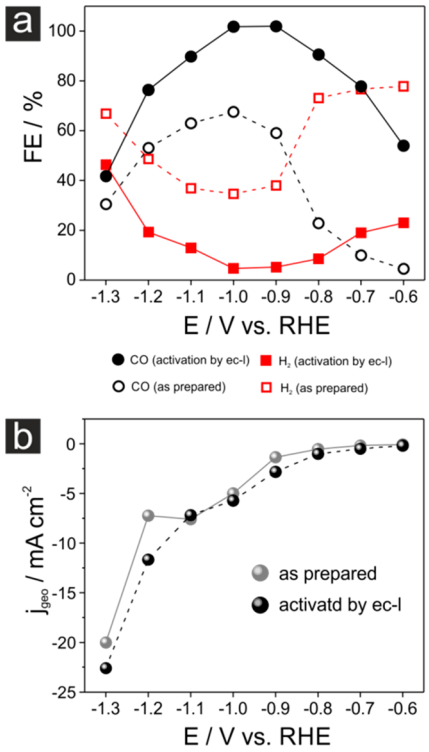

Figure 7. (a) *ec*-CO_2RR product distribution of 1 h lasting electrolysis experiments comparing the as prepared Ag-NW catalysts and those pretreated by an electrochemical looping (E_{vertex} = −1.3 V vs RHE, see Figure 3e). (b) Steady-state total current densities of the electrolysis experiments which correspond to the data in panel a.

product distribution of the Ag-NW catalyst after the successful deprotection of the Ag-NWs. For comparison purposes, the corresponding 1 h lasting *ec*-CO_2RR experiments of the as-prepared Ag-NW catalysts are also provided. CO efficiencies of ∼100% are obtained after the ec-l preconditioning (E_{vertex} = −1.3 V vs RHE) in the potential range between −1.0 and −1.1 V. These efficiencies are competitive in comparison to previously published data.[20,21,63,75] Table S6 provides a comprehensive overview of the relevant benchmark studies that have used Ag as the *ec*-CO_2RR catalyst material, while Figure 7b demonstrates again that only the product selectivity is changed by the ec-l treatment, and not the overall reaction rate. The total (steady-state) current densities remain largely unaffected by electrochemical looping.

XPS Analysis. Our analysis of the *ec*-CO_2RR product distribution (Figures 3 and 7a) clearly demonstrates an activation of the Ag-NW catalyst by the chemical looping but lacks deeper mechanistic insights into the chemical origin of the observed improved CO selectivity. Therefore, complementary XPS experiments were performed to provide information on the compositional changes of the catalyst surface. Figure 8a–c depicts spectra of the Ag3*d*, Cl2*p*, and N1*s* photoemissions that are representative of the as-prepared Ag-NW catalyst prior to its deprotection. These results demonstrate that both chloride and PVP are present on the surface of the as-prepared Ag-NWs, as indicated in the schematics of Figure 9. The performed electrolysis experiments clearly show that the HER does not effectively contribute to the deprotection of the desired catalyst (Figure 4b).

Figure 8d,e displays the integrated intensities of the N1*s* and Cl2*p* emissions normalized to the one of the respective Ag3*d* emissions. These data can be used to assess the effectiveness of the surfactant removal depending on the particular pretreatment protocol that is applied. Note that the (I_{Cl2p}:I_{Ag3d}) ratios are generally lower than the corresponding (I_{N1s}:I_{Ag3d}) values, irrespective of the applied pretreatment. One possible reason for this observation is that a layered structure of the surfactant shell was covering the Ag-NWs. Chloride is likely to be chemisorbed and would therefore be in direct contact with the Ag-NW surface.

These halide anions are considered to play a crucial role in the initial nucleation stage of Ag-NW formation (self-seeding via AgCl nuclei).[32] Furthermore, the (100) textured sidewalls of the Ag-NWs in particular exhibit a strong tendency toward specific chloride adsorption, which can result in a maximum (saturation) surface coverage of Θ = 0.5 ML (normalized to the number of surface atoms on the [100] surface) when a Ag(100)-c(2 × 2)-Cl surface ad-layer is formed.[76−78] The high-molecular-mass PVP polymer (M_w = 1 300 000 g mol^{-1}) presumably constitutes the outermost shell of the as deposited Ag-NW. A "coiling" of the linear PVP around the Ag-NW is discussed in the literature, where the pyrrolidone acts as the anchor group of the polymer backbone to free metallic sites on the surface (Ag−O or Ag−N coordination).[32] Considering the high molecular mass of the PVP, it is likely that hydrophobic effects lead to an enhanced PVP agglomeration on the Ag-NWs beyond monolayer coverages. This layered configuration of surfactants, as depicted in Figure 9 (left panel), could also contribute to the reduced intensity observed in the Cl2*p* emission of the chloride that accumulated at the "buried" interface.

The electrochemical activation treatments applied to the Ag-NW catalysts exhibit strong variations in the PVP removal efficiency. The treatments in which H_2 was the exclusive electrolysis product (protocols 2 and 3 in Figure 8d) were less effective, while those using postsynthesis deprotection approaches involving the formation of CO (protocol 4 and 5 in Figure 8d) were more effective. The optimal PVP removal characteristics that were observed for the electrochemical looping approach (E_{vertex} = −1.3 V vs RHE) are in full agreement with our electrolysis data (Figures 4b and 7a). The XPS results also confirm that the PVP (and its removal) is the main origin for the observed hysteresis effects in the product distribution (Figure 3).

Interestingly, all pretreatments that were applied herein led to the near-complete removal of the chemisorbed chloride (Figure 8e). The origin of the chloride removal is the potential-dependent electrostatic repulsion of the chloride anions at the negatively polarized electrode surface.

https://dx.doi.org/10.1021/acscatal.0c02026
ACS Catal. 2020, 10, 8503−8514

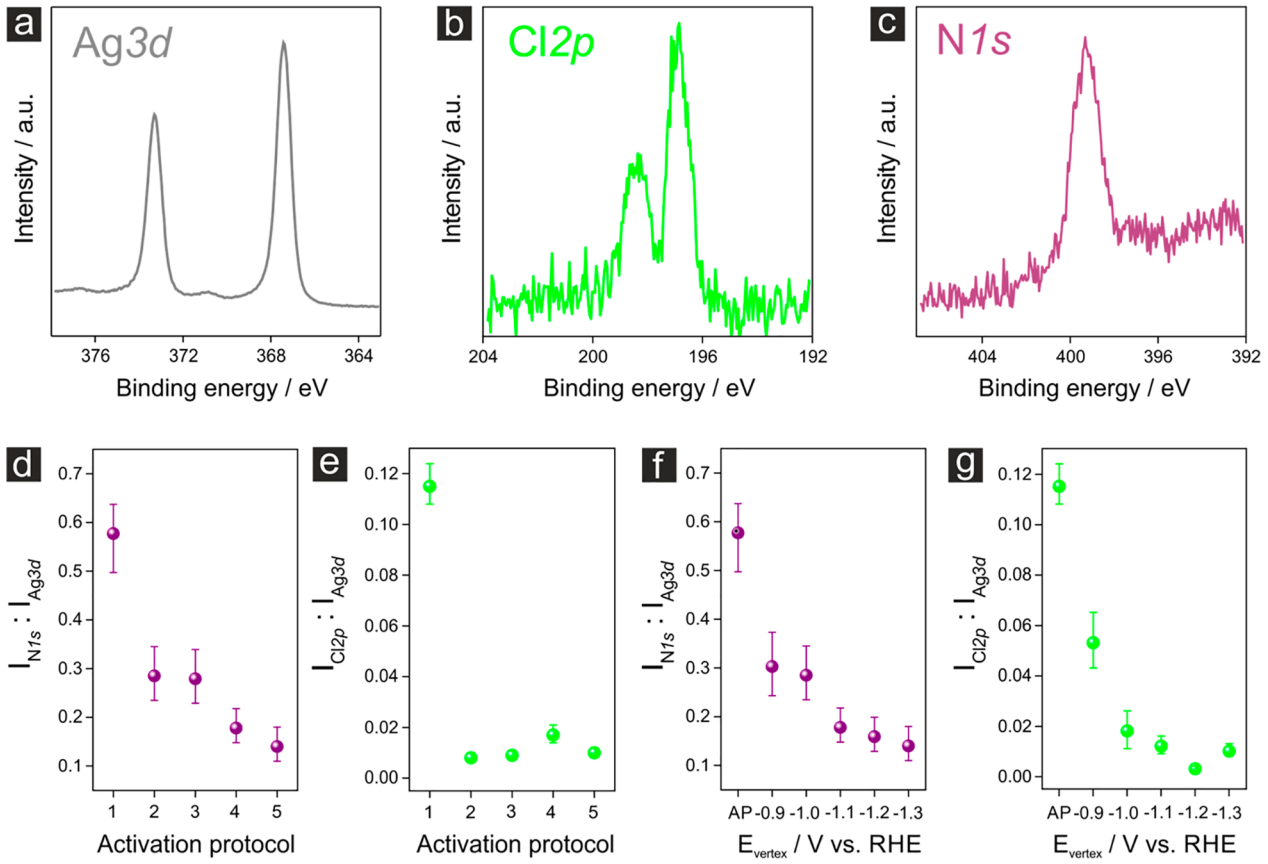

Figure 8. (a–c) Representative XPS spectra of the Ag3*d*, Cl2*p*, and N1*s* emissions derived from the Ag-NW catalyst on the GC support electrode (see Figure 2a–c). (d, e) Integrated intensities of the N1*s* and Cl2*p* emissions normalized to the corresponding integrated intensity of the Ag 3d emission; the digits on the *x*-axis indicate the respective catalyst activation protocols. **1**, as prepared; **2**, galvanostatic electrolysis in Ar-saturated (CO_2-free) 0.5 M $KHCO_3$ solution at $j = -3$ mA cm^{-2}, the total transferred charge was $Q = 115.3$ C; **3**, electrochemical looping (ec-l) in Ar-saturated 0.5 M $KHCO_3$ solution, the vertex potential was $E_{vertex} = -1.3$ V vs RHE, the total transferred charge was $Q = 895.9$ C; **4**, galvanostatic electrolysis in CO_2-saturated 0.5 M $KHCO_3$ solution at $j = -3$ mA cm^{-2}, the total transferred charge was $Q = 115.3$ C; **5**, electrochemical looping (ec-l) in CO_2-saturated 0.5 M $KHCO_3$ solution, the vertex potential was $E_{vertex} = -1.3$ V vs RHE, the total transferred charge was $Q = 115.3$ C (the activation conditions correspond to those in Figure 2b). (f, g) Integrated intensities of the N1*s* and Cl2*p* emissions normalized to the corresponding integrated intensity of the Ag3*d* emission measured after the electrochemical looping (ec-l) treatment; the respective vertex potentials are indicated on the *x*-axis (the activation conditions correspond to those in Figure 3).

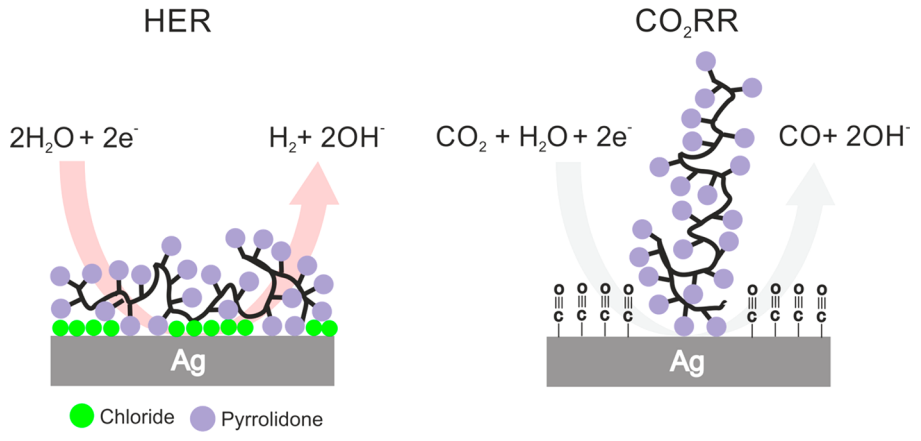

Figure 9. Schematics demonstrating the PVP and Cl terminated Ag surface which is still active for the HER (left panel) and the Ag surface which is activated upon CO production through PVP and Cl removal (right panel).

From these observations it can safely be concluded that it is the remaining PVP that disturbs the *ec*-CO_2RR rather than the chemisorbed chloride. Our analyses were further complemented by an extra XPS inspection of the catalyst films subjected to the systematic electrochemical looping experiments presented in Figure 3a–d. The results of this analysis are depicted in Figure 8f,g and clearly demonstrate that the vertex potential E_{vertex} and the width of the potential window that were applied to the catalysts in the electrochemical looping are necessary for the effectiveness of the surfactant removal. The

https://dx.doi.org/10.1021/acscatal.0c02026
ACS Catal. 2020, 10, 8503–8514

surface concentration of adsorbed chloride could be reduced to the minimum possible quantity when vertex potentials of E_{vertex} = −1.1 V vs RHE were applied, whereas the PVP surface coverage continued to decrease to an applied vertex potential of E_{vertex} = −1.3 V vs RHE. Our XPS results are also in full agreement with the working hypothesis made on the basis of the electrolysis data presented in Figure 3 and confirm that compositional changes at the catalyst surface are the origin of the hysteresis features observed in the electrochemical analysis (see also Figure S15). Complementary ^{1}H NMR measurements suggest that the PVP is removed structurally intact from the Ag surface. There are no PVP degradation products observed in the electrolyte after the electrolysis.

CONCLUSIONS AND OUTLOOK

Here, we demonstrate that the presence of surfactants (e.g., chloride and in particular PVP) on the surface of the colloidal silver catalyst negatively impacts the *ec*-CO_2RR selectivity and instead favors the HER in electrolysis reactions carried out in CO_2-saturated aqueous 0.5 M bicarbonate electrolytes.

The present work clearly demonstrates the importance of complete surfactant removal for the catalyst performance evaluation which might otherwise be superimposed by "transient artifacts", in particular in the initial stage of electrolysis (time scale of hours).

Electrochemical looping—a sequence of potentiostatic electrolysis experiments with defined starting, vertex, and ending potentials—has been demonstrated to be highly effective in the deprotection of catalysts, provided that CO is formed as the main electrolysis product. The chemical nature of the reaction product formed during electrolysis is found to be vital to the effectiveness of the activation of the catalysts via surfactant removal. An extended potential window in the electrochemical looping pretreatment, spanning from E_{start} = −0.6 V vs RHE to E_{vertex} = −1.3 V vs RHE, yields substantially improved CO efficiencies, which attained FE_{CO} = 100% at −1.0 V (j_{CO} = −5.8 mA cm^{-2}) and −1.1 V vs RHE (j_{CO} = −6.5 mA cm^{-2}). This improvement in the product selectivity relative to the as-prepared Ag-NWs is in agreement with the observed decrease in the normalized PVP surface concentration. This catalyst deprotection protocol is also transferable to C-supported Ag-NW catalyst systems.

Our future research will address the application of these electrochemically activated Ag-NW catalysts in flow-cell electrolyzer systems in detail in order to demonstrate the importance of the environment (gaseous versus aqueous/liquid) for surfactant removal under *operando* experimental conditions.

ASSOCIATED CONTENT

Supporting Information

The Supporting Information is available free of charge at https://pubs.acs.org/doi/10.1021/acscatal.0c02026.

Additional data and figures including a photograph, calibration curve, XPS spectrum, product distributions, white-light interferometric characterization, hysteresis characteristics, CO efficiencies, SEM images, TEM images, optical photographs, electrochemical looping, and ^{1}H NMR analysis (PDF)

AUTHOR INFORMATION

Corresponding Authors

Yuhui Hou − *Department of Chemistry and Biochemistry, University of Bern, Bern 3012, Switzerland;* orcid.org/0000-0003-1616-562X; Email: yuhui.hou@dcb.unibe.ch

Peter Broekmann − *Department of Chemistry and Biochemistry, University of Bern, Bern 3012, Switzerland;* orcid.org/0000-0002-6287-1042; Email: peter.broekmann@dcb.unibe.ch

Authors

Huifang Hu − *Department of Chemistry and Biochemistry, University of Bern, Bern 3012, Switzerland*

Menglong Liu − *Department of Chemistry and Biochemistry, University of Bern, Bern 3012, Switzerland*

Ying Kong − *Department of Chemistry and Biochemistry, University of Bern, Bern 3012, Switzerland*

Nisarga Mysuru − *Department of Chemistry and Biochemistry, University of Bern, Bern 3012, Switzerland*

Changzhe Sun − *Department of Chemistry and Biochemistry, University of Bern, Bern 3012, Switzerland*

María de Jesús Gálvez-Vázquez − *Department of Chemistry and Biochemistry, University of Bern, Bern 3012, Switzerland*

Ulrich Müller − *Surface Science and Coating Technology, Empa, Swiss Federal Laboratories for Materials Science and Technology, Dübendorf 8600, Switzerland*

Rolf Erni − *Electron Microscopy Center, Empa, Swiss Federal Laboratories for Materials Science and Technology, Dübendorf 8600, Switzerland;* orcid.org/0000-0003-2391-5943

Vitali Grozovski − *Department of Chemistry and Biochemistry, University of Bern, Bern 3012, Switzerland*

Complete contact information is available at: https://pubs.acs.org/10.1021/acscatal.0c02026

Notes

The authors declare no competing financial interest.

ACKNOWLEDGMENTS

The financial support by the CTI Swiss Competence Center for Energy Research (SCCER Heat and Electricity Storage) is gratefully acknowledged. P.B. acknowledges the financial support by the Swiss National Science Foundation (SNSF) via Project 200020_172507. H.H., M.L., Y.K., and C.S. acknowledge the financial support by the Chinese Scholarship Council (CSC). Y.H. acknowledges the financial support by the University of Bern.

REFERENCES

(1) Change is in the air. *Nat. Catal.* **2018**, *1* (2), 93−93.

(2) Jhong, H.-R. M.; Ma, S.; Kenis, P. J. A. Electrochemical Conversion of CO_2 to Useful Chemicals: Current Status, Remaining Challenges, and Future Opportunities. *Curr. Opin. Chem. Eng.* **2013**, *2* (2), 191−199.

(3) Jones, J.-P.; Prakash, G. K. S.; Olah, G. A. Electrochemical CO_2 Reduction: Recent Advances and Current Trends. *Isr. J. Chem.* **2014**, *54* (10), 1451−1466.

(4) Whipple, D. T.; Kenis, P. J. A. Prospects of CO_2 Utilization via Direct Heterogeneous Electrochemical Reduction. *J. Phys. Chem. Lett.* **2010**, *1* (24), 3451−3458.

(5) Durst, J.; Rudnev, A.; Dutta, A.; Fu, Y.; Herranz, J.; Kaliginedi, V.; Kuzume, A.; Permyakova, A. A.; Paratcha, Y.; Broekmann, P.; Schmidt, T. J. Electrochemical CO_2 Reduction - A Critical View on Fundamentals, Materials and Applications. *Chimia* **2015**, *69* (12), 769−776.

(6) Samavati, M.; Santarelli, M.; Martin, A.; Nemanova, V. Production of Synthetic Fischer−Tropsch Diesel from Renewables: Thermoeconomic and Environmental Analysis. *Energy Fuels* **2018**, *32* (2), 1744−1753.
(7) Haas, T.; Krause, R.; Weber, R.; Demler, M.; Schmid, G. Technical photosynthesis involving CO_2 electrolysis and fermentation. *Nat. Catal.* **2018**, *1* (1), 32−39.
(8) Hori, Y.; Wakebe, H.; Tsukamoto, T.; Koga, O. Electrocatalytic Process of CO Selectivity in Electrochemical Reduction of CO_2 at Metal Electrodes in Aqueous Media. *Electrochim. Acta* **1994**, *39* (11−12), 1833−1839.
(9) Hori, Y.; Kikuchi, K.; Suzuki, S. Production of CO and CH_4 in Electrochemical Reduction of CO_2 at Metal-Electrodes in Aqueous Hydrogencarbonate Solution. *Chem. Lett.* **1985**, *14*, 1695−1698.
(10) Hoshi, N.; Kato, M.; Hori, Y. Electrochemical reduction of CO_2 on single crystal electrodes of silver Ag(111), Ag(100) and Ag(110). *J. Electroanal. Chem.* **1997**, *440* (1−2), 283−286.
(11) Boles, M. A.; Ling, D.; Hyeon, T.; Talapin, D. V. The surface science of nanocrystals. *Nat. Mater.* **2016**, *15* (2), 141−153.
(12) Back, S.; Yeom, M. S.; Jung, Y. Active Sites of Au and Ag Nanoparticle Catalysts for CO_2Electroreduction to CO. *ACS Catal.* **2015**, *5* (9), 5089−5096.
(13) Gabardo, C. M.; Seifitokaldani, A.; Edwards, J. P.; Dinh, C.-T.; Burdyny, T.; Kibria, M. G.; O'Brien, C. P.; Sargent, E. H.; Sinton, D. Combined high alkalinity and pressurization enable efficient CO_2 electroreduction to CO. *Energy Environ. Sci.* **2018**, *11* (9), 2531−2539.
(14) Salvatore, D. A.; Weekes, D. M.; He, J.; Dettelbach, K. E.; Li, Y. C.; Mallouk, T. E.; Berlinguette, C. P. Electrolysis of Gaseous CO_2 to CO in a Flow Cell with a Bipolar Membrane. *ACS Energy Lett.* **2018**, *3* (1), 149−154.
(15) Larrazábal, G. O.; Strøm-Hansen, P.; Heli, J. P.; Zeiter, K.; Therkildsen, K. T.; Chorkendorff, I.; Seger, B. Analysis of Mass Flows and Membrane Cross-over in CO_2 Reduction at High Current Densities in an MEA-Type Electrolyzer. *ACS Appl. Mater. Interfaces* **2019**, *11* (44), 41281−41288.
(16) Liu, Z.; Yang, H.; Kutz, R.; Masel, R. I. CO_2 Electrolysis to CO and O_2 at High Selectivity, Stability and Efficiency Using Sustainion Membranes. *J. Electrochem. Soc.* **2018**, *165* (15), J3371−J3377.
(17) Verma, S.; Kim, B.; Jhong, H.-R. M.; Ma, S.; Kenis, P. J. A. A Gross-Margin Model for Defining Technoeconomic Benchmarks in the Electroreduction of CO_2. *ChemSusChem* **2016**, *9* (15), 1972−1979.
(18) Martín, A. J.; Larrazábal, G. O.; Pérez-Ramírez, J. Towards sustainable fuels and chemicals through the electrochemical reduction of CO_2: lessons from water electrolysis. *Green Chem.* **2015**, *17* (12), 5114−5130.
(19) Kan, C. X.; Zhu, J. J.; Zhu, X. G. Silver nanostructures with well-controlled shapes: synthesis, characterization and growth mechanisms. *J. Phys. D: Appl. Phys.* **2008**, *41* (15), 155304.
(20) Liu, S.; Sun, C.; Xiao, J.; Luo, J.-L. Unraveling Structure Sensitivity in CO_2 Electroreduction to Near-Unity CO on Silver Nanocubes. *ACS Catal.* **2020**, *10*, 3158−3163.
(21) Liu, S.; Tao, H.; Zeng, L.; Liu, Q.; Xu, Z.; Liu, Q.; Luo, J.-L. Shape-Dependent Electrocatalytic Reduction of CO_2 to CO on Triangular Silver Nanoplates. *J. Am. Chem. Soc.* **2017**, *139* (6), 2160−2163.
(22) Zhang, S. H.; Jiang, Z. Y.; Xie, Z. X.; Xu, X.; Huang, R. B.; Zheng, L. S. Growth of silver nanowires from solutions: A cyclic penta-twinned-crystal growth mechanism. *J. Phys. Chem. B* **2005**, *109* (19), 9416−9421.
(23) Xi, W.; Ma, R.; Wang, H.; Gao, Z.; Zhang, W.; Zhao, Y. Ultrathin Ag Nanowires Electrode for Electrochemical Syngas Production from Carbon Dioxide. *ACS Sustainable Chem. Eng.* **2018**, *6* (6), 7687−7694.
(24) Sun, Y. G.; Yin, Y. D.; Mayers, B. T.; Herricks, T.; Xia, Y. N. Uniform silver nanowires synthesis by reducing $AgNO_3$ with ethylene glycol in the presence of seeds and poly(vinyl pyrrolidone). *Chem. Mater.* **2002**, *14* (11), 4736−4745.
(25) Li, X.; Wang, L.; Yan, G. Review: Recent research progress on preparation of silver nanowires by soft solution method and their applications. *Cryst. Res. Technol.* **2011**, *46* (5), 427−438.
(26) Li, B.; Ye, S.; Stewart, I. E.; Alvarez, S.; Wiley, B. J. Synthesis and Purification of Silver Nanowires To Make Conducting Films with a Transmittance of 99%. *Nano Lett.* **2015**, *15* (10), 6722−6726.
(27) Jiu, J.; Araki, T.; Wang, J.; Nogi, M.; Sugahara, T.; Nagao, S.; Koga, H.; Suganuma, K.; Nakazawa, E.; Hara, M.; Uchida, H.; Shinozaki, K. Facile synthesis of very-long silver nanowires for transparent electrodes. *J. Mater. Chem. A* **2014**, *2* (18), 6326−6330.
(28) Xia, Y.; Xiong, Y.; Lim, B.; Skrabalak, S. E. Shape-Controlled Synthesis of Metal Nanocrystals: Simple Chemistry Meets Complex Physics? *Angew. Chem., Int. Ed.* **2009**, *48* (1), 60−103.
(29) Coskun, S.; Aksoy, B.; Unalan, H. E. Polyol Synthesis of Silver Nanowires: An Extensive Parametric Study. *Cryst. Growth Des.* **2011**, *11* (11), 4963−4969.
(30) Gao, Y.; Jiang, P.; Song, L.; Liu, L. F.; Yan, X. Q.; Zhou, Z. Q.; Liu, D. F.; Wang, J. X.; Yuan, H. J.; Zhang, Z. X.; Zhao, X. W.; Dou, X. Y.; Zhou, W. Y.; Wang, G.; Xie, S. S. Growth mechanism of silver nanowires synthesized by polyvinylpyrrolidone-assisted polyol reduction. *J. Phys. D: Appl. Phys.* **2005**, *38* (7), 1061−1067.
(31) Kim, M. J.; Alvarez, S.; Chen, Z.; Fichthorn, K. A.; Wiley, B. J. Single-Crystal Electrochemistry Reveals Why Metal Nanowires Grow. *J. Am. Chem. Soc.* **2018**, *140* (44), 14740−14746.
(32) Sun, Y.; Xia, Y. Large-Scale Synthesis of Uniform Silver Nanowires Through a Soft, Self-Seeding, Polyol Process. *Adv. Mater.* **2002**, *14* (11), 833−837.
(33) Sun, D.; Xu, X.; Qin, Y.; Jiang, S. P.; Shao, Z. Rational Design of Ag-Based Catalysts for the Electrochemical CO_2 Reduction to CO: A Review. *ChemSusChem* **2020**, *13* (1), 39−58.
(34) Mourdikoudis, S.; Liz-Marzán, L. M. Oleylamine in Nanoparticle Synthesis. *Chem. Mater.* **2013**, *25* (9), 1465−1476.
(35) Yang, H.-J.; He, S.-Y.; Tuan, H.-Y. Self-Seeded Growth of Five-Fold Twinned Copper Nanowires: Mechanistic Study, Characterization, and SERS Applications. *Langmuir* **2014**, *30* (2), 602−610.
(36) Jin, M.; He, G.; Zhang, H.; Zeng, J.; Xie, Z.; Xia, Y. Shape-Controlled Synthesis of Copper Nanocrystals in an Aqueous Solution with Glucose as a Reducing Agent and Hexadecylamine as a Capping Agent. *Angew. Chem., Int. Ed.* **2011**, *50* (45), 10560−10564.
(37) Ung, D.; Cossairt, B. M. Effect of Surface Ligands on CoP for the Hydrogen Evolution Reaction. *ACS Appl. Energy Mater.* **2019**, *2* (3), 1642−1645.
(38) Luo, M.; Hong, Y.; Yao, W.; Huang, C.; Xu, Q.; Wu, Q. Facile removal of polyvinylpyrrolidone (PVP) adsorbates from Pt alloy nanoparticles. *J. Mater. Chem. A* **2015**, *3* (6), 2770−2775.
(39) Lopez-Sanchez, J. A.; Dimitratos, N.; Hammond, C.; Brett, G. L.; Kesavan, L.; White, S.; Miedziak, P.; Tiruvalam, R.; Jenkins, R. L.; Carley, A. F.; Knight, D.; Kiely, C. J.; Hutchings, G. J. Facile removal of stabilizer-ligands from supported gold nanoparticles. *Nat. Chem.* **2011**, *3* (7), 551−556.
(40) Naresh, N.; Wasim, F. G. S.; Ladewig, B. P.; Neergat, M. Removal of surfactant and capping agent from Pd nanocubes (Pd-NCs) using tert-butylamine: its effect on electrochemical characteristics. *J. Mater. Chem. A* **2013**, *1* (30), 8553−8559.
(41) Cargnello, M.; Chen, C.; Diroll, B. T.; Doan-Nguyen, V. V. T.; Gorte, R. J.; Murray, C. B. Efficient Removal of Organic Ligands from Supported Nanocrystals by Fast Thermal Annealing Enables Catalytic Studies on Well-Defined Active Phases. *J. Am. Chem. Soc.* **2015**, *137* (21), 6906−6911.
(42) Rioux, R. M.; Song, H.; Grass, M.; Habas, S.; Niesz, K.; Hoefelmeyer, J. D.; Yang, P.; Somorjai, G. A. Monodisperse platinum nanoparticles of well-defined shape: synthesise characterization, catalytic properties and future prospects. *Top. Catal.* **2006**, *39* (3−4), 167−174.
(43) Hou, Y.; Bolat, S.; Bornet, A.; Romanyuk, Y. E.; Guo, H.; Moreno-García, P.; Zelocualtecatl Montiel, I.; Lai, Z.; Müller, U.; Grozovski, V.; Broekmann, P. Photonic Curing: Activation and Stabilization of Metal Membrane Catalysts (MMCs) for the

https://dx.doi.org/10.1021/acscatal.0c02026
ACS Catal. 2020, 10, 8503−8514

Electrochemical Reduction of CO_2. *ACS Catal.* **2019**, *9* (10), 9518−9529.
(44) Bartholomew, C. H. Mechanisms of catalyst deactivation. *Appl. Catal., A* **2001**, *212* (1−2), 17−60.
(45) Shaw, S.; Tian, X. C.; Silva, T. F.; Bobbitt, J. M.; Naab, F.; Rodrigues, C. L.; Smith, E. A.; Cademartiri, L. Selective Removal of Ligands from Colloidal Nanocrystal Assemblies with Non-Oxidizing He Plasmas. *Chem. Mater.* **2018**, *30* (17), 5961−5967.
(46) Aliaga, C.; Park, J. Y.; Yamada, Y.; Lee, H. S.; Tsung, C.-K.; Yang, P.; Somorjai, G. A. Sum Frequency Generation and Catalytic Reaction Studies of the Removal of Organic Capping Agents from Pt Nanoparticles by UV−Ozone Treatment. *J. Phys. Chem. C* **2009**, *113* (15), 6150−6155.
(47) Rosen, E. L.; Buonsanti, R.; Llordes, A.; Sawvel, A. M.; Milliron, D. J.; Helms, B. A. Exceptionally Mild Reactive Stripping of Native Ligands from Nanocrystal Surfaces by Using Meerwein's Salt. *Angew. Chem., Int. Ed.* **2012**, *51* (3), 684−689.
(48) Doris, S. E.; Lynch, J. J.; Li, C. Y.; Wills, A. W.; Urban, J. J.; Helms, B. A. Mechanistic Insight into the Formation of Cationic Naked Nanocrystals Generated under Equilibrium Control. *J. Am. Chem. Soc.* **2014**, *136* (44), 15702−15710.
(49) Nelson, A.; Zong, Y.; Fritz, K. E.; Suntivich, J.; Robinson, R. D. Assessment of Soft Ligand Removal Strategies: Alkylation as a Promising Alternative to High-Temperature Treatments for Colloidal Nanoparticle Surfaces. *ACS Mater. Lett.* **2019**, *1* (1), 177−184.
(50) Menard, L. D.; Xu, F. T.; Nuzzo, R. G.; Yang, J. C. Preparation of TiO_2-supported Au nanoparticle catalysts from a Au-13 cluster precursor: Ligand removal using ozone exposure versus a rapid thermal treatment. *J. Catal.* **2006**, *243* (1), 64−73.
(51) Ansar, S. M.; Perera, G. S.; Ameer, F. S.; Zou, S. L.; Pittman, C. U.; Zhang, D. M. Desulfurization of Mercaptobenzimidazole and Thioguanine on Gold Nanoparticles Using Sodium Borohydride in Water at Room Temperature. *J. Phys. Chem. C* **2013**, *117* (26), 13722−13729.
(52) Hasché, F.; Oezaslan, M.; Strasser, P. In Situ Observation of the Thermally Induced Growth of Platinum-Nanoparticle Catalysts Using High-Temperature X-ray Diffraction. *ChemPhysChem* **2012**, *13* (3), 828−834.
(53) Li, D. G.; Wang, C.; Tripkovic, D.; Sun, S. H.; Markovic, N. M.; Stamenkovic, V. R. Surfactant Removal for Colloidal Nanoparticles from Solution Synthesis: The Effect on Catalytic Performance. *ACS Catal.* **2012**, *2* (7), 1358−1362.
(54) Safo, I. A.; Oezaslan, M. Electrochemical Cleaning of Polyvinylpyrrolidone-capped Pt Nanocubes for the Oxygen Reduction Reaction. *Electrochim. Acta* **2017**, *241*, 544−552.
(55) Safo, I. A.; Dosche, C.; Özaslan, M. Effects of Capping Agents on the Oxygen Reduction Reaction Activity and Shape Stability of Pt Nanocubes. *ChemPhysChem* **2019**, *20* (22), 3010−3023.
(56) Bong, S.; Jang, B.; Han, D.; Piao, Y. Effective Electrochemical Activation of Oleate-Residue-Fouled Pt Nanoparticle Catalysts for Methanol and Formic Acid Oxidation. *ACS Omega* **2019**, *4* (23), 20330−20334.
(57) Sun, Y. G.; Gates, B.; Mayers, B.; Xia, Y. N. Crystalline silver nanowires by soft solution processing. *Nano Lett.* **2002**, *2* (2), 165−168.
(58) Sun, Y. G.; Mayers, B.; Herricks, T.; Xia, Y. N. Polyol synthesis of uniform silver nanowires: A plausible growth mechanism and the supporting evidence. *Nano Lett.* **2003**, *3* (7), 955−960.
(59) Hori, Y. Electrochemical CO_2 Reduction on Metal Electrodes. In *Modern Aspects of Electrochemistry*; Springer: New York, 2008; pp 89−189.
(60) Dutta, A.; Rahaman, M.; Luedi, N. C.; Mohos, M.; Broekmann, P. Morphology Matters: Tuning the Product Distribution of CO_2 Electroreduction on Oxide-Derived Cu Foam Catalysts. *ACS Catal.* **2016**, *6* (6), 3804−3814.
(61) Dutta, A.; Rahaman, M.; Mohos, M.; Zanetti, A.; Broekmann, P. Electrochemical CO_2 Conversion Using Skeleton (Sponge) Type of Cu Catalysts. *ACS Catal.* **2017**, *7* (8), 5431−5437.
(62) Rahaman, M.; Dutta, A.; Broekmann, P. Size-Dependent Activity of Palladium Nanoparticles: Efficient Conversion of CO_2 into Formate at Low Overpotentials. *ChemSusChem* **2017**, *10* (8), 1733−1741.
(63) Dutta, A.; Morstein, C. E.; Rahaman, M.; Cedeño López, A.; Broekmann, P. Beyond Copper in CO_2 Electrolysis: Effective Hydrocarbon Production on Silver-Nanofoam Catalysts. *ACS Catal.* **2018**, *8*, 8357−8368.
(64) da Silva, R. R.; Yang, M.; Choi, S.-I.; Chi, M.; Luo, M.; Zhang, C.; Li, Z.-Y.; Camargo, P. H. C.; Ribeiro, S. J. L.; Xia, Y. Facile Synthesis of Sub-20 nm Silver Nanowires through a Bromide-Mediated Polyol Method. *ACS Nano* **2016**, *10* (8), 7892−7900.
(65) Niu, Z.; Cui, F.; Kuttner, E.; Xie, C.; Chen, H.; Sun, Y.; Dehestani, A.; Schierle-Arndt, K.; Yang, P. Synthesis of Silver Nanowires with Reduced Diameters Using Benzoin-Derived Radicals to Make Transparent Conductors with High Transparency and Low Haze. *Nano Lett.* **2018**, *18* (8), 5329−5334.
(66) Jiang, P.; Li, S.-Y.; Xie, S.-S.; Gao, Y.; Song, L. Machinable Long PVP-Stabilized Silver Nanowires. *Chem. - Eur. J.* **2004**, *10* (19), 4817−4821.
(67) Li, Y.; Cui, F.; Ross, M. B.; Kim, D.; Sun, Y.; Yang, P. Structure-Sensitive CO_2 Electroreduction to Hydrocarbons on Ultrathin 5-fold Twinned Copper Nanowires. *Nano Lett.* **2017**, *17* (2), 1312−1317.
(68) Clark, E. L.; Ringe, S.; Tang, M.; Walton, A.; Hahn, C.; Jaramillo, T. F.; Chan, K.; Bell, A. T. Influence of Atomic Surface Structure on the Activity of Ag for the Electrochemical Reduction of CO_2 to CO. *ACS Catal.* **2019**, *9* (5), 4006−4014.
(69) Kuhl, K. P.; Hatsukade, T.; Cave, E. R.; Abram, D. N.; Kibsgaard, J.; Jaramillo, T. F. Electrocatalytic Conversion of Carbon Dioxide to Methane and Methanol on Transition Metal Surfaces. *J. Am. Chem. Soc.* **2014**, *136* (40), 14107−14113.
(70) Liu, X. Y.; Xiao, J. P.; Peng, H. J.; Hong, X.; Chan, K.; Norskov, J. K. Understanding trends in electrochemical carbon dioxide reduction rates. *Nat. Commun.* **2017**, *8*, 15438.
(71) Hammer, B.; Morikawa, Y.; Nørskov, J. K. CO Chemisorption at Metal Surfaces and Overlayers. *Phys. Rev. Lett.* **1996**, *76* (12), 2141−2144.
(72) Zhu, S.; Li, T.; Cai, W.-B.; Shao, M. CO_2 Electrochemical Reduction As Probed through Infrared Spectroscopy. *ACS Energy Lett.* **2019**, *4* (3), 682−689.
(73) Schmitt, K. G.; Gewirth, A. A. In Situ Surface-Enhanced Raman Spectroscopy of the Electrochemical Reduction of Carbon Dioxide on Silver with 3,5-Diamino-1,2,4-Triazole. *J. Phys. Chem. C* **2014**, *118* (31), 17567−17576.
(74) Ichinohe, Y.; Wadayama, T.; Hatta, A. Electrochemical reduction of CO_2 on silver as probed by surface-enhanced Raman scattering. *J. Raman Spectrosc.* **1995**, *26* (5), 335−340.
(75) Liu, S.; Wang, X.-Z.; Tao, H.; Li, T.; Liu, Q.; Xu, Z.; Fu, X.-Z.; Luo, J.-L. Ultrathin 5-Fold Twinned Sub-25 nm Silver Nanowires Enable Highly Selective Electroreduction of CO_2 to CO. *Nano Energy* **2018**, *45*, 456.
(76) Fu, H.; Jia, L. L.; Wang, W. N.; Fan, K. N. The first-principle study on chlorine-modified silver surfaces. *Surf. Sci.* **2005**, *584* (2−3), 187−198.
(77) Bowker, M.; Waugh, K. C.; Wolfindale, B.; Lamble, G.; King, D. A. THE ADSORPTION OF CHLORINE AND CHLORIDATION OF AG(100). *Surf. Sci.* **1987**, *179* (2−3), 254−266.
(78) Lamble, G. M.; Brooks, R. S.; Campuzano, J. C.; King, D. A.; Norman, D. STRUCTURE OF THE C(2 × 2) COVERAGE OF CL ON AG(100) - A CONTROVERSY RESOLVED BY SURFACE EXTENDED X-RAY-ABSORPTION FINE-STRUCTURE SPECTROSCOPY. *Phys. Rev. B: Condens. Matter Mater. Phys.* **1987**, *36* (3), 1796−1798.

https://dx.doi.org/10.1021/acscatal.0c02026
ACS Catal. 2020, 10, 8503−8514

7. Limitations of Identical Location SEM as a Method of Degradation Studies on Surfactant Capped Nanoparticle Electrocatalysts

Authors: Yuhui Hou, Noémi Kovács, Heng Xu, Changzhe Sun, Rolf Erni, María de Jesús Gálvez-Vázquez, Alain Rieder, Huifang Hu, Ying Kong, Menglong Liu, Benjamin J. Wiley, Soma Vesztergom, and Peter Broekmann.

***Journal of Catalysis*, 394, 58-66 (2021). DOI: 10.1016/j.jcat.2020.12.006**

Highlight: Identical location scanning electron microscopy (IL-SEM) is an important characterization tool in the field of electrocatalysis to study morphology changes of catalysts caused by the catalyzed reaction. However, the electron beam (the local probe) itself may introduce unintended effects leading to structural and/or chemical alterations of the surface areas probed by the electron beam. A passivating carbonaceous layer was observed on PVP-capped Ag nanocubes (Ag-NCs) after their exposure to the SEM electron beam which led to the (partial) deactivation of the Ag-NCs. This was proven by structural alterations which typically occurred during electrolysis in case of Ag-NCs not exposed to the electron beam whereas Ag-NCs exposed to the electron beam did not show any on these typical alterations.

Contribution: I helped to prepare the glassy carbon electrodes, conducted some parts of the electrochemical experiments and have been involved in the discussion of the results.

Journal of Catalysis 394 (2021) 58–66

Contents lists available at ScienceDirect

Journal of Catalysis

journal homepage: www.elsevier.com/locate/jcat

Limitations of identical location SEM as a method of degradation studies on surfactant capped nanoparticle electrocatalysts

Yuhui Hou [a,1,*], Noémi Kovács [a,b,1], Heng Xu [c], Changzhe Sun [a], Rolf Erni [d], María de Jesús Gálvez-Vázquez [a], Alain Rieder [a], Huifang Hu [a], Ying Kong [a], Menglong Liu [a], Benjamin J. Wiley [c], Soma Vesztergom [a,b,*], Peter Broekmann [a]

[a] University of Bern, Department of Chemistry and Biochemistry, Freiestrasse 3, 3012 Bern, Switzerland
[b] Eötvös Loránd University, Department of Physical Chemistry, Pázmány Péter sétány 1/A, 1117 Budapest, Hungary
[c] Duke University, Department of Chemistry, French Family Science Cen 2214, NC–27708 Durham, NC, USA
[d] Swiss Federal Laboratories for Materials Science and Technology (EMPA), Electron Microscopy Center, Überlandstrasse 129, CH–8600 Dübendorf, Switzerland

ARTICLE INFO

Article history:
Received 14 October 2020
Revised 11 December 2020
Accepted 12 December 2020
Available online 23 December 2020

Keywords:
Electrocatalysis
CO_2 reduction
Electron microscopy
Under-beam contamination
Carbon
Polyvinylpyrrolidone (PVP)

ABSTRACT

Identical location scanning electron microscopy (IL–SEM) has become an important tool for electrocatalysis research in the past few years. The method allows for the observation of the same site of an electrode, often down to the same nanoparticle, before and after electrochemical treatment. It is presumed that by IL–SEM, alterations in the surface morphology (the growth, shrinkage, or the disappearance of nanosized features) can be detected, and the thus visualized degradation can be linked to changes of the catalytic performance, observed during prolonged electrolyses. In the rare cases where no degradation is seen, IL–SEM may provide comfort that the studied catalyst is ready for up-scaling and can be moved towards industrial applications. However, although it is usually considered a non-invasive technique, the interpretation of IL–SEM measurements may get more complicated. When, for example, IL–SEM is used to study the degradation of surfactant-capped Ag nanocubes employed as electrocatalysts of CO_2 electroreduction, nanoparticles subjected to the electron beam during pre-electrolysis imaging may lose some of their catalytic activity due to the under-beam formation of a passive organic contamination layer. Although the entirety of the catalyst obviously degrades, the spot mapped by IL–SEM reflects no or little changes during electrolysis. The aim of this paper is to shed light on an important limitation of IL–SEM: extreme care is necessary when applying this method for catalyst degradation studies, especially in case of nanoparticles with surface-adsorbed capping agents.

1. Introduction

Due to the ever-increasing consumption of fossil fuels, gigatons of CO_2 are released yearly to the atmosphere, expediting global warming [1]. A possible way of mitigating the effects of atmospheric CO_2 is to reduce it electrochemically. Electrochemical reduction does not only allow CO_2 to be regarded as a valuable raw material instead of an environmentally dangerous waste, but it may also provide a solution for the storage of excess renewable (hydro-, solar or wind) energy [2].

Mostly due to this, electrochemical CO_2 reduction —a process that was first described more than 150 years ago [3]— has recently become the forefront of electrochemical research [4]. Searching for the term "electrochemical CO_2 reduction" on the website of ACS Publications yields 3334 research papers about this topic, only from the past year; Google Scholar, when searched for the same term and for the same period of time, gives $>$ 17000 matches. A majority of these publications are original research papers that describe new catalyst materials, which —somewhat remarkably— all exhibit excellent qualities when applied for CO_2 reduction. This means that by covering electrodes with the newly invented catalysts, and carrying out electrolyses of solutions that contain CO_2 dissolved in some form, high current densities of CO_2 reduction can be achieved at relatively low overpotentials, and the process may in an ideal case yield only one or just a few desired products [4].

* Corresponding authors at: University of Bern, Department of Chemistry and Biochemistry, Freiestrasse 3, 3012 Bern, Switzerland (Y. Hou); Eötvös Loránd University, Department of Physical Chemistry, Pázmány Péter sétány 1/A, 1117 Budapest, Hungary (S. Vesztergom).
E-mail addresses: yuhui.hou@dcb.unibe.ch (Y. Hou), vesztergom@chem.elte.hu (S. Vesztergom), peter.broekmann@dcb.unibe.ch (P. Broekmann).
[1] These authors contributed equally.

https://doi.org/10.1016/j.jcat.2020.12.006
0021-9517/

Compared to the tremendous amount of research invested in the design of new electrocatalyst materials for CO_2 electroreduction, technologies that operate on an industrial scale are still rare. Undoubtedly, the most important obstacle that hinders the application of newly developed catalysts on an industrial level is an issue of stability: catalysts that may show remarkable features in lab experiments tend to degrade and lose their performance over prolonged use. This may especially be true for catalysts owing their activity to a fine structure, such as colloidally synthesized nanoparticles that are especially prone to degradation over long-time operation. In case of these catalysts, studying (electro-)mechanical degradation and its effects on the catalytic performance has to be the first step of technological up-scaling.

Although many *operando* techniques (*e.g.*, X-ray diffraction, scattering or absorption, as well as Raman spectroscopies [5,6]) can provide an insight to nanoparticle transformations occurring during CO_2 reduction, it is still more common to use *ex situ* electron microscopic (EM) techniques to observe, in particular, the structural changes that electrocatalysts suffer during CO_2 reduction.

In order to apply EM in an electrocatalysis study, the catalyst has to be sampled before and after it is made subject to electrochemical treatment. When comparing images taken before and after electrolysis, we usually work under two implicit assumptions: *(i.)* that the areas scanned before and after the electrolysis are either physically the same, or are both representative of the sample as a whole; and *(ii.)* that any changes we observe are indeed caused by the electrochemical treatment and not by other operations, *e.g.,* the pre-electrolysis scanning of the sample, careless sample transportation, exposition to air or to chemicals, etc.

The former of the above two assumptions can readily be made explicit, for example, if identical location scanning or transmission electron microscopies (IL–SEM or IL–TEM) are employed. IL–TEM was first described by a work of Mayrhofer et al. in 2008 [7], and the first report on the application of IL–SEM by Hodnik et al. [8] followed not much later, in 2012. In early studies, the catalyst material was loaded on a TEM finder grid (made of gold) to facilitate identical location imaging [7]. Later it was found that it is enough to apply a small incision (a cross-like scratch) on other (*e.g.*, graphite) holders to relocate the scanned site after electrolysis, which rendered the use of finder grids unnecessary. Due to the fact that IL–EM is able to visualize changes of a catalyst surface, often down to the details of individual nanoparticles, IL–EM found immediate application in catalyst degradation studies on a variety of target reactions [9,10].

In the field of CO_2 electrolysis, IL–EM became a prominent method of studying catalyst degradation [11–21], mainly because it is considered (and, starting from its discovery, often advertised as) a non-destructive method. It is usually assumed that if a given catalyst preserves good performance characteristics over longer periods of electrolysis, and neither IL–SEM nor IL–TEM reveal any structural degradation, the catalyst is stable and can be considered a potential candidate for up-scaled (*e.g.*, flow cell) studies [15].

Unfortunately, however, the situation is not this simple, especially because, in some cases, the pre-electrolysis EM imaging does affect the future catalytic performance of the sampled catalyst areas. For example, in the literature of IL–TEM studies of electrocatalysts, there are reports on the electron beam induced shrinkage (as well as some ripening) of Pt nanoparticles used in fuel cells [22]. Based on these results, Arenz and Zana strongly recommend that in order to check if the electron beam changes the sample, TEM analysis following the electrochemical measurements should also be performed at pristine locations; *i.e.*, locations which have not been previously exposed to the electron beam [23].

For IL–SEM, probably based on the assumption that the electron dose is much lower than in the case of TEM, no such warning was given, and it is indeed not likely that the beam used under SEM conditions could induce similar sintering effects observed in TEM. The sintering of nanoparticles may however not be the only way an electron beam can alter a catalyst surface: another, equally important phenomenon —namely, the under-beam formation of a passive layer— should also deserve attention.

That electron bombardment of a conducting sample *in vacuo*, where only slightest traces of organic vapours occur, can result in the coverage of the sample with a non-conducting layer of polymerized carbon compounds was first noticed by Lariviere Stewart [24] in 1934 — that is, four years before von Ardenne built the first SEM [25]. That electron bombardment, especially during focusing, can also cause changes to the surface of a sample inside an SEM was first noticed as early as 1946 by Marton et al. [26]. Recently, two reviews from Postek et al. [27,28] discussed some issues of interpreting SEM images: the second part [28] was entirely devoted to the issue of electron beam-induced specimen contamination.

Postek et al. [28] pointed out that the origin of beam-induced contaminations can both be the sample itself and the vacuum system of the SEM. While the cleanliness of the latter can be significantly improved (for example, by the replacement of diffusion pumps with turbomolecular ones backed by dry backing pumps in modern instruments), the history of the specimen prior to entering the vacuum system still remains important [28]. In case of samples with significant organic content, organic molecules remaining on the sample surface can break, undergo polymerization, and get "pinned" to the sample by the beam during scanning [28]. Depending on the electron dose, the formed carbonaceous layer can grow at a rate of a few nanometers/seconds over the sample surface, even if only low accelerating voltages are used.

It is interesting to note that although under-beam contamination is a well-studied subject in the literature of SEM (see [27,28], as well as the references cited therein), studies on the effect of under-beam contamination/passivation on the future electrochemical behaviour of the sample are scarce, and are mostly focused on corrosion and not on electrocatalytic properties [29]. Yet, as we are going to demonstrate in this paper, under-beam passivation can practically disable the sampled part of a catalyst, especially if it contains organic remnants (capping agents) from the synthesis process. While other parts of the catalyst (not affected by the electron beam before electrolysis) remain active and very often degrade significantly during the catalysed process, the part of the sample affected by pre-electrolysis scanning remains intact, and probably entirely passive, due to the carbonaceous film formed on it under the beam.

Here we demonstrate, by IL–SEM studies on polyvinylpyrrolidone (PVP) functionalized Ag nanocubes used as electrocatalysts for CO_2 reduction, a catalytic activity disabling effect of a passive carbonaceous layer that is known to be formed under the electron beam during pre-electrolysis SEM scans [30]. The aim of this paper is to emphasize the necessity of extreme care being taken not to misinterpret IL–SEM studies that seemingly demonstrate excellent catalyst stability.

2. Experimental

Catalyst preparation. Ag nanocubes (Ag NCs) were prepared by an upscaled synthesis route described elsewhere [31]. As support, a glassy carbon plate (2 mm thickness, Alfa Aesar, type 1) was mirror-polished (0.5 μm alumina suspension, Buehler), was thoroughly rinsed with ultrapure water and ethanol, dried, and masked with an inert PTFE tape to leave an 0.8 cm × 1 cm geometric surface area open for catalyst coating.

In order to form a carbon-supported Ag NC catalyst, 5.6 mg of the as-prepared Ag nanocubes [31] (in the form of powder) was dispersed in 6 cm^3 isopropanol (VLSI Selectipur, BASF) by a 1-hour sonication. 1.5 mg of technical carbon powder (Vulcan XC 72R, Cabot, USA) was also dispersed in 3 cm^3 isopropanol by 1-hour of sonication, and the two suspensions were subsequently mixed by sonicating for 30 min. The resulting suspension was dried overnight under vacuum conditions, yielding a C-supported Ag NC catalyst powder. This powder was re-dispersed in 1.5 cm^3 of isopropanol containing 75 $\mu\ell$ of a Nafion solution (Aldrich, 5 wt% dissolved in a mixture of lower aliphatic alcohols and water). The obtained dispersion was subjected to sonication for 30 min, and for each electrode, 25 $\mu\ell$ of the resulted ink was drop-cast onto the glassy carbon plate and dried in a vacuum oven.

An Ag NC catalyst without carbon support was prepared by dispersing 22 mg of the as-prepared Ag NCs in 6 cm^3 isopropanol by 1-hour sonication and spin-coating 75 $\mu\ell$ of this suspension onto a glassy carbon support in three steps over 1 minute, using 1000 min^{-1} rotation rate on an Ossila spin coater.

Both the C-supported and the unsupported Ag NC catalysts were exposed to a UV-ozone atmosphere (PSD Series, Novascan, operated with air at atmospheric pressure) for 12 min.

For studies on a gas diffusion electrode (GDE, experimental details were described elsewhere [15]) the suspension of carbon-supported Ag NCs was drop-cast on the hydrophobic surface of a Sigracet 39 BC (Fuel Cell Store) GDE, and the nanocubes were percolated through the porous body of the GDE by a vacuum filtration system placed on the rear side of the electrode, followed by air-drying at ambient conditions lasting 30 min. No UV-ozone treatment was applied to the thus prepared, Ag NC-modified GDE. The GDE was used as part of the gas flow cell described in [15], combined with a Sustainion alkaline membrane (X37-50 RT, Dioxide materials) and an anode compartment containing 2 mol dm^{-3} KOH solution.

XPS Characterization. X-ray photoelectron spectroscopy (XPS) studies were carried out using a Thermo ESCALAB 250 XI instrument at a pass energy of 30 eV using monochromated Al K-α line ($h\nu = 1486.7$ eV). Charge correction was based on the position of the C*1s* peak (284.8 eV). The XPS spectra were subjected to a Shirley background subtraction and were analysed using the CasaXPS software.

Electrocatalysis studies. For all electrochemical experiments, a potentiostat/galvanostat (Metrohm Autolab 302N, The Netherlands) was used to control the potential, current density, and transferred charge. The electrolysis experiments were carried out using a custom-built, air-tight, H-type glass cell. Apart from the working electrode that was prepared as described above, the three-electrode arrangement consisted of a "leakless" Ag|AgCl|3 mol dm^{-3}KCl reference (Pine) and a Pt-foil (1.5 cm × 0.5 cm, Goodfellow) counter electrode. For electrolyses, 0.5 mol dm^{-3} $KHCO_3$ (ACS grade, Sigma-Aldrich) electrolyte solutions were prepared with ultrapure water (Milli-Q by Merck Millipore) and were saturated with CO_2 (99.999%, Carbagas, Switzerland). During the experiments, continuous gas flow was maintained through the electrolyte solution. To avoid possible fluctuations in CO_2 solubility caused by a change in the ambient temperature, all electrochemical experiments were performed at 20 °C, by immersing the H-type cell into a thermostated water bath. Automatic *IR* compensation was applied following the determination of the cell resistance by positive feedback. For the sake of comparability, all potentials given herein were converted to the reversible hydrogen electrode (RHE) scale. The reported current densities were normalized to the geometric surface area.

Gaseous products generated in the cell were detected by connecting the purging gas outlet to a GC analyzer (SRI Instruments Multigas Analyzer Nº3). The continuous flow of the carrier CO_2 gas through the electrolysis cell carried volatile reaction products from the head-space into the sampling loops of the gas chromatograph. The partial current I_i, corresponding to the formation of a gaseous product *i*, can be calculated [32] as

$$I_i = x_i n_i F v_m, \quad (1)$$

where x_i denotes the mole fraction of the products, determined by GC using an independent calibration standard gas (Carbagas); n_i is the number of electrons involved in the reduction reaction to form a particular product ($n = 2$ for both CO and H_2 formation); $F = 96485.3$ C mol^{-1} is Faraday's constant; and v_m is the molar CO_2 gas flow rate measured by a universal flowmeter (7000 GC flowmeter, Ellutia) at the exit of the electrochemical cell.

The Faradaic efficiency (*FE*) of a given reaction product can be determined by dividing the respective partial current, determined from Eq. (1), by the total current measured electrochemically. A thermal conductivity detector (TCD, for the detection of H_2) and a flame ionization detector (FID, for the detection of CO) were applied in our studies. We found that in the studied system H_2 and CO are the only two detectable products, accounting for 100% ± 5% of the current density that was electrochemically measurable. The electrochemically measured current densities were thus subdivided into partial current densities by taking into account the chromatographically determined concentration ratios, as will be shown later in Fig. 2. During operation, aliquots were analysed in intervals of 20 min during steady state electrolyses.

EM Measurements. EM analysis was conducted with a Zeiss Gemini 450 SEM with an InLens secondary electron (SE) and a backscatter electron detector (BSD). An accelerating voltage of 1.5 kV (probe current of 20 pA) and 5.0 kV (probe current of 120 pA) were applied for SE and BSD imaging, respectively. For high-angle annular dark-field scanning transmission electron microscopy (HAADF–STEM) combined with energy-dispersive X-ray spectroscopy (EDX) and TEM imaging, an FEI Titan Themis (equipped with a SuperEDX detector) was used with an acceleration voltage of 300 kV.

3. Results and discussion

In colloidal nanoparticle synthesis, PVP is a widely applied shape-control agent that promotes the growth of specific crystal faces while hindering others [33,34]. In the synthesis of Ag NCs used in this study, PVP —by strongly binding to the (100) facets of Ag—, facilitated the formation of almost perfect nanocubes of side lengths of about 100 nm, as shown in Fig. 1a. The XPS spectrum (Fig. 1b) of a catalyst prepared without carbon support clearly exhibits a strong Ag*3d* signal, as well as a small peak that can be assigned to the N*1s* excitation of the PVP molecules adsorbed on the surface of the nanocubes. As shown in Fig. 1b, the applied UV-ozone treatment resulted in a significantly decreased N*1s* peak intensity. The peak has not disappeared, however, which hints that some PVP still remained on the surface despite the UV-ozone treatment.

Although the adsorbed PVP could, in principle, inhibit the catalytic activity of the nanocubes [35,36], the UV-ozone treated, C-supported Ag NCs showed good performance when applied for the electroreduction of CO_2. This is demonstrated by Fig. 2a, showing the current density and the product distribution as a function of the applied electrode potential. The current densities shown in Fig. 2a were averaged for 1-hour electrolyses carried out in CO_2 saturated 0.5 mol dm^{-3} $KHCO_3$ solutions: for the electrolyses at different potentials, fresh solutions and newly prepared catalysts were applied.

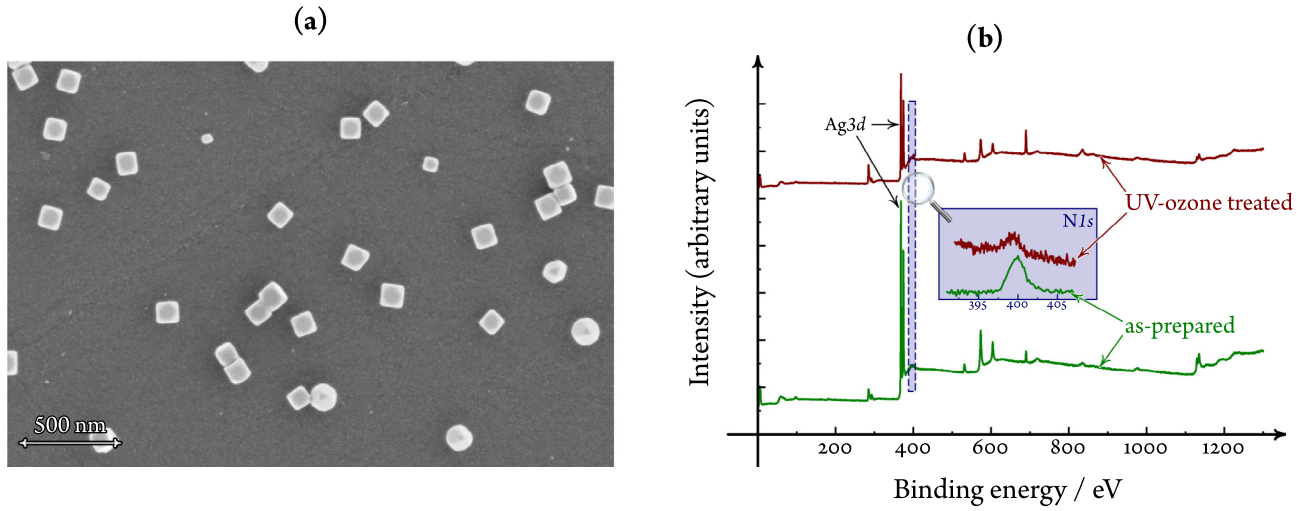

Fig. 1. Scanning electron micrograph **(a)** and X-ray photoelectron survey **(b)** of the unsupported Ag NC catalyst. XPS spectra are shown in **(b)** for the as-prepared catalyst (green curve) and for the catalyst made subject to UV-ozone treatment (red curve) as well. (For interpretation of the references to colour in this figure legend, the reader is referred to the web version of this article.)

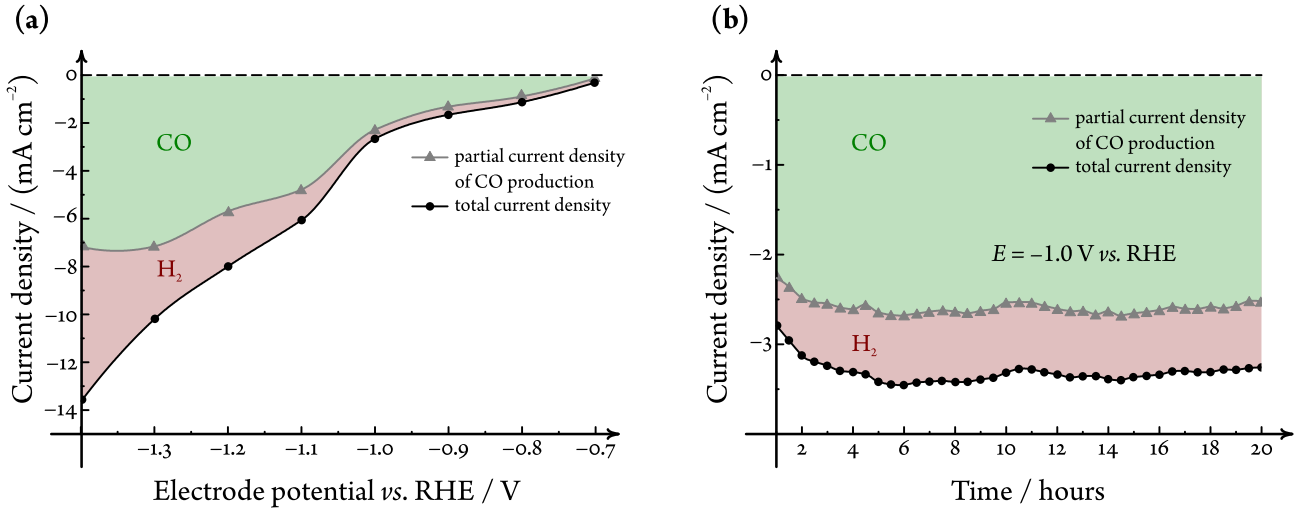

Fig. 2. The electrocatalytic performance of carbon-supported Ag nanocubes, used as catalysts of CO_2 electroreduction in a CO_2-saturated 0.5 mol dm^{-3} $KHCO_3$ solution. **(a)** Potential dependence of the current density and the product distribution, as determined by means of online gas chromatography in an H-type cell for 1-hour electrolyses. Each electrolysis (data points) were carried out using a freshly prepared catalyst and a fresh solution. Curves were created by interpolation. **(b)** Time dependence of the catalytic performance, as determined by a single electrolysis experiment lasting 20 hours, with subsequent chromatographic head-space analysis (data points). The curve was created by interpolation.

It is known that on Ag, the primary product of CO_2 reduction is CO [37]. The same is true for the carbon-supported Ag NCs, with the addition that compared to plain silver —*e.g.*, a silver foil [14]— the Ag nanocubes exhibit a broader overpotential range for CO production. That is, only a little amount of H_2 is formed at potentials less negative than −1.1 V *vs.* RHE, and CO_2 reduction generally prevails over hydrogen evolution in the entirety of the studied potential range ($-1.3\ \text{V} < E < -0.7\ \text{V}$). This observation is in agreement with other reports on nanoparticulate silver catalysts of CO_2 electroreduction [38].

In order to check the stability of the catalyst, we chose the moderate potential value of −1.0 V *vs.* RHE for a prolonged operation study. As shown in Fig. 2b, the catalyst preserved both its overall activity and its relative selectivity towards the production of CO (the Faradaic efficiency of CO formation was about 80%) for an electrolysis lasting 20 hours.

Nevertheless, since catalysts can maintain their macroscopic activity even as they undergo partial deactivation or decomposition [39], we carried out IL–SEM investigations of the working electrode surface, which —although the overall activity remained unchanged— indeed revealed some degradation.

In Fig. 3 we compare two scanning electron micrographs of the same spot of a working electrode surface; one recorded before (Fig. 3a) and one after (Fig. 3b) a 20-hours electrolysis treatment at −1.0 V *vs.* RHE, similar to the one used to obtain the data of Fig. 2b. Fig. 3a shows highly isotropic Ag NCs of a side length of about 100 nanometers, distributed evenly on the supporting carbon matrix. As revealed by Fig. 3b, the nanocubes undergo some slight deformation and shrinkage during electrolysis, and, more prominently, some subnanometer sized particles appear on the surface. EDX mapping (Fig. 3c) confirmed that these small particles consist of silver, and are most probably formed as a debris of nanoparticle degradation due to the mechanical impact of gas evolution [16].

In order to get a clearer view of the degradation process of Ag NCs, the above SEM experiment was repeated with a working elec-

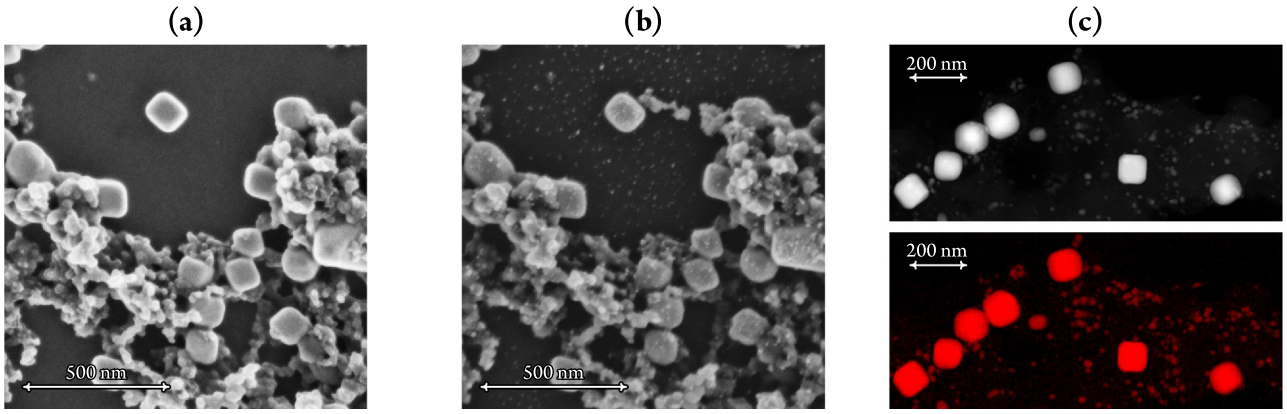

Fig. 3. IL–SEM investigation of the degradation of carbon-supported Ag nanocubes, used as catalysts of CO_2 electroreduction. The same spot of the working electrode surface is shown just before **(a)** and right after **(b)** the electrode was used for a 20-hours electrolysis of a CO_2-saturated 0.5 mol dm^{-3} $KHCO_3$ solution at an electrode potential of −1.0 V *vs.* RHE. The formation of subnanometer sized Ag particles during electrolysis is revealed by the HAADF–STEM (gray-scale) and EDX scans (red-scale) in **(c)**, recorded post-electrolysis at a pristine location that has not been subjected to an electron beam before.

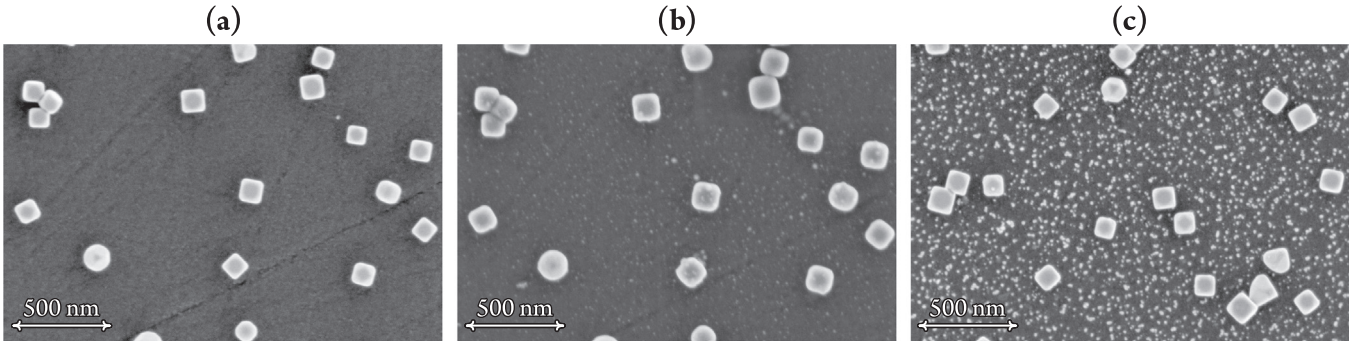

Fig. 4. SEM investigation of the degradation of non-supported Ag nanocubes, used as catalysts of CO_2 electroreduction. The same spot of the working electrode surface is shown just before **(a)** and right after **(b)** the electrode was used for a 20-hours electrolysis of a CO_2-saturated 0.5 mol dm^{-3} $KHCO_3$ solution. A different spot of the same sample is shown after electrolysis in **(c)**.

trode prepared without the supporting carbon matrix (see the Experimental section for details).

The as-prepared electrode surface is shown in Fig. 4a, exhibiting cubic shaped Ag nanoparticles distributed on the glassy carbon electrode substrate. Somewhat surprisingly, the SEM image of the same spot, recorded after a 20-hours electrolysis, shows practically no degradation and the appearance of just a little amount of the subnanometer sized particles, as shown in Fig. 4b. What is even more surprising is that if we record an SEM micrograph with the same configuration, just of a different spot of the sample —that was not scanned before electrolysis—, the picture gets quite different. Fig. 4c clearly shows slightly deformed Ag nanocubes, along with a significant amount of Ag debris formed during electrolysis.

The micrographs of Fig. 4 very clearly reveal an important pitfall of IL–SEM analysis; namely, that due to electron beam-induced changes of the catalyst surface during the pre-electrolysis scan, the sample may get at least partially deactivated for the catalysed process. Due to its decreased electrocatalytic activity, the pre-scanned area of the sample may show no or little changes during the electrolytic process, while other spots (that were not affected by pre-electrolysis SEM scanning) preserve their activity and, in turn, exhibit significant degradation. In other words, the often advertised nondestructiveness of IL–SEM [8,9] should not be taken as granted — at least, not for all catalyst types.

That the effect shown in Fig. 4 can indeed be explained by pre-electrolysis electron beam–sample interactions is further demonstrated by Fig. 5, showing an SEM micrograph of a working electrode surface obtained after electrolysis. Only a part (a rectangular segment) of this sample was scanned by SEM before electrolysis took place, and despite that the sample was exposed

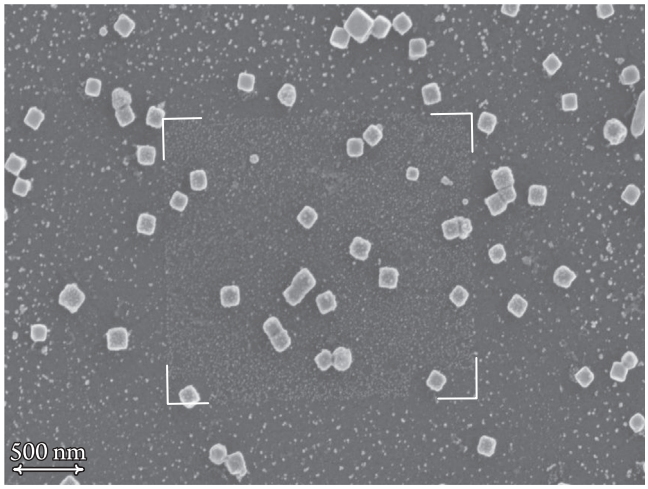

Fig. 5. SEM micrograph of a sample of non-supported Ag NC catalyst taken after a 40-hours electrolysis at −1 V *vs.* RHE in a CO_2-saturated 0.5 mol dm^{-3} $KHCO_3$ solution. A rectangular segment of the sample —shown in the image by its corners— was also scanned before electrolysis. This pre-scanned area exhibits different degradation features compared to the rest of the surface.

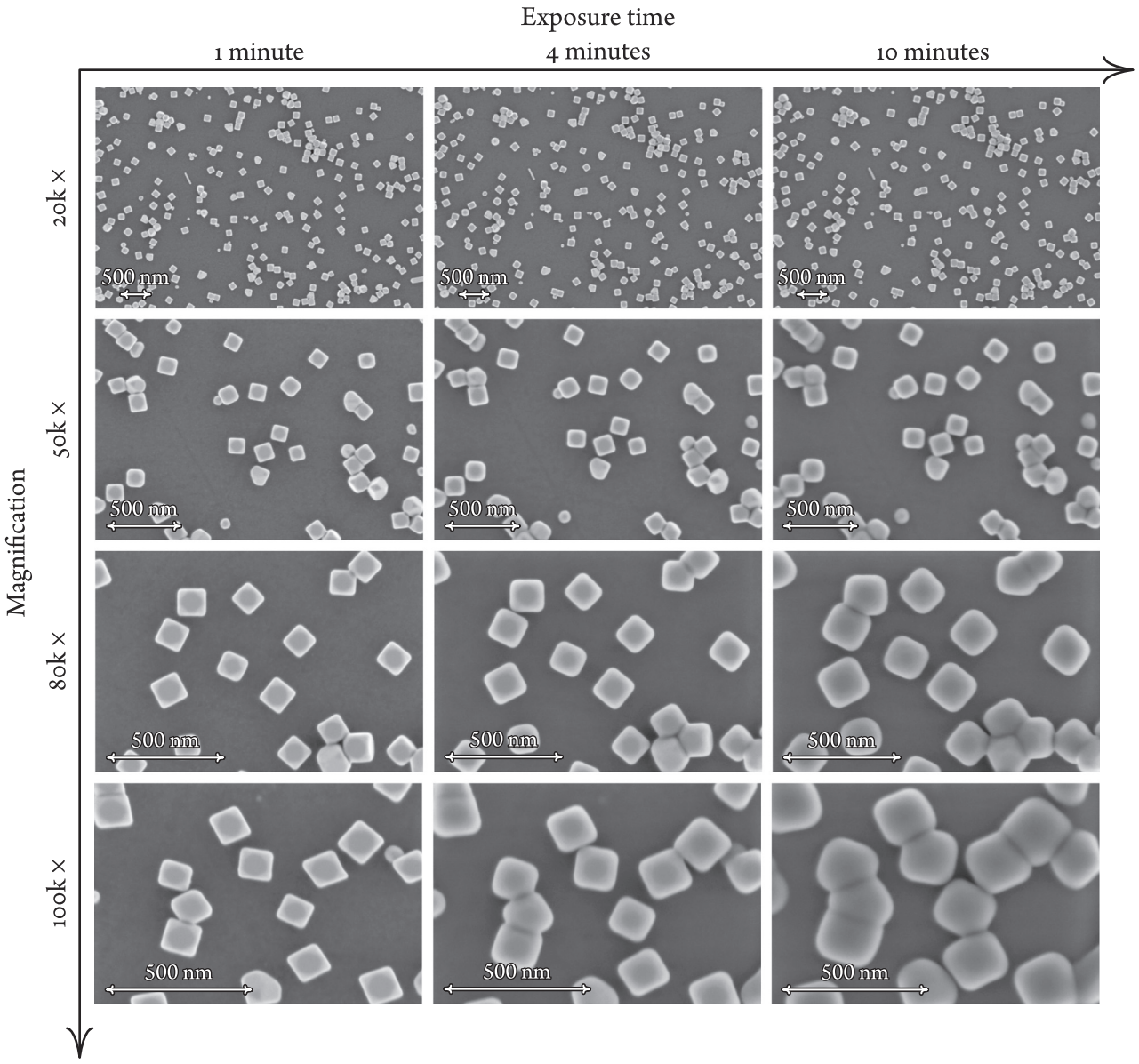

Fig. 6. SEM micrographs of a catalyst surface, obtained using different magnifications and after different scanning times. The applied accelerating voltage was 1.5 kV.

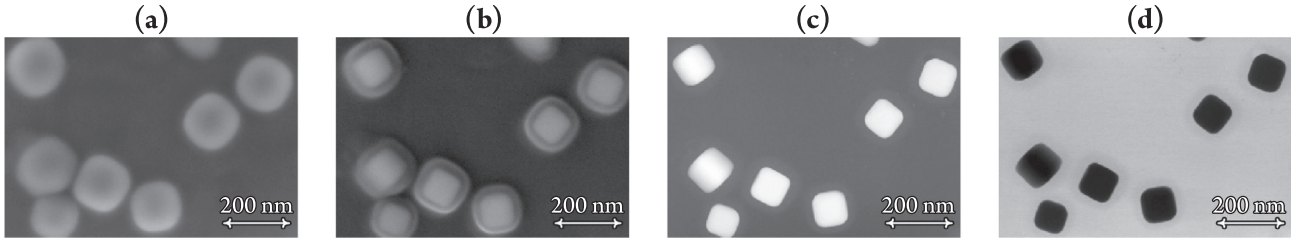

Fig. 7. Electron microscopic images of Ag NCs after electron beam irradiation was carried out for 10 min with a scanning electron beam of 1.5 kV accelerating voltage. **(a)** Secondary electron SEM image taken at 1.5 kV acceleration voltage. **(b)** Secondary electron SEM image obtained at 20 kV. **(c)** HAADF–STEM image taken at 300 kV. **(d)** TEM bright field image taken at 300 kV.

to the electron beam only for a short time, a marked difference can be observed between the degradation features of the pre-scanned segment and the rest of the surface area. Most notably, the coverage of the pre-scanned area with the subnanometer sized Ag particles is less pronounced, compared to other sites. This hints that the electron beam exerts an effect not only on the Ag nanoparticles but also on the underlying glassy carbon substrate.

Note that provided we refrain from long-time exposure of the sample to the electron beam, the above-described electron beam irradiation effect is hardly noticeable *per se*. Yet, as shown by Fig. 5, even the irradiation damages that remained undetected dur-

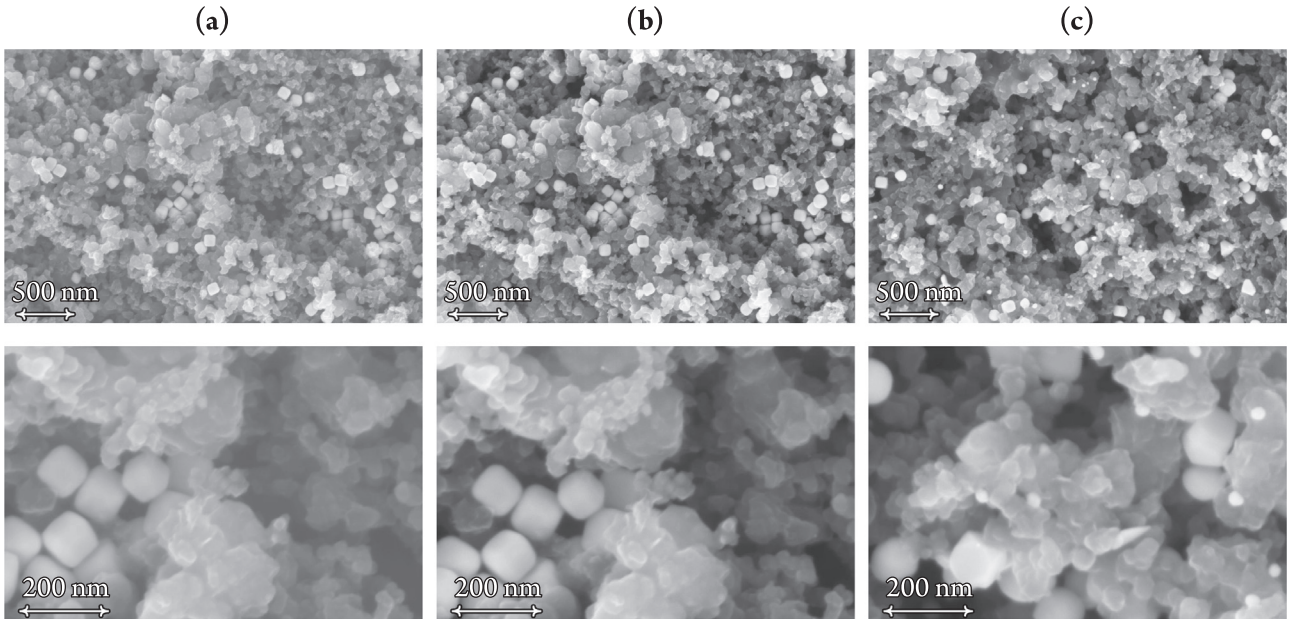

Fig. 8. SEM micrographs of different magnification of a GDE modified by Ag NCs. Identical locations are shown prior to **(a)** and after **(b)** a potentiostatic electrolysis at −2.0 V *vs.* an Ag | AgCl | 3 mol dm^{-3} KCl(aq) reference electrode consuming 1600 C cm^{-2}. A different location is shown after the electrolysis in **(c)**.

ing pre-electrolysis EM scanning can prove significant when the sample is used for electrolysis and scanned afterwards.

To demonstrate the irradiation effect in itself, we carried out prolonged SEM scans on one of our catalyst samples. As revealed by Fig. 6, the effect of contamination (as visualized by the growth and even the apparent merging of the nanocubes) is more pronounced when larger magnifications are applied (*i.e.*, when the beam is more focused) or when the sample is scanned for longer times.

At first glance, the growing and subsequently merging nanocubes shown in Fig. 6 may resemble the coalescence of Pt nanoparticles observed by Chorkendorff et al. under *in situ* TEM conditions [22]. Note, however, that under TEM conditions, the accelerating voltage and the electron dose are both much higher than in SEM. Accordingly, the main feature that Chorkendorff et al. described in their study was a shrinkage (and not a growth) of most nanoparticles, with only a few of these displaying actual coalescence [22]. Shrinkage in this study was shown to be an effect of both the high electron dose and the oxidizing atmosphere. None of these are characteristic of our SEM measurements; thus in our case, it seems more straightforward to presume that the beam has little effect on the nanocubes themselves, and it is rather the under-beam formation of a carbonaceous passive layer what is seen in Fig. 6.

Although the SEM images recorded at an accelerating voltage of 1.5 kV may not allow a clear distinction between the core of the nanoparticles and the contamination layer formed around them (Figs. 6 and 7a), the contamination layer can be visualized by EM scans at higher (20 kV) accelerating voltage (Fig. 7b). That under the formed carbonaceous contamination layer the Ag nanocubes preserve their original shape can be confirmed by the HAADF–STEM and the TEM bright field images shown in Figs. 7c and d, respectively.

It is of worth noting that the contamination layer is most probably formed by the PVP capping agent, remnants of which remain adsorbed on the Ag nanocubes despite the applied UV–ozone treatment, and then get polymerized and pinned to the electrode surface by the electron beam [28]. Based on the electrocatalytic degradation pattern shown by Fig. 5, we can assume that some PVP may also remain on the substrate, forming there a carbonaceous shell that is however presumed to be not as thick as on the surfaces of the nanocubes, where PVP is primarily adsorbed.

The under-beam formation of the passive layer on the surface of nanoparticulate catalysts seems to block the pre-scanned surface even if entirely different settings, and much harsher electrolysis conditions, compared to what was described before, are applied. This is demonstrated by Fig. 8, where we modified a gas diffusion electrode (GDE) with carbon-supported Ag NCs (this time, without the application of UV-ozone treatment), and performed electrolysis by applying a potential of −1.4 V *vs.* RHE, thus passing through a total charge amount of 1600 C cm^{-2}. While the identical location SEM images of Fig. 8a and b show no trace of degradation, particle deformation and the appearance of newly formed, small particles is clearly shown by the SEM micrograph of Fig. 8c, recorded at a random spot after the electrolysis. Although as pointed out in [40], in fact any organic contaminations of a catalyst sample may act as source of material for the formation of passive carbonaceous crust layers, the prominent role of PVP in this process is further supported by our numerous IL–SEM studies on PVP-free catalysts, where no such contamination effects were ever seen [11–20].

4. Concluding remarks

No effort has so far been made to demonstrate the effect of capping-agent related under-beam passive layer formation on the catalytic behaviour of nanoparticle type electrocatalysts. This is considered worrying, particularly because of the emerging popularity of IL–SEM-based stability studies where the pre-electrolysis scanning can contaminate (and consequently disable) the catalyst sample in a way that the post-electrolysis scan would deceivingly show no degradation.

Using PVP-functionalised Ag nanocubes as model catalysts of CO_2 reduction, we demonstrated how under-beam contamination (a carbonaceous, passive crust formed over the catalyst particles) might account for artefacts in IL–SEM studies in such a way that the experimenter is provided with false comfort with regard to the stability of the catalyst. This paper was written with the aim to direct attention to this possible pitfall of IL–SEM studies, which

may especially emerge when IL–SEM is applied on electrocatalysts prepared by a synthesis route involving capping agents.

Apart from the issues that PVP remnants can cause in the interpretation of IL–SEM experiments, it should also be emphasized that shape-forming surfactants may exert further unwanted effects also on the essential catalytic properties. *E.g.*, in case of the system studied here we have to note that if no action (in our case, UV-ozone treatment) is taken to remove (at least most of) the adhering PVP remnants, this will negatively affect both the selectivity and the stability of the catalyst. In our case omission of the UV-ozone treatment resulted, for example, in the overall Faradaic efficiency (toward CO production) dropping from ~ 80% to ~ 65%, and a further dropping to below 50% over 2 hours of electrolysis (under conditions similar to those applying for Fig. 2b). The removal of capping agents may be based on plasma/thermal annealing [41] (note that the UV-ozone treatment we applied here proved to be far from ideal), or it may even rely on mere electrochemical methods. Namely, it was recently shown in two independent studies (by our group [42] and by Pankhurst et al. [43]) that capping agent remnants may effectively be removed by the harsh cathodic potentials applied during CO_2 electrolysis. Needless to say, the latter "*operando* activation" method [42] does not work for capping agents baked to the catalyst surface by the electron beam in an IL–SEM scenario.

Declaration of Competing Interest

The authors declare that they have no known competing financial interests or personal relationships that could have appeared to influence the work reported in this paper.

Acknowledgement

Support by the CTI Swiss Competence Center for Energy Research (SCCER Heat and Electricity Storage) is gratefully acknowledged. P. B. acknowledges financial support from the Swiss National Foundation (grant 200020–172507). S. V. acknowledges support from the National Research, Development and Innovation Office of Hungary (NKFIH grant FK135375). N. K. and M. de J. G.-V. acknowledge the financial support by the Swiss Government Excellence Scholarships for Foreign Scholars (ESKAS).

References

[1] D.R. Feldman, W.D. Collins, P.J. Gero, M.S. Torn, E.J. Mlawer, T.R. Shippert, Observational determination of surface radiative forcing by CO2 from 2000 to 2010, Nature 519 (7543) (2015) 339–343, https://doi.org/10.1038/nature14240.
[2] S. Nitopi, E. Bertheussen, S.B. Scott, X. Liu, A.K. Engstfeld, S. Horch, B. Seger, I.E. L. Stephens, K. Chan, C. Hahn, J.K. Nørskov, T.F. Jaramillo, I. Chorkendorff, Progress and perspectives of electrochemical CO2 reduction on copper in aqueous electrolyte, Chem. Rev. 119 (12) (2019) 7610–7672, https://doi.org/10.1021/acs.chemrev.8b00705.
[3] E. Royer, Réduction de l'acide carbonique en acide formique, Compt. Rend. Hebd. Séances Acad. Sci. 70 (1870) 731–732.
[4] H.-R.M. Jhong, S. Ma, P.J.A. Kenis, Electrochemical conversion of CO2 to useful chemicals: Current status, remaining challenges, and future opportunities, Curr. Opin. Chem. Eng. 2 (2) (2013) 191–199, https://doi.org/10.1016/j.coche.2013.03.005.
[5] A.D. Handoko, F. Wei, Jenndy, B.S. Yeo, Z.W. Seh, Understanding heterogeneous electrocatalytic carbon dioxide reduction through operando techniques, Nature Catal. 1 (12) (2018) 922–934, https://doi.org/10.1038/s41929-018-0182-6.
[6] A. Bergmann, B. Roldán Cuenya, Operando insights into nanoparticle transformations during catalysis, ACS Catal. 9 (11) (2019) 10020–10043, https://doi.org/10.1021/acscatal.9b01831.
[7] K.J.J. Mayrhofer, J.C. Meier, S.J. Ashton, G.K.H. Wiberg, F. Kraus, M. Hanzlik, M. Arenz, Fuel cell catalyst degradation on the nanoscale, Electrochem. Commun. 10 (8) (2008) 1144–1147, https://doi.org/10.1016/j.elecom.2008.05.032.
[8] N. Hodnik, M. Zorko, M. Bele, S. Hočevar, M. Gaberšček, Identical location scanning electron microscopy: A case study of electrochemical degradation of PtNi nanoparticles using a new nondestructive method, J. Phys. Chem. C 116 (40) (2012) 21326–21333, https://doi.org/10.1021/jp303831c.
[9] N. Hodnik, S. Cherevko, Spot the difference at the nanoscale: Identical location electron microscopy in electrocatalysis, Curr. Opin. Electrochem. 15 (2019) 73–82, https://doi.org/10.1016/j.coelec.2019.03.007.
[10] J.C. Meier, I. Katsounaros, C. Galeano, H.J. Bongard, A.A. Topalov, A. Kostka, A. Karschin, F. Schüth, K.J.J. Mayrhofer, Stability investigations of electrocatalysts on the nanoscale, Energy Environ. Sci. 5 (11) (2012) 9319, https://doi.org/10.1039/c2ee22550f.
[11] M. Rahaman, A. Dutta, A. Zanetti, P. Broekmann, Electrochemical reduction of CO2 into multicarbon alcohols on activated Cu mesh catalysts: An identical location (IL) study, ACS Catal. 7 (11) (2017) 7946–7956, https://doi.org/10.1021/acscatal.7b02234.
[12] A. Dutta, M. Rahaman, M. Mohos, A. Zanetti, P. Broekmann, Electrochemical CO2 conversion using skeleton (sponge) type of Cu catalysts, ACS Catal. 7 (8) (2017) 5431–5437, https://doi.org/10.1021/acscatal.7b01548.
[13] P. Moreno-García, N. Schlegel, A. Zanetti, A. Cedeño López, M.deJ. Gálvez-Vázquez, A. Dutta, M. Rahaman, P. Broekmann, Selective electrochemical reduction of CO2 to CO on Zn-based foams produced by Cu^{2+} and template-assisted electrodeposition, ACS Appl. Mater. Interfaces 10 (37) (2018) 31355–31365, https://doi.org/10.1021/acsami.8b0989.
[14] A. Dutta, C.E. Morstein, M. Rahaman, A. Cedeño López, P. Broekmann, Beyond copper in CO_2 electrolysis: Effective hydrocarbon production on silver-nanofoam catalysts, ACS Catal. 8 (9) (2018) 8357–8368, https://doi.org/10.1021/acscatal.8b01738.
[15] M.deJ. Gálvez-Vázquez, S. Alinejad, H. Hu, Y. Hou, P. Moreno-García, A. Zana, G. K.H. Wiberg, P. Broekmann, M. Arenz, Testing a silver nanowire catalyst for the selective CO2 reduction in a gas diffusion electrode half-cell setup enabling high mass transport conditions, CHIMIA Int. J. Chem. 73 (11) (2019) 922–927, https://doi.org/10.2533/chimia.2019.92.
[16] Y. Hou, S. Bolat, A. Bornet, Y.E. Romanyuk, H. Guo, P. Moreno-García, I.Z. Montiel, Z. Lai, U. Müller, V. Grozovski, P. Broekmann, Photonic curing: Activation and stabilization of metal membrane catalysts (MMCs) for the electrochemical reduction of CO2, ACS Catal. 9 (10) (2019) 9518–9529, https://doi.org/10.1021/acscatal.9b03664.
[17] Y. Hou, R. Erni, R. Widmer, M. Rahaman, H. Guo, R. Fasel, P. Moreno-García, Y. Zhang, P. Broekmann, Synthesis and characterization of degradation-resistant Cu@CuPd nanowire catalysts for the efficient production of formate and CO from CO2, ChemElectroChem 6 (12) (2019) 3189–3198, https://doi.org/10.1002/celc.201900752.
[18] M.deJ. Gálvez-Vázquez, P. Moreno-García, H. Guo, Y. Hou, A. Dutta, S.R. Waldvogel, P. Broekmann, Leaded bronze alloy as a catalyst for the electroreduction of CO2, ChemElectroChem 6 (8) (2019) 2324–2330, https://doi.org/10.1002/celc.201900537.
[19] A.V. Rudnev, K. Kiran, A. Cedeño López, A. Dutta, I. Gjuroski, J. Furrer, P. Broekmann, Enhanced electrocatalytic CO formation from CO_2 on nanostructured silver foam electrodes in ionic liquid/water mixtures, Electrochim. Acta 306 (2019) 245–253, https://doi.org/10.1016/j.electacta.2019.03.102.
[20] A. Dutta, I.Z. Montiel, R. Erni, K. Kiran, M. Rahaman, J. Drnec, P. Broekmann, Activation of bimetallic AgCu foam electrocatalysts for ethanol formation from CO2 by selective Cu oxidation/reduction, Nano Energy 68 (2020) 104331, https://doi.org/10.1016/j.nanoen.2019.104331.
[21] W.T. Osowiecki, J.J. Nussbaum, G.A. Kamat, G. Katsoukis, M. Ledendecker, H. Frei, A.T. Bell, A.P. Alivisatos, Factors and dynamics of Cu nanocrystal reconstruction under CO2 reduction, ACS Appl. Energy Mater. 2 (11) (2019) 7744–7749, https://doi.org/10.1021/acsaem.9b01714.
[22] S.B. Simonsen, I. Chorkendorff, S. Dahl, M. Skoglundh, J. Sehested, S. Helveg, Direct observations of oxygen-induced platinum nanoparticle ripening studied by in situ TEM, J. Am. Chem. Soc. 132 (23) (2010) 7968–7975, https://doi.org/10.1021/ja910094r.
[23] M. Arenz, A. Zana, Fuel cell catalyst degradation: Identical location electron microscopy and related methods, Nano Energy 29 (2016) 299–313, https://doi.org/10.1016/j.nanoen.2016.04.027.
[24] R. Lariviere Stewart, Insulating films formed under electron and ion bombardment, Phys. Rev. 45 (7) (1934) 488–490, https://doi.org/10.1103/physrev.45.488.
[25] M. von Ardenne, Das elektronen-rastermikroskop, Z. Phys. 109 (9–10) (1938) 553–572, https://doi.org/10.1007/bf01341584.
[26] L. Marton, N.N. Das Gupta, C. Marton, Modifications of specimens in electron microscopy, Science 104 (2689) (1946) 35–36, https://doi.org/10.1126/science.104.2689.35.
[27] M.T. Postek, A.E. Vladár, Does your SEM really tell the truth?—How would you know? Part 1, Scanning 35 (6) (2013) 355–361, https://doi.org/10.1002/sca.21075.
[28] M.T. Postek, A.E. Vladár, K.P. Purushotham, Does your SEM really tell the truth?—How would you know? Part 2, Scanning 36 (3) (2013) 347–355, https://doi.org/10.1002/sca.21124.
[29] B. Luo, Y. Fang, J. Li, Z. Huang, B. Hu, J. Zhou, Improved stability of metal nanowires via electron beam irradiation induced surface passivation, ACS Appl. Mater. Interfaces 11 (13) (2019) 12195–12201, https://doi.org/10.1021/acsami.9b00875.
[30] S.F. Tan, M. Bosman, C.A. Nijhuis, Molecular coatings for stabilizing silver and gold nanocubes under electron beam irradiation, Langmuir 33 (5) (2017) 1189–1196, https://doi.org/10.1021/acs.langmuir.6b03721.

[31] S.H. Im, Y.T. Lee, B. Wiley, Y. Xia, Large-scale synthesis of silver nanocubes: The role of HCl in promoting cube perfection and monodispersity, Angew. Chem. 117 (14) (2005) 2192–2195, https://doi.org/10.1002/ange.200462208.
[32] A.V. Rudnev, Online chromatographic detection, in: K. Wandelt (Ed.), Encyclopedia of Interfacial Chemistry, Elsevier, Amsterdam, 2018, pp. 321–325, https://doi.org/10.1016/b978-0-12-409547-2.13564-4.
[33] J. Zhang, Q. Wang, X. Zhang, J. Wang, M. Guo, B.J. Wiley, C. Li, C. Hu, Carbamide promoted polyol synthesis and transmittance properties of silver nanocubes, Inorg. Chem. Front. 3 (4) (2016) 547–555, https://doi.org/10.1039/c5qi00256g.
[34] K.M. Koczkur, S. Mourdikoudis, L. Polavarapu, S.E. Skrabalak, Polyvinylpyrrolidone (PVP) in nanoparticle synthesis, Dalton Trans. 44 (41) (2015) 17883–17905, https://doi.org/10.1039/c5dt02964c.
[35] N. Naresh, F.G.S. Wasim, B.P. Ladewig, M. Neergat, Removal of surfactant and capping agent from Pd nanocubes (Pd-NCs) using tert-butylamine: Its effect on electrochemical characteristics, J. Mater. Chem. A 1 (30) (2013) 8553, https://doi.org/10.1039/c3ta11183k.
[36] D. Ung, B.M. Cossairt, Effect of surface ligands on CoP for the hydrogen evolution reaction, ACS Appl. Energy Mater. 2 (3) (2019) 1642–1645, https://doi.org/10.1021/acsaem.9b00240.
[37] Y. Hori, Electrochemical CO_2 reduction on metal electrodes, in: C.G. Vayenas, R.E. White, M.E. Gamboa-Aldeco (Eds.), Modern Aspects of Electrochemistry, Vol. 42, Springer, New York, 2008, pp. 89–189, https://doi.org/10.1007/978-0-387-49489-0.
[38] D. Sun, X. Xu, Y. Qin, S.P. Jiang, Z. Shao, Rational design of Ag-based catalysts for the electrochemical CO2 reduction to CO: A review, ChemSusChem 13 (2019) 39–58, https://doi.org/10.1002/cssc.201902061.
[39] A. Moysiadou, X. Hu, Stability profiles of transition metal oxides in the oxygen evolution reaction in alkaline medium, J. Mater. Chem. A 7 (45) (2019) 25865–25877, https://doi.org/10.1039/c9ta10308b.
[40] M. Zorko, B. Jozinović, M. Bele, N. Hodnik, M. Gaberšček, SEM method for direct visual tracking of nanoscale morphological changes of platinum based electrocatalysts on fixed locations upon electrochemical or thermal treatments, Ultramicroscopy 140 (2014) 44–50, https://doi.org/10.1016/j.ultramic.2014.02.006.
[41] I. Puspitasari, E. Skupien, F. Kapteijn, P. Kooyman, Au capping agent removal using plasma at mild temperature, Catalysts 6 (2016) 179, https://doi.org/10.3390/catal6110179.
[42] H. Hu, M. Liu, Y. Kong, N. Mysuru, C. Sun, M. d. J. Gálvez-Vázquez, U. Müller, R. Erni, V. Grozovski, Y. Hou, P. Broekmann, Activation matters: Hysteresis effects during electrochemical looping of colloidal Ag nanowire catalysts, ACS Catal. 10 (2020) 8503–8514. https://doi.org/10.1021/acscatal.0c02026.
[43] J.R. Pankhurst, P. Iyengar, A. Loiudice, M. Mensi, R. Buonsanti, Metal–ligand bond strength determines the fate of organic ligands on the catalyst surface during the electrochemical CO2 reduction reaction, Chem. Sci. 11 (2020) 9296–9302, https://doi.org/10.1039/d0sc03061a.

8. Size-Dependent Structural Alterations in Ag Nanoparticles during CO_2 Electrolysis in a Gas-Fed Zero-Gap Electrolyzer

Authors: Huifang Hu, Menglong Liu, Ying Kong, Iván Zelocualtecatl Montiel, Yuhui Hou, Soma Vesztergom, Alexander V. Rudnev and Peter Broekmann.

***ChemElectroChem*, 2022, 9, e202200615. DOI: 10.1002/celc.202200615**

Highlight: The effect of the NP size on the catalyst degradation behavior during ec-CO_2RR was studied using a semi-zero-gap electrolyzer cell and PVP-capped Ag-NPs (10, 40, and 100 nm) as model catalysts. Differently sized Ag-NPs underwent distinct structural alteration during a galvanostatic ec-CO_2RR. The initial size distribution of the Ag-NPs determines how the catalyst degrades during electrolysis (e.g., via cathodic corrosion, agglomeration, coalescence etc.).

Contribution: I helped to prepare the GDEs and performed the electrochemical experiments. I also contributed to the total nitrogen content determination and to the discussion of the results.

ChemElectroChem

Research Article
doi.org/10.1002/celc.202200615

Chemistry Europe
European Chemical Societies Publishing

www.chemelectrochem.org

Size-Dependent Structural Alterations in Ag Nanoparticles during CO_2 Electrolysis in a Gas-Fed Zero-Gap Electrolyzer

Huifang Hu,[a] Menglong Liu,[a, b] Ying Kong,[a, b] Iván Zelocualtecatl Montiel,[a, b] Yuhui Hou,[a] Alexander V. Rudnev,*[a, c] and Peter Broekmann*[a, b]

Ag nanoparticles (NPs) are efficient electrocatalysts for electrochemical CO_2-to-CO conversion. However, NPs are thermodynamically unstable and can undergo structural alterations under electrolysis operating conditions. These structural changes may play a crucial role in the deterioration of CO_2 reduction reaction (CO_2RR) performance on the long-term electrolysis time scale. Here, we studied the effect of NP size on NP degradation during CO_2RR. Polyvinylpyrrolidone-capped 10, 40, and 100 nm Ag NPs deposited on a gas diffusion electrode were used as testbed catalysts in a gas-fed zero-gap electrolyzer. Inductively coupled plasma mass spectrometry indicated insignificant catalyst-material detachment after galvanostatic CO_2 electrolysis. Scanning electron microscopy analysis showed that smaller NPs tended to agglomerate during CO_2 electrolysis. 100 nm NPs formed agglomerates consisting of only two-three NPs and underwent pronounced fragmentation with the formation of particles several nanometers in size. The fragmentation was associated with cathodic corrosion of Ag NPs under conditions of intensive CO_2RR and hydrogen evolution.

Introduction

Electrochemical CO_2 conversion is a promising approach for the storage of renewable electricity in a sustainable manner and the production of synthetically or industrially valuable platform chemicals.[1] Currently, research on the electrochemical approach is driven primarily by the technological demand for catalyst and electrolyzer configurations that provide selective and stable progress of CO_2 reduction reaction (CO_2RR).

CO_2RR in H-type electrochemical cells (two-compartment cells with a membrane separating the cathode and anode compartments) suffers from mass transport limitations, owing to the low concentration of CO_2 in electrolyte solutions. The use of a zero-gap gas-flow electrolyzer unit with a gas diffusion electrode (GDE) overcomes these limitations, thus resulting in current densities of CO_2RR above 300 mA cm^{-2}.[2–5] Modern commercial GDEs consist of a carbon fiber support (CFS) and a microporous layer (MPL) with the catalyst layer deposited on the MPL.[6] In the zero-gap configuration, a humidified CO_2 gas diffuses through a porous gas diffusion layer (CFS and MPL) of the GDE to the active sites of the catalyst.

Metallic nanoparticles (NPs) deposited on a GDE can be used as efficient electrocatalysts for CO_2 reduction. High selectivity for CO_2-to-CO conversion has been achieved, for example with nanoparticulate or nanostructured Ag catalysts.[7–11] Relatively low loading of nanoparticulate catalyst material can be used to achieve a CO_2RR current density at an industrially relevant level. However, owing to their small size, NPs are thermodynamically unstable and can therefore undergo structural alterations under electrolysis operating conditions. Degradation mechanisms for fragmentation, reshaping, poisoning, agglomeration, dissolution (redeposition), detachment, and Oswald ripening have been reported for NPs under CO_2RR at negative potentials.[12,13] NP fragmentation can be considered as a phenomenon of cathodic corrosion.[14]

Although NP-catalyst degradation behavior during CO_2RR has been intensively studied in H-type and one-compartment cells (e.g., see Refs. [12,15–20]), the conclusions obtained in these studies might not be directly applicable to the zero-gap electrolyzer configuration.[2] In the latter case, the investigation of catalyst degradation has been hindered by the precipitation of (bi)carbonate salt at a three-phase GDE interface within several or few tens of minutes, thus severely suppressing CO_2RR.[2,3,21–23] Nevertheless, the study of NP-catalyst structural changes during CO_2RR in a zero-gap electrolyzer under harsh conditions (high current densities) is extremely important, because NP degradation is crucial for CO_2RR performance on the long-term electrolysis time scale.

Multiple factors affect NP degradation behavior. In our previous work, we have studied the effect of a capping agent on structural alterations of spherical Ag NPs after CO_2RR in a zero-gap electrolyzer.[3] Ag NPs 40 nm in size were stabilized by

[a] H. Hu, M. Liu, Y. Kong, I. Z. Montiel, Dr. Y. Hou, Dr. A. V. Rudnev, Prof. P. Broekmann
Department of Chemistry, Biochemistry and Pharmaceutical Sciences
University of Bern
Freiestrasse 3, 3012 Bern, Switzerland
E-mail: peter.broekmann@unibe.ch
alexander.rudnev@unibe.ch
[b] M. Liu, Y. Kong, I. Z. Montiel, Prof. P. Broekmann
National Centre of Competence in Research (NCCR) Catalysis
University of Bern
Freiestrasse 3, 3012 Bern, Switzerland
[c] Dr. A. V. Rudnev
A. N. Frumkin Institute of Physical Chemistry and Electrochemistry
Russian Academy of Sciences
Leninskii pr. 31 bld. 4, 119071 Moscow, Russia

Supporting information for this article is available on the WWW under https://doi.org/10.1002/celc.202200615

four capping agents: branched polyethylenimine (PEI), polyvinylpyrrolidone (PVP), polyethylene glycol (PEG), and citrate. Although the NPs displayed identical size distributions, they differed in their activity toward CO_2RR in terms of faradaic efficiency for CO formation, FE_{CO}, and current densities in the course of potentiostatic electrolysis. Thus, the structural changes in NPs occurring during electrolysis were also affected by the chemical nature of the capping agent. Here, continuing our investigation of the degradation behavior of Ag NP catalysts, we focused on the effect of NP size on structural changes during CO_2RR in a zero-gap electrolyzer (the corresponding configuration has been described in detail in Refs. [3,23], Figure S1). Catalyst inks were prepared from commercially available PVP-capped 10, 40, and 100 nm Ag NPs. Through a set of post-electrolysis analyses of the NP-catalyst, we show that degradation pathways substantially depend on the initial NP size. Smaller NPs tend to agglomerate during CO_2 electrolysis. In particular, 10 nm NPs form agglomerates up to 200 nm in the longest dimension. In addition, 100 nm NPs form agglomerates consisting of only two or three NPs, and undergo pronounced fragmentation, thus forming large amounts of particles several nanometers in size, which are redeposited on the MPL. The fragmentation appears to be associated with cathodic corrosion of Ag NPs at negative potentials under conditions of intensive CO_2RR and hydrogen evolution reaction (HER).

Results and Discussion

Characterization of As-Prepared Ag NPs Deposited on GDE

The as-prepared Ag NP catalyst deposited on the GDE (Figure S2) was analyzed with scanning electron microscopy (SEM) (Figure 1a, e and i). The respective size distributions are shown in Figure 2. SEM images before electrolysis indicated that the

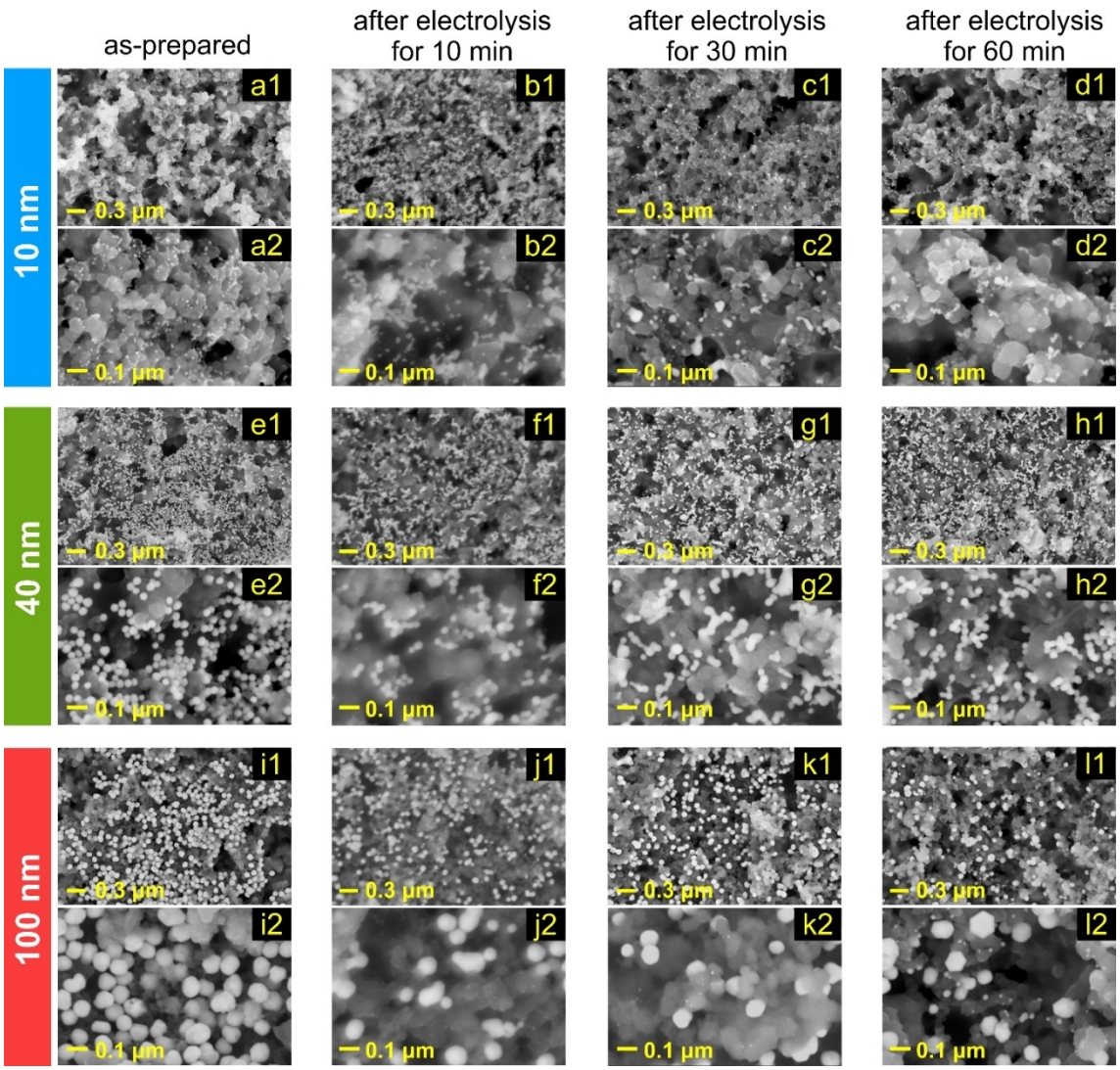

Figure 1. Representative SEM images of Ag NP-catalyst on GDEs. The size of NPs: (a–d) 10 nm, (e–h) 40 nm, (i–l) 100 nm. The SEM images were recorded (a, e, i) before ("as-prepared") and (b–d, f–h, j–l) after galvanostatic CO_2 electrolyses ($j = -283$ mA cm^{-2}) for different time (different passed charge): (b, f, j) 10 min (169.7 C cm^{-2}), (c, g, k) 30 min (509.2 C cm^{-2}), (d, h, l) 60 min (1018.4 C cm^{-2}). Two images of different magnification are shown for each sample.

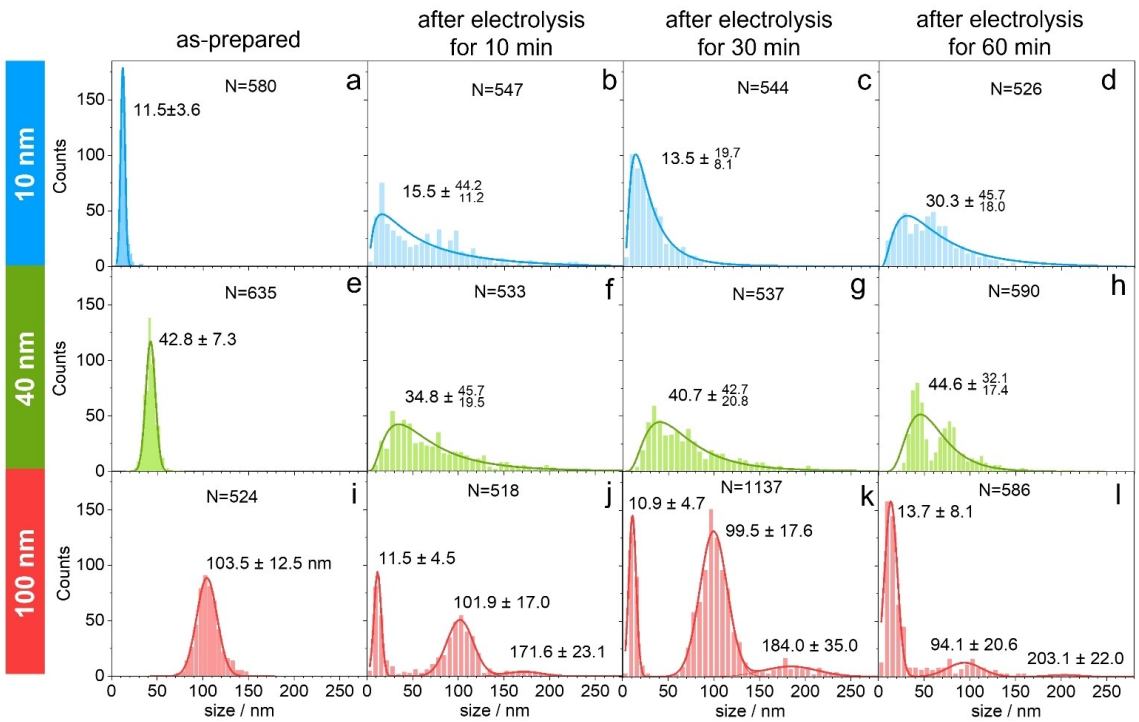

Figure 2. Histograms showing the particle size distribution of Ag NPs of different size: (a–d) 10 nm, (e–h) 40 nm, (i–l) 100 nm. The data were obtained for NP-catalysts (a, e, i) before and (b–d, f–h, j–l) after CO_2 electrolysis at $j = -283$ mA cm^{-2} for a certain time: (different passed charge): (b, f, j) 10 min (169.7 C cm^{-2}), (c, g, k) 30 min (509.2 C cm^{-2}), (d, h, l) 60 min (1018.4 C cm^{-2}). Expectation ranges of the particle size are shown for the fitted peak(s). Number of particles analyzed (*N*) is given in the graphs.

Ag NPs were fairly uniformly distributed over the MPL surface. Size analysis demonstrated a normal distribution of NP sizes on the GDE surface before electrolysis. The estimated mode values were close to the values indicated by the manufacturer (the values are given in the graphs, Figure 2). Inductively coupled plasma mass spectrometry (ICP-MS) data demonstrated that the actual mass loading for NPs of different sizes was nearly identical (Table 1). However, according to SEM data the number of NPs on the GDE surface (in terms of volume or mass) appeared dissimilar. The amount (volume and mass) of 10 nm NPs on the GDE surface seemed to be significantly less than those of 40 and 100 nm NPs. This finding is explained by the greater penetration of smaller NPs inside the GDE layers during drop-cast deposition. The cross-sectional SEM images in Figure 3 distinguished the boundary between MPL and CFS. The energy-dispersive X-ray spectroscopy (EDX) mapping of Ag demonstrated the presence of Ag NPs inside both MPL and CFS (Figure 3). Moreover, 10 nm NPs were distributed fairly uniformly in the microporous layer, with greater density around cracks and at the boundaries between microporous and microfiber layers. The amount of 10 nm NPs on the surface of the GDE was similar to that inside the microporous layer. This finding was supported by individual EDX spectra (cf. spectrum 1 with spectra 2 and 6 in Figure 3b). Spectrum 3 recorded at the area close to the microporous/microfiber layer boundary showed an enhanced Ag signal. The EDX mapping and spectra 4 and 5 unambiguously indicated that 10 nm NPs penetrated into the CFS.

A slightly less uniform distribution of 40 nm NPs was observed inside MPL (Figure 3c) with increased density on the top surface of MPL, at cracks, and around the MPL/CFS boundary. A smaller amount of Ag NPs was observed in CFS. This observation was supported by individual EDX spectra (Figure 3d). Spectra 1 to 3 showed Ag signals of slightly higher intensity than those in the spectra recorded at areas 4 and 5. A large fraction of 100 nm NPs after deposition were located on

Table 1. Loading of Ag in NP-catalyst as calculated from the drop-cast amount and as estimated by ICP-MS.

Ag NP-catalyst	Calculated loading [μg cm^{-2}]	Loading by ICP-MS [μg cm^{-2}]		
		As-prepared	After electrolysis[a]	After recovery experiments[b]
10 nm	300	290.52 ± 11.8	267.80 ± 20.7	266.65 ± 9.4
40 nm	300	297.31 ± 16.6	289.43 ± 17.0	277.04 ± 18.0
100 nm	300	303.02 ± 4.8	287.78 ± 18.2	270.68 ± 13.8

[a] After electrolysis at −283 mA cm^{-2} for 60 min. [b] After 2nd electrolysis at −283 mA cm^{-2} for 60 min.

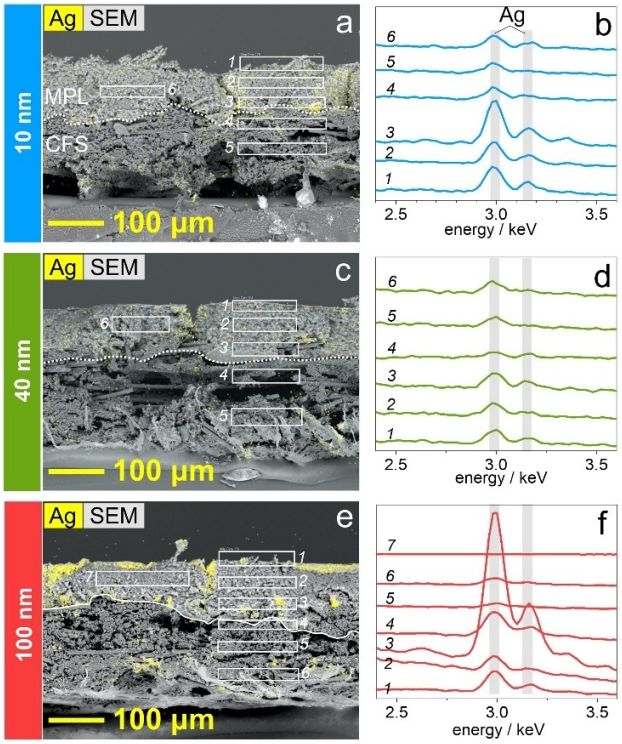

Figure 3. (a, c, e) Representative cross-sectional side-view SEM images and overlapped EDX Ag mapping of the microporous and microfiber GDE layers with deposited Ag NPs of different sizes: (a) 10 nm, (c) 40 nm, (e) 100 nm. Dotted lines indicate boundaries between MPL and CFS. (b, d, f) EDX spectra recorded for respective areas of GDE cross-sections (see numbering).

top of the MPL (Figure 3e). High density of NPs was also observed at cracks and at the MPL/CFS boundary, whereas NPs were scarcely detected inside MPL and CFS far from large cracks. This result was confirmed by EDX spectra (Figure 3f): spectra recorded at areas inside the layers (2 and 7 in MPL and 5 and 6 in CFS) showing weak or absent Ag signal, whereas the signal was stronger on the top of MPL (spectrum 1) or around the MPL/CFS boundary (spectra 3 and 4). These findings indicated that larger particles (such as 100 nm) scarcely penetrated through/into micropores of MPL, but a portion of these NPs passed through the MPL via cracks and accumulated at the MPL/CFS boundary.

Note that we used the same Ag mass loading for all NP-catalysts. Thus, the surface area of NP-catalysts would certainly depend on their initial size. In addition, the data in Figure 3 clearly show that a large fraction of particles penetrates the GDE and might not participate in the electrolysis reaction. Moreover, the amount of Ag NPs penetrated in CFS layer strongly depends on initial NP size. Estimation of the electroactive area of Ag NPs and the appropriate comparison of surface areas are hardly possible when solely based on the mass loading and size distribution data.

CO_2 Electrolysis: Loss of CO_2RR Performance

Figure 4 shows the *FE*s of three detected products (CO, H_2, and $HCOO^-$) formed during CO_2 galvanostatic electrolysis at $j = -283\ mA\,cm^{-2}$ for 60 min (passed charge $q = 1018.4\ C\,cm^{-2}$). The initial FE_{CO} was ~90–93% and was nearly identical for NPs of different sizes (Figure 4), in agreement with findings form studies on the size effect on CO_2RR. Au NPs and Cu NPs ~5 nm or larger have been reported to show similar CO_2RR performance in terms of faradaic efficiency.[24,25] Only smaller NPs showed a significant change in the product distribution. Typically, the use of Cu and Au NPs with sizes below 5 nm markedly increased faradaic efficiency of hydrogen formation, FE_{H2}, and decreased CO_2RR efficiency.[24,25]

However, over time or with a passed charge, the FE_{CO} drastically decreased, whereas the FE_{H2} correspondingly increased. No clear correlation was observed between the NP size and the CO_2RR performance deterioration. The fastest deterioration occurred for 40 nm NPs, whereas the slowest deterioration was observed for 100 nm NPs. The rate of FE_{CO} decrease over time was moderate for 10 nm NPs. Formate was also produced in a detectable amount in our experiments. Typically, FE_{HCOO-} increased over time, reaching ~11% after 60 min of CO_2 electrolysis ($1018.4\ C\,cm^{-2}$).

The rapid loss in CO_2RR performance has been found to be associated primarily with potassium (bi)carbonate precipitation on the GDE.[2,3,21–23] The (bi)carbonate precipitation is caused by increased local alkalinity leading to an undesirable reaction of CO_2 with hydroxide ions. Several processes induce an increase in local pH. (i) CO_2RR and HER consume protons from water molecules, thus forming hydroxide ions. (ii) Driven by both

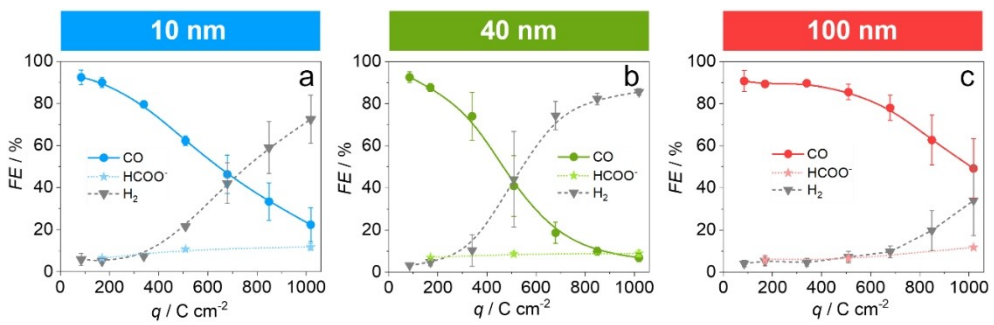

Figure 4. *FE*s of CO, $HCOO^-$, and H_2 versus charge passed during galvanostatic CO_2 electrolyses (at $j = -283\ mA\,cm^{-2}$) employing Ag NP-catalysts. The size of NPs: (a) 10 nm, (b) 40 nm, (c) 100 nm. The total electrolysis time is 60 min.

chemical and electric potential gradients, K^+ ions penetrate even the anion exchange membrane.[26] (iii) Finally, the percolation of anolyte (KOH) from the anode compartment via membrane defects leads to flooding of the GDE. The electrolyte solution penetrating into GDE substantially slow down CO_2 diffusion to the active catalytic sites in MPL, thus, hindering CO_2RR consequently promoting HER.[23] On the other hand, the flooding of GDE induces the formation of (bi)carbonate at the three-boundary GDE interface. Because of the limited solubility of potassium (bi)carbonate (lower than the solubility of KOH), the salt precipitates and also leads to blocking of CO_2RR active sites.[21] The precipitation also results in a decreasing electrode potential during the galvanostatic CO_2 electrolysis (Figure S3). The potential at the beginning of the electrolysis at $j = -283\ mA\,cm^{-2}$ is around -1.7 V irrespective of the NP size and decreases with time, as the precipitate forms.

We also note that the precipitation issue may be affected by the amount of PVP-capping agent in the catalyst ink. Previously, we reported that PVP is present in ink not only as a capping agent adsorbed on Ag NPs but also in a dissolved/dispersed form (excess PVP).[3] The adsorption of PVP from ink on the GDE after catalyst drop-casting may change the interfacial properties of the electrode and influence the precipitation behavior. Alinejad et al. have recently demonstrated that a PVP-capped Au NP-catalyst displays worse CO_2RR performance (in terms of FE_{CO} and current density) than a PVP-free Au NP-catalyst in both an H-cell and a zero-gap electrolyzer.[27] Herein, we estimated the PVP content in supernatant solutions (Table 2). To quantify PVP surfactant, we determined the total nitrogen content in the supernatant solution (TN_{sup}), i.e., excess PVP, and in the solution of NPs redispersed in water after removal of excess PVP (TN_{NP}). We assumed that TN_{NP} corresponded to PVP directly attached to NPs. The data indicated that TN_{sup} (excess PVP) was approximately an order of magnitude higher than TN_{NP} (PVP on NPs) (Table 2). The results also indicated that the excess PVP decreased with NP size. That is, the concentration calculated for a PVP monomer, $c_{VP,sup}$, in the case of 100 nm NPs was half that for 10 nm NPs (135 vs. 250 ppm). Thus, the relatively slow deterioration of CO_2RR performance in the case of 100 nm NPs (Figure 4c) might also have been due to the smaller amount of PVP in the catalyst ink. The effect of PVP on the precipitation issue during CO_2 electrolysis in a zero-gap electrolyzer will be the focus of our follow-up work.

Despite the deterioration in CO_2RR performance associated with (bi)carbonate precipitation at the GDE, clear alterations in the NP-catalyst structure occurred after CO_2 electrolysis. These structural changes might lead to CO_2RR performance losses, which occur less rapidly than losses due to salt precipitation but can become considerable during long-term CO_2 electrolysis. Of particular concern, NPs with certain preferential orientations (e.g., cubic NPs) display higher activity (lower overpotential) toward CO_2RR.

The structural disordering of such shaped NPs leads to catalyst deactivation.[20] In contrast, the degradation of even spherical NPs with no preferential surface orientation can lead to performance losses. For example, NP agglomeration decreases the electrochemically active surface area, whereas corrosion may promote the detachment of NPs, i.e., the loss of the contact between the catalyst and the support.

To confirm the fact that the large decrease in FE_{CO} within 60 min of CO_2 electrolysis (as shown in Figure 4) was associated primarily with (bi)carbonate precipitation, we performed so-called "recovery" experiment (Figures S4-S6). In this experiment, the GDE after the 1st electrolysis was washed accurately in water to remove the salt precipitate and used again in the 2nd electrolysis (details in Experimental Section). Of note, the washing procedure did not lead to any loss in Ag NP catalysts. ICP-MS data demonstrated nearly identical mass loading of Ag after the 1st and 2nd electrolyses (Table 1). Simultaneously, the washing allowed for removal of nearly all (bi)carbonate precipitate (as previously demonstrated by EDX analysis in Ref. [3]). Figure S4 shows the comparison of *FE*s for CO and H_2 production in the 1st and 2nd galvanostatic electrolyses at $j = -283\ mA\,cm^{-2}$. The CO_2RR performance almost completely recovered for the washed GDE: the initial FE_{CO} in the 2nd electrolysis was equal to or slightly less than that in the 1st electrolysis. The FE_{CO} decrease and the FE_{H2} increase over time (passed charge) were slightly faster in the case of the washed GDE in the 2nd electrolysis. However, beyond structural changes in NP catalysts, these effects may be associated with many other factors such as (partial) removal of the capping agent, PVP, slight changes in hydrophilicity of GDE, and/or remaining residual salt precipitate after the washing procedure.

CO_2 electrolysis was also performed at two other current densities in addition to $j = -283\ mA\,cm^{-2}$: -141 and $-566\ mA\,cm^{-2}$ (Figures S7–S12). In all cases, the charge passed during electrolysis was $509.2\ C\,cm^{-2}$, and therefore the electrolysis duration differed: 60 min at $-141\ mA\,cm^{-2}$, 30 min at $-283\ mA\,cm^{-2}$, and 15 min at $-566\ mA\,cm^{-2}$. When the FE_{CO} and FE_{H2} were plotted vs. electrolysis time (Figure S8), the deterioration rate of CO_2RR performance was higher at higher applied current density. However, when we compared data for the same charge passed, the decrease in FE_{CO} was highest for the lowest current density used (Figure S7). Overall, we concluded that the size of NPs had no considerable effect on CO_2RR performance deterioration, regardless of electrolysis duration or current density. This finding is in agreement with the conclusion that performance losses were due mainly to salt

Table 2. TN values for supernatant (TN_{sup}) and redispersed NPs (TN_{NP}) solutions after the removal of excess PVP and calculated respective concentrations of PVP monomers (vinylpyrrolidone, $c_{VP,sup}$ and $c_{VP,NP}$) assuming one nitrogen atom per monomer. The Ag content in the samples was 0.5 $mg\,mL^{-1}$.

Samples	TN_{sup} [ppm]	$c_{VP,sup}$ [ppm]	TN_{NP} [ppm]	$c_{VP,NP}$ [ppm]
10 nm	31.5	250	2.8	22
40 nm	21.7	172	2.3	18
100 nm	17.0	135	1.3	10

precipitation. We also observed that increasing the current density of CO_2 electrolysis increased in FE_{HCOO^-} up to 17–19% (Figure S9). However, this change in the product distribution did not appear to depend on NP size: FE_{HCOO^-} increased with current density similarly for 10, 40, and 100 nm NPs. The dependencies of the electrode potential on the passed charge or time are also rather similar for NPs of different sizes (Figure S10). In general, the potential decreases during the galvanostatic electrolysis reaction. This decrease scales with the cathodic current applied.

Structural Changes in Ag NPs after CO_2 Electrolysis

The structural changes in NP catalysts were analyzed by SEM after CO_2 electrolyses. Because of massive salt precipitation, the GDE underwent the water washing procedure, as in the "recovery" experiments. A comparison of Ag mass loading estimated by ICP-MS before and after electrolysis indicated only a minor decrease (Table 1).

Representative SEM images of the Ag NP-catalyst layer after CO_2 electrolysis at $j = -283\ mA\,cm^{-2}$ are shown in Figure 1 for the three studied sizes of NPs. The size distributions of NPs are presented in Figure 2. Expected particle size ranges (mode ± deviation) were determined from the histograms shown in Figure 2, fitted by either symmetric Gaussians or asymmetric (skewed) log-normal functions.

The SEM images demonstrated that Ag NPs underwent agglomeration after CO_2 electrolysis even within 10 min (Figure 1). The agglomeration was characteristic for all three sizes of NPs under study. Furthermore, we observed the appearance of smaller particles after electrolysis with 100 nm NP catalyst (Figure 1j–l). From the fitting of NP size distribution, we made the following observations. In the case of 10 nm NPs, the size distribution was fitted by a log-normal function. The mode value increased with increasing electrolysis time (charge passed) from 11.5 up to 30.3 nm (Figure 2b–d), with some particles/agglomerates reaching 100 nm or greater (the longest dimension). Such agglomerated NPs were not observed before electrolysis, and as-prepared NPs had a fairly narrow expected range. In the case of 40 nm NPs (Figure 2f–h), the size distribution was also log-normal. Nevertheless, the mode value did not substantially shift after electrolysis; thus, a large fraction of NPs retained their initial size. Simultaneously, the expected range became broader, and skewness appeared with a larger contribution from agglomerated particles (as in the case of 10 nm NPs). The number of NPs smaller than 40 nm also increased after CO_2 electrolysis, thus indicating a degradation mechanism associated with partial NP fragmentation. The degradation behavior of 100 nm NPs was different. Three populations of NPs were distinguished and fitted with Gaussians (Figure 2j–l). The size distribution in the population with the mode value close to the initial value (100 nm) became broader after electrolysis: the deviation increased from 12.5 nm for the as-prepared catalyst up to 20.6 nm for the catalyst after 60-min electrolysis. Simultaneously, the mode value of this population slightly decreased from 103.5 to 94.1 nm after electrolysis, thus, suggesting fragmentation of the NPs. A new population with a mode value of approximately 11–13 nm appeared after 10 min of CO_2 electrolysis. The number of these small NPs and the expected range of the population appeared to increase with electrolysis time (charge passed). SEM images in Figure 1j–l clearly displayed an increased number of small NPs. The formation of the small NPs was consistent with the decrease in the mode value of the initial NP distribution. Additionally, we resolved the third population with the mode value, which changed from 171.6 nm to 203.1 nm with increasing electrolysis time (Figure 2j–l). This population typically consisted of two or three agglomerated NPs. The agglomeration of 10 nm NPs was much more severe during CO_2 electrolysis: a large fraction of agglomerates exceeded the initial NP size by factors of 10 to 20 (Figure 2b–d). Thus, the agglomeration of 100 nm particles was a slower process than that for 10 nm NPs. On the basis of our results, we concluded that 100 nm NPs are more likely to undergo fragmentation than agglomeration.

Interestingly, we also observed the faceting of individual 100 nm NPs after electrolysis. For the as-prepared samples, virtually all NPs were spherical without any distinguishable facets. SEM images in Figure 5 (more images in Figure S13) showed that NPs underwent extensive restructuring and, after 60 min of electrolysis, acquired clear facets. Facet formation was characteristic of the cathodic corrosion process.[28,29] Although the mechanism of cathodic corrosion is not yet fully understood, it has been observed for many metals including Ag.[30] Elnagar et al. have demonstrated the formation of a (111) facet on a polycrystalline Au wire after cathodic polarization in concentrated KOH solution (5–20 M).[31] Au faceting was observed at −1.5 V vs. RHE (reversible hydrogen electrode) and became more pronounced at more negative potentials. After polarization at −3.5 V vs. RHE for just 60 s, the voltammetric response of Au wire was nearly identical to that for an Au(111) single crystal electrode. The authors in ref.[31] have concluded that HER and high near-surface concentration of K^+ ions are essential for the cathodic corrosion process and faceting. Such conditions can be fulfilled during CO_2 electrolysis in a gas-fed electrolyzer. Typically, the GDE cathode potential during galvanostatic polarization at $j = -283\ mA\,cm^{-2}$ is between −1.75 and −1.95 V, whereas high alkalinity and K^+ concentration are achieved because of HER and CO_2RR, K^+ ion penetration and KOH solution flooding via the membrane. In the case of 40 nm NPs the faceting was observed but in much

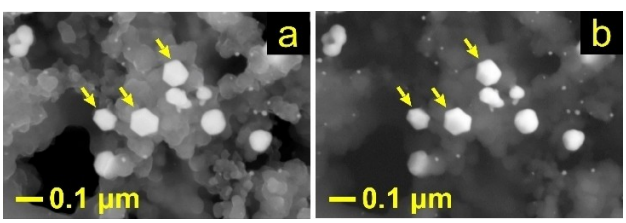

Figure 5. Representative SEM images of 100 nm Ag NP-catalysts on GDE after passing $1018.4\ C\,cm^{-2}$ during CO_2 electrolysis (60 min) at $j = -283\ mA\,cm^{-2}$. NPs indicated by arrows display clear faceting. Images were acquired using (a) InLens SE and (b) BSD detectors.

less extent than for 100 nm NPs. Figure S14 demonstrates a few faceted NPs for a sample after the "recovery" experiment, i.e., two electrolyses at $j=-283$ mA cm^{-2} for 60 min each. For small NPs (10 nm), we did not observe pronounced faceting after CO_2 electrolysis, possibly because of insufficient SEM resolution as well as the tendency of the smaller particles to agglomerate.

The faceting of spherical NPs in this study (Figure 5) was opposite from the degradation behavior of cubic Ag NPs with the initial facet orientation of (100).[2] During electrolysis, the Ag nanocubes underwent fragmentation and changed their cubic shape, becoming more spherical during CO_2 electrolysis. Similarly, the fragmentation and destruction of (100) facets were found for cubic Cu NPs.[20]

In addition, we performed a reference experiment employing the 100 nm NP-catalyst, where we fed the GDE with Ar+H_2O (no CO_2). Under these conditions only HER takes place at the cathode. Note, no precipitate was observed at the cathode after 60 min of electrolysis at $j=-283$ mA cm^{-2}. This might be the reason why the electrode potential was much more stable during the water electrolysis than that in the course of CO_2 electrolysis (Figure S15a). Nevertheless, the MPL layer of the GDE was wet after the water electrolysis probably likely due to the KOH flooding. The SEM analysis after the electrolysis in the absence of CO_2 demonstrates much less pronounced formation of small clusters as compared to the samples after the CO_2 electrolysis at the same current density (Figure S15). This finding suggests that the fragmentation of 100 nm Ag NPs is more pronounced during CO_2RR (on CO_2-fed GDE). One possible explanation of this observation is that the (bi)carbonate precipitation on the CO_2-fed GDE blocks diffusion pathways for CO_2, H_2O, K^+, and OH^- ions and, thus, may lead to a greater local increase in alkalinity as compared to the situation where only Ar and H_2O are fed through the GDE.

Recently, we have reported that excess PVP influences the degradation behavior of 40 nm Ag NPs: the removal of excess PVP leads to more pronounced agglomeration of NPs after CO_2 electrolysis.[3] We assumed that excess PVP adsorbed on the carbon support rendered NPs immobile and thus hindered their agglomeration. The estimation of TN in NP-catalyst samples demonstrated a smaller amount of excess PVP in the case of larger NPs (cf. TN_{sup} values in Table 2). Thus, a greater tendency for agglomeration might be expected for NP catalysts containing smaller amounts of excess PVP. However, we observed an opposite trend: although the 100 nm NP-catalyst contained a smaller amount of excess PVP, the agglomeration was more characteristic for 10 and 40 nm NP catalysts (Figures 1 and 2). This result indicated that NP size plays a more decisive role in degradation behavior than excess PVP content observed in our experiments.

The SEM analysis of Ag NP catalysts after CO_2 electrolysis at different current densities (but with the same passed charge equal to 509.2 C cm^{-2}) is shown in Figures S11 and S12. For the 10 nm NPs, the increase in current density (−141, −283, and −566 mA cm^{-2}) had a minor effect on the degradation behavior: the NPs tended to agglomerate at any current density (Figures S11a–d, S12a–d). The agglomeration of 40 nm NPs appeared to be more severe with increasing current density of electrolysis (Figures S11e–f, S12e–f). At $j=-566$ mA cm^{-2}, the NP size could scarcely be estimated because of massive agglomeration, whereas at $j=-141$ mA cm^{-2}, many agglomerates consisted of two NPs, thus resulting in an additional peak in the size distribution histogram at 79.7 nm (Figure S12f). For 100 nm NPs, the agglomeration was insignificant at low current density $j=-141$ mA cm^{-2} (Figure S12j). At higher current densities (−283 and −566 mA cm^{-2}), the difference in degradation behavior was minor (Figure S12k,l). At all current densities, the 100 nm NPs tended toward fragmentation with the formation of small particles with a mode size of 11–18 nm (Figure S12j–l).

We also performed SEM analysis of 40 nm catalyst after the "recovery" experiment, i.e., after the 2nd electrolysis at $j=-283$ mA cm^{-2} (product distribution data are shown in Figures S4, S5). The comparison of the morphology and size distribution of the NP catalysts after the 1st and 2nd electrolyses (Figure 6a–c) demonstrated further agglomeration and fragmentation of NPs in the 2nd electrolysis: the expected range became broader, and the deviations increased for both directions (toward smaller and larger sizes; Figure 6c). Thus, the continuation of CO_2 electrolysis after reactivation of GDE by removal of (bi)carbonate precipitate led to further degradation (agglomeration and fragmentation) of Ag NPs. SEM analysis of the 100 nm catalyst after the "recovery" experiment demonstrates even more pronounced changes in size distribution as compared to that after the 1st electrolysis (Figure 6d–f). The mode value of the population of small particles formed in the 1st electrolysis increased from 13.7 to 25.3 nm accompanied by a broadening of the expectation range. This finding suggests that at least part of small clusters agglomerated (in parallel to

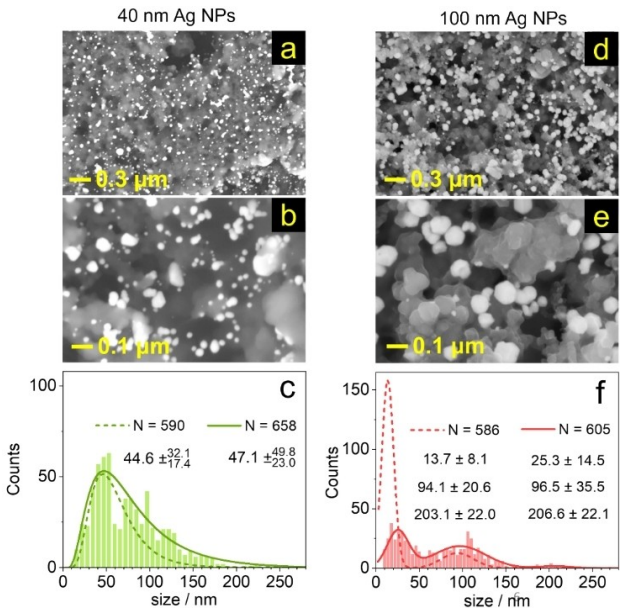

Figure 6. (a, b, d, e) SEM images and (c, f) size histograms and fitting (solid line) of (a–c) 40 nm and (d–f) 100 nm NP-catalysts after "recovery" experiment, i.e., 2nd electrolysis at $j=-283$ mA cm^{-2}. The fitting curves of size distribution for NP-catalysts after the 1st electrolysis are also shown by dashed lines. Number of particles analyzed (*N*), mode values, and deviations are given in the graphs.

the formation of new small clusters due to fragmentation) in the course of the 2nd electrolysis. Moreover, some 100 nm NPs display signs of severe degradation of after the 2nd electrolysis as indicated in Figure S6.

Raw data and unprocessed measurement files serving as a basis of this article can be found elsewhere.[32]

Conclusion

Herein, we studied the effect of NP size on NP degradation behavior during CO_2 electrolysis in a gas-fed zero-gap electrolyzer. For this purpose, we performed galvanostatic electrolyses with PVP-capped spherical Ag NPs of different initial sizes (10, 40, and 100 nm). Post-electrolysis SEM and size-distribution analyses were used to explore structural changes. ICP-MS analysis of Ag loading before and after electrolysis showed no considerable detachment of the NP-catalyst, regardless of the NP size. However, SEM data demonstrated clear structural changes in NPs on the surface of GDE after electrolysis. The smallest 10 nm NPs underwent mainly agglomeration during galvanostatic CO_2 electrolysis, thus leading to the formation of larger agglomerates with the longest distance up to 200 nm. For 40 nm NPs, agglomeration was also prevalent, although the fragmentation of NPs with the formation of smaller clusters was also detected. The size distribution of both 10 and 40 nm NPs after CO_2 electrolysis was fitted well with a log-normal function, with a pronounced skewness toward larger sizes. In the case of 100 nm NPs, two new populations were distinguished with mode values of 11–13 nm and 170–200 nm after electrolysis. The mode values, particularly for the population of larger agglomerates, increased with electrolysis time (charge passed). The 100 nm NPs tended to form agglomerates consisting primarily of two or three initial particles. The population of smaller particles (mode of approximately 11–13 nm) was formed because of the fragmentation of initial NPs. The fragmentation appeared to be associated with cathodic corrosion of Ag NPs at negative potentials under conditions of intensive CO_2RR and HER. The GDE flooding with KOH solution, additional penetration of K^+ ions via a membrane, and accumulation of OH- ions due to cathodic reactions may facilitate the cathodic corrosion of Ag catalyst. Another sign of cathodic corrosion is the faceting of NPs, which was clearly distinguishable for the 100 nm NP-catalyst. We emphasise that the NP mass loading may also affect the degradation behavior. Simultaneously, the correlation between the structural changes and the CO_2RR performance losses in a zero-gap electrolyzer was not able to be established because of the flooding and the harsh salt precipitation at the GDE within a short time (minutes). However, the results clearly indicated that on a long-term time scale, structural changes in catalysts play important roles in CO_2RR performance. NP agglomeration would decrease the electrochemically active surface area, whereas fragmentation/corrosion would promote the detachment of NPs.

Experimental Section

Catalyst Preparation

PVP-capped Ag NPs of different sizes (~10 nm, ~40 nm, ~100 nm, and 1 mg mL^{-1} in water) were purchased from NanoComposix. Subsequently, 1 mL of as-received Ag NP suspension was diluted to 1.627 mL by the addition of isopropanol (VLSI Selectipur, BASF, Germany). Then 0.1765 mg of carbon powder (Vulcan XC 72R, Cabot, USA) was dispersed in 353 μL isopropanol by sonication for 1 hour. The two suspensions were subsequently mixed, and after the addition of 20 μL Nafion solution (5% Nafion, 15–20% water, Sigma–Aldrich), the new suspension with an Ag NP concentration of 0.5 mg mL^{-1} was sonicated for 5 min to yield a homogeneous catalyst ink. Next, 75 μL of the above suspension of carbon-supported Ag NPs was drop-cast on the hydrophobic surface of a GDE (circle with diameter d of 4 mm; Sigracet 36BB, Fuel Cell Store), as shown in Figure S2. The electrodes were dried under ambient conditions. The mass loading was 300 ± 17 μg cm^{-2} (Table 1), as determined by inductively coupled plasma mass spectrometry (ICP-MS). A GDE (Sigracet 36BB) circle (d = 4 mm) with an Ag-NP catalyst was inserted into the hole (d = 4 mm) in the center of a larger-area GDE (d = 20 mm, Freudenberg H23C8, Fuel Cell Store), as illustrated in Figure S2, and the assembled electrode was further inserted in an electrolyzer.

Assembly of Gas-Fed Zero-Gap Cell

The electrolyzer used in this work has been described elsewhere (Figure S1).[2,3] It consists of a stainless-steel cell body with gas flow channels used to feed the CO_2 from the backside of the GDE. The prepared electrode was placed on the top of the gas flow channels, with its catalyst modified surface facing upward. Subsequently, a hydroxide-functionalized Sustainion alkaline membrane (X3750 RT, Dioxide materials) and a PTFE (polytetrafluoroethylene) anolyte compartment were placed on top of the GDE. Then 10 mL of 2.0 M KOH was used as an electrolyte in the anolyte compartment. An Ag/AgCl (3M KCl, double junction design, Metrohm) electrode and Ir wire (99.9%, Goodfellow GmbH) were used as reference and counter electrodes. The counter electrode was placed inside a glass capillary tube with a glass frit. The PTFE anolyte compartment had a central orifice of 3 mm diameter at its bottom, thereby providing direct contact between the electrolyte and the underlying anion-exchange membrane, whereas the GDE cathode was prevented from direct contact with the supporting anolyte. Thus, we defined the geometric area of the GDE electrode as the area of this orifice, i.e., 0.0707 cm^2. During electrolysis, a humidified CO_2 stream (17 mL min^{-1}, 99.999%, Carbagas, Switzerland) was continuously fed through the gas flow channels of the cell body, adjacent to the GDE.

Electrochemical Measurements and Product Distribution Studies

CO_2 electrolysis was performed at room temperature (22 ± 1 °C) in galvanostatic mode with an ECi-200 potentiostat (Nordic Electrochemistry). The reported current and charge densities were normalized to the geometric surface area (0.0707 cm^2). The gaseous products of CO_2RR were quantitatively analyzed by on-line gas chromatography (SRI Instruments). A thermal conductivity detector for detecting H_2 and a flame ionization detector with a methanizer for detecting CO and hydrocarbons were applied in our studies. Among the possible dissolved products, only formate was detected in all experiments performed. Formate anions forming during CO_2 electrolysis diffused via the anion-exchange membrane to the

anode compartment. Thus, formate was quantified by ion chromatography (Metrohm Ltd., Switzerland) analysis of anolyte samples collected after CO_2 electrolysis.

The faradaic efficiency (FE_i) of the gaseous product was calculated[33] as:

where x_i denotes the molar fraction of the products determined by gas chromatography with an independent calibration standard gas (Carbagas), n_i is the number of electrons involved in the reduction reaction to form a particular product ($n_i = 2$ for both CO and H_2 formation), $F = 96485.3\ C\,mol^{-1}$ is Faraday's constant, v_m is the molar CO_2 gas flow rate measured by a universal flowmeter (7000 GC flowmeter, Ellutia), and I is the current set for the galvanostatic electrolysis.

The faradaic efficiency of formate FE_{HCOO^-} is calculated as:

$$FE_{HCOO^-} = \frac{C_{HCOO^-} V_{anolyte} F n_{HCOO^-}}{Q} \times 100\,\% \quad (2)$$

where c_{HCOO^-} denotes the formate concentration in the anolyte determined by ion chromatography, $V_{anolyte}$ is the volume of anolyte in the electrolyzer, n_{HCOO^-} is the number of electrons involved in the formation of formate ($n_{HCOO^-} = 2$), and Q is the passed charge during galvanostatic CO_2 electrolysis. Every data point of FE (FE_{CO}, FE_{H2}, and FE_{HCOO-}) was obtained from three independent experiments with new GDEs, and error bars represent standard deviations.

In the "recovery" experiments, the GDE after the 1st electrolysis was carefully placed onto the surface of Milli-Q water in a beaker with the catalyst layer facing downward. Water was exchanged at least five times every 15 min. Then the GDE was dried and again used for the electrolysis (2nd electrolysis). Details have been previously reported.[3]

SEM and EDX

For morphological analysis of catalysts, a Zeiss Gemini 450 scanning electron microscope equipped with the InLens secondary electron (InLens SE) and back-scattering detectors was used. SEM images obtained with the InLens SE detector are presented herein unless otherwise specified. An acceleration voltage of 5 kV and currents of 120 pA and 200 pA were applied at a working distance of 2.9–4.0 mm. The particle size was measured in Smile View software, and the particle size distribution was based on size estimations of 500–1100 individual particles and agglomerates for each catalyst in three randomly selected areas. The particle/agglomerate size was defined as the longest dimension in the case of anisotropic NPs (Figure S16). EDX spectra and 2D surface elemental maps of samples were obtained with AZtec 5.0 software (Oxford Instruments). An acceleration voltage of 10 kV and a current of 1000 pA were applied at a working distance of 8.5 mm for EDX measurements.

ICP-MS

The Ag mass loading of the electrodes was determined with a NExION 2000 ICP-MS instrument (Perkin Elmer). The Ag NPs on the GDE were dissolved in 1 mL HNO_3 (69.3 %, BASF SE, Ludwigshafen, Germany). The obtained solutions were further diluted with 3 % HNO_3 solution by a factor of 1000 and injected into the ICP-MS instrument to obtain the actual content of Ag on GDEs.

Total Nitrogen Content Determination

To quantify PVP surfactant in the dispersion of Ag NPs, we determined the total nitrogen content (TN). Sample solutions with Ag NPs (Ag content is 0.5 mg mL^{-1}) were diluted by a factor of 4. Then 100 μL of diluted solution (Ag content is 0.125 mg cm^{-3}) was further centrifuged to separate NPs from the supernatant. The centrifugation rate was 35000 rpm (for 40 min) for solutions with 40 and 100 nm NPs, whereas a solution with 10 nm NPs was centrifuged for 40 min at 35000 rpm, then 40 min more at 50000 rpm. The obtained supernatant was further fed into a DIMATOC 2100 instrument (Dimatec, Essen, Germany) to determine TN in supernatant solution (TN_{sup}). The organic compounds were oxidized at 850 °C on a Pt catalyst to CO_2/NO. A non-dispersive infrared gas sensor with a reflective diffuser and a chemiluminescence detector was used to detect NO. The separated NPs were further redispersed in Milli-Q water, and these prepared dispersions with the same Ag content (0.5 mg mL^{-1}) were again analyzed to determine the TN_{NP}.

Acknowledgements

The work in this publication was part of NCCR Catalysis (grant number 180544), a National Centre of Competence in Research funded by the Swiss National Science Foundation. A. R. acknowledges support from the Ministry of Science and Higher Education of the Russian Federation. M. L., Y. K., and H. H. acknowledge financial support from the Chinese Scholarship Council (CSC). Open Access funding provided by Universität Bern.

Conflict of Interest

The authors declare no conflict of interest.

Data Availability Statement

The data that support the findings of this study are available from the corresponding author upon reasonable request.

Keywords: carbon dioxide electroreduction · cathodic corrosion · gas diffusion electrodes · nanoparticle agglomeration · nanoparticle degradation

[1] P. De Luna, C. Hahn, D. Higgins, S. A. Jaffer, T. F. Jaramillo, E. H. Sargent, *Science* **2019**, *364*, eaav3506.
[2] M. de Jesus Gálvez-Vázquez, P. Moreno-García, H. Xu, Y. Hou, H. Hu, I. Z. Montiel, A. V. Rudnev, S. Alinejad, V. Grozovski, B. J. Wiley, M. Arenz, P. Broekmann, *ACS Catal.* **2020**, *10*, 13096–13108.
[3] M. Liu, Y. Kong, H. Hu, N. Kovács, C. Sun, I. Zelocualtecatl Montiel, M. d J Gálvez Vázquez, Y. Hou, M. Mirolo, I. Martens, J. Drnec, S. Vesztergom, P. Broekmann, *J. Catal.* **2021**, *404*, 371–382.
[4] J. He, Y. Li, A. Huang, Q. Liu, C. Li, *Electrochem. Energy Rev.* **2021**, *4*, 680-717.
[5] Y. Gu, J. Wei, X. Wu, X. Liu, *Sci. Rep.* **2021**, *11*, 11136.
[6] Y. Wu, S. Garg, M. Li, M. N. Idros, Z. Li, R. Lin, J. Chen, G. Wang, T. E. Rufford, *J. Power Sources* **2022**, *522*, 230998.
[7] A. Salehi-Khojin, H.-R. M. Jhong, B. A. Rosen, W. Zhu, S. Ma, P. J. A. Kenis, R. I. Masel, *J. Phys. Chem. C* **2013**, *117*, 1627–1632.

[8] A. V. Rudnev, K. Kiran, A. Cedeño López, A. Dutta, I. Gjuroski, J. Furrer, P. Broekmann, *Electrochim. Acta* **2019**, *306*, 245–253.
[9] Q. Lu, J. Rosen, F. Jiao, *ChemCatChem* **2015**, *7*, 38–47.
[10] S. Liu, H. Tao, L. Zeng, Q. Liu, Z. Xu, Q. Liu, J.-L. Luo, *J. Am. Chem. Soc.* **2017**, *139*, 2160–2163.
[11] W. H. Lee, Y.-J. Ko, Y. Choi, S. Y. Lee, C. H. Choi, Y. J. Hwang, B. K. Min, P. Strasser, H.-S. Oh, *Nano Energy* **2020**, *76*, 105030.
[12] S. Popović, M. Smiljanić, P. Jovanovič, J. Vavra, R. Buonsanti, N. Hodnik, *Angew. Chem. Int. Ed.* **2020**, *59*, 14736–14746; *Angew. Chem.* **2020**, *132*, 14844–14854.
[13] C. Spöri, J. T. H. Kwan, A. Bonakdarpour, D. P. Wilkinson, P. Strasser, *Angew. Chem. Int. Ed.* **2017**, *56*, 5994–6021; *Angew. Chem.* **2017**, *129*, 6088–6117.
[14] B. Vanrenterghem, M. Bele, F. R. Zepeda, M. Šala, N. Hodnik, T. Breugelmans, *Appl. Catal. B* **2018**, *226*, 396–402.
[15] Y. Hou, N. Kovács, H. Xu, C. Sun, R. Erni, M. d J Gálvez-Vázquez, A. Rieder, H. Hu, Y. Kong, M. Liu, B. J. Wiley, S. Vesztergom, P. Broekmann, *J. Catal.* **2021**, *394*, 58–66.
[16] J. Huang, M. Mensi, E. Oveisi, V. Mantella, R. Buonsanti, *J. Am. Chem. Soc.* **2019**, *141*, 2490–2499.
[17] J. Huang, N. Hörmann, E. Oveisi, A. Loiudice, G. L. De Gregorio, O. Andreussi, N. Marzari, R. Buonsanti, *Nat. Commun.* **2018**, *9*, 3117.
[18] W. T. Osowiecki, J. J. Nussbaum, G. A. Kamat, G. Katsoukis, M. Ledendecker, H. Frei, A. T. Bell, A. P. Alivisatos, *ACS Appl. Energ. Mater.* **2019**, *2*, 7744–7749.
[19] H. Yun, J. Kim, W. Choi, M. H. Han, J. H. Park, H.-s. Oh, D. H. Won, K. Kwak, Y. J. Hwang, *Electrochim. Acta* **2021**, *371*, 137795.
[20] P. Grosse, D. Gao, F. Scholten, I. Sinev, H. Mistry, B. Roldan Cuenya, *Angew. Chem. Int. Ed.* **2018**, *57*, 6192–6197; *Angew. Chem.* **2018**, *130*, 6300–6305.
[21] M. E. Leonard, L. E. Clarke, A. Forner-Cuenca, S. M. Brown, F. R. Brushett, *ChemSusChem* **2020**, *13*, 400–411.
[22] L.-C. Weng, A. T. Bell, A. Z. Weber, *Energy Environ. Sci.* **2019**, *12*, 1950–1968.
[23] Y. Kong, H. Hu, M. Liu, Y. Hou, V. Kolivoška, S. Vesztergom, P. Broekmann, *J. Catal.* **2022**, *408*, 1–8.
[24] R. Reske, H. Mistry, F. Behafarid, B. Roldan Cuenya, P. Strasser, *J. Am. Chem. Soc.* **2014**, *136*, 6978–6986.
[25] H. Mistry, R. Reske, Z. Zeng, Z.-J. Zhao, J. Greeley, P. Strasser, B. R. Cuenya, *J. Am. Chem. Soc.* **2014**, *136*, 16473–16476.
[26] J. J. Kaczur, H. Yang, Z. Liu, S. D. Sajjad, R. I. Masel, *Front. Chem.* **2018**, *6*, 263.
[27] S. Alinejad, J. Quinson, G. K. H. Wiberg, N. Schlegel, D. Zhang, Y. Li, S. Reichenberger, S. Barcikowski, M. Arenz, *ChemRxiv*. **2021**. DOI: https://doi.org/10.26434/chemrxiv-2021-1t50s-v3.
[28] M. M. Elnagar, J. M. Hermann, T. Jacob, L. A. Kibler, *Curr. Opin. Electrochem.* **2021**, *27*, 100696.
[29] T. J. P. Hersbach, I. T. McCrum, D. Anastasiadou, R. Wever, F. Calle-Vallejo, M. T. M. Koper, *ACS Appl. Mater. Interfaces* **2018**, *10*, 39363–39379.
[30] J. Feng, D. Chen, A. S. Sediq, S. Romeijn, F. D. Tichelaar, W. Jiskoot, J. Yang, M. T. M. Koper, *ACS Appl. Mater. Interfaces* **2018**, *10*, 9532–9540.
[31] M. M. Elnagar, J. M. Hermann, T. Jacob, L. A. Kibler, *Electrochim. Acta* **2021**, *372*, 137867.
[32] H. Hu, M. Liu, Y. Kong, Y. Hou, I. Zelocualtecatl Montiel, A. V. Rudnev, P. Broekmann, *Zenodo* **2022**. DOI: https://doi.org/10.5281/zenodo.6840454.
[33] A. V. Rudnev, in *Encyclopedia of Interfacial Chemistry* (Ed.: K. Wandelt), Elsevier, Oxford, **2018**, pp. 321–325.

Manuscript received: June 2, 2022
Revised manuscript received: July 18, 2022
Accepted manuscript online: August 4, 2022

Appendix

1. List of publications

I. **M. Liu**, H. Hu, Y. Kong, I. Zelocualtecatl Montiel, V. Kolivoška, A. V. Rudnev, Y. Hou, R. Erni, S. Vesztergom, and P. Broekmann, The role of ionomers in the electrolyte management of zero-gap MEA-based CO_2 electrolysers: A Fumion vs. Nafion comparison. *Applied Catalysis B: Environmental* 335 (2023) 122885.

II. **M. Liu**, Y. Kong, H. Hu, N. Kovács, C. Sun, I. Zelocualtecatl Montiel, M. D. J. Gálvez Vázquez, Y. Hou, M. Mirolo, I. Martens, J. Drnec, S. Vesztergom, and P. Broekmann, The capping agent is the key: Structural alterations of Ag NPs during CO_2 electrolysis probed in a zero-gap gas-flow configuration. *J. Catal*., 2021, 404, 371-382.

III. H. Hu, **M. Liu**, Y. Kong, I. Z. Montiel, Y. Hou, A. V. Rudnev, and P. Broekmann, Size-dependent structural alterations in Ag nanoparticles during CO_2 electrolysis in a gas-fed zero-gap electrolyzer. *ChemElectroChem*, 2022, 9 (17), e202200615.

IV. Y. Kong, **M. Liu**, H. Hu, Y. Hou, S. Vesztergom, M. J. Gálvez-Vázquez, I. Zelocualtecatl Montiel, V. Kolivoska, and P. Broekmann, Cracks as efficient tools to mitigate flooding in gas diffusion electrodes used for the electrochemical reduction of carbon dioxide. *Small Methods*, 2022, e2200369.

V. H. Hu, **M. Liu**, Y. Kong, N. Mysuru, C. Sun, M. D. J. Gálvez-Vázquez, U. Müller, R. Erni, V. Grozovski, Y. Hou, and P. Broekmann, Activation matters: Hysteresis effects during electrochemical looping of colloidal Ag nanowire catalysts. *ACS Catal*., 2020, 10 (15), 8503-8514.

VI. H. Hu, Y. Kong, **M. Liu**, V. Kolivoška, A. V. Rudnev, Y. Hou, R. Erni, S. Vesztergom, and P. Broekmann, Effective perspiration is essential to uphold the stability of zero-gap MEA-based cathodes used in CO_2 electrolysers. *J. Mater. Chem. A* (2023).

VII. Y. Kong, H. Hu, **M. Liu**, Y. Hou, V. Kolivoška, S. Vesztergom, and P. Broekmann, Visualization and quantification of flooding phenomena in gas diffusion electrodes used for electrochemical CO_2 reduction: A combined EDX/ICP–MS approach. *J. Catal*., 2022, 408, 1-8.

VIII. C. Sun, Y. Hou, N. Lüdi, H. Hu, M. D. J. Gálvez-Vázquez, M. Liechti, Y. Kong, **M. Liu**, R. Erni, A. V Rudnev and P. Broekmann, Improving the lifetime of hybrid CoPc@MWCNT catalysts for selective electrochemical CO_2-to-CO conversion. *J. Catal*., 2022, 407, 198-205.

IX. Y. Hou, N. Kovács, H. Xu, C. Sun, R. Erni, M. D. J. Gálvez-Vázquez, A. Rieder, H. Hu, Y. Kong, **M. Liu**, B. J Wiley, S. Vesztergom and P. Broekmann. Limitations of identical location SEM as a method of degradation studies on surfactant capped nanoparticle electrocatalysts. *J. Catal*., 2021, 394, 58-66.

2. Conferences

Oral presentation on NCCR WP-1 online meeting. 28th June, 2021. ETH Zurich, Switzerland;

Poster presentation on NCCR Catalysis site visit. 7-8th October, 2021. Bern, Switzerland;

Poster presentation on 15th International Fischer Symposium. 12-16th June, 2022. Kloster Seeon, Germany;

Poster presentation on NCCR Catalysis Annual Event 2022 Symposium. 27-28th September. Bern, Switzerland;

Poster presentation on International Summer School on Electrocatalysis and Electroorganic Synthesis 2023. 28-31th August. Interlaken, Switzerland.

3. Acknowledgements

I would like to express my deepest gratitude to my supervisor Prof. Peter Broekmann, who accepted me to the PhD program four years ago. Peter not only generously provides his expertise when we seek guidance but also cares for and encourages us wholeheartedly, the latter is often more important during a PhD study.

I'm extremely grateful to Dr. Yuhui Hou, who guided me on my application for the scholarship for my PhD study, as well as on the research field of electrochemical CO_2 reduction. Her knowledge as well as her encouragement are greatly appreciated.

I'm very grateful to Dr. Soma Vesztergom, who shared his insights during our scientific discussion, which have expanded my scientific vision; he also warmly invited me to have a Hungarian lunch when I visited Budapest in 2021.

I'm also grateful to Prof. Wenjing Hong (Xiamen University) and Prof. Christina Roth (University of Bayreuth) for their kind acceptance of my invitation to be the external referee for my PhD work. Special thanks to Prof. Matthias Arenz (University of Bern), for providing us with the semi-zero gap electrolyzer and accepting the invitation to be the chair of my PhD defense.

I would like to thank the China Scholarship Council for providing financial support for my study abroad.

I want to thank Dr. Pavel Moreno-García, Dr. Abhijit Dutta, Dr. Vitali Grozovski, Dr. Alexander Rudnev, Dr.Viliam Kolivoška, and Dr. Noémi Kovács, who offered help without hesitation whenever I asked. Many thanks to Rene Büler, Nicola Lüdi, Mike Liechti, Dennis Tsubasa Flury, Lorine Gaudin, Valery Rauchwerger, and Levi Widmer, our former and current lab engineers and technicians, who helped create outstanding research conditions in the lab.

I'm grateful to Dr. Huifang Hu, who kindly helped me to get used to the life here when I first arrived in Bern, she is more than kind and sincere. I'm also thankful to Dr. Qi Huang, Dr. Heng Liu, Dr. Jia Du, Dr. Ying Kong, Sinan Li, Shan Wu, and Cong Wang, for the happy memories of skiing, hiking, gathering and other social activities.

I have had the pleasure of meeting Alan Rieder, Aline Bornet, Dr. Iván Zelocualtecatl Montiel, Liliana Gálvez-Vázquez, Dr. María de Jesús Gálvez-Vázquez, Mario García-Rodríguez and Renan Lopes Munhos, who are the most wonderful friends I could have hoped for.

Thanks to my former and current colleagues, Dr. Kiran Kiran, Dr. Yuzhen Wang, Jonas Simon Forner, Julia Anna Lorenzetti, Anna Iarchuk, Yaqiang Li, Nandu Ashtaman, it was a pleasure working with you all in the lab.

I would also like to thank Beatrice Thönen, Beatrice Frey, Beatrice Niederhauser, and many others from human resources, workshop, material shop, IT support, and facility maintenance group, for their kind help.

I am grateful for the facilities offered by the University of Bern, especially the sports course. I learned skiing tennis and climbing from excellent coaches, and participated in badminton, swimming, archery, boxing, and other courses. I met great people through these fun and relaxing activities.

Last but not least, I would like to thank my parents for their unconditional love. They have always been supportive of my pursuit and who I want to become. To my dear sister and brother-in-law, thank you for always being there when I was down, and for being family. To my dear brother, his wife, my niece, and my nephew, it is nice to have you and call you family.

I have spent a bit more than four years in Bern by now, I have to say that I have enjoyed the time here. It was purely by chance that I came to study in Bern. My friend Chuanliang Huang recommended Prof. Peter Broekmann when I was looking for a host professor, Dr. Yuhui Hou had a short “interview” with me and some months later she told me that, she thought I was either a very easy-going person or a strange person, I hope I am the former. When I was thinking about coming to Switzerland or not, I thought “Switzerland seems to be a nice place because I love natural landscapes”, and now I realize it is the people I met here that truly amazed me. I wonder if I could meet another professor like Peter, if I could meet such nice people like you. I will always be grateful for the time I spent here and the people I met in Switzerland.

4.致我的父母 (Dedication to my parents)

在我博士论文的最后，我想特别地感谢我的父母，没有他们的支持，四年前我不可能完成硕士研究生的学习，更不要说完成博士学习了。

父亲和母亲在亲戚介绍下相亲认识、结婚。后面有了我姐、我以及我弟。他们考虑过把我们留给爷爷奶奶照顾，然后出去打工（当时很多人这么做）。但为了更好地照顾我们，他们决定留在家乡的镇上，开了一家五金店。不得不提的是，在他们的辛苦劳动下，这个店铺的收入供我们进入县城最好的初中、市里最好的高中，负担了我们大学甚至是研究生期间的花费。

我的父母在日常生活中潜移默化地教导我们。 他们对人耐心、友善，彼此相爱，认真地扮演好自己在生活中的每一个角色。父亲高中毕业后拜师学做木匠，出师后自己又收了几个徒弟。 他曾经告诉我们，他的木工手艺比他的同龄人都好，我对此毫不怀疑。结婚开办五金店后，他非常努力地拓广业务。他先后学习了涂料制作、管道安装、制作和安装门窗等等。我的妈妈是一个坚强的女人，尽管生活对她并不友善。我的父亲是最小的孩子，身体也最差。我五岁左右的时候他感染了肺结核，这在当时的中国是致命的。 他很幸运的活了下来，治疗的副作用使他患上了肝病和胃病。直到我上中学，母亲每天都给我父亲开小灶，帮助他身体恢复。我上中学那年，奶奶去世了，次年，弟弟意外被严重烧伤。 母亲在医院内外照顾了他大约半年的时间。 当我和姐姐都进入市里读高中时，妈妈又在出租屋照顾了我们一年。在我们姐弟陆续开始上大学时，生活似乎慢慢变得轻松，尽管经济压力越来越大。 她对生活从来没有过多的抱怨。 作为女儿、妻子和母亲，她全身心地投入到我们的家庭中，她很少只做自己。

我的学习并不不太好。 大学毕业后，我去了一家电镀公司，工作期间，父亲一直鼓励我继续深造。我花了两年时间才考上研究生。当我想继续攻读博士学位时，我得到了父亲的全力支持。其实回想起来，无论我们想尝试什么，他都会支持。无法想象父亲在看到我完成博士学业时该有多么开心和骄傲，可惜我父亲永远无法看到这一天了。三年前，他被诊断出患有非霍奇金 T 细胞淋巴癌，于 2023 年 8 月去世。他总是对生活抱有积极的态度，即使在得知这个淋巴癌一般只有两年左右生存期以及癌症后期他的身体条件已经不支持他继续治疗的时候，他仍对我们说“没什么大不了的”。他用自己的全部意志和力量与癌症抗争到了最后一刻。面对逆境，我只愿有他一半的勇气。

我对父母的感激之情无以言表，他们教导我追求目标，努力学习，永不放弃。是他们坚定不移的支持和引导，我才能够义无反顾地追逐自己的梦想。爸妈，谢谢你们!

(English version here)

I would like to express my gratitude to my parents at the end of my thesis. Without their support, I would never have been able to complete my master's studies four years ago, let alone my PhD.

My parents met on a blind date arranged by one aunt, got married, and gave birth to the three of us: my sister, me, and my brother. After having three children, they decided to settle down in town and focus on raising us. Later, they opened a hardware store. I have to mention that with the small

store, my hard-working parents managed to send us into the best mid-school in the county and best high school in the city. They even covered our college and master's degree expenses.

Beyond financial support, my parents imparted wisdom and values through their everyday actions. They were patient and kind to people, they loved each other, and they played their role in life seriously. My father chose his career and always did it well. He learnt to be a carpenter from his master after high school study, and later took on several apprentices himself. He used to tell us that he was more efficient in his craft than his peers, and I have no doubt about that. After opening the hardware store, he worked very hard to expand. He learned plumbing, made and installed windows and doors, painting mixtures, etc.

My mom is a strong woman even though life has not been kind to her. My father was the youngest child and the weakest health-wise. He got tuberculosis when I was around five, which was fatal in China at that time. He was lucky to survive, but suffered from liver and stomach problems (side effects of the treatments). Until the time I went to mid school, my mom had always been cooking extra meal for my dad every day to help him recover. My grandma passed away the year I entered mid-school and the year after, my brother was accidently injured in a fire. My mom took care of him in and out of the hospital for about half a year. When my sister and I both entered the high school in the city, mom spent another year taking care of us at our rental apartment. As my siblings and I headed off to college, life seemed to be getting easier, though financial pressure was mounting. She never complained too much about life. She devoted herself to our family as a daughter, wife, and mother, she rarely is just herself, a woman without her own wants and needs.

I wasn't very good with school work. After graduating from college, I went to an electro-coating company. My father always encouraged me to continue my studies. It took me two years to start my master's degree. When I wanted to continue studying for a PhD, I got full support from my father. He was onboard with whatever we wanted to try.

Looking back on my past, I realize the wisdom of my parents. I hope I have the open mind and heart to continue learning. I cannot imagine how happy my father will be when he sees the day I finish my PhD, but he will never see it. He was diagnosed with non-Hodgkin's lymphoma three years ago and passed away in August 2023. He always had a positive outlook on life and he liked to say to us "it was no big deal" when things didn't go as planned, even when he knew that the living time is generally two years for the cancer. He fought cancer with all his will and strength till the end. I can only wish to be half as brave as him in face of adversity.

I am grateful beyond words to my parents, who taught me to pursue my goals, study hard, and never give up. Their unwavering support and guidance is what makes it possible for me to chase my dream without hesitation.

5. Declaration of consent

Declaration of consent

on the basis of Article 18 of the PromR Phil.-nat. 19

Name/First Name: Liu Menglong

Registration Number: 19-125-772

Study program: Chemistry and Molecular Sciences

Bachelor ☐ Master ☐ Dissertation ☑

Title of the thesis: Stability of zero-gap CO2 electrolyzer for electrochemical CO production

Supervisor: Prof. Dr. Peter Broekmann

I declare herewith that this thesis is my own work and that I have not used any sources other than those stated. I have indicated the adoption of quotations as well as thoughts taken from other authors as such in the thesis. I am aware that the Senate pursuant to Article 36 paragraph 1 litera r of the University Act of September 5th, 1996 and Article 69 of the University Statute of June 7th, 2011 is authorized to revoke the doctoral degree awarded on the basis of this thesis.
For the purposes of evaluation and verification of compliance with the declaration of originality and the regulations governing plagiarism, I hereby grant the University of Bern the right to process my personal data and to perform the acts of use this requires, in particular, to reproduce the written thesis and to store it permanently in a database, and to use said database, or to make said database available, to enable comparison with theses submitted by others.

Bern, 10.08.2023

Place/Date

Signature Menglong Liu